An exploration of the measured and modelled thermal characteristics of structural thermal breaks in UK buildings.

PhD. Thesis (iCASE)

Joe Pemberton

Sponsored by:

UoS & Farrat Isolevel

Contents

Foreword by Professor Richard Fitton, Professor William Swan and Oliver Farrell

This PhD thesis is the work of Joe Pemberton, who was working in a collaboration between the University of Salford and Farrat Isolevel. Unfortunately, on the 17th of April 2023 Joe passed away unexpectedly. He was very near the completion of his PhD, with his viva already arranged. The supervisory team, Professor Richard Fitton and Professor Will Swan, compiled the latest version of Joe's PhD, which was submitted to the external examiners. This version is entirely Joe's work, as such there are a few small gaps. However, Joe had undertaken a considerable amount of work to an exceptionally high standard, which the examiners identified as deserving of a posthumous award. Richard, Will and Oliver Farrell, CEO of Farrat Isolevel, are proud of the work Joe undertook with us and are pleased that we have had the opportunity to publish this thesis on Joe's behalf

If you have any queries regarding Joe's work, please contact r.fitton@salford.ac.uk

Abstract

This research explores the measured and modelled thermal characteristics of structural thermal breaks (STBs) in UK buildings. Thermal bridging (TB) in building envelopes can significantly affect the fabric heat loss of a building, leading to higher energy consumption for space heating. This study aims to enhance understanding of the effectiveness of STBs in mitigating thermal bridging, thereby reducing energy use and CO_2 emissions.

A methodology was developed, which provided a unique combination of experimental measurements and finite element (FE) modelling. The research investigates point thermal bridges created by structural-point-connection façade penetrations. In-situ measurements were taken under controlled conditions at the Salford Energy House and were used to inform FE models, to provide more accurate evaluations when compared to current practice.

The findings indicate a gap exists between some of the methods of modelling thermal breaks in the UK and in-situ measured values. This "performance gap" therefore should not only be studied to be further and understood, but also a rigorous methodology should be developed to measure thermal breaks out in the field.

The research contributes the current knowledge in this area by proposing a robust experimental design and validated FE models for evaluating the thermal performance of structural thermal breaks. These can hopefully guide future work in this area not only for researchers and practitioners, but for those developing models and thermal brakes themselves.

Lists (tables, figure, equations)

Tables

Figures

Equations

Nomenclature

Symbol	Description	Unit
f_{Rsi}	Critical temperature factor	1
T, θ	Temperature	K
Φ, q'	Heat flow rate	W
A	Area	m^2
k	Conductivity	W/m.K
h	Convective HTC	$W/m^2.K$
$\dot{q}$	Heat generation	W/m^3
α	Thermal diffusivity	m^2/s
τ	Time change	s
ρ	Density	Kg/m^3
c	Specific heat capacity	KJ/Kg.K
E_b	Black body emissive power	W/m^2
σ	Stefan-Boltzmann constant	W/m^2K^4
ε	Emissivity	1
F_g	Geometrical view factor	1
R-value R	1D HTC (resistance)	m^2K/W
U-value U	1D HTC (transmittance)	W/m^2K
ψ	Linear-transmittance (Psi-value)	W/mK
χ	Point-transmittance (Chi-value)	W/K
q	Heat flux	W/m^2
L_{2D}	2D thermal coupling coefficient	W/mK
L_{3D}	3D thermal coupling coefficient	W/K
l	Length	M
H	Heat-loss coefficient	W/K
H_s	Heat-loss coefficient due to presence of point-bridge	W/K
ΔU	Change in U-value	W/m^2K
Y	Periodic thermal transmittance	W/K
f	Decrement factor	1
$\hat{q}_i$	Complex amplitude of heat flux	W/m^2
$\hat{T}_e$	Complex amplitude of the harmonic temperature excitation	K
φ_r	Phase difference	1
θ_r	Angular shift	1
W	Radiation power by IR camera	W
v	Velocity (wind speed)	m/s
I_{tb}	Incidence factor (Infrared)	1
$I_{tb_{HFM}}$	Incidence factor (HFM)	1
Q_{tb}	Heat flow – TB section	W
Q_{1D}	Heat flow – 1D section	W
q_x	Heat flow rate for each pixel, of height ‘x’	W/m
q_{xu}	Heat flow rate without TB influence	W/m
q_{xTB}	Additional heat flow rate due to the TB	W/m
q_{TB}	TB heat flow	W/m

1.0 Introduction

‘Thermal-Bridging’ (TB) is a term used in building physics that categorise weak points in a building’s thermal envelope which cause condensation issues and allow heat to escape. TB can increase space heating loads by 30% (T. G. Theodosiou & Papadopoulos, 2008) (Šadauskienė et al., 2015) (Ascione et al., 2012) whilst other sources (BC Hydro, 2016) suggest that neglecting major TB, like balconies, result in a 20 – 70% of the total heat flow through the building envelope .

Many typologies exist, although they are generalised into two forms, linear-TB and point-TB, causing two- and three-dimensional heat-flows, respectively (BS EN ISO 10211 (BSI, 2017c) *ISO 52019-2:2017* (BSI, 2017a)). All relevant standards are covered in the literature review; ISO 10211 is the core focus since in these works, point-TB-transmittances were studied caused by structural-point-connection façade penetrations: a representative steel-beam cantilever was used to develop an in-situ experimental design in the laboratory, using both measurement and modelling techniques.

Structural Thermal-Breaks (STB’s) can isolate heat-flow through such structural penetrations whilst retaining structural integrity; their performance evaluation is not fully understood, although a 20-65% reduction in heat-flow is seen when comparing connections with and without a STB – depending on the configuration (Ben Larbi et al., 2017). Some objectives in this research include improving understanding for practitioners/designers/specifiers to characterise and treat this type of structural TB – where designing-out the problem is impossible. Expanding the knowledge around the impacts of structural TBs – and their potential reduction using STB solutions – widens the adoption of low-energy building designs within the construction industry. Implementing the STB measure improves the outcome of Building Performance Evaluation (BPE) by lowering CO_2 emissions and energy consumption requirements for space heating.

TB locally reduces the temperature of the wall, creating cold spots. These cold spots can, in some cases, cause condensation (on the surface or within the structure, damage the structure) and mould growth (Ward & Sanders, 2016) which can be mitigated by implementing STB solutions. Not only do these solutions enhance occupancy comfort, building health, and hygiene, it also enriches design flexibility providing architects more creative freedom whilst adhering to building energy regulations.

If TBs are neglected or erroneously evaluated a large uncertainty in performance can be expected. This disparity between the expected/designed and the actual/constructed details thermal performance, is known as the Performance Gap (PG) and is experienced in many aspects of building performance analysis (Johnston et al., 2015b; Marshall et al., 2017; Zero Carbon Hub, 2013; Zou et al., 2019). One-dimensional physical measurement, such as heat flux and temperature, have effectively been used to reduce PGs (Marshall et al., 2018) by calibrating whole building energy simulation tools and model sensitivities. Unfortunately, since two- and three-dimensional effects are more complex in nature, with no current standardised way of directly measuring the heat flux, they cannot be precisely understood/categorised/captured with one single measurement methodology and evaluated in the same manner. Alternatively, Finite Element (FE) analysis software is relied upon to simulate construction scenarios, numerically modelling the multi-dimensional heat-transfer, crucially capturing temperature and heat flux distributions through the geometry with which the TB-transmittances can be quantified. The metrics generated can then be more accurately utilised in whole building energy modelling (C. Gorse et al., 2016) or included in Standard Assessment Procedures (SAP) tools for Buildings Performance Evaluation (BPE) – which has a recently updated standard BS 40101:2022 (BSI, 2022) – compared with the current methods using generic off-the-shelf linear-transmittances values (BS EN ISO 14683 (BSI, 2017h)).

Evaluating the energy performance of building requires reviewing numerous standards covering the various aspects of building physics, all of which are summarised in document *52019-2:2017 Energy Performance of Buildings* (BSI, 2017a), dictating how all standards link together for a total BPE. Guidance on how to model bespoke numerical calculations of various TB typologies is available in standard BS EN ISO 10211 *numerical evaluation of TBs in construction – heat flows and surface temperatures – detailed calculations* (BSI, 2017c) and will be the focus of this study. Amongst other standards, it is implemented in publications the BR497 (Ward & Sanders, 2016) and IP1/06 (Ward, 2006) released by the British Research Establishment (BRE). They publish off-the-shelf tabulated TB-transmittance values for basic construction scenarios and show worked examples of the numerical methods that quantify TB-transmittances under steady-state conditions using FE.

Thermal FE analysis requires assumptions, which can contribute to the building's overall energy PG. One school of thought (adopted in these works) to reduce this gap in knowledge, is to gather a greater understanding of the assumptions necessary to accurately parameterise these FE models with physical measurement.

Appropriately then, this research aims to establish an experimental design capable of quantifying point-TB-transmittances by using in-situ measurements (taken from an investigated TB) to inform the FE software – more accurately evaluating and characterising a specific system compared to the standardised approach of assuming boundary conditions.

1.1 Background and Justification

To justify the research undertaken, some background around the problem will be covered, answering: what the problem is, why the problem exists, and how extensive the problem is.

Current UK government statistics around domestic energy consumption and carbon emission in buildings are reviewed in the following section. The key focus is around domestic space heating, highlighting that action must be taken to improve building fabric performance of the existing and new building stock to reduce overall energy consumption and carbon emission. A significant amount of energy is used to heat homes, making performance measures such as STB increasingly important.

1.1.1 Energy consumption and emissions in buildings – space heating

According to the 2019 UK government Department of Business, Energy, and Industrial Strategy (BEIS), transport remained the top contributor to total energy consumption and emissions whilst domestic energy was a close second (BEIS, 2020). However, in 2020, overall consumption fell revealing the significance of the global pandemic (BEIS, 2021a). As the transport, industry, and service sectors all reduced, the domestic sector increased, see Figure 1:

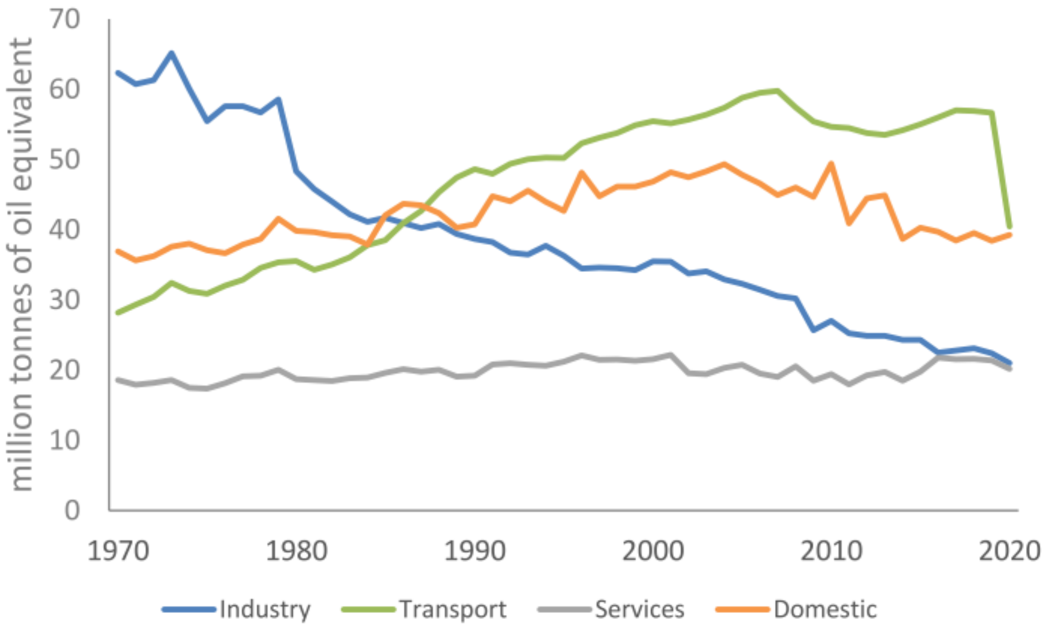

Figure 1 – Shows consumption by sector (BEIS, 2021a).

After 15 years of consecutive decrease in domestic energy consumption, a 2.3% increase was seen in the 2020 – even larger when accounting for the temperature correction – with a 4% increase in electricity and 2% in gas (BEIS, 2021a). Figure 2 shows domestic energy consumption (and the temperature corrected consumption) compared to the annual average temperature. One would expect that if the average annual temperature increases, the space heating demand would decrease, but this is not the case.

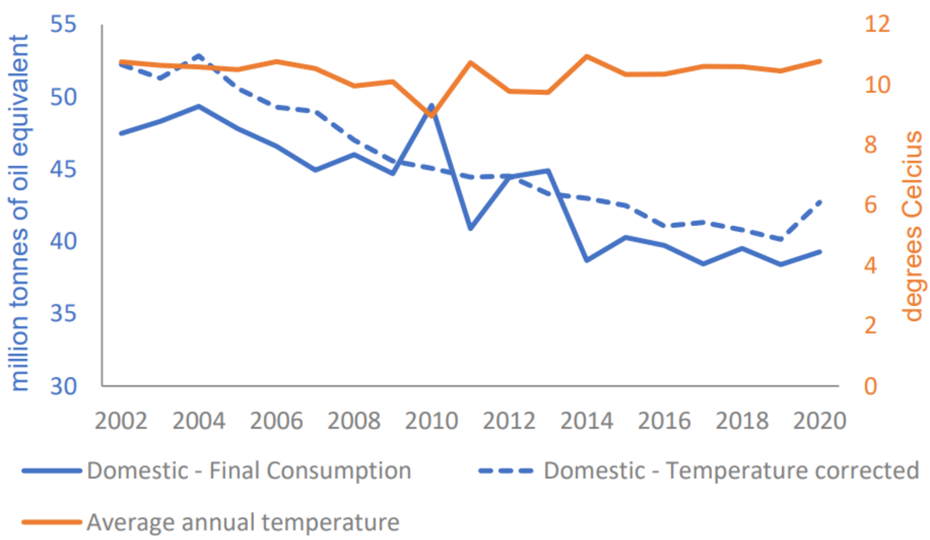

Figure 2 – Shows domestic consumption, temperature-corrected consumption, and average annual temperatures (BEIS, 2021a).

This is directly attributed to lockdown curfews and restrictions as the critical mass of the population were told to reduce mobility unless essential and work from home where possible. Also, businesses in both the industrial and service sectors were closed. Since people are adapting to post-pandemic life and realising the success/benefits of working from home, it is likely that consumption in the building sector will increase further – accordingly, employing measures to improve energy performance in buildings in both new and existing building stock is essential.

As of 2019, the domestic sector was responsible for 29% of the total energy use (BEIS, 2020) in the UK, of which, around 82.8% of domestic energy consumption is for space and water heating (Ma et al., 2019). Space heating is responsible for around 17% of the total energy CO_2 emissions in the UK (BEIS, 2021b), illustrated in the following Figure *3* & Figure *4*:

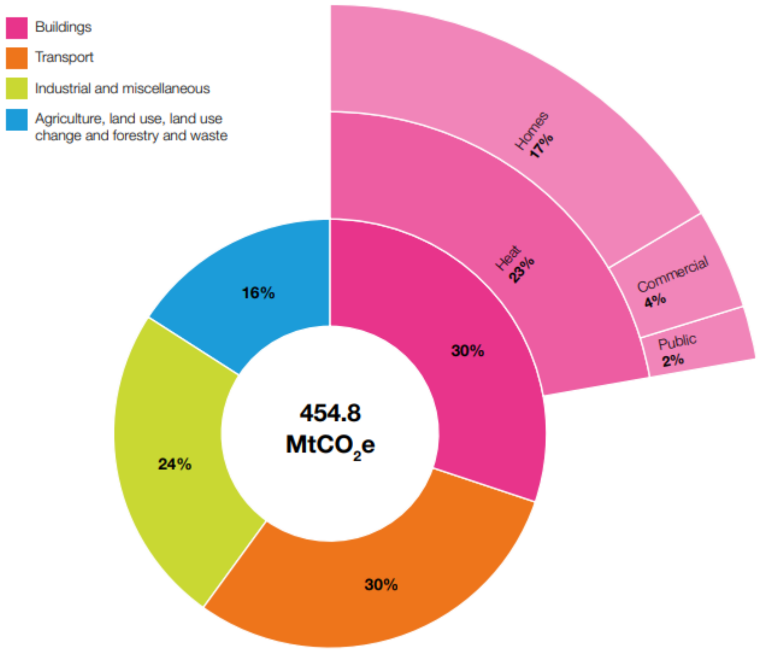

Figure 3 – Shows UK emissions in 2019 (BEIS, 2021b).

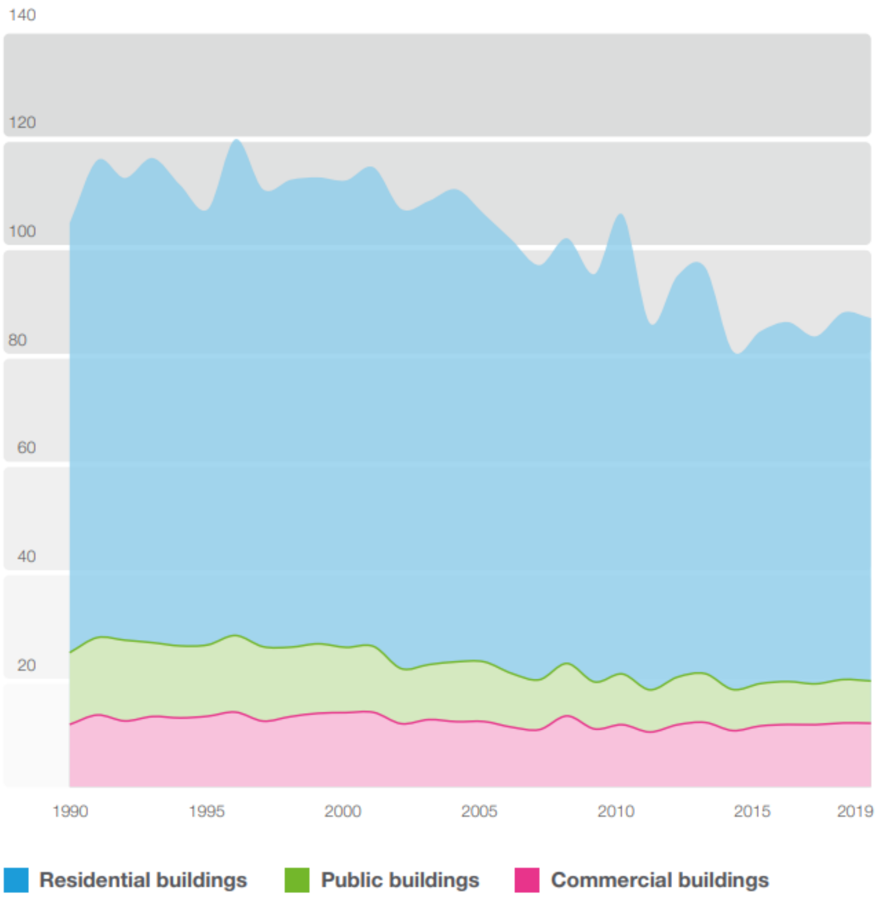

Figure 4 – Shows the direct emissions from heating buildings (BEIS, 2021b).

Agreeably, historical data from the Housing Energy Fact File 2013 suggests that space heating is the largest contributor to domestic energy, which has increased from 58% in 1970 to 62% in 2011, see Figure 5:

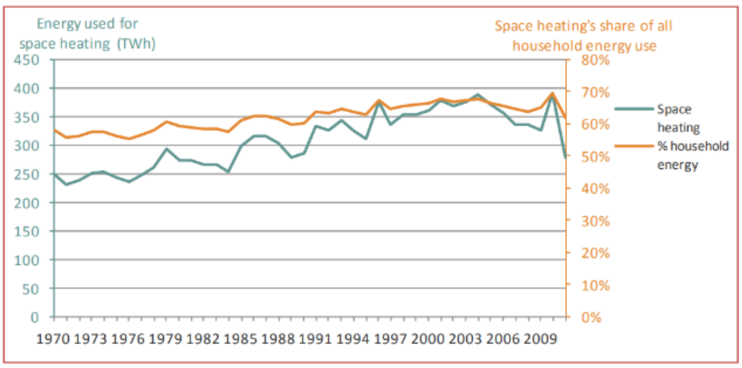

Figure 5 – Household energy use for space heating (TWh) *(Palmer & Cooper, 2013)*.

To give an overview of domestic energy consumption by category, (Fitton, 2016) depicted the percentage usage of household energy with data taken from the Cambridge Housing Model (CHM), see Figure 6:

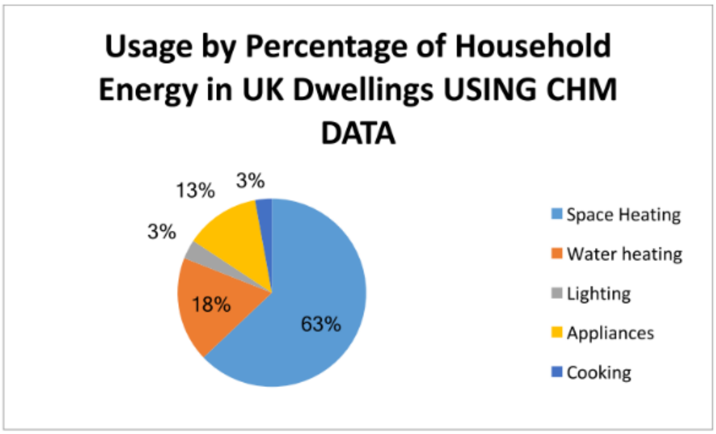

Figure 6 – Usage by percentage of household energy (Fitton, 2016; GOV.UK, 2015, 2019b).

The CHM (GOV.UK, 2015) uses English Housing Survey 2011 data (GOV.UK, 2019a) in SAP which estimates energy use and CO_2 emissions for all homes in England. Underpinning the 2013 Housing Energy Fact File and Energy Consumption in the UK, this model was developed by Cambridge Architectural Research helping to inform housing policy decisions. The model is still under development and has been published to encourage feedback (GOV.UK, 2015).

National calculation methods such as the UK's regulatory compliance tools, SAP (Standard Assessment Procedure), RdSAP (Reduced data Standard Assessment Procedure) (BRE, 2017), and SBEM (Simplified Building Energy Model) can all be used for BPE (BSI, 2017h, 2017c), amongst others.

Gas is primarily used for space heating (BEIS, 2021c). Savings in gas consumption in 2019 from measures installed in the previous year, range from 4% for loft insulation to 18% for solid wall insulation (BEIS, 2021c), illustrated in the following Figure 7**:**

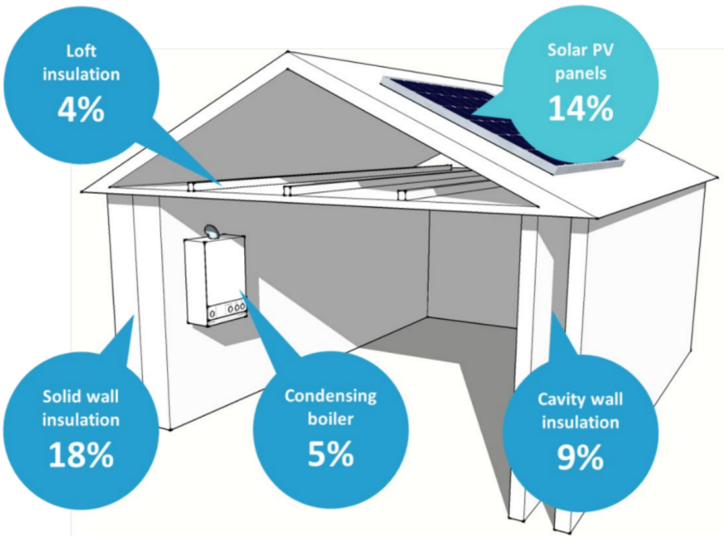

Figure 7 – Shows measures and % saving in gas consumption from 2018 to 2019 (BEIS, 2021c).

Since the UK housing stock is relatively old compared to other European countries, with many properties pre-dating the Victorian era, a lot of these older builds have poor insulation and require high energy demand to maintain occupancy comfort levels. Retrofitting dwellings with more efficient insulation or boilers has proven to relieve energy demand and reduce overall consumption (BEIS ECUK, 2018).

As a step toward achieving the target set within the 2008 climate change act (UK Government, 2008) – of an 80% reduction in carbon emissions by 2050 compared to 1990 levels, the UK government targeted a 68% reduction in emissions by 2030 (GOV.UK, 2020). Since the COP26 agreement (UN climate change conference in 2021), the UK government has put into law that they will achieve net zero carbon emissions by the year 2050 (COP26, 2022; GOV.UK, 2022). It is clear these targets are being seriously considered and actions are being taken to reduce overall emissions.

This section highlighted that a significant amount of energy is used to heat buildings in the UK, strengthening and reinforcing the importance to improve energy performance of buildings.

Justifiably then, implementing solutions such as STBs in high performing new builds to minimise the impact of TB, becomes increasingly relevant. Hoping to advance the knowledge and understanding around TB within the construction industry, encourage the uptake of STB design solutions, the focus in this research is to develop an experimental design to address TB, combining measurement and modelling, capable of thermally evaluating point-connections in the building fabric, in-situ.

The following section reviews some relevant legislative directives, policies, and regulations driving the initiative to decarbonise and improve the energy performance of building, including quality assurance processes.

1.1.2 Legislative directives, policies, and regulatory drivers

Since buildings are responsible for a great deal of the energy consumption and energy emissions, this section focuses on the institutions driving policies for energy improvement, illustrating the importance of sustainability in the built environment.

The European Green Deal proposal, presented on the 14 July 2021 (European Union, 2021b), targets a 55% reduction in greenhouse gas emissions by 2030 compared to 1990 levels. According to the upgraded regulatory framework the European Commission proposed in December 2021, (European Union, 2021a), buildings account for 40% of the total energy consumption in the EU which equates to around 36% of CO_2 emissions (de Sousa Dias Prata & de Sousa Dias Prata Joana, 2017; European Union, 2021c). Thus, buildings are the single largest consumer of energy in Europe, 80% of which is used for heating, cooling, and domestic hot water (European Union, 2021a). Consequently, the directive covers a wide range of measures supporting national EU governments in enhancing building performance.

The Renovation Wave Strategy and Action Plan were published in 2020 as part of the European Green Deal, aiming to double annual energy renovations in the next 10 years with 3 identified focus areas: tackling energy poverty and worst-performing buildings, public buildings and social infrastructure, and decarbonising heating and cooling (European Union, 2020).

Working alongside these strategies, the revised EPBD promotes policies aimed at achieving a highly energy efficient and decarbonised EU building stock by 2050 (European Union, 2021a). As of 2030 all new private buildings will be zero carbon-emission, but public buildings have until 2027. It also forces member states to integrate national building renovation plans into national energy and climate plans – stating they will need to phase out fossil fuels in heating and cooling by 2040 (European Union, 2021a).

The rising pressure for European member states to enforce schemes (OFGEM, 2021) which combat these growing concerns of energy consumption and carbon emissions in buildings, drives the concept of NZEB (nearly zero-emission buildings) – a building with very high energy performance requiring minimal power, mostly sourced renewably.

The global investment in energy efficient buildings is monitored by the IEA, shown in their Energy Efficiency Market Report (International Energy Agency, 2018, 2021).

The 2019 UK government amended the 2008 Climate Change Act altering the previous commitment (targeting an 80% reduction in emissions by 2050, compared to 1990 levels) to a target of net zero (100% reduction) by 2050 (UK Gov, 2019).

ECO (energy company obligations), is a government energy efficiency scheme to help reduce the carbon emissions and fuel poverty in Great Britain (GOV, 2018). The main obligation of the scheme (Home Heating Cost Reduction Obligation), forces obligated suppliers to improve the ability of low income, fuel poor, and vulnerable households to heat their homes – including actions that result in heating savings, such as replacing broken heating systems or upgrading inefficient heating systems (ofgem, 2018). Essentially it requires large energy companies to boost efficiency of homes, passing costs onto consumers via energy bills (Black, 2021). Similar incentives such as the emissions trading scheme, fuel duty tax, contracts for difference, and the climate change levy all strive toward a net-zero, sustainable future (UK Parliament, 2021).

A Building Performance Evaluation (BPE), evaluating the efficiency of a building in the design, development, and post construction stages, represents a continuous-improvement approach such that every aspect of the design, construction and occupancy is scrutinized and ideally enhanced, with regards to quality and efficiency (Preiser et al., 2018).

CIBSE 'Guide A' defines the main criteria for the design of buildings in terms of comfort, health, energy demand issues, and carbon emissions (CIBSE, 2021). Guidance is provided regarding the quality of the design – by introducing logical processes, for engineers to carry out relevant calculations and make decisions – in a consistent, repeatable, and auditable manner.

As mentioned, SAP is the UK governments recommended energy assessment tool for residential dwellings, where the Reduced Data version (RdSAP) is used for existing dwellings (BRE, 2017). Future developments of the methodology, SAP / RdSAP 11, is expected to come into force in 2025 to support the net zero commitment, alongside the Future Homes Standard update of the Building Regulations (GOV.UK, 2021).

Building Regulations in the UK, *Approved Document Part L (England and Wales) Conservation of fuel and power' Volume L1A and L1B*, for new and existing dwellings, respectively (HM Government, 2021a), contain the design standards, requirements, and regulations for target fabric efficiency and CO_2 emissions, covering quality of construction and commissioning – regulating dwelling emission rates and dwelling fabric energy efficiency – focussing on subjects such as: TB, party walls and other thermal bypasses, air permeability and pressure testing. Volume L2A and L2B, is a similar document addressing new and existing buildings other than dwellings (HM Government, 2021b).

Complying with these Building Regulations, Simplified Building Energy Models (SBEM) is a government approved methodology used to calculate the energy required to heat, cool, ventilate, and light a non-residential building over a 12-month period when used under normal circumstances. Results include emissions and energy consumption before assigning a numerical rating. The higher the rating the less energy efficient the building is (EnergyTest, 2017).

Energy Performance Certificates (EPC) rate a buildings efficiency level; schemes such as LEED (USGBC, 2019), passive house, and BREEAM are used worldwide and within EU legislative frameworks to rank building energy performance.

The Accredited Construction Details (ACDs) guide is published within Part L of the approved Building Regulations (HM Government, 2007) and supports SAP compliance. The guide provides examples of construction details in which TB effects are limited to a reasonably low level (HM Government, 2007) and is presented in two main sections. The first section discusses thermal performance principles in construction (insulation continuity, airtightness), whilst section two provides large scale indicative drawings of thermal insulation and airtightness provisions for specific construction interfaces. Similarly, the Enhanced Construction Details guide offers a catalogue of construction designs with yet greater performance specifically aimed at reducing TB impacts, providing metrics for SAP calculation (Energy Saving Trust, 2008) – otherwise bespoke numerical modelling should be utilised to evaluate the TB transmittances for a more precise value of the individual TB details performance.

Approved building regulations require that numerical assessments quantifying heat loss caused by TB should be carried out by 'a person with suitable expertise and experience' – following the guidance set out in BR497 (Ward & Sanders, 2016) and IP 1/06 (Ward, 2006) (BRE documentation) – and that provisions be made to limit excessive heat losses and condensation risk through TB.

The European based PassivHaus Institute (PHI) endeavours to create a zero-carbon future (Passivhaus Institute, 2021) both in domestic (Designing Buildings Wiki, 2021a), and non-domestic applications (Designing Buildings Wiki, 2021b), with several UK approved building assessors able to issue quality assured Passivhaus Certificates. The process is seen below in Figure 8, below:

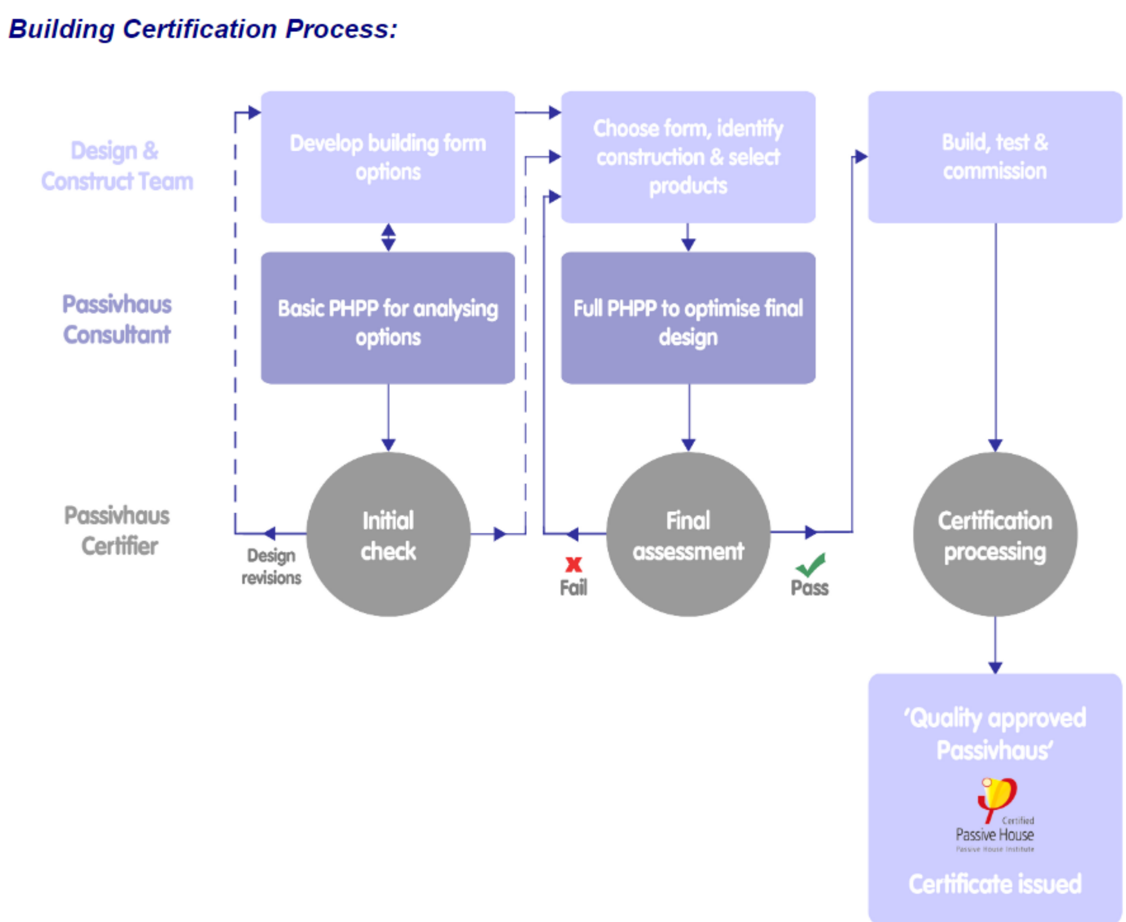

Figure 8 – Building certification process (Passivhaus-Trust, 2019).

To achieving high Passivhaus standards typically involves; very high levels of insulation, extremely high-performance windows with insulated frames, airtight building fabric, ‘TB free’ construction, a mechanical ventilation system with highly efficient heat recovery, and accurate design modelling using the Passive House Planning Package (PHPP) (Passivhaus-Trust, 2019), similar to the UK’s SAP.

Buildings may not be described as a Passivhaus unless it has been modelled in the PHPP and meets all the requirements of the Passivhaus Standard criteria, established by the PHI to certify buildings (Broome et al., 2015).

PHPP is a guide containing everything necessary for designing a properly functional Passive House; based on an excel (or equivalent) spreadsheet, with different worksheets containing the respective inputs and calculations, it prepares an energy balance and calculates the annual demand of the building based on user inputs relating to the building’s characteristics (Passipedia, 2019), forming the basis for quality assurance and certification. The results from the software are collated in a well-structured verification sheet (see Figure 9), the verification flow is seen in Figure 10.

Specific building demands with reference to the treated floor area

				Requirements	Fulfilled?*
	Treated floor area	156,0	m^2		
Space heating	Heating demand	14	$kWh/(m^2a)$	15 $kWh/(m^2a)$	yes
	Heating load	10	W/m^2	10 W/m^2	yes
Space cooling	Overall specif. space cooling demand		$kWh/(m^2a)$	-	-
	Cooling load		W/m^2	-	-
	Frequency of overheating (> 25 °C)	1,6	%	-	-
Primary energy	Heating, cooling, auxiliary electricity, dehumidification, DHW, lighting, electrical appliances	60	$kWh/(m^2a)$	120 $kWh/(m^2a)$	yes
	DHW, space heating and auxiliary electricity	33	$kWh/(m^2a)$	-	-
	Specific primary energy reduction through solar electricity	25	$kWh/(m^2a)$	-	-
Airtightness	Pressurization test result n_{50}	0,2	1/h	0,6 1/h	yes

* empty field: data missing; '-': no requirement

Figure 9 – Verification sheet (Passipedia, 2019).

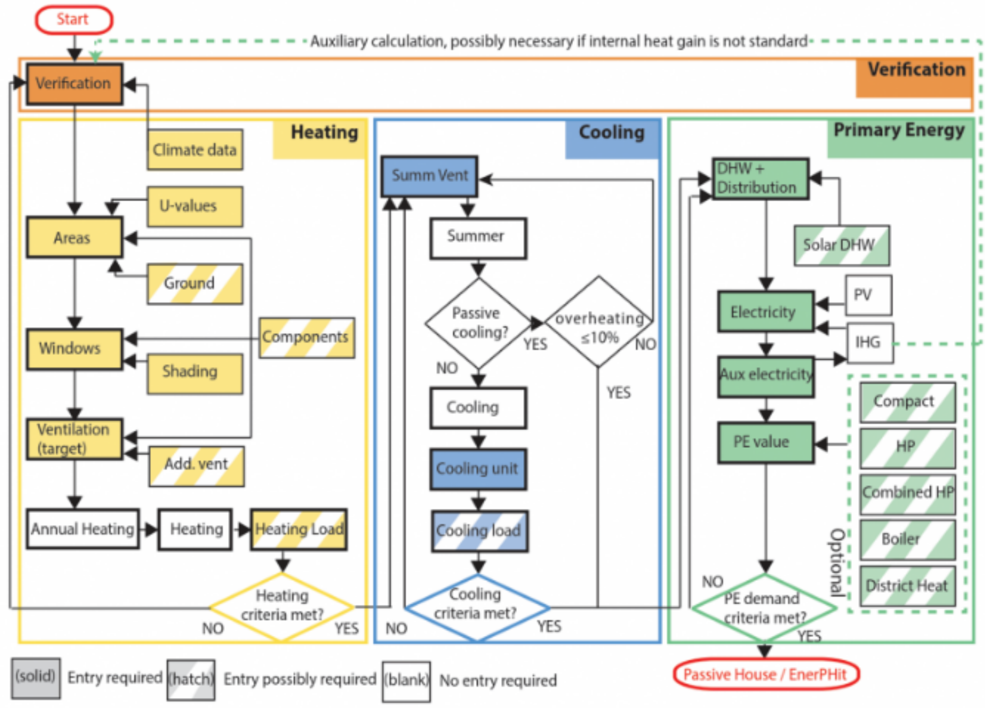

Figure 10 – Flow chart showing how the PHPP works (Passipedia, 2019).

The first edition of PHPP was released in 1998 and has been continuously developed and validated since (Passipedia, 2019).

It is clear that these policy and regulatory drivers call for a far more robust understanding of energy and buildings, particularly around the fabric performance of a building. If NZEB and zero-carbon, as will be introduced in the UK in 2025, are to be policy options, a more detailed consideration of heat loss, one that better includes TB, will need to be considered (Touloupaki & Theodosiou, 2017a).

The following section gives an appraisal of the basic heat transfer mechanisms in building physics related to the assessments of energy performance.

1.1.3 Building Physics and Performance definitions

Energy consumption in buildings is a physics problem, hence the following section briefly covers an introduction to basic building physics definitions and metrics that need to be considered when reviewing and evaluating a buildings energy performance.

Energy and heat have different definitions. Energy is measured in Joules ‘J’; the amount of energy that transfers/transforms per second [J/s] is a Watt [W], commonly known as power – or in this context, heat (J. P. Holman, 1972).

Amongst other energy metrics categorising a buildings energy performance, Heat Transfer Coefficients (HTC), defined as the “heat flow rate divided by the temperature difference between two environments” (BSI, 2017g), categorise each mode of heat loss, whether it be by ventilation or fabric transmittance. The sum of the ventilation and fabric transmittance is known as the buildings HTC and, with units [W/K], they describe the energetic transfer per temperature differential between conditioned and ambient environments (NSAI, 2017). When summed, these determine the total energetic loss (BSI, 2017a) from a building.

The building envelope is the barrier between the conditioned internal environment and the ambient external environment, resisting all modes of heat transfer (conduction, convection, and radiation), air, water, light, and noise (Sadineni et al., 2011). The fabric considers windows, walls, roofs, floors etc. or anything separating the internal conditioned environment from the outside. Walls are usually comprised of multiple layers of structural or insulating materials, possibly with intentional air cavities for ventilation – it is the first element to consider for improving a buildings energy performance.

The metric used to describe heat transmittance through walls is known as the U-value. With units [W/m^2K], it is defined as the one-dimensional heat transfer between environments per effective area and degree differential between conditioned and ambient environment (air-to-air) (BSI, 2018a). It can be calculated analytically or measured directly following standardised methodologies (BSI, 2014, 2018b). The U-value must not be confused with conductance (surface-to-surface) since the surfaces are exposed to environmental conditions, hence the surface resistance (SR) – encapsulating the convective and radiative transmittances – must be included within the determination. The reciprocal of the U-value transmittance is the resistance [m^2K/W]. Both provide a deterministic energetic loss through planar, opaque wall elements, if the temperature difference between environments and the façade area are known where 1D heat flow is realised.

Another important metric is the air permeability. Defined as 'air leakage rate per the envelope area across the building envelope' in the internationally recognised testing methodologies: (BSI, 2015a) *and a US standard* (ASTM, 2022) *and, at building level, is the second consideration for improving energy performance. Air infiltration of conditioned spaces pulls ambient temperature air in and discharges the conditioned air. Qualitative IR* (Pearson, 2011) *can highlight poor detailing causing infiltration. The metric for airtightness (synonymous with air-filtration) is ACH (air change per hour). Quantitative assessments of air-tightness, such as blower door testing* (Johnston et al., 2015a)*, can produce the ACH metric, which is essentially a volumetric flow rate through the space. The heat loss via this mode can be determined if the density and specific heat capacity of the space are known* (BSI, 2017b)*. Unlike TB, validated in-situ measurement and physical testing* (Marshall et al., 2017) *justifies possibilities to either design-out or retrofit a solution to air-tightness issues*.

TB, however, does not have the same level of supporting guidance and established standardised documentation (T. Theodosiou et al., 2019) for quantification using direct measurement. Therefore, it has remained relatively untreated (Touloupaki & Theodosiou, 2017b, 2017a), despite the advancements made in fabric insulation quality *and air-tightness performance* (Gaspar et al., 2016) to meet regulations. However, as the insulation resistance increases, so does the percentage contribution of TB (Berggren & Wall, 2013; T. Theodosiou et al., 2017, 2019; T. G. Theodosiou et al., 2015) thereby increasing the relevance of TB measures – such as STBs.

Some basic definitions and the major contributors to heat loss in buildings were reviewed in this section, illustrating that established/standardised test methods are available for U-value and ACH quantification, but are lacking for TB analysis. Following on from this the implications of the current industry response to the TB are exampled.

1.1.4 Current industry response to the problem

Disregarding STB in construction is a real concern with some developers/contractors/steel-fabricators/structural engineers/architects wrongly assuming that the STB solutions are not cost-optimal, leading to their mistreatment (sometimes neglected, or poorly constructed – either in the designed material choice or neglect in workmanship). This shows knowledge and guidance ought to be enriched through thorough scientific research – encouraging accurate BPE and cost-optimised designs, including STB. Better understanding around the importance of STBs and their proper install will hopefully generate a significant uptake of these solutions, ultimately, increasing human comfort and design flexibility, whilst reducing energy use and carbon emissions.

If unaddressed, TB is said to increase the fabric heat loss by 30% (Passive House, 2015), agreed with by the BRE (BRE, 2022).

The accredited thermal details (HM Government, 2007) states the Elemental Method 2002 edition of Approved Document L1 provides average overall standards for U-values, in which, the proportion of overall heat-loss due to TB in recently constructed dwellings is between 10 and 15% – though this can be substantially higher with certain construction systems or dwellings with particularly poor detailing.

The National Energy Code of Canada for buildings state that for minor and major insulation penetrations (minor: wall ties, studs; major: balconies, structural members) which cover less than 2% of the cross-sectional area, need not be accounted for in the calculation of the effective thermal resistance of penetrated wall area. However, (Ge et al., 2013) showed that in typical high-rise multi-unit residential buildings with balconies forming 4% to the cross-sectional area of the building façade contributes 11% to the energy consumption depending on the thermal performance of the windows and opaque walls.

Similarly, (BC Hydro, 2016) showed minimising TBs in Canadian multi-unit residential buildings, results in a 10% saving in energy. Additionally, this showed neglecting major TB, like balconies, can result in an underestimation around 20 – 70% of the total heat flow through the building envelope.

Disregarding impacts of TB but adopting highly efficient insulation and window installations will not produce an optimum reduction in a building's energy use. As mentioned, increasing the wall fabric resistance to improve building performance can induce more significant TBs (Whale, 2012). (T. G. Theodosiou & Papadopoulos, 2008), (Šadauskienė et al., 2015), and (Ascione et al., 2012) have shown that TB in buildings can cause an increase of up to 30% in space heating load.

Unaccounted effects of TB in some buildings can cause an increase up to 35% of thermal loads than initially calculated (T. G. Theodosiou & Papadopoulos, 2008); causing heating requirements in reality to be 30% higher than initially calculated. TB can cause a reduction in the total thermal resistance of the clear field wall by around 40% (Kośny, J., Curcija, C., Fontanini, A.D., Liu, H. and Kossecka, E., 2016).

Comparing measured energy consumption with and without the presence of TB found thermal losses increased by 9% due to TB. (Bianchi et al., 2014) continuously monitored the internal and external conditions affecting a case study building (purpose built for research), whilst using a novel measurement of linear-TB using IR techniques quantifying their transmittance. (Ambrosini et al., 2015; Ascione et al., 2014; Asdrubali et al., 2012; Benko, 2002; O'grady, 2018; O'Grady et al., 2017a, 2017b, 2018) introduced a measurement method for linear-transmittance quantification. The methods include both HFM and IR techniques to capture the surface temperature and flux gradient leading into a linear-TB and validated against numerical simulation solutions. This topic is discussed in greater detail in the literature review since it resonates well with current study.

With data from test rooms, (Gao et al., 2008) showed one-dimensional heat flow assumptions cause an underestimation of the total heat flow through envelopes containing TB by about 10-40% for certain building envelopes. Furthermore, TB can lead to a potential increase in total heat losses through the building envelope by 9-19%. This was concluded by using a low order additional heat loss model considering TB – allowing coupling with existing 1D transient thermal simulation software – shortening the burdensome 3D calculation.

(Baba & Ge, 2016a) performed experiments regarding annual heating and cooling loads under four scenarios: direct 3D modelling, equivalent wall method, equivalent U-value method; and without TB in the design. Simulation results have shown that the presence of TB increases the annual heating load by 18-30% and the annual cooling load by 20% for hot climates.

An improved version of the Equivalent U-value (which alters the U-value of the wall to represent a TB detail, simplifying the 1D analysis) is the Combined Thermal Properties (CTP) method. (Gomes et al., 2013) included light steel framing with this new method; results show an increase in peak thermal loads of 10% and an increase of annual energy use by 5%.

Using solid metal profiles to fix building envelopes' insulation layers, reduce the thermal resistance of the assembly by half – proving to be a major cause of TB (Šadauskienė et al., 2015). (Ben Larbi et al., 2017) focused on steel-to-steel STB products consisting of a highly thermally resistive PVC material showing how the thermal and mechanical effects are influenced under different configurations. Numerical simulations show that, depending on the configuration the STB products studied, reductions in TB transmittance of 20-65% were found, compared to a connection without a thermal break. For the same configurations the use of stainless-steel fasteners oppose to carbon steel reduces the TB effect by a further 17-37%. In a further study it was shown that the TB was reduced by 30-60% compared with a fixing without a STB (Larbi et al., 2017).

Embedding sensors in and around an experimental mock-up of a thermal break solution in a guarded hot box, (Dikarev et al., 2016) showed that results from numerical modelling were in good agreement with measured temperatures – validating the numerical assessment.

Similarly, (Garay et al., 2014) found 2D TBs contributes 10-20% to heat loss. Model re-calibration techniques utilised embedded sensors monitoring crucial performance metrics. The accessible locations to deploy sensors around the investigated detail (concrete linear bridge junction) were compared, as were the sensitivities of these parameter. A later paper, amalgamating two standards (Martinez et al., 2017) (combining dynamic and TB transmittance calculations) was developed and applied to an adapted case study including 3D TB (Garay Martinez, 2018), finding that: taking experimental measurements to parameterise and re-calibrate models, hybridising numerical and experiment performance assessment, is successful and necessary.

Point thermal breaks isolating heat loss caused by steel anchors in ventilated façade systems were analysed (T. Theodosiou et al., 2017, 2019; T. G. Theodosiou et al., 2015). Numerical software: Abaqus software was utilised in 2015, Ansys in 2017, and COMSOL in 2019. In their research it was shown that in new smart double-skin ventilated façades, the importance of parameters like point TB are in most cases overlooked, and neglecting their presence can lead to a significant underestimation of the total heat flows through the building envelope by 5-20%.

Table 1 consolidates sources showing the impact TB has on the building fabric as a percentage:

% Contribution to fabric heat loss	Reference
10-15%	(HM Government, 2007)
9-19%	(Gao et al., 2008)
35%	(T. G. Theodosiou & Papadopoulos, 2008)
30%	(Whale, 2012). (T. G. Theodosiou & Papadopoulos, 2008), (Šadauskienė et al., 2015), and (Ascione et al., 2012)
5-10%	(Gomes et al., 2013)
11%	(Ge et al., 2013)
9%	(Bianchi et al., 2014)
20 – 70%	(BC Hydro, 2016)
5-20%	(T. G. Theodosiou et al., 2015)
40%	(Kośny, J., Curcija, C., Fontanini, A.D., Liu, H. and Kossecka, E., 2016)
18%	(Baba & Ge, 2016a)
25%	(T. Theodosiou et al., 2019).

Table 1 – Percentage contributions to fabric heat loss due to TB.

Table 2 consolidates sources showing the percentage reduction in TB-transmittance when thermal breaks are utilised:

% TB-transmittance reduction using Thermal Breaks	Sources
30%	(Sallée et al., 2014)
10%	(BC Hydro, 2016)
20-65% (Carbon Steel Bolts)	(Ben Larbi et al., 2017)
17-37% (Stainless Steel Bolts)	(Ben Larbi et al., 2017)
10-23%	(T. Theodosiou et al., 2017).

Table 2 – Shows the % TB-transmittance reduction when using thermal breaks.

Concluding this section, it becomes clear from (T. Theodosiou et al., 2019) that implementing advanced energy-efficient systems into buildings needs an integrated approach that goes beyond building energy codes aimed at providing sustainable buildings which operate as predicted in the design stage.

What is lacking is in-situ analysis methods of as-built details. Only thermal models – created by trained modellers – must be trusted, often informed using manufacturing details, engineering drawings, and assumed boundary conditions. This idealises the investigated detail somewhat and contributes to the energy PG (Rye & Scott, 2012).

Addressing structural TB by developing a measurement and modelling experimental design (accurately quantifying their transmittances in-situ) improves understanding and expands knowledge, which is needed to treat TB impacts, either by altering design or implementing STB solutions.

1.2 Aim & objectives

This research aims to develop an in-situ experimental design quantifying structural point TB transmittance caused by steel beam façade penetrations, enabling an impact assessment of STB solutions within steel-to-steel connection interfaces. Informed numerical models will be re-calibrated using measurements taken from a specific construction system and compared with standardised numerical approaches to determine the associated PG.

1.2.1 Aim

The overall aim of this research is to understand the impact of TB in point-connections and establish appropriate experimental and modelling processes to support industry and researchers in better understanding the phenomena.

The binding hypothesis for these topics is captured in the following question: “is the PG a combination of other gaps, such as the measurement gap, and the data gap in models?” (Fitton, 2016). This is illustrated in the following diagram see Figure 11:

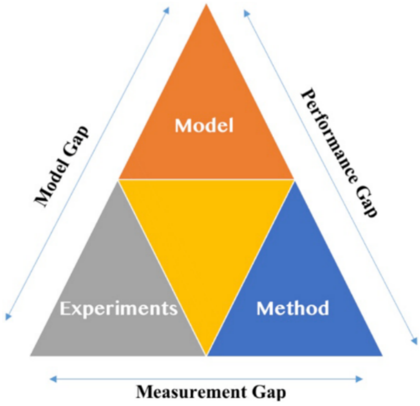

Figure 11 – Hypothetical gaps contained within the PG (Fitton, 2016).

Improving understanding of the principal phenomena shortens this PG and encourages the uptake of TB treatments. STB solutions help relieve regulatory pressures to reduce CO_2 emissions and energy consumption caused by space heating, enabling a more energy-efficient, longer-lasting, hygienic, cost-optimal, built environment – whilst expanding architectural creative freedom.

1.2.2 Objectives

The identified elements of the PG informed the development of the following research objectives:

- Identify the causes of the PG in both measurement and thermal FE modelling.
- Understand and criticise existing methodologies assessing building performance.
- Explore assumptions in modelling building performance.
- Design and conduct experiments to correlate the performance of STB solutions by comparing results using standardised numerical modelling to simulations informed with physical measurement.
- Formulate findings and provide insights/recommendations related to the evaluation of this nuanced TB and break product.

1.2.3 Original contributions to knowledge

The proposed body of research makes an original contribution to knowledge in the following areas:

- Calibrating models using measured data (taken in and around bespoke structural TB details and STB solutions) to reflect real world performance. The numerical estimation maps the multi-dimensional heat flows and complex temperature distributions through a FE model of the investigated detail. Informing the model using measurements reduces some uncertainties stemming from assumptions in the model data and enables quantification of the accepted TB transmittance metric with greater accuracy compared with standard numerical assessments.

- An experimental design is developed by testing a range of STB products in a well-instrumented laboratory under climatic-controlled conditions; emulating steady-state conditions allows validation of novel measurement methodologies and theory which the adopted grey-box parametric model re-calibration method can then be verified against. Ensuring a thorough understanding of the measurement uncertainties hopes to produce a robust interpretation of heat loss and cold spots cause by structural point-connections.

- Energy performance practitioners are provided with a greater understanding of possible evaluation methods assessing the associated heat loss and corresponding cold spots attributed to structural TBs in-situ, post construction.

- Broadening the knowledge around the impacts of STB solutions increases their application and accurate inclusion in whole building energy performance calculations. Also, enhanced understanding of the problem allows them to be treated further up the design stage

1.2.4 Limitations to the study

We may find that the only way to gather sensible metrics to train the model is by embedding sensors. Experimentally, flux sensors capture 1D heat flow but are deployed in these works within a structural connection causing a 3D flux. These point-measurements (amongst other, such as air and surface temperatures) are used to calibrate FE models – which is solely relied upon for TB quantification. Hence, systematic errors may be inherent.

For in-situ testing, this would require access to the investigated construction prior to completion; deploying the sensors; then waiting for the development, so as a temperature differential can applied. This is not only invasive, but potential risk for damaged sensors is high which cannot be replaced post construction. It also requires collaborating with the development teams for on-site access post-build. This may warrant supervisory access and re-evaluation of the research ethics.

When in-situ, each case is unique: neighbouring TBs (sliding-doors and windows) are commonly found on balcony details; also, complex envelope layers differ between designs. Capturing these architectural circumstances in the lab is difficult and true representativeness is hard to achieve.

Dynamic condition testing would further develop the understanding of the TB phenomena. However, evaluation is not well known or standardised. Hybridising standardised methods of 'steady-state TB calculation' and 'dynamic heat-transfer' may advance estimation of the TB-transmittance and its transient behaviour. This is particularly interesting to diurnal/annual whole building energy performance simulation that consider this type of TB in the construction.

TB-transmittance is sensitive to SR conditions which may vary dramatically across one façade in-situ, making it difficult to evaluate structural TBs holistic effect on a building design (e.g., convection and radiation are increased due to high wind speeds at elevation, and greater solar incidence on south facing orientations).

Situational measurements taken from real structural TB constructions would enrich the analysis of bespoke details in FE. It would be desirable that experimental in-situ testing considers many conditions and situations – preferably of a modular construction allowing alteration of STB solutions and comparisons without a thermal break if required.

COVID-19, budget cuts, and lack of collaboration from the industry made it impossible for actual real-world balconies to be tested in-situ. Instead, steady-state conditions within the EH labs were relied upon in the experimental data capture.

This research attempts to develop an experimental method capable of evaluating steel-to-steel TBs in-situ, where STBs can be implemented within the connection interface, with greater accuracy and a reduced PG by informing models using measurements. Erroneous TB evaluations can cause many detrimental implications; enabling a wider appreciation of their impacts encourages uptake in their treatment, such as better designs or thermal break installation, which ultimately encourages a more comfortable, cost-optimal, sustainable future for buildings, whilst aligning regulation with modern architectural wants.

In the following literature review section, legislation, relevant directives, mandates, and policies - informing building regulation, will be briefly outlined.

2.0 Literature review

Direct TB measurement methodologies do not exist, and numerical solutions are required to accurately quantify their complex nature, giving reason as to why addressing TB is the last consideration for building performance improvement.

As mentioned, TB can be categorised into two forms, linear and point, causing 2D and 3D heat flows, respectively. Their causation is due to fabric penetrations, discontinuities in the envelope (materials conductivity and thickness), or differences between heat emitting and absorbing surface areas (BSI, 2017c). It is the unpredictable multi-dimensional nature of the heat flux which makes direct measurement so difficult.

Reiterating, linear-TB are non-repeating TB which have a uniform cross-section along one of the three orthogonal axes (BSI, 2017c). The psi-value (or 'Ψ-value') measured in [W/mK], is the quantity describing linear transmittance. These are accounted for along with U-values in whole building BPEs. Common examples of linear-TB (windows, doors, intermediate floors, corner junctions, etc) are listed in building regulations: 'Accredited Construction Details' (HM Government, 2007) with improved versions in the 'Enhanced Construction Details' by the Energy Saving Trust (Energy Saving Trust, 2008).

Whereas, point-TB is a repeating localised TB whose influence can be represented by a point-thermal transmittance, or chi-value ('χ-value') which is measured in [W/K], a quantity describing its influence on the total heat-flow through the building envelope (BSI, 2017c). Less significant examples, such as façade fixings (Šadauskiene et al., 2015; T. Theodosiou et al., 2017, 2019; T. G. Theodosiou et al., 2015), are commonly accounted for directly within an adjusted U-value (BSI, 2017b), whereas substantial examples like structural beam penetrations, linking external features (such as balconies or passageways) to the buildings substructure (Ben Larbi et al., 2017; Larbi et al., 2017, 2019), need a more thorough analysis.

Generally speaking, both TB typologies cause a path of least resistance for heat to escape from buildings and induce localised cold spots, increasing condensation and mould risk. Condensation develops at a dewpoint where warm humid air meets a cold surface. This can occur on the internal surface or within the wall structure, interstitially. Interstitial condensation can cause material degradation and/or structural damage. Mould formation not only looks bad, but pathogens can cause serious respiratory harm to occupancy health (Broome et al., 2015; CIBSE, 2021; GOV.UK, 2019a; HM Government, 2007; Whale, 2012; Zero Carbon Hub, 2013).

The BRE (Ward, 2006) provides guidance assessing the risk of surface condensation and mould growth. The minimum internal surface temperature and air temperatures (external and internal) are required to calculate the so called 'temperature factor', defined in equation 1:

$$f_{Rsi} = \frac{T_{si} - T_e}{T_i - T_e} \qquad (1)$$

Where 'f_{Rsi}' is the temperature factor, 'T_{si}' is the internal surface temperature, 'T_e' is the external air temperature, and 'T_i' is the internal air temperature.

To limit the risk of condensation or mould, the temperature factor should be greater than or equal to a critical value (f_{CRsi}) – shown in a later section. However, the local humidity is also a consideration which depends on the buildings operational humidity; typically swimming pools or laundrettes have a greater humidity than residential buildings, hence, a larger critical temperature factor must be achieved (Ward & Sanders, 2016).

These are calculated under steady-state conditions following BS EN ISO 13788 (BSI, 2012a); the internal surface resistance is increased to 0.25 [m^2K/W] on **all** internal surfaces to account for obstructions usually found in domestic buildings, such as cupboards, beds, etc. although, the critical values reported by the BRE in their information paper IP 1/06 (Ward, 2006) were calculated considering the lower internal surface resistances dependant on heat flow direction (Ward & Sanders, 2016) – surface resistances are explained in a later section.

The continuing global population growth (Office for National Statistics, 2019, 2020) will inevitably encourage a significant uptake of high-rise residential buildings for inner-city domestic housing. With this increase (Office for National Statistics, 2020), one can safely assume the demand for balconies will also increase with people's desire for outdoor living space, creating potentially huge TB impacts (Ge et al., 2013). In some high-rise buildings in Canada, 50% of the elevation consists of 3D envelope structural detailing (Kosny & Desjarlais, 1994), illustrating huge potential for STB solutions in cantilever balcony connections.

Currently, standardised TB quantification relies on FE modelling methodologies. The experimental design in these works aims to combine in-situ measurement with modelling, evaluating a system featuring a steel-to-steel point-TB connection interface. In understanding the limitations of measurement and modelling, TB transmittance evaluations can be analysed more accurately than standardised numerical estimation, hoping to highlight and reduce the associated PG by considering precise measurement uncertainties to inform simulations.

Measurement techniques have in-built errors, some of which are allowed for in standards exposing imperfections in methodological techniques that are sometimes open to interpretation, hence accurate building performance characterisation is not guaranteed.

Resulting from the absence of specific guidance for TB assessment, neglecting point-TB simplifies the calculation of the heat-flow through the envelope (Kuusk et al., 2017). One outcome of this is that there is no treatment of these point-TB's (Oh et al., 2016), leading to, in many cases, large deviations between predicted and actual thermal losses through the envelope (T. G. Theodosiou & Papadopoulos, 2008). This section highlighted PG issues with respect to TB. The following section expands the discussion around energy PG in more detail.

2.1 Issues when characterising Thermal Bridging

The energy PG is the difference between the actual and estimated energy performance of a building. A mathematical percentage, positive or negative, can be calculated using equation 2, showing under or over estimations of BPE, respectively (Fitton, 2021b).

$$PG = \frac{Actual\ Consumption - Theoretical\ Consumption}{Theoretical\ Consumption} * 100 \qquad 2$$

It is not uncommon to find this gap throughout global academic research, the results of which vary drastically and can be apprehensive. A collection of results can be found in Table 3:

Country	Sample Size	Average PG	Reference
Italy	6	45%	(Ballarini & Corrado, 2009)
Germany	3400	30%	(Galvin, 2014)
UK	25	50%	(Johnston et al., 2015b)
Canada	3400	74%	(Rouleau et al., 2018)
Switzerland	50000	11%	(Cozza et al., 2020)

Table 3 – Global examples of recent energy PG studies including average PGs and sample sizes of the studies (Fitton, 2021b).

In the UK, it was found that the range of PG falls between +5% and -140% when comparing HTC measurement of new build UK dwellings (Johnston et al., 2015b) to the predicted buildings HTC.

Some construction methods and models of assessment (like practiced by Passivhaus) are more robust than others, with significantly less PG issues. Research found an average PG around 8% (Mitchell & Natarajan, 2020) in a study of 97 builds. A larger study of over 2000 Passivhaus and 130 EnerPHit standard retrofitted homes (Johnston et al., 2020) all exhibited low PG, better than the minimum prescribed standard demonstrating that this problem can be overcome – closing the gap by utilising correct methods of construction and assessment models.

Many causes of PG exist, a lot of which are known but some remain unknown, therefore the so called "energy pathology" is an area of research which investigates this (Mclean & Fitton, 2017). It has been developing worldwide since the 1960s by establishing new methods of measurement, improving modelling assumptions, and reducing the PG.

There is a growing body of evidence suggesting the importance to address the PG within the construction industry, specifically in BPE (C. Gorse et al., 2012; C. A. Gorse et al., 2013; Johnston et al., 2015a). The gap has been identified to be between steady-state predictive building models and in-situ measured thermal performance of the building fabric – even when the model is based on the actual building design. (Marshall et al., 2017) used DesignBuilder to model a pre-1920's Victorian end-terrace to recognise and reduce the gap between modelled and measured energy performance. Model specifics were derived from a measured survey of the Salford EH facility – a well-instrumented laboratory built within a climate-controlled chamber. Electric co-heating tests were performed to calculate the HTC; an 18.5% difference was demonstrated between modelled and measured data. From this, the model was re-calibrated informed by accurate air permeability and U-value in-situ measurements. In doing this, the PG was reduced to 2.4% when using the modified model.

(Marshall et al., 2017) reviewed many works regarding the discrepancies between modelled and in-situ measurements, when assessing U-values (Tye, 1977), (Lecompte, 1990), (Zero Carbon Hub, 2013), (Hens et al., 2007). Similarly, (Swan et al., 2015) identify the need for more work on practices, issues of data collection, and analysis to be undertaken to reduce the PG. In their paper, domestic energy issues are addressed by BPE practitioners; insights from both academic and industry-based practitioners acknowledge not only practicalities of building performance studies, but also future considerations for these types of studies. Issues regarding experimental design, data collection error, and fieldwork practicalities are not uncommon to any data collection and analysis exercise of this type. The PG between designed and actual performance of buildings was the major issue raised by many of the interviewees.

PGs not only arise because of inadequate predictive techniques; assumptions are often not well enough informed by what really happens in practice (T. G. Theodosiou & Papadopoulos, 2008). Similarly, (Bordass et al., 2004) shows the opportunity that the Energy Performance of Building Directive (EPBD) has to report actual energy use clearly, grading buildings, and relate expectations transparently to the design stage. Good practice guides published by 'Zero-Carbon Hub' are aimed at addressing the PG

(Zero Carbon Hub, 2013) proving that the construction industry is also realising this issue. A study by the BRE investigated three buildings, all with different BREEAM (British Research Establishment Environmental Assessment Method) ratings from various years, analysing the energy PG (Abdul & Hadi, 2016). The exemplar buildings within this study did not meet the operational savings in use; several factors were highlighted showing that achieving the intended performance in practice is difficult.

Post Occupancy Performance Evaluation (POPE) in Leadership in Energy and Environmental Design (LEED) buildings provide necessary feedback loops for designers, building managers, and occupants. Since some strategies can positively effect behaviour in one respect but negatively impact others, establishing an evidence-based guide for assessing building performance against its predicted goals in terms of physical metrics and perceived occupancy comfort, spurs future research aiding designers to balance the pros and cons of green systems and manage PGs (Preiser et al., 2018).

(Asdrubali et al., 2014) found that the in-situ measured values of thermal transmittance are almost always higher than the calculated ones. Several factors contribute to this difference: the performance data declared by building material manufacturers are often overestimated for marketing reasons; thermal performance of building elements and materials are measured under idealised laboratory conditions; the installation of insulation may not be perfect; external conditions (wind and rain) can affect the in-situ measurements. This gap becomes important with building certification schemes such as LEED and BREEAM, that assign points (Kubba, 2017), ranking the construction.

Clearly, measurement and modelling both have different PG contributors leading to differences between the expected and actual performance of the analysed component. The extent of these issues has not gone unnoticed in literature: PG issues almost always exist when comparing predictive with actual evaluation (Abdul & Hadi, 2016; Asdrubali et al., 2014; Bordass et al., 2004; Hens et al., 2007; Jack et al., 2017; Kubba, 2017; Lecompte, 1990; Mangematin et al., 2012; Marshall et al., 2017, 2018; Preiser et al., 2018; Subbarao et al., 1988; Tye, 1977; Zero Carbon Hub, 2013). The following section explains the measurement gap associated with HTC, U-value, and Air-permeability, before expanding the discussion to modelling associated PG and TB assessment.

2.1.1 Measurement Gap

Measurements are never perfectly exact; even with standardised measurement methodologies for HTC, U-value, and airtightness, issues around precision and accuracy remain – some of which can be found in the literature and are discussed in the next section – illustrating that the way the building performance is measured can be a contributing factor to the PG.

2.1.1.1 HTC

The Heat Transfer Coefficient (HTC) is defined in BS EN ISO 13789 as the "heat flow rate divided by the temperature difference between two environments" (BSI, 2017g). The standard provides a calculation method, encompassing all modes of heat transfer in steady-state numerical analysis. Whether used to predict annual energy consumption or to estimate energy efficiency of a building, this modelled metric can be compared with experimental measurements of completed buildings – evaluating the PG (Deb et al., 2021; Jones et al., 2016).

Co-heating (described more thoroughly in a later section) is a method in which the global fabric heat loss can be measured, quantifying the buildings HTC. Although there are many approaches to this method, a UK report by the National House Builders Council Foundation (NHBCF) studied the same standard test house to assess the differences in measurement techniques. Carried out by six teams, their measurements ranged by 20.4W/K (or 30%) (Butler et al., 2013), see Figure 12:

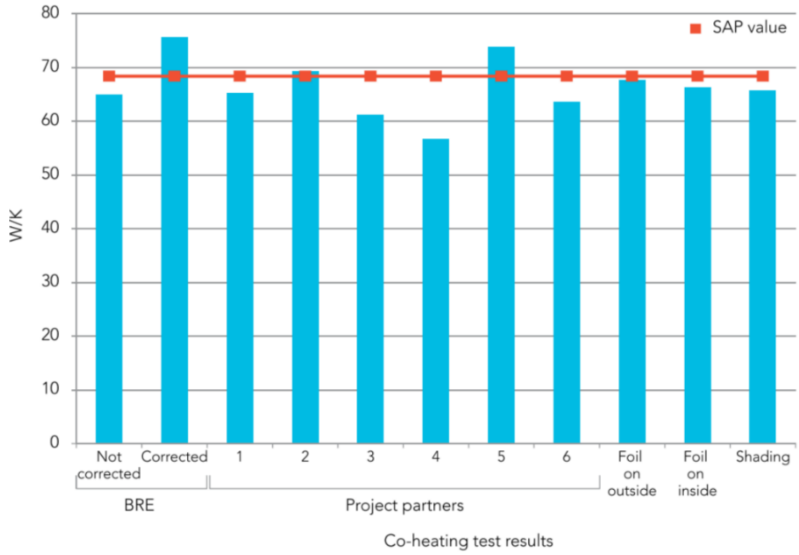

Figure 12 – Co-heating tests carried out on the same building by different researchers (Butler et al., 2013).

21 mechanisms were demonstrated (Stamp, 2015) that may affect uncertainty in co-heating methods. Some examples include moisture from the drying out process in new builds, measurement periods involved, and data analytics determining the final HTC value, suggesting improvements can be made in testing and standardisation. The CEN standard for co-heating testing (CEN/TC 89, 2020) is progressing to hopefully address these issues.

(C. Gorse et al., 2012; C. A. Gorse et al., 2013; Johnston et al., 2015a) highlights the PG. A mixture of green retrofits and low-energy new-builds (39 buildings in total) were tested using the co-heating test and compared against the designed values to assess the PG. And average PG of 26% was found but it may be as high as 58% or as low as –9% (C. A. Gorse et al., 2013).

Similarly, a later paper quantifies the PG in 25 dwellings, newly built to 2006 Part L1A regulation. Although variations were seen, findings show most dwellings had considerable PGs. Closer analysis suggests the poorest performing buildings (mid-terrace) tend to have the largest PGs, the reason being thermal bypassing occurs through party-walls which were not accounted for in the regulated evaluations (Johnston et al., 2015a).

2.1.1.2 U-value

The U-value ('fabric transmittance' defined earlier) can be determined analytically using a physics-based approach, which one can trust with little ambiguity. However, when measured in-situ, many mechanisms such as moisture levels, workmanship, porosity, density, and material properties can vary evaluation – not to mention oscillating internal and external boundary conditions (e.g., wind, rain, and solar radiation). Therefore, the U-value is constantly changing in a dynamic system (Fitton, 2021b). Simplifications can be applied utilising models to determine the metric, and, in some cases, model evaluations deviate from the analytical expectations.

(Hulme et al., 2014) compared the default modelled value – used in RdSAP – of a solid masonry wall with no cavities (2.1 [W/m^{2}K]), with measurements from field trials assessing 85 walls applying the in-situ measurement standard BS EN ISO 9869-1 (BSI, 2014). The median value was measured to be 1.59 [W/m^{2}K], differing by approximately 32% to the RdSAP value: authors alluded that the walls moisture content was overestimated in the calculation. The regulatory model has adjusted the standard U-value for solid wall construction to 1.7 [W/m^{2}K] – reflecting reality more accurately. The old value was used for over a decade and overestimated the U-value (assuming a less thermally resistive wall) causing consumers, policies, and decision makers underestimated the performance of these walls.

In-situ U-value measurement has a number of standards: from the United States ASTM C1155 (ASTM, 2013b) and the internationally recognised BS EN ISO 9869 (BSI, 2014) each with individual distinctions leading to differences in techniques. This can have a significant effect on the results; in a study caried out at the UoS EH, the way variables are measured and used in analysis to calculate the U-value were compared investigating (uninsulated solid brick) under steady-state conditions, taking measurements from three points on the same wall. Even though the same wall was studied, the way measurements were collected and analysed caused variation in the U-value estimate Figure 13.

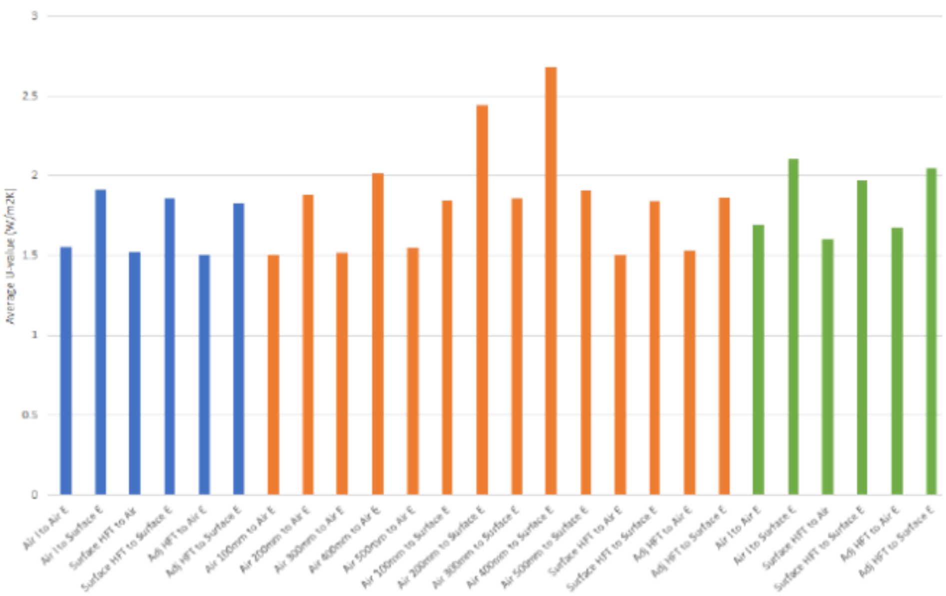

Figure 13 – Illustrating U-value variations caries out on the same wall areas, with different temperature sensor placements and data analysis: U-values range from 1.5-2.6 [W/m^{2}K] (Fitton, 2021b).

Significate issues are illustrated since all calculated values comply with at least one of the various measurement standards, showing a range of around 1.1 [W/m^{2}K]. If these values are expanded into a BPE, large differences in the calculated HTC are expected (Fitton, 2021b).

Similarly, since small heat fluxes were detected by sensors (even more so for well insulated buildings), minuscule changes in single measurements can cause differences in the calculated measurand, which can be affected by many variables: sensor-to-surface contact, heating patterns, wind, rain, etc, and moisture effects in the fabric of the wall (from climatic conditions or of the drying of new builds). Moist brick/mortar reduces its thermal resistance and depending on material a 10-98% increase in conductivity can be seen (Budaiwi & Abdou, 2013; Papadakos et al., 2021).

Due to these number of issues, such a simple measurement can have serious error margins – this also explains the large uncertainty figures denoted in standards (BSI, 2014) (up to +/- 28%) for these measurements (Fitton, 2021b).

2.1.1.3 Air-permeability

Air-permeability (defined earlier) of a building is pertinent to its energy performance, it can be measured following standards (BSI, 2015a) or (ASTM, 2022). The metric deals with unintended gaps in structure (caused by poor workmanship, bad design, or expanding/contracting components/elements). Pressure tests, where a fan is used to generate a pressure differential of around 50 Pa (N/m^2) between the internal and external environments, can measure the buildings permeability. Although, often a figure is stipulated in the design stage: a typical UK design value is 5 m^3/m^2h, although <10 m^3/m^2h is the maximum allowed for new homes in the UK (Crawley et al., 2019)**.** Over many years of research, issues of airtightness have been found in new and existing homes, cited as one of the most significant contributors to the PG (Johnston et al., 2015b; Marshall et al., 2017).

However, we cannot assume that standardised measurements are perfect since all measurements are subject to some error: researchers have been investigating the errors and uncertainty associated with these test methods finding external wind speed at the time of testing significantly increases uncertainty levels – the greater the wind speed the larger the uncertainty (Carrié & Leprince, 2016), illustrated in the following Figure 14:

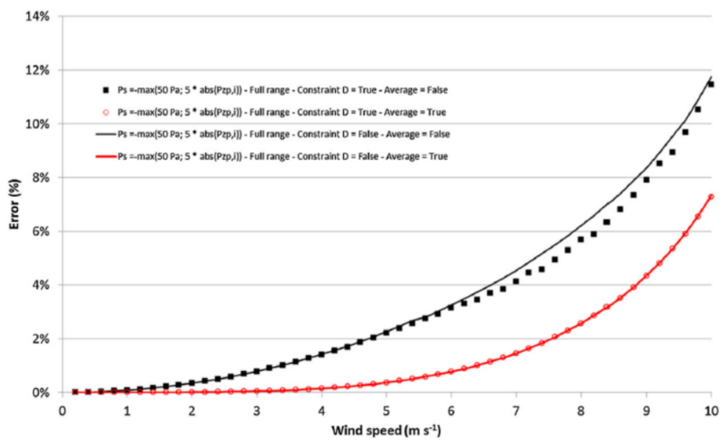

Figure 14 – Maximum error due to wind speed (Carrié & Leprince, 2016).

The authors here found that a combined uncertainty ranging between 6-12% should be used for windspeeds between 6-10m/s.

This section illustrated that not only do sensor errors cause measurement uncertainty, but the way standardised methods are implemented in practice also affect accuracy and precision (Fitton, 2021b), all of which contribute to the so called 'Measurement Gap'. The 'Modelling Gap' is discussed in the following section.

2.1.2 Modelling Gap

The energy PG can also be seen when modelling buildings energy performance which are generally caused by modelling assumptions. (Lomas et al., 1997) attempted to identify errors in building energy simulations, 25 combinations of models and modellers were compared finding discrepancies between the results from modelling teams – with some software packages reporting different outcomes with different users. User errors ranging from incorrect inputs, inconsistent parameterisation, calculation errors, interpretation of results, oversimplification, and misidentification of HVAC systems are the largest contributors to this gap – but also the way different models deal with physical parameters such as TB or solar gains differ. This is seen in (Strachan et al., 2016) where the data from a well measured case study building was shared with 21 other modelling teams around the globe. Several mechanisms of modelling error were identified. Most significant of all was user error, but the way models cope with physical parameters such as TB, long-wave radiation, internal convection, and transmission of heat gain through glazing, differed simulation outcomes.

Reporting similar issues to Strachan and Lomas, a recent paper (Roberts et al., 2019) carried out a small study investigating overheating in homes using modern software and compared simulation results with data from a well measured case study. Four separate modelling software were utilised which failed to predict the measurements accurately: familiar issues of user error were reported along with incorrect U-value calculations of components within the model (Fitton, 2021b).

Concluding this section, the modelling gap is broadly caused by both user error and software capability to predict heat transfer in building physics.

2.1.2.1 Thermal Bridging Performance Gap

As mentioned, the critical aspects effecting building performance (fabric and airtightness) have been addressed thoroughly through attainable measurement leading to optimised designs and best practice guidance (Anderson, 2006; CIBSE, 2021; NBS, 2016; Passivehaus, 2015). In contrast to the measurement methodologies mentioned previously, the multi-dimensional nature of TB cannot be measured directly (BSI, 2017c) since only 1D heat flow or point temperature measurements can be taken (BSI, 2014). Although some novel attempts have been made to measure 2D linear-TB's (Ambrosini et al., 2015; Ascione et al., 2014; Asdrubali et al., 2012; Benko, 2002; O'grady, 2018; O'Grady et al., 2017a, 2017b, 2018), there are no standard measurement methods. This encourages bad practice within the construction industry; neglecting TB (Ge et al., 2013), making assumptions (BSI, 2017h), or erroneously evaluating (Dilmac et al., 2007) their contribution to whole building energy performance – all causing PGs (Janssens et al., 2007).

Numerical software, vitally capturing the complex heat paths and temperature distributions through any bespoke 2 or 3-dimensional building element (BSI, 2017c; Ward & Sanders, 2016), is essential for TB evaluation. Idealisations in model generation and assumptions in simulation parameterisation are examples of gaps in modelling data knowledge. Minimising this is an objective for the experimental design in these works by combining measurement and modelling, therefore understanding the uncertainty in measurements or methodologies is imperative.

TB is a relatively new consideration in building physics, hence the influx of novel numerical methods to calculate multi-dimensional heat-flow in recent years (Baba & Ge, 2016b; Ge & Baba, 2017; Kośny & Kossecka, 2002; Kossecka & Kosny, 1997, 2005). These methods have informed the uptake of bespoke numerical simulation software adapting the FE (finite-element) methods, amongst others, to address TB in buildings. Similarly, simplification of complex TB heat-flows allows implementation into 1D building energy modelling software enabling analysis of the holistic TB impact on the whole building energy performance. (Ascione et al., 2012, 2013). Understanding the holistic impact of TBs and their heat paths highlights the importance – on a macro scale – that these details be addressed rather than ignored or over-simplified.

Standard BS EN ISO 14683 (BSI, 2017h) offers default transmittance values, for some common TB typologies, to be incorporated into BPE models – with an accuracy of around ± 50%. Using TB catalogues (Passive House, 2021) and/or manually calculating transmittance values provides an accuracy of ± 20%. However, the most accurate TB transmittance is determined by numerical calculation in accordance with BS EN ISO 10211 with a typical accuracy of ± 5% (BSI, 2017h, 2017c).

In the UK, the BRE provide guidance and best practice to quantify the TB effect (BRE, 2017; Ward, 2006; Ward & Sanders, 2016). Evaluating transmittance caused by linear- or point-TB is difficult to measure or calculate analytically, therefore numerical methods have been developed to predict this multi-dimensional heat flow. Procedures for various construction types can be seen in BR 497 (Ward & Sanders, 2016), summarising from BS EN ISO 10211 (BSI, 2017c). Internationally, PassivHaus (BRE, 2019b) offer the highest level of certification in terms of buildings energy performance. Their Passive House Planning Package (PHPP) is another standard assessment procedure for surveying buildings (Passipedia, 2019) and assessing energy performance, similar to UK's SAP. PassivHaus deal with TB in a same manner as the BRE: both institutes aim for a TB free building design but where unavoidable, they heavily rely on simulation software and/or thorough on-site surveys by experienced technicians (Ward & Sanders, 2016) to quantify TB for their energy assessments.

This section highlights the main PG contributors in building physics. In terms of TB FE analysis, PG issues stem from applying assumptions within the model; the simulation response is very sensitive to the prescribed surface resistance. In these works, models are informed with physical measured therein PG caused by each must be considered. TB impacts and their mitigation using thermal breaks are described in the following section using examples from literature showing the current state-of-the-art whilst illustrating the lack of standardised quantitative measurement methods of TB evaluation.

2.2 Characterisation and modelling thermal bridges

Understanding the principles of heat transfer are essential for measuring, characterising, and modelling TB, hence, in this section, the heat transfer mechanisms relevant to building physics are explained whilst outlining the standardised approaches for their analysis.

2.2.1 Heat transfer in buildings

Heat-transfer supplements the first and second laws of thermodynamics by predicting the energy transfer taking place due to a temperature difference (J. Holman, 1988). Thermodynamics deals with systems of equilibrium, whereas heat-transfer explores how heat energy is transferred and predicts the rate at which the exchange happens. Hence, heat-transfer-rate is the desired output of analysis. The three modes of heat-transfer are conduction, convection, and radiation (J. P. Holman, 1972).

Conduction refers to the transfer through solid bodies induced by lattice vibration and free transport of electrons. The rate is determined by understanding, the material conductivity, thickness, area, and temperature difference. The governing formula, Fourier's law of conduction (J. P. Holman, 1972), is shown below in equation 3:

$$q = -K.A.\frac{\partial T}{\partial x} \qquad 3$$

Where $'q'$ is the heat [W], 'K' is the conductivity [W/mK], 'A' is the area under consideration [m^2], '∂T' is the respective temperature differential [K], and '∂x' is the change in thickness of material [m].

Convection obeys Newtons law of cooling (Munson et al., 2013), see equation 4:

$$q = hA(T_w - T_\infty) \qquad 4$$

Where $'q'$ is the heat [W], 'h' is the convective coefficient [m^2K/W], 'A' is the area [m], 'T_w' is surface temperature [K], and 'T' is the ambient fluid temperature [K].

Evaluation of the convection coefficient 'h' is often achieved empirically or through dimensional analysis; implementing sensitive variables affecting the thermal boundary layer (usually derived from fluid flow speed, viscosity, or surface roughness). However, off-the-shelf assumptions are usually used to characterise the phenomena (BSI, 2017b).

Thermal radiation is a type of electro-magnetic radiation caused by a temperature difference (J. P. Holman, 1972). It is governed by the Stefan-Boltzmann Law, adapted from 'Planks blackbody radiation law' (J. Holman, 1988) which shows that a blackbody is an idealised object that radiates according to the fourth power temperature differential '$T_1^4 – T_2^4$'; because of this, Stefan-Boltzmann introduced a proportionality constant 'σ' (5.667×10^{-8} [W/m^2K^4]) (J. P. Holman, 1972). This holds true for idealised blackbodies (J. P. Holman, 1972), however, a dimensionless ratio known as the emissivity 'ε', must be applied to 'grey-bodies' to account for an objects reflectivity in an unideal reality. It is a ratio of the 'grey-bodies' radiance to the ideal 'blackbody' radiance at the same temperature and spectral interval. Radiation travels in straight lines so surface orientation must also be considered, since not all the radiation leaving one surface will reach the other – some will be lost to the surroundings (J. P. Holman, 1972) – to account for this a view factor 'F_g' is applied, see equation 5:

$$q = \varepsilon F_g \sigma A(T_1^4 - T_2^4) \qquad 5$$

Where 'q' is the heat [W], 'ε' is the emissivity, 'F_g' is the view factor, 'σ' is the proportionality constant [W/m^2K^4], 'A' is the area [m^2], and '$T_1^4 – T_2^4$' is the temperature difference $[K]$.

Heat-transfer in the built environment uses a combination of these modes of transfer, especially the total heat loss through the building fabric, known as transmittance, which incorporates all these mechanisms into a single metric (U-value).

As well as fabric transmission, other contributing HTCs are categorised as transmissions through the ground, unconditioned space (ventilation), and to adjacent buildings, hence estimations can be made of the building's total energy demand.

The overarching supporting standard *Energy Performance of Buildings - Hygrothermal performance of building components and building elements PD CEN ISO/TR 52019-2:2017* (BSI, 2017a) underpins the association of all the relevant standards, establishing a structure for assessing the energy performance of new and existing buildings in the general EPB framework. It explains and justifies all the relevant standards regarding energy performance in buildings, supporting correct understanding and use of the current methodologies. Figure 15 depicts linkages between standard documents:

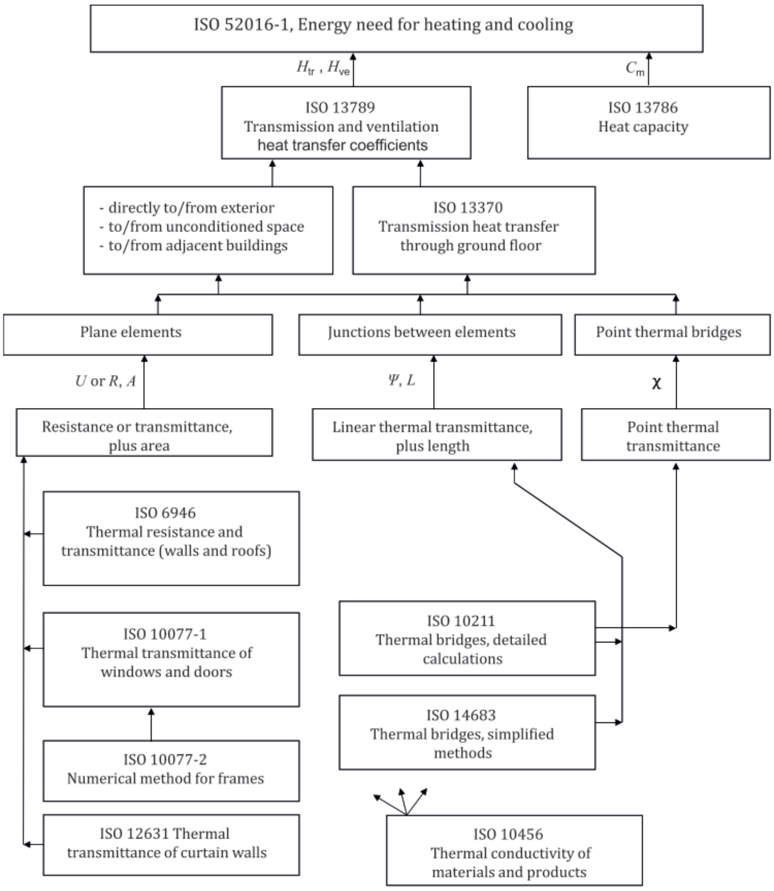

Figure 15 – Linkages between documents (BSI, 2017a).

Within BS EN ISO 7345 (BSI, 2018a) *Thermal Performance of Buildings and Building Components – Physical Quantities and Definition* thermal insulation physical quantities, their symbols, and units are defined. These are referred to in all subsequent standards, of which, the first to mention is *BS EN ISO 13789 (Thermal performance of buildings-Transmission and ventilation heat transfer)* which specifies a calculation method for determining the thermal performance of a whole building or part of it – and provides conventions for estimating individual HTCs. The total transmission of the building is calculated in equation 6, unifying all transmission and ventilation HTCs (BSI, 2017g).

$$H_{tr} = H_d + H_g + H_u + H_a \qquad 6$$

Subscripts 'tr', 'd', 'g', 'u', 'a' refer to transmission heat transfer, direct transmission through the envelope, transmission through the ground, transmission through unconditioned spaces, and transmission between adjacent buildings, respectively. These are calculated individually using separate standards.

The total HTC – as a combination of all other transmission coefficients – can then be multiplied by the average temperature difference to determine the total energetic loss [kWh] from the building.

The transmission of heat from adjacent buildings, 'H_a', is covered by BS EN ISO 13789:2017 (BSI, 2017g) with a simple calculation if the direct HTC between conditioned space and the adjacent building, their respective temperatures, and the ambient temperature, are known. The transmission of heat transfer to the ground, 'H_g', is covered by BS EN ISO 13370 (BSI, 2017e) providing calculation methods for the coefficient on a weekly, monthly, or annually basis – considering the dynamic nature caused by thermal inertia of the ground. Dynamic thermal characteristics (heat capacity and thermal mass) are covered more thoroughly in BS EN ISO 13786 (BSI, 2017f).

The transmission of heat through unconditioned spaces, 'H_u', incorporates both ventilation 'H_{ve}' and direct transmission between environments 'H_d' in its calculation. The ventilation component 'H_{ve}' is calculated using the density [kg/m^3], specific heat [J/Kg.K], and air flow rate [m^3/h], see equation 7:

$$H_{ve} = \rho . c_p . q \tag{7}$$

Where 'H_{ve}' is the ventilation heat transmission coefficient, 'ρ' is the density of air [kg/m^3], 'c_p' is the specific heat capacity of air [J/Kg.K], and 'q' is the volumetric flowrate [m^3/s] (BSI, 2017g).

The direct transmission between environments, 'H_d', through the separating building envelope fabric, see equation 8:

$$H_d = \sum_i A_i . U_i + \sum_k l_k . \Psi_k + \sum_j \chi_j \tag{8}$$

Where, 'H_d' is the direct fabric HTC [W/K], 'A_i' is the area of element 'i' of the building envelope [m^2], 'U_i' is the thermal transmittance of element 'i' of the building envelope [W/m^{2}K], 'l_k' is the length of the linear-TB$_k$ [m], 'Ψ_k' is the linear thermal transmittance of the linear-TB$_k$ [W/mK], and 'χ_j' is the point thermal transmittance of the point-TB$_j$ [W/K].

Analytical calculations apply theory in a logical way to quantifiably diagnose a problem. When the problem complexity increases, analytical solutions become impractical. Numerical approximations, on the other hand, break a complex problem down into simpler subdivisions enabling a faster solution – typically calculated using computer software. Another way to determine building physics parameters is by experimental measurement; methods include both destructive and non-destructive, either in laboratory or in-field (in-situ) conditions.

The following section addresses the standardised methodologies of HTC analysis in building physics. Firstly, analytical calculations are described, followed measurement techniques, and finally numerical estimations.

2.2.2 Analytical calculations – building fabric transmittance and resistance (U-value)

Often, especially in new-builds, prior knowledge of construction materials and their thermo-physical properties are well understood, therefore the U-value can be analytically calculated as per *BS EN ISO 6946 "Building components and building elements – Thermal resistance and thermal transmittance – calculation methods"* (BSI, 2017b), by summing up all the thermal resistances from each contributing mechanism (conductance and SR), see equation 9:

$$U = \frac{1}{\sum R_{th}} = \frac{1}{R_{si} + R_{\lambda} + R_{se}} \qquad 9$$

Where, 'R_{th}' the total thermal resistance, 'R_{λ}' is the conductive resistance, and 'R_{si}' and 'R_{se}' are the internal and external surface resistance, respectively, which both encapsulate convective and radiative mechanisms of heat transfer.

Conductance theory (BSI, 2017b, 2018a) obeys Fourier's law. Calculation complexities can arise if the conductivity is considered temperature dependant (Dascalaki et al., 1993), also evidence shows that moisture content (wet brick or mortar) alters the conductivity, adding uncertainty to the conductivity assumption (Budaiwi & Abdou, 2013; Papadakos et al., 2021). Neglecting these factors to simplify the calculation, the thermal resistance due to conduction 'R_{λ}' [m^2K/W] is seen in equation 10:

$$R_{\lambda} = \frac{dx}{\lambda} \qquad 10$$

Where 'λ' [W/mK] and 'dx' [m] are the thermal conductivity and the thickness of the material, respectively. BS EN ISO 10456 (BSI, 2007) gives typical design values for the thermophysical properties (conductivity, density, specific heat capacity, and water vapor resistance factor) of many materials.

The SRs (surface resistance) 'R_{si}' and 'R_{se}' encapsulate both radiative and convective modes of transfer between environment and surface, internally and externally, respectively. Conventional assumptions, based on heat flow direction for external and internal environments, are provided for plane surfaces in the absence of specific boundary layer conditions: Annex C of BS EN ISO 6946 details empirical calculations to estimate the convective (based on wind speed) and radiative (based on emissivity and considering the mean thermodynamic temperature of the surface including its surroundings) coefficients, whilst instructing how to combine these components and calculate the respective total SR (BSI, 2017b).

NCM utilise knowledge of the building structure, properties, and conditions to estimate the building performance analytically. Although these analytical estimations prove useful, huge gaps remain between actual and designed performance, demonstrated by comparing theoretical methodologies with experimental measurement (Fitton, 2021b), hence the physical measurements relevant to building physics are described in the following section.

2.3 Measurements

Although measurements are tangible and alleviate some PG caused by analytical assumptions, they do not flawlessly interpret reality. Aspects such as sensor capabilities, operating conditions, human error, etc, all contribute to some uncertainty in the measurement, which, as a scientist, should be understood to a reasonable level of confidence.

When applying standardised assumptions in analytical calculations evaluating buildings HTC in practice, many idealisations are required leading to a disparity between the intended and actual energy performance in buildings. These PGs can stem from a multitude of sources, especially in old buildings since construction materials degrade over time (Kordatos et al., 2013). Other PGs typically affecting new builds manifest from: manufacturers overestimating specifications, poor workmanship in the construction (on any level) causing a detrimental impedance to the insulating barrier, or as shown in these works, neglecting to treat TB.

In this section, methods measuring SR, calorific losses (hot box, co-heating), transmittance (HFM and IR), and finally some novel TB measurement techniques are discussed.

2.3.1 Surface resistance (SR)

As mentioned, BS EN ISO 6946 provides analytical calculation methods of the thermal resistance and (its reciprocal) the thermal transmittance of opaque building elements and components (BSI, 2017b).

However, the SR can be measured directly (Evangelisti et al., 2016) since the flux (transferring heat from air-to-surface) and the driving temperature differential between air-and-surface, can both be measured, see equations 11 & 12:

$$q = \frac{\theta - \theta_s}{R_s} \qquad 11$$

Where, 'q' is the density of heat flow [W/m^2], $\boldsymbol{\theta}$ is the air temperature (internal or external); $\boldsymbol{\theta_s}$ is the surface temperature; and $\boldsymbol{R_s}$ is the SR [m^{2}K/W] (BSI, 2017b). Rearranging for 'R_s':

$$R_s = \frac{dT}{q} \qquad 12$$

Where 'dT' is the temperature differential in [°K] between air and surface.

This measurement encapsulates both radiative and convective transmission mechanisms; it is a sensitive parameter necessary for an accurate transmittance estimation, or for further use in model parameterisation (Evangelisti et al., 2017).

2.3.2 Laboratory measurement (hot box)

A laboratory-based heat transfer experiment, 'Hot Box Testing', is a method which in essence measures the calorific loss through an investigated specimen, usually a sample of a building envelope. The tests are designed in accordance with BS EN ISO 8990:1996 (BSI, 1996a) which refers to procedures given in standards:

- EN 12567-1 (BSI, 2010) Thermal performance of windows and doors – Determination of thermal transmittance by the hot-box method.
- EN 12412-2 (BSI, 2003) Thermal performance of windows, doors and shutters – Determination of thermal transmittance by hot box method-Part 2: Frames.
- EN 1946-4 (BSI, 2000) Thermal performance of building products and components – Specific criteria for the assessment of laboratories measuring heat transfer properties – Part 4: Measurements by hot box methods
- EN 1745 (BSI, 2012b) Masonry and masonry products – Methods for determining thermal properties.
- EN 1934 (BSI, 1998) Thermal performance of buildings – Determination of thermal resistance by hot box method using heat flowmeter – Masonry

BS EN ISO 8990-1996 (BSI, 1996a) presents two different approaches to the hot box tests. In general both methods rely on monitoring the power input to sustain an internal temperature, and by knowing the heat losses through the walls and flanking elements of the apparatus, the heat loss through the investigated test sample can be derived.

Firstly, the 'Calibrated hot box' method involves two highly insulated connected chambers, thermally separated by the investigated specimen. Several calibrated tests, over a wide range of temperatures are carried out to accurately quantify the precise heat loss through the external walls, edges, and corners, allowing accurate predictions of the heat loss through the test sample.

Secondly, the 'Guarded hot box' method uses a slightly different apparatus. A metering box, situated inside a guarded hot box (highly insulated container), houses a small study sample to test at a hot condition. This way the temperature and air movement inside and outside the metering box needs to be controlled ensuring no heat transfer through the metering box walls.

The main difference in these methods is that calibration is not required in the guarded hot box and the test area for the specimen is a lot smaller (Prata et al., 2018).

(Ghazi Wakili & Tanner, 2003) compared hot box testing with HFM and numerical calculation methods finding good agreement between the three approaches, especially when the model is refined with measurement. (Asdrubali & Baldinelli, 2011) compared the Russian, American, and international standards for hot box apparatus. A maximum deviation of 3% was found between the three methods when applied to determine the thermal resistance of the same test sample.

(Martin, Campos-Celador, et al., 2012) used a guarded hot box facility (metering box) to test the dynamic behaviour of a TB, comparing experimental results with numerical calculation. Limitations in using the metering box primary stem from the size of the monitoring area, also, the guarded hot box caused noticeable multi-dimensional flux which distorted the results. Still, the largest comparable differences found between the measurement and the standardised numerical calculation method (BS EN ISO 10211) was 8%.

In conjunction with a 'Calibrated hot box' apparatus, a laboratory based experiment (Prata et al., 2018) used HFM and thermocouples to measure the flux and temperature gradients across the surface of a corner-corner linear TB junction, see Figure *16*:

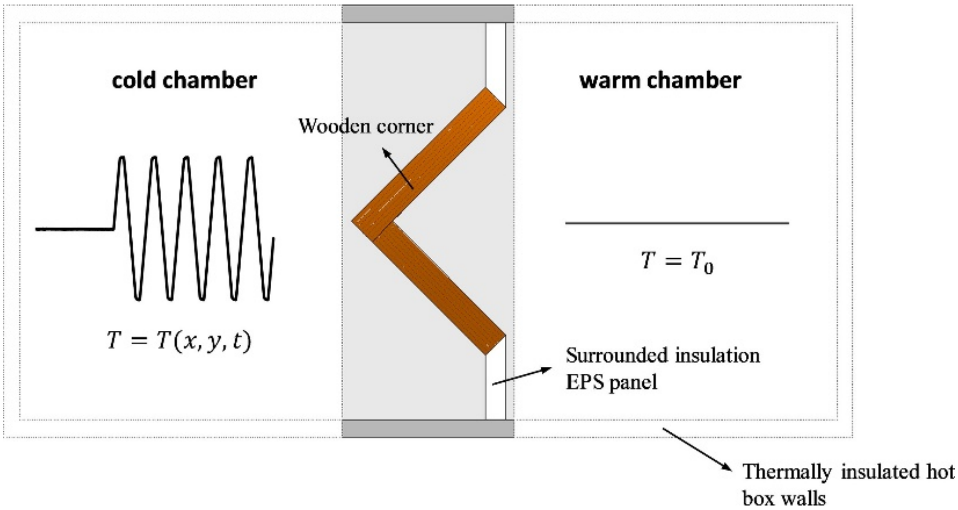

Figure 16 – Top view of test chamber (Prata et al., 2018).

Internally, an array of 44 thermocouples were fixed to the test specimen in a line to measure the surface temperature gradient leading into the corner, up to about 0.6m from the corner – 2 extra sensors monitored the hottest and coldest surface temperatures, both externally and internally. HFM and thin-film flux sensors, measuring the heat flux through the wall, were positioned in the centre of the panel and near the corner, on each side, see Figure *17*:

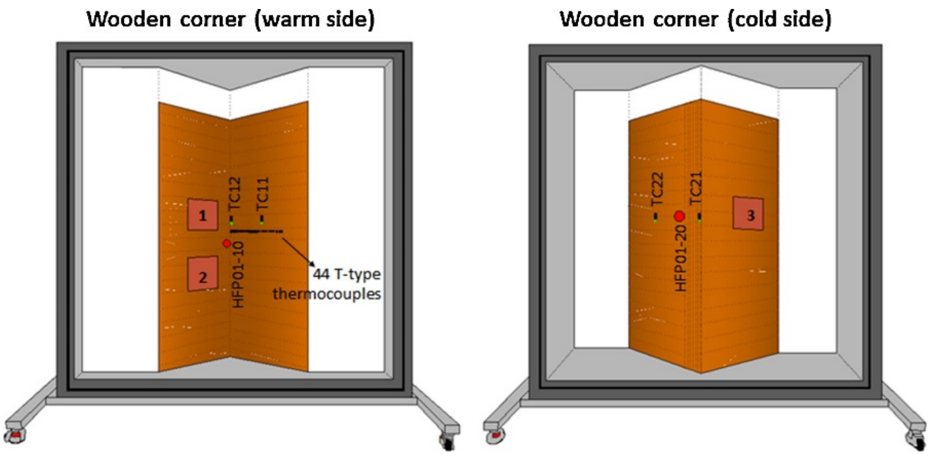

Figure 17 – Each side of the linear TB studied (Prata et al., 2018).

As expected, the maximum surface temperatures and minimum heat flux occur in the middle of the panel (away from the TB), whilst the maximum heat flux and minimum surface temperatures were observed in the corner (closest to the TB) (Prata et al., 2018).

By analysing the time-series measurements of the internal and external surface temperature and fluxes, evaluated at intermittent surface locations leading into the corner (Prata et al., 2018), the dynamic testing results from the 'Calibrated hot box' experiment showed a higher thermal phase lag and amplitude at the corner.

Where in-situ measurement methods quantifying TB are seldom found in literature due to the lack of standardised guidance, this novel measurement technique evaluating linear-TB transmittance is refreshing. Conversely, in-situ HTC and U-value evaluation are standardised as it is somewhat easier to capture 1D heat flow with measurement: these are discussed in the following section.

2.3.3 Total HTC measurement (co-heating)

Co-heating testing is a one-dimensional measurement method (Jack et al., 2017) (Mangematin et al., 2012), (Subbarao et al., 1988) (Alzetto et al., 2018) (C. A. Gorse et al., 2013) (C. Gorse et al., 2012) similar to hot box testing (Prata et al., 2018) (Martin, Campos-Celador, et al., 2012) (BSI, 1996b) in that they both measure the calorific losses either from the entire building or through an element, offering interesting experimental opportunities to capture TB behaviours.

Direct measurements of the total HTC is possible which negates the necessity to assume conditions or have any prior knowledge of the construction (Mangematin et al., 2012). Co-heating is a common method to evaluate whole-building thermal performance (Bauwens & Roels, 2014) and as such various methods have been developed:

- PRISM (Princeton scorekeeping method) (Fels, 1986)
- STEM (short term energy monitoring) (Subbarao et al., 1988).
- PSTAR (primary and secondary terms analysis and renormalisation) (Johnston et al., 2012)
- MPR (measured performance rating)
- QUB (quick measurements of energy efficiency of buildings)
- VeriTherm (quick overnight screening test) (Cambridge Consultants, 2021)

Essentially, co-heating monitors the heat power input to maintain a constant internal temperature in a building as well as the temperature differential between environments. This allows calculation of the total HTC [W/K] (Alzetto et al., 2018; Bauwens & Roels, 2014; Farmer et al., 2016; Johnston et al., 2012).

2.3.4 In-situ Transmittance (U-value) measurement

To evaluate the transmittance through a wall; estimations, either analytical calculations or in-situ measurement are widely accepted (BSI, 2018b). Building Regulation Part L (HM Government, 2017) state guidance can be found in: BR 443 (Anderson, 2006), BS EN ISO 9869 (BSI, 2017b), or CIBSE Guide Section A3 (CIBSE, 2021) for non-destructive measurement and calculation methods estimating fabric transmittance (U-value). Also, guidance is provided regarding destructive testing, however this is less often practiced.

2.3.4.1 Destructive methods

Primarily an analytical calculation standard, BS EN ISO 6946 – Annex C (BSI, 2017b) describes two destructive methods measuring fabric transmission: the sampling method (boring a whole to determine the thickness, moisture content, and density of the respective wall layers) or the endoscope method (also requires drilling a small hole allowing the thickness to be determined, this causes less damage but can only visually inspect, therefore seen as less accurate, especially for moisture content). These methods are only generally exercised to explain unexpected U-value measurements, to apply correction factors due to thermal inertia, or, to examine workmanship, structural integrity, and moisture content (BSI, 2014).

Destructive sampling involves taking a core sample from a wall to be investigated, the thickness and conductivities of each layer can then be determined and applied to analytical calculations (BSI, 2017b). Comparing this destructive method with the standardised non-destructive measurement method, (Desogus et al., 2011) found differences between the methods of 8% and 18%, depending on temperature difference.

2.3.4.2 Non-destructive

The preferred standard measurement method in the UK is BS EN ISO 9869-1 (BSI, 2014) which shows two non-destructive methods – average and dynamic – developed using HFM instruments.

BS EN ISO 9869 "*Thermal insulation – building elements – in-situ measurement of thermal resistance and thermal transmittance – Part 1*" (BSI, 2014) describes the measurement methodology to calculate the U-value. Thermal resistance and conductance (surface-to-surface) are defined, explaining how they relate to fabric transmission. Also, the measurement apparatus and relevant calibration procedures for HFM (heat flux meter) and temperature sensors are described. Experimental procedures advise the correct installation of sensors, mentioning the importance of identifying appropriate measurement area (which should be indicative of one-dimensional heat flux and avoid inhomogeneities, cracks, TB, influence from heating or cooling systems, fans etc.) and the use of thermal paste to encourage good thermal contact between the HFM sensor and wall – similar guidance is given regarding the proper install of surface and air temperature sensors (BSI, 2014). Identification of potential inhomogeneities within the studied wall is possible following qualitative infrared thermography advice in accordance with BS EN ISO 6781:1983, revised in 2015 (BSI, 2015b).

Regarding data collection, sensor signals should be recorded at fixed intervals continuously or a period of complete days. At least 72 hours of acquisition time is advised depending on the thermal mass, temperature differential, or method chosen (BSI, 2014). The simpler **averaging method** assumes the conductance or transmittance can be calculating by dividing the mean density of heat flow rate by the mean temperature difference.

By computing the estimate after each measurement, asymptotic convergence is observed, providing between ±14–28% uncertainty; this uncertainty estimation is based on RSS and arithmetic sum, respectively, both of which consider external conditions for in-situ measurement.

The more **sophisticated dynamic method** is designed to better address thermal inertia and is more applicable to heavy walls with large thermal mass (BSI, 2014). Annex A and B show the averaging and dynamic methods in greater detail. (Gaspar et al., 2016) compared these two U-value measurement methods with theoretical assumptions finding that, over 3 case-studies smaller differences were obtained using the dynamic method over the average method in every case, although acceptable agreement was found using the average method.

The American Society for Testing and Materials International (ASTM International) have similar standards: ASTM C1155 (ASTM, 2013b) *"Determining Thermal Resistance of Building Envelope Components from the In-Situ Data"* and ASTM C1046 (ASTM, 2013a) "*In-Situ Measurement of Heat Flux and Temperature on Building Envelope Components"* consider dynamic conditions. Also, ASTM C518-17 (ASTM, 2015) the *'American Standard Test Method for Steady-state Thermal Transmission Properties by Means of the Heat Flow Meter Apparatus'* covering the steady-state measurement of thermal transmission using heat flow meters.

BR 443 – *Conventions for U-value calculations* (Anderson, 2006) guides the use of the measurement methods by identifying their appropriateness depending on construction type, providing information regarding their use, and presenting data relevant to typical UK constructions. These methods comply with building regulations and U-values obtained can be used in relevant SAP or SBEM calculations.

Comparing theoretical and measured U-values, a range between 4% to 75% was found in a study by (Asdrubali et al., 2014). Further, (Evangelisti et al., 2015) showed differences between theoretical and measured U-values between 17% and 153%. Authors generally owe this deviation to a lack of knowledge of the thermophysical properties of the wall and its thickness (for analytical calculation) and experimental systematic errors.

Infrared Thermography (IRT) is another non-destructive method, and as mentioned can be employed qualitatively to highlight potential faults in the building envelope (Balaras & Argiriou, 2002; Lucchi, 2017a, 2017b, 2018; Martín Ocaña et al., 2004) (Garrido et al., 2018) advising proper installation of HFM (BSI, 2018b) which should avoid thermal anomalies such as damaged areas or moisture content (Rosina & Spodek, 2003) (Barreira et al., 2012) which distort the heat flux leading to erroneous measurements (Asdrubali et al., 2012; Atsonios et al., 2018; Bros-Williamson et al., 2014; BSI, 2018b; Nardi et al., 2017; Rye & Scott, 2012).

The following section describes how IRT can be used quantitatively to measure the fabric U-value. First explaining radiation theory and instrument calibration, the standardised methods are presented followed by novel techniques, external surveys, automation, post-processing, and finally applications relevant to TB detection.

2.3.5 Infrared

Quantitative infrared methods measuring the transmittance (U-value) are standardised in BS EN ISO 9869-2 (BSI, 2018b), which is explained later. First, the IR theory (briefly discussed later in the equipment section) and instrument calibration will be described.

There are three sources of radiation received by the camera detector: emission from the object; emission from the atmosphere; and reflected radiation from the surroundings. The assumption is made that the target object is opaque (i.e. zero transmission of infrared radiation through the object) (T. Taylor et al., 2014) and that atmospheric emission varies with air temperature, humidity, and distance from the object (Barreira et al., 2012).

IRT detects the radiant thermal energy which is emitted from bodies and then translates it to temperature values (Walker, 2004). Radiant thermal energy is the energy emitted by the body itself, together with the energy reflected by the surroundings across the surface of the body (Kylili et al., 2014). The total radiant energy emitted by an object is related to its emissivity and temperature according to Stefan-Boltzmann's Law see equation 13.

$$R = \varepsilon \sigma T^4 \qquad (13)$$

Where, R is the irradiance [Wm^{-2}]; ε is the emissivity; σ is the Stefan-Boltzmann constant $5.67x10^{-8}$ $[Wm^{-2}K^{-4}]$, and T is the temperature [K].

The emissivity of an object varies with its temperature, the wavelength of radiation, and the angle at which it is viewed, although this can usually be ignored considering the typical temperature and wavelength variations found within buildings. Similarly, no significant emissivity variation is seen for angles up to 45° from perpendicular (Pearson, 2011). Advice suggest that the final image taken must not be perpendicular to the target object in order to avoid the camera seeing a reflection of its own lens, known as the "Narcissus effect"(Asdrubali et al., 2012).

A sensitivity analysis performed by (Fokaides & Kalogirou, 2011) deduced that the 'reflected apparent temperature' and the assumed 'emissivity' of the buildings surface are the most sensitive variables in the U-value calculation using the IRT method which have significant importance regarding precision of the results.

2.3.5.1 Calibrating (IR)

Ensuring the 'reflective apparent temperature' and object 'emissivity' are calibrated in the IR camera is crucial to the accuracy of the quantified surface temperature values in the image (Marshall et al., 2018; Mauriello et al., 2019; Nardi et al., 2018; O'grady, 2018). This is briefly explained later in the 'equipment' section: basically, using another measurement instrument to quantify the temperature of a target point, the emissivity and reflected apparent temperature settings in the camera are adjusted until the temperatures match.

Calibrating thermal images typically assigns an object a single value of emissivity. Objects with high emissivity emit relatively higher proportions of IR radiation and reflect lower proportions of radiation from the surroundings – providing a more reliable surface temperature compared with low emissivity objects. Low emissivity surfaces, like windows or mirrors, act as reflectors of IR radiation, therefore it is difficult to take surface temperature measurements using thermography (T. Taylor et al., 2014).

The total radiation reflected by a body depends on the temperature of the surroundings, the objects emissivity, and reflectivity. Reflectivity of opaque bodies can be calculated with equation 14:

$$\rho = 1 - \varepsilon \tag{14}$$

Where 'ρ' is the reflectivity and 'ε' is the emissivity.

For the purpose of calibration, the surrounding area is considered as a uniform black body and is assigned an effective temperature (T. Taylor et al., 2014).

The reflected temperature of the surroundings is calculated by measuring the average temperature of the surrounding surfaces that exchange infrared radiation with the target objects. This should not compensate for reflection or atmospheric attenuation and measurements should be averaged in proportion to their view factor with the target object (T. Taylor et al., 2014).

(Datcu et al., 2005) showed alternatively, a highly reflective and diffusive aluminium mirror can be placed on a target object to measure the reflective temperature. Similarly, (Fokaides & Kalogirou, 2011) and (Asdrubali et al., 2012) used a crumpled and re-flattened aluminium foil to the same effect. The values of emissivity, distance from the target, atmospheric temperature, relative humidity and ambient temperature of the surroundings are entered into the IR camera or image analysis software to calibrate the thermal image.

All of the above needs to be considered for acurate quantification of U-value measurement – which is explained in the subsequent sections.

2.3.5.2 U-value measurement (IR)

BS EN ISO 9869-2 (BSI, 2018b) stipulates quantitative infrared methods measuring fabric transmittance (U-value) in-situ. The working principles are described: irradiance drives the relationship of the fluid-surface heat transfer coefficient and the temperature difference between surface and air, see equation 15 & 16:

$$Q = h(\theta_n - \theta_s)A \tag{15}$$

Where 'Q' is heat flux [W], 'h' is the fluid-surface heat transfer coefficient [W/m^{2}K], 'A' is the area [m^2], 'θ_n' is the environmental temperature, and 'θ_s' is the surface temperature [K].

This evaluates the heat transfer through the walls fluid boundary layer considering both radiative and convective mechanisms, which in theory should remain constant through the wall where 1D heat flux is realised. Applying the environmental temperature differential and wall area, the U-value can be calculated using equation 16:

$$U = \frac{Q}{(\theta_{ni} - \theta_{ne})A} \tag{16}$$

Where 'U' is the transmittance, 'θ_{ni}' is the internal environmental temperature, and 'θ_{ne}' is the external environmental temperature.

The standard explains how the fluid-surface heat transfer coefficient 'h' (equation *16*) – as a combination of radiation and convection – can be calculated accurately using ET sensors (to determine the **E**nvironmental **T**emperatures externally and internally), HTC sensors, thermocouples, and calibrated IR thermography.

Measurement rules:

- Measured area position should be away from any cooling or heating devices and avoid drafts, also, it should be free of visual interference impeding the field of view for the IR camera.
- Environmental temperature difference must be greater than 10°C.
- Inside region must be sealed, avoiding temperature fluctuations.
- Follow calibration procedure.
- Recommended measurement period of 3 days or until measurements converge to within 10%.

Since many factors can affect the accuracy of IR measurement, annex D and E of BS EN ISO 9869-2 (BSI, 2018b) illustrates an example of a thorough uncertainty analysis that should be conducted for this U-value estimation method.

The U-value measurement procedure using IR (Nardi et al., 2018) is summarised in Figure 18 below:

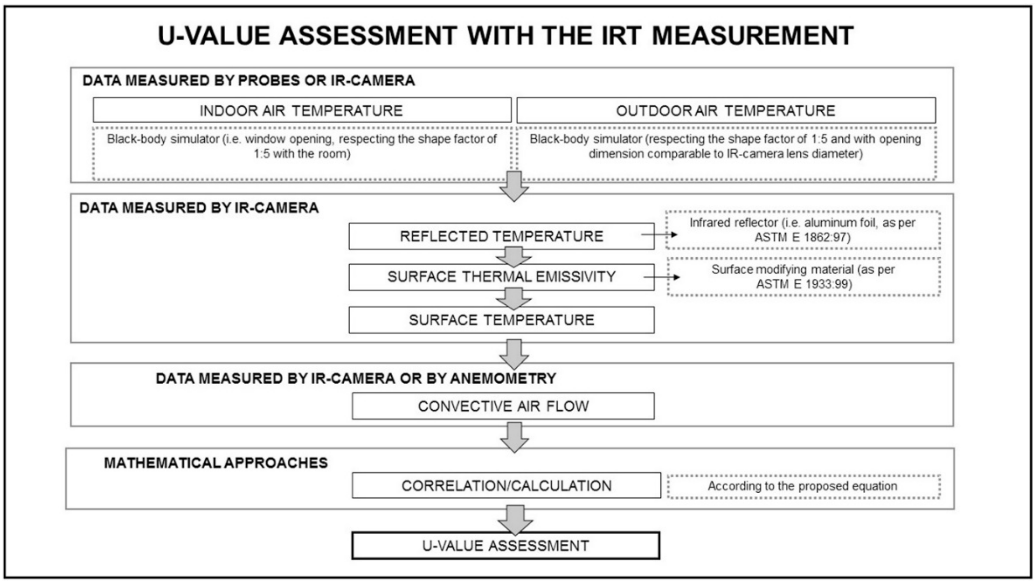

Figure 18 – IRT assessment of U-value procedure (Nardi et al., 2018).

Research has conducted investigation of both inside and outside surveys; internal measurements have controllable boundary conditions (Albatici et al., 2013; Simões et al., 2014) whereas external measurements are affected by environmental conditions (Tejedor et al., 2017, 2018).

When performing outdoor quantitative IRT surveys, important parameters include: wind speed influence (Albatici et al., 2015; Hoyano et al., 1999; Nardi et al., 2014); solar radiation (overcast skies are advised and the recommended time of day for surveys is early morning before sunrise, or late in the evening after sunset – to avoid solar radiation) (Dall'O' et al., 2013; Fokaides & Kalogirou, 2011; Nardi et al., 2014, 2016); the target distance from the camera; air temperature difference (Albatici & Tonelli, 2010; Dall'O' et al., 2013; Fokaides & Kalogirou, 2011; Hoyano et al., 1999; Marino et al., 2017); apparent surface temperature (Albatici & Tonelli, 2010; Fokaides & Kalogirou, 2011; Kato et al., 2007; Madding, 2008; Marino et al., 2017); reflective temperature (Albatici et al., 2015; Dall'O' et al., 2013); object emissivity (Albatici et al., 2015; Albatici & Tonelli, 2010; Dall'O' et al., 2013; Fokaides & Kalogirou, 2011).

Authors have made modifications to this standardised U-value measurement depending on the situation the method is applied. (Nardi et al., 2016) presented equations 17 & 18 describing a walls transmittance using infrared, adapting the equations first seen in (Madding, 2008) which includes the radiative ('$4\varepsilon\sigma T_m^3$') and convective ('h_c') terms and the internal ('T_{in}') and external ('T_{out}') environmental air temperatures:

$$U = \frac{4\varepsilon\sigma T_m^3\left(T_s - T_{refl}\right) + h_c(T_s - T_{in})}{T_{in} - T_{out}} \quad (17)$$

Where 'T_m' is the mean,

$$T_m = \frac{T_s + T_{refl}}{2} \quad (18)$$

Emissivity and the Stefan-Boltzmann constant are together multiplied by the third power of the mean temperature difference (averaged between the internal wall temperature T_s and the reflected temperature T_{refl}). The reflected apparent temperature 'T_{refl}' is measured by the IR camera in calibration.

(Fokaides & Kalogirou, 2011) modified this equation by involving the third power of the surface temperature (instead of the mean temperature), see equation 19:

$$U = \frac{4\varepsilon\sigma T_s^3\left(T_s - T_{refl}\right) + h_{in}(T_s - T_{in})}{T_{in} - T_{out}} \tag{19}$$

Where, 'ε' is the emissivity, 'σ' is the Stefan-Boltzmann constant, 'T_s' is the surface temperature, 'T_{refl}' is the reflected apparent temperature, 'T_{in}' is the internal air temperature, 'T_{out}' is the external air temperature, and 'T_s' is the internal convective heat transfer coefficient.

Both of these equations (*17*& *19*) obtain the U-value as a ratio of the sum of the radiative and convective heat transfers to the difference in temperature between environments.

(Dall'O' et al., 2013) proposed a different balance for transmittance based on external surveys, utilising the empirical external convective coefficient (Jürges equation) equation 20 & 21:

$$U = \frac{h_{out}(T_s - T_{out})}{T_{in} - T_{out}} \tag{20}$$

With,

$$h_{out} = 5.8 + 3.8054v \tag{21}$$

Where T_s, T_{out}, and T_{in} are the outside wall, outdoor air and indoor air temperatures, respectively. The external convective coefficient h_{out} (Jürges' equation) is manageable with wind speed v <5m/s.

This was implemented for external surveys in (Albatici et al., 2015) who refined a calculating formula from previous works including a radiative term as well as a modified Jürges equation for external convection (equation 22):

$$U = \frac{\varepsilon\sigma\left({T_s}^4 - {T_{out}}^4\right) + 3.8054(T_s - T_{out})}{T_{in} - T_{out}} \tag{22}$$

Due to the variability of external parameters such as wind speed, internal surveys have favourable experimental conditions. In which case, the method by (Fokaides & Kalogirou, 2011) (considering the surface temperature rather than the mean, ass seen in) provides more reliable results.

For this reason equation *17* was adopted by (Marshall et al., 2018) who suggested using IRT is more representative of the overall fabric heat loss than point measurements (such as heat flow meter methods), finding large variations in U-values across a homogeneous wall when comparing high and low-resolution IRT with HFM methods, however it proved to be time intensive. Taking one image of the entire wall is considered a low-resolution image, whereas high-resolution images are stitched together from multiple images of the wall in post-processing – increasing resolution. Recommendations were made to apply the high-resolution technique in a real building (not the lab where conditions can be controlled) to investigate its feasibility, also increasing data capture to identify if low-resolution techniques are sufficient (Marshall et al., 2018).

Compared to point HFM measurements, IRT assessment offers an opportunity to fully understand the U-value distribution across a wall, since inherent inhomogeneous compositions of the building envelope (changes to material thermal conductivity or thickness) produce variation to the wall's resistance. Not only can IRT better identify U-value distributions over the building envelope, but TB can be detected. (Garrido et al., 2018) builds on an automatic detection criterion developed by other authors, attempting to reduce the number of falsely identified TBs and increasing the number of real TBs detected. Thermal imaging performed by a human operator involves subjective interpretation, relying on operator expertise, therefore an automation of this interpretation is a proposed solution. This demonstrates an example where IRT and computer modelling can be used together to support the identification and assessment of insulation defects in building façades (T. Taylor et al., 2014). Furthermore, the thermographic image may highlight defects which can be assessed with heat transfer models to determine their heat loss. Heat transfer modelling can be used to calculate an expected surface temperature distribution over a building element – comparing the modelling results to the thermography obtained from in-situ surveys can improve diagnostic capabilities (T. Taylor et al., 2014). (Zalewski et al., 2010) also employed IRT to visualise TBs in an industrial light-weight construction, containing insulating material between metal trusses, water vapour barriers, and the internal and external facings, numerically (using TRISCO software) validating experimental heat flux measurements. The author then showed the effect of breaking the TB with an insulating layer of plasterboard which reduced the heat losses and increased the minimum internal surface temperature, decreasing the overall impact of TB.

The following Table 4 collates the reviewed of literature focused on IRT assessment of building fabric either qualitatively or quantitatively (to estimate U values or TB-transmittances using thermography) in the lab or in-situ. Finally, the measurement chapter is concluded by reviewing the few novel measurement methods, quantifying TB-transmittance, found in literature.

#	Reference	Qualitative/Quantitative	Lab/in-situ
1	(Albatici & Tonelli, 2010)	Qualitative	In-situ
2	(Albatici et al., 2013)	Qualitative	Lab
3	(Albatici et al., 2015)	Quantitative	In-situ
4	(Asdrubali et al., 2012)	Quantitative	Lab
5	(Atsonios et al., 2018)	Quantitative	In-situ
6	(Balaras & Argiriou, 2002)	Qualitative	In-situ
7	(Dall'O' et al., 2013)	Qualitative	Lab
8	(Datcu et al., 2005)	Qualitative	In-situ
9	(Fokaides & Kalogirou, 2011)	Quantitative	Lab
10	(Garrido et al., 2018)	Quantitative	In-situ
11	(Hoyano et al., 1999)	Qualitative	In-situ
12	(Kato et al., 2007)	Quantitative	In-situ
13	(Lucchi, 2017)	Qualitative	In-situ
14	(Madding, 2008)	Qualitative	In-situ
15	(Marino et al., 2017)	Quantitative	In-situ
16	(Marshall et al., 2018)	Quantitative	Lab

17	(Martín Ocaña et al., 2004)	Qualitative	In-situ
18	(Mauriello et al., 2019)	Quantitative	In-situ
19	(Nardi et al., 2014)	Quantitative	In-situ
20	(Nardi et al., 2016)	Quantitative	Lab
21	(O'grady, 2018)	Quantitative	Lab
22	(Rosina & Spodek, 2003)	Qualitative	In-situ
23	(Simões et al., 2014)	Quantitative	Lab
24	(Taylor et al., 2014)	Qualitative	In-situ
25	(Tejedor et al., 2017, 2018)	Quantitative	In-situ
26	(Zalewski et al., 2010)	Qualitative	Lab

Table 4 – Reviewed literature of IRT methods

Although any standardised assessment methodologies evaluating are lacking, there are a few novel measurement techniques quantifying TB in construction some of which are included in the Table 4. The following section reviews their development and other categorisation methods.

2.3.6 Novel measurement techniques quantifying thermal bridging

In 2002, (Benko, 2002) quantified TB effects using infrared thermography. Using only the outdoor thermography of a building slab, the surface temperature of the TB and undisturbed zone were recorded simultaneously. These two temperatures were used in the calculation of the introduced parameter – 'ES', the energy saving factor, a ratio between heat losses through a building component with and without a TB, see equation 23.

$$ES = \frac{\dot{Q}_j}{\dot{Q}_{si}} = \frac{h_j A_j (T_j - T_{envi})}{h_{si} A_{si} (T_{si} - T_{envi})} \quad (23)$$

Where the numerator relates to the heat flow rate influenced by a TB and the denominator relates to the undisturbed section of the wall.

Assuming constant SR for the TB zone and the undisturbed zone, as well as defining the surface temperature of the TB 'T_j' as the average temperature 'T_{avg}' and the surface temperature of the undisturbed zone 'T_{si}' as the minimum temperature 'T_{min}', the area ratio $a = A_J/A_{si}$ is introduced, where 'A_j' is the area of the TB and 'A_{si}' is the area of the undisturbed zone.

The energy saving factor ES can then be written as equation 24:

$$ES = a \frac{(T_{avg} - T_{envi})}{(T_{min} - T_{envi})} \quad (24)$$

The higher this value, the greater the influence the TB has. This factor indicates the TB impacts but does not show the actual heat loss caused by the bridge.

Building on this, (Asdrubali et al., 2012) introduced a parameter 'I_{tb}' (incidence factor of a TB) able to estimate the TB effects on building as a percentage increase of the U-value transmittance, using only information of temperature dispersion from thermographs. A window frame TB was investigated initially in a lab, followed by two in-situ floor beam TB. The IR and HFM methods were compared with CFD analysis showing promising results.

To evaluate the 'I_{tb}', consider a homogenous part of the wall where 1D heat-flow is assumed (unaffected by the TB). Under steady-state conditions, the surface temperature is a function of the SR, thicknesses, and thermal conductivities of the constituting layers, see equation 25:

$$Q_{1D} = h_{1D_i} A_{1D} \left(T_i - T_{1D_{is}}\right) \tag{25}$$

Where 'h_{1D_i}' is the reciprocal of the internal SR (considering the convection and radiative heat-transfer), 'A_{1D}' is the area considered, 'T_i' and '$T_{1D_{is}}$' are the inner air and surface temperatures, respectively.

Introducing a TB into this area, the temperature is no longer uniform across the entire surface. Using an IR camera, the thermogram provides a temperature value associated to each pixel, hence, heat-flux evaluation is possible in each pixel using equations 26:

$$Q_{tb} = h_{tb_i} A_{pixel} \sum_{P=1}^{N} \left(T_i - T_{pixel_{is}}\right) \tag{26}$$

Where the subscript '$_{pixel}$' refers to the individual pixels within the thermogram. Further, if 'N' is the number of pixels that compose the entire area, equation 27:

$$A_{1D} = N A_{pixel} \tag{27}$$

Assuming the same SR is effecting the walls surface, coefficient 'h_{1D_i}'='h_{tb_i}', therefore 'I_{tb}' becomes a ratio between the TB thermal loss and the hypothetical U-value of the wall (calculated without the effect of the TB – i.e., the 1D section), see equation 28:

$$I_{tb} = \frac{Q_{tb}}{Q_{1D}} = \frac{h_{tb} A_{pixel} \sum_{P=1}^{N} \left(T_i - T_{pixel}\right)}{h_{1D} A_{pixel} \sum_{P=1}^{N} (T_i - T_{1D})} = \frac{\sum_{P=1}^{N} \left(T_i - T_{pixel}\right)}{N (T_i - T_{1D})} \tag{28}$$

Therefore, the incidence factor determines the percentage increase in thermal transmittance, equation 29:

$$U_{tb} = U_{1D} * I_{tb} \tag{29}$$

Where 'U_{1D}' is the U-value of the wall, 'I_{tb}' is the incidence factor, and 'U_{tb}' is the thermal transmittance increase due to TB.

If temperature values are obtained from the same image, error sources are minimised (Asdrubali et al., 2012).

A similar quantitative measurement using infrared technologies is suggested by (O'Grady et al., 2018). This alternative approach to the incidence factor method requires calculating a new parameter, the M-value, focusing on multiple TB in the building envelope caused by windows.

The 'I_{tb}' is determined slightly differently: three rows of pixels in the IR image are selected forming a line leading into a TB from an undisturbed location. The centre line is reconstructed by averaging the temperatures from the neighbouring eight pixels, smoothing the surface temperature gradient. The length of the pixel, 'l_x', depends on the distance the camera is from the target.

where 'T_{sx}', 'T_{sur}', and 'T_i' are temperatures of the pixel, surroundings, and internal air, the heat-flow rate for each pixel, 'q_x', on the IR line is determined by including the convective 'h_{cx}' and radiative 'h_{rx}' heat-transfer rates on the internal face, as per equation 30:

$$q_x = l_x[h_{cx}(T_i - T_{sx}) + h_{rx}(T_{sur} - T_{sx})] \tag{30}$$

Determining the heat-flow without the influence of a TB 'q_{xu}', then, subtracting this value from the heat-flow for each pixel q_x – per pixel in the IR line – the extra heat-flow rate due to the TB can be found q_{xTB} (O'grady, 2018) applying equation 31:

$$q_{xTB} = q_x - q_{xu} \tag{31}$$

Summing up 'q_{xTB}' for all pixels on the IR line, the TB heat-flow rate 'q_{TB}' is found using equation 32:

$$q_{TB} = \sum q_{xTB} \tag{32}$$

Dividing this by the imposed temperature difference between environments, the psi-value 'ψ' (linear transmittance) is determined (O'Grady et al., 2017b) in equation 33:

$$\psi = \frac{q_{TB}}{T_i - T_e} \tag{33}$$

Using this method, (Bianchi et al., 2014) categorised nine TBs in terms of incidence factor and overall contribution to energy loss in a building.

Validating the 'I_{tb}' method with hot-box and numerical software, (O'Grady et al., 2018) assessed windows and steel framing in walls (O'Grady et al., 2017a) utilising equations 25 – 33.

As mentioned, HFM can also be used to evaluate the 'I_{tb}' (Asdrubali et al., 2012; Baldinelli et al., 2018) adopting equation 34:

$$I_{tb_{HFM}} = \frac{Q_{tb}}{Q_{1D}} = \frac{\varphi_{1D}A_{1D} + \varphi_{tb_1}A_{tb_1} + \varphi_{tb_2}A_{tb_2} + \varphi_{tb_3}A_{tb_3}}{\varphi_{1D}\left(A_{1D} + A_{tb_1} + A_{tb_2} + A_{tb_3}\right)} \quad (34)$$

Where, 'φ_i', are the measured heat fluxes leasing into the TB with the corresponding sensor areas, and 'I_{tbHFM}' is the incidence factor via HFM method.

The transient linear-thermal transmittance of the corner of a room was analysed using this method, validated with numerical code. Thermal imaging identified 1D heat-flow in a homogeneous region in the wall, around 1m away from the corner. HFM measured the 1D heat-flow in this identified region and ten thin-film flux sensors were positioned leading into the bridge, see Figure 19:

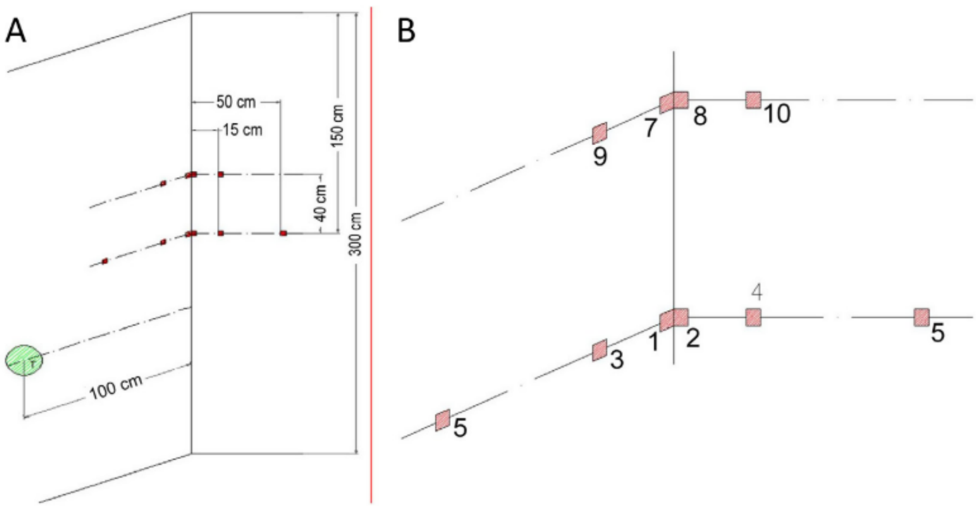

Figure 19 – Arrangement of thin flux sensors (Ascione et al., 2014).

Thermocouples were used to measure the internal and external air temperatures. All measurements were averaged to 60mins, for a full day. The numerical calculation was simulated over 10 days repeating the same recorded weather profile achieving stable initial temperatures condition. Deviations between modelled and measured data appeared, since; wind, rain, solar, thermal inertia, etc. are hard to model exactly. Maximum deviation of 12% were found (Ascione et al., 2014), although on average the results balance close to zero, suggesting a validated code. These approaches indicate a wide number of possibilities in terms of TB evaluation in both laboratory and in-situ experiments. The author performed numerical analysis with FLUENT (CFD tool); boundary conditions adhere to relevant standards – replicating reality by prescribing forced convection externally and natural convection internally.

(Bianchi et al., 2014) applied the HFM 'I_{tb}' methodology, developed by previous authors (Asdrubali et al., 2012), continuously monitoring full-scale building. Flux, air, and surface temperatures were monitored allowing comparison with the IR method. Variation between these two approaches was less than 1%, however the simplicity of the building studied could be considered as a simplifying factor, therefore it was suggested for further work to apply this methodolgy to real operating buildings.

The 'I_{tb}' is greatly affected by the accuracy of the thermographic image. Both (Asdrubali et al., 2018) and (Baldinelli et al., 2018) developed a validated mathematical algorithm to enhance the image resolution, improving energy loss assessment. Hot box experiments were conducted investigating three types of TB prior to thermographic surveys which employed the enhancement algorithm, comparing 'I_{tb}' results using the IR and HFM methods with good agreement between the methods. The image reconstruction and enhancement algorithm that is applied is based on the mathematical theory of the sampling Kantorovich operators, together with a suitable thresholding method based on histogram analysis associated to the thermographic image. Reconstruction algorithms better define the temperature trend retrieved from infrared camera usually portrayed by a pixel resolution. Kantorovich operators essentially reconstructs the 2D thermal signal with a scaling factor of 'R=2', the choice for this scaling factor is explained in previous works (Costarelli et al., 2017; Costarelli & Vinti, 2013) regarding seismic engineering (Cluni et al., 2014, 2015).

The algorithm enhances the image from 320*240 pixels up to 640*480 pixels, producing a more defined image with a higher number of pixels in the area used for determining the 'I_{tb}' (Asdrubali et al., 2018). Environmental conditions: air temperature, and relative humidity were measured and used for calibration in the post-processing of the IR image.

When the effective lengths of the TB and U-value 'U_{1D}' of the wall are known, the 'I_{tb}' is shown to relate to TB linear transmittance (psi-value 'ψ') in the following equation 35:

$$\psi = (I_{tb} - 1)\, U_{1D}(l_{tb} + l_{1D}) \tag{35}$$

Where 'ψ' is the linear thermal transmittance of the TB and 'l_{tb}' and 'l_{1D}' are the length of the zone effected by the TB and the length of the undisturbed zone caught by the thermogram, respectively.

The geometrical boundaries of materials generating the TB can be extracted defining a threshold parameter by analysing the probabilistic temperature distributions (histogram). Interpreting these, two peaks representing the homogeneous temperature areas – undisturbed and disturbed areas see Figure 20 below.

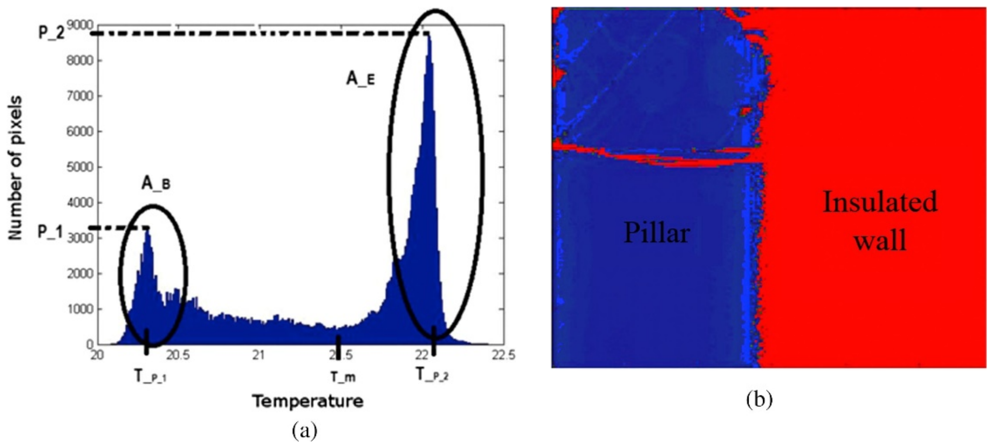

Figure 20 – Probabilistic histogram (left), corrected image (right) (Baldinelli et al., 2018).

Between the two peaks it is possible to identify a minimum value associated with a threshold temperature 'T_m' which identifies the TB geometry, segmenting it from the background. The geometrical interpretation of the TB using this method, mapped the exact position and shape with errors no more than 1cm. (Asdrubali et al., 2018; Baldinelli et al., 2018)

It is clear attempts have been made to quantify linear-TB by employing various novel experimental measurements (HFM and IRT), validated using numerical software. However, point-TB is less often addressed with physical measurement, although their quantification using numerical methods are demonstrated (Nimiya et al., 1999; Šadauskiene et al., 2015; T. Theodosiou et al., 2017, 2019). (Šadauskiene et al., 2015) found that point-TB in the form of aluminium façade anchors can increase the U-value of the wall by 30% comparing models with and without a thermal break. In the study point-TB transmittance evaluation using FE software (Heat3) was compared with the results from a novel dimensionless approach, considering various conductivities and thicknesses of the baring wall and insulating layers. The following section reviews some available thermal modelling software with which building physics phenomena, and specifically TB, can be evaluated.

2.4 Modelling

Most simulation programs solve the governing heat transfer equations by considering 1D flow through an envelope. Multidimensionality (2D and 3D) considerably increase the complexity of analytical solutions, although some programs can perform an integral approach of the thermal interactions which support design decisions (Hensen, 1992), such as finite element/volume/difference methods – proposed to solve the multidimensional heat transfer problems – used in conjunction with the international standard BS EN ISO 10211. This standard guides the steady-state calculation of TB transmittance; however, numerous authors highlight the importance of considering dynamic conditions when calculating this transmittance. Various dynamic simulations of TB can be seen in literature, the BEM (boundary element method) (Wrobel & Brebbia, 1981), for example, was developed for transient heat transfer analysis of TB. Using this theorem a corner bridge investigated, (Tadeu et al., 2011) highlighting the importance of dynamic TB assessment by showing that current steady-state analysis underestimates the linear transmittance and overestimates the minimum internal surface temperature.

When exposed to fluctuating temperature differentials, thermal mass (Balaras, 1996) induces a time delayed response of stored heat. This becomes an important property when modelling the energy performance of a building under dynamic conditions (Sadineni et al., 2011). Transient analysis of TB still remains a challenge (T. Theodosiou et al., 2019), only linear-TB have been assessed dynamically in research (Al-Sanea & Zedan, 2012; Berggren & Wall, 2018; Garay Martinez, 2018; Martinez et al., 2017) and require consideration of material density and the specific heat capacity.

Due to the complexities of modelling TB dynamically (Pipes, 1957), simplified numerical methods have been established such as the such as 'Equivalent wall', or 'Equivalent U-value' (replacing the wall section with an arbitrary material featuring properties reproducing the TB characteristics, in terms of conduction and transfer dynamics), oppose to direct 3D modelling.

The 'Equivalent Wall' method is defined: "The thermally equivalent wall is a simple structure that has the same dynamic behaviour of a complex structure and can be used as a substitute for it in building energy simulation design" (Kossecka & Kosny, 1997). This has been implemented by a number of authors (Quinten & Feldheim, 2016) (Baba & Ge, 2016a; Ge & Baba, 2017) (Martin, Escudero, et al., 2012) demonstrating 1D analysis of 2D or 3D TB.

Similarly, the 'Equivalent U-value' method simplifies the analysis of a complicated TB feature, by altering the thermal conductivity and material thickenss in the homogeneous wall, adjusting its transmittance to reflect the wall containing the TB (Baba & Ge, 2016a). Although it may not represent the actual dynamic thermal behaviour exactly, the density and specifc heat is set to reflect the thermal mass of the structure. Several authors have applied these methods to determine the U-value. In (Peng & Wu, 2008) three methods were presented: synthetic temperate, surface temperature, and frequency response. The difference between the methods and design values ranged from 3-7% for one wall studied, and 6-24% in another. (Jiménez et al., 2009) used the same dataset to estimate the U-value for a component applying three linear models: CTSM (continuous-time stochastic models), LORD software (a deterministic and lump RC model), and MATLAB system identification toolbox to model the linear transfer functions. Bayesian analysis combined with a simple lumped thermal mass model was compared a non-thermal mass model and a single mass model, these were both compared with measurement results from the averaging method in BS EN ISO 9869-1 (BSI, 2014), finding similar results for all studied walls (Biddulph et al., 2014). An iterative model evaluating thermal resistance for a multilayer wall dynamically, was validated numerically and experimentally (Tadeu et al., 2015). Findings showed a relative error around 8% between the expected value and model evaluation.

These simplification methods become less necessary as technology improves and computational cost decreases, hence bespoke FE TB analysis software and powerful multi-physics tools become academically and commercially accessible options.

Dynamic transmittances through TB are a huge factor yet to be addressed in any standards, therefore, (Martinez et al., 2017) proposed a hybridization of two standards (*BS EN ISO 13786:2017 – Thermal performance of building components - Dynamic thermal characteristics - Calculation methods* (BSI, 2017f) with *BS EN ISO 10211:2017 – TBs in building construction-Heat flows and surface temperatures - Detailed calculations* (BSI, 2017c)) could address this gap in knowledge. This hybrid method of evaluation was later applied to a 3D TB case study – façade anchors (Garay Martinez, 2018). A concrete intermediate floor junction, from a previous study (Garay et al., 2014), was retrofitted with EWI (External Wall Insulation), substantially reducing the heat transfer in a 1D study. The EWI was fixed to the substrate with mechanical anchors – causing the 3D effect – which became a relevant contributor to heat loss. Interestingly, the surplus heat loss due to the 3D anchors was 16% (with 5cm EWI) and 48% (when 20cm EWI), showing: the better the 1D façade insulation, the more detrimental TB becomes, as other authors have agreed (Berggren & Wall, 2013; T. Theodosiou et al., 2017, 2019; T. G. Theodosiou et al., 2015).

The following sections explore whole building energy modelling tools and examines the available 2D, 3D and Multiphysics modelling software tools for TB analysis.

2.4.2 Whole building energy modelling

Direct modelling of 2D and 3D TB components in whole building 1D energy modelling programs achieves greater accuracy than simplification techniques mentioned earlier, however, the increased complexity requires much higher computing power. (Purdy & Beausoleil-Morrison, 2001) performed whole building energy modelling to test the significance of various simulation input parameters aiming to reduce complexity and identify insignificant parameters which then be ignored.

(Déqué et al., 2001) developed a two-stage 2D modelling approach. The first stage utilises Sisey software to calculate the steady state TB linear transmittance generating a reduced dynamic model. These reduced models are then integrated with the other envelope components and simulated in a separate program, Clim 2000, assessing the holistic impacts in terms of energy, emissions, and in some case, vapour diffusion. The authors found an increase in accuracy between 5-7% when comparing the dynamic simulation incorporating detailed 2D TBs, to a normal steady-state simulation model that included tabulated values from standards.

Developed by the Fraunhofer institute of building physics (Fraunhofer, 2018c), WUFI is simulation program capable of modelling transient multi-dimensional (Fraunhofer, 2018a) heat transfer and moisture transport through walls and other multi-layered building components (Fraunhofer, 2018b) exposed to user-defined weather profiles, ventilation, HVAC, and internal loads (Fraunhofer IBP, 2017).

(Kirimtat et al., 2016) reviews previous studies about simulation modelling of shading in buildings from 1996 to 2015, using whole building energy performance software. The review covers the simulation tools: ADELINE, Autodesk VIZ 4, Bsim, Daysim, DesignBuilder, DIVA for Rhino, DOE-2 (department of energy), EnergyPlus, Ecotect, ESP-r, Evalglare, iDbuild, amongst others, showing what, where, and why they were used in previous literature.

Developed by the Lawrence Berkeley National Laboratories Simulation Research Group for the U.S. department of energy, DOE-2, is a free, open source, and cross platform (DOE, 2018). It can predict energy performance with hourly simulations of the user defined model parameters: graphical orientation, building layout and position, building materials, envelope details, conditioning systems, operating schedules, and weather data.

DesignBuilder (DesignBuilder Software Ltd, 2021) is another example of whole building dynamic simulation software; its user-friendly interface enables the engineers to model HVAC, daylight, airflow, cost, energy, and carbon, helping designers to optimise solutions by minimising energy consumption, carbon emissions, and cost; whilst maximising occupancy comfort. This was used in (Baba & Ge, 2016a; Marshall et al., 2017, 2018). The engine behind DesignBuilder is EnergyPlus – an independent simulation program with no graphical user interface – it only reads and writes inputs and outputs as text files, performing energy and thermal load simulations, as well as calculating cooling loads defined by thermal comfort setpoints. Daylight manipulation for dynamic simulation can integrated, performing heat and mass transfer. OpenStudio is a similar software tool supporting EnergyPlus which allows users to quickly create geometry for simulation.

The Belgian building research institute (Tilmans & Van Orshoven, 2010) provided a comparison table of TB analysis FE software. Each software is categorised by type of analysis (heat-transfer only, if air and moisture transports are included, or if Multiphysics is considered), 2D or 3D, steady-state or transient, free form or rectangular, automatic psi-value calculation, type of license available, and what standard validation has been applied, see Figure 21.

Name	Type	2D/3D	SS/TR	FF/RECT	ψ-value	License	Validation
Heat transfer software							
AnTherm [36]	H-T (1)	3D	SS	R	Y	commercial	EN ISO 10211:2007 EN ISO 10077-2:2003
Argos (2) [37]	H-T	2D	SS	FF	Y	commercial	
Bisco / Bistra [38] / [39]	H-T	2D	SS / TR	FF	Y	commercial	EN ISO 10211:2007 EN ISO 10077-2:2003
Champs-bes [40]	HAM-T	2D	TR	R		free	EN ISO 10211:2007
David32 [41]	H-T	3D	SS	R		free	EN ISO 10211:2007
Delphin [42]	HAM-T	2D	TR	R		commercial	EN ISO 10211:2007 HAMSTAD Benchmarks 1 to 5 EN 15026:2007
Flixo [43]	H-T	2D	SS	FF	Y	commercial	EN ISO 10211:2007 EN ISO 10077-2:2003
FramePlus [44]	H-T					commercial	
HAMLab [45]	HAM-T	3D	TR	FF		free	(3)
Heat2 [46]	H-T	2D	TR	R	Y	commercial	EN ISO 10211:2007 EN ISO 10077-2:2003
Heat3 [47]	H-T	3D	TR	R	Y	commercial	EN ISO 10211:2007
KOBRA v3.0w (4) [48]	H-T	3D	SS	R	Y	free (5)	EN ISO 10211:2007
KOBRU86 / Sectra [49] / [50]	H-T	2D	SS / TR	R	Y	commercial	EN ISO 10211:2007
RadTherm [51]	H-T	3D	TR	FF		commercial	
Solido [52]	H-T	3D	SS	FF		commercial	EN ISO 10211:2007
TAS ambiens [53]	H-T	2D	TR	FF		commercial	EN ISO 10211:2007
Therm [54]	H-T	2D	SS	FF		free	EN ISO 10211:2007 (6)
Trisco / Voltra [55] / [56]	H-T	3D	SS / TR	R	Y	commercial	EN ISO 10211:2007
UNorm [57]	H-T	3D	SS	R	Y	free	EN ISO 10211:2007 EN ISO 10077-2:2003
WUFI 2D 3.2 [58]	HAM-T	2D	TR	FF		commercial	EN ISO 10211:2007
General purpose software							
Ansys multiphysics [59]	M-Phys	3D	TR	FF		commercial	
Ansys CFX [60]	M-Phys	3D	TR	FF		commercial	
Fluent [61]	M-Phys	3D	TR	FF		commercial	
Phoenics [62]	M-Phys	3D	TR	FF		commercial	
Comsol multiphysics [63]	M-Phys	3D	TR	FF		commercial	EN ISO 10211:2007
SAMCEF thermal [64]	H-T	3D	TR	FF		commercial	

Figure 21 – Software comparison table *(Tilmans & Van Orshoven, 2010)*.

The characteristics of these software indicate that a whole building design projects can be developed from concept to completion – from the early design stage.

Although these whole building energy models evaluate the buildings emission, consumptions, and hygrothermal performance which can inform the early design stage, there are no options for the inclusion of point-TB, although some offer options to prescribe linear transmittance for common junctions. In general, either 'equivalent wall' or 'equivalent U-value 'methods are adopted to encapsulate TB effects in whole building energy models – calculated prior using separate bespoke 2D or 3D numerical tools. There are numerous numerical software options which can evaluate 2D or 3D TB in construction however, they must satisfy the validation cases in the annex C of BS EN ISO 10211 – these are discussed further in the following section.

2.4.3 2-Dimensional analysis

THERM, developed by Lawrence Berkeley National Laboratory (Lawrence Berkeley National Laboratory, 2012), is a 2-dimensional FE heat-transfer analysis software, capable of modelling complex geometries in steady-state conditions. Mainly applied to components such as windows, walls, foundations, roofs, and doors; and other components where TBs are concerned – the flux and temperature distributions can be estimated allowing analysis of heat loss and condensation risk inferring possible structural damage caused by moisture. The aforementioned 'equivalent U-value' and solar heat gain coefficients can be calculated using THERM (Ge et al., 2013), which can then be implemented to aid whole building annual energy performance evaluation.

A similar software, HTFlux 2D is capable of analysing heat and moisture transport, dynamically (HTflux, 2018). It applies the well-known Glaser method (GLASER 2D algorithm) and enables the user to determine condensation dew points and evaporation rates.

In (Larbi, 2005) used BISCO (Physibel), a 2D numerical simulation software, to analyse 3 types of linear bridge junctions: floor-wall, slab-on grade floor-wall, and roof-wall, each assessed considering both concrete and masonry wall. The numerical simulation results were compared against a proposed statistical model based on regression (non-linear ordinary least square estimation) minimising the sum of the variances (squared deviation) of the chosen coefficients. Chosen coefficients for the statistical model were each estimated and acknowledged by applying the adjusted R-squared value and the t-statistic, assessing how well the estimate fits the model. These statistical regression coefficients were presented along with the psi-value. The proposed statistical and simulation models, generated for each variant studied, found a global relative error of around 10%.

2.4.5 3-Dimensional analysis

Most packages offer both 2D and 3D thermal analysis. For example, PSI-Therm is ISO-validated, capable of generating geometry within the software and determining heat flux and temperature distributions. Using FE mesh generation, automatic calculations of the psi-values (linear thermal transmittance), chi-values (point-TB transmittance), and f_{Rsi} values (critical temperature factors) enables the user to deduce the energetic significance of any investigated detail whilst identifying detrimental anomalies in the design, offering potential for design optimisation (PSI THERM, 2018). The 3D feature comes with a boundary condition database for analysis according to BR497 and Passive House conventions.

AnTherm (Antherm, 2020) is dedicated to TB analysis (Tudiwer et al., 2019). It allows 3D transient simulations and easy import of DXF files. The software creates a matrix of thermal coupling coefficients which are then automatically used to calculate the linear and point thermal transmittance of the TB. It is not only ISO validated (steady state), but also calculates the harmonic, periodic or transient thermal coupling coefficients. Vapour diffusion and hygric coupling coefficients can also be generated.

Heat3 is a 3-D transient and steady-state heat transfer program (Blomberg, 1996; Šadauskienė et al., 2015). Heat2 is the 2-D version, capable of 2-D simulation. Both calculate thermal coupling coefficients according to ISO 10211 and satisfy the validation cases.

The British Research Establishment (BRE) provide thermal analysis modelling for components within the construction industry, utilising the software tool TRISCO developed by Physibel (Physibel, 2017a). TRSICO is a 3D simulation tool, again, satisfying 5the validation examples in the annex C of BS EN ISO 10211. Similar to TRISCO, Physibel have developed a dynamic tool VOLTRA. This requires additional input parameters: material densities, specific heat, and solar reflection (as a function of angle of incidence) and transmission factors. The software allows the thermal conductivity and specific heat values to be set as dependant on temperature – which is useful in fire simulations and for evaluating transient behaviours. Dynamic boundary conditions are time dependant functions, these can be set in the form of constant, steps, periodic, climate values, or fire curves (Physibel, 2017b).

2.4.6 MultiPhysics

The mentioned numerical heat-transfer software such as Heat3, and the Physibel products (VOLTRA and TRISCO) are bespoke for TB analysis (Physibel, 2017a, 2017b) – amongst other building physics applications. However, trusted multi-physics software developers have been used in literature to perform 3D heat transfer analysis: Dassault Systemes ABAQUS (O'grady, 2018; T. G. Theodosiou et al., 2015), COMSOL Multi-physics Heat-transfer Module (T. Theodosiou et al., 2019), and ANSYS

(Ascione et al., 2012; Dikarev et al., 2016; O'Grady et al., 2018), are examples capable of evaluating 3D heat-transfer through TB and much more – beyond the needs of this research.

"COMSOL Multi-Physics" is an all-encompassing physics modelling software including a heat transfer add-on (COMSOL, 2021). Conduction, convection, and radiation capabilities can be used to analyse thermal transfers in buildings – specialised features can be used to assess surface or interstitial condensation and evaporation, latent heat effects, moisture transport, or complex eddy-based turbulent mixing of heat and moisture in air can be incorporated.

Similarly, in ANSYS Multiphysics, fluid forces, thermal effects, structural integrity, or electromagnetic radiation, can be prescribed simultaneously – providing a comprehensive understanding of the products performance (ANSYS, 2021).

The point TB analysis published by Theodosiou utilised a variety of available software; ABAQUS was utilised in 2015, ANSYS in 2017, and COMSOL in 2019 (T. Theodosiou et al., 2017, 2019; T. G. Theodosiou et al., 2015). They proved in these works that each software package can capture the complex 3D heat flows and temperature distributions through TB construction elements and are all suitable for analysis.

The chosen modelling software in these works is ABAQUS. This was justified by comparing the available bespoke software; free demonstration versions, and student versions were reviewed.

Each software reviewed is capable of modelling TB and have been proved to satisfy the validation cases in BS EN ISO 10211. Table 5 below shows some of the reviewed bespoke TB analysis software and popular multi-physics packages capable of TB analysis, comparing attributes (2D/3D/Multiphysics, standard validations, steady or dynamic, and licenses):

Software	2D/3D/MP	Validated	SS/TR	License
THERM	2D	10211 10077-2	SS	Open source
BISCO	2D	10211 10077-2	SS	Commercial
TRISCO	3D	10211 10077-2 13370 1745	SS	Commercial
VOLTRA	3D	13370 11855-2	TR	Commercial
HTFlux	2D	10211 10077-2	SS/TR	Commercial
AnTherm	3D	10211 10077-2	SS/TR	Commercial
Psi-Therm	2D/3D	10211 10077-2 13788	SS	Commercial
Heat 3	3D	10211 10077-2	SS/TR	Commercial
Heat 2	3D	10211 10077-2	SS/TR	Commercial
COMSOL	3D	10211 10077-2	SS/TR	Commercial
ANSYS	3D		SS/TR	Commercial

ABAQUS	3D	10211 10077-2	SS/TR	Commercial

Table 5 – Compares the reviewed software for bespoke TB analysis.

To conclude this section, ABAQUS (ABAQUS, 2021) is a multi-physics package with capabilities of, steady or transient analysis and provides advanced features which resonates well with the research objectives. The superior model generation functionality over most other options was a desirable trait and it is compatible with other CAD software and meshing engines easing import and export of complex assemblies for rapid design alterations. **As mentioned, this study utilises ABAQUS software because of the superior acoustic modules compared to other MP packages since the software is shared by staff from other departments in Farrat.**

The calculation methods to be used with the abovementioned software are shown in the following section.

2.4.1 Numerical thermal bridge estimations

As mentioned, structural TB is difficult to quantify with point-measurements, therefore validated numerical FE modelling is entrusted to provide dependable predictions. Trusting standardised values (CIBSE, 2021), guides (BSI, 2017h), and building regulations (NBS, 2018a) could cause inadequate evaluations of whole building energy performance assessments. Numerical modelling is a non-invasive, non-destructive, repeatable, and a relatively fast method of assessing structures in terms of heat and temperature compared to experimentations – proving a useful tool for product development and comparison.

The linear thermal transmittance (Ψ-value) can be estimated using available methods found in BS EN ISO 14683 *TBs in building construction – Linear thermal transmittance – Simplified methods and default values* (BSI, 2017h). However, point-TB is not supported by the default values and manual methods in this document, and numerical calculation methods are advised for their evaluation. The accuracy of the methods determining the linear transmittance vary drastically. If default values are used (as shown in Annex C of BS EN ISO 14683) an accuracy up to ±50% can be expected, whereas accuracies of ±20% can be expected if manual calculation methods or TB catalogues are used, but the most advisable method is to use numerical calculations as per BS EN ISO 10211 achieving accuracies of ±5%.

Strict rules regarding numerical calculation procedures for TB are standardised in (BSI, 2017c) BS EN ISO 10211 *thermal bridges in building construction - Heat flows and surface temperatures - Detailed calculations*. The standard explains the steady-state calculation procedure, defines terms, quantities, symbols, initial conditions, and boundary conditions which analysis must adhere to. Moreover, in Annex C, four validation cases are presented: two for 2-dimensional and two for 3-dimensional analysis which the chosen numerical code/software must satisfy to prove its validity. Supporting documentation from the BRE, BR 497 and information paper IP 1/06 show examples of analysis (Ward, 2006; Ward & Sanders, 2016) applying BS EN ISO 10211 to evaluate common linear TB's.

Summarising the numerical calculation rules in BS EN ISO 10211 (BSI, 2017c), ensuring robust model validation, the steps are re-iterated:

Step 1 – Define the cut-off planes.

- Generally, cut-off planes are positioned 1m away from the TB.
- Unless a symmetry plane is closer, then use that.

- Simplifications can be made – for thin layers; quasi-homogeneous layers; or changes to the external or internal surface position or interfaces.

Step 2 – Apply boundary conditions and thermal resistances and conductivities.

- For conductivities use international convention BS EN ISO 10456 (BSI, 2007).
- Air layers and cavities – resistances can be found in accordance with BS EN ISO 6946, EN 673, BS EN ISO EN 10077-2 depending on the building element.
- Boundary conditions must consist of temperatures, SR, or heat fluxes. Temperatures can be freely chosen but should represent reality (typically, temperatures of 20°C and -5°C should be applied, internally and externally, respectively, to reflect worst-case-scenario in northern European climates), whereas SR depends on the direction of the heat flux BS EN ISO 6946 (BSI, 2017b), but should be slightly adjusted when evaluating condensation risk BS EN ISO 13788 (BSI, 2012a).

Step 3: Test cases for software validation

- 4 different cases are provided in the annex of BS EN ISO 10211, two for 2D and two for 3D validations.

As mentioned, any chosen software or numerical code used to calculate TB must adhere to the above steps.

Calculating conduction problems only requires FE analysis, although FE is capable of a lot more. This eliminates the need to model complex turbulent fluid flow with CFD (Computational Fluid Dynamics) which drastically increases computational cost. However, the convective and radiative transfers cannot be ignored entirely, so representative SR are prescribed at model boundaries exposed to environments (BSI, 2017c).

The generated geometrical model is discretised (divided into cells) creating a mesh, each with several nodes which Fourier's conduction equation and energy conservation laws are applied to. Whilst considering the initial conditions and boundary conditions, a full system of equations can be constructed which is a function of temperature at each node. Direct or iterative solutions determine a temperature field and interpolation can derive the temperature at any chosen point allowing calculation of heat-flows (BSI, 2017c).

Modelling requirements specify that a mesh convergence study (or grid independency tests) is necessary. That is, the number of elements within a model is increased and the simulation response is compared with the previous iteration, if the responses are within a tolerance (±1% dictated by the standard), the courser mesh is acceptably accurate (BSI, 2017c). This reduces unnecessary computational cost and is best practice when meshing models for simulation. Adiabatic cut-off planes – where no heat-transfer can takes place – are suggested to be prescribed at a plane of symmetry or 1m away from the TB, whichever is closer (BSI, 2017c; Viot et al., 2015).

The numerical output from the thermal simulation determines the coupling coefficient. The coupling coefficient describes the total energetic loss through the component between the boundaries. Both 2D and 3D simulations calculate coupling coefficients, referred to as 'L_{2D}', [W/mK], and 'L_{3D}', [W/K], respectively (BSI, 2017c; Ward, 2006; Ward & Sanders, 2016). The relationship between '$L_{3D,i,j}$' and thermal transmittances is given in the following equations 36 – 38:

$$L_{3D,i,j} = \sum_{k=1}^{N_k} U_{k(i,j)}.A_k + \sum_{m=1}^{N_m} \psi_{m(i,j)}.l_m + \sum_{n=1}^{N_n} \chi_{n(i,j)} \quad 36$$

The linear-thermal transmittance:

$$\psi_{m(i,j)} = L_{2D} - \sum_{j=1}^{N_j} U_j.l_j \quad 37$$

The point-thermal transmittance:

$$\chi = L_{3D} - \sum_{i=1}^{N_i} U_i.A_i - \sum_{j=1}^{N_j} \psi_j.l_j \quad 38$$

Where,

'χ' is the point-thermal transmittance [W/K],

'L_{3D}' is the 3D coupling coefficient [W/K] (total energetic loss divided by the applied temperature differential),

'U_i' is the 1D transmittance (U-value) [W/m^{2}K],

'A_i' is the area the 1D U-value is effective over [m^2],

'ψ_j' is the psi-value (ψ-value) [W/mK],

'l_j' is the length over which the psi value exists [m].

Analysing point-transmittance in the absences of any linear transmittance, means part of the equation can be ignored, although, this 3D metric (χ) is seldom used in whole building energy assessments. Instead, the 2D counterpart, ψ-values (linear transmittances) are reported and converted from 3D simulations which encapsulates any point bridging within the linear metric. Therefore, the output from the 3D simulation needs to be properly assessed by the modeller to accurately report a 2D metric. BRE documentation (Ward, 2006) only deals with the non-repeating 2D linear-TB, giving guidance on limiting the condensation risk and mould growth. Generally, numerically calculating the linear thermal transmittance requires subtracting the 1D heat flow through the plane building elements (U-values), from the total calculated heat flow through the model, deducing the additional heat flow associated with the TB junction (Ward & Sanders, 2016); relevant SAP methods for various typologies are presented. The '*Certified Thermal Detail and Product Scheme'* categorises thermal performance metrics (BRE, 2019a), providing transmittances of products and details to be used in the design stage. However, only 2D-transmttance metrics (BRE, 2019a) are listed – even for 3D details (point-TB).

Steady-state software TRISCO (Physibel) with 3D capabilities is favoured by the BRE for calculating transmittances of 3D balcony junctions; following SAP E23 (for balcony assessment) (Ward & Sanders, 2016) the 3D analysis captures the TB transmittance within a 2D metric. Their procedure is as follows:

- The total energetic loss [W] resulting from a simulation is generated, then, by applying the prescribed temperature difference, the 3D coupling coefficient 'L3D' [W/K] is attained.

- The analytical U-value – multiplied by its area – is subtracted (noting dimensions used – internal/external).

- This leaves a residual energy metric [W/K] which is further divided by the user-defined model depth of the simulated model, deducing the linear-transmittance [W/mK] of the investigated 3D model, describing the heat loss per m wall length.

- In this manner, a 2D linear transmittance (psi-value) can be reported for 3D details and listed in their publication Certified product list' (BRE, 2019a)

It can then be appreciated that correct dimensional assessment of geometry, representing the 1D areas, is crucial in the calculation of the ψ-value (linear thermal transmittance). In UK Building Regulations the U-value applies between finished internal faces of the external building elements (NBS, 2018b); i.e. ignoring partition walls and intermediate floors of the same premises, but not the separating walls or floors between different premises (Ward, 2006), see Figure 22. This means the ψ-values depends on the specific construction of the junction and the area over which the relevant U-values are being applied.

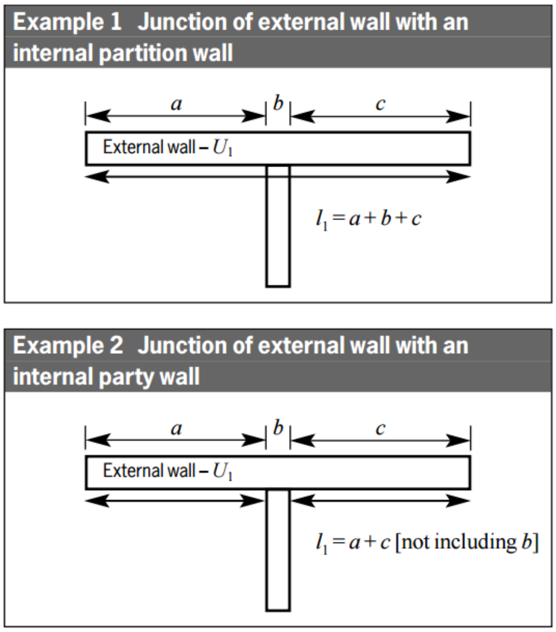

Figure 22 – Illustrating correct lengths to choose for 1D heat flow in ψ calculation (Ward, 2006).

When determining the 'ψ' and 'χ' values, it is necessary to state the dimensions (internal or external) which have been used (BSI, 2017d), so they can be accounted for correctly in BPE.

A similar method, which resonates well with this study, is a simple subtraction of models, with and without the TB discontinuity (Ben Larbi et al., 2017)(Šadauskiene et al., 2015).

Point-thermal transmittance 'χ' of a component within a building envelope is defined by 3D methodology as the difference between the specific heat-loss through an area with (H_s) and without (H) components' causing the point-TB (Šadauskienė et al., 2015). i.e., see equation 39:

$$\chi = H - H_s \quad 39$$

If this point-thermal transmittance is repetitive throughout the envelope, the effect can be accounted for by quantifying how many 'n' occur in 1m^2 of the envelope; then multiplying the amount by the point-transmittance value 'χ' – acquiring the weighted effect in 1m^2 (Luscietti et al., 2014), see equation 40:

$$\Delta U = \chi . n \quad 40$$

This adjusted U-value 'ΔU' can then be added the overall heat-transmittance coefficient 'U' obtained from 1-D analysis of the insulated wall – unaffected by TB. As seen in the BS EN ISO 6946 (BSI, 2017b) using equation 41.

$$U = U_i + \Delta U \quad 41$$

Another important metric derived from thermal simulation of TB is the minimum internal surface temperature, with which, the temperature factor can be determined. This is explained in the next section.

Critical internal temperature factor (fRsi)

Briefly mentioned earlier, numerical modelling not only calculates the TB transmittance but can also determine the minimum internal surface temperature of the structure which is used to calculate the temperature factor. The internal temperature factor is a dimensionless quantity ranging from 0 to 1 and is calculated by dividing the difference between the minimum internal surface temperature and external air temperature, by the internal and external air temperature difference as shown as equation 42 from the standard ISO EN BS 13788 (BSI, 2012a):

$$\mathrm{f_{Rsi}} = \frac{(\mathrm{T_{min}} - \mathrm{T_e})}{(\mathrm{T_i} - \mathrm{T_e})} \quad 42$$

Where f_{Rsi} is the temperature factor, T_e is the external air temperature, T_i is the internal operative temperature (the arithmetic mean value of the internal air temperature and the mean radiant temperature of all surfaces surrounding the internal environment), and T_{min} is the minimum internal surface temperature at the thermal bridge location.

If the temperature factor is equal to 1, the internal surface temperature at the thermal bridge is the same as the internal air temperature building, if it equals 0 then the internal surface temperature at the thermal bridge is the same as the external air temperature.

Numerical calculation assumes steady-state conditions and, compared to transmittance calculations in the norm BS EN ISO 10211 (BSI, 2017c), an elevated internal surface resistance must be applied (0.25 [m^{2}K/W] on all internal surfaces oppose to 0.13 [m^{2}K/W]) to consider cupboards, beds, draws etc., or any other wall obstructions impeding the internal convective and radiative heat transfer mechanisms

(BSI, 2012a). However, the critical temperature values reported by the BRE in their information paper IP 1/06 (Ward, 2006) IP 1/06, shown in Figure 25 and Figure 26 below, compensate for the use of lower internal SR when modelling to their guidance (Ward & Sanders, 2016).

The temperature factor is a property of the construction and depends only on the geometry and material properties, not on the imposed air temperatures (Ward & Sanders, 2016). Therefore, once it has been calculated for any environmental temperatures, it can be used to determine the surface temperature for any other set of air temperature conditions by rearranging equation 42 above to equation 43 below:

$$T_{min} = T_e + f_{Rsi} * (T_i - T_e) \tag{43}$$

Dependent upon climatic zones and buildings operation, this f_{Rsi} must be above a critical value f_{CRsi} to meet hygiene criteria, since the colder the climatic condition (or the higher the buildings operative humidity), the higher the requirement will be for the temperature factor. If the critical temperature factor is achieved, the formation of mould and condensation can be averted.

The Passive House have provided an experimentally derived table (see Figure 23) listing the criteria for all climate zones (see Figure 24) in their documentation (Passivhaus Institut, 2022).

Climate zone	Hygiene criterion[8]	Comfort criterion	Efficiency criteria			Moisture criteria[6]	
	$f_{Rsi=0.25\,m^2K/W}$ ≥[3]	U-value of the installed window[1] ≤	U-value of the exterior building component $U_{opaque} * f_{R\,PHI}$[2] ≤	Purely opaque details $f_{Rsi=0.25\,m^2K/W}$ ≥[3]	Absence of thermal bridges Ψ_a ≤[4]	Condensation	Ma limit according to DIN EN ISO 13788 ≤
	[-]	[W/(m²K)]	[W/(m²K)]	[-]	[W/(mK)]	[-]	[g/m²]
1 Arctic	0.80	0.45 (0.35)	0.09	0.90	0.010[5]	Condensation should be completely evaporated at the end of 12 months	200[7]
2 Cold	0.75	0.65 (0.52)	0.12	0.88			
3 Cool, temperate	0.70	0.85 (0.70)	0.15	0.86			
4 Warm,temperate	0.65	1.05 (0.90)	0.25	0.82			
5 Warm	0.55	1.25 (1.10)	0.50	0.74			
6 Hot	None	1.25 (1.10)	0.50	0.74			
7 Very hot	None	1.05 (0.90)	0.25	0.82			

1 applies for vertical windows with a test size of 1.23*1.48 m. The criteria for other transparent building components can be taken from the relevant certification criteria. Value in brackets: respective reference glazing.
2 $f_{R,\,PHI}$: Reduction factor: always 1, exception: areas in contact with the ground and towards the unheated basement in the climate zones 1-4: 0.6; e.g. for climate zone 3 the U-value criterion becomes 0.25 W/(m²K).
3 $f_{Rsi=0.25\,m^2K/W}$ ≥ see Section 3.8.
4 as a thermal bridge loss coefficient based on external dimensions and length. Specific constructions such as inner edges are exempted from this criterion.
5 Geometric thermal bridges, where the insulation thickness around the junction is consistent, but the calculation methodology results in a Psi-value of > 0.010 W/(mK), are exempt from this criterion.
6 These criteria are based on the Glaser Method and allow an assessment of the likelihood of the occurrence of interstitial condensation during the winter. This method brings more reliable results for lightweight and airtight components used in cool and non-humid locations away from the equator that do not contain materials with a large water or heat storage capacity. Where the criteria are not met following this approach, a dynamic simulation according to EN 15026 can be carried out to provide greater detail. It is the responsibility of the architect to ensure the appropriate assessments have been carried out for specific buildings, which may include more detailed analyses than those carried out for this certification. In addition on-site measurements like airtightness testing as well as trained tradespeople help to ensure construction quality.
7 The Ma limit (maximum accumulated moisture content) is based on the ISO 13788 and reflects the maximum amount of condensate in order to prevent run-off of liquid water from watertight surfaces. It may make sense in certain cases to calculate a more specific Ma limit according to the materials present in the wall, roof and floor constructions.
8 For door thresholds the dew point criterion applies according to section 6.

Figure 23 – Experimental critical temperature factors for various construction types and applications taken from the passive house documentation (Passivhaus Institut, 2022).

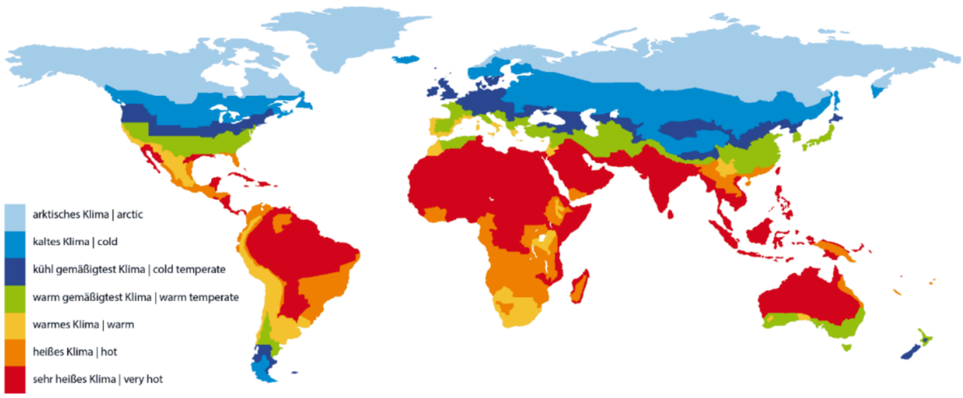

Figure 24 – Climatic zones, taken from passive house documentation (Passivhaus Institut, 2022).

Similarly, the BRE (Ward, 2006) have given indicative f_{CRsi} values for different building types. Figure 25 shows a table taken from IP1/06 which addresses buildings with absorbent internal surfaces wherein mould growth needs avoiding.

Table 1 Critical temperature factors for avoiding mould growth in buildings

Type of building	f_{CRsi}
Dwellings; residential buildings; schools	0.75
Swimming pools (including a dwelling with an indoor pool)	0.90

Figure 25 – Critical temperature factors for avoiding mould growth in buildings (Ward, 2006).

From the same published BRE information paper (Ward, 2006), Figure 26 shows a second table which addresses buildings with non-absorbent internal surfaces with only the risk of surface condensation.

Table 2 Critical temperature factors for limiting the risk of surface condensation

Type of building	f_{CRsi}
Storage buildings	0.30
Offices, retail premises	0.50
Sports halls, kitchens, canteens; buildings heated with un-flued gas heaters	0.80
Buildings with high humidity, eg swimming pools, laundries, breweries	0.90

Figure 26 – Critical temperature factor limiting the risk of surface condensation (Ward, 2006).

Although, with present knowledge, it is unclear how much condensation is acceptable within the wide diversity of building types and variety of operative use. For example, overnight condensation which evaporates during the day is acceptable, whereas condensation build-up over many days may cause surface corrosion – or condensate may drip and cause problems. Therefore, inferring the level of risk is complex (Ward, 2006).

The next section will cover topics specific to the current research such as embedding sensors to recalibrate thermal models with measurement, and a review of thermal breaks in construction connections.

2.5 Measurement informed models

Since model recalibration using well defined physical measurements is thought to reduce the PG in TB evaluation, this section reviews possibilities of embedding sensors at critical locations – within structural TB connections – to better inform and validate thermal models. This resonates well with these works; this section covers a few examples of using embedded before reducing the review to thermal break solutions.

Numerical calibration is achieved by measuring specific model input parameters from real conditions, as shown in (Dikarev et al., 2016; Garay Martinez, 2018) where measurements were taken using embedded thermocouples, thin-film heat-flux sensors, and HFM. A sensitivity analysis was done over thirty-six different TB details, identifying that the internal insulation has the largest impact on the linear-transmittance value. Similarly, the conductivity of the bearing wall material impacts the result more than its thickness (Capozzoli et al., 2013)(T. Theodosiou et al., 2019). Since each TB is unique, it is important to gather a much physically measured data as possible from the investigated construction detail to inform steady-state numerical models with the following: internal and external air temperatures, flux (at critical locations), SR, material thicknesses, conductivities, and a detailed dimensional description of all elements in the modelled geometry.

(Garay Martinez, 2017, 2018; Garay et al., 2014; Martinez et al., 2017) calibrated models with measurements taken around a concrete linear-bridge (intermediate floor junction). Measurements were taken over a long period of time and, in the re-calibration of the thermal model, attempts were made to fit the model estimate to the real-world data by comparing various model calibration iterations. Sensitive parameters and the measurement locations affecting the model re-calibration were compared finding that SR parameterisation, and the surfaces which they apply to, were the most sensitive (Garay et al., 2014).

Thermal-breaks

Because building regulations and policy drivers are pushing for a more sustainable built environment, fitting measures such as EWI becomes an appealing solution. But, as shown in some cases, the more resistive the wall is, a greater magnitude of point-TB transmittance is observed. Hence, increasing the importance to implement thermal break solutions to isolate point connections. Some solutions are highlighted in the following section.

Thermal-breaks influence on heat-flow reduction through TB can be seen in (Ghazi Wakili et al., 2007), where Glass Fibre Reinforce Plastic (GFRP) replaced highly conductive steel compression reinforcement rods – commonly found in concrete balcony details. Thermocouples were glued to critical sites of two balcony details (one unbroken, the other including the thermal break) before cement was poured and tested in a guarded hot-box experiment. The thermal break design was built up to portray reality with brick layers, plaster rendering (left for 3 months for the humidity to achieve equilibrium moisture content), and insulation layer – with further thermocouples attached between layers to better support the verification of steady-state numerical analysis. Assessed with numerical analysis and embedded sensor measurement under steady-state condition within a hot box, the linear-transmittance was calculated numerically in accordance with BS EN ISO 10211. Compared to a conventional concrete slab (0.55W/mK), the informed model of the measured proposed system produced a linear transmittance of 0.2 W/mK and increased the minimum internal surface temperature to 19.9'C from 16.2'C in a conventional through.

A similar thermal break experiment also used embedded sensors to calibrate a thermal numerical model. Thermocouples were fixed on critical sites within and around a concrete balcony connection, with and without a reinforced thermal break insulation (Dikarev et al., 2016) and tested in a guarded hot-box apparatus. Using ANSYS, a numerical model was validated when comparing probe point values in the simulation with the experimental measurements at critical locations, calculating a linear transmittance of 0.12 W/mK with thermal break in the connection oppose to the conventional concrete connection (0.58 W/mK).

(Ge et al., 2013) showed concrete-to-concrete floor slab extensions can be thermally broken by sandwiching a low conductivity material within the connection. Using 2D software, THERM, linear thermal transmittance calculations showed the thermal break solution reduced the overall U-value of the balcony by 72-85% and raised the minimum floor surface temperature from 6.1'C to 12.5'C. When these 2D evaluations were carried forward into eQuest, evaluating their holistic impact on a high-rise building, finding an overall reduction in space heating loads of 5-11%.

Although thermally breaking concrete-to-concrete cantilever connections can reduce their thermal impacts, this type of proposed thermal break product (Schöck Ltd, 2022), can generate greater vibration and deflection when compared to steel-to-concrete or steel-to-steel cantilever connections – limiting the designed balcony length because large deflections and vibrations are undesirable for occupancy comfort and acoustic isolation (Schneider & Fischer, 2008). This becomes more significant as the demand for greater outdoor living space in high-rise flats increases where longer balconies are an appealing design trait in new developments. A recent technical paper proved the use of thermally broken structural steel-to-steel cantilever balcony connections, can provide the same thermal efficiency with less vibration and deflection (Akarcay et al., 2020) compared with competing concrete-to-concrete thermal break solutions. Therefore, thermally broken steel-to-steel cantilever balcony supports could provide the solution to this growing problem, allowing architects more freedom to design longer balconies whilst retaining structural and thermal integrity.

Slim thermal breaks were shown to alleviate the impact of TB (Sallée et al., 2014) in Vacuum Insulated Panels (VIP) and External Thermal Insulation Complex System (ETICS), reducing the heat loss by 30% and 50%, respectively. Interrupting direct contact using STB pads reduces the overall heat loss through a connection, the magnitude of which is closely related to the thickness of the pad and its conductivity. Using thermal breaks on this type of modern façade fixing can reduce the point TB transmittance by 10-23% depending on substrate wall conductivity (T. Theodosiou et al., 2017). However, steel bolt anchors, fixing the bracket to the substrate, penetrate the STB causing a heat bypass and reducing the effectiveness of the solution (T. Theodosiou et al., 2017) (T. Theodosiou et al., 2019). Consequently, in a further study, a thin thermally insulating material acting as a washer, separated the steel fastener from the bracket. Although, its limited thickness showed that this is not a promising solution to the problem in the study (T. Theodosiou et al., 2019). The point-TB solution was included in a whole building analysis comparing two scenarios: A) representing moderate thermal insulation including steel anchors and no break, and B) NZEB national framework insulation including chemical anchors and thermal breaks. Point-bridging was found to constitute a large proportion of the heat flow through the envelope in a whole building energy performance assessment, even more than 25% was presented according to this study (T. Theodosiou et al., 2019).

New double skin smart facades have become more popular in modern designs which sometimes feature aluminium anchors fixed to the concrete substrate. These generate point-TBs since the insulation layer is penetrated by a material with a conductivity around 5000 times higher than that of the insulating material. Theodosiou showed in 2015 (T. G. Theodosiou et al., 2015) that neglecting this type of construction point-TB may lead up to a 5-20% underestimation of the heat loss through the façade envelope, depending on a variety of reasons (unventilated/ventilated cavity, shape of aluminium façade anchor, insulation thickness, inner wall resistance). It was also concluded that although the thermal insulation has a contribution to the magnitude of the TB transmittance, it is less significant than material conductivity variations of the substrate wall.

Ben Larbi showed that, in a joint study between the mechanical and thermal performance of STB pads within a steel-to-concrete balcony connection, a 30-65% reduction of heat flow was seen (Ben Larbi et al., 2017), depending on the configuration.

Focusing on the thermal analysis (Ben Larbi et al., 2017; Larbi et al., 2017), in the first study, two steel-to-concrete connections were compared, extended-end-plate vs extended-end-plate with a saddle see Figure 27 & Figure *28*.

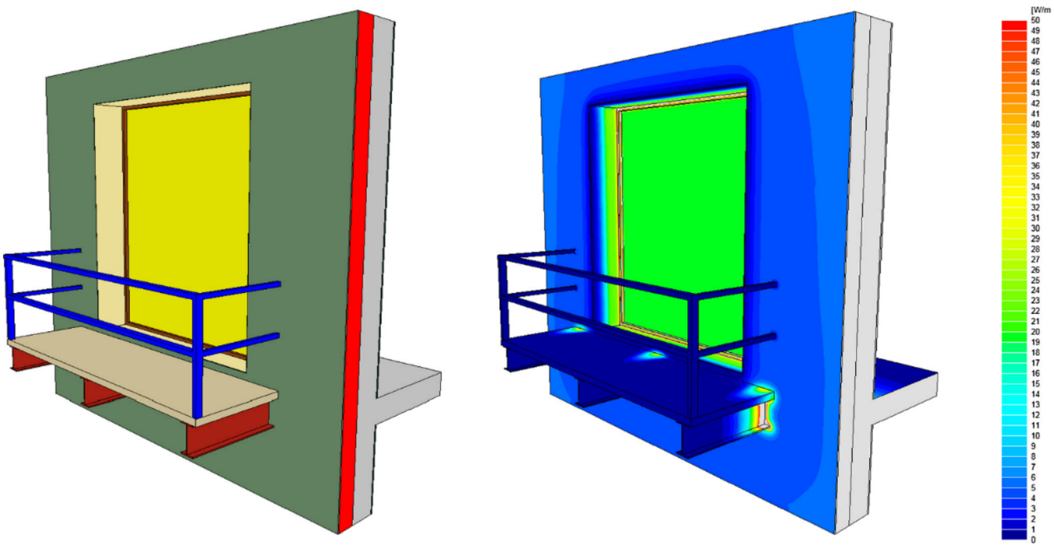

Figure 27 – Shows modelled connection and heat flux from the thermal simulation results (Ben Larbi et al., 2017; Larbi et al., 2017).

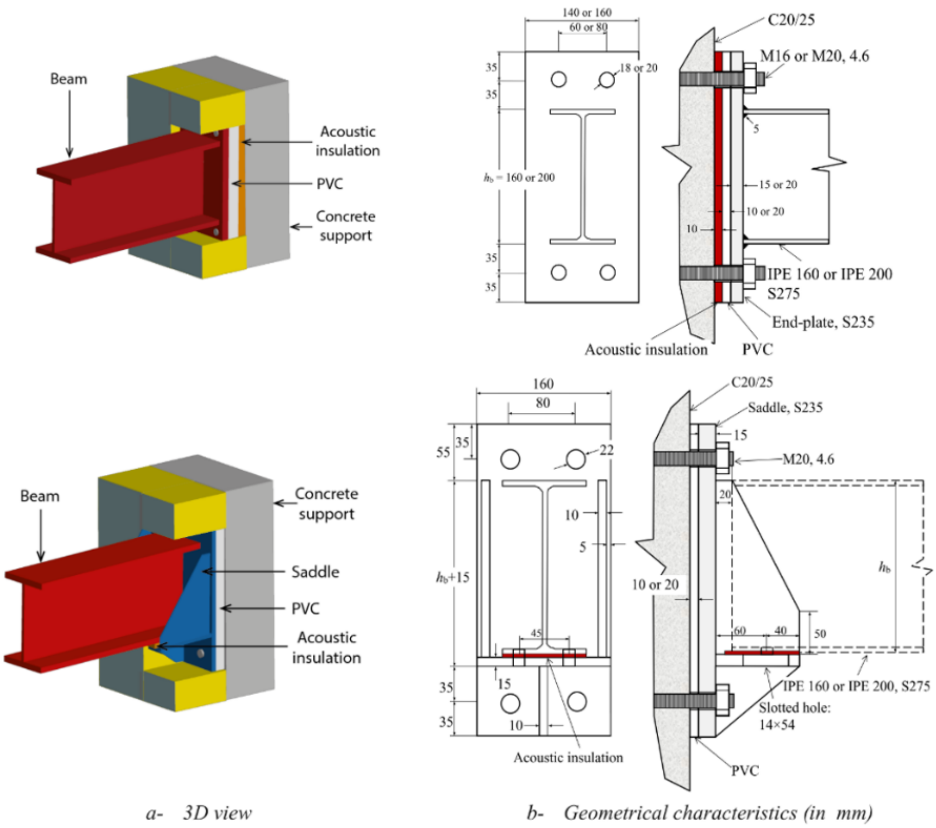

Figure 28 – Illustrates the saddle and STB connection (Ben Larbi et al., 2017; Larbi et al., 2017).

In the later study, the case studies were adapted slightly based on findings from the previous analysis see Figure *29*: supplementary considerations such as bolt position and additional insulation were included. Thermal analysis found a reduction of 20-65% in heat transfer when applying the STB solution in the connection (Larbi et al., 2017).

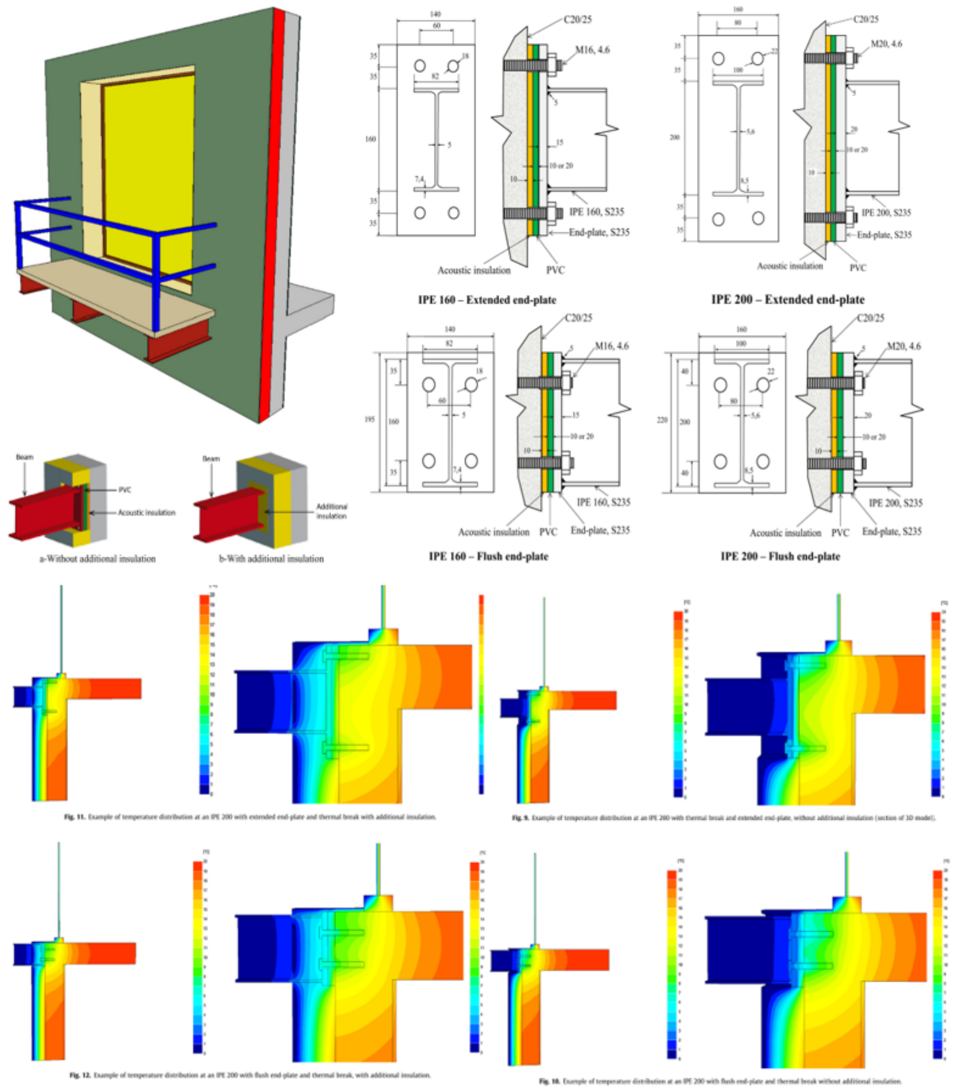

Figure 29 – Illustrates STB tested (Ben Larbi et al., 2017).

Thermal model comparisons provided informative insights – especially regarding the fasteners used to fix the steel to the supporting concrete; a 17%-37% reduction was attributed to using stainless over carbon steel fasteners, undoubtably due to the disparity in thermal conductivities of the fasteners – stainless steel has a conductivity (17 W/mK) around a third of carbon steel (50 W/mK) (CIBSE, 2021). Critical findings from both reports are lacking from a thermal perspective since model input parameters were not measured, instead, standardised assumptions were applied, leading to a probable PG.

It is clear that the importance of understanding/categorising/evaluating TB is being taken seriously and attempts are being made to evaluate the effectiveness of STB solutions, yet no TB measurement methods are standardised – numerical simulation software is solely relied upon to quantify TB-transmittances. Some experiment shown here use physical measurement to improve the numerical predictions, however, both the modelling data gap (between measurement and the model) and measurement gap (between the method and the measurement) could both contribute to the overall gap in energy PG. By understanding the causations, this gap can be reduced.

It is therefore hypothesised that robust model parameterisation is achievable by re-calibrating FE models with physical measurements (taken from critical locations) – more accurately estimating the TB-transmittance (and any STB solution) of point connections in-situ.

In these works, FE models will be supplemented with measurements from a lab-based experimentation in a climatic controlled facility. An experimental design will be developed aiming for later application in-situ. Physical measurements (U-value, SR, and environmental temperatures) from the investigated experimental detail will be used to calibrate model parameters. Parameters will be adjusted – within their sensible ranges – until probed model values match their corresponding experimentally measured estimates from embedded flux and surface sensors.

3.0 Research methodology

The overall aim of this research is to understand the impact of TB in point-connections and establish appropriate experimental and modelling processes to support industry and researchers in better understanding the phenomena.

Hoping to support industry and researchers in better understanding the phenomena around TB through structural point-connections, this research aims to establish appropriate experimental and modelling processes by evaluating STB solutions isolating steel-to-steel interfaces. The philosophical approaches to meet this aim are outlined in this chapter.

Dubbed the Research Onion (Saunders et al., 1997), the stages and elements involved in developing a final research design, seen in Figure 30 below, aims to help students and researchers methodologies.

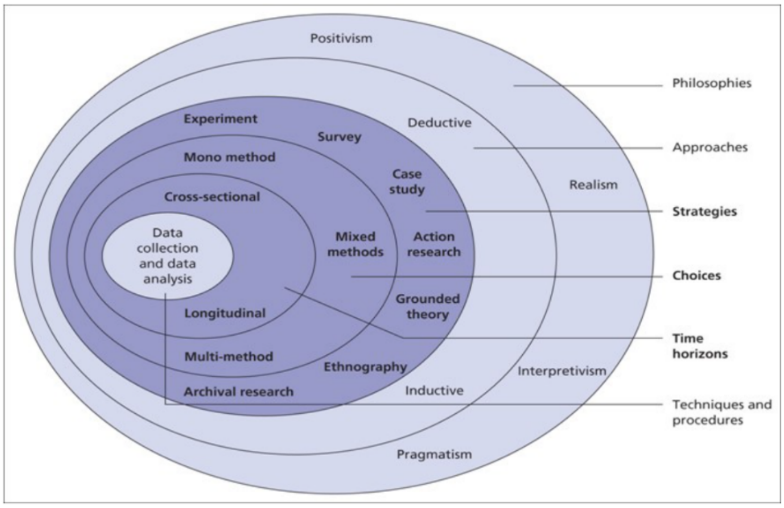

Figure 30 – The Research Onion (Saunders et al., 1997).

There are six main layers. In sequential order from outside to in, the Philosophy, Approach, Strategy, Choices of Methods, Time Horizons, and finally, Data Collection and Analysis.

The philosophical principles, concerning the view from which the research is conducted, are studied in terms of ontology and epistemology. The former governs how one understands the existence of the information and its authenticity, whilst the latter describes how one can obtain valid information for the research. Academic studies usually take a positivist or interpretivist position, which assumes the knowledge and subject being studied are independent from one another, and that the individual observer formulates their own understanding and perception of reality, respectively. Hence, in general, quantitative studies follow a positivism approach, whereas qualitative studies follow an interpretivism approach (Saunders et al., 1997).

The path through the onion adopted in these works is illustrated in Figure 31, below.

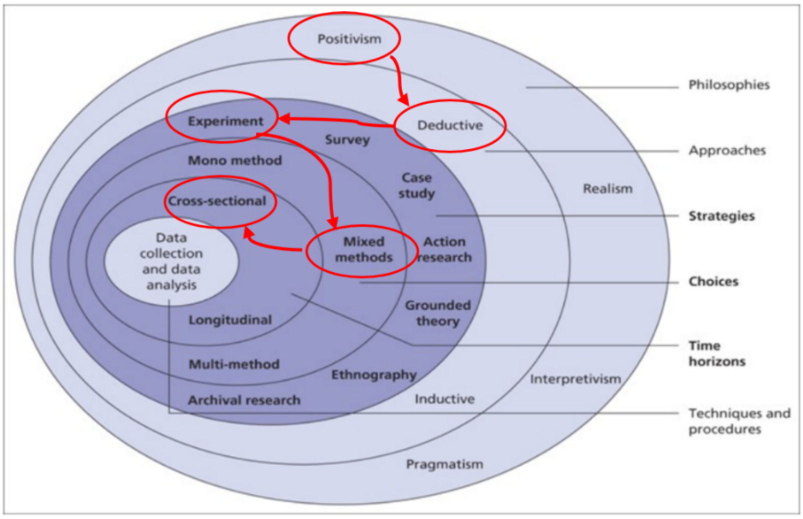

Figure 31 – The path taken through the research onion within these works.

3.1 Research Paradigm

The research paradigm may be viewed as a set of basic beliefs that deal with first principles. It is based and defined considering three variables: the ontology, epistemology, and the methodology (Scotland, 2012) (Elshafie, 2013; Rashid Shah & Al-Bargi, 2013)

3.1.1 Ontology

Ontology is the philosophy of existence. It categorises the philosophical assumptions questioning what we can know from the form and nature of reality. For example, if a 'real world' is assumed then we can know how things really are and really work. i.e. only questions relating to real existence and action are permissible, other questions – acting on matters of aesthetics or morality – fall outside the scope of scientific inquiry (Guba & Lincoln, 1994). In these works, the positivism paradigm is followed exercising a 'real' ontology, in that, knowledge is considered knowable and objective.

3.1.2 Epistemology

The epistemology categorises the nature of the relationship between the would-be knower and what can be known (Guba & Lincoln, 1994). This is constrained by the adopted ontology and now not just any relationship can be presupposed. For example, if a 'real' reality is the assumed ontology, a scientific method (quantitative) governs the relationship between the knower and objective reality to discover how things really are and work. Therefore, an 'objectivist' epistemology is realised in this work allowing the inquirer to pursue a 'real' reality.

3.1.3 Methodological approach

The methodology questions how the would-be knower would find out what is knowable. Again, this is constrained by other answers given, that is, not just any method can be applied (Guba & Lincoln, 1994). Following the ontology and epistemology definitions of 'realism' and 'objectivism', respectively, the methodology adopted is one of 'experimental' – implying the ability to be objective and a real world to be objective about. Therefore, this work follows the scientific method in a linear structure: hypothesis, data collection, analysis, conclusion, and discussion (Creswell, 2009) see Figure 32 showing the flow of the scientific method.

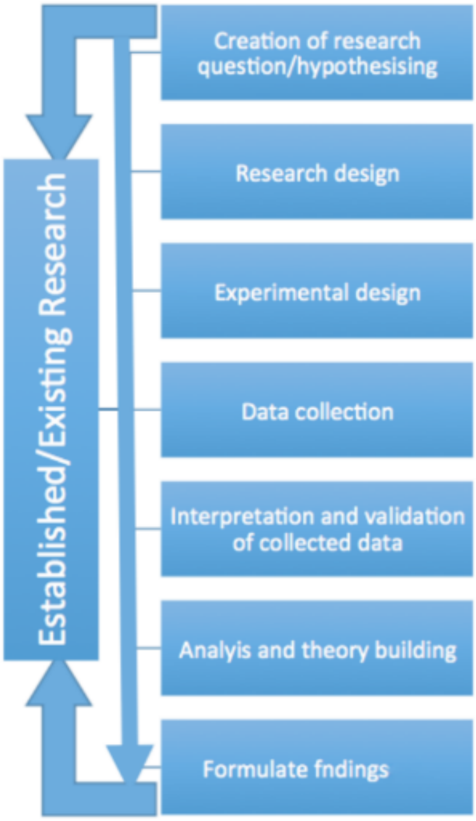

Figure 32 – Shows the research structure and the flow of the scientific method process (Fitton, 2016).

Experiments are subject to a peer review process and external scrutiny; hence, attempts were made to ensure transparent findings, whilst falling in-line with the scientific methods and good practice for experimental design.

As mentioned, all experiments were facilitated by the EH Labs at the University of Salford.

Key experimental issues when in the lab, include: the variables in a test, uncertainty in measurement, and data analysis. Initially, the measurement equipment and the associated errors will be described in the following section.

3.1.4 Variables in a test

To improve the accuracy of measurement, the OFAT (One-Factor-At-a-Time) approach (Xu et al., 2015) was adopted – proven by other researchers to provide accurate findings. Applying OFAT, the value of one factor varies while the rest are fixed. Unquestionably, this approach could determine the impact altering a variable has on a given output – which resonates well with the current study.

Emphasis is made throughout data acquisition to collect robust estimates of variables, allowing accurate observations of differences in physical measurements, testing of hypothesis/theory, and model parameterisation and re-calibration – ultimately leading to accurate TB quantification (Kothari, 2004).

The possible value a measured estimate of a variable has is a consequence of the measurement system employed (JCGM, 2008). This is an extremely important aspect of any measurement, shedding light on the tolerance a particular measurand has (Baker, 2009) – especially when the measurement is subsequently used to inform a numerical FE model. Any measured findings are therefore somewhat redundant without describing the uncertainty interval around the quantity (Moffat, 1988), this is discussed in the following section.

3.1.5 Uncertainty in measurement

The word 'error' in scientific measurements does not carry the usual connotation associated with the word 'mistake'; you cannot eliminate them by being careful. Instead, it refers to the inevitable uncertainty existing in all measurements (J. R. Taylor, 1982). Therefore, the error in a measurement result can be defined as the difference between the true and measured value.

For single measurements, the results will have associated uncertainty (Moffat, 1988) caused by the errors arising from various limitations in measurement:

- Instrumental limitation: increment granularity of measurement instrument
- Systematic errors: caused by observational mistakes during measurement affecting the accuracy in measurement, creating a shift from the true value.
- Random errors: caused by random variations affecting precision, e.g., unnoticed variation in measurement technique.

The difference between accuracy and precision in measurement can be seen in the following Figure *33*.

:

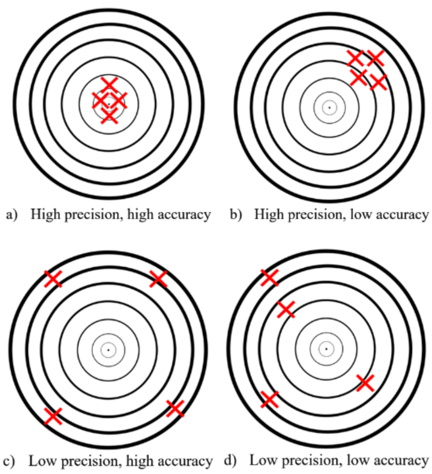

Figure 33 – Illustrating examples of accuracy and precision.

- Precision is about consistency and repeatability. i.e., good precision has a tight grouping.
- Accuracy is about how close it is to the true value. i.e., the average is close to the centre of the target.

We cannot confidently state what this error might be if the true value is unknown, hence, the concept of uncertainty is introduced which refers to the possible range a measurement value may have (Moffat, 1988).

According to (Prasad, 2016), measurement uncertainties are categorised into systematic and random uncertainties:

Systematic uncertainty (bias error), caused by the individual measuring device and affects the accuracy in the measurement. Generally, these can be found using calibration curves or denoted in manufacturer datasheets as an absolute (±unit) or relative (±%) error. However, they could also be reported as standard deviations affecting a measurand.

Random uncertainty (precision or repeatability error) is seen over a set of readings, showing whether the measurements are repeatable.

In multiple sample calculations, both 'Systematic' and 'Random' uncertainty components contribute to the total uncertainty (Moffat, 1988; Prasad, 2016). Using the RSS (root sum square) method (Kline & McClintock, 1953), these components are combined in quadrature to determine a total uncertainty for measurement.

Applying these concepts, *JCGM 100:2008 Evaluation of measurement data – Guide to the expression of uncertainty in measurement* (GUM method) is an internationally recognised standard guiding measurement uncertainty analysis (JCGM, 2008), and is the chosen method for uncertainty analysis in this research.

In this method, the uncertainties are grouped into Type-A or Type-B; synonymous with 'Random' and 'Systematic' uncertainties, and are associated with 'precision' and 'bias' errors, respectively.

Type-A uncertainties are deduced through repeated measurements and are assumed to follow some common probability distribution, describing the precision of the given dataset and is calculated using the standard deviation 'sd' and sample size 'N', see equation 44:

$$\mathrm{uA} = \frac{\mathrm{sd}}{\sqrt{\mathrm{N}}} \tag{44}$$

Whereas, Type-B uncertainties are obtained by applying the RSS, combining all systematic measurement errors (remaining constant throughout a single test) in quadrature using equation 45.

$$\mathrm{uB} = \sqrt{\mathrm{e}^1 + \mathrm{e}^2 + \cdots + \mathrm{e}^\mathrm{n}} \tag{45}$$

Where 'uB' is Type B uncertainty, and 'e^i' are the considered instrument errors.

These standard uncertainties are combined in quadrature into a 'combined standard uncertainty' of a single measurement 'uC' using equation 46 (JCGM, 2008).

$$\mathrm{uC} = \sqrt{\mathrm{uA}^2 + \mathrm{uB}^2} \tag{46}$$

Single measurement uncertainty analysis is relatively simple compared to multiple measurement since the errors are from one measuring device and one type of measurement. When two different types of measurements are recorded from two different types of measuring devices and used to calculate a measurand, since it is a function of multiple input variables, the uncertainties (systematic and random) ought to be properly propagated to describe the 'total combined standard uncertainty'.

Using an example (see equation 47), consider a measurand, 'Y', calculated from several measured inputs:

$$Y = \frac{M}{X} \tag{47}$$

'Y' can be expressed as (equation 48) a function of the two input variables:

$$Y = f\{M, X\} \tag{48}$$

Where each input variable could itself, also be a function of other measurements.

The estimate of the measurand, 'y', is written as equation 49:

$$y = f\{m, x\} \tag{49}$$

The 'total combined standard uncertainty' of the estimate 'y' is determined with equation 50:

$$u_c(y) = \sqrt{\left(\frac{\partial y}{\partial m} . u_c(m)\right)^2 + \left(\frac{\partial y}{\partial x} . u_c(x)\right)^2} \tag{50}$$

Where, the partial derivative terms '$\partial y/\partial m$', and '$\partial y/\partial x$' are the 'sensitivity coefficients' of the input variable; and '$u_c(m)$', and '$u_c(x)$' are the 'combined standard uncertainties' of each input variable – calculated by combining individual measurement precision (Type A) and instrument accuracy (Type B) uncertainty estimations in quadrature, as follows in equation 51:

$$u_c(m) = \sqrt{\left(\frac{\sigma_m}{\sqrt{N}}\right)^2 + (\delta_m)^2} \quad \text{and} \quad u_c(x) = \sqrt{\left(\frac{\sigma_x}{\sqrt{N}}\right)^2 + (\delta_x)^2} \tag{51}$$

Where, '$u_c(m)$' and '$u_c(x)$' are the 'combined standard uncertainty' of the input variables, 'σ_{xi}' is the standard deviation of that variable, 'N' is the number of samples, and 'δ_{xi}' is the relative uncertainty of the instrument.

Sensitivity is a measure of how much an input variable contributes to an output (Moffat, 1988) which, in uncertainty calculation, is found by taking the partial derivative [$\partial y/\partial m$] of the function with respect to the variable in question (Prasad, 2016) (Lewis et al., 2005). It can also be found experimentally by observing how the measurand alters when one input estimate is changed, whilst the rest are held constant (JCGM, 2008).

In most cases propagating errors in this way to evaluate the 'total combined standard uncertainty' is sufficient in describing the measurand uncertainty. However, uncertainty confidence intervals can be determined by expanding an uncertainty estimation to show how confident the uncertainty is.

Confidence is defined as: an estimate of the probability that a repeated experiment will find a similar value. i.e. the confidence statement is a probabilistic description that a measurement will fall within the standard deviation of the mean measurement when a study is repeated (Carpi & Egger, 2008).

The 'expanded uncertainty' can be calculated using equation 52 by applying a coverage factor 'k' to the 'total combined standard uncertainty':

$$u(y)_{expanded} = k * u_c(y) \qquad 52$$

Table 6 below, shows the common distributions, their confidence level, and coverage factor – the choice depends on the probability distribution and required confidence. (Lewis et al., 2005).

Distribution	Parameter	Confidence Level	Coverage Factor
Normal	1 standard deviation	67.7%	1
Normal	2 standard deviations	95.5%	2
Normal	3 standard deviations	99.7%	3
Rectangular	Semi-range	100%	$\sqrt{3}$
Triangular	Semi-range	100%	$\sqrt{6}$

Table 6 – Shows common distributions, their confidence level, and coverage factor for a desired expanded uncertainty (Lewis et al., 2005).

Usually, using simplified standardised uncertainty in BS EN ISO 9869-1 (BSI, 2014) for the U-value measurement overestimates the uncertainty; it states the thermal transmittance measurement uncertainty margin lies between ±14-28%. Some authors studies fall in-line with this assumed uncertainty; (Desogus et al., 2011) compared destructive and non-destructive U-value assessments finding a disparity of ±7% and of ±16% when temperature differentials of 10°C and 7°C were applied in measurement, respectively. Other authors have suggested a higher uncertainty by comparing the calculated with the measured U-value; (Asdrubali et al., 2014) found a difference up to ±43%, whilst (Evangelisti et al., 2015) found a difference up to ±153%, in the worst-cases analysed. These authors put the large deviations down to unknown stratigraphy across the internal face or an inaccurate thermal conductivity value was used in the analytical calculation in BS EN ISO 6946 (BSI, 2017b).

Other sources of error can stem from: sensor placement, stratification of the internal air, contact between sensor and wall surface, and instrument precision (Cesaratto & De Carli, 2013). (Meng et al., 2015) showed a measurement error up to 6% when thermocouples were improperly pasted and up to 26%

when heat flux plates are improperly pasted. Some of these errors can be minimised by taking long-term measurements or with steadier conditions (J. R. Taylor, 1982).

Using a statistical approach to analyse the error in a U-value measurement (Baker, 2009), the uncertainty was reduced to approximately ±5.75% – this is also the favoured value for U-value uncertainty used in (Fitton et al., 2017).

Although there are various methods to calculate the uncertainty budget in a measurement, similarities between the understandings are stark; it is scientifically crucial to understand the possible values of a measurement estimation.

The uncertainty analysis in these works followed the GUM method (JCGM, 2008), propagating the errors when calculating the heat flux, SR, and U-value measurands.

In the following section, data acquisition methods, equipment, and instruments are described. Then aims/objectives/etc. are presented before the literature review of building physics related to by study: policies, heat transfer appraisal, analytical methods, the current measurement methods, numerical calculations, modelling numerical simulation theory, and software.

3.1.6 Data Collection

For the reasons mentioned above, uncertainty in the measurement data must be analysed. Both SR and U-value calculations followed relevant measurements standards, therefore, since the calculation involves multiple single measurements, proper propagation is needed in evaluation.

Calculation of U-value (transmittance) measurement used the averaging method in BS EN ISO 9869-1 (BSI, 2014), whereas the SR measurement uses the method defined in BS EN ISO 6946 (BSI, 2014, 2017h, 2018b). Microsoft Excel will be used to compute the minutely data, calculating measurement averages and analyse uncertainty.

Using only the U-value measurand calculation as an example, heat flux and temperature difference (air-to-air) are captured simultaneously (BSI, 2014). Temperature and flux, measured with thermocouples and HFM, respectively, have associated instrument errors which, in general, are listed in the manufacturer specifications (Hukseflux, 2021a). The U-value is determined by dividing the heat flux by the temperature differential (BSI, 2018b), therefore errors associated with each individual measurement ought to be properly captured within the uncertainty analysis of the estimated U-value (Baker, 2009) measurand which requires propagating their errors (JCGM, 2008).

Qualitative IR was used to position sensors and highlight any presence of surrounding anomalies effecting 1D assessments (BSI, 2018b).

Quantitative IR using surface temperatures from internal surveys is standardised in BS EN ISO 9869-2 (BSI, 2018b). Novel measurement procedures seen in literature (Benko, 2002; Bianchi et al., 2014; O'grady, 2018) utilised this by calculating the incidence factor of a linear-TB, a metric estimating the TB-transmittance. A similar method (Asdrubali et al., 2012) utilises HFM to evaluate the same TB and is a comparable novel measurement method.

Within in the EH labs, the experimental design will be initial developed in a preliminary experiment testing model re-calibration by comparing novel measurement methods with FE results to vindicate its efficacy when quantifying a simpler linear transmittance (psi-value) using measurements taken from the same experimental investigation. This aims to identify sensitive parameters and categorise potential methodological improvements.

Using learnings from the preliminary experimentation, the experimental design will be developed further in a second experiment, applying the same FE calibration to a 3D point-TB. This type of TB relies solely on FE quantification with no comparable measurement. Embedded sensors will collect measurements from within the investigated structural TB connection for model re-calibration.

Final development of the experimental design will investigate a representative steel-to-steel configuration penetrating a lightweight rainscreen-cladding system that conforms to building regulation. Employing OFAT to test 6 thermal break variants (5mm, 25mm over three different materials: TBL, TBF, TBK), the impact of the STB solutions can be scrutinised, whilst developing the in-situ experimental design of measurement and modelling for field testing.

Of course, every effort was made to maintain unanimous conditions across all test phases to compare their thermal characteristics and, endeavours to minimise uncertainty was practiced (such as: calibrating sensors, using thermal paste to ensure sound thermal contact, initial qualitative IR, use of high emissivity and reflective tape in thermography, etc).

3.1.7 Equipment

When choosing sensors for measurement in the built environment, it is important to consider three major elements: their range, accuracy, and cost. In the next section, the possible sensors – to measure temperature and heat flux – will be described and compared justifying their choice.

3.1.7.1 IR

The physics of radiation is briefly touched on here and discussed further later. Essentially, any object with a temperature above absolute zero (0[K]) will radiate within a range of wavelengths from 0 to infinity. Most temperatures commonly found in a building physics context are within the infrared part of the electromagnetic spectrum. Generally, the higher the temperature of an object, the more infrared radiation it emits (Balaras & Argiriou, 2002).

The energy irradiated from the object, W_{obj}, is the only term of interest for quantitative analysis since it is a function of the object temperature. W_{refl} is the reflective power from the surrounding ambient objects, depending on their temperature. W_{atm} is the atmospheric emission, depending on air temperature, relative humidity, and distance from the object – see Figure 34 for illustration.

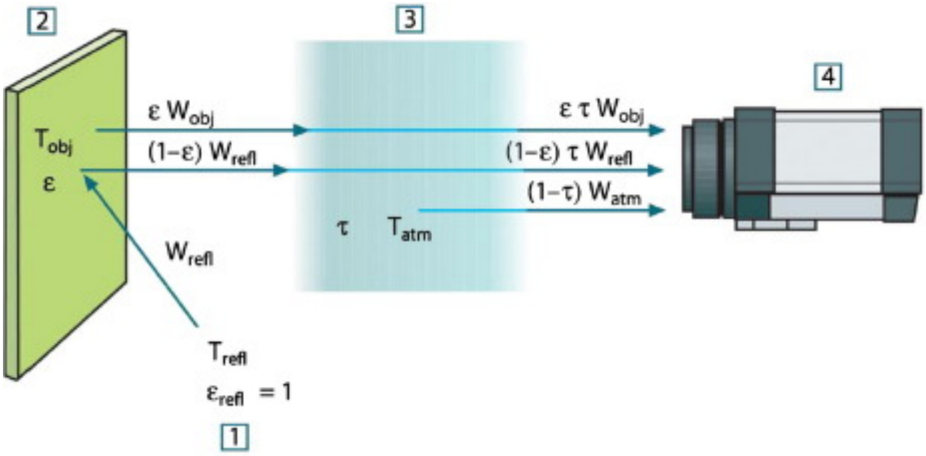

Figure 34 – Sketch illustrated by FLIR Systems (Flir Systems, 2019).

Three cameras were used in these works: handheld FLIR camera was used for qualitative surveys and two Optris cameras were used for quantitative transient thermography: one with a resolution of 640x480 pixels, the other with a resolution of 382x288 pixels, both with the same accuracy of ±2°C or ±2% (Optris, 2021).

To perform quantitative surveys, calibration is necessary. The most important parameter for calibrating the IR camera, is the emissivity. Following BS EN ISO 18434 (BSI, 2008b), a piece of black tape with known emissivity is applied to the target surface and the temperature recorded after inputting the emissivity value to the camera. Removing the tape, a second temperature is record in the same location on the target object, where the tape was. The emissivity is then adjusted on the camera until the temperatures match (Asdrubali et al., 2012). The other method, depicted in the same standard (BSI, 2008b), the contact method, requires using the cameras measurement function to define a measurement point or area in the centre of thermogram. Then, using another measurement instrument to quantify the temperature of this point, the emissivity of the camera is then adjusted until the temperatures match.

3.1.7.2 Thermistors

Made from ceramic semiconductors, the thermistor (thermally sensitive resistor) is an active device since it does not produce its own output; a current source detects the resistance in the sensor, which varies depending on the temperature. Various types are available (low to moderate cost in general) of two distinct categories: NTC (negative temperature coefficients) and PTC (positive temperature coefficients), meaning the resistance drops and increases, respectively, with an increasing temperature (Capgo, 2014b; Ramsden, 2000). The metal oxides which they are formed from characterise the sensors resistive behaviour by doping various additive elements. Iron, nickel, cobalt, copper, and manganese are commonly used for NTC devices; whilst barium, strontium, and lead titanates are commonly used for PTC.

The Temperature vs Resistance curves are distinctly difference for NTC and PTC. NTC curves exhibit an exponential decay with decreasing temperature, whilst PTC curves display a sudden change in resistance at a prescribed temperature (see Figure 35) – called a switch temperature (in the range of 60-120°C) – hence there main applications, are self-regulators for heating elements, but not exclusively.

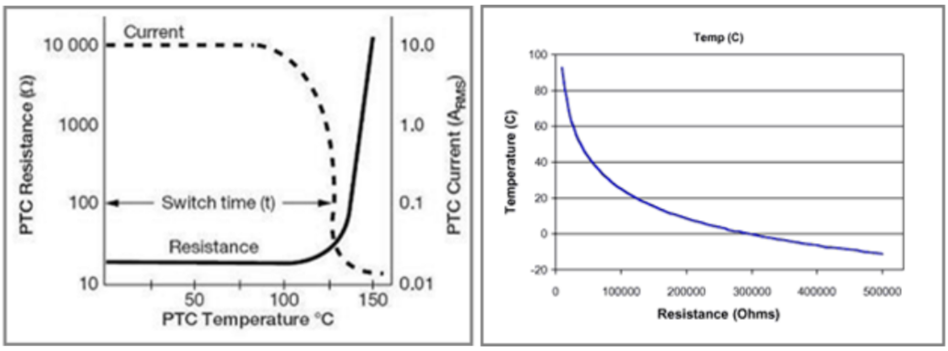

Figure 35 – PTC curve vs NTC curve (StirlingSensors, 2019).

PTC sensors have two groups (ee power, 2020): 'Silistor' (using silicone as the semi-conductive material) and 'Switching', that exhibit linear and highly non-linear curves, respectively (see Figure 36).

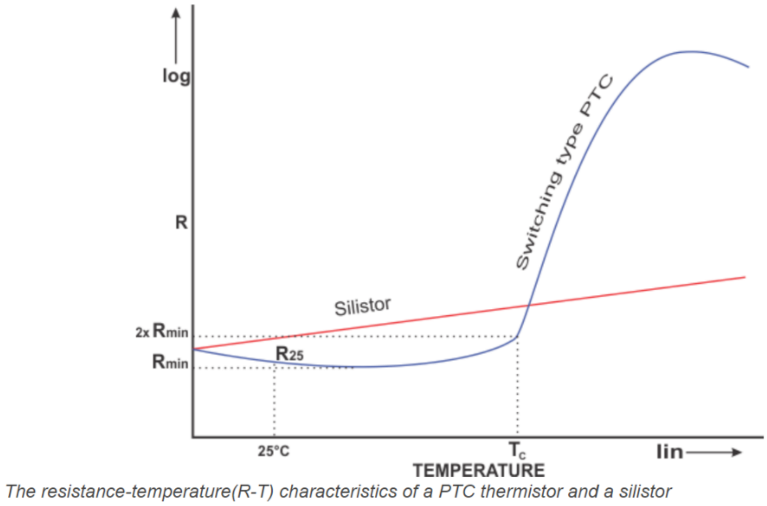

Figure 36 – PTC thermistor comparison between 'Silistor' and 'Switching' types (ee power, 2020).

NTC thermistors have a working range between -55°C and +200°C and the change in resistance due to temperature is non-linear, causing a challenge to compute the temperatures accurately in analogue circuits (ee power, 2020). Digital circuits have somewhat solved this problem by enabling precise computation: interpolating values of the recorded resistance ('B' values, that allow linear approximation between two temperature points) or, solving an approximation equation of the characteristic NTC curve (Steinhart-hart equation) (ee power, 2020).

In summary, thermistors have a high sensitivity and response time; primarily due to the large resistance change over small temperature variations – providing a high resolution, making it highly accurate (typically, ±0.05°C).

RTD's (Resistance Temperature Detector) are also temperature sensors which measures the temperature dependant resistance. Much like a thermistor, it is an active device and requires a small current to be passed through the sensor generating a voltage, therein deducing its resistance. The change in resistance due to temperature is considered linear, therefore a simple interpolation can easily evaluate a temperature from recorded signals. (ee power, 2020) unlike thermistors, see Figure 37:

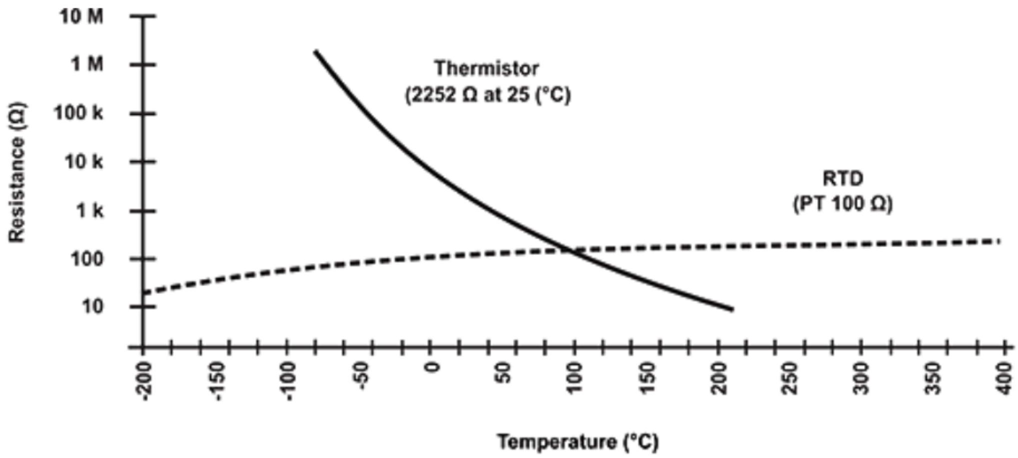

Figure 37 – NTC vs RTD (Temperature vs Resistance graph) (ee power, 2020).

The PT100 sensor is a Platinum Resistance Thermometer (PRT) – a type of RTD – manufactured to 100 Ω at 0°C; and , as you can see from Figure 37 the resistance increases as the temperature increases, just not as dramatically as the thermistor, illustrating the RTD's potential shortcomings in accuracy (ee power, 2020).

That said, the accuracy of an RTD's can range between ±0.1℃ -1℃, which is considerably acceptable in most applications and a much greater range of temperatures can be detected. There are various types of RTD sensors offering different qualities dictated by their composition (commonly either platinum, nickel, or copper) (Capgo, 2014a; Ramsden, 2000) which change their resistance, altering accuracy and working range.

For example, a PRT, as mentioned in the above example, can be manufactured as 'Flat Film' or 'Wire Wound' acceptable for low and high temperature ranges, respectively. 'Flat Film' features a platinum resistor embedded in a ceramic substrate, coated in glass or epoxy for protection. 'Wire Wound' on the other hand, features a length of fine coiled platinum wire around a ceramic or glass core, covered in a protective coating. The latter is much more expensive but has a faster response time and greater accuracy. Therefore, the choice depends on the application as their cost can vary dramatically (StirlingSensors, 2019).

To illustrate this, the difference between a PT100 and PT1000 is shown in Figure 38, taken from (Thermo-Sensor, 2021).

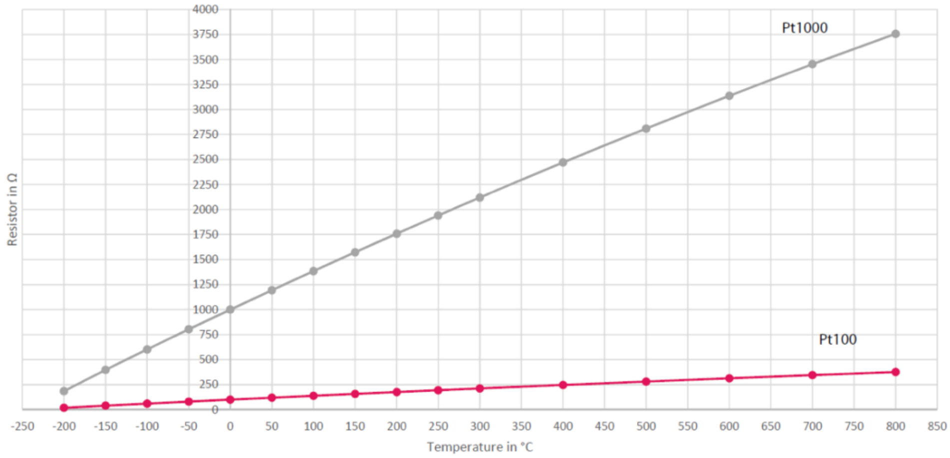

Figure 38 – Comparison between PT100 and PT1000 (Thermo-Sensor, 2021).

PT1000 is a PRT with a known resistance of 1000Ω at 0°C, whereas the PT100 has a 100Ω resistance at 0°C (BSI, 2008a). This generates a larger gradient, hence greater resolution when interpreting the measured temperature.

An RTD sensor resistance can be measured using a 2-wire configuration, but the resistance in the copper lead wires – carrying the signal from the detector to the logger – will be causing errors since they also exhibit a resistance. Using sensors with minimal wire resistance compared to sensor resistance minimises this error. Figure 39 shows alternative configurations to mitigate against this. Three or four-wire configurations compensate for the wire resistances by subtracting them from the total resistance – reducing the measurement errors – allowing a more accurate measure of the sensor resistance change proportional to temperature (StirlingSensors, 2019).

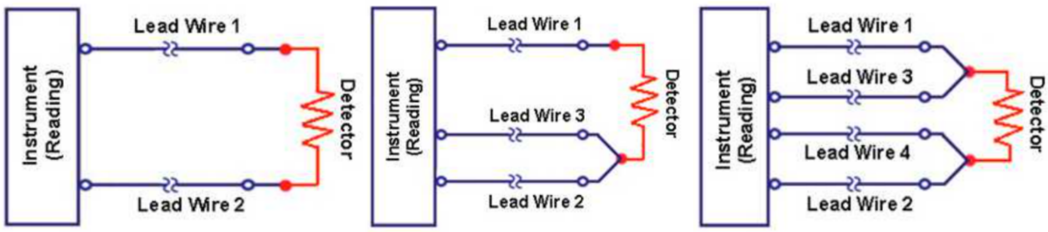

Figure 39 – From left to right, see the two, three, and four-wire RTD circuits (StirlingSensors, 2019).

In the three-wire configuration, the average of one lead wire resistance can be calculated and subtracted, making it more accurate than the two-wire configuration. The four-wire configuration is more accurate still by removing average resistances from both lead wires. The application of the four-wire configuration is warranted only if the lead wires are extremely long or extremely precise and accurate measurements are required (StirlingSensors, 2019).

The main difference between the thermistor and the RTD is that they are made from metal oxides and pure metal, respectively. Thermistors have much higher thermal coefficients of resistance, offering much higher sensitivities and accuracy. Although this makes it possible to measure temperature changes to one hundredths of a degree, thermistors have a highly non-linear relationship complicating interpolation and their operating temperature ranges are limited. Both sensors succumb to the same shortcoming of self-heating – due to some of the energy, from the required current to detect the sensor resistance, dissipating within the active sensors – since they are resistors after all.

Thermocouples are also temperature sensors but characteristically different in that these are passive sensors which do not need any current to produce a measurable voltage. The principle is based on the Seebeck effect: joining two dissimilar metals in a loop, one can observe a temperature change at the connection point when a voltage is applied to the other end (Pollock, 1991).

3.1.7.3 Thermocouples

The conductivity of a material depends on the capability of electrons to flow from the valance band to the conduction band. A metal is considered a good conductor since the valance and conductance bands overlap allowing electrons to flow to the conduction band easily, whereas good insulators, on the other, feature a band gap. Each material has its own Fermi level – a hypothetical energy level of an electron. Used in band structure theory in solid state physics, the position of the Fermi level in relation to the band energy of the molecule is crucial in understanding the electrical properties of the material; in thermodynamic equilibrium the fermi level would have 50% probability of being occupied by an electron (Kittel, 2004).

Joining two dissimilar metals together causes electrons to flow from one material, in which the electrons are less bound, to the other. When in contact, the Femi levels of the dissimilar metals balance, caused by electrostatic potential between the two joined dissimilar metals – also known as a contact potential, measured in coulombs. If a closed circuit exists (i.e., joining two ends forming a loop consisting of two dissimilar metals), there is no electro motive force since the two contact potentials oppose each other, cancelling the current flow. However, when one junctions' temperature is increased compared to the other, a current is formed, inducing an emf if the two dissimilar metals have different Fermi levels (Hosch, 2009).

Seebeck first discovered this in 1821, noticing that joining two dissimilar metals caused a compass needle to deflect when a temperature difference was observed along the wire. He thought he had found a way of converting thermal energy into electrical energy, later it was shown that the magnetic field produced was a result of the electron diffusion current generating an emf due to Lenz's law (Salman, 2003).

This concept is used to measure temperature with great accuracy since the temperature gradient has a liner relationship with the measured voltage, the magnitude of which depends on the materials comprising the thermocouple (Rowe, 2016). Directly proportional, the voltage and temperature differentials are defined with the temperature-dependant Seebeck coefficient '$-S(T)$', under open circuit conditions with no current flow, see equation 53:

$$\Delta V = -S(T) * \Delta T_{1-2} \tag{53}$$

The voltage can be measured passively from an open end of the thermocouple circuit, as seen in Figure *40*, applying this in the characteristic function (equation 53), pairs of thermocouple materials can be categorised at known fixed temperatures to establish the Seebeck coefficient for that pair (Pollock, 1991).

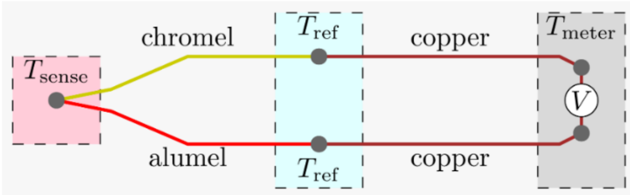

Figure 40 – K-type thermocouple diagram (Rowe, 2016).

The various types of thermocouples are shown in the following Figure 41:

ANSI/ASTM	°C Temperature Range	Standard	Special
T	-200° to -67° -67° to -62° -62° to 125° 125° to 133° 133° to 370°	± 1.5% T ± 1° ± 1° ± 1° ± 0.75% T	± 0.8% T* ± 0.8% T* ± 0.5° ± 0.4% T ± 0.4% T
J	0° to 275° 275° to 293° 293° to 760°	± 2.2° ± 2.2° ± 0.75% T	± 1.1° ± 0.4% T ± 0.4% T
E	-200° to -170° -170° to 250° 250° to 340° 340° to 870°	± 1% T ± 1.7° ± 1.7° ± 0.5% T	± 1°* ± 1°* ± 0.4% T ± 0.4% T
K	-200° to -110° -100° to 0° 0° to 275° 275° to 293° 293° to 1260°	± 2% T ± 2.2° ± 2.2° ± 2.2° ± 0.75% T	— — ± 1.1° ± 0.4% T ± 0.4% T
N	0° to 275° 275° to 293° 293° to 1250°	± 2.2° ± 2.2° ± 0.75% T	± 1.1° ± 0.4% T ± 0.4% T
R or S	0° to 1260° 1260° to 1480°	± 1.5° ± 0.25% T	± 0.6° ± 0.1% T
B	870° to 1700°	± 0.5% T	± 0.25%
C**	0° to 426° 426° to 2315°	± 4.4° ± 1% T	— —

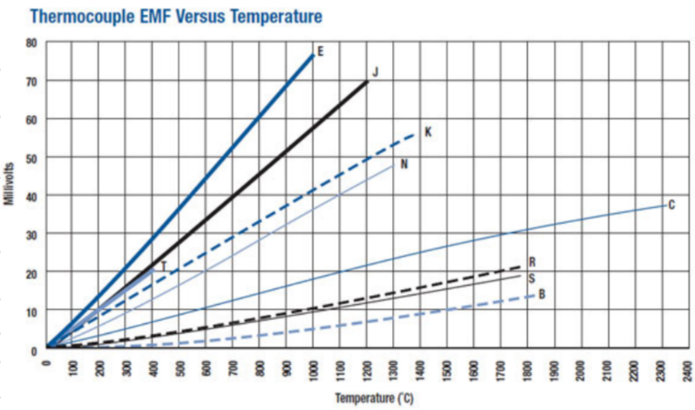

Figure 41 – Property comparison of thermocouple types (Thermometrics Corporation, 2012).

Conductor materials are seen in Figure 42:

T/C Type	Conductor +	Conductor –	T/C Junction Continuous Temperature range °C	INTERNATIONAL IEC 584-3:1989 BS 4937 P.30:1993
E	Ni-CR	Cu-Ni Constantan	0 to +800	
J	Fe	Cu-Ni Constantan	0 to +750	
K	Ni-Cr	Ni-Al	0 to +1100	
N	Ni-Cr-Si Nicrosil	Ni-Si-Mg Nisil	0 to +1100	
R	Pt-13Rh	Pt	0 to +1600	
S	Pt-10Rh	Pt	0 to +1600	
T	Cu	Cu-Ni Constantan	-185 to +300	
B	Pt-30Rh	Pt-6Rh	+200 to +1700	

Thermo-couple	Material (+/–)	Class 1 Tolerance	Class 2 Tolerance	Class 3 Tolerance
Type E	Chromel / Constantan	-40 to +375 : ±1.5°C +375 to +800 : ±0.4%	-40 to +333 : ±2.5°C +333 to +900 : ±0.75%	-200 to -167 : ±1.5% -167 to +40 : ±2.5°C
Type J	Iron / Constantan	-40 to +375 : ±1.5°C +375 to +750 : ±0.4%	-40 to +333 : ±2.5°C +333 to +750 : ±0.75%	N/A
Type K	Chromel / Alumel	-40 to +375 : ±1.5°C +375 to +1000 : ±0.4%	-40 to +333 : ±2.5°C +333 to +1200 : ±0.75%	-200 to -167 : ±1.5% -167 to +40 : ±2.5°C
Type N	Nicrosil / Nisil	-40 to +375 : ±1.5°C +375 to +1000 : ±0.4%	-40 to +333 : ±2.5°C +333 to +1200 : ±0.75%	-200 to -167 : ±1.5% -167 to +40 : ±2.5°C
Type R & Type S	Platinum–Rhodium / Platinum	0 to +1100 : ±1°C +1100 to +1600 : ±(1°C+0.003* (t°C-1100°C))°C	0 to +600 : ±1.5°C +600 to +1600 : ±0.25%	N/A
Type T	Copper / Constantan	-40 to +125 : ±0.5°C +125 to +350 : ±0.4%	-40 to +133 : ±1°C +133 to +350 : ±0.75%	-200 to -67 : ±1.5% -67 to +40 : ±1°C
Type B	Platinum–Rhodium / Platinum–Rhodium	N/A	+600 to +1700 : ±0.25%	+600 to +800 : ±4°C +800 to +1700 : ±0.5%

Figure 42 – Thermocouple type comparison (StirlingSensors, 2019).

The dominant temperature measurement instrument used in this research is the T-type thermocouple (see Figure 43) because their cost is low with suitable operating ranges and sensitivity for monitoring the built environment.

Figure 43 – T-type thermocouples.

Illustrating the comparison between the three temperature sensors mentioned, see Figure 44:

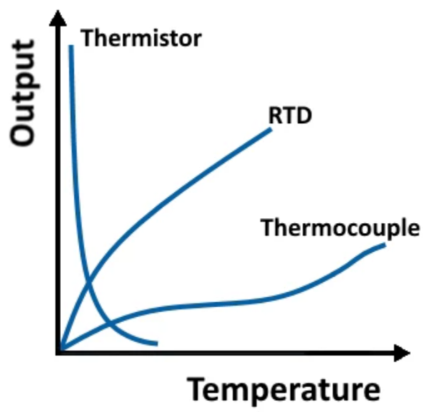

Figure 44 – Comparison of the available temperature sensors (NI, 2021).

T-type thermocouples were used in all experiments in these works measuring both internal and external, air and surface temperatures. Like all thermocouples, they measure temperature directly using the Seebeck effect (Pollock, 1991) (Rowe, 2016). T-type is made from combining copper and constantan (a copper and nickel alloy) featuring a temperature range of around -185°C to +370°C making it suitable for the expected ranges typically experienced in building physics (Wilkerson, 2012).

Only T-type thermocouples, with an error of ±1°C, were used in measurement throughout all experiments – comprised of Nickle and Constantan (Nickle-copper alloy) with a working temperature range of -180°C to +300°C, making it a suitable choice for temperature measurements within the built environment.

3.1.7.4 HFM – Thermopile

Hukseflux detail the working principles of their HFM (Heat Flux Meter) sensor 'HFP01' in a manufacturer specification report (Hukseflux, 2021b). Essentially, this is a thermopile transducer device which records electrical voltage signals that are proportional to heat flux [W/m^2].

A thermopile allows the heat flux to be measured directly (greenTEG, 2021), passively, since it does not require power; thermocouples are connected in series, creating pairs, with junctions either side of a thermal resistive layer, quite literally piling up thermocouples. This generates a voltage proportional to the temperature difference (Pineda & Rezaniakolaei, 2017), hence, the heat flux through the thermal resistance layer can be determined (if its average conductivity and thickness are known) by applying Fourier's law of conduction (ASTM, 2015; FluxTeq, 2018; Hukseflux, 2021a), see Figure 45 below:

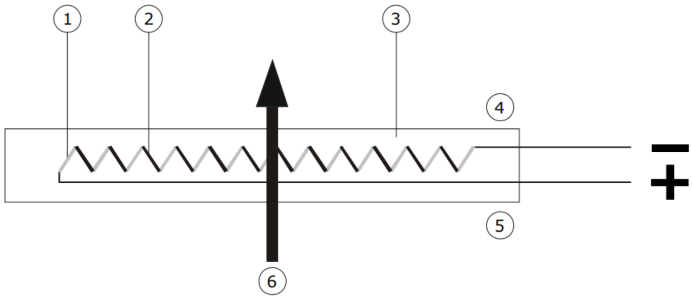

Figure 45 – Example of thermopile transducer from (Hukseflux, 2021b) shows a heat flux (6) transmitting through (3) the sensor body, from the hot (5) side to the cold (4) side. Both (1) and (2) are dissimilar metals creating thermocouple junctions, located on the opposite surfaces (hot and cold).

This concept is illustrated again by FluxTeq in Figure 46:

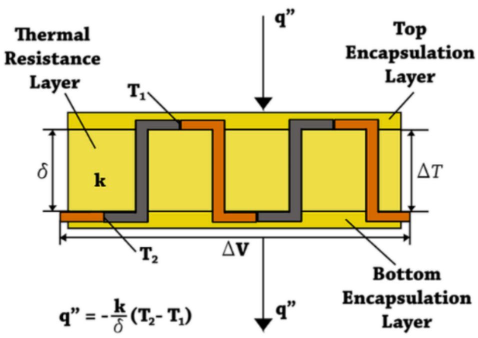

Figure 46 – Depictions by and FluxTeq (FluxTeq, 2018).

ASTM C518-17 (ASTM, 2015) the *'American Standard Test Method for Steady-state Thermal Transmission Properties by Means of the Heat Flow Meter Apparatus'* covers the steady-state measurement of thermal transmission using heat flow meters. It also shows the working principles of the transducer sensor (thermopile), and that the temperature coefficient of the transducer sensitivity depends on the type of temperature detectors used in the transducer (thermocouple material type in the thermopile) and the core material creating the thermally resistive layer with a known conductivity and thickness. Higher voltage can be obtained by adding more thermocouple pairs in series (ASTM, 2015) or by using alternative thermocouple configuration see Figure 47.

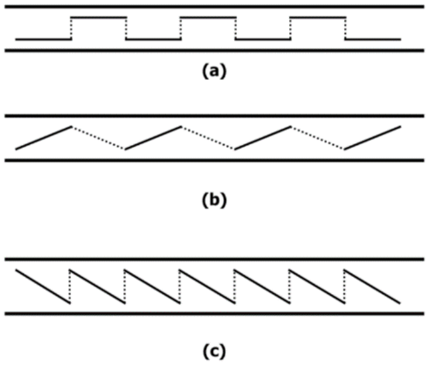

Figure 47 – Comparing possible thermocouple configurations in a thermopile (ASTM, 2015).

The document ASTM C518-17 (ASTM, 2015) refers the reader to equivalent international standard ISO 8301:1991 (BSI, 1991a). Similarly, BS EN ISO 9869 (BSI, 2014) – again, illustrating the working principle of the heat-flow meter transducer (thermopile) showing the essential properties to consider for their construction in Figure *48* – again, refers the reader to the same standard ISO 8301 (BSI, 1991a) since the HFM calibration methods to evaluate new sensors use absolute methods (achieving a known calibration factor with an accuracy of ±2%) such as the 'Guarded Hot Plate Apparatus' ISO 8302:1991 (BSI, 1991b), or a 'Heat-Flow Meter Apparatus' ISO 8301 (BSI, 1991a), on various materials, at various temperatures, and fluxes (BSI, 2014).

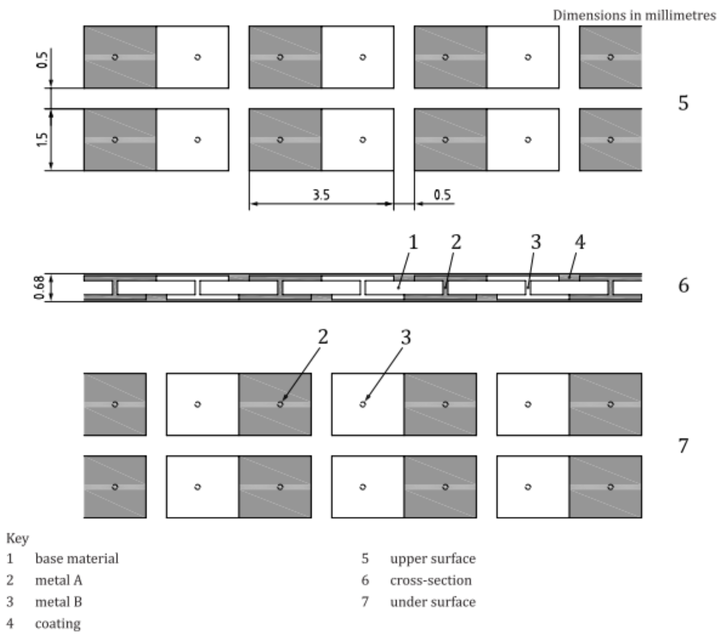

Figure 48 – ISO 9869-1 shows a depiction of a heat flow meter construction (BSI, 2014).

The contributing factors to a typical uncertainty budget when measuring heat flux with Hukseflux sensors are: the calibration, temperature dependence, conductivity of the surrounding environment, and the appropriateness of the measurement location (Hukseflux, 2021a). Generally, their sensors have an uncertainty of ±3%, under factor calibration reference condition following ASTM C1130 (ASTM, 2017). With a coverage factor of two (i.e., k = 2), measurements of heat flux may attain ±6%. The temperature dependence specification is 0.1 [%/°C], meaning for every °C deviation from the calibration reference temperature of 20°C, 0.1% relative uncertainty should be added to the budget.

The placement of these sensors can also cause resistance errors; BS EN ISO 9869-1 (BSI, 2014) states typical uncertainties during in-situ measurement of ±20% showing a possible range of ±14-28% depending on the method of combining uncertainties. Other than the obvious in-situ uncertainty causation (weather factors, etc.), these could stem from a multitude of sources such as contact resistance (caused by air gaps between the sensor and the wall), or deflection error (BSI, 2014; Hukseflux, 2021a) (caused by added resistance due to the transducer itself, deflecting the isotherms – see Figure 49 & Figure 50).

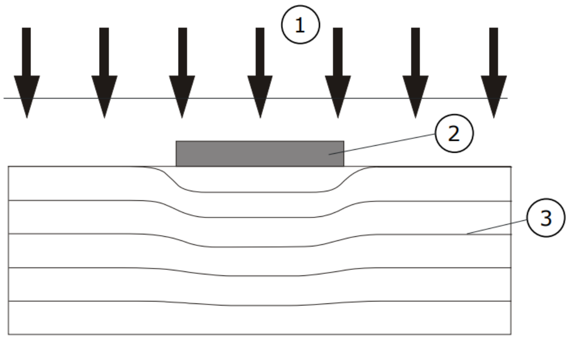

Figure 49 – Shows deflection in isotherms due to the increased resistance from sensor placement (Hukseflux, 2021a).

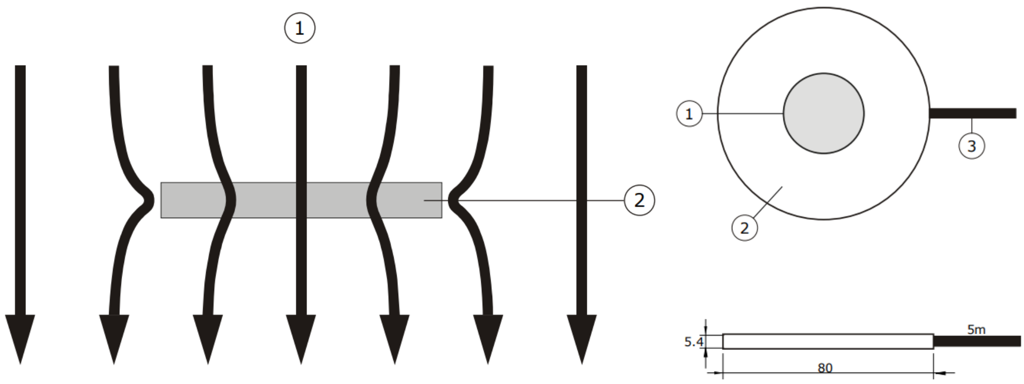

Figure 50 – (LHS) shows maximum deviations in flux occur at the sensor edge, (RHS) shows Hukseflux sensors dimensions (Hukseflux, 2021a).

Due to the large flux errors at the edges (see LHS of Figure 50), Hukseflux have guarded the sensing area with a ceramic ring (see RHS of Figure 50), successfully mitigating the uncertainty to the point that Hukseflux actually discouraging users to apply the correction formulas in BS EN ISO 9869 since they rely on assumptions of the surrounding material properties and the contact resistance (BSI, 2014; Hukseflux, 2021a).

The associated errors within the sensors will be used in the uncertainty analysis later in the experimental methodology. It is also important to include the data logger error within the uncertainty analysis. The equipment is explained in the next section.

Flux measurements will be taken using heat flow meters (FluxTeq and Hukseflux) sensors. Milli-volt (mV) readings are detected and recorded by the datalogger, which, in analysis needs to be converted into a flux using the heat flux sensor sensitivity coefficient. With units of micro-volts per flux [$\mu V/(W/m^2)$], this is unique to each sensor and is derived in calibration by the manufacturer and declared with the calibration conditions on the calibration certificate. This usually comes with a linear interpolation equation to scale the sensitivity coefficient depending on the operating temperature range, i.e., the value depends on the working temperature; if calibration was at 25°C then the declared value is only true for this temperature. The true working temperature should be used to scale the conversion coefficient for accurate flux measurement (FluxTeq, 2018).

3.1.7.5 Data Loggers

Dataloggers are programmed electronic devices which record data over time. Mostly, these devices can be configured to collect data in a specified way by using computer interface software or, in some case, using the local hardware (keypad or LCD screen). The channels on the data logger need to be configured to the signal (analogue or digital) it will receive (depending on the sensor) and the desired granularity (time-frequency).

Campbell Scientific, priding themselves in providing "Rugged Monitoring" offer a wide range of measurement and control instrumentation for multi-purposes, including dataloggers (Campbell Scientific Inc, 2021), see f*Figure 51* below. They suggest the main purchase considerations for data loggers are primarily: the site environment, measurement type and quality, programming flexibility, data storage, communications, and power requirements.

Figure 51 – Image show a typical Campbell scientific data logger (Campbell Scientific Inc, 2021).

A similar company, Graphtec (Graphtec Corporation, 2005), also offer a range of measurement recording loggers, however precision measurement instrumentation can become expensive. An example can be seen in the following Figure 52:

Figure 52 – Image shows a typical Graphtec data logger.

There are many potential loggers on the market with a vast price range, therefore careful consideration is needed when choosing the logger, ensuring it is fit for purpose and within budget.

Novus field loggers have 8 universal analogue input channels capable of receiving voltage, amperes, or resistance readings at rates of up to 1000/second (Novus Automation Inc, 2021), see the following Figure 53:

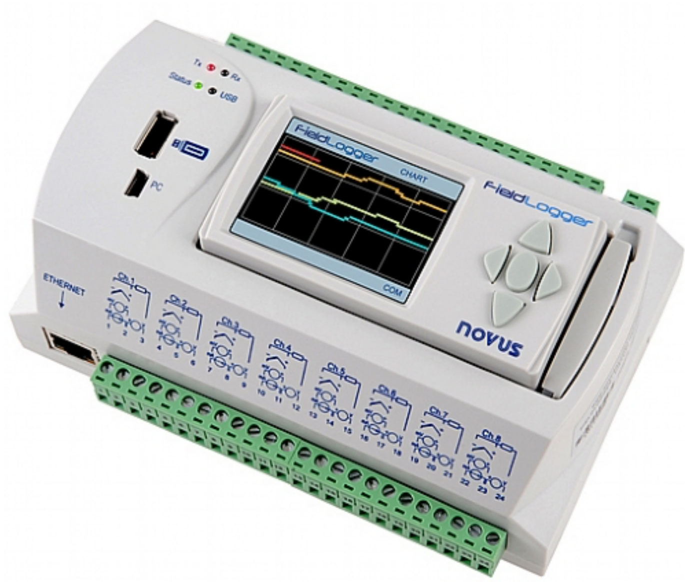

Figure 53 – Image shows the Novus data logger.

The data can be saved either in the internal flash drive memory, SD card, or USB. This data can be accessed and downloaded to many formats including .csv file manually or remotely (if the device is configured to a network through an ethernet interface).

These capabilities not only allow the data to be remotely viewed via a web page, but logger communication enables channels to be augmented with extenders (see Figure 54 below) where an array of ‘slave’ logger channels can be linked to one ‘master’ datalogger which disseminates the configuration. This is useful if more than 8 channels are required.

Figure 54 – Image shows Novus DigiRail used for channel augmentation.

Augmenting the Novus FieldLogger with channel extenders (via RS485 Modbus) allows all the data to be captured using one data logger, at the same time instant. Therefore, each measurement will have the same time stamp for clear comparison in data processing, avoiding the time-consuming pitfalls of matching up timestamps from different data sets when post-processing. The downside to the extenders is that large negative signals cannot be registered rendering them inapplicable for heat flux meters, however thermocouples can still be detected.

The voltage signals from each sensor are recorded using dataloggers (Graphtec and Novus). These are configured defining: the logging interval time and the sensor signal type, for each channel. As mentioned, each of these loggers have associated errors (typically 0.01-0.001%), which need to be incorporated in the propagation of errors in the uncertainty analysis.

3.2 Experimental measurement and modelling methods

Philosophical approaches, described in an earlier section ‘Research Methodology’, explain the research paradigm adopts a scientific experimental positivist methodology, dictated by the philosophical ontology and epistemology which are considered ‘realist’ and ‘objectivist’, respectively, following a linear structure: hypothesis, data collection, analysis, conclusion, and discussion (Creswell, 2009),

A robust experimental design will be developed in laboratory conditions, exploiting interactions between numerical modelling and collections of measurements.

As shown, structural TB is difficult to quantify with point-measurements therefore validated numerical FE modelling is entrusted to provide dependable predictions. Numerical modelling is a non-invasive, non-destructive, and relatively fast method of thermally assessing structures. However, as seen from the reviewed literature, it is not easy to develop models to accurately evaluate the energy performance of as-built constructions.

With no standardised TB measurement methods, some authors have developed novel measurement techniques quantifying 2D linear-TB. And, although the aim in these works is to assess point-TB, applying these novel techniques in a preliminary experiment, offers an opportunity to compare direct measurement of TB-transmittance with a calibrated model, developing the experimental design.

If the model recalibration technique is validated in this first experiment, it will be applied in a second experiment, investigating point-TB; using measured data to re-calibrate a FE thermal model – quantifying the TB transmittance with improved accuracy compared with standardised numerical approaches.

3.3 Pilot experimental design development

The experimental design aims to evaluate the energy performance of in-situ point TB connections by re-calibrating thermal models using physical measurement, categorising specific systems. It is developed within laboratory-controlled testing undertaken in the Energy House (EH) facility at the University of Salford (UoS) – where climatic-conditions can be controlled to quasi-steady-state.

With the EH, dynamic complexities effecting real-world measurements for BPE are minimised, since temperatures and complex convective and radiative fluid-surface heat transfer mechanisms can be fixed – this not only allows rapid testing but reduces variability inherent with field testing. Steady-state analysis is unaffected by thermal inertia (caused by thermal mass), therefore admittance (a thermophysical property describing the materials ability to store and dissipate heat) can be ignored. Idealising a scenario in such a way reduces uncertainty in measurements, allowing novel measurements techniques, analytical theories, or numerical approaches – predicting the energy-performance within the built-environment – an accurate affirmation.

Using this facility, the experimental design (model re-calibration) will be validated; specific scenarios can be recreated, then comparisons can be drawn against existing peer-reviewed novel measurement methods developed to measure simpler 2D linear-TB.

The method will be applied to analyse and characterise the heat flow through a 3D point-TB in the form of a steel beam cantilever, representing a single balcony support arm with which STB variations can be tested under laboratory-controlled conditions.

Eventually, in-situ measurements and data processing methods can be applied to thermally evaluate various situations in the field; typically focussing on steel-to-steel beam connections (cantilever supports or a column sections) in new-builds under dynamic conditions, but realistically, the connections could steel-to-concrete or concrete-to-concrete.

3.4 Pilot experiment 1 – Linear-transmittance

To validate the proposed model calibration initially, comparisons were drawn between novel measurements (using IR and HFM techniques) quantifying the 2D linear TB effect of a corner-corner wall junction (Ascione et al., 2014; Asdrubali et al., 2012; Baldinelli et al., 2018; O'grady, 2018). This is a common LTB primarily caused by large differences in heat emitting and heat absorbing surface areas. Lots of examples can be found within the EH labs, but the most fitting is a junction between two external walls in the upstairs bedroom, hence this was chosen for experimental investigation.

3.4.1 The Energy House facility

The EH is a fully furnished pre-1920's Victorian end-terrace, solid wall construction (made from locally reclaimed materials), representative of around 20% of the UK building stock (Alzetto et al., 2018). This common domestic building is built within a climatic controlled testing chamber (Marshall et al., 2017) – see Figure 55

The chamber is controlled using chiller and HVAC systems capable of emulating dynamic/steady weather condition including wind, solar, and rain. Temperatures can be held to ±1°C, over a range between -12°C and +30°C. Robust control of the external environmental conditions allows rapid testing, whilst the vast sensor network records temperature, flux, or humidity measurements at a fine granularity (Marshall et al., 2018).

Using laboratory-controlled facilities the situation is idealised minimising heat storage effects and volatile changes in SR (experienced in-situ due to solar and/or wind speed variations). Quasi-steady-state conditions, seldom found in-situ environments, were exploited in this study to develop the experimental design – measurement calibrated models – producing less uncertainty inherent with in-situ data capture. Normally, in-situ measurements are required to be captured over long time periods to reduce signal noise in the measurement enough that average values converge. Using the EH labs, not only is the acquisition time is drastically reduced, but theory and measurement methods (both novel and standardised) can be validated confidently.

Figure 55 – EH laboratory: end-terrace built inside a climatic chamber.

The wall composition is well known: 5 courses of English bond (no cavity), two layers of brick (222.5mm think), 12.5mm hard-wall plaster coat with internal plaster skimmed finish. Although, previous researchers (Fitton, 2021a) found a range of U-values (1.5-2.6 [W/m^2K]) when measuring the

EH wall depending on the sensor placement and data analytics, suggesting inconsistencies in wall composition.

In a full building energy model of the energy house, (Ji et al., 2014) considered a value of 2.05 [W/m^{2}K] for external walls in a numerical model. The assumed U-value used in energy models has a significant effect on the outcome. Therefore, in (Marshall et al., 2018) standard reference U-values from CIBSE Guide A (CIBSE, 2021), SAP (Li et al., 2015), and BR443(Anderson, 2006) (with values of 2.09, 2.1, and 1.75 [W/m^{2}K], respectively) were compared with a model informed using physical measurements. The three in-situ measurement methods (BSI, 2014), HFM, low-resolution IRT, and high-resolution IRT, resulted in 1.57, 1.72, 1.52 [W/m^{2}K], showing that standardised U-values are often overestimated – agreeable by other authors (Baker, 2011; Doran, 2001; Rye & Scott, 2012).

3.4.2 Description of measurement

Two novel measurement methods quantified the linear transmittance from the corner of the room in the upstairs bedroom (two external wall junction) of the EH facility at the University of Salford. The 'incidence factor of the TB', a factor describing the increased transmittance compared with the 1D (unaffected) zone, was measured using both HFM and IR. This allowed comparison against the numerical modelling method proposed in these works (FE simulation, re-calibrated using physical measurements), assessing/validating its effectiveness before being applied later quantifying point-transmittance.

While small HVAC and internal-heating fluctuations were observed, quasi steady-state temperatures were held either side of the investigated TB aiming for 21℃ inside and 5℃ outside – maintaining around a 16℃ difference. These conditions were held 2-day prior to testing, mitigating heat storage as a source of error. Averages were taken over the last 12hr steady-state periods and used for analysis.

High emissivity tape was applied to the wall leading into the corner from the 1D unaffected zone – to better capture the true surface temperature gradient with IR – highly reflective strips indicated distance aiding thermogram postprocessing. The set-up is shown in Figure 56.

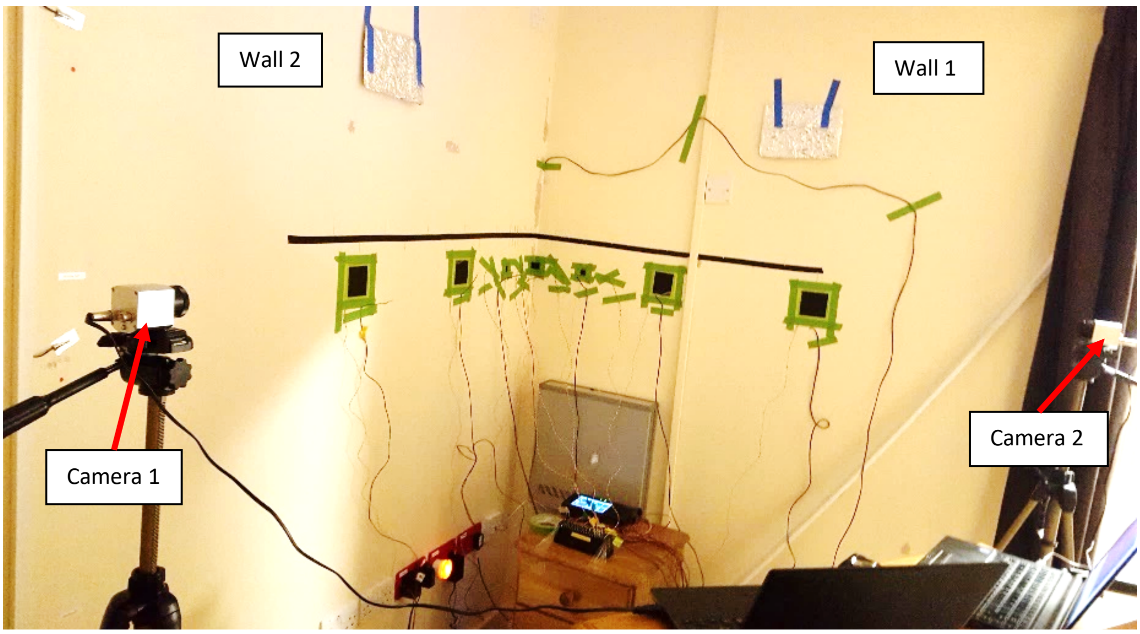

Figure 56 – Experimental set up of corner-corner transmittance experiment.

Internal infrared and heat flux plate measurement methods were applied simultaneously. All measurements taken from the experimental set-up were used to inform the model, ensuring robust model parameterisation and a fair comparison between measurement result and simulation output.

Measurement instruments include:

- Infrared camera Optris (x2)
- T-type Thermocouple (x 16 used) are a copper/Constantan coupling. In general, operating temperature ranges for this type are between -250℃ to 350℃ with an accuracy of ±1℃ or ±0.75% – whichever is greater.
- FluxTeq (large) x4, sensing area dimensions: 8.8cm x 9.5cm, with a sensitivity of 70-90 mV/(W/cm^2),
- FluxTeq (small) x4, sensing area dimensions: 2.54cm x 2.54cm, with a sensitivity of 9 mV/(W/cm^2).

Both Novus and Graphtec dataloggers were used in this experiment, simultaneously, due to resource availability and number of channels required.

Time-series thermography was performed utilising Optris thermal cameras which captured the temperature gradient leading into the bridge across the high emissivity line (Asdrubali et al., 2012). Camera 1 focused on wall 1 whilst the camera 2 focused on wall 2 (seen in Figure 56), synchronised to recording minutely data.

- Phase 1 – positioned cameras perpendicular from the wall, 1m away
- Phase 2 – positioned cameras perpendicular from the wall, 0.5m away

Optris PI 640 (with an accuracy of ±2℃ or ±2%, and resolution of 640x480 pixels) was used (see fFigure 57) in tandem with Optris Pi 450 (with and accuracy: ±2℃ or ±2%, and a resolution of 382x288 pixels) (Optris, 2021).

Figure 57 – Optris PI 640.

Initially (in phase 1), the IR images captured a 1m wall length to analyse, before being positioned closer to the wall capturing a 0.5m length to analyse in a later phase (phase 2). This decision was made from qualitative IR identifying that the greatest temperature gradient occurred within 100mm from the corner-corner TB. Hence a more concentrated view of 500mm, focusing on this gradient, was hypothesised to produce a more reliable quantification via the IRT method.

Following the calibration procedure in BS EN ISO 18434 (BSI, 2008b) a crumpled and flattened piece of aluminium foil was attached to the wall (seen in Figure *56*), the cameras emissivity was set to 1 and the reflected apparent temperature of the surrounding radiative heat sources was recorded. Then a location with a known temperature measurement (realised by fixing a T-type thermocouple to the wall with highly reflective tape – protecting the reading from radiative sources) was targeted with the IR camera and the emissivity settings was adjusted until the temperature reading on the thermogram matched that on the measured target.

Time-series thermogram data was logged with Optris GmbH – PI Connect software, using an individual laptop for each camera. The software saves .csv files displaying a temperature value for each pixel in the resolution.

Approximately 720 thermograms were analysed, covering the last 12hrs of the test period after 2-day conditioning. The Optris cameras saved each image to a directory as .csv files. Each cell in the file represented a pixel in the IR camera and had a value associated to a surface temperature. The high-ε tape line was identified in the image and a line, leading from the 1D heat transfer zone (highest temp) into the corner TB (lowest temp), was established (see Figure 58).

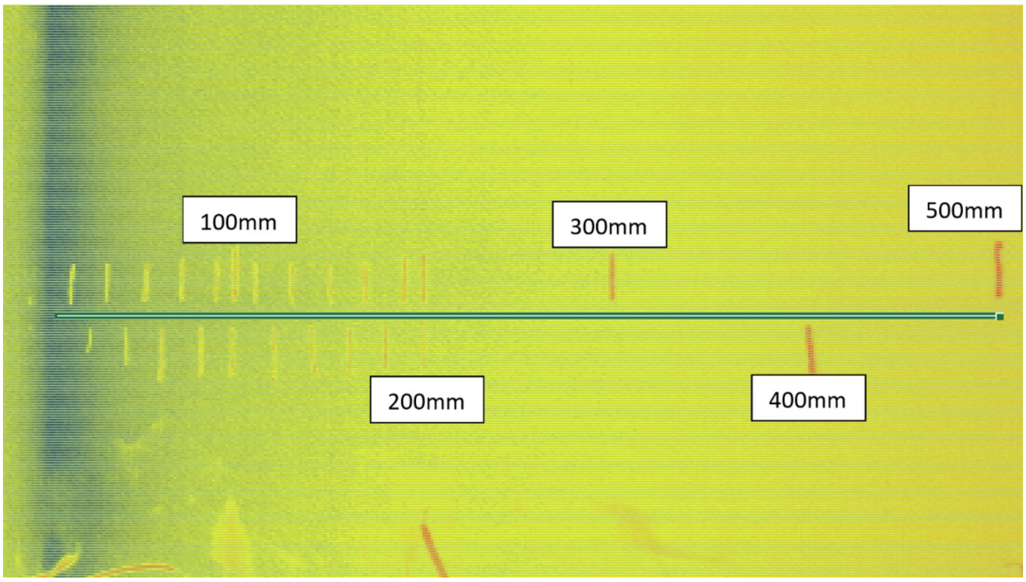

Figure 58 – Camera 1, Wall 1, Close view (Phase 2).

To develop the image, the .csv cells were made square, and colour conditional formatting was applied: higher temperatures set to red, lower temperatures set to blue, and yellow in between. The IR line for analysis is highlighted running directly into the TB along the high-ε tape surface and highly reflective indicators mark distances every 10 mm up to 500mm away.

As per literature (Asdrubali et al., 2012; O'grady, 2018), each pixel in the centre row was averaged using their neighbouring 8 pixels to smooth the IR line. This process was automized utilising python code ('pandas' library .csv manipulator): performing this process on each .csv in the directory then printing the time stamped IR line into a fresh Excel workbook (Figure *59*). Cam 1, wall 1, close (phase 2), captured the cleanest and most representative data therefore this was chosen for the IRT analysis.

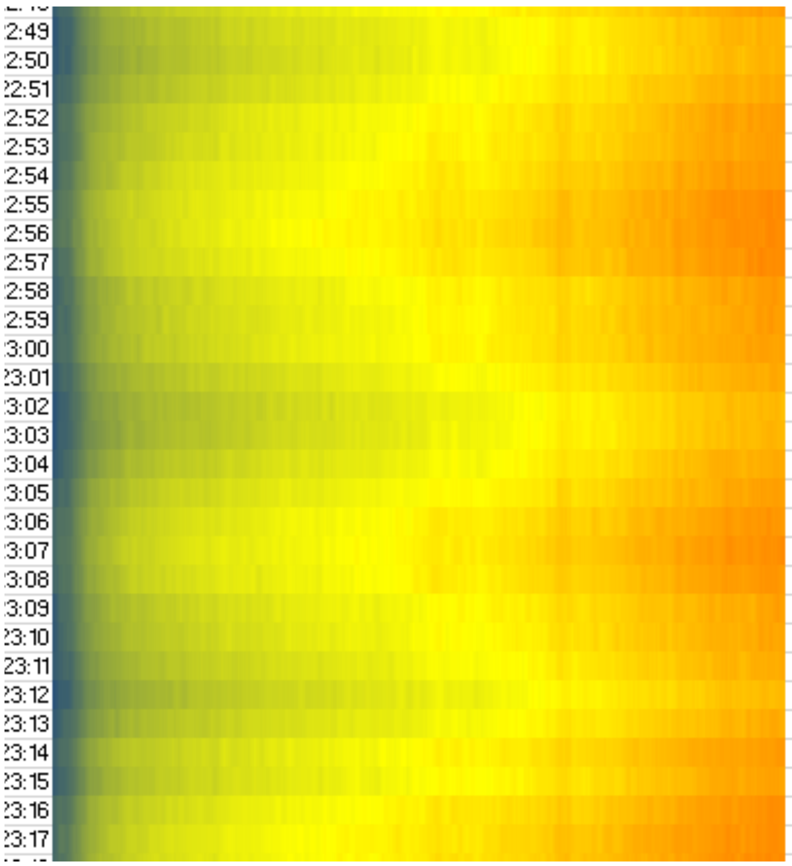

Figure 59 – Fresh workbook with IR lines, 0.4m long, from each .csv printed against timestamp.

The incidence factor was calculated for each IR line using equation 54, then averaged over the last 12-hour windowed period.

$$I_{tb_{IR}} = \frac{\sum_{P=1}^{N}\left(T_i - T_{pixel}\right)}{N(T_i - T_{1D})} \tag{54}$$

Where, '$I_{tb_{IR}}$' is the incidence factor using IR, 'T_i' is the internal air temperature, 'T_{pixel}' is surface temperature of the pixel, and 'T_{1D}' is the surface temperature of the unaffected zone, away from the corner, experienceing 1D flux.

The heat flux and temperature signals were also recorded minutely for the duration of the experiment then averaged for the last 12 hours.

FluxTeq (Figure 60) are approximately 600 microns thick, with a heat flux range of ±150kW/m^2, and a temperature range between -50°C to +120°C, featuring embedded T-type thermocouples. Using an in-house conduction-based calibration system developed by (FluxTeq LLC, 2022) calibration allocates a sensitivity specific to each sensor 'S_{Calib}', which, with units of [µV/(W/m^{2}K)], is used to convert the voltage signal to a heat flux (providing results of up to 5% accuracy). This has an associated sensor uncertainty attached within the calibration certificate from the manufacturer, typically in the range of +/-0.03 [μV/(W/m^{2}K)].

Figure 60 – FluxTeq thin film flux sensors, small (left), large (right).

Manufacturer calibration was at 25°C, therefore if operative temperatures deviate drastically, a multiplication factor 'M.F.' can be determined to adjust the conversion coefficient 'S_{Calib}' using the following equations 55 & 56:

$$M.F. = [0.00334 * T_{\circ C} + 0.917] \tag{55}$$

$$S_{T_{\circ C}} = M.F. * S_{Calib} \tag{56}$$

Where '$T_{\circ C}$' is the operation temperature, and '$S_{T_{\circ C}}$' is the temperature dependant sensitivity coefficient.

The array of thin film flux sensors (FluxTeq) (x8 in total, x4 on each wall) and a thermocouples were positioned leading into the TB directly beneath the high-ε tape (see Figure *56*), to record the corresponding flux values for the I_{tb_HFM} calculation, evaluated with equation 57:

$$I_{tb_{HFM}} = \frac{Q_{tb}}{Q_{1D}} = \frac{\varphi_{1D}A_{1D} + \varphi_{tb_1}A_{tb_1} + \varphi_{tb_2}A_{tb_2} + \varphi_{tb_3}A_{tb_3}}{\varphi_{1D}\left(A_{1D} + A_{tb_1} + A_{tb_2} + A_{tb_3}\right)} \tag{57}$$

Where, '$I_{tb_{HFM}}$' is the incidence factor using the HFM method, 'Q_{tb}' is the heat loss through the TB [W], 'Q_{1D}' is 1D heat loss [W], 'φ_{1D}' is the measured flux [W/m^2] , and 'A_{1D}' is the area over which the flux was measured [m^2].

U-value measurements of each wall were also simultaneously calculated using these sensors applying the in-situ BS EN ISO 9869 averaging method (BSI, 2014). Average measurements of U-values, fluxes, and surface temperatures were also referred to in the model parameterisation, shown below in Table 7:

	Ext Air	Int Air	Min Flux	Max Flux	Min Surf T	Max Surf T	U-value
	°C	°C	W/m^2	W/m^2	°C	°C	W/m^{2}K
Measured Average	5.3	21.3	25.1	29.4	15.2	18.2	**1.6**

Table 7 – This shows the internal/external air temperatures, min and max flux and surface temperature, and U-values measurements averaged over a 12hr period.

As expected, the maximum flux and minimum temperature were both measured directly in the TB, whilst the maximum temperature and minimum flux were recorded in the 1D (unaffected zone).

Uncertainties were assumed from the BS EN ISO 9869 (BSI, 2014) standardised average method (the lesser of the two options = ±14%) for calculating U-values, even though experiments took place within a laboratory environment (not in-situ where environmental conditions have greater effect on measurement uncertainty) where (Baker, 2009) suggests a smaller uncertainty of +/-5.75%. These provide some tolerance for the 2D FE thermal model parameterisation.

In this experiment, equation 54 was used to calculate the incidence factor from thermographic measurement and equation 57 was used to calculate the incidence factor from heat flux measurements. Since the incidence factor can be defined as the ratio between the TB and the 1D heat transmittance (Q_{tb} and Q_{1D}, respectively in equation 58):

$$I_{tb}Q_{1D} = Q_{tb} \tag{58}$$

Applying the U-value and analysis dimensions (lengths of 1D and TB affected zone), the psi-value from each method can be determined from equation 59:

$$\psi = (I_{tb} - 1)U_{1D}(l_{tb} - l_{1D}) \tag{59}$$

The lengths of the 1D and TB affected zones were taken as the total length of the IR line and array length of flux plates used to calculate the incidence factor, respectively. The heat flux evaluation of the incidence factor was assessed over a total wall length around 1m, assuming l_{tb} was 0.9 and l_{1D} was 0.1m. Whereas, the IRT method considered half that (0.5m), assuming l_{tb} was 0.45 and l_{1D} was 0.05m.

Novel measurement method comparison shows close agreement (see Table 8):

	I_{HFM}	I_{IR}
Incidence Factor	1.16	1.3
PSI-value [W/mK]	0.2	0.19

Table 8 – Incidence factor and psi-values from HFM and IR measurements.

The heat flux method obtained an incidence factor of 1.16 whereas the IRT method found 1.3. Considering the measured U-value of **1.6 [W/m^{2}K]** and applying an analysis length of (0.9-0.1=0.8m) for the HFM method, and (0.45-0.05=0.4m) for the IRT method, in equation 59, the psi-values were calculated as 0.20 [W/mK], and 0.19 [W/mK], for HFM and IRT methods, respectively.

(Asdrubali et al., 2012) also showed close agreement between methods of linear transmittance calculation comparing the CFD analysis, infrared, HFM method. The HFM method has the largest limitations – mainly due to difficulties locating the sensors correctly to capture the flux gradient approaching the 2D linear-TB, from the 1D zone.

3.4.3 Description of Thermal FE analysis

Data was captured simultaneously in the experiment and the novel linear TB measurement methods were in close agreement. The same physical measurements were used to parameterise and recalibrate a FE thermal model of the corner-corner wall junction.

3.4.3.1 Calibrating a FE thermal model:

By calibrating models, like seen in (Garay et al., 2014), it is possible to change the scenario to suit the simulation describing the invested detail (altering only structural dimensions, thermophysical properties, or SRs).

In sequential order, firstly the model geometry is generated using engineering drawings for known dimensions and manufacturer details for thermal properties, relative to the investigated construction detail.

- Gathering and applying this information should generate a similar representation (Dikarev et al., 2016). However, tolerances must be considered since any measurement is subject to uncertainty. Hence taking samples to test their conductivity (using a FoxFlowMeter apparatus for example) is advisable where possible.

Mesh independency / Convergence study (Iodice et al., 2016) (O'Grady et al., 2018) ,

- Refine mesh (double the elements) from previous – simpler – simulation.
- Note the change in results.
- When the iteration results converge to less than 1%, the simpler mesh of the final iterations provides sufficient accuracy (Ascione et al., 2013).

Calibration via measurements

- The boundary conditions (SR and air temperature measurements) are applied to the respective internal and external wall surfaces in the model (Martinez et al., 2017).
- The first calibration iteration is simulated with these conditions and results analysed:
    - Overall [W] metric is generated – total energetic losses between environments.
    - Isotherms – temperature gradient distribution through/across the model
    - Flux and Temperature at nodes – averaged at a point (or over an area) of interest.

- The surface temperatures and flux measurements, either from an array leading into the TB or embedded around the STB, for example, were used as response values (i.e., the model was probed at the same location the measurements were taken).
- Considering the accuracies and uncertainties of the measurement sensors (Sun & Reddy, 2006), the model parameters (thermophysical properties of the wall and thickness of wall layers – effecting conduction) were altered – within their sensible ranges – to inform the model re-calibration, until probed values to match their measured counterpart within tolerance dictated by uncertainty analysis.
- When the values match (within tolerance of accuracies/uncertainties) a calibrated status is achieved.

Calibrated status

- Once the model parameters used to set-up the simulation are a robust representation of the investigated wall (Šadauskiene et al., 2015), the steady-state metric describing the extra transmittance caused by the TB can be evaluated by applying the measured estimates for SR and air temperature (Ward & Sanders, 2016) in the calculation.

The generated TB transmittance metric can be compared against standardised methods of simulation (using BS EN ISO 6946 boundary conditions (BSI, 2017b) instead of in-situ values, other novel measurement methods of linear transmittance, or against TB atlases as seen in the standard BS EN ISO 14683 (BSI, 2017h) (or other TB atlases (BC Hydro, 2016; Little & Beñat, 2011; Passive House, 2021)).

An illustration of the calibration workflow is shown in Figure 61 below:

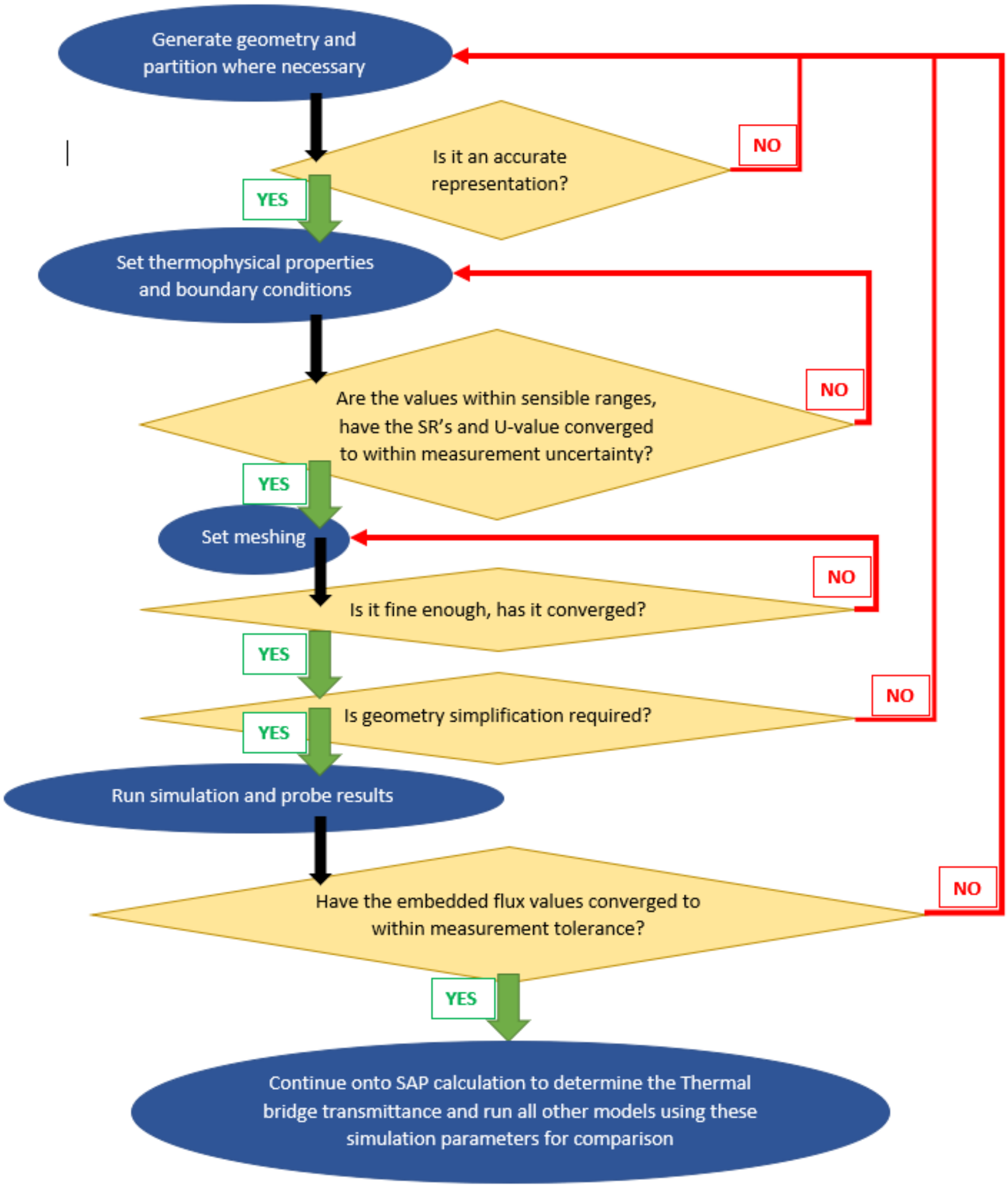

Figure 61 – Homemade flow chart depicting the re-calibration workflow.

Essentially, initial values were taken from manufacturer details (or accurately measured in the FoxFlowMeter) to parameterise the model and inform re-calibration by altering within sensible ranges until the probed model values match the experimentally measured values – considering measurement uncertainty.

3.4.4 In this experiment SECTION HEADING

Sensible ranges (Anderson, 2006; BSI, 2007) for the wall layers (brick [0.6-1.2W/mK], plaster [0.2-0.25W/mK], and skim [0.2-0.25W/mK]) correlate to the measured U-value, suggesting suitable thermophysical properties and boundary conditions (SRs are dependent on heat flow direction – taken from standard BS EN ISO 6946 (BSI, 2017b)) were used in model parameterisation, see Table 9.

Calibration	
Thickness [m]	Conductivity [W/mK]
0.225	0.7
0.013	0.2
0.005	0.2
Ext BC	25 [W/m^{2}K] @ 21[°C]
Int BC	7.7 [W/m^{2}K] @ 5[°C]
U	1.72 [W/m^{2}K] (7.5% difference)

Table 9 – Calibrated model parameters.

These assumed values produce a U-value of 1.72 [W/m^{2}K] which is approximately 7.5% different than the measured and within the assumed measurement uncertainty interval (±14%). The following describes the simulation set-up.

Abaqus/Standard FE heat transfer software assembled the simple 2D geometry of the investigated corner, where material properties and boundary conditions from Table 9 were applied, before meshing generated 22001 8-node quadratic heat transfer quadrilateral elements, see Figure 62) below.

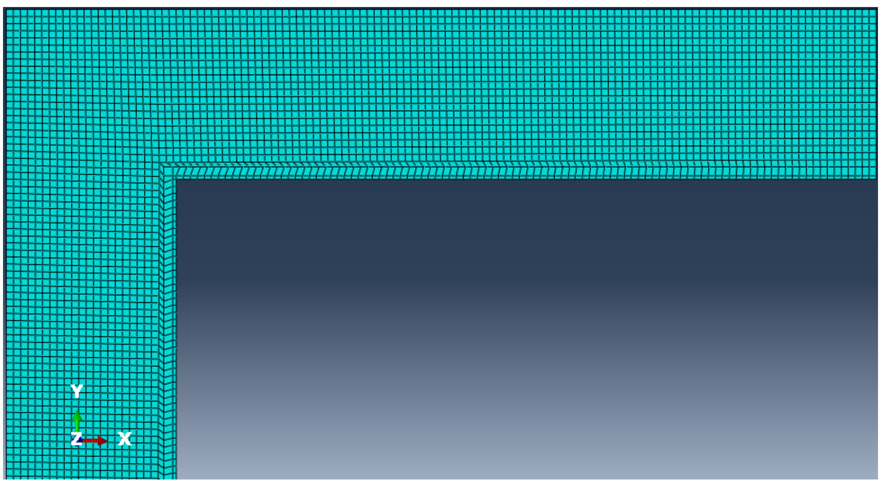

Figure 62 – Structured quadratic meshing of the studied linear bridge.

A convergence study was performed to optimise mesh size; the mesh quality was increased to include approximately 545000 quad elements. The difference in coupling coefficients was less 0.002% therefore adequate accuracy is achieved at a much lower computational cost, hence subsequent calibration iterations adhered to courser meshing of around 22000 elements.

3.4.6 Calibration results

Measured U-values and surface temperatures used informing model calibration are in Table 10 below, comparing the % difference between modelled and measured estimates:

	Ext Air	Int Air	Min Flux	Max Flux	Min Surf T	Max Surf T	U-value
	°C	°C	W/m^2	W/m^2	°C	°C	W/m^2K
Measured Average	5.3	21.3	25.1	29.4	15.2	18.2	1.6
Uncertainty	±1°C	±1°C	±5%	±5%	±	±	±14%
Calibrated Model	5	21	27.5	37	15	17.5	1.72
% Difference	5.7	1.4	9.56	20.5	1.3	3.85	7.5%

Table 10 – Measurements compared against calibrated model estimations.

As mentioned, SRs were prescribed as per BS EN ISO 6946, in the form of a surface-fluid HTC 7.7 and 25 [W/m^2K] for internal and external surfaces, respectively.

The models were examined by investigating the model nodes (using result visualisation tools – 'probing' the critical nodes from the simulation results). Probed values from the thermal model had good agreement when compared with corresponding measurements, however, some comparisons showed larger differences than others. Table 10 shows the comparison of most values fall within 10%, although the 'U-value' was calibrated considering the uncertainty expectation within BS EN ISO 9869-1 (BSI, 2014) of 14%, providing greater freedom to achieve good agreement when comparing other values. Although, (Baker, 2009) proposed a figure of +/-5.75% – agreed by other authors (Fitton et al., 2017) – as an uncertainty for U-value measurement within the lab environment.

The 'max flux' has the largest difference from its measured estimation, deviating by 20.5%, and as expected, this appears in the corner where minimum surface temperature occurs – directly in the corner.

The reason for this large deviation stems from the difficulty in measuring an accurate heat flux value in the corner since a 1D device is attempting to capture a 2D effect; the sensors closest to the bridge experiences large flux gradients across its sensing face, they are 1" square so average values over this area contribute to the measured signal. This will reduce the recorded flux compared to the probed value in the model because in the model, the nodal values directly in the corner are probed providing a higher flux than the average over 1" square (measured). Therefore, the location of the heat flux sensor in the corner is the largest cause of error leading to this discrepancy.

Similarly, the wall thickness directly in the corner could also have unnoticed plaster or paint finish build up – again reducing the measured flux. Consideration must be given that the measurement instrument is designed to capture 1D flux but experiences 2D flux in this application.

Following BS EN ISO 10211, to attain the psi-value from the simulation, the entire internal surface was selected to retrieve the total energetic loss [W] through the solid body (i.e., coupling coefficient) from ABAQUS results. Since this was a 2D simulation the coupling coefficient generated is per m depth with units [W/m]. This was then divided by the prescribed temperature difference in the simulation (creating a familiar metric [W/mK]) before subtracting the analytical U-value (multiplied by its respective length) determining the linear-transmittance (BSI, 2017c; Ward & Sanders, 2016).

This experiment shows that the adopted recalibration method adequately predicts the linear transmittance of this TB, see Table 11 below.

	I_{HFM}	I_{IR}	FE simulation
Incidence Factor	1.16	1.3	
PSI-value [W/mK]	0.2	0.19	0.19375

Table 11 – Compares results for Psi-value (IR, HFM, and FE).

There was close agreement between both novel measurement methods. Each method produced a different 'incidence factor' but when applied to equation 59 with their respective analysis lengths, a very similar psi-value is found (see Table 11). The FE simulation, informed with physical measurements from the unique/individual situation, employed the modelling rules (BS EN ISO 10211) and calculation methods (BRE 497) (BSI, 2017c; Ward & Sanders, 2016), resulted in an astounding resemblance/similarity in the calculated psi-value.

Some limitations in measurement include misalignment when locating high-e line in the image – therefore only the best quality most representative data (from camera 1 – close-up of wall 1 in phase 2) was processed for the IR technique.

The time-series IR created a lot of data; a thermograph image was taken every minute from two cameras over one week and stored to respective directories. This produced over 20,000 images for each phase (far- and close-view). Each of these images needed to be processed by first isolating the high-e line in the thermogram, averaging each pixel from its neighbouring 8 pixels (see Figure 58), then extracting the IR line to a separate Excel workbook (see Figure *59*). This was a cumbersome task hence python code was employed to automate this process and data was reduced by windowing over a steady-state periods.

Heat flux positioning and attachment methods followed the standardised advice in BS EN ISO 9869-1, although, inherent errors in these point flux measurements will exist caused by the two-dimensional nature of the heat flux directly in the corner (i.e., 1D instruments are attempting to capture 2D effects). Silicone paste was used between sensor and the wall to close any air gaps, but other sources of error may be present: unknown skim thickness (plater build-up in the corner) for example. Also, the convection is reduced in the corner of a room, reducing the SR, which would affect the point flux measurement.

FE modelling is limited since assumptions are required to set the environmental conditions, wall thickness, and material conductivity. New builds are somewhat easier to model correctly with greater certainty of the true wall layer dimensionality and thermophysical properties. These are readily available from manufacturer details and building designs, and negligible degradation can be assumed which is inherent in weathered old-existing building stock – with large uncertainties in their thermophysical properties.

Reflecting on the findings and limitations, the model results are very sensitive to SR (m^2K/W) – prescribed in the model as its reciprocal, the surface-fluid HTC (W/m^2K). Therefore, in future studies these should be measured, not assumed from standards. Also, proper uncertainty analysis is lacking for measurands (standard uncertainty was used from ISO 9869 (BSI, 2014)). Understanding this metric is crucial as the measured uncertainty provides a tolerance and determines a range, expanding the possibilities the true value could potentially be within, aiding initial parameterisations and convergence of the observed variable in model re-calibration.

Concluding this initial experiment; compared to the novel measurement methods, the calibrated FE model successfully evaluated the linear-transmittance of the studied TB, proving the efficacy of the simulation tools. To that end, this method of quantifying TB in construction will be developed/tested further when applied to analyse/evaluate a 3D TB – where no direct measurement exists. Taking these learnings forward, SR measurements with a full uncertainty analysis, using the GUM method, will be considering.

3.4.5 Calculation workflow

BS EN ISO 10211 explains how to numerically calculate TB transmittance under steady-state conditions. Software capability validation, rules for simulation, and calculation equations are provided, see equation 60:

$$\psi_{m(i,j)} = L_{2D} - \sum_{j=1}^{N_j} U_j . l_j \qquad (60)$$

Where '$\psi_{m(i,j)}$' is the psi-value, 'L_{2D}' is the coupling coefficient, 'U_j' is the U-value of the flanking elements, and 'l_j' is the length over which the U-value is considered.

BR 497 (Ward & Sanders, 2016) is based on the aforementioned standards and provides guidance regarding calculation methods quantifying TBs in construction. see example in Figure *63*:

Figure 8 shows a 2D horizontal cross-section of the normal corner junction of a simple masonry wall with flanking elements A and B, whence the Ψ-value is calculated from:

$$\Psi = L^{2D} - (U_A \times \ell_A) - (U_B \times \ell_B) \quad \text{(W/m·K)} \qquad (3)$$

where:

L^{2D} = thermal coupling coefficient

U_A and U_B = U-values (W/m·K) of the flanking elements A and B

ℓ_A and ℓ_B = lengths (m) over which U_A and U_B apply.

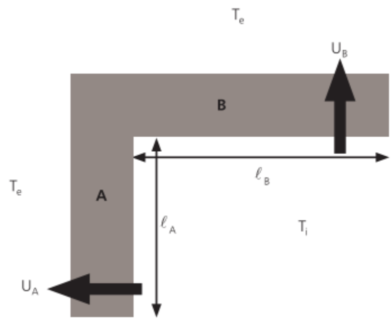

Figure 8: 2D model of a wall corner junction

Figure 63 – Showing calculation of linear transmittance from numerical simulation *(Ward & Sanders, 2016)*.

Although the procedure is slightly different for 2D or 3D scenarios, the essence of each calculation requires subtracting the analytical U-value of the known wall (1D transmittance), multiplied by its respective length (2D) or area (3D), from the coupling coefficient (simulation output) which estimates the total energetic heat loss between environments. The residual heat transfer is attributable to the TB-transmittance.

SRs are applied considering BS EN ISO 6946 suggestions: 0.04 and 0.13 [m^2K/W] (prescribed in the simulation as their reciprocal, the surface-fluid HTC, at 25 and 7.7 [W/m^2K]), for external and internal surfaces, respectively. All simulations prescribe temperatures at these surfaces, usually 20°C internally and 0°C externally providing a 20°C difference reflecting typical thermal comfort conditions. However, since this research aims at calibrating models to the actual bespoke conditions effecting individual construction details, the measured temperatures are considered in simulation. The isotherms are extracted from the simulation output in Figure 64:

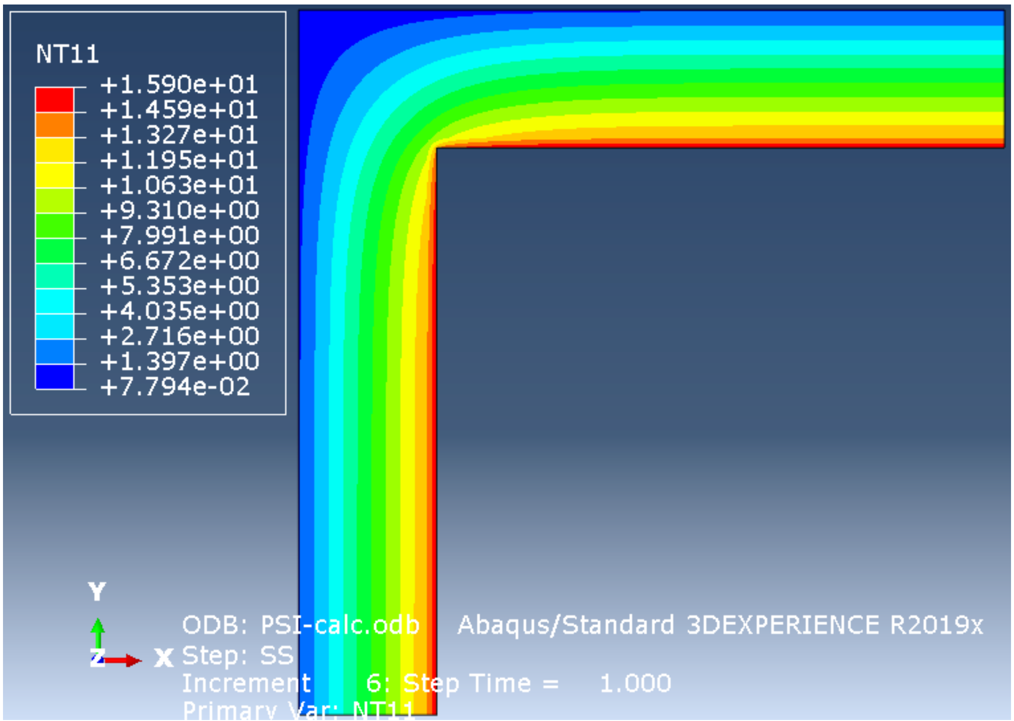

Figure 64 – 2D calibrated model of the investigated corner wall junction. Visualisation of the nodal temperature (NT) isotherms.

The internal walls are 1m in length following standardised advice. The isotherms are level where 1D heat transfer occurs and start to bend as they approach the corner. This effect is generally owed to the difference between internal and external surface areas; the external surface area is larger therefore more heat is emitted compared with the smaller internal surface area where heat is absorbed.

3.5 Pilot experiment 2 - Point-transmittance

Balconies are becoming a popular design feature in multi-story high-rise residential buildings offering greater outdoor space for the occupant (Sapphire balconies Ltd, 2022). However, they cause point-TB by puncturing the thermal envelope with steel-beams to structurally support a cantilever balcony. STBs solutions in point connections like this can mitigate condensation occurrence and help meet the buildings energy performance requirement, yet no standardised measurement method exists because the complex heat flux cannot be measure directly. Therefore, evaluation relies entirely on numerical calculation following standardised guidance. This reliance is expected to generate considerable PGs due to the necessary assumptions of sensitive parameters such as SR. This experimental design phase focuses on these causations and seeks to develop a reliable in-situ evaluation method using measured parameters oppose to assumed values to parameterise the FE thermal simulation, reflecting estimations of their actual in-situ performance more accurately.

In this stage, the experimental design will be developed in the measurement of a STB in a point connection within the EH – a well instrumented climatic-controlled test facility, described earlier. Aiming to reduce the PG, the measured uncertainty intervals provide a tolerance with which to parameterise and re-calibrate a FE thermal model – exclusively relied upon to quantifying the TB. Embedding sensors within the STB interface to measuring flux will be compared against the corresponding probed simulation value. When this probed model value falls within the uncertainty of the measured value, the model will be considered robustly parameterised to the specific investigated construction detail.

In the next section, a full account of the experiment is described, specifying the tested STB product, test facility, conditions, assumptions, set-up, scenarios, instruments, and sensors used in measurements. The results from measurements will be reported (with their associated uncertainties) which are carried forward for model calibration. Applying the modelling method, comparisons with and without a STB can be drawn. Calibrated models quantifying the TB transmittance characterise the effectiveness of the break solution whilst isotherm graphics illustrate the implications of TB and STB impacts. Concluding with limitations, both in measurement and modelling, further works are discussed suggesting adaptations to the experimental design.

Figure 65 below, shows the poly-resin composite material STB product tested (25mm Farrat TBK) – it has a compressive strength similar to steel with a conductivity similar to wood:

Figure 65 – Farrat 25mm TBK STB (conductivity = 0.187 W/mK).

Other available material properties are reported in the following Table 12:

Properties	Farrat TBK		Notes
Compressive strength	Characteristic	312 MPa	BS EN 1990 Eq. (D.1)
	Design	250 MPa	BS EN 1993-1-8 (Y_{M2}=1.25) (UK NA)
Elastic modulus		5178 MPa	
Thermal conductivity		0.187 [W/mK]	
Density		1465 [kg/m^3]	
Water Absorption		0.14%	
Long term creep		20%	% Increase of initial strain (Serviceability Limit State)

Table 12 – Material properties of Farrat TBK material (Farrat, 2021).

Learnings from the preliminary experiment suggested the model was sensitive to SR values; these were measured in this 3D TB experiment unlike the previous linear-TB experiment (where standardised SR values were assumed).

Other limitations include situational irregularities that guidance (BSI, 2014) advises to avoid: the internal face featured obstructions (see Figure 70); convection altering excitations from door drafts; stratification (see Figure 68); and proximity to radiators give more credence to the importance of measuring SR, see Figure 70.

The EH (seen earlier in Figure *55*) test facility at the UoS facilitated testing. Since no natural structural 3D-point-TB existed in the EH, slight modifications were made to feature one: a 0.5m long steel-beam cantilever (universal beam UB_152x89x16 with a 20mm thick endplate 200mm x 160mm) – representing a single cantilever support – was anchored to the external wall. This produced a point-penetration in the thermal envelope where STB solutions can be implemented and tested, allowing measurement of the characteristic 3D heat transfer through this TB, see in Figure 66 Figure *67* :

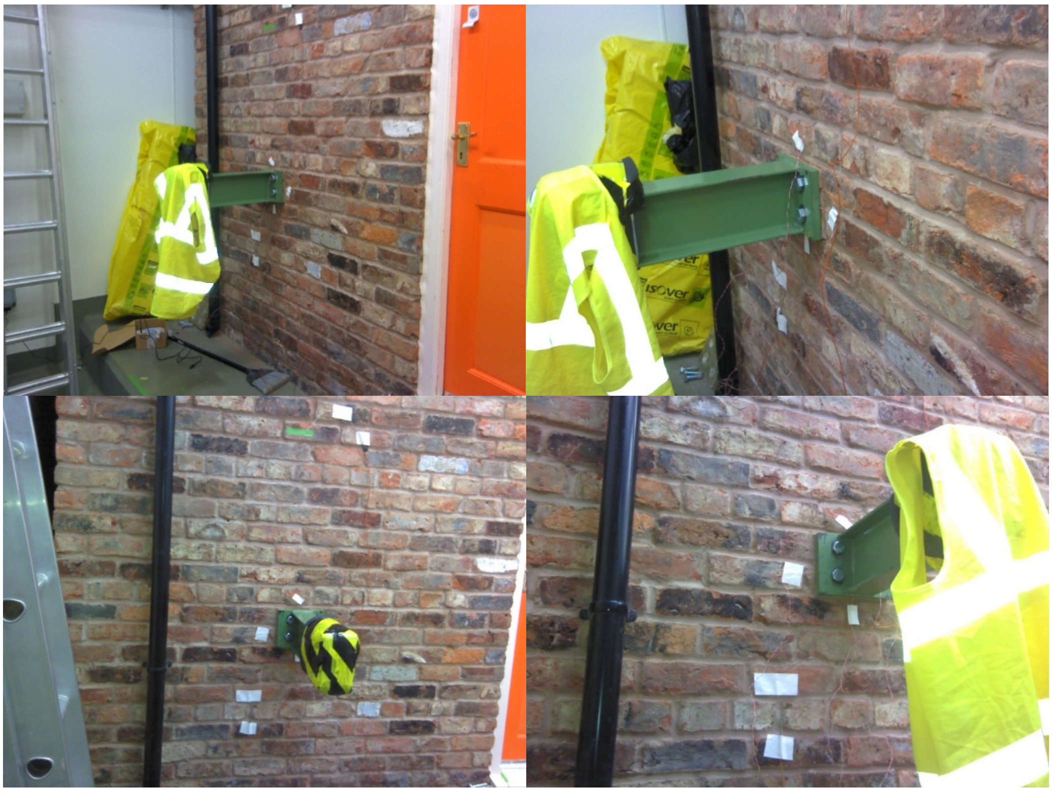

Figure 66 – Modification to EH wall.

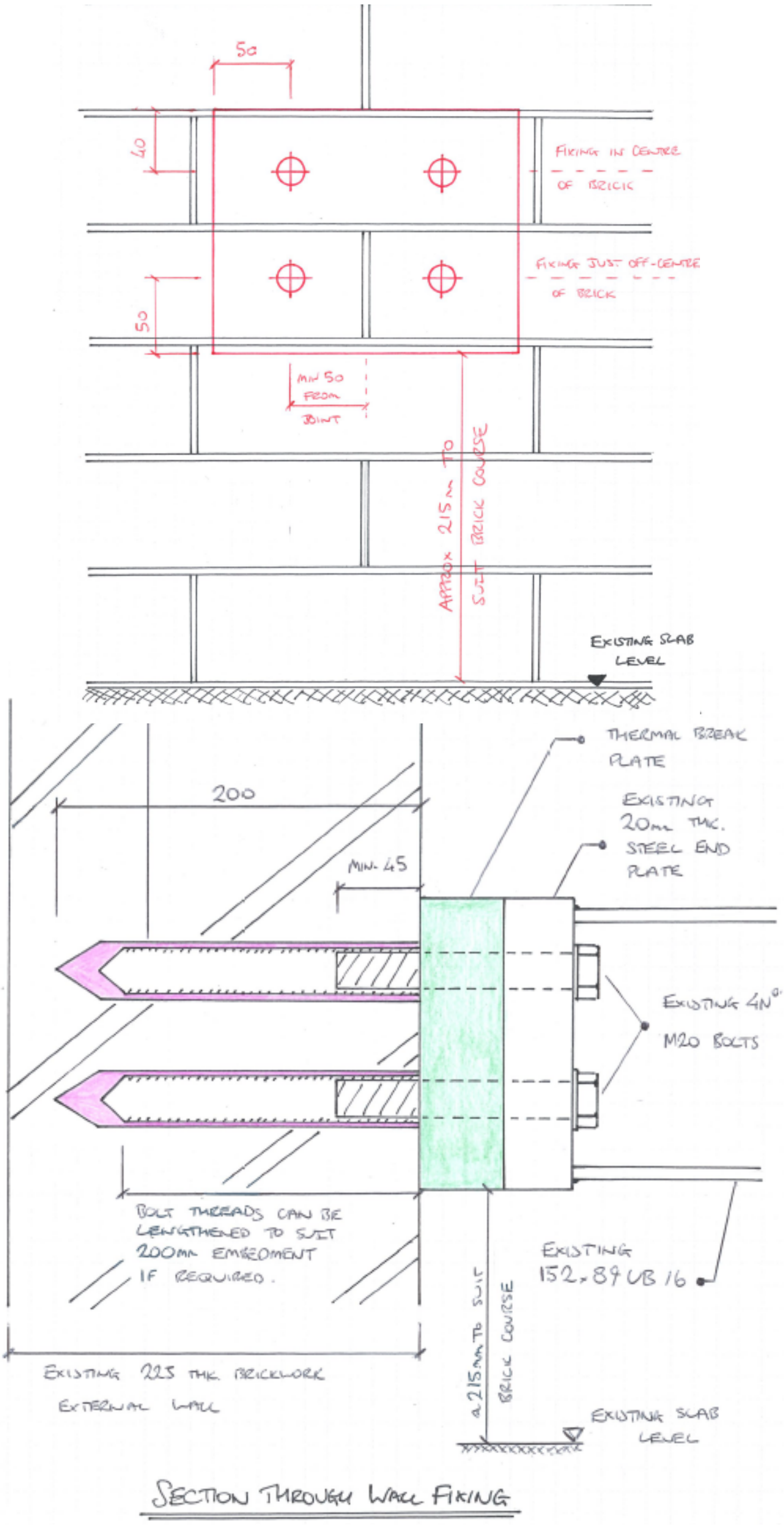

Figure 67 – Structural engineering drawing of anchored installation.

3.5.1 Conditions & assumptions in measurement

The test location featured undesirable conditions affecting experimental measurement integrity. This section clarifies the problems and surmises their solutions, attempting to mitigate their effect.

To reduce stratification, fans excited internal air flow, increasing convection, and homogenising the surface temperature see Figure 68.

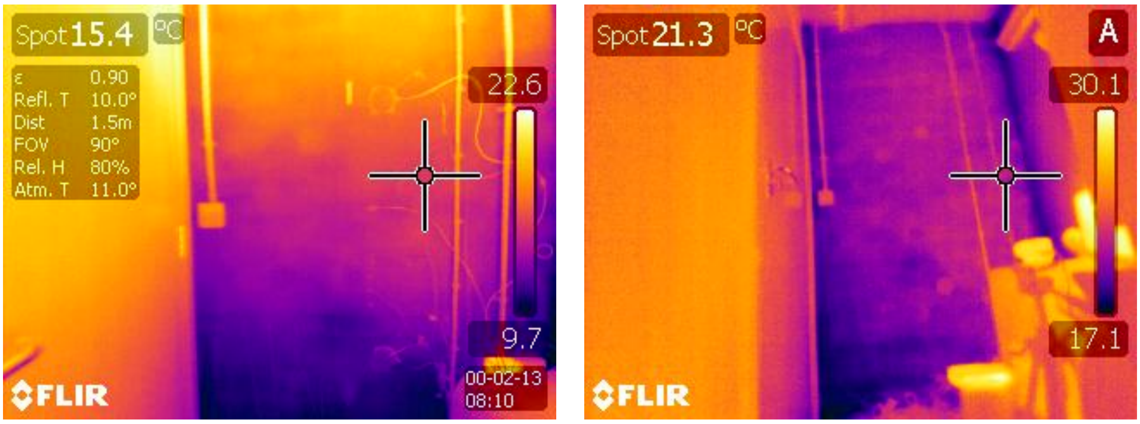

Figure 68 – (LHS) Illustrates internal stratification showing a 9°C difference in internal air temperature. This issue was rectified by exciting the internal flow and excluding drafts (RHS).

Causes of this effect include cold air drafts filtrating up from under the door, hot updrafts caused by a nearby radiator, and physical obstructions interrupting the natural buoyancy driven internal convection. When the fans were used, upper and lower sensor locations converged to the same temperature and air velocity. These measurement locations were also used to calculate the internal SR.

The interface between steel beam and masonry had significant gaps in the connection, detrimental to the experiment since a 1mm air gap can have a resistance of 0.04 [m^2K/W] (Anderson, 2006; BSI, 2017b). Hence, to mitigate this, a soft sand/cement mix was applied to the surface of the brick generating a decent thermal contact by eliminating air gaps, see Figure 69.

Figure 69 – Attempts to promote a perfect thermal contact between wall and beam.

3.5.2 Sensor array

Internally, a T-type thermocouple array ran parallel to the high-ε tape linking the unaffected to the affected zone (using vertical and horizontal lengths intersecting at the cold spot) whilst two heat flux meters (Hukseflux) were installed in unaffected zones, all located with qualitative IR. 20 channels in the Graphtec logger were used, see Figure 70 Figure 71, and Table 13 below illustrating the internal sensor array.

T-type thermocouples monitored internal and external air temperatures – used to set up the simulation and U-value calculation (with heat flux), considering the proper error propagation in uncertainty analysis.

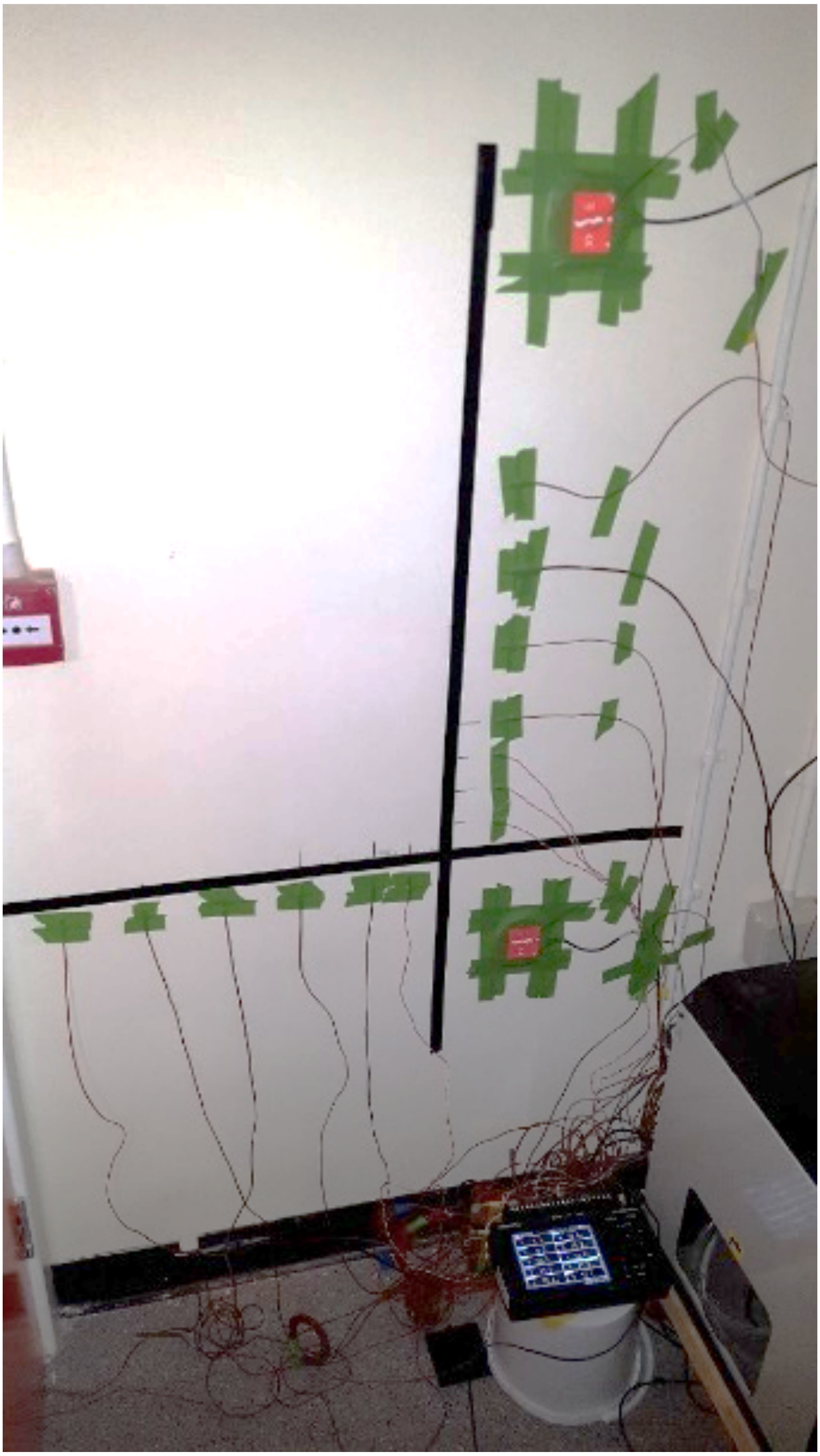

Figure 70 – Internal sensor array.

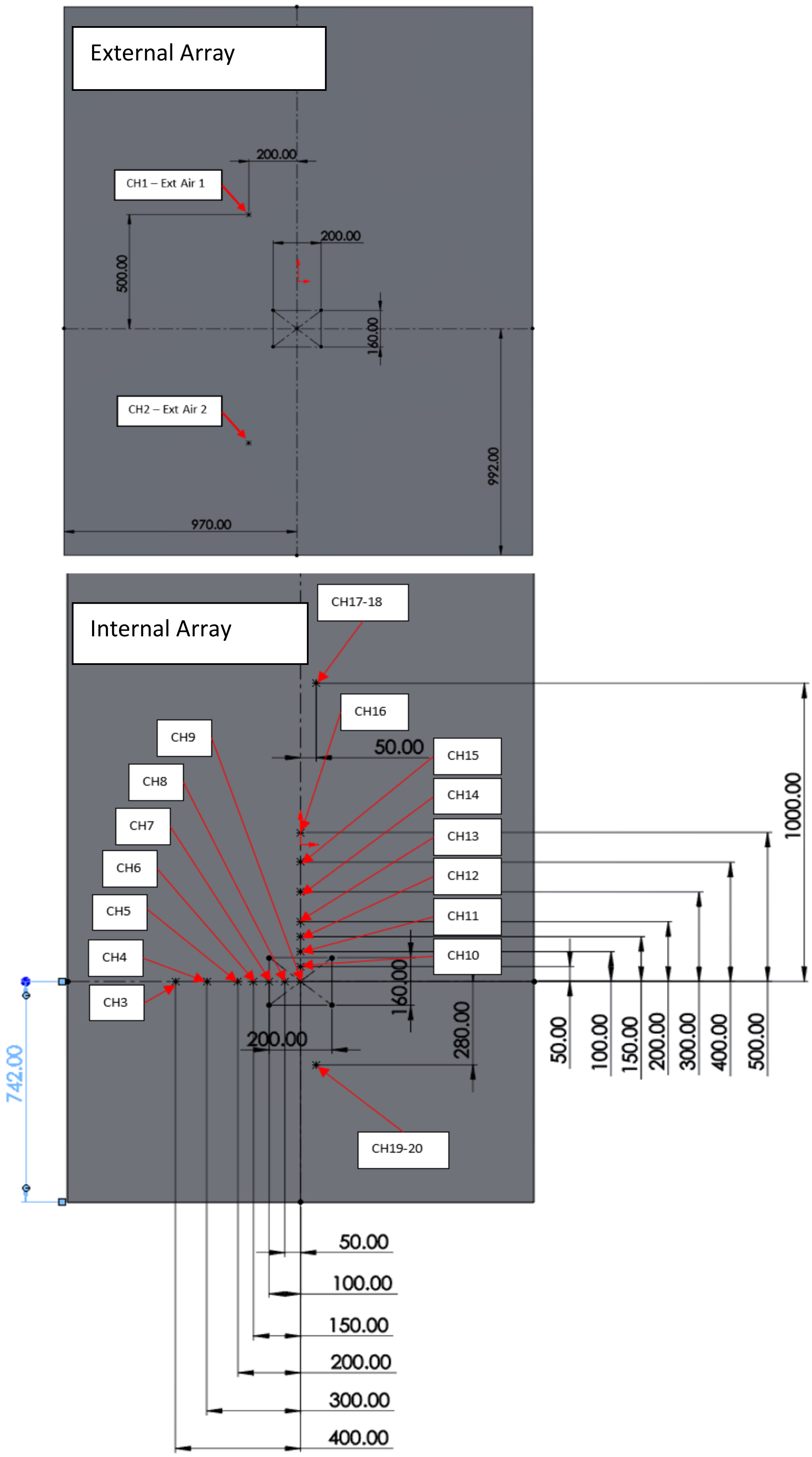

Figure 71 – Schematic of external (top) and internal (bottom) sensor array.

Channel (Graphtec)	Sensor	Measurement	Unit	Error	Uncertainty
1	T-type thermocouple	External Air Temperature	°C	± 1 °C	± 1%
2	T-type thermocouple	External Air Temperature	°C	± 1 °C	± 1%
3	T-type thermocouple	Internal Surface Temperature	°C	± 1 °C	± 1%
4	T-type thermocouple	Internal Surface Temperature	°C	± 1 °C	± 1%
5	T-type thermocouple	Internal Surface Temperature	°C	± 1 °C	± 1%
6	T-type thermocouple	Internal Surface Temperature	°C	± 1 °C	± 1%
7	T-type thermocouple	Internal Surface Temperature	°C	± 1 °C	± 1%
8	T-type thermocouple	Internal Surface Temperature	°C	± 1 °C	± 1%
9	PT100	Internal Surface Temperature	°C	± 1 °C	± 0.5%
10	PT100	Internal Surface Temperature	°C	± 1 °C	± 0.5%
11	PT100	Internal Surface Temperature	°C	± 1 °C	± 0.5%
12	PT100	Internal Surface Temperature	°C	± 1 °C	± 0.5%
13	T-type thermocouple	Internal Surface Temperature	°C	± 1 °C	± 1%
14	T-type thermocouple	Internal Surface Temperature	°C	± 1 °C	± 1%
15	T-type thermocouple	Internal Surface Temperature	°C	± 1 °C	± 1%
16	T-type thermocouple	Internal Surface Temperature	°C	± 1 °C	± 1%
17	Huxeflux	Heat Flux (Internal)	W/m^2	± [W/m^2]	± 6%
18	T-type thermocouple	Internal Air Temperature	°C	± 1 °C	± 1%
19	Huxeflux	Heat Flux (Internal)	W/m^2	± [W/m^2]	± 6%
20	T-type thermocouple	Internal Air Temperature	°C	± 1 °C	± 1%

Table 13 – Graphtec channels with sensor system uncertainties (absolute and relative).

3.5.2.1 Embedded Sensor array

To measure the heat flux through the break itself, four 'FluxTeq' thin-film flux sensors (measuring flux and temperature) were embedded within the connection, either side of the break

Measurements were compared with the model probed responses for re-calibration. Each FluxTeq embedded sensor requires 2 channels. Therefore the 8 channel Novus field logger was used for these sensors exclusively see Figure 72 and Table 14.

Averages were recorded over a steady 12hr period for each phase and were used as either input or response parameters for calibration purposes.

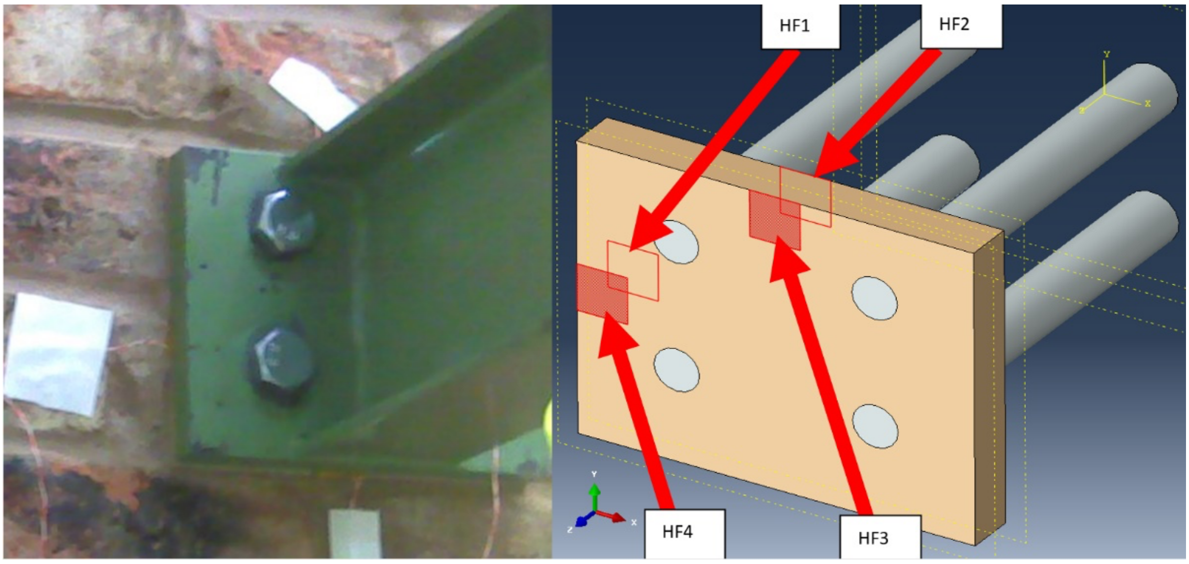

Figure 72 – Shows location of the embedded sensors around the STB, located in the centre of each edge, in between the bolt fixings.

Channels (Novus)	Sensor	Measurement	Unit	Absolute Uncertainty	Relative Uncertainty
1	FluxTeq	Heat Flux	W/m^2	±0.03 [W/m^2]	± 5%
2	T-type	Temperature	°C	± 1°C	± 1%
3	FluxTeq	Heat Flux	W/m^2	± 0.03[W/m^2]	± 5%
4	T-type	Temperature	°C	± 1°C	± 1%
5	FluxTeq	Heat Flux	W/m^2	± 0.03 [W/m^2]	± 5%
6	T-type	Temperature	°C	± 1°C	± 1%
7	FluxTeq	Heat Flux	W/m^2	± 0.03 [W/m^2]	± 5%
8	T-type	Temperature	°C	± 1 °C	± 1%

Table 14 –Novus Channels with embedded sensors – system uncertainties (absolute and relative).

The logger also introduces a systematic error which applies to all signals detected; Novus is assumed to be 0.1%, as per manufacturer specification.

3.5.3 Scenarios

To understand the impact of the STB, four test phases were performed changing one factor at a time (OFAT): bare wall – with and without a STB, and an externally insulated wall – with and without a STB. i.e.:

- Phase 1 – Bare wall, steel only
- Phase 2 – Bare wall, steel broken with STB
- Phase 3 – EWI wall, steel only
- Phase 4 – EWI wall, steel broken with STB

Since this is not representative of where these STB products are usually utilised, attempts were made to exacerbate the TB effect by retrofitting EWI (external wall insulation) to the wall in phases 3+4. The hypothesis being, the beam itself bridges more insulation, increasing the relative effects of bridging, hence, a greater reduction can be measured when applying the STB solution.

EWI layers comprised of soft mineral wool glued to EPS on plasterboard, chosen such that when retrofitted to the wall, the soft mineral wool would close the airgaps caused by the rough wall surface, see Figure 73.

Figure 73 – The external wall insulation was retrofitted to the brick.

A small sample was taken of the chosen stratigraphy and the effective thermal conductivity was tested at various compression thicknesses in the 'Heat-flow-meter'. Results are shown below in Figure 74:

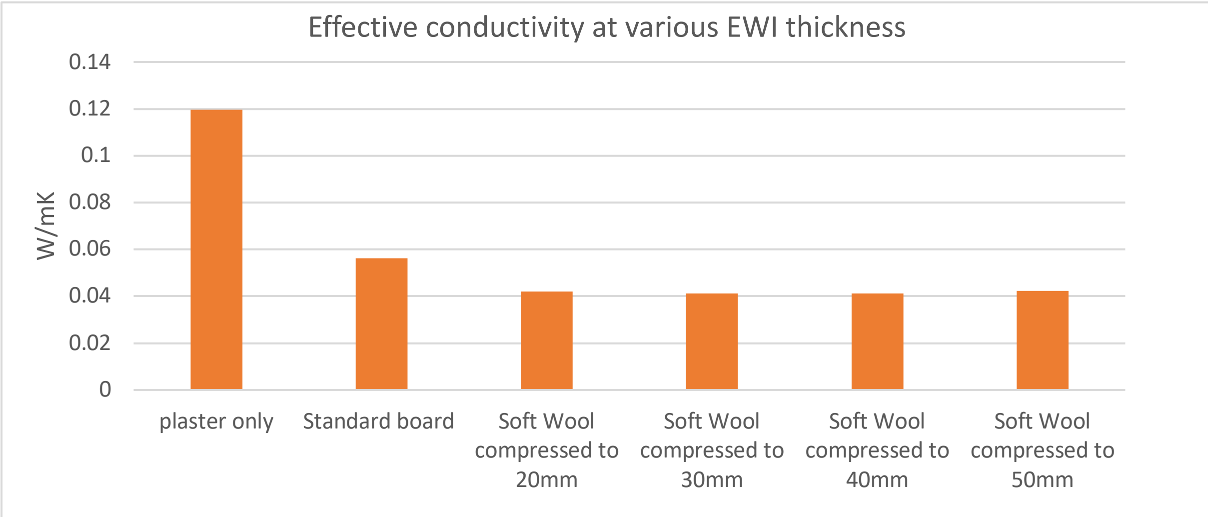

Figure 74 – Measured equivalent conductivity of EWI compressed to varying thicknesses.

The retrofitted thickness can be measured in-situ and the effective conductivity interpolated against the graph in Figure 74 for model calibration purposes.

3.5.4 Measurement Results

Type A and B standard uncertainties will be analysed for each measurement estimate. Where these estimates are used to calculate a measurand (such as a U-value or SR), the propagation of errors – following the GUM method (Guide to the expression of uncertainty in measurement) JCGM 100:2008 (JCGM, 2008) – allows the combination of uncertainties from multiple measurement estimations. Equations are defined in a previous section. The following section will apply these equations in the uncertainty analysis, with the respective errors of the component parts, for each measurand calculation.

3.5.4.1 SR Measurement

Due to exciting the internal air flow, it was deemed necessary to understand the internal surface-fluid HTC [W/m^{2}K]. Therefore, measurements (fluid/surface heat flux along with local air and surface temperatures) were captured on each surface exposed to the internal and external environments (using FluxTeq and thermocouples, see Figure *75*). Using equation 61, the measurand was calculated – encapsulating both the convective and radiative terms in one expression (CIBSE, 2021) (François et al., 2020a) (François et al., 2020b).

$$\mathrm{SR} = \frac{1}{\frac{Q}{Ta - Ts}} \quad 61$$

Where, ‘SR’ is the SR [m²K/W], Q is the heat flux [W/m^2], ‘Ta’ is the air temperature [K], ‘Ts’ is the surface temperature [K].

This measurement provides a more authentic reflection of the unique conditions experienced, compared to applying standardised assumptions, providing greater accuracy when prescribing values in the simulation.

The measurements taken from the investigated set-up (structural-steel TB with and without a break) will again be used to calibrate the parameters within a 3D FE model, since this is the only way to quantify point-TB transmittance. However, learnings from the preliminary experiment suggest understanding measurement uncertainties is vital since all measurements are subject to uncertainty. Laboratory-controlled measurements improve the confidence in the uncertainty since sources are less volatile and can be identified clearly unlike dynamic field work: radiative mechanisms cause concern if large solar irradiance incidences on the external face, however, since the test took place in a controlled facility, associated error caused by this mechanism did not significantly affect the measurement. Similarly, other weather factors (rain) and high wind speeds were avoided.

Figure 75 – Air and surface temperatures in conjunction with surface heat flux measurements allow direct measurement of SR.

These were taken on 2 locations internally and externally then the values were windowed over a steady-period and averaged.

	Phase1 [W/m^{2}K]	Phase2 [W/m^{2}K]	Phase3 [W/m^{2}K]	Phase4 [W/m^{2}K]
External	4.64 ± 0.21	4.64 ± 0.21	4.64 ± 0.21	4.64 ± 0.21
Internal	22.87 ± 11.42	22.87 ± 11.42	22.87 ± 11.42	22.87 ± 11.42

Table 15 – Measured values for surface-fluid HTC [W/m^{2}K, the reciprocal of the SR [m^{2}K/W].

Input parameters can be adjusted within their confident uncertainty intervals to calibrate the model.

The sensitivities of ‘dT’ and the ‘flux’ estimates to the calculated measurand were calculated then multiplied with the combined standard uncertainty for the respective estimate. These were then combined in quadrature (RSS – squared and summed before square-rooting).

The temperature measurements using T-type thermocouples assumed an error from the manufacturer specification of ±1 [°C]. In the calculation of SR, the temperature difference (dT) was considered as one variable, however it is determined through subtraction of two measured averages – each with an associated error. Therefore, these errors were initially propagated in quadrature, hence ‘dT’ has an absolute error of ±1.4 [°C] which was taken forward for the uncertainty analysis of the calculated measurand.

Type-B uncertainties for flux measurement assumed manufacturer errors of ± 0.03 [W/m^2K] in the flux conversion coefficient – which was scaled dependant on temperature using the linear interpolation calibration formula – and ± 5% of the average flux. The embedded T-type (within the FluxTeq) assumed a manufacturer error of ± 1 [°C].

The standard Type-B uncertainty, propagated properly, is then combined with the Type-A (precision uncertainty) for each measurement prior to final SR calculation.

Somewhat opposing the standardised assumptions (of 25 and 7.7 W/m^2K surface-fluid HTC, externally and internally, respectively) in BS EN ISO 6946 (BSI, 2017b), the measured surface-fluid HTC values came to an average of 22.87 ±11.42 [W/m^2K] (±50%) and 4.64 ± 0.21 [W/m^2K] (±5%), internally and externally, respectively.

Compared to the standardised values, the increase in internal surface-fluid HTC was massively affected when eliminating internal stratification by exciting the air with a fan. In addition, the decrease in external surface-fluid HTC was attributed to lack of weather conditions (as mentioned: solar, wind, rain).

The reason for considerable differences in their uncertainties when propagated is primarily due to very small differences between surface and air temperatures, which increases their sensitivity in the propagation of errors. For example, externally an average temperature difference of 1.4 [°C] was maintained, oppose to an average temperature difference of 0.64 [°C] internally. Also notable, the external flux measurement was far more stable than the internal measurement, reducing the precision error further.

3.5.4.2 U-value Measurement – EH wall in experiment 2 (3D point bridge)

Hukseflux sensors measured the heat flux for the U-value analysis following guidance in BS EN ISO 9869-1 – the averaging method. Since steady-state conditions were realised in the experiment, this method allowed rapid, accurate data capture with low computational cost in processing.

The measured mV’s were converted to fluxes using the sensitivity coefficient; manufacturer calibration suggests an absolute error (specific to the individual sensor) from calibration certificates, an uncertainty of ±3% (k = 1), and a drift of 0.1% per °C deviation from the calibration temperature, 20°C. An expanded uncertainty (k = 2) of 6% was used, and since the operating temperature was close to the calibration temperature (20°C) no additional % were added to the uncertainty budget. Therefore, the measured flux estimate W/m^2 is approximately ± 6%.

Steady-state was achieved. The temperature difference 'dT', used to calculate the measurand was initially analysed; since it is a subtraction of two measurements, each with an absolute error of ±1°C. Again, these were combined in quadrature, estimating a dT error of ± 1.4°C (square root of 2).

The sensitivity of each input variable, flux 'Q' and temperature difference 'dT', were derived from partial differentials of the U-value calculation – with respect each input variable following the GUM method (JCGM, 2008) described in the previous section.

Combining the Type-A and B standard uncertainties for each measured input estimate in quadrature, before propagation in its final calculation, defines the total estimated uncertainty of the average measurand. The following graph in Figure 76 shows each U-value measurement and the expanded uncertainty interval (k = 2) for each phase.

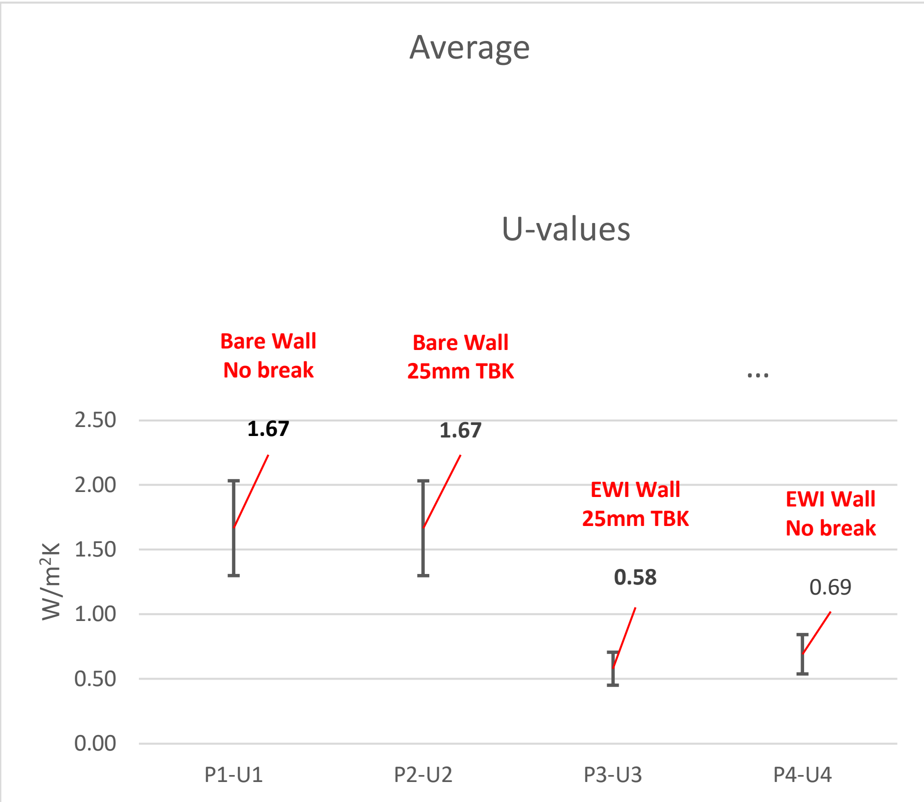

Figure 76 – Average U-values for each phase with an uncertainty of 11% and confidence interval of 95%.

Measurement averages and their uncertainties were calculated from a 12hr steady-state period of minutely data (720 data points). The U-value uncertainty estimate varied over the phases, see

$$U = \overline{U} \pm \delta_U \qquad 62$$

Phase 1 (Bare brick)	$U_1 = 1.67 \pm 0.14$ $(\pm 8.5\%)$
Phase 2 (Bare brick)	$U_2 = 1.67 \pm 0.15$ $(\pm 9.1\%)$
Phase 3 (EWI)	$U_3 = 0.58 \pm 0.06$ $(\pm 11.0\%)$

Phase 4 (EWI)	$U_4 = 0.69 \pm 0.05 \ (\pm 7.4\%)$

Table 16 presenting each U-value and its uncertainty in the form of equation 62:

$$U = \overline{U} \pm \delta_U \quad (62)$$

Phase 1 (Bare brick)	$U_1 = 1.67 \pm 0.14 \ (\pm 8.5\%)$
Phase 2 (Bare brick)	$U_2 = 1.67 \pm 0.15 \ (\pm 9.1\% \,)$
Phase 3 (EWI)	$U_3 = 0.58 \pm 0.06 \ (\pm 11.0\%)$
Phase 4 (EWI)	$U_4 = 0.69 \pm 0.05 \ (\pm 7.4\%)$

Table 16 – Average U value measurements and their uncertainty at a 95% (k=2) level of confidence.

Retrofitting EWI improved the U-value achieving between 0.58 ± 0.06 and 0.69 ± 0.05 [W/m^{2}K] oppose to pre-retrofit U-value 1.67 ± 0.2 [W/m^{2}K] (the revised uncertainty of this averaged U-value has combined the two measured uncertainties from the different methods in quadrature – attaining ± 0.2). As hypothesised, increasing the overall fabric resistance should exacerbate the relative TB effect and prove that the greater the wall resistance, the more detrimental the bridging effect.

The measured averages of external and internal air temperatures, and maximum and minimum internal surface temperatures are seen in Table 17:

Measurements	Ext air Temp [Input]	Int air Temp [Input]	Min Surf Temp	Max Surf Temp
[Units]	[°C]	[°C]	[°C]	[°C]
Phase1	5.88 ±1°C	23.39 ±1°C	20.04 ±1°C	22.47 ±1°C
Phase2	6.10 ±1°C	23.35 ±1°C	20.14 ±1°C	22.52 ±1°C
Phase3	5.61 ±1°C	23.35 ±1°C	21.35 ±1°C	22.97 ±1°C
Phase4	5.69 ±1°C	28.95 ±1°C	25.89 ±1°C	28.31 ±1°C

Table 17 – Experimental measurement results (Graphtec) averaged over a 12hr period.

The uncertainties in the single temperature measurement considered manufacturer error for T-type thermocouples of ±1°C. The measured averages of the embedded flux are seen in Table 18 below:

Measurements	HF1	HF2	HF3	HF4
[Units]	[W/m^2]	[W/m^2]	[W/m^2]	W/m^2]
Phase1	51.16 ± 2.76	40.98 ± 2.21	55.71 ± 3.00	50.32 ± 2.71
Phase2	29.99 ± 1.62	16.71 ± 0.9	24.44 ± 1.32	16.96 ± 0.91
Phase3	34.86 ± 1.88	38.58 ± 2.08	31.73 ± 1.71	38.07 ± 2.05

Phase4	201.77± 10.87	103.17 ± 5.56	140 ± 7.54	74.04 ± 3.99

Table 18 – Experimental measurement average and uncertainty of embedded flux (Novus) averaged over a 12hr period.

All uncertainties in the embedded flux measurements were calculated regarding the same bias uncertainty and since the precision error was so low – due to a low standard deviation and a high sample size – a ubiquitous uncertainty of 5.39% (k = 1) was found.

The following grapahs (in Figure 77) show average temperature and flux measurements with their expanded uncertainties, for each phase: Phase1 (top left), Phase2 (top right), Phase 3 (bottom left), and Phase 4 (bottom right). In each phase, the temperature graphs (top) show internal air temperature, maximum internal surface temperature, minumum internal surface temperature, and external air temperatures (from left-to-right), whilst the embedded flux (bottom) shows each measured average and expanded uncertaitnty.

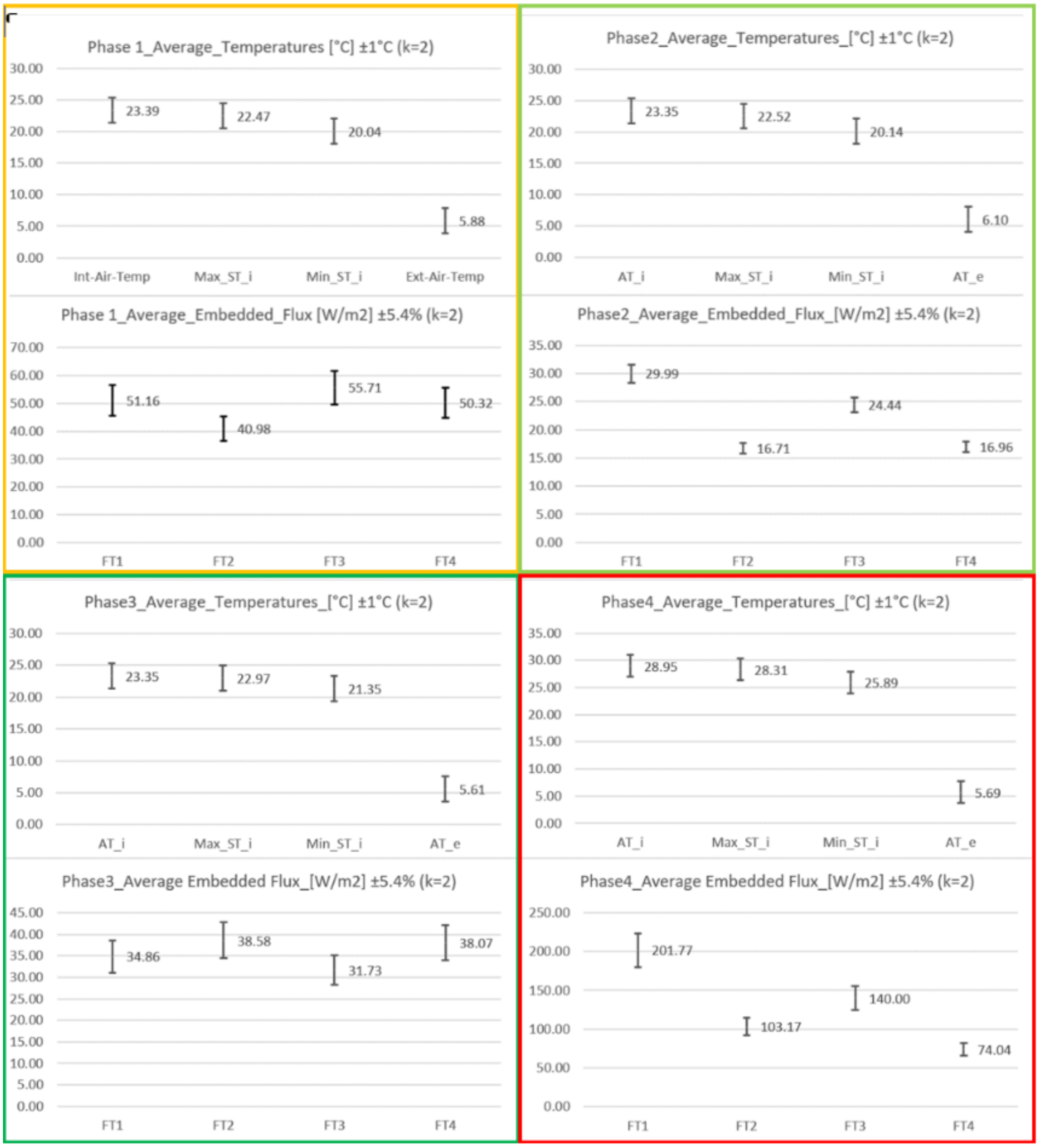

Figure 77 – Average measurements of embedded flux sensors including their uncertainty for phases 1-4.

Phase 1 had no break (simply a steel beam anchored to the wall) whilst Phase 2 included a 25mm Farrat TBK STB in the connection and reductions in embedded fluxes can be seen. Phase 4 had EWI fitted (to exacerbate the bridge effect) with no STB. The magnitude of the embedded flux was noticeably reduced in Phase 3 where the STB was fitted, see Figure 77.

The latter phases were far better suited for the use of this type of sensor since these thin-film flux sensors were embedded within the junction and surrounded by EWI, isolated from the external environment, unlike the former set-up, where the sensors were directly exposed to environmental (convective and radiative) conditions.

In the phases where no break was used (Phase 1&4), the embedded sensors were sandwiched between steel and brick/mortar to capture point measurements of heat flux through the connection.

Figure 78 shows the heat flux isotherm (LHS) in the connection illustrating the gradient volatility, the RHS shows sensor displacement from two views:

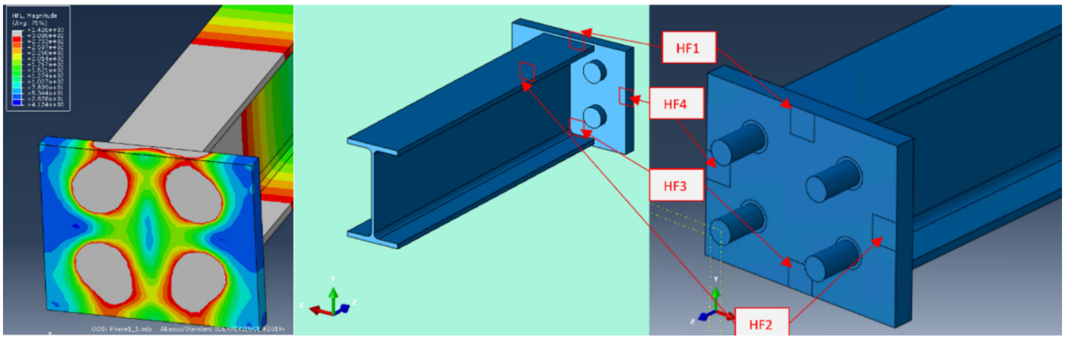

Figure 78 – Shows a cross-section view of the heat flux in the connection (LHS). The two RHS images show the sensor locations in Phases 1 & 4 (without a STB).

In the phases with a thermal break (Phases 2&3), the embedded flux sensors were situated either side of the break to capture the flow through the break (see configuration in Figure 79 below), sandwiched between differing materials (steel-TBK, and TBK-brick/mortar).

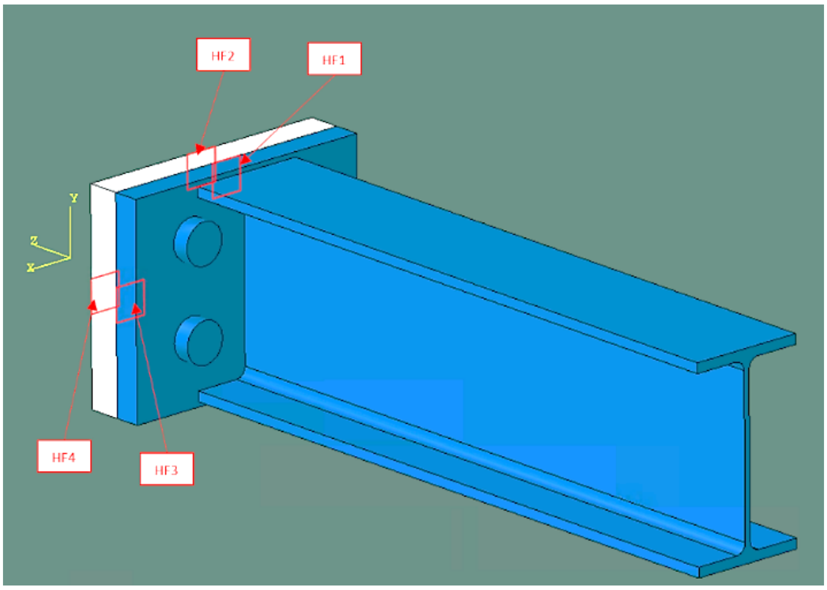

Figure 79 – Embedded flux sensor locations in phases 2 & 3 (with a STB).

As mentioned, these measurements will be used further in model parameterisation and re-calibartion of a thermal simulation to quantifying the point-TB transmittance. The following section describes the modelling method and transmittance calulation before comparing the results and suggesting adjustments to develop the experimental design.

3.5.5 Modelling methods

Steady-state heat transfer FE analysis in ABAQUS calculated the conduction through the investigated construction detail. Convective and radiative transfers were represented as SRs (prescribed as surface-fluid HTCs) in the models at surface boundaries exposed to environments (BSI, 2017c), along with temperature.

3.5.5.1 Mesh

The model is meshed dividing the geometry into many elements (Figure *80*) each with 4 nodes. The conduction equation and energy conservation laws are then applied to these nodes populating a system of equations as a function of temperature. By direct or iterative solutions, a temperature distribution field is determined, and interpolation calculates the heat flows (BSI, 2017c).

As seen in the previous experiment, modelling requirements specify that a mesh convergence study is necessary: the number of elements within a model is increased and the simulation response is compared with the previous iteration, if the responses are within a tolerance (dictated by the standard), the courser mesh is acceptably accurate. This reduces unnecessary computational cost, see Table 19. The standard also specifies that adiabatic cut-off planes, where no heat-transfer can take place, are located at planes of symmetry, or 1m away from the TB, whichever is closer (BSI, 2017c; Viot et al., 2015).

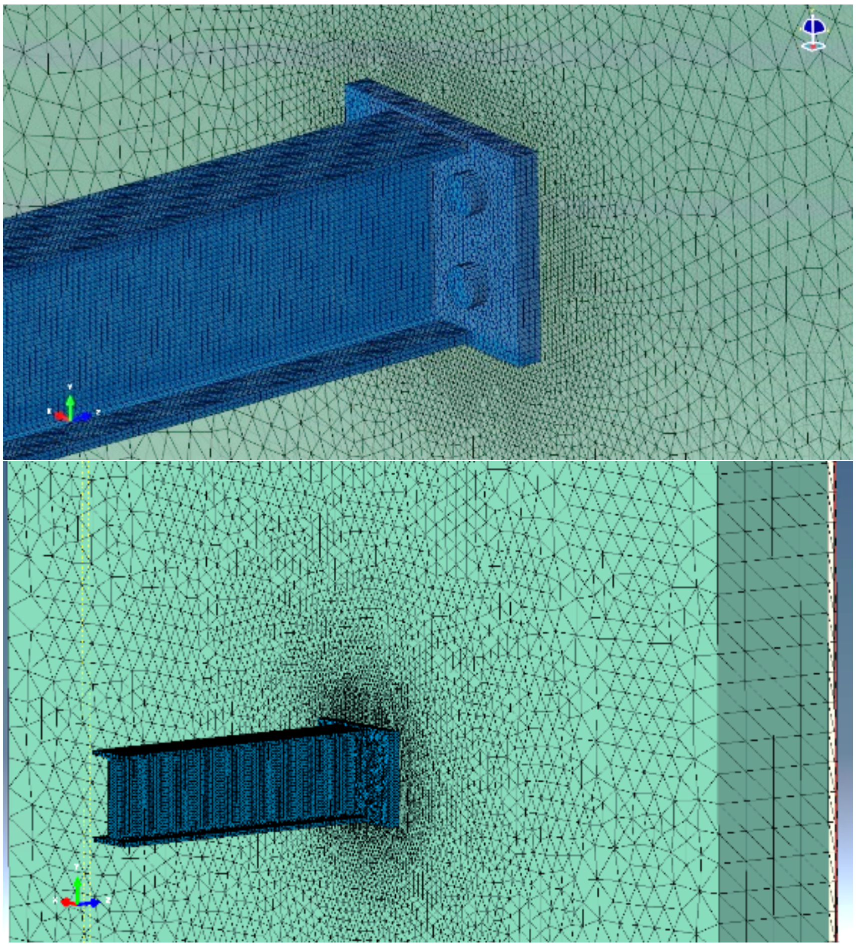

Figure 80 – Shows localised mesh refinement around the area of interest, focusing on the connection, in Phase 1 is shown as an example.

Phase	Type of element	Number of nodes
1	4-node tetrahedra	1004149
2	4-node tetrahedra	1048142
3	4-node tetrahedra	1262304
4	4-node tetrahedra	1203562

Table 19 – Meshing for each phased modelled, (Global:0.05, Local:0.005).

For all phases, the model geometry and material properties were set to reproduce the measured U-value (seen in Table 16) the tolerance of their adjustable range is dictated by uncertainty analysis (seen previously in Figure 76). The final calibrated model parameters are shown below in Table 20.

	Phase 1+2 Conditions	Phase 3+4 Conditions

Material	Thickness [m]	Conductivity [W/mK]	Thickness [m]	Conductivity [W/mK]
Brick	0.225	0.7	0.225	0.7
Plaster	0.013	0.2	0.013	0.2
Skim	0.005	0.2	0.005	0.2
TBK	0.025	0.187	0.025	0.187
EWI	~	~	0.05	0.05
Internal Temperature [°C]		23°C	Internal [°C]	P3(23°C), P4(29°C)
Internal SR		25[W/m^{2}K]	Internal	25[W/m^{2}K]
External Temperature [°C]		6°C	External [°C]	6°C
External SR		4.85[W/m^{2}K]	External	4.85[W/m^{2}K]

Table 20 – Calibrated thermophysical properties: final parameters.

Analytically, the U-value is dependent on properties contributing to the total thermal resistance of the wall: SRs, material thickness, and their conductivities. Measured SRs as seen in Table 15: 22.87 ± 11.42 W/m^{2}K (±50%) and 4.64 ± 0.21 W/m^{2}K (±5%) were applied to models internal and external surfaces, respectively. Probed model values are later compared with embedded flux sensors and surface temperature measurement estimations in Table 22.

3.5.5.2 Calculations

Referring to the BRE publications (Ward, 2006; Ward & Sanders, 2016) and ISO 10211 (BSI, 2017c) – regarding numerical calculation methods of TB in construction for the chi-value (χ-value) calculation (see equation 63) the coupling coefficient is found by dividing the total energetic loss [W] by the applied temperature differential [K]. Then, the analytical U-value [W/m^{2}K] multiplied by its effective area [m^2] (theoretical loss without presence of TB), is subtracted. This finds the residual energy left over attributable to the TB effect:

$$\chi = L_{3D} - \sum_{i=1}^{N_i} U_i \,.\, A_i - \sum_{j=1}^{N_j} \psi_j . l_j \qquad 63$$

Where 'χ' is the point-thermal transmittance [W/K], 'L_{3D}' is the 3D coupling coefficient [W/K] (total energetic loss divided by the applied temperature differential), 'U_i' is the 1D U-value [W/m^{2}K], 'A_i' is the area the 1D U-value is effective over [m^2], 'ψ_j' is the psi-value (ψ-value) [W/mK], 'l_j' is the length over which the psi value exists [m] (BSI, 2017c).

In this 3D experiment there was no linear transmittance, therefore, this part of the equation can be ignored. Paradoxically, this 3D metric is seldom used in industries whole building energy performance SAP calculations. Instead, either an adjusted U-value is determined considering the point transmittance, or the 2D psi-values (linear transmittances) are reported and converted from 3D simulations.

Balconies are, in some situations, a special case where a steel-support penetrating the insulation creates a point TB (with 3D effects) occurring on an existing linear TB (with 2D effects). To fully capture this multi-dimensional heat flow, the BRE use 3D modelling software TRISCO (Ward & Sanders, 2016) and follow SAP E23 (balcony assessment) in BR 497 (Ward & Sanders, 2016) adhering to ISO 10211 (BSI, 2017c). This is a 2D procedure and is therefore adapted in this case: a 3D model of the investigated balcony is created to include the steel support, then the coupling coefficient from the 3D simulation is calculated which the temperature difference is applied to before subtracting the analytical U-value – multiplied by its area. This deduces a [W/K] value which is then divided by the user defined model depth, finding the linear transmittance [W/mK] applicable to the modelled depth.

In this manner, a 2D linear transmittance (psi-value) encapsulates both 3D and 2D effects in the construction detail and can be reported in the 'Certified product list' (BRE, 2019a) as a linear transmittance, allowing it to be understood and used correctly in BPE.

The BRE publication titled 'Certified thermal details and product scheme' (BRE, 2019a) reports psi-values for specific products in which bespoke thermal modelling was performed. Companies will pay for the privilege of having their product listed in the scheme – this provides architects, structural engineers, and building designers with a thermal metric for specific thermal details and solutions.

The model in the 3D experiment reported on in this paper, was 2m deep. Therefore, the difference between the chi- and psi-value was a factor of 2 (i.e., mathematically, the linear transmittance is exactly half that of the point transmittance).

3.5.7 Interim Findings

Each model used consistent meshing methods: Table 19 shows mesh type and number of nodes. Local refinement increased the number of elements in the region of interest (concentrating analysis at the beam/wall connection), as seen previously in Figure *80*.

Percentage differences between modelled values and their corresponding measurement is shown in Table 22. In all phases, the probed model values generally remained at very close agreement to the measurements, however, probing the model for embedded sensors values displayed some rogue estimations. This could be due several reasons: un-perfect contact when positioning, inconsistent locations, or air gaps. Similarly, the embedded thin film flux sensors were more exposed to external conditions in phases 1 & 2, whilst in the final phases, the embedded sensors were completely isolated from the external convection (or any radiative) interference. The phases with the STB showed closer agreement than the phases without, possibly because smaller fluxes were registered.

Probing the embedded flux values from the model results show a slight flux in the x- and y-directions, not just in the z-direction. see Figure 81. This is possibly caused by the bolts allowing heat to bypass the STB, creating a differential between the edge of the break and the bolt. So, when averaged over the area (at the sensor locations), a deviation in modelled flux magnitude is observed compared to the measurement.

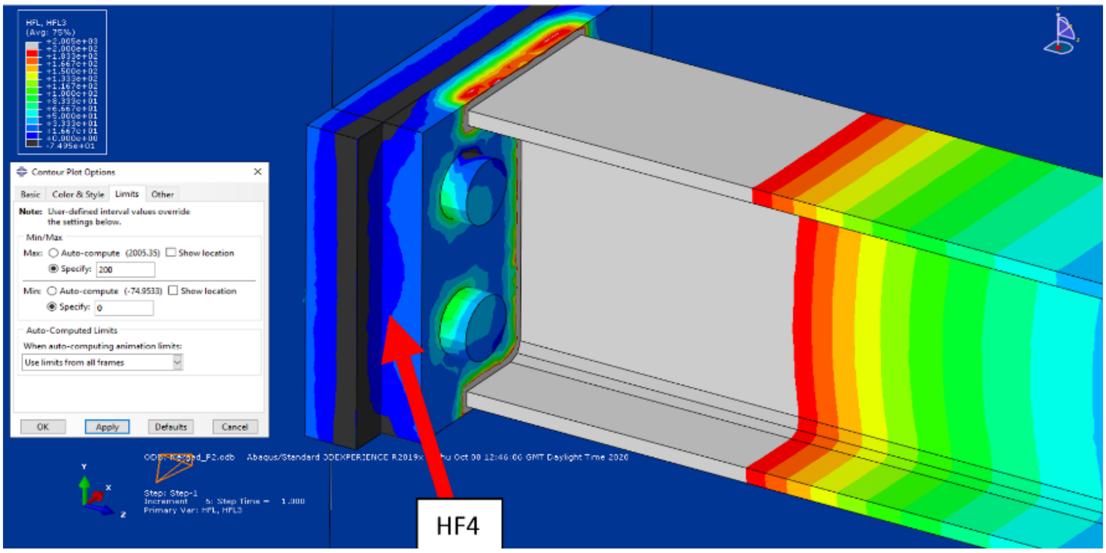

Figure 81 – Shows stripped-back model to illustrate complex heat paths at the point of embedded sensor (HF4).

Considering the inherent drawbacks in embedding 1D point measurement sensors in a 3D heat flow connection, overall agreement was acceptable for these fluxes (around 50% different).

Table 20 shows the calibrated parameters used in the final model simulation and Table 21 shows the calculated psi-value (following the standardised BRE methods) for each phase and the corresponding reduction when the STB solution was applied. A 6.73% reduction in TB-transmittance is seen between phases 1+2 (where no external wall insulation was) raising the minimum internal temperature by a meagre 0.1°C, and a 15.43% reduction in TB-transmittance is seen between phases 3+4 (when external wall insulation was retrofitted to exacerbate bridging) raising the minimum internal temperature by 4-5°C. We can see an increase in overall TB-transmittance when EWI is retrofitted, proving: the greater the wall resistance, the more detrimental the TB impact (Berggren & Wall, 2013; T. Theodosiou et al., 2017, 2019; T. G. Theodosiou et al., 2015). Moreover, the higher the resistance of the wall, the more benefit can be gained from STB solutions (see graph in Figure 83).

Since the greatest STB impact was observed in the later phases, Figure 84 compared phases 3+4 (with EWI); heat loss is reduced, and a greater minimal internal surface temperature is achieved when the break solution is used.

Figure 85 & Figure 86 show cross-section views of temperature isotherms through the centre of the connection and through the anchoring bolt, respectively, for each phase. Again, illustrating the STB solutions capacity to level out the isotherms – indicative of reduced heat loss and increased internal surface temperature.

In Figure 88, a closer examination of the isotherms through the connection is seen by focusing the limits of the temperature scale to visualise the impact of the STB solution in each phase; less disturbances in isotherms is observed with STB in the connection.

The aim of this experiment was to test the experimental design when evaluating a 3D structural TB connection in terms of energy and minimum internal temperature, whilst observing any improvement when incorporating STB solutions. The experimental design seeks to provide a more accurate assessment of a STB solution in-situ by prescribing measurements in simulations rather than parameterising the thermal model using standard assumptions (boundary conditions or material properties).

Experiments were carried out in the EH labs at the UoS and since no point-bridge connection existed to test STBs, modifications were made to include an arbitrary steel beam, emulating a single cantilever balcony structural support (not an actual representative detail).

Emulating quasi-steady-state conditions reduced errors induced from thermal storage effects and allowed reliable, repeatable data capture.

SR spot measurement were taken to supplement the model set-up, as were the environmental air temperatures. The U-value assessment informed the material thickness and conductivity in the model. SR and transmittance measurands were calculated using single flux, air temperature, and surface temperature measurements.

Embedded sensors captured the heat flux in the connection which were used as simulations responses. Considering the calculated uncertainty intervals (analysed following the GUM method) as tolerances in re-calibration, when comparing probed values of embedded flux with their measurements, model parameters were adjusted within sensible ranges (dictated by the uncertainty in measurement) in subsequent iterations until the model response best fits the measurements.

In the first situation (without EWI), a 6.73% reduction in transmittance is caused using a STB solution, whereas, in the second situation (with EWI) the transmittance was reduced by 15.43% (Table 21). The efficacy of STB has been proven and allows comparison between other documented TB metrics. The psi-value [W/mK], a 2D metric, was calculated from a 3D simulation by following the BRE advice taken from BS EN ISO 10211. The 'Building Envelope TB Guide' (BC Hydro, 2016) shows the linear transmittances for a range of balcony examples: poor (1 W/mK), regular (0.5 W/mK), improved (0.35 W/mK), and efficient (0.2 W/mK), see Figure 82.

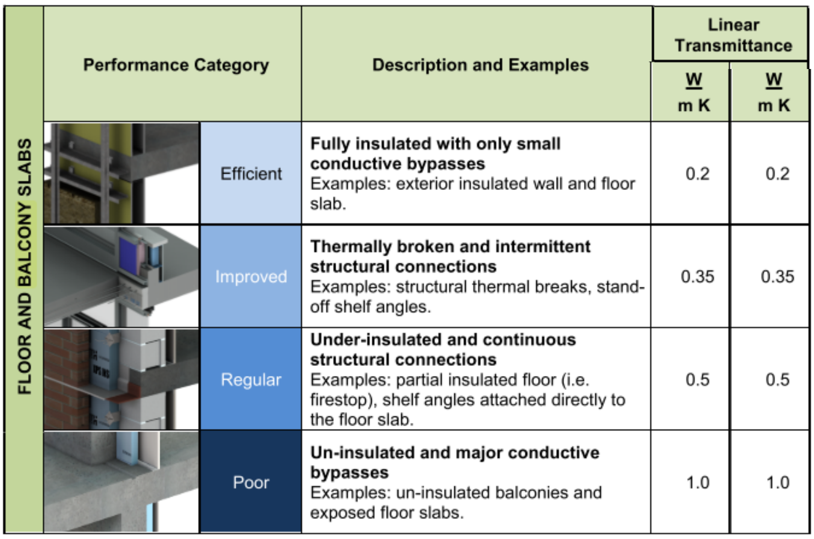

FLOOR AND BALCONY SLABS

Performance Category	Description and Examples	Linear Transmittance W/m K	W/m K
Efficient	**Fully insulated with only small conductive bypasses** Examples: exterior insulated wall and floor slab.	0.2	0.2
Improved	**Thermally broken and intermittent structural connections** Examples: structural thermal breaks, stand-off shelf angles.	0.35	0.35
Regular	**Under-insulated and continuous structural connections** Examples: partial insulated floor (i.e. firestop), shelf angles attached directly to the floor slab.	0.5	0.5
Poor	**Un-insulated and major conductive bypasses** Examples: un-insulated balconies and exposed floor slabs.	1.0	1.0

Figure 82 – Balcony linear transmittance values (BC Hydro, 2016).

Similar catalogues from Passive House Institute (PHI) (Passive House, 2015) or the UK building regulation approved documents ACD (HM Government, 2007) also exist.

Comparing this to the psi-values calculated in this experiment: even when forcing the worst-case scenario (phase 4) – using EWI to exacerbate the TB effect – an efficient-improved status is maintained with a transmittance of 0.2145 [W/mK] according to Figure 82 (BC Hydro, 2016). Meaning the TB falls within the worst-case scenario.

This maybe because only an arbitrary 3D TB was realised in the experiment and, although a structural point-TB was modified into the wall to represent a single balcony support, the structural beam itself did not penetrate the wall. The anchors caused most of the TB hence the detriment of transmittance losses is minimal compared to what could be expected in a real steel-to-steel balcony case study.

However, reductions were seen in heat loss (6.73-15.43% depending on wall composition) when the STB solution was used utilised, and the minimum internal surface temperature was raised from 20.56℃ to 20.61℃ in phase 1 & 2, and from 21.62℃ to 26.5℃ in phase 4 & 3. One can therefore hypothesise that when the STB solutions are utilised in the correct position (in-line with the insulating envelope), greater improvement in transmittance and minimum internal temperature are observed.

That said, this study is of one connection (beam to brick), with no surrounding windows, doors (or any other TB elements) like seen in real balcony case studies. Having only one TB source focussed attention on the STB impact without worry of unnoticed influencing factors causing errors.

3.5.6 Modelling Results

We saw minimal discrepancy in the measured U-values between Phases 1&2 (bare wall) – 1.67 ± 0.14 to 1.67 ± 0.15 [W/m^{2}K] (to 2 decimal places) – which is expected when analysing the same wall. Although, slight variations were seen in U-value measurement between Phases 3&4 (with EWI retrofitted). This was unexpected since the uncertainty analysis boundaries did not overlap considering the measurement between 0.58 ± 0.06 and 0.69 ± 0.05 [W/m^{2}K] with (k=1), expanding this combined propagated uncertainty assuming a normal distribution (k=2), the U-values are 0.58 ± 0.12 and 0.69 ± 0.1 [W/m^{2}K], with a 95% confidence level, see Table 22 which shows all modelled U-values and environmental conditions, both internally and externally, were within the measured uncertainty.

The values are agreeable assuming an average of 0.64 ± 0.15 [W/m^{2}K] for phases 3&4, and 1.67 ± 0.2 [W/m^{2}K] for phases 1&2, with the same confidence. The revised uncertainty is due to the averaging of the values; uncertainties are combined in quadrature.

Conditions were set using measurements of temperature and SRs: all models assumed internal and external SRs as surface-fluid HTC's: 22.87±11.42 [W/m^{2}K] and 4.64±0.21 [W/m^{2}K] at their respective temperatures.

Psi-value results and % reduction when break is used can be seen in Table 21:

	Phase1	Phase2	Phase3	Phase4
Psi-Value [W/mK]	0.104	0.097	0.1814	0.2145
% Reduction	6.73%		15.43%	

Table 21 – Impact of STB numerically: % reduction when used in each case.

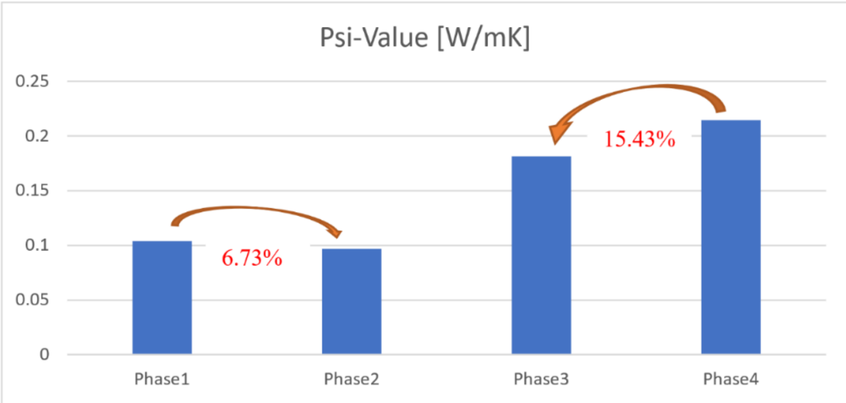

Figure 83 – Graph comparing modelled TB transmittance between phases.

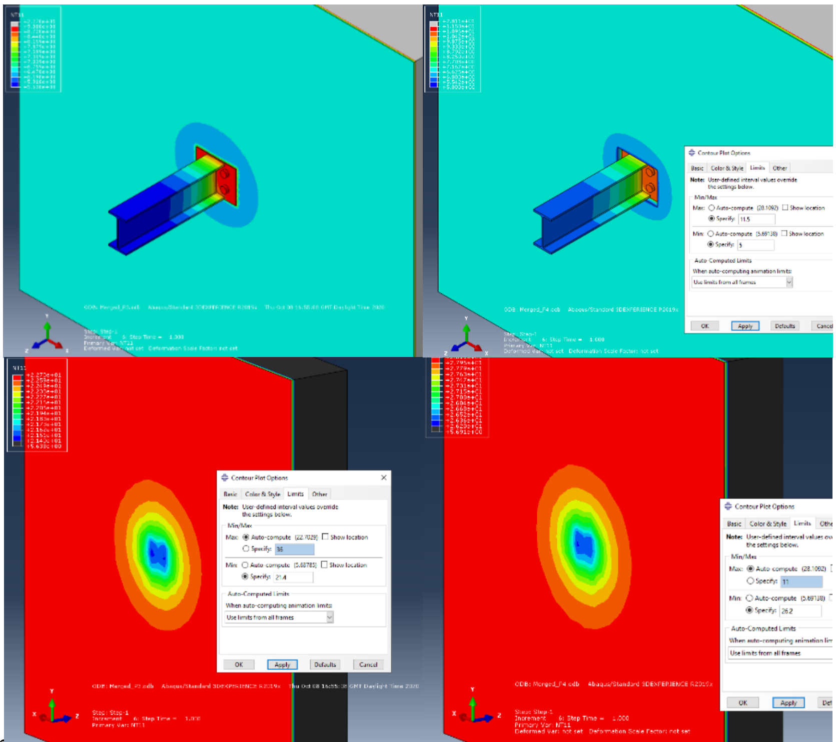

Figure 84 – 3D comparison between Phase 3 (with Break) and 4 (without break) featuring EWI, external view top, internal view bottom.

The next figures show a cross-section directly through the centre of the beam (Figure 85) and a slightly adjusted cross-section position (Figure 86) cutting the model directly through the anchor bolts.

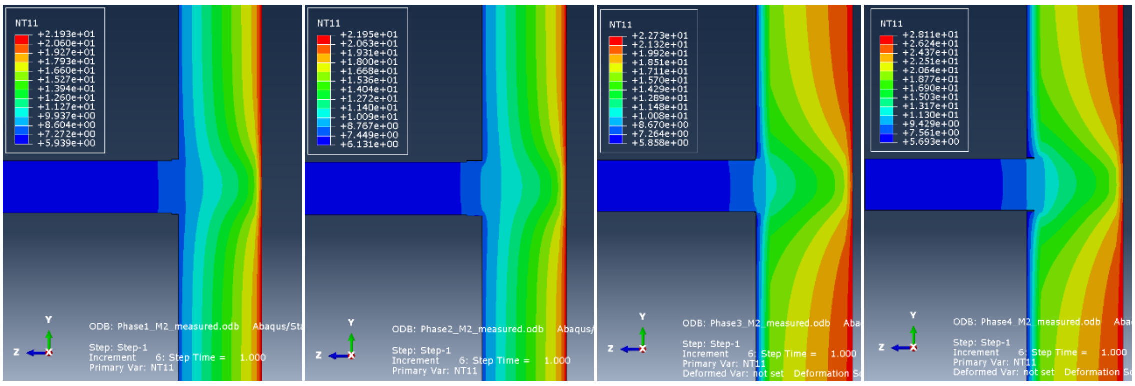

Figure 85 – Left to Right, Phase 1-4, cross-section of isotherm through centre of beam.

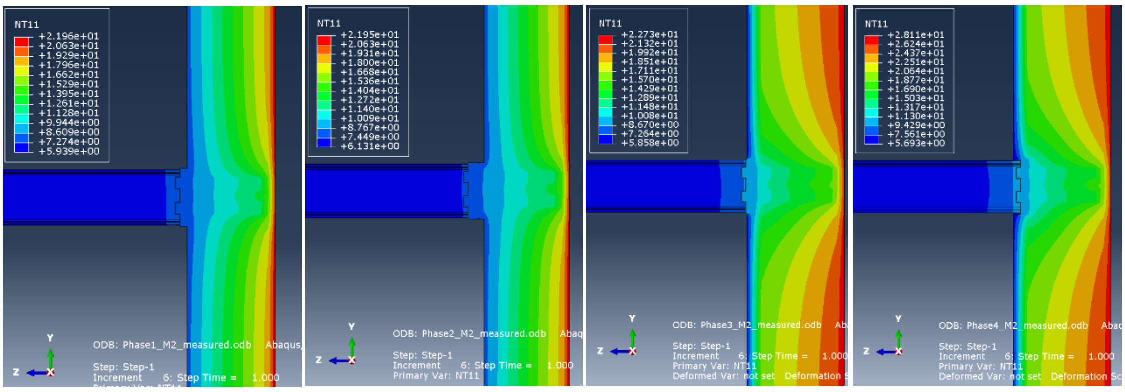

Figure 86 – Left to Right, Phase 1-4, cross-section of isotherm through centre of bolts and anchors.

The cross section through the bolts deviates the isotherms noticeably more illustrating the effect of the masonry anchors.

The following images examine temperature isotherms of cross-sections through the centre of the TB allowing visual comparison in bare wall phases 1&2 (without and with STB, respectively, seen in Figure 87) followed by EWI phases 4&3 (without and with STB, respectively, seen in Figure *88*).

In the top image the limits to the temperature scale were not adjusted, whereas in the bottom images the temperature scale limits are adjusted, illustrating isotherm deflection. The maximum and minimum were set focusing on the temperature gradient through the TB break junction.

Because the measured internal temperature conditions for phases 3 & 4 were different (23°C and 29°C, respectively), the illustrated example considered identical conditions i.e., 23°C and 6°C, for internal and external temperatures in each simulation – producing a fair visual comparison between phases.

Phase 1 & 2 comparison:

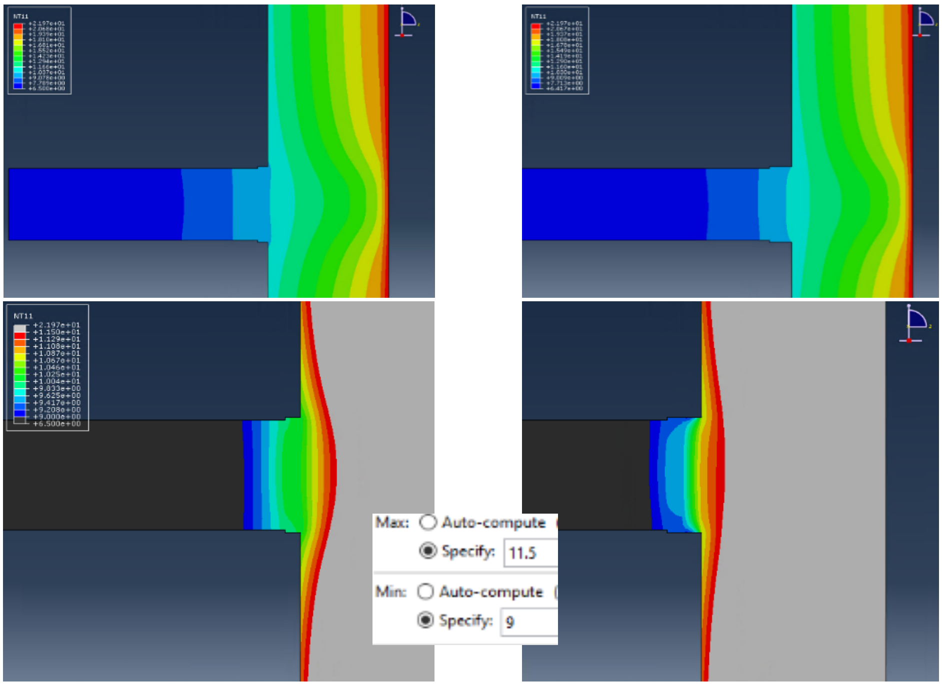

Figure 87 – Phase 1 (LHS) & Phase 2 (RHS), temperature is scaled between 9°C and 11.5°C.

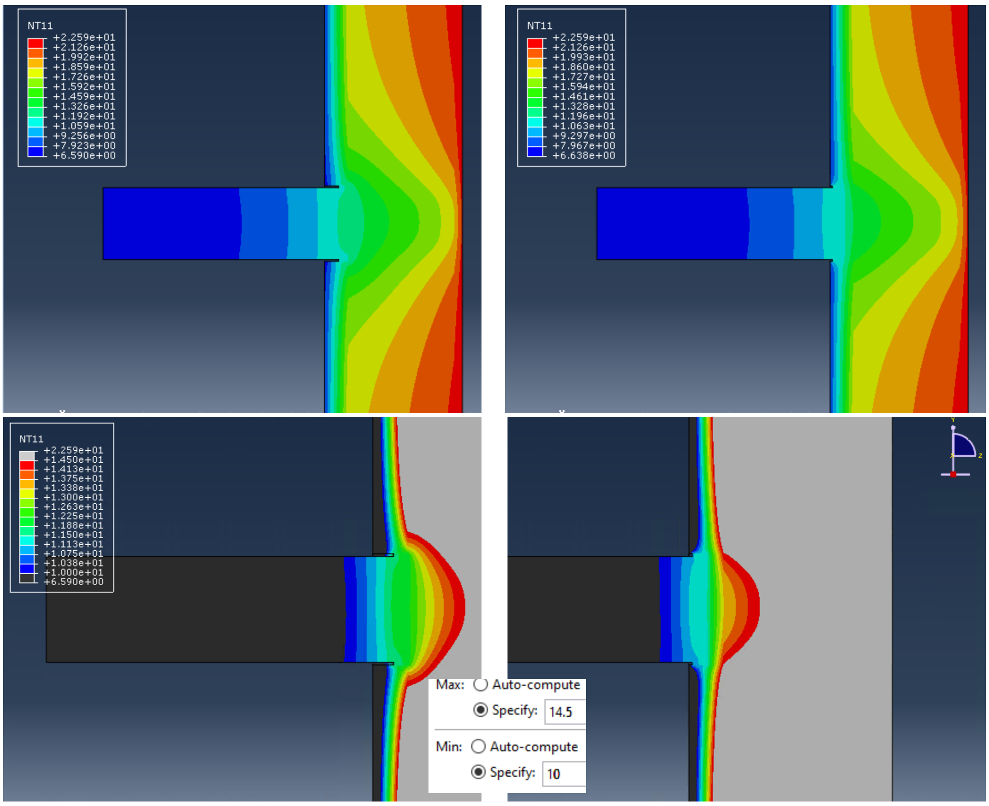

Figure 88 – Phase 4 (LHS) & Phase 3 (RHS), temperature is scaled between 10°C and 14.5°C.

Comparison table:

	Ext Condition	Int Condition	Min Surf Temp	Max Surf Temp	U-value	HF1	HF2	HF3	HF4
	°C	°C	°C	°C	W/m^2K	W/m^2	W/m^2	W/m^2	W/m^2
Phase 1 – without break (bare wall)									
Measured	5.88	23.39	20.04	22.47	1.67	51.16	40.98	55.71	50.32
Uncertainty	±1	±1	±1	±1	± 0.20	±2.76	±2.21	±3.00	±2.71
Modelled P1	6	23	20.56	21.97	1.52	52.23	23.07	53.17	23.76
% Difference	2%	1.7%	2.6%	2.2%	9%	2%	43.7%	4.6%	52.8%
Phase2 – with break (bare wall)									
Measured	6.10	23.35	20.14	22.52	1.67	29.99	16.71	24.44	16.96
Uncertainty	±1	±1	±1	±1	± 0.20	±1.62	±0.90	±1.32	±0.91
Modelled P2	6	23	20.61	21.97	1.52	29.45	16.2	23.7	16.04
% Difference	1.6%	1.5%	2.3%	2.4%	9%	1.8%	3%	3%	5.4%
Phase3 – with break (EWI retrofit)									
Measured	5.61	23.35	21.35	22.97	0.64	34.86	38.58	31.73	38.07
Uncertainty	±1	±1	±1	±1	± 0.20	±1.88	±2.08	±1.71	±2.05
Modelled P3	6	23	21.62	22.6	0.6033	51.89	19.62	21.1	18.92
% Difference	7%	1.5%	1.3%	1.6%	5.7%	49%	49%	33.5%	50%
Phase4 – without break (EWI retrofit)									
Measured	5.69	28.95	25.89	28.31	0.64	201.77	103.17	140.00	74.04
Uncertainty	±1	±1	±1	±1	± 0.20	±10.87	±5.56	±7.54	±3.99
Modelled P4	6	29	26.5	28.4	0.6033	136.6	75.52	132.8	75.5
% Difference	5.4%	1.7%	2.4%	3%	5.7%	33%	27%	5.1%	2%

Table 22 – Calibration results compared against mean measurements % differences.

3.5.8 Implication on further modelling

The TB-transmittance metric (point or linear), like the U-value, is independent of temperature i.e., regardless of the temperature difference used in calculation, the value remains the same. However, the TB metric is sensitive to SRs. Future studies should explore deeper investigation, possibly considering:

- Internal convection: convection may have to be adjusted locally to specific surfaces in FE models (Garay Martinez, 2018; Garay et al., 2014; Martinez et al., 2017). Measuring this variable in as many places as possible could help refine the model calibration techniques achieving more accurate simulations in subsequent experimentation.

- Building orientation and elevation: comparing the effect of SR on TB-transmittance would be an insightful investigation if SR are considered a dynamic function of wind-speed and solar.

- Dynamics need to be considered in subsequent experimentation, altering the experimental design, if necessary, to suit in-situ measurement campaigns.

- On-site real case studies would be preferred to further the experimental investigations, where climatic conditions cannot be controlled.

- Surrounding TBs (windows and doors) effect on STB solutions.

4.0 Final experiment

The final experiment attempts to develop the in-situ experimental measurement design further by applying the proposed model parameterisation and re-calibration exercise using well understood measurements taken from a representative construction detail where STBs are used in real buildings.

After experiment 1 (linear-bridge 2D transmittance corner-corner wall investigation), comparing IR and HFM measurement methods with an informed FE simulation software, confirmed that accurate model calibration could reproduce experimental measurements – albeit with some PG issues. A second study focussed on a 3D point-bridge under steady-state laboratory conditions to develop the experimental design further. Some of these preliminary PG issues were addressed by taking additional measurements (surface-fluid HTC) and performing more in-depth analysis of their uncertainty. However, since additional error sources were noticed (such as, stratification seen through the thermocouple sensor array and qualitative IR, airgaps in the connection, etc) further situational modifications were made (EWI, internal fans, soft mortar connecting brick to steel to improve the thermal contact). Other experimental limitations noticed include proximity to other bridges, penetration depth of cantilever beam (anchored to chemically fixed wall bushes), steady conditions oppose to dynamic, and unreal workmanship.

From this experiment, taking any meaningful measurement of this type of TB in a working construction site became obvious, raising concerns that more or different obstructions maybe present onsite: interferences, or blockages may restrict access or cause erroneous data capture in-situ. To embed sensors within a construction detail, site access is required in the steelwork phase to deploy the one-use sensors, which could easily become damaged during the completion of the building.

Therefore, due to the shortcomings of the previous investigations, the final data capture was initially aimed to monitor a live balcony in-situ. This required liaising with construction contractor from many departments and levels. Unfortunately, the contractor pulled out of the agreement close to the date forcing the study to develop its own system with which to test STBs within a representative construction under real external conditions. Manufacturing a bespoke test rig (similar to a hot box) was discussed but was quickly disregarded as too expensive when various sizes of test-rigs were proposed – this was not helped by the Covid-19 outbreak causing financial uncertainty and diminishing cashflow forecasts.

In light of the unforeseen issues, the University of Salford offered the EH labs to facilitate final experimentation: investigating a representative steel-to-steel balcony support configuration (a similar example is seen in Figure *89*), with which a variety of STBs can be tested under steady-state conditions.

Figure 89 – Steel beam cantilever balcony support example.

4.1 Steel

The actual steel configuration design of representative steel-to-steel cantilever balcony support is detailed in Figure 90:

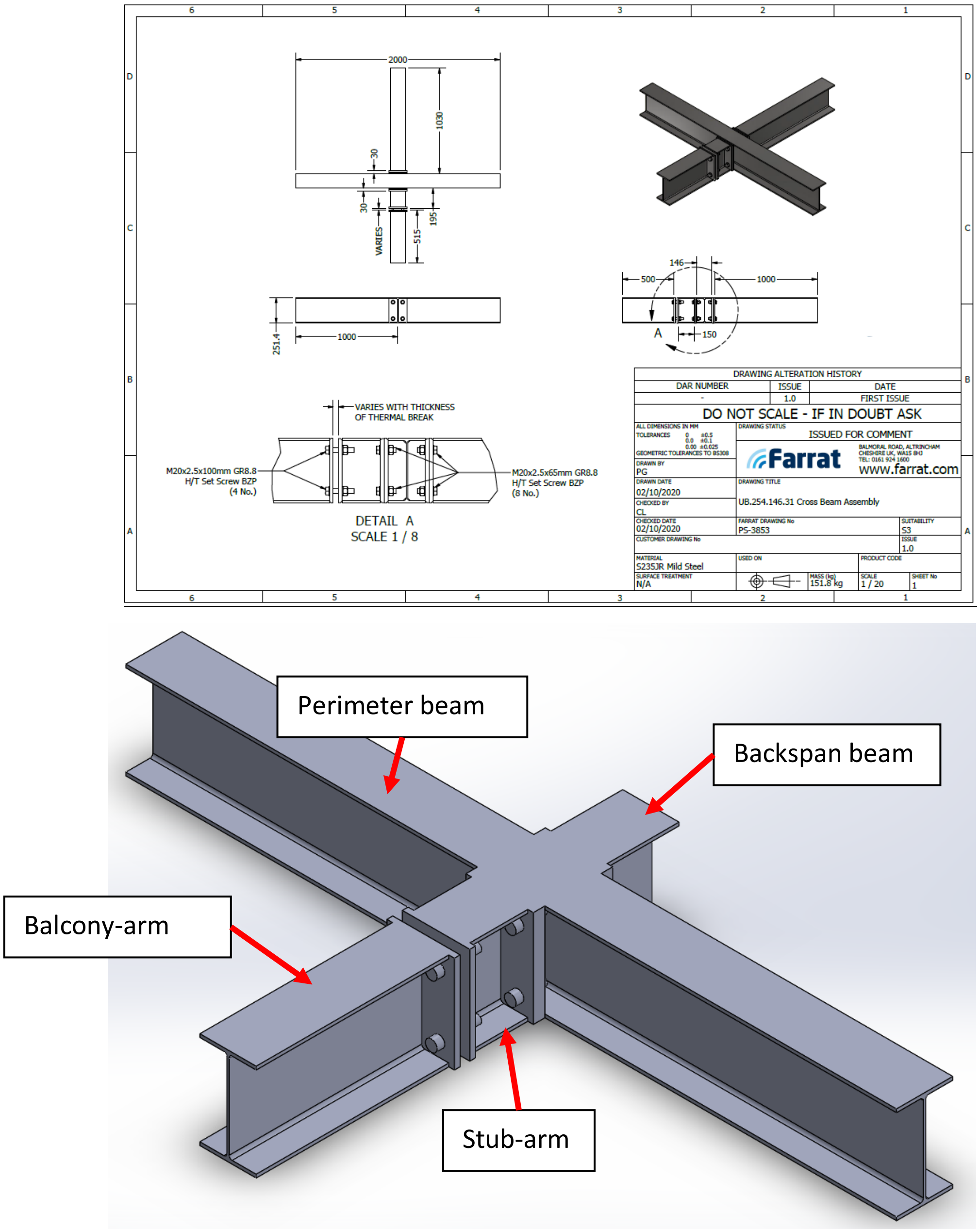

Figure 90 – Steel crossbeam assembly.

It was aiming to represent a worst-case scenario featuring a perimeter beam with a backspan beam at the stub-arm and balcony-arm location.

4.2 Breaks

Farrat STBs come in three materials, ranging in thickness from 5mm – 25mm. Therefore, this final experiment applied six breaks in the steel-to-steel: the thickest and thinnest breaks of each material, see Figure 91:

Figure 91 – Tested Farrat STBs. 5mm and 25mm pads of each material: TBL, TBK, TBF.

The material properties are specified by the manufacture and published in Farrats technical brochure (Farrat, 2020), see Figure 92.

MATERIAL PROPERTIES	FARRAT TBF*	FARRAT TBK	FARRAT TBL
Characteristic Compressive Strength, fck (N/mm², MPa)	460	312	89
Design value for compressive strength, fcd (N/mm², MPa)	368	250	70
Compresion Modulus (N/mm², MPa)	6800	4100	2586
Density (Kg/m³)	2100	1465	1137
Water Absorption (%)	0.40	0.14	0.48
Thermal Conductivity (W/m-k)	0.200	0.187	0.292
Colour (may vary)	Grey	Amber	Black
Thicknesses available (mm) +	5, 10, 15, 20 & 25	5, 10, 15, 20 & 25	5, 10, 15, 20 & 25
Maximum sheet size (mm)	1000 x 1200	2400 x 1200	2500 x 1250
Temperature resistance (°Celsius)	+550 short term (Max) +300 long term (Max) -120 (Min)	+250 short term (Max) +210 long term (Max) -180 (Min)	+170 short term (max) +110 long term (max) -40 (min)
Thickness tolerances (mm)++	+/- 0.5 (TBF 5) +/- 0.7 (TBF 10) +/- 1.05 (TBF 15) +/- 1.4 (TBF 20) +/- 1.75 (TBF 25)	0 / +0.2 (TBK 5, 10 and 15) 0 / +0.3 (TBK 20 and 25)	0 / +0.25 (TBL 5) +0.2 / +1.5 (TBL 10) +0.3 / +2.5 (TBL 15, 20 and 25)

Figure 92 – Material properties of the available Farrat structural thermal grades (Farrat, 2020).

4.3 Specimen wall

The experimental wall construction aims to represent new-builds where steel penetrations supporting balconies primarily exist. Complying with building regulations criteria regarding high energy new builds, a U-value around 0.18 W/m^{2}K (GOV, 2021) was targeted. The wall was conceptualised to meet these targets bearing in mind safety, location of testing, representativeness, and cost.

4.3.1 Cross section

A light-weight rainscreen cladding system design was realised (see Figure 93) comprised of (from external to internal): plywood (9mm), external airgap (50mm), OSB (11mm), PIR (100mm), internal airgap (50mm), and EPS on plasterboard (20+10mm, respectively), generating an analytical transmittance U-value of around 0.18 [W/m^{2}K], considering the material properties in Table 23. This replaced the first-floor window 1.16m x 1.64m in the heated conditioning void (neighbouring the EH test house), allowing the experiment to make use of the climatic chamber once again for external conditions.

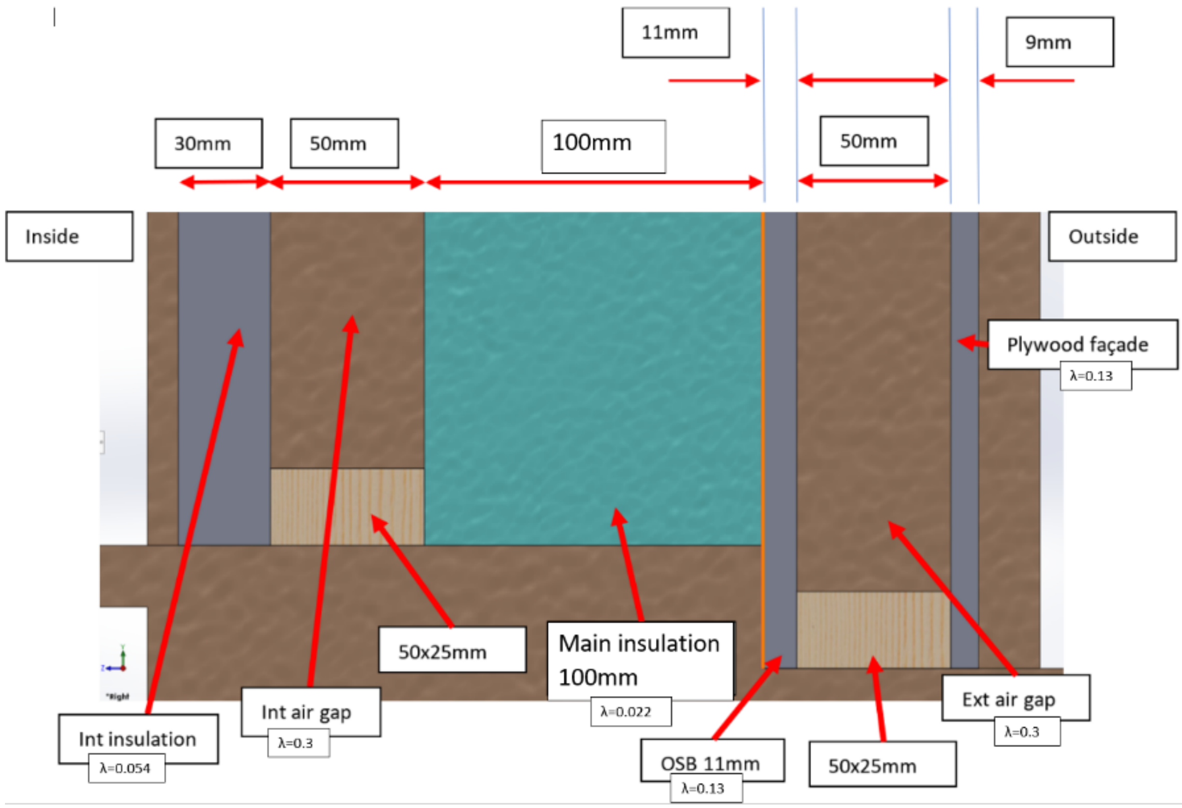

Figure 93 – Shows the cross-section of the specimen wall labelling the thickness and material conductivity of each layer.

Layer	Materials:	Conductivity (Man Spec) [W/mK]	Thickness [m]	$R_{Thermal}$ [m^2K/W]
Plywood	Plywood	0.13	0.009	.009/.13
	Air gap (External)	0.3	0.05	.05/.3
	OSB outer-leaf	0.13	0.011	.011/.13
	Main insulation (PIR)	0.022	0.1	.1/.022
Air gap (External)	Air gap (internal)	0.3	0.05	.05/.3
Inner insulation	Inner insulation (EPS Plaster)	0.054	0.03	.03/.054
		Internal SR = 0.13 [m^2K/W]		
		External SR = 0.04 [m^2K/W]		
	U-value [W/m^2K]			0.174

Table 23 – Shows the material conductivity and thickness of each layer. The U-value has been calculated using the standard surface-fluid HTC's, 25 [W/m^2K] and 7.7 [W/m^2K] for external and internal, respectively.

4.3.1 Materials (Fox flow meter)

Materials were tested using the Fox Flow meter to measure the conductivity of each wall layer and each break material. Table 24 shows the measured conductivities and their assumed uncertainty.

Components	Materials:	Conductivity (Man Spec) [W/mK]	Difference [% change]	Conductivity (Measured) [W/mK]	Uncertainty [W/mK]	Uncertainty [%]
Plywood	Plywood	0.13	21%	0.1026	+/- 0.0274	+/- 26.7%
OSB outer-leaf	OSB	0.13	26%	0.0963	+/- 0.0337	+/- 35%
Main insulation	PIR	0.022	0%	0.022	+/- .004	+/- 18%
Inner insulation	EPS Plaster	0.054	11%	0.048	+/-.0096	+/- 19.8%
TBK	Resin polymer	0.182	5.5%	0.172	+/- 0.015	+/- 8.7%
TBF	Mineral based	0.2	1.5%	0.197	+/- 0.003	+/- 1.5%
TBL	Rubber compound	0.292	12%	0.256	+/- 0.036	+/- 14%

Table 24 – Shows the various material conductivities, both measured using the Fox Flow Meter and from the manufacturer specification with their assumed uncertainty range.

300mm square samples were cut and their conductivity was tested at various temperature ranges and fluxes, akin to the exposed conditions in the experiment. The measurement average can be compared with specification from the manufacturer. Noticeably, each tested materials conductivity was underestimated compared with manufacturer specification, this difference was exploited, and the associated uncertainty was altered such that each manufacturer specified value was within the confidence interval. This underestimation was attributed to the presence of a small airgap around the edges of the samples, increasing thermal resistance which reduces the calculated flux.

The main insulations (PIR) conductivity measurement uncertainty was assumed as +/-20% because the manufacture specification was so close. This assumption was the same for the 'inner insulation' (EPS on plasterboard) and thought to be a conservative uncertainty estimation – but not too dissimilar to the other measurement uncertainties.

Again, for the CV wall and steelwork, the uncertainty was broadly assumed as +/-20% since these could not be measured, hence manufacture specifications were considered, seen in Table 25.

Components	Materials:	Conductivities [W/mK]	Ranges [W/mK]
CV wall	Brick	0.65	+/-.13 (20%)
Steelwork	Steel	50	+/- 10 (20%)

Table 25 – Materials Brick and Steel which could not be measured in the Fox Flow meter.

The following images in Figure 94 show the Fox Flow Meter (LaserComp Fox314) and the materials tested for conductivity. The apparatus consists of two parallel hotplates which compress a sample between them. When the sample is loaded between the plates care must be taken that no dust is present. Using the WinTherm32 software, a temperature difference, mean temperature, automatic thickness detection and instruments calibration are defined in the settings.

The software then produces a graph illustrating when the data converges, a flux and conductivity is then reported for that prescribed temperature difference and mean temperature – deducing an equivalent conductivity for that material. Effort was made to ensure that the mean temperature is similar to the operating temperature likely to be experienced in the experiment.

Figure 94 – Shows the 4 wall materials (from top to bottom on the LHS: plywood, EPS on plaster board, OSB, and PIR) and the 3 break materials (bottom RHS) tested in the Fox Flow Meter (top RHS) LaserComp Fox314.

4.4 Conditioning Void (CV) window hole

As mentioned, the window was removed from upstairs in the conditioning void (CV) to facilitate the experimental test rig. The CV acts as a neighbour to the EH when required for testing and can be heated and conditioned like a normal domestic building. The size of the window hole can be seen in Figure 95 & Figure *96* below:

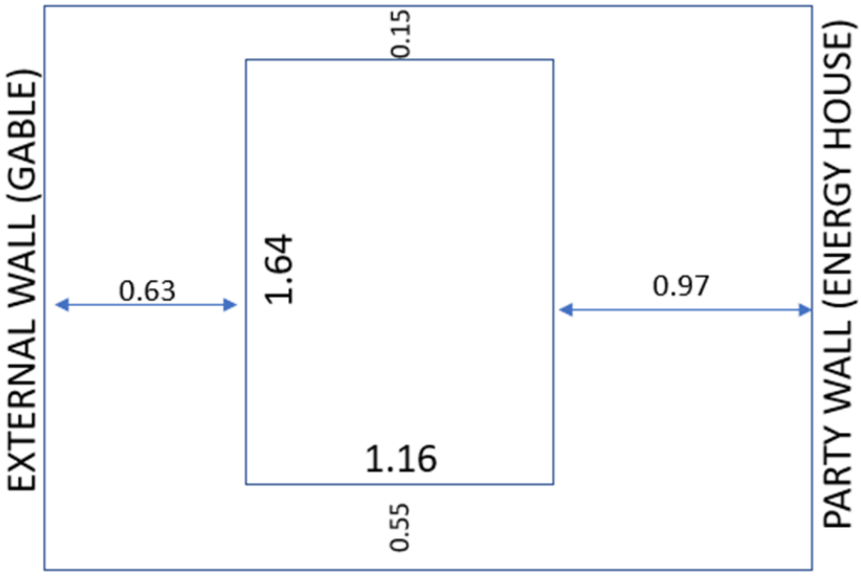

Figure 95 – Shows the measured window hole sizes (internal veiw).

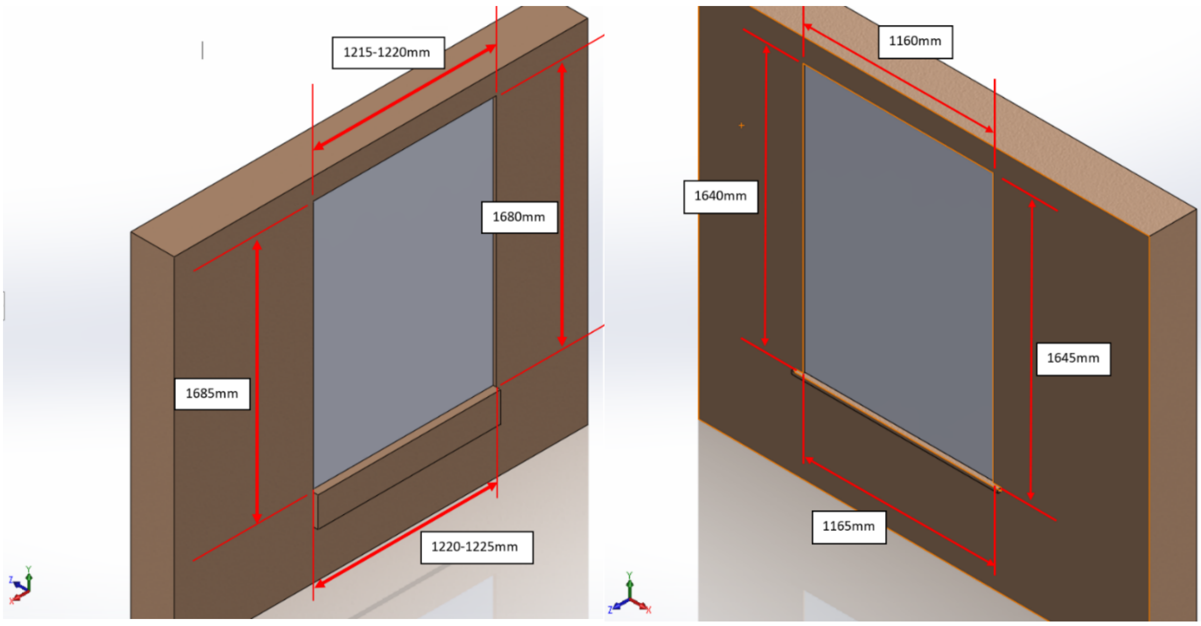

Figure 96 – Shows the measured window hole sizes (external view LHS and internal view RHS).

Notice the hole is not square and, the external opening (roughly 1222x1685mm) is slightly larger than the internal (roughly 1160x1640mm); hence care must be taken when cutting the wall layers to ensure a tight fit, leaving minimal gaps at the edges.

To support the steel internally, size ‘0’ adjustable support props can be fixed to the floor and clamped to the steelwork in 3 places, see Figure 97. The cantilever section is self-supported from these 3 internal supports and required no external support.

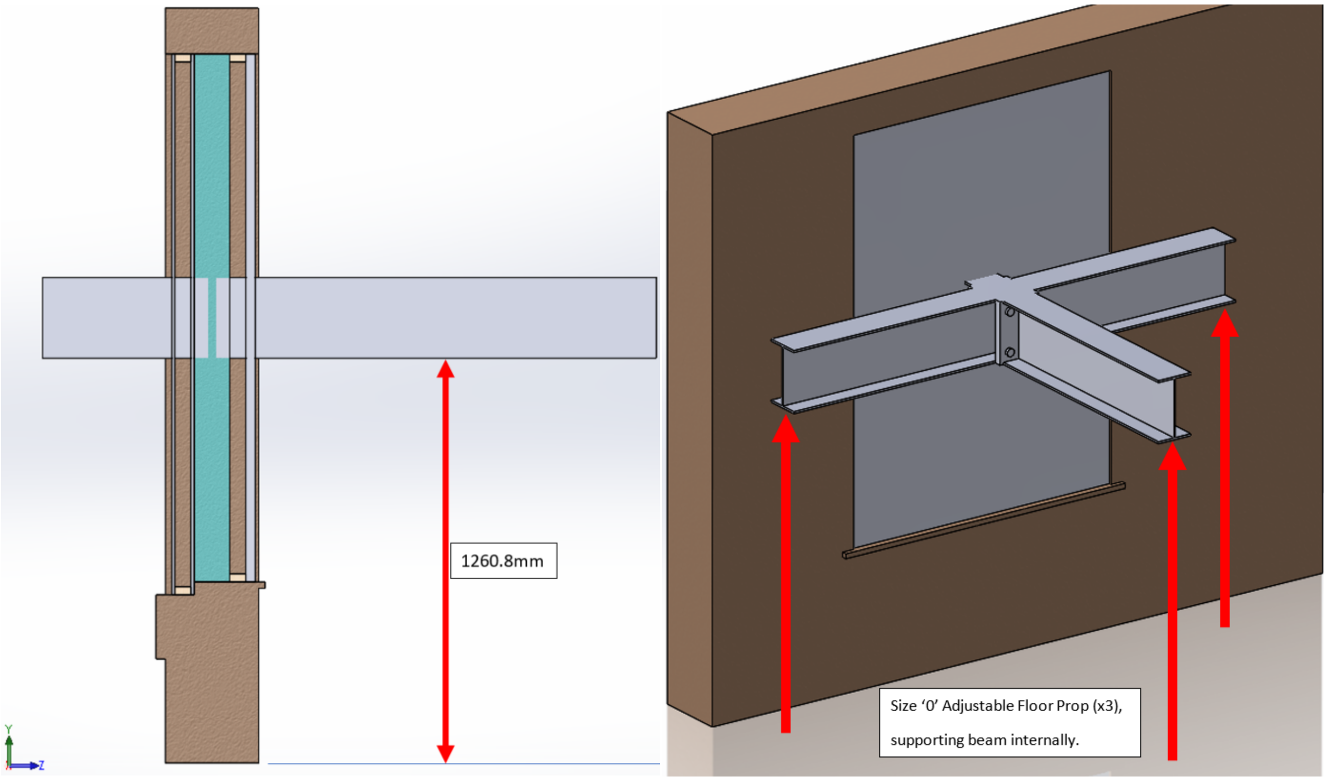

Figure 97 – LHS (side view) shows the modelled specimen positioned within the CV wall, RHS (isometric) internal.

The internal distance from the floor to the bottom of the specimen is approximately 1260.8mm, therefore a size 0 adjustable prop would support it from the three highlighted positions internally.

4.4.1 Real space for test

In the following Figure 98 & Figure 99, the window was removed and replaced with a 100mm thick ridged insulation panel in preparation for the specimen install.

Figure 98 – External view of the window hole prior to specimen install.

Figure 99 – Internal view of the window hole prior to specimen install.

4.5 Flanking loss verification simulation

This location, however, could still potentially cause erroneous data if the flanking loss, at the edge of the specimen where it meets the CV wall, have a detrimental influence on the heat flow through the connection. Therefore, preliminary modelling was performed to assess if the window hole was sufficiently big enough so as not to incur flux interference at the break connection from the specimen edge, before install.

Comparisons can be made between the 'specimen alone' and 'including the CV wall' at various model dimensions. The first models were made to the specimen dimensions (**1.64m*1.16m)** dictated by the window hole in the CV wall; 'specimen alone' model featured only the specimen wall at (1.64x1.16m) whilst the 'including CV wall' model featured the CV stratigraphy (approx. 9inch or 225mm brick with plaster and skim) at the entire wall dimensions (2.76x2.34m), as per the previous Figure 93, Figure *95*, Figure 96. This provides a baseline model comparison of the planned experimental situation.

Both models assumed the same conditions: the surface-fluid HTCs were set to 25 and 7.7 [W/m^{2}K], externally and internally, respectively. The temperature difference was 20°C achieved by setting the external and internal to 5°C and 25°C, respectively.

Figure 100 Figure 101 compare 'including CV wall' LHS and 'specimen alone' RHS. Figure 100 depicts the nodal temperature (top row) and heat flux magnitude (bottom row) viewed from the internal face, scaling set to 25-22[°C] and 30-0[W/m^2], respectively. Whilst Figure 101 depicts the same metrics but from the external face with scaling adjusted to 7.8-5[°C] and 8-0[W/m^2], respectively.

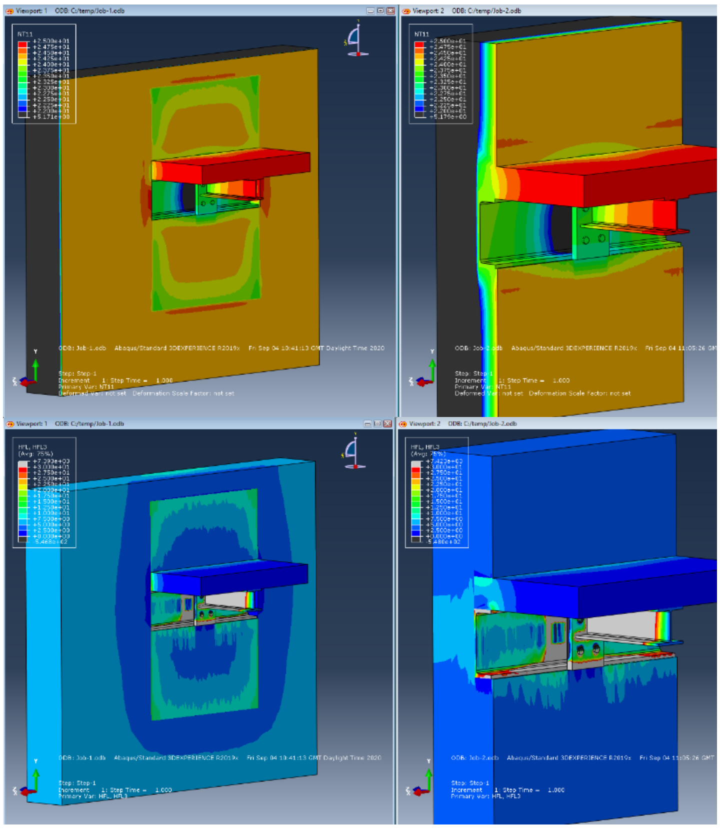

Figure 100 – Shows internal screenshots of the specimen in the CV wall (left-hand side) and the specimen alone (right-hand side). Nodal temperatures (top) scales set to 25-22[°C] and heat flux magnitude (bottom) scales set to 30-0[W/m^2].

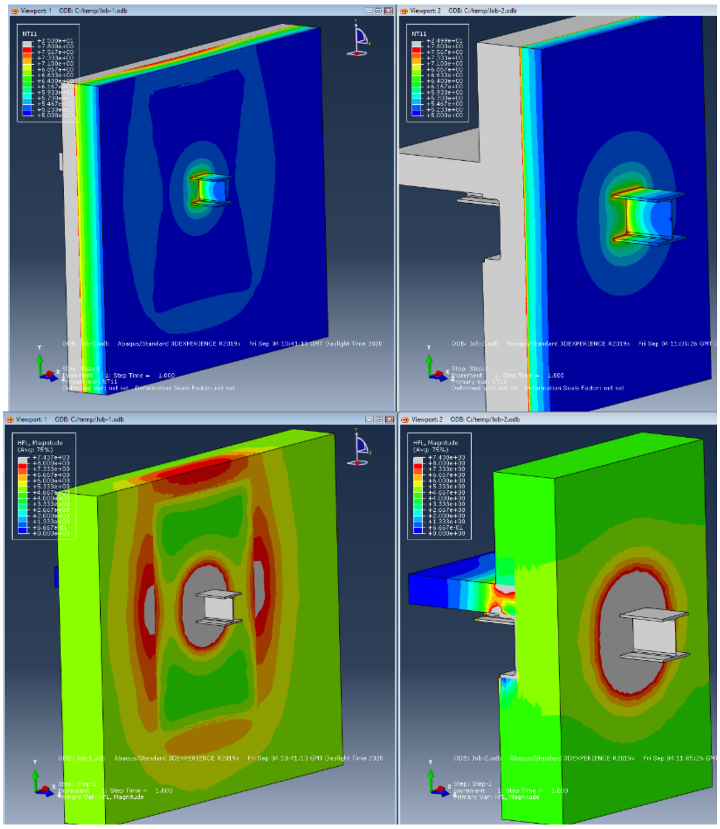

Figure 101 – Shows external screenshots of the specimen in the CV wall (left-hand side) and the specimen alone (right-hand side). Nodal temperatures (top) scales set to 7.8-5 [°C] and heat flux magnitude (bottom) scales set to 8-0[W/m^2].

To probe the model a path of nodes was made, see Figure 102, and used to plot nodal temperatures against, see Figure 103. Surface temperature plots on the internal face start in the centre of break and lead towards the bottom edge through the centre of the model on the internal face:

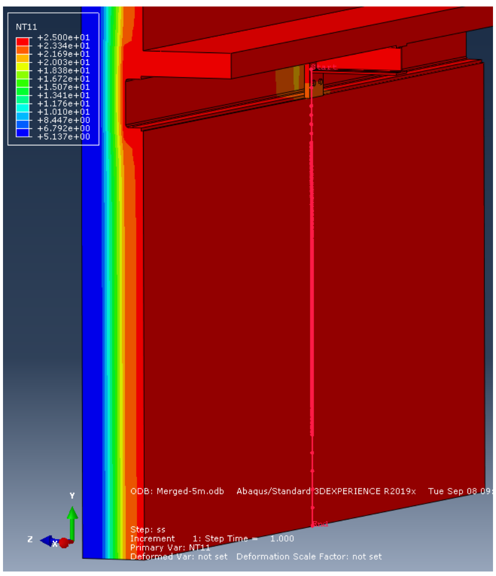

Figure 102 – Shows the nodal path plotted on the modelled geometry.

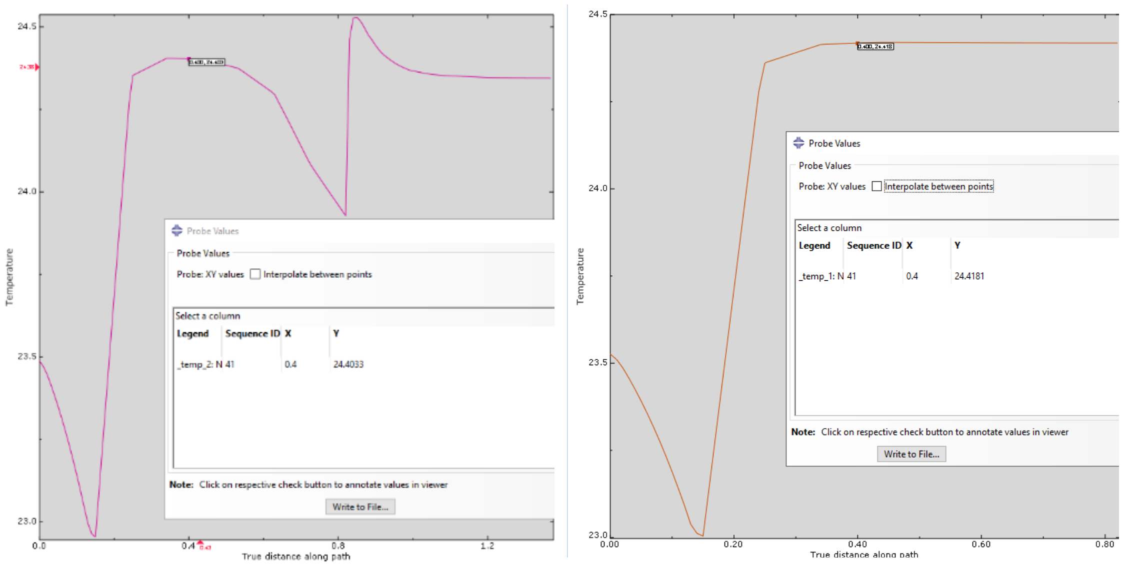

Figure 103 – Shows the asymptotic temperature gradient leading from the centre of the model to the edge. The specimen in the CV wall LHS, and alone RHS.

Comparing the plotted distance/temperature graphs (Figure 103), the alone model without flanking losses (RHS), asymptotes to a temperature of 24.4℃ occurring at 0.4m away. The model featuring the specimen in the CV wall (LHS) where flanking interference is expected, reaches the same temperature of 24.4℃ at the same distance of 0.4m away. This proves that the flanking losses at the edges of the specimen, cause little detriment to the 3D heat flow through the point-TB.

To vindicate this further, the specimen will be analysed at 1mx1m then subsequently increased incrementally by 0.5m up to 5mx5m. Initially, the specimen will be analysed alone, then the specimen in a 5m square wall (same stratigraphy as CV wall) will be analysed.

The only factor to change throughout the model variations is the size, all conditions and thermophysical properties were kept the same.

The following figures show the incremental size increase of the 'specimen alone' model, expanding from 1mx1m to 5mx5m in 0.5m increments. Figure 104 shows the nodal temperatures (top group) and the heat flux (bottom group) from the internal face setting the scale limits to 25-22[℃] and 30-0[W/m^2], respectively.

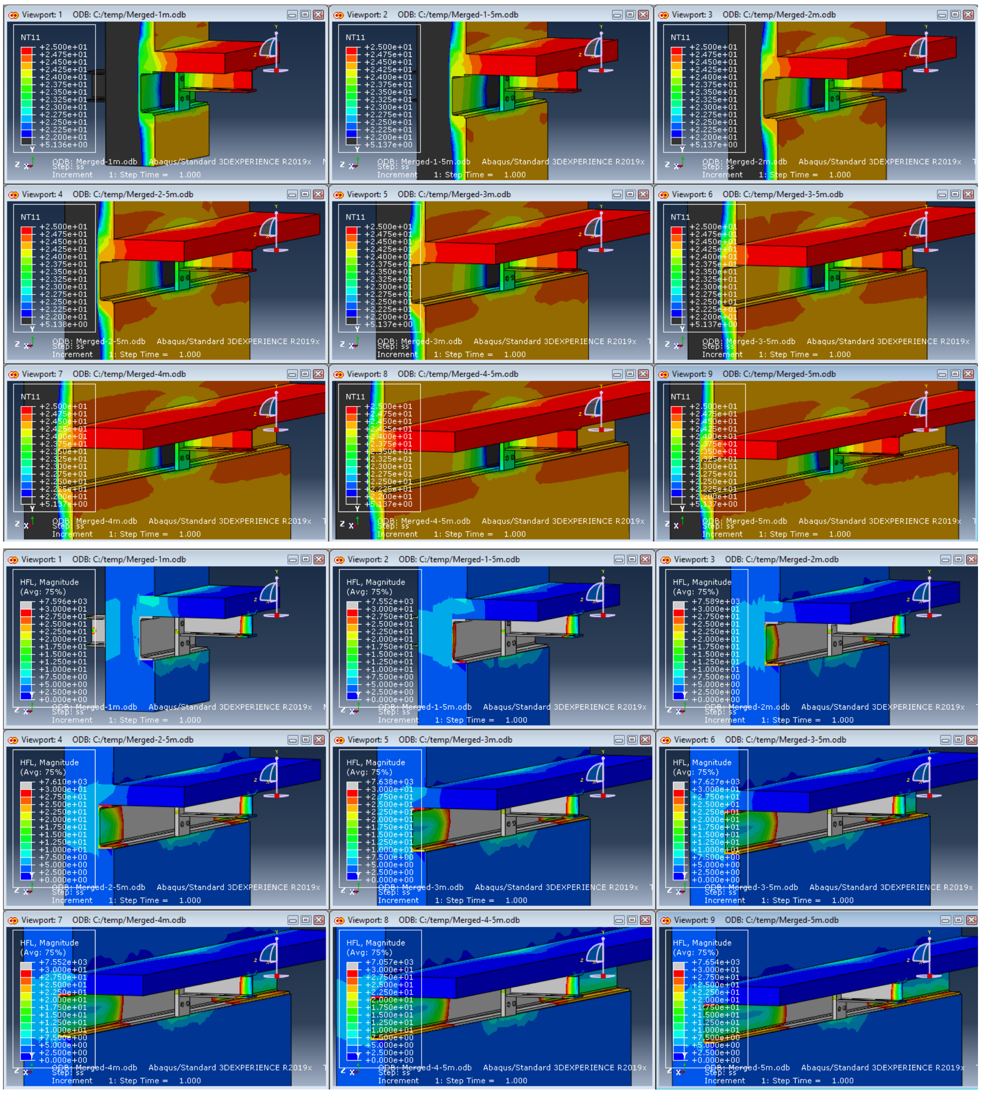

Figure 104 – Shows the internal face of the models expanding from 1-5[m^2] in 0.5[m] increments. The top images are nodal temperature with scales set to 25-22[°C] and the bottom images are the heat flux magnitude with scales set to 30-0[W/m^2].

The following figures show the incremental size change of the 'specimen alone' model, expanding from 1[m^2] to 5[m^2] in 0.5m increments. Figure 105 shows the nodal temperatures and the heat flux from the external face setting the scale limits to 6.22-5[°C] and 8-0[W/m^2], respectively.

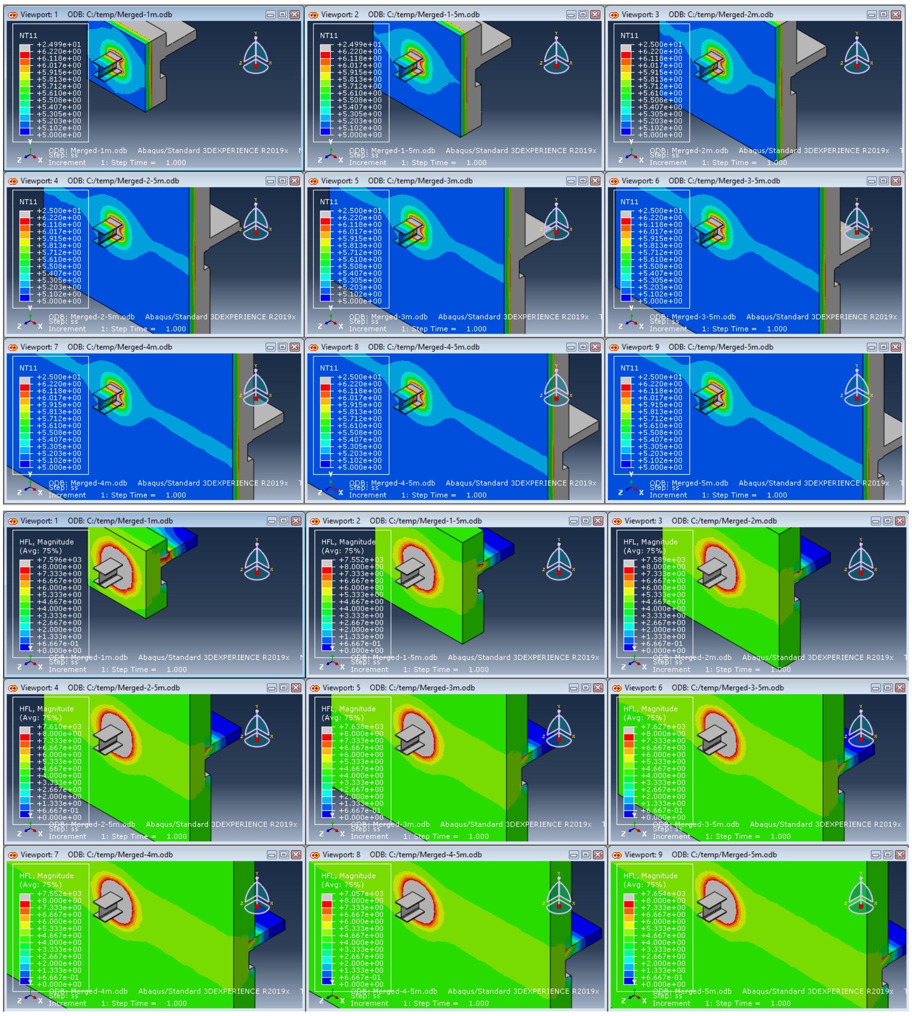

Figure 105 – Shows the external face of the models expanding from 1-5[m^2] in 0.5[m] increments. The top images are nodal temperature with scales set to 6.22-5[°C] and the bottom images are the heat flux magnitude with scales set to 8-0[W/m^2].

The temperature was plotted against the path plot distance in Figure 106 for each expanded model size.

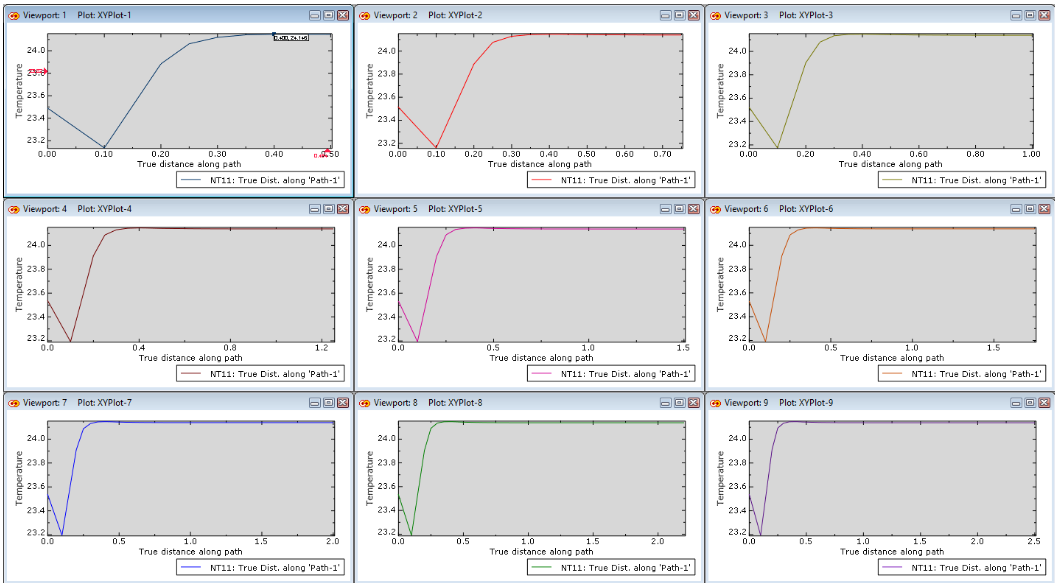

Figure 106 – Shows temperature against distance for each model size.

This shows a unanimous asymptotic surface temperature value of approx. 24.14 ℃ occurring at 0.4m along the length of the path – 0.4m away from the centre of the break.

The following Figure 107 shows heat flux plotted against the same path in each model size:

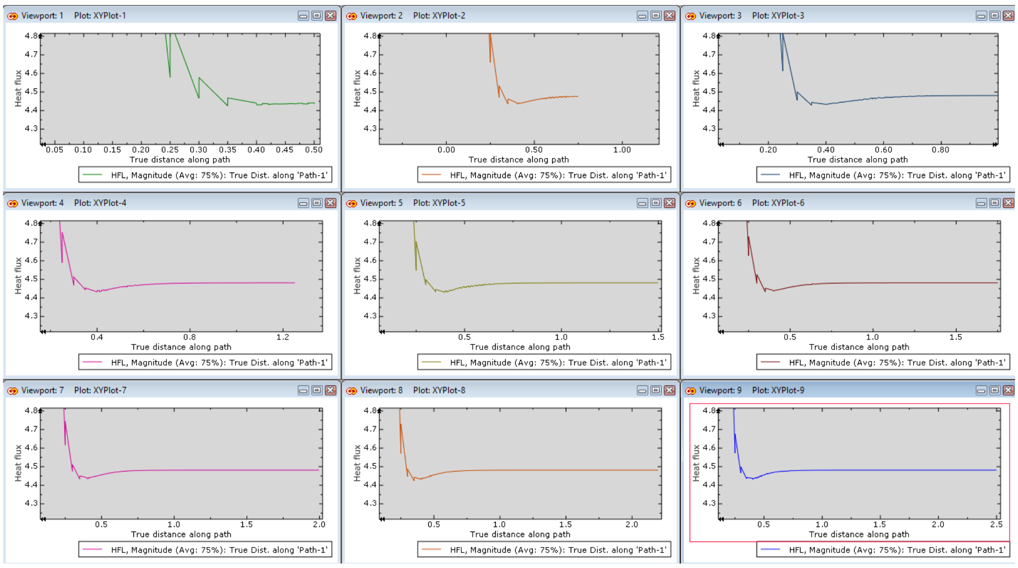

Figure 107 – Shows heat flux against distance for each model size.

The graphs were scaled to encapsulate the heat flux asymptote in each model. 4.43 – 4.48 [W/m^2] occurred between 0.4m – 0.5m along the path, like the temperature location.

As mentioned, in order to further check that flanking losses do not distort the 3D heat flow through the break connection, the ‘specimen in CV wall’ compared a 1mx1m specimen in a 5mx5m CV wall up to a 4.5mx4.5m specimen in a 5mx5m CV wall. The internal view is seen in Figure 108 showing nodal temperatures (top) and the heat flux (bottom) from the internal face setting the scale limits to 25-22[°C] and 30-0[W/m^2], respectively. Lastly the dimensions of the actual setup were considered (bottom RHS of Figure 108).

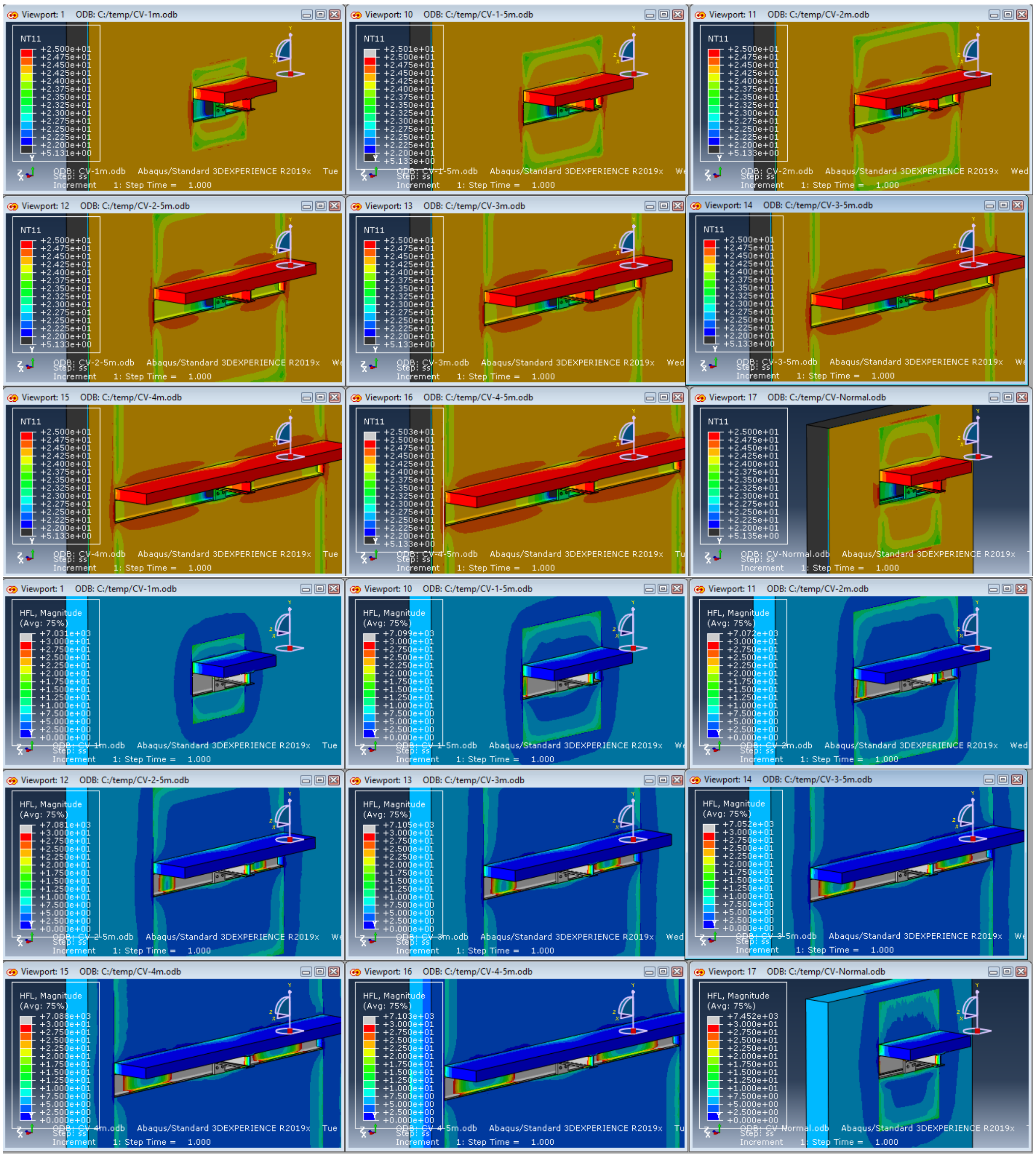

Figure 108 – Shows the internal face of the models expanding from 1-4.5[m^2] in 0.5[m] increments, inside a 5[m^2] CV wall. The top images are nodal temperature with scales set to 25-22[°C] and the bottom images are the heat flux magnitude with scales set to 30-0[W/m^2].

The ‘specimen in CV wall’ compared a 1m s in a 5m s CV up to a 4.5m s in a 5msq CV wall. The external view is seen in fFigure 109 showing the nodal temperatures (top images) and the heat flux (bottom images) from the internal face setting the scale limits to 6.21-5[°C] and 8-0[W/m^2], respectively. Lastly the dimensions of the actual setup are considered (bottom RHS of Figure 109).

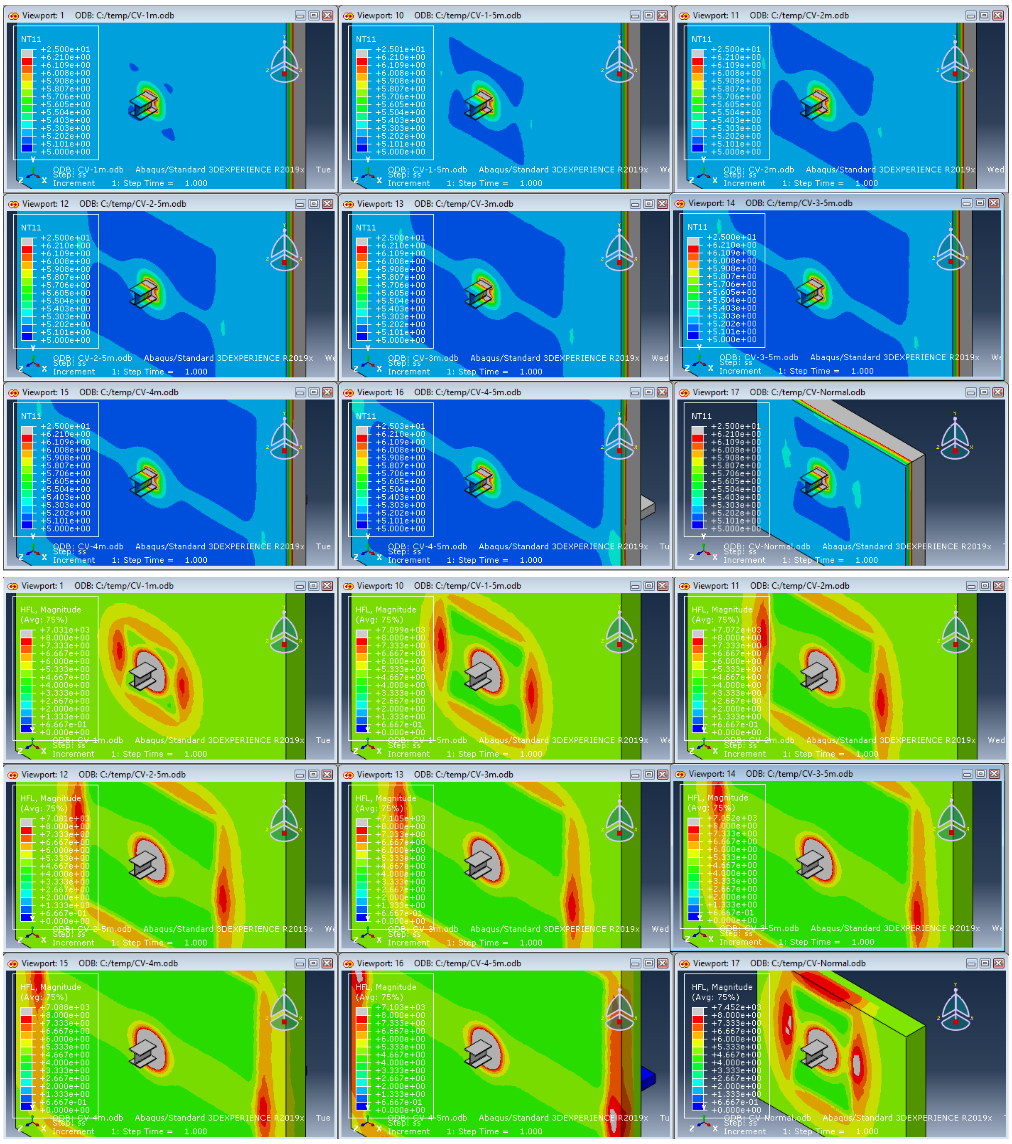

Figure 109 – Shows the internal face of the models expanding from 1-4.5[m^2] in 0.5[m] increments, inside a 5[m^2] CV wall. The top images are nodal temperature with scales set to 6.21-5[°C] and the bottom images are the heat flux magnitude with scales set to 8-0[W/m^2].

The temperature was plotted against the path plot distance in Figure 110 for each expanded model size.

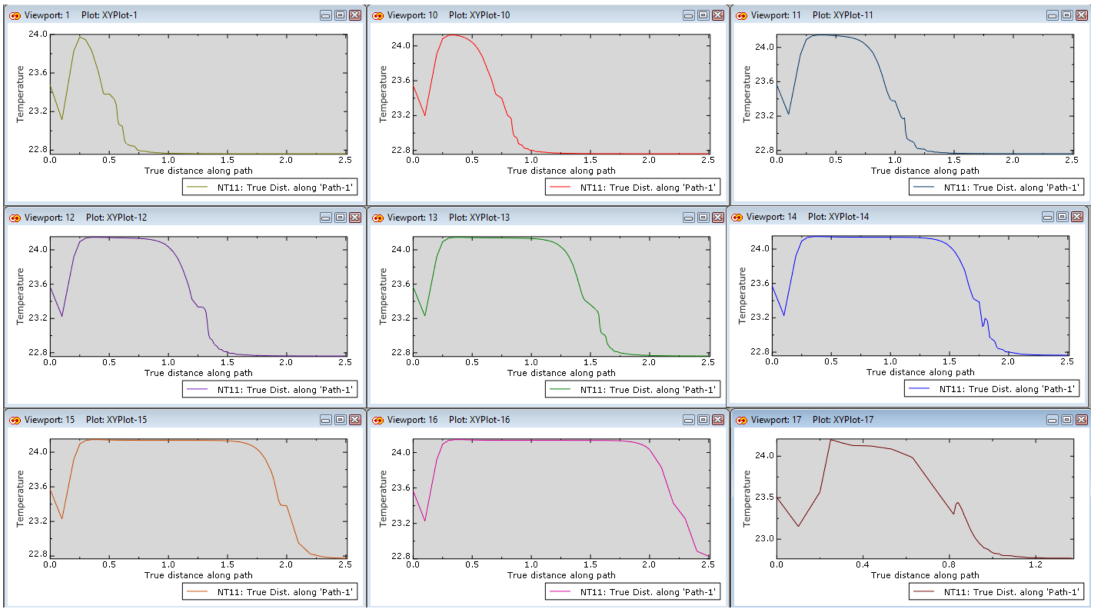

Figure 110 – Shows temperature against distance for each model size.

The asymptote value in large models converged to 24.14 [W/m^{2}K] at 0.4m. In the normal model, at 0.4m the value converged to 24.12 [W/m^{2}K] dropping to 24.102 [W/m^{2}K] at 0.5m before tailing off towards specimen edge.

This shows that not massive detriment is experienced due to flanking losses on 1D heat flow zone suggesting the TB effect is unaffected by the flanking loss.

The following shows heat flux plotted against the same path in each model size, see Figure 111:

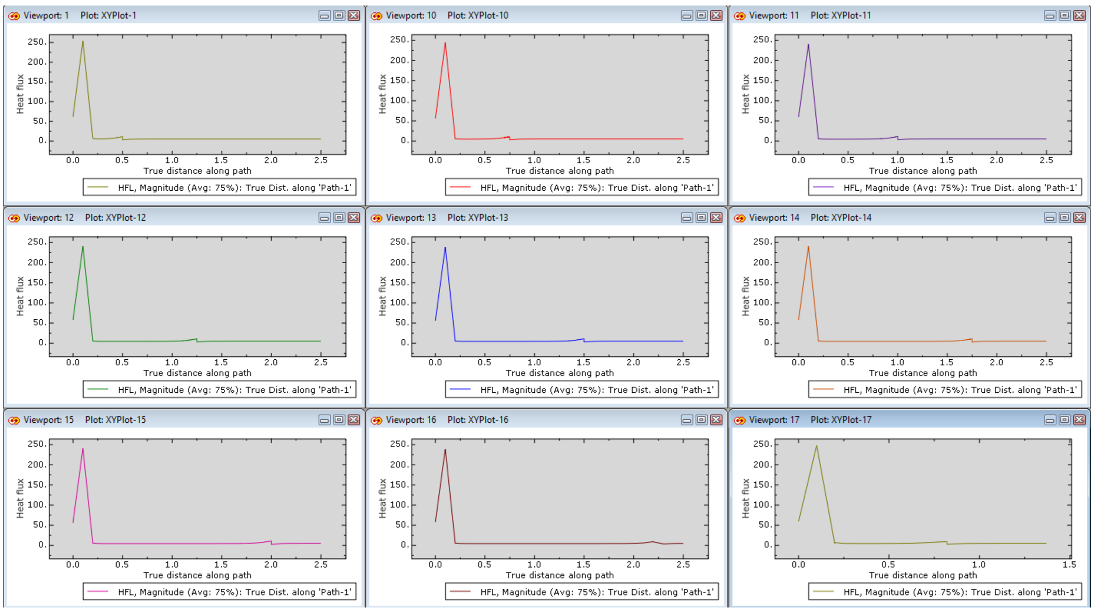

Figure 111 – Shows heat flux against distance for each model size.

This tells a similar story; asymptote relates to 0.35-0.5m. Again, showing the actual specimen size will suffice, avoiding flanking loss interference.

4.6 Construction & installation

Confident that the flanking losses would not detrimentally interfere with the flux through the STB connection, materials were purchased, and steel work design was fabricated by a third party. The planned steps are illustrated in the following Figure 112:

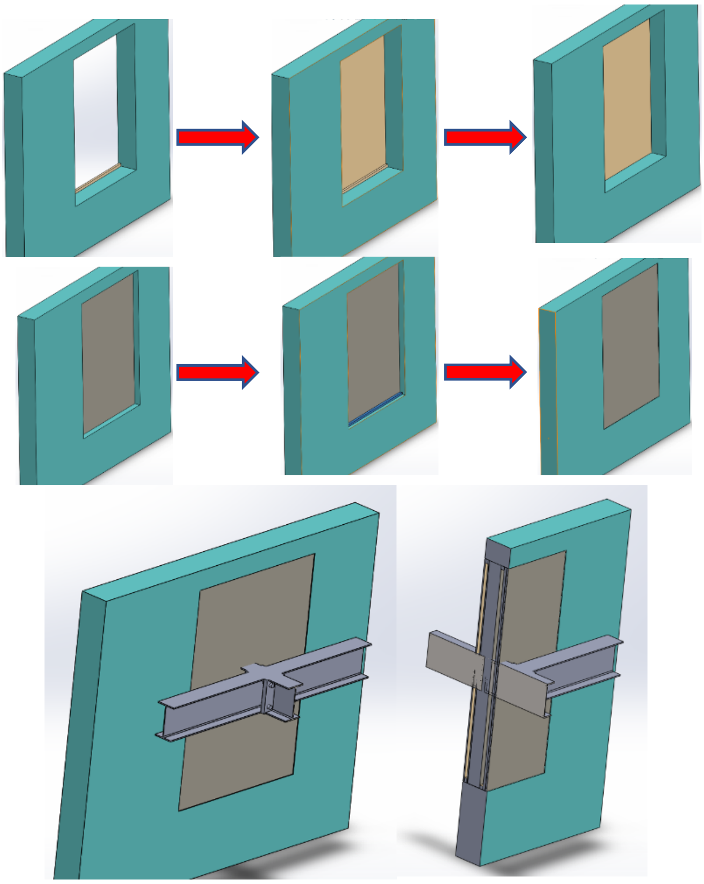

Figure 112 – Shows the planned steps.

Firstly, all materials were cut to their correct respective sizes: considering the wonkiness of the window, each panel was measured and cut individually. The OSB then the PIR were each battened in, externally and internally, respectively, using 25x50mm timber – fixed at the bottom and each side, see Figure 113**.** The timber battens were fixed to the masonry not only to hold the OSB and PIR but also provide a fixing for the external finish (plywood) and the internal finish (EPS on plasterboard).

The plywood and the EPS on plasterboard were each fixed from the external and internal faces to the timber battens, respectively – finishing each façade wall and creating their respective 50mm air gaps.

The actual steps were photographed and can be seen in the following Figure 113**,** Figure 114, & Figure 115.

4.6.1 Actual construction

Figure 113 – Shows the timber battens fixed externally to the masonry securing the OSB in position and providing an anchor to fix the external plywood.

Figure 114 – Shows the external façade. Plywood has been fixed to the timber battens.

Figure 115 – Shows the internal view of the OSB (LHS), PIR battened in internally (centre), EPS on plasterboard internal finish secured to the internal battens (RHS).

Qualitative IR and transmittance monitoring were performed in a preliminary 'BASELINE' test, see Figure 116. This validated the flanking loss prediction and verified that the constructions measured U-value is close to the analytical designed value.

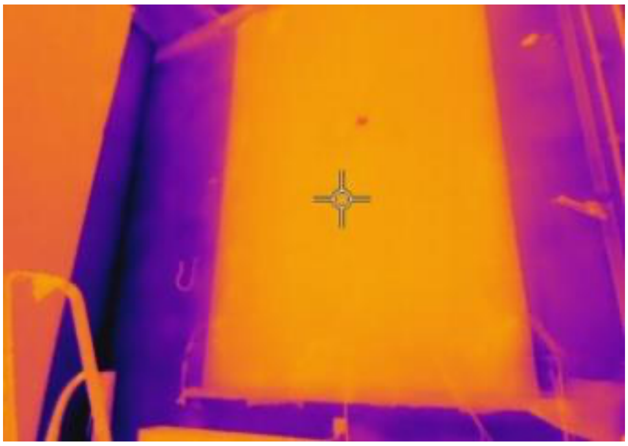

Figure 116 – Shows qualitative IR: LHS is the external view showing a colder surface temperature on the specimen indicating a higher resistance. RHS is the internal view, conversely, showing a hotter surface temperature on the specimen, again indicating a higher resistance than the surrounding CV wall. This was hypothesised since the target U-value (0.18 W/m^2K) is less than the surrounding wall.

A hole was then cut to accommodate the steelwork, see Figure 117:

Figure 117 – Shows the through hole cut into the specimen wall from internal (LHS) and external (RHS) faces.

To guarantee a modular steelwork assembly, enabling easy and safe alterations of the STBs, the stub arm (connecting the balcony arm to the edge beam) had the 4 x M20 bolts welded in position – see Figure 118:

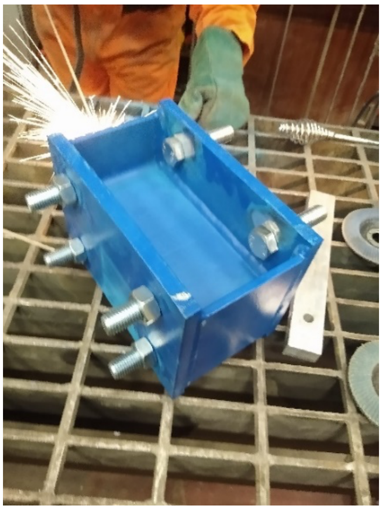

Figure 118 – Shows the bolts being welding in position on the stub arm beam section.

In doing so, when altering the break only the balcony arm needs to be removed externally.

As planned the steel was mounted on adjustable props, providing structural support, and allowing the height to be set accurately, see Figure 119:

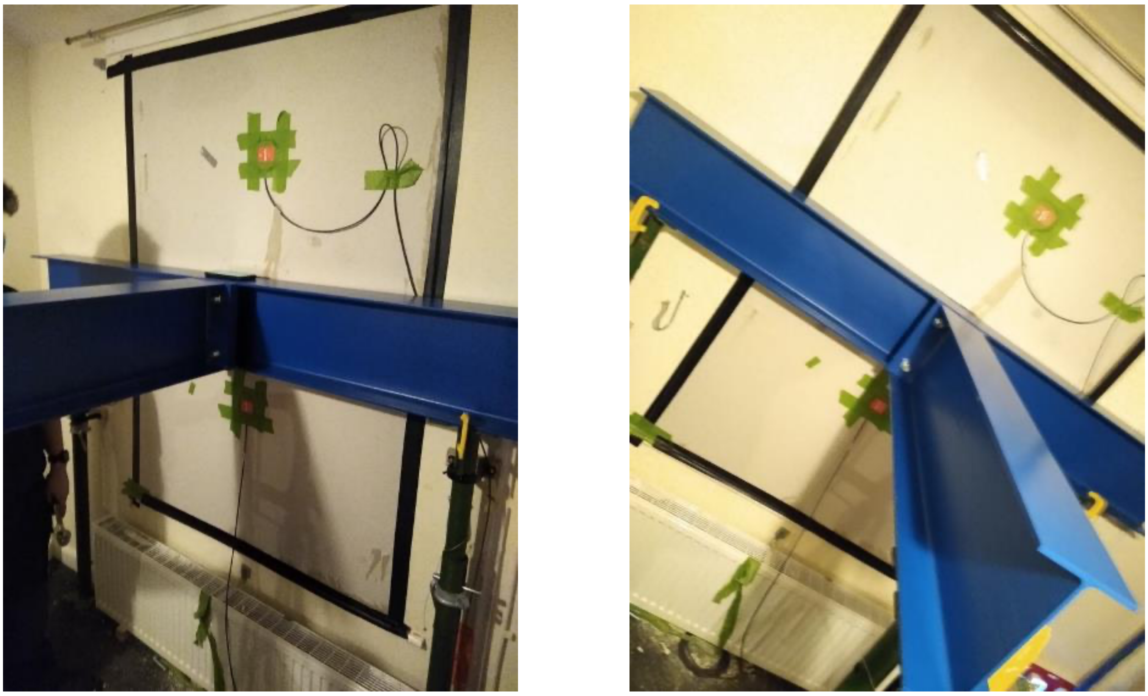

Figure 119 – Shows the internal steelwork clamped on top of props. The props were fixed to the floor and wall with screws where possible for extra protection.

4.7 Sensors, distribution

The sensor array in the initial test utilised FluxTeq sensors – later to be embedded within the steel connection to capture the flux on the intermediate faces within the air gap (i.e., 2 within the inner gap on the EPS and PIR, and two in the outer gap fixed to the OSB and Plywood). The hypothesis being that the embedded T-type thermocouple within the FluxTeq sensor along with the air temperature measurement within the gap could help understand the SR (or surface-fluid HTC) within the air gaps. This could be useful information later in the modelling.

1. **Baseline**

Air temperatures, surface temperatures, and heat flux, were monitored in 2 locations on each environmentally exposed surface. The gathered metrics were used for calculation of both the U-value and SRs measurands at these positions. The remaining channels monitored the air temperatures in each air gap and the flux on the 4 internal surfaces within the air gaps (Ply, OSB, PIR and EPS) see Figure 120.

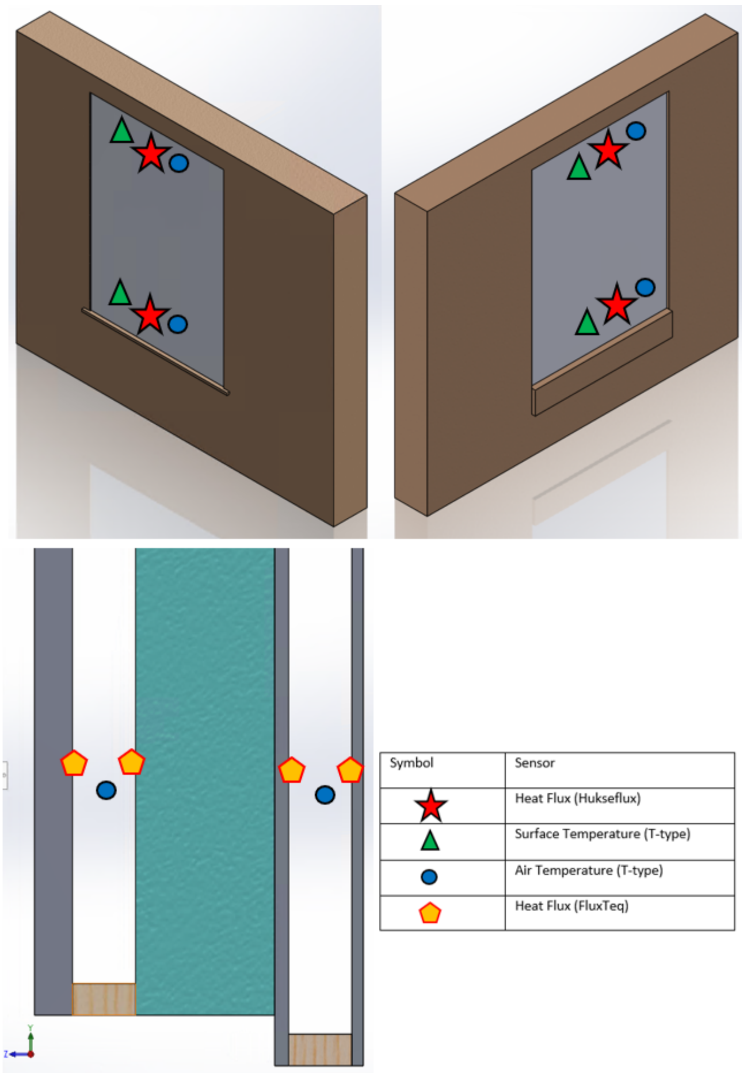

Symbol	Sensor
★	Heat Flux (Hukseflux)
▲	Surface Temperature (T-type)
●	Air Temperature (T-type)
⬟	Heat Flux (FluxTeq)

Figure 120 – Shows the internal view (top left), external view (top right), and the cross-section through the wall (below).

A ledged of symbols referring to sensors is also provided. 6 channels are used in total on each side (internal and external) to capture two air temperatures, two surface temperatures, and two heat flux (Hukseflux HFM) signals. Each air gap, internal and external, had an air temperature and two thin film flux plates (FluxTeq). The FluxTeq had temperature and flux sensing capabilities therefore 5 channels were utilised per air gap.

With the air temperature, surface temperature, and heat flux both the U-value and SR can be calculated. This was the case for each Hukseflux sensor (internal and external) and each internal FluxTeq sensor attached to surfaces within the airgaps. The internal SR calculations were deemed erroneous on account of misleading temperature readings and such small difference between surface and air temperature.

2. Steel Beam Only

Similarly, in the phases where the steel beam was installed, the sensor array captured the same air and surface temperatures local to surface HFM, twice on each environmental surface, as well as the gaps air temperatures, see Figure 121.

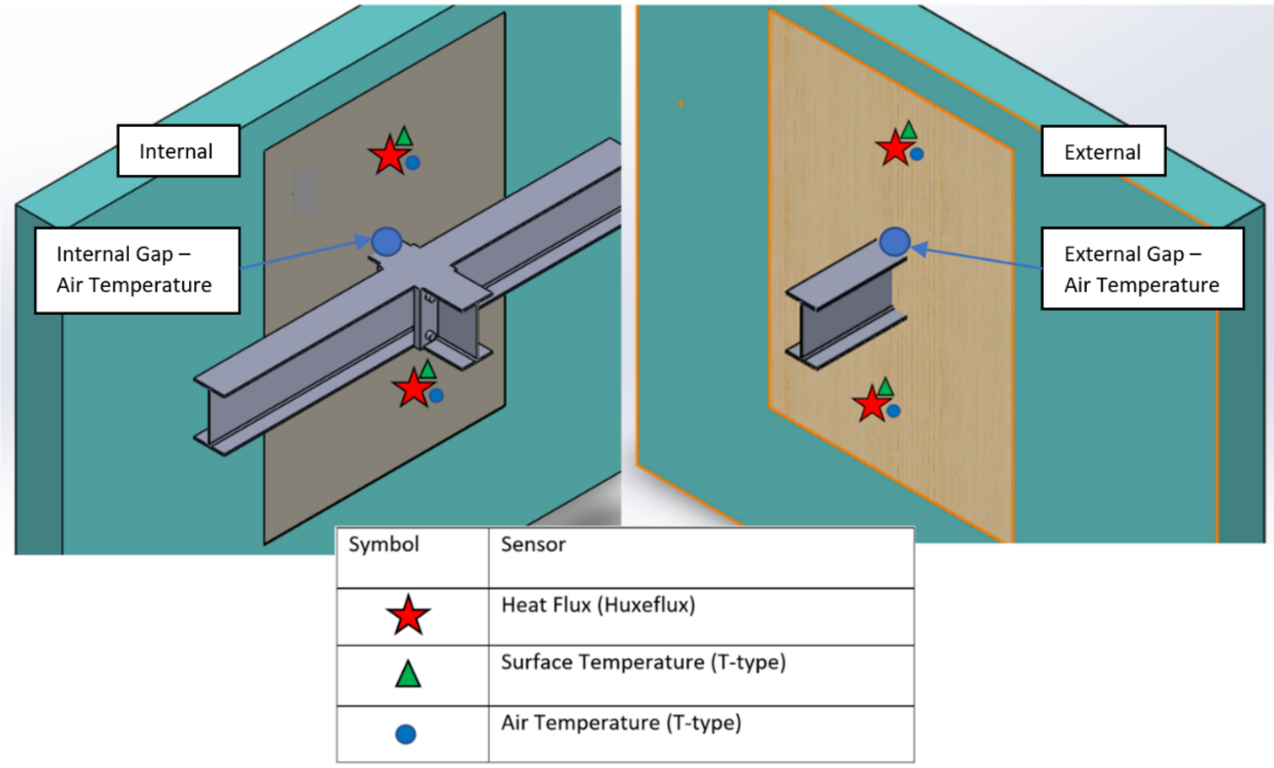

Figure 121 – Shows steel phase sensor distribution: the environmental air, and surface temperatures, also external heat flux sensor locations and internal air gap air temperature sensor locations.

The embedded flux array in the steel phases was altered attempting to capture the complex heat paths through the connection. These will monitor the flux through the connection with and without a STB.

To achieve this in the steel only phase (without any STB), the 4 FluxTeq sensors, measuring both 1D heat flux and temperature, were deployed as follows in Figure 122:

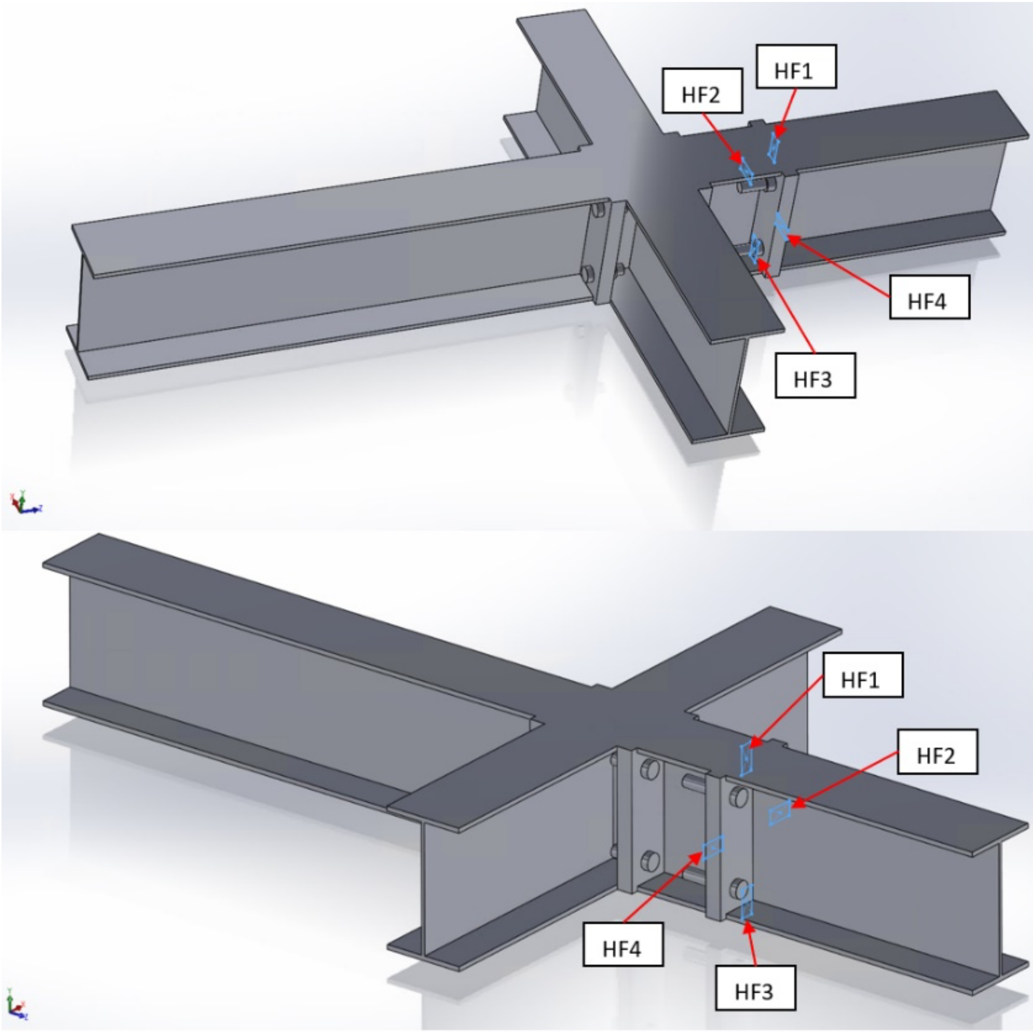

Figure 122 – Shows the embedded sensor array to capture the most extreme heat flux across the gradient in the steel-to-steel connection.

3. STB phases

In the STB phases of the experiment, the embedded array situated the thin film flux sensors either side of the STB as follows in Figure 123 & Figure 124:

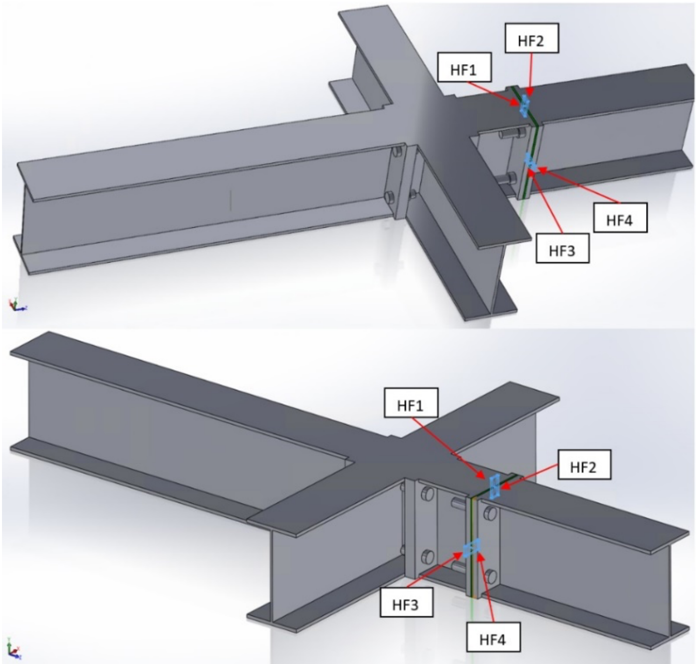

Figure 123 – Shows the embedded sensor array to capture the most extreme heat fluxes across the gradient in the connection using 5mm breaks.

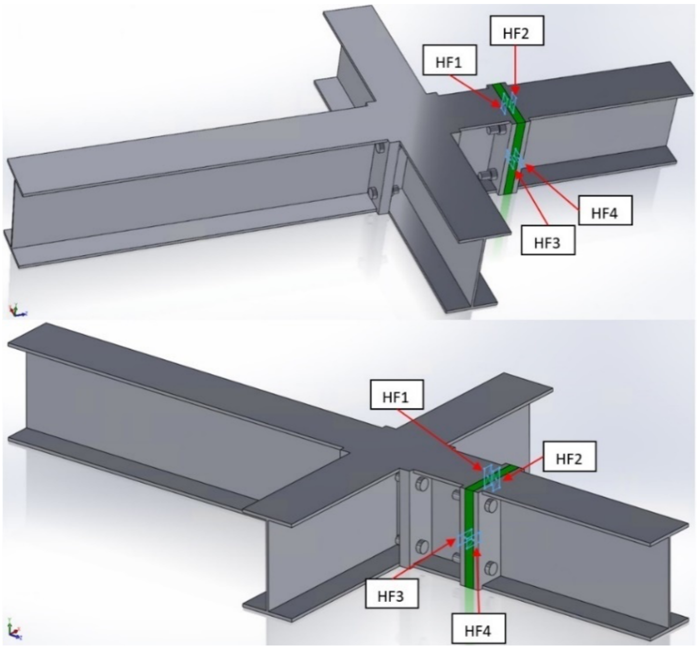

Figure 124 – Shows the embedded sensor array to capture the most extreme heat fluxes across the gradient in the connection using 25mm breaks.

In both the steel only and the STB cases, the thin film flux (FluxTeq) sensors were positioned to monitor the maxima and minima fluxes in the connection. The maximum heat flux in the STB is hypothesised to be at the top or bottom section (where the web meets the flange), whereas minima was expected to occur at the side (furthest point from web or flange), see Figure 125.

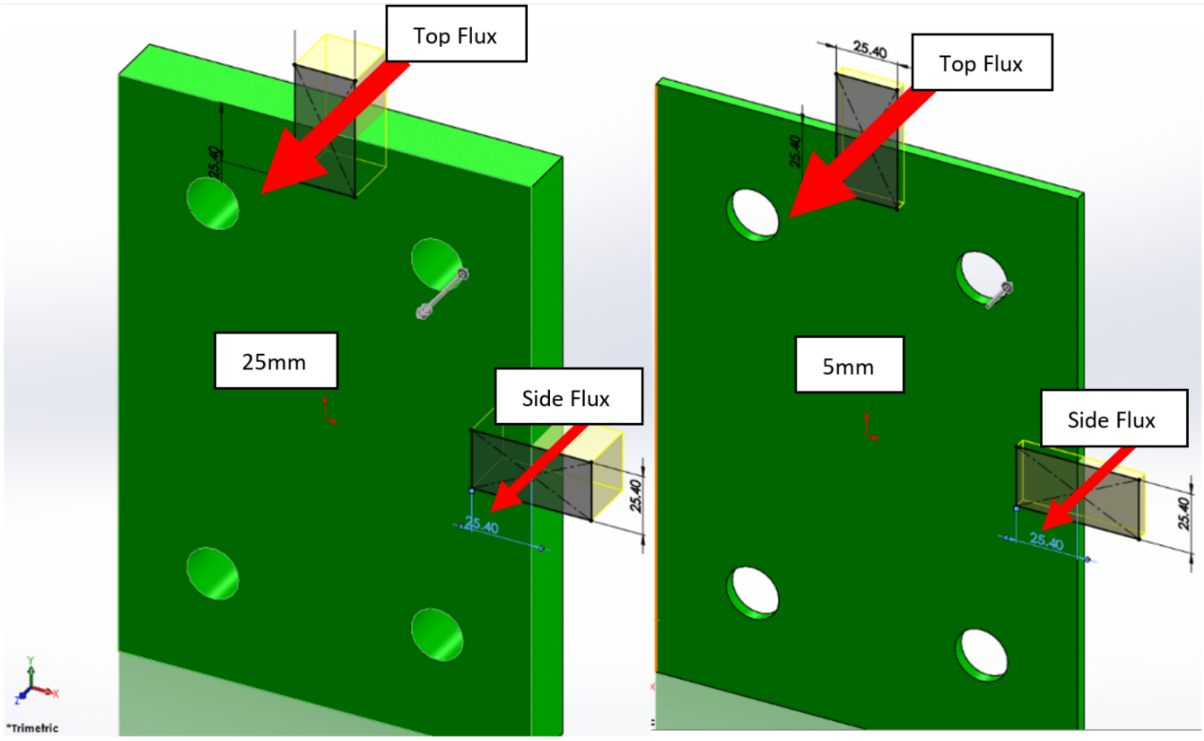

Figure 125 – Shows 25mm (left) and 5mm (right) break illustrating the top and side flux measurement locations in each case.

This is because the highly conductive steel profile (web and flange) causes the greatest connecting heat path, experienced in the centre of either the top or bottom (where the web and flange meet) of the break. Conversely, the furthest away from the web and flange, in the middle of either side, experiences the least heat flux due to less connecting heat paths.

To highlight this issue a preliminary comparison is made between no STB 'Steel Only', TBK 5mm, and TBK 25mm. All simulated under the TBK 25mm calibrated settings for comparison. The only factor to change was the break thickness. Each comparison in the following Figure 126 Figure 127 used the same scale limits over each model to illustrate the differences between no break, a 5mm TBK, and a 25mm TBK.

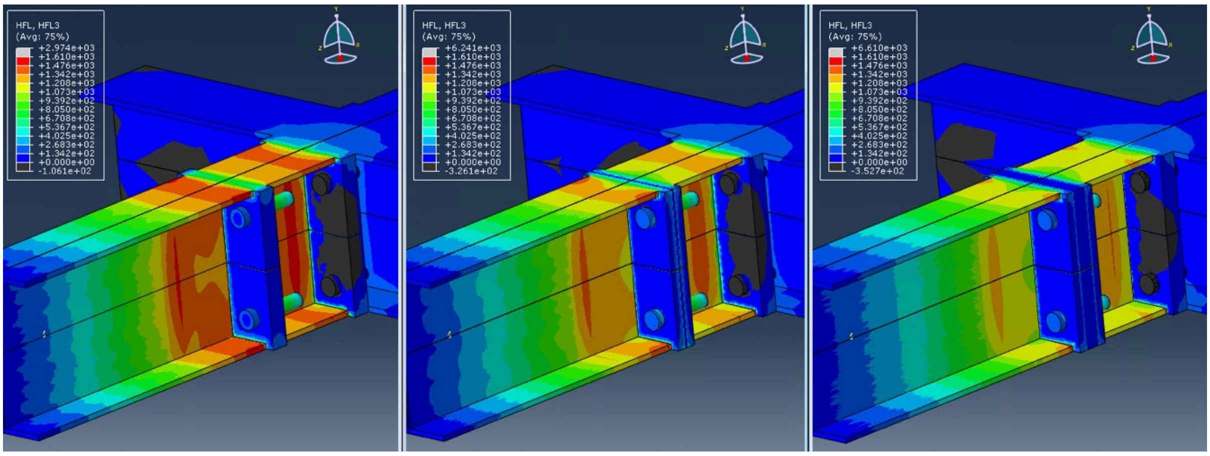

Figure 126 – Shows from left to right: SO, model, TBK5 model, and the TBK25 model under the TBK25 settings. Heat Flux z-axis 0 – 1610 [W/m^2].

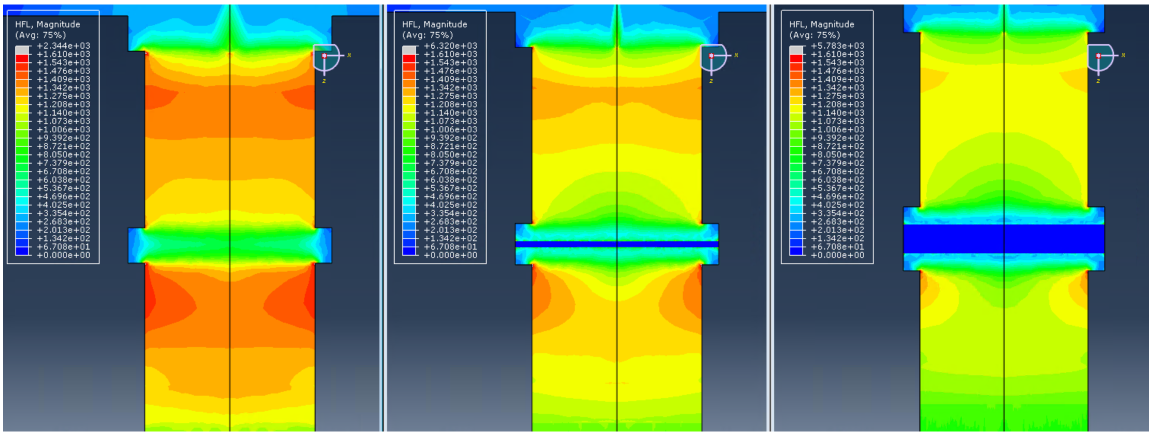

Figure 127 – Shows top view from left to right: 'SO model', TBK5 model, and the TBK25 model under the TBK25 settings. Heat Flux z-axis 0 – 1610 [W/m^2].

The followings figures show the same models but focussing the view on the break connection. The scale limits are adjusted to a tighter range, see Figure 128 & Figure 129:

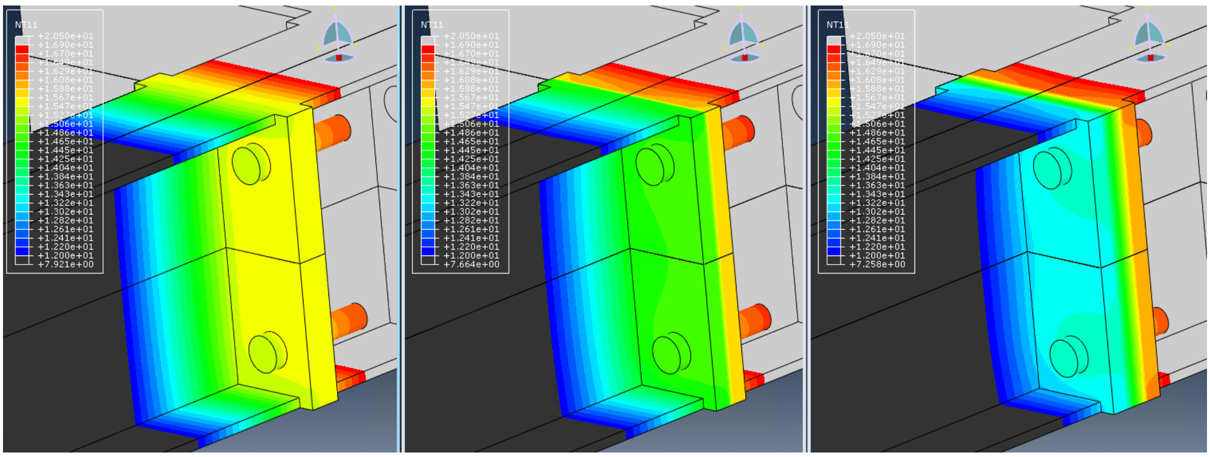

Figure 128 – Shows from left to right: ‘SO’ model, TBK5 model, and the TBK25 model under the TBK25 settings. Nodal Temperature set between 12 – 16.9 [°C].

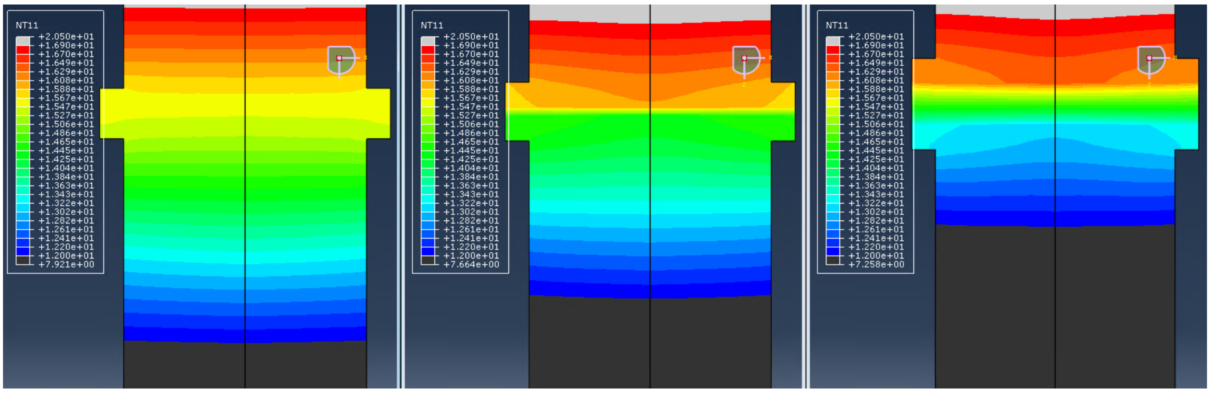

Figure 129 – Shows top view from left to right: ‘SO’ model, TBK5 model, and the TBK25 model under the TBK25 settings. Nodal Temperature set between 12 – 16.9 [°C].

To visualise the flux and temperature gradients the embedded sensors are likely to experience, the following Figure 130 shows a cross-section view of the ‘Steel Only’ model at the Steel-Steel interface – where sensors are deployed:

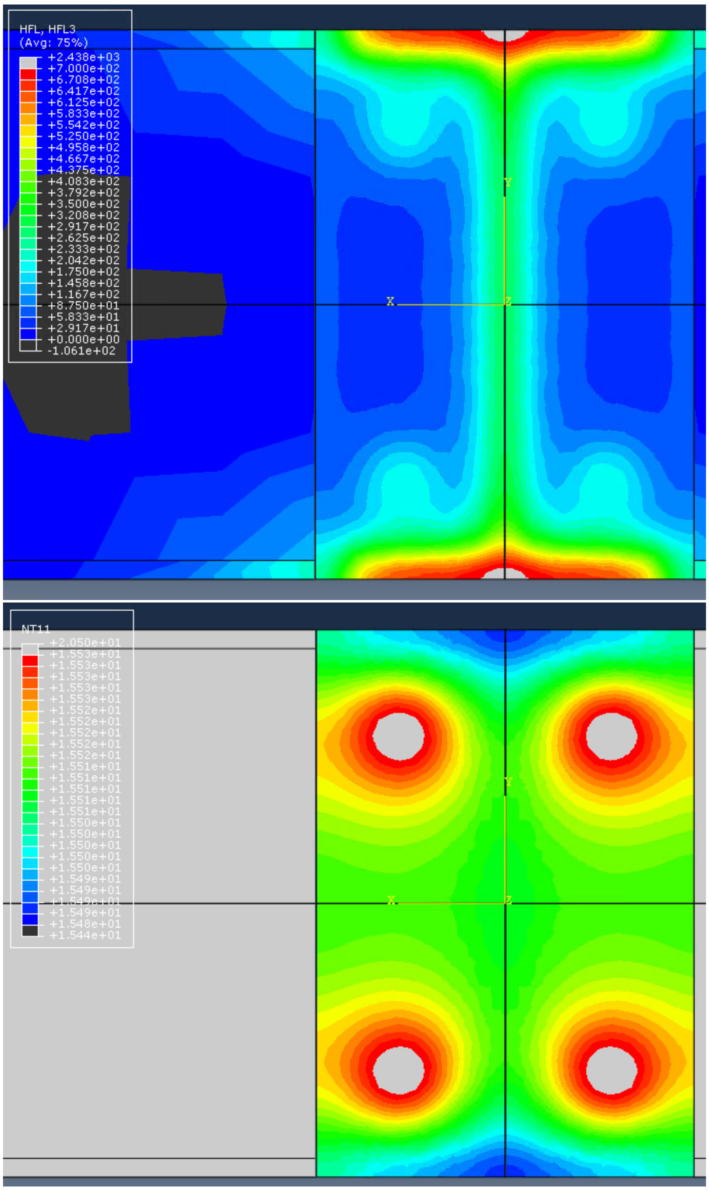

Figure 130 – Steel only, at the connection interface location – heat flux is scaled to 0 – 700 [W/m^2] (top), same view but nodal temperature set to 15.485 – 15.535 (0.05[°C] range) (bottom).

The top image illustrates just how drastic the flux gradient is within the connection. The scale for flux is set to 0 – 700 [W/m^2], the maximum magnitude surpasses the scale limits and the minimal is approximately 20 – 50 [W/m^2] occurring furthest away from the web and flange. It is obvious that the maximum measured flux across this gradient occurs at both the top and bottom locations (where the web and flange meet), conversely, the minimum occurs at the sides (away from the web and flange).

The bottom image shows nodal temperatures of the same cross-section view. The scale was set with a 0.05 [°C] temperature range. The hottest temperatures occur in the bolts, whilst the coldest locations are at the web/flange joint.

Figure 131 illustrates the flux and temperature gradients at the connection between the internal contact interface between break and the ‘stub arm section’ (LHS), and the external contact interface between the ‘balcony arm section’ and break (RHS):

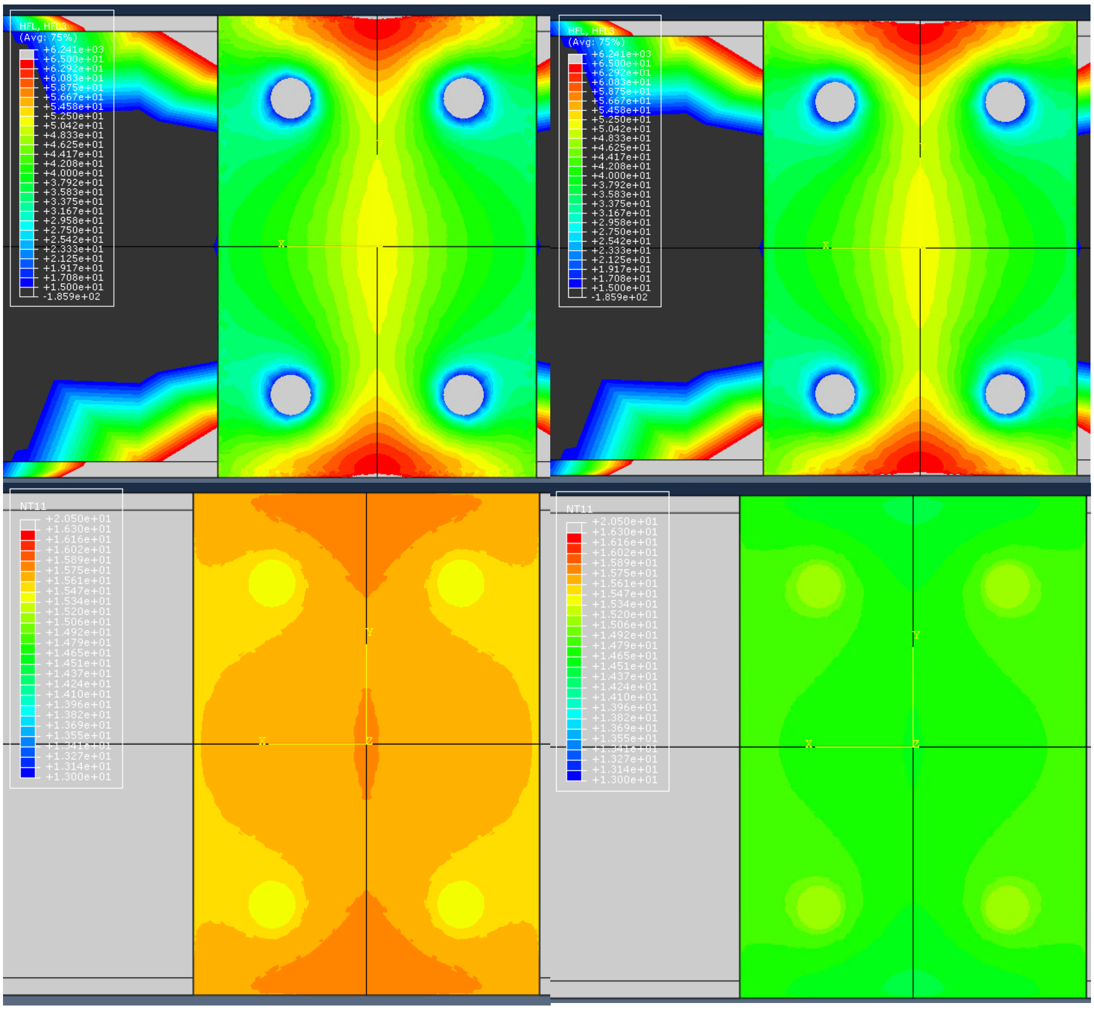

Figure 131 – Shows the TBK5 cross-section at internal (LHS) and external (RHS) contact of the STB, heat flux (top) scale set to 15 – 65 [W/m^2], nodal temperature (bottom) scale set to 13 – 16.3 [°C].

The same ranges were set for the variables, 15 – 65 for HF and 13 – 16.3 [°C] for temperature, in the following comparison featuring a 25mm break. The connection between the internal contact interface between break and the ‘stub arm section’ (LHS), and the external contact interface between the ‘balcony arm section’ and break (RHS), see Figure 132:

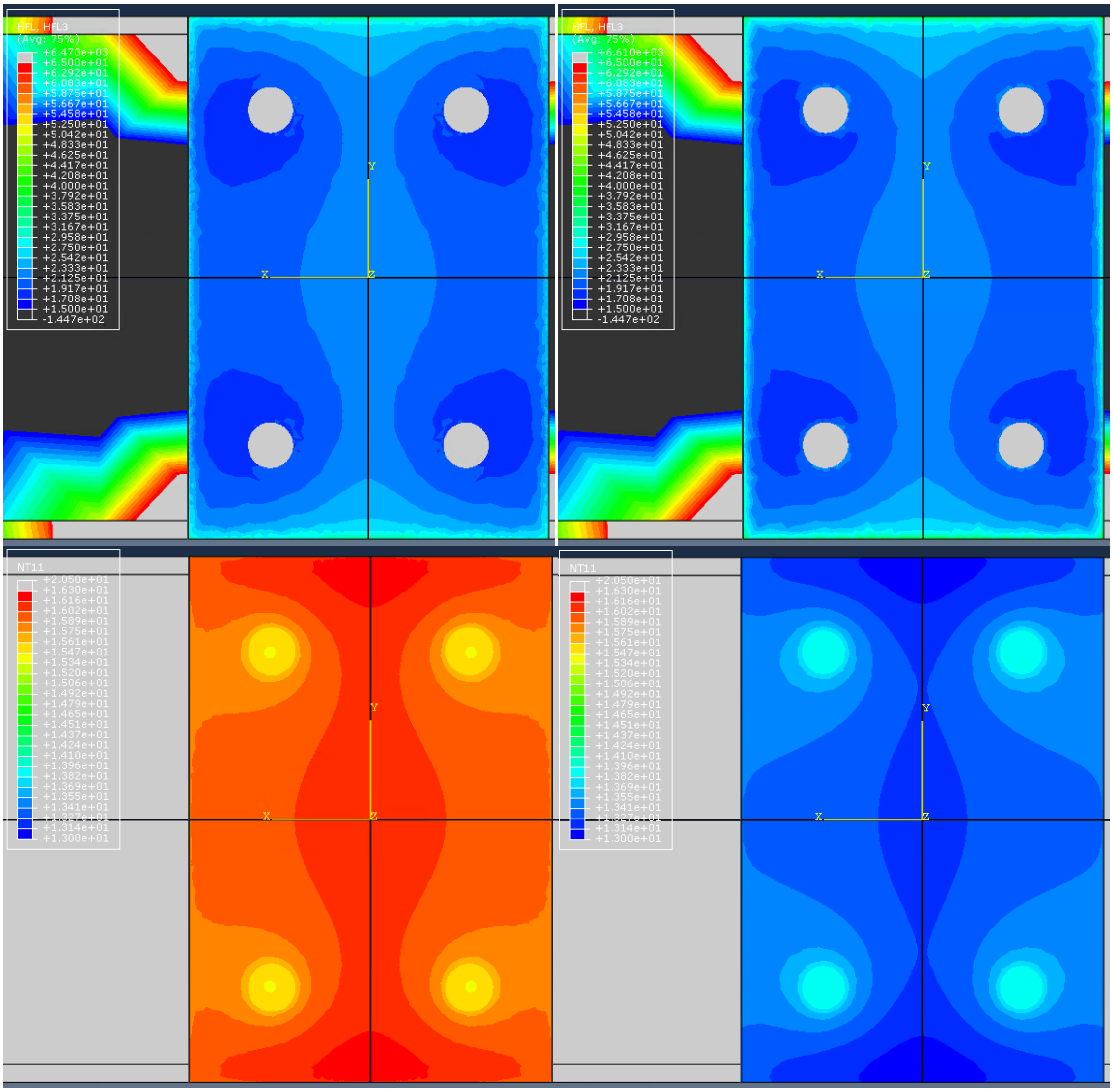

Figure 132 – Shows the TBK 25 cross-section at internal (LHS) and external (RHS) contact of the STB, HFL3 (top) setting range 15 – 65 [W/m^2], Nodal Temperature (Bottom) setting range 13 – 16.3 [°C].

Comparing the top images in both figures above, no huge difference can be seen between the internal and external locations in terms of flux. However, they both show that the highest measured flux location is experienced at the top and bottom of the break (where the web and flange meet) and the lowest measured flux location is experienced at the side (furthest away from the web and flange). Comparing the heat flux screenshots of the 5mm and 25mm variants, it is easily noticed that the TBK25mm experiences considerably less flux compared with the TBK5mm.

Similarly, the difference between the external and internal temperature gradients are obvious. The internal is hotter than the external in both cases: roughly 1.55 [°C] and 3.3 [°C] difference between internal and external, for the 5mm and 25mm variants, respectively. Compared the 5 mm variant with the 25mm variant, the hot side is hotter, and the cold side is colder in the thicker break connection. This shows the thicker break is restricting the isotherms more effectively and better resists heat flow.

The following Figure 133, Figure *134*, Figure *135*, & Figure *136* show the cross-section through the centre of the connection (i.e., at the steel-steel interface, 2.5mm in from edge of 5mm break, and 12.5mm in from edge of 25mm break), splitting the break in the connection.

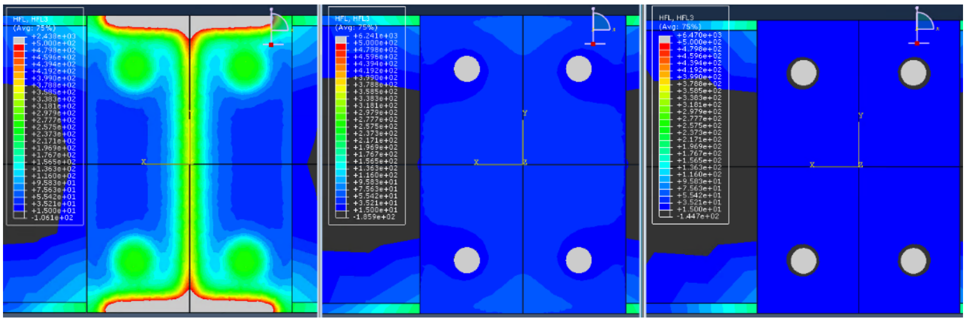

Figure 133 – Scale set to 15 – 500 [W/m^2] HF, left to right SO, TBK5, TBK25.

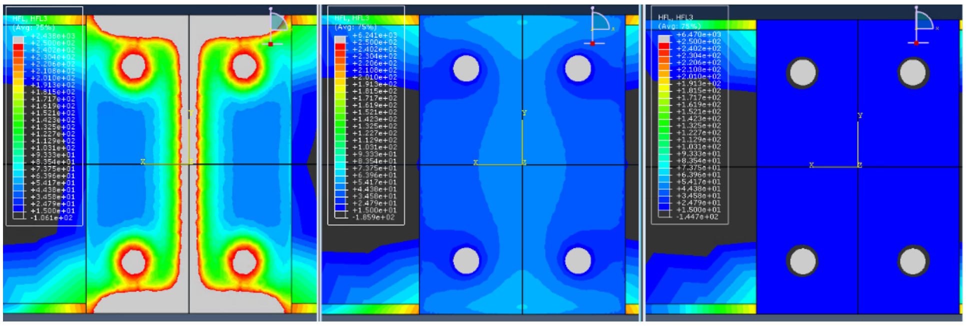

Figure 134 – Scale set to 15 – 250 [W/m^2] HF, left to right SO, TBK5, TBK25.

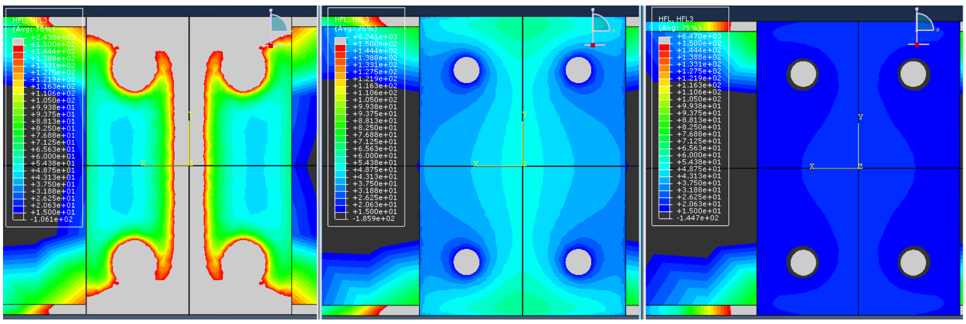

Figure 135 – Scale set to 15 – 150 [W/m^2] HF, left to right SO, TBK5, TBK25.

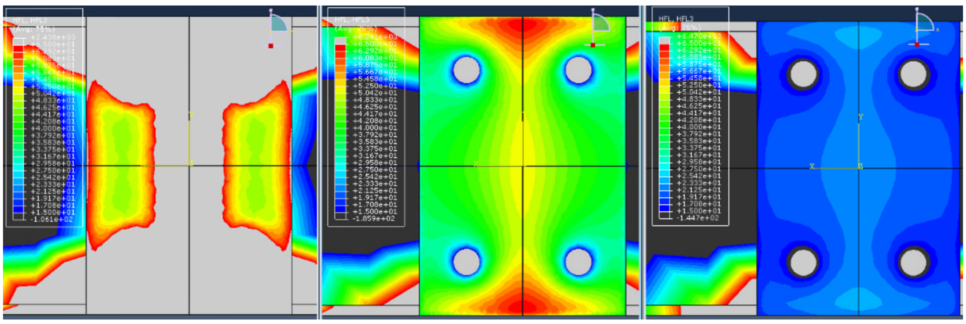

Figure 136 – Scale set to 15 – 65 [W/m^2] HF, left to right SO, TBK5, TBK25.

In the steel only connection the highest flux is seen at the top of the connection where the web meets the flange. This is also a similar trend in the STB connections, but the greatest flux is seen in the bolts themselves due to the change in material.

This is illustrated further in the following Figure 137 to Figure 140 showing the temperature gradients and Figure 141 to Figure 144 show heat flux through the steel and break connection:

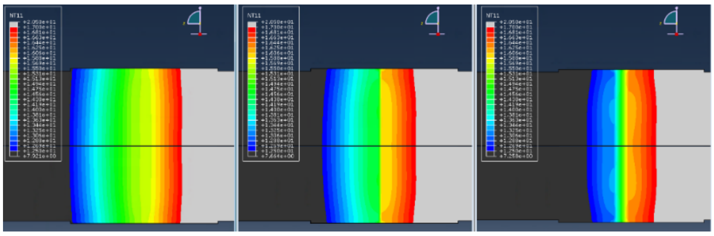

Figure 137 – Shows from left to right SO, TBK5, TBK25 nodal temperature range 12.5 – 17 [°C] – Left hand view.

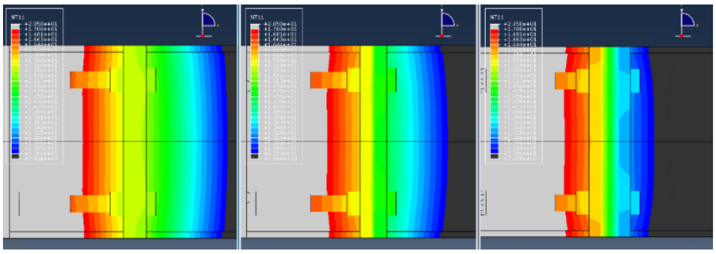

Figure 138 – Shows from left to right SO, TBK5, TBK25 nodal temperature range 12.5 – 17 [°C] – Right hand view.

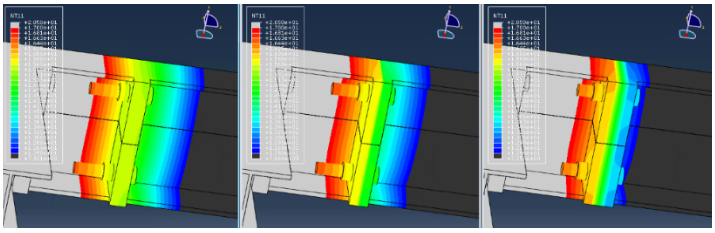

Figure 139 – Shows from left to right SO, TBK5, TBK25 nodal temperature range 12.5 – 17 [°C] – Isometric view.

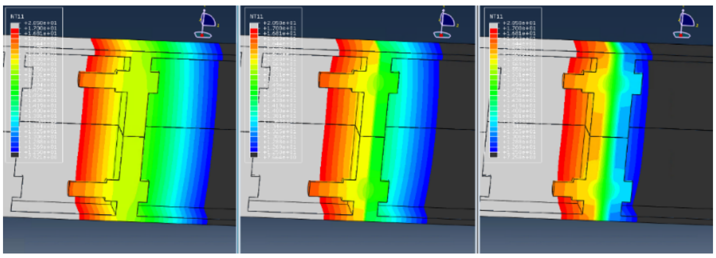

Figure 140 – Shows from left to right SO, TBK5, TBK25 nodal temperature range 12.5 – 17 [°C] – Cross-section through the bolts.

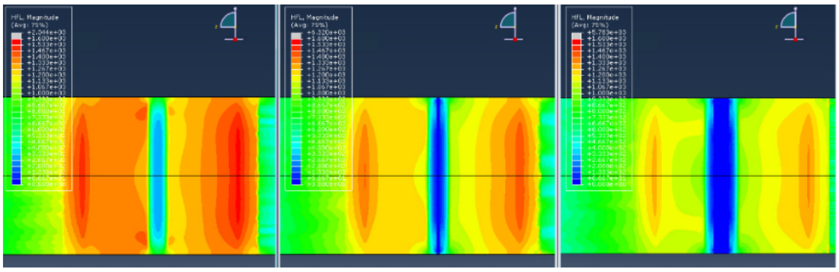

Figure 141 – Shows from left to right SO, TBK5, TBK25 heat flux range 0 – 1600 [W/m^2] – Left hand view.

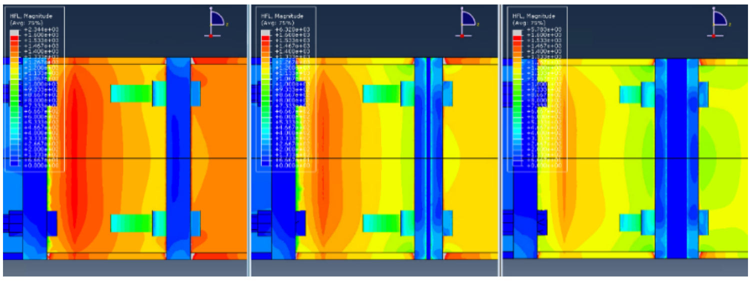

Figure 142 – Shows from left to right SO, TBK5, TBK25 heat flux range 0 – 1600 [W/m^2] – Right hand view.

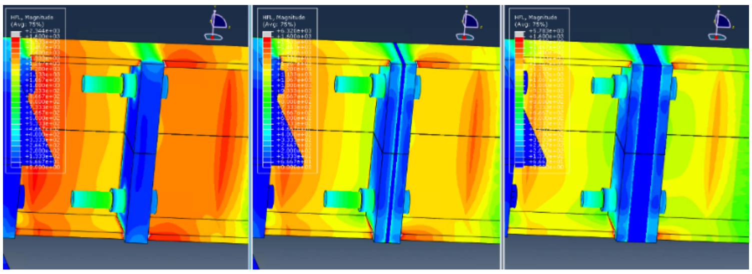

Figure 143 – Shows from left to right SO, TBK5, TBK25 heat flux range 0 – 1600 [W/m^2]– Iso-view.

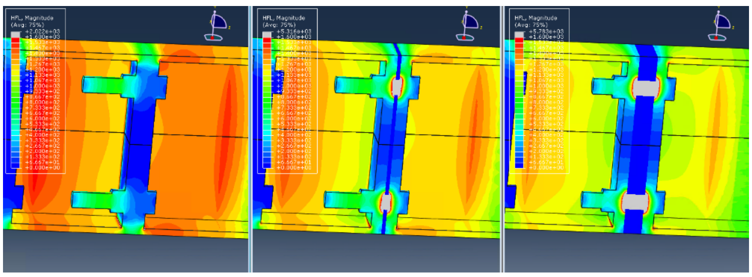

Figure 144 – Shows from left to right SO, TBK5, TBK25 heat flux range 0 – 1600 [W/m^2] – Cross-section through the bolts.

4.8 Measurements

The measurements were used to process the U-value and the SR values. BS EN ISO 9869 averaging method was followed to calculate the transmittance and BS EN ISO 6946 aided calculation of surface-fluid HTC. The former is deduced from the sum of recorded fluxes divided by the sum of the recorded temperature difference (air-to-air), whilst the latter is deduced using the dT between the surface and air temperatures local to the HFM.

4.8.1 Calculations

The chosen data samples to analyse are justified by visualising the external temperatures and fluxes over time. Once steady periods with sufficient prior conditioning were windowed. All single measurements are averaged and used to calculate their respective measurands.

The heat flux is calculated by converting the [mV] signals from the heat flux plates or thin film sensors, recorded by the data logger, to flux readings [W/m^2]. This is done by applying the conversion coefficient, using equation 64. With units of ([µV]/[W/m^2]), the mV signal reading is simply divided by the coefficient scaled to ([mV]/[W/m^2]). This estimates the flux at points of interest and can be further processed into surface-fluid HTC (SR's) or U-values.

$$\mathrm{Flux}\left[\frac{\mathrm{W}}{\mathrm{m}^2}\right] = \frac{\text{sensor signal [mV]}}{\text{coversion coeff}\left[\frac{\mu\mathrm{V}}{\left[\frac{\mathrm{W}}{\mathrm{m}^2}\right]}\right]} * 1000 \tag{64}$$

For SR or U-values, temperature differences between surface-fluid and air-to-air are required, respectively. Therefore, single temperature measurements, taken using T-type thermocouples for both air and surface, are processed respectively using equation 65 & 66.

$$\mathrm{dT_{s-f}} = \mathrm{T_s} - \mathrm{T_a} \tag{65}$$

Where '$\mathrm{dT_{s-f}}$' is the temperature difference between fluid-and-surface, '$\mathrm{T_s}$' is the surface temperature, and '$\mathrm{T_a}$' is the air temperature.

$$\mathrm{dT_{a-a}} = \mathrm{T_1} - \mathrm{T_2} \tag{66}$$

Where '$\mathrm{dT_{a-a}}$' is the air-to-air temperature difference, '$\mathrm{T_1}$' is the air temperature of environment 1, and '$\mathrm{T_2}$' is the air temperature of environment 2.

The U-values and SR can then be calculated using equation 67 & 68, respectively:

$$U = \frac{\text{Flux}}{dT_{a-a}} \qquad (67)$$

Where ‘U’ is the transmittance [W/m^{2}K] (U-value) calculated by dividing the flux with the air-to-air temperature difference.

$$SR = \frac{dT_{s-f}}{\text{Flux}} \qquad (68)$$

Where ‘SR’ is [m^{2}K/W] (reciprocal of surface-to-fluid HTC) calculated by dividing the surface-to-fluid temperature difference by the flux.

4.8.2 Uncertainty

Each voltage signal (mV) is subject to the same datalogger uncertainty of +/-0.15%. Precision error is deduced and combined with the logger uncertainties (single measurement of temperature or heat flux include their respective instrument accuracy errors) in quadrature as per the GUM method.

The Type A precision uncertainty was deduced for each signal measurement using the s.d. (standard deviation) and the N (count), see equation 69:

$$uA = \frac{sd}{\sqrt{N}} \qquad (69)$$

Where ‘uA’ is Type A uncertainty, ‘sd’ is the standard deviation over the sample and ‘N’ is the size of the sample.

The logger uncertainty and associated instrument error – for example, T-type thermocouples +/-1℃ – are applied within the Type B bias uncertainty, considered using equation 70.

$$uB = \sqrt{e^1 + e^2 + \cdots + e^n} \qquad (70)$$

Then, the combined standard uncertainty ‘uC’ can be deduced by joining the Types A & B in quadrature (see equation 71) – following the GUM method (JCGM, 2008).

$$uC = \sqrt{uA^2 + uB^2} \qquad (71)$$

The calibration coefficient ‘S’– converting the mV signals into Flux – is found in the manufacturer specification. In this experiment both FluxTeq and Hukseflux HFM were used, each have differing associated instrument errors.

The calibration coefficients – used to convert the voltages into fluxes – apply the instruments errors, calibration uncertainty, and operating temperature condition uncertainty contributors to their single measurement before propagation in the measurand calculation. Care must be taken not to consider the same uncertainty twice within the propagation of errors (JCGM, 2008).

FluxTeq have +/- 0.03[μV], 5% calibration, and a linear scaling equation for the coefficient depending on temperature. Whereas Hukseflux have a +/- x [μV] independent to each sensor. It also states that +/- 3% (k=1) should be added to the uncertainty budget, the manufacture specification explains why and was discussed in the equipment section previously.

Illustrating the uncertainty analysis and using the FluxTeq as an example (see equation 72), the bias uncertainties are summed in quadrature to attain combined standard uncertainty for the calibration coefficient ‘S’ first. Whilst the ‘mV’ reading has the datalogger uncertainty applied. This generates ‘$\mathrm{u(S)}$’ and ‘$\mathrm{u(mV)}$’, respectively. The average flux then becomes a calculated measurand and as such needs to be properly propagated using the errors in the single measurements to understand its associated uncertainty. Since Flux=mV/(mV/Flux) the sensitivities first need to be found and multiplied by the corresponding uncertainty before being summed in quadrature to combine the uncertainties of the measurand.

$$\mathrm{F} = \frac{\mathrm{mV}}{\mathrm{S}} \tag{72}$$

Consider F as a function of the mV and S.

Sensitivities are the partial derivatives of this relationship (JCGM, 2008), seen in the following equations 73 & 74:

$$\frac{\partial \mathrm{F}}{\partial \mathrm{mV}} = \frac{1}{\mathrm{S}} \tag{73}$$

$$\frac{\partial \mathrm{F}}{\partial \mathrm{S}} = \frac{-\mathrm{mV}}{\mathrm{S}^2} \tag{74}$$

Understanding the combined standard uncertainty in S and the mV, the propagation of errors method follows equation 75:

$$\mathrm{u(F)} = \sqrt{\left(\frac{\partial \mathrm{F}}{\partial \mathrm{mV}} * \mathrm{u(mV)}\right)^2 + \left(\frac{\partial \mathrm{F}}{\partial \mathrm{S}} * \mathrm{u(S)}\right)^2} \tag{75}$$

The same approach used in this example is applied in the SR and U-value calculations. However, small dT's in the SR-value calculations cause large sensitivities which lead to a large uncertainty.

4.9 Scenarios

Testing commenced by producing a baseline data set of the proposed wall to eventually be bridged with steel (representing cantilever balcony support) with which STB variants can be tested – measurements are supplemented into thermal simulation determining TB transmittance metrics.

Initial baseline measurements of the un-bridged wall will be taken followed by sequential alterations: bridged wall (Steel Beam with no break), breaking the bridge with Farrat STBs: TBL/TBK/TBF materials at thicknesses of 5mm & 25mm.

4.10 Conditions

Ideally, dynamic conditions were sought after since this is what affects real details in-situ. However, since the DEEP Retrofit project was running in the same facility, the experimental conditions mirrored them used in DEEP. This was almost always steady-state, although some charging and discharging dynamics could be extrapolated.

Therefore, once again, the experimental conditions will exploit the EH steady-state capabilities, holding the environmental temperatures within sensible limits typically experienced in Northern European climates (20°C internally, 5°C externally) maintaining at least a dT>10°C and ensuring 12hrs of prior conditioning to eliminate any thermal inertia influence.

5.0 Measurement results

Some anomalies were seen due to the test-rig proximity to the HVAC outlet – differences between embedded fluxes were seen when comparing the HVAC and Chiller results. This was thought to be due to forced convection of conditioned air filtrating behind the web and flange of the steel from the external wall, shown later in Figure 148 & Figure 149. This was only discovered when the first break was being tested – after the Steel Only set-up, hence re-capturing data from the initial unbroken phase was required.

Other causes for re-capturing data included: loosing data due to datalogger errors and, since the FluxTeq sensors are very flimsy and broke easily, cutting recesses into the breaks to accommodate the FluxTeq sensors (see Figure 145) was thought necessary. Adequate silicone heat sink gel was applied encouraging a perfect thermal contact between sensor and surface.

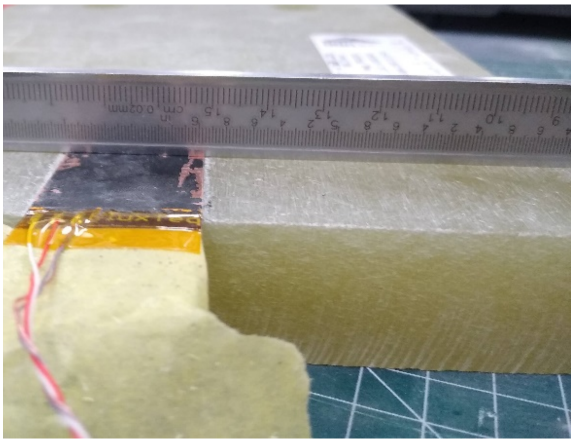

Figure 145 – FluxTeq sitting flush in recess cut into STB pad.

Because of other experiments, the "DEEP retrofit" project, frequent construction work needs to be done to the EH test facility. Therefore, some occasions in the data acquisition will show inactive chamber conditioning. The following graph in Figure 146 shows the external air temperatures through the total acquisition period of the TBK 25mm variant as an example:

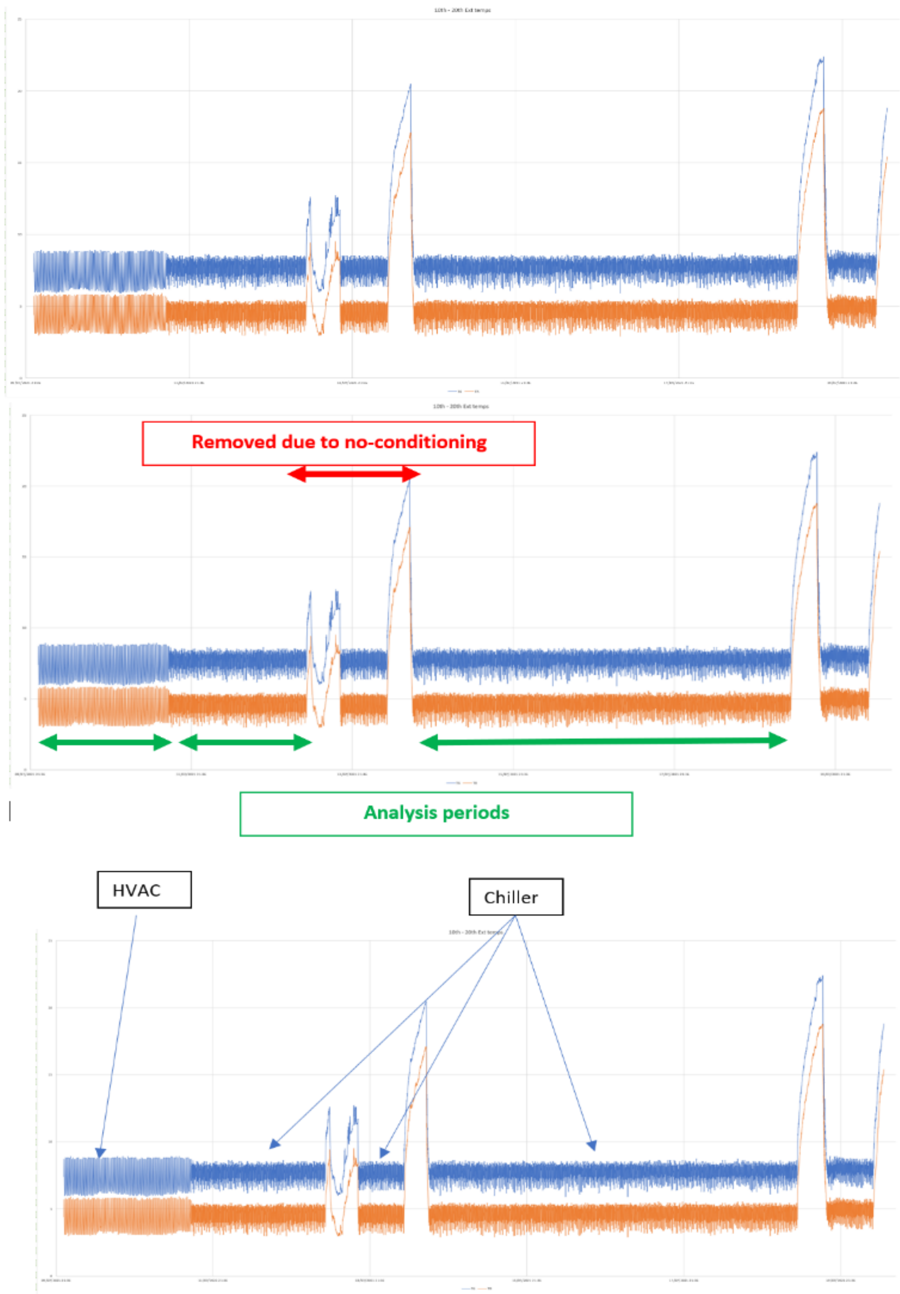

Figure 146 – External air temperatures captured during the TBK 25mm phase, illustrating the windowed steady-state analysis periods.

The spikes in these external temperatures are the occasions where the chamber conditioning was turned off. The analysis periods are shown where other dynamic data (charging and discharging) was removed to isolate steady conditions. The same was applied to all captured data, the following Figure 147 shows the TBF 25mm data (external temperature/time) as an example:

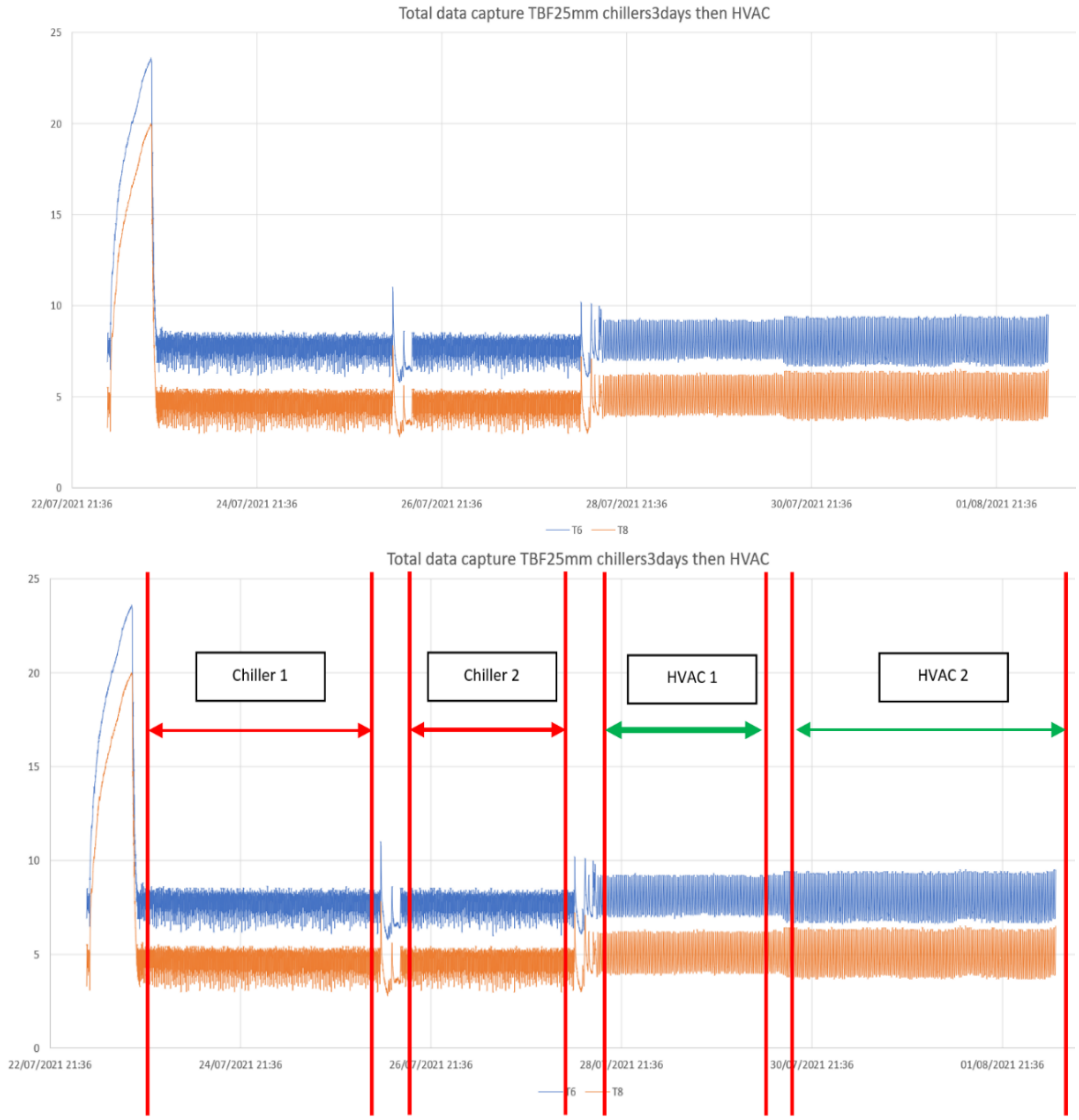

Figure 147 – Windowed data TBF25mm external temperatures / time.

Interest arose due to the unpredictable alterations of fluxes embedded in the break. Figure 148 shows the external temperatures at the bottom (in grey) and the 4 embedded fluxes – both averaged and noisy.

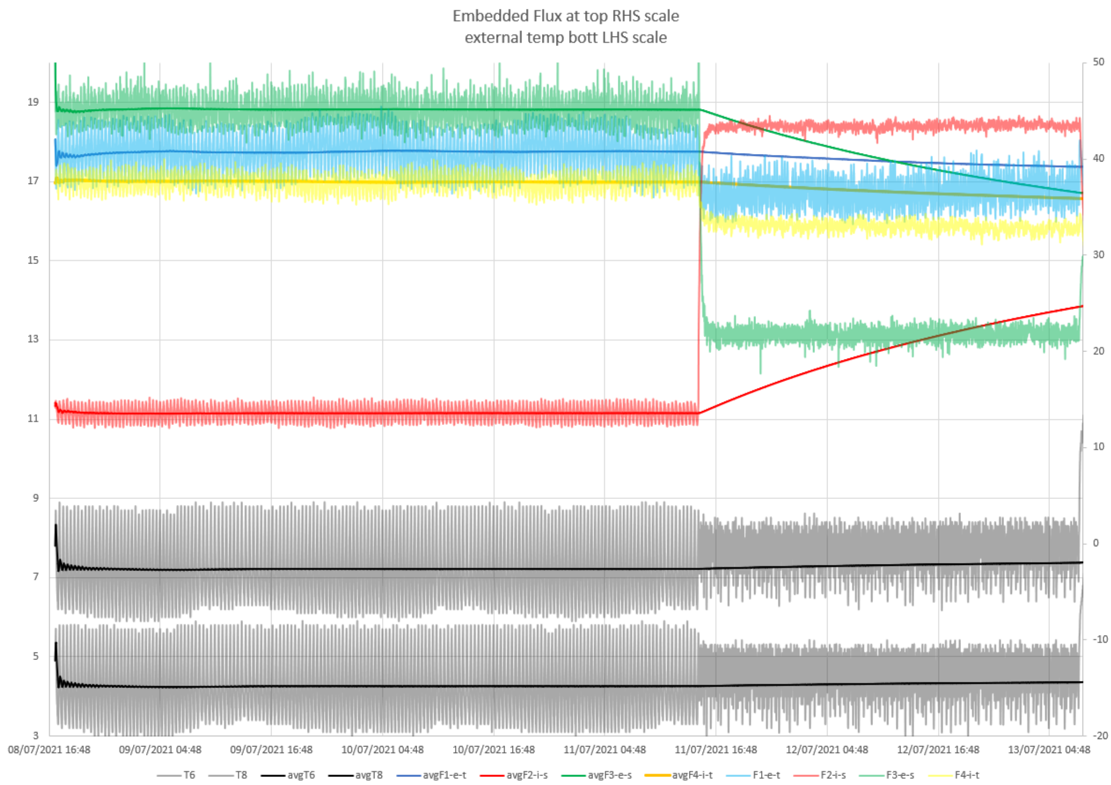

Figure 148 – LHS scale is the embedded Heat Flux [W/m^2] (4 colours represent the 4 sensors), RHS scale [°C] is the external air temperature (grey), depicting alteration in heat flux magnitude dependent upon the conditioning tool used – HVAC or Chiller.

It was noticed that the embedded heat flux depends on the conditioning tool used. Figure 148 illustrates a change from HVAC to Chiller, notice the difference in the grey signals noise (external air temperature), at which point the embedded fluxes change.

The top fluxes (blue and yellow) both drop in magnitude slightly but remain relative to one and other, whereas the side fluxes (red and green) almost swap magnitude. This was very confusing as this anomaly was observed in every phase.

Figure 149 illustrates this further, showing TBK25 (top), TBF25 (middle), TBL25 (bottom) windowed around the moments of change in conditioning tool:

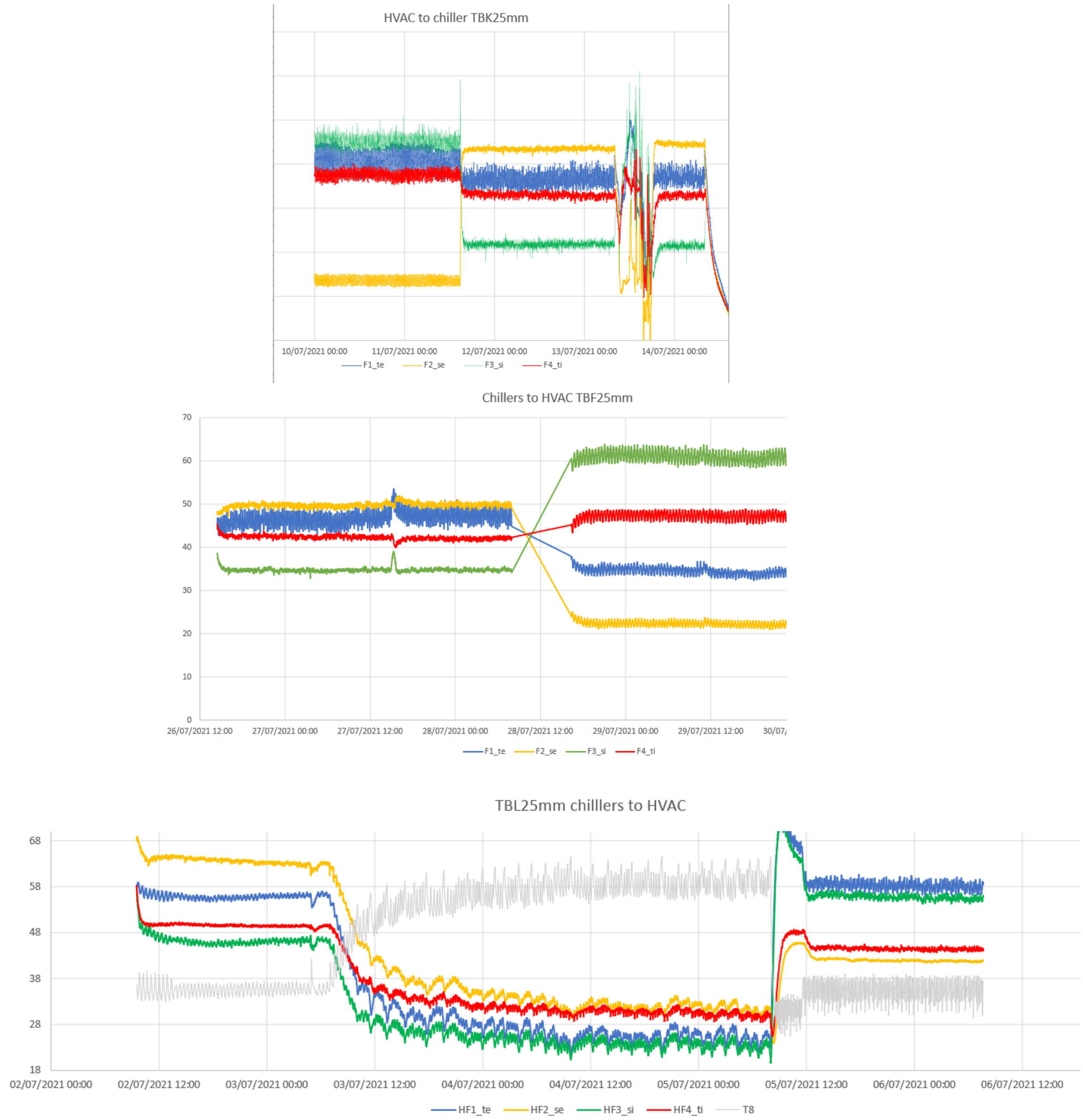

Figure 149 – Illustrating moment of change between the condition tools, the top graph shows the TBF25mm variant transitioning from HVAC to Chiller, the middle graph shows the TBF25mm variant transitioning from Chiller to HVAC, the bottom graph shows the TBL25mm variant transitioning from Chiller to HVAC

It was thought that due to proximity to the HVAC outlet in the conditioning chamber, forced air convection was filtrating around the beam's web and flange, increasing sensor exposure to higher convective mechanisms – affecting the measured heat flux within the connection. The Chiller unit was far away from the test-rig and did not directly force cooled air over the balcony arm beam-section, it also reduced external temperature fluctuations. Therefore, the chiller conditioning was considered more robust data and used in analysis.

The following chart (Figure 150) shows the total timeline of acquisition:

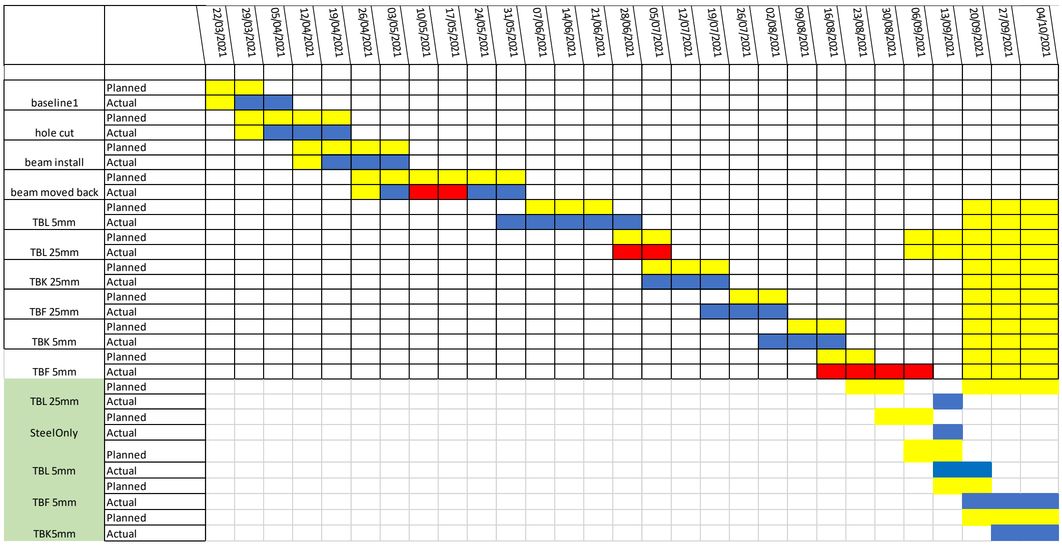

Figure 150 – Yellow = planned, Blue = actual, red = error in capture, green = recaptured phases.

The installed wall was measured initially to ensure the design was correct to regulation before a hole was cut to accommodate the steelwork (representing an edge-beam at a single cantilever balcony junction, featuring a balcony arm and stub connection protruding externally balanced with backspan protruding inward). Testing commenced in March 2021 and completed in October 2021, see Figure 150. In that time all phases were tested, and measurements logged ready for analysis and FE simulation calibration to quantify the TB-transmittance.

The data was captured until a representative window could be extracted and analysed. This was realised when steady-state conditions have been held long enough using Chiller conditioning tools, to both eliminate thermal mass storage interference and reduce the precision error to a negligible effect – caused by large data sets.

From the initial data capture it was clear that some phases needed revisiting due to the aforementioned reasons. These phases were, Steel Only, TBL25, TBL5, TBF5, TBK5. In other words, the only phases done right the first time were TBK25 and TBF25. Approximately 12 hours of minutely data was seen as more than adequate to represent the thermal performance as long as the facility was pre-conditioned prior to monitorisation. The analysis windows are in Table 26:

Phase	Analysis period	Sample size
Baseline	29/03/21 07:30 - 01/04/21 08:51	4402 samples
Steel Only	16/09/21 14:24 - 17/09/21 09:01	1118 samples
TBL5	17/09/21 11:00 - 20/09/21 07:23	2580 samples
TBF5	20/09/21 18:00 - 21/09/21 12:29	1110 samples
TBK5	29/09/21 16:59 - 30/09/21 09:30	992 samples
TBL25	14/09/21 13:00 - 16/09/21 11:00	2760 samples
TBF25	26/07/21 14:26 - 28/07/21 07:56	2491 samples
TBK25	11/07/21 15:00 - 13/07/21 08:00	2461 samples

Table 26 – Analysis windows.

Each of these phases will be shown in the following section. Justifying the windowed data, initially a time-lapse of the external temperatures measured in each experiment will be plotted, followed by the U-value measurand, environmental temperatures plotted against time. Then, the average of these values and SR-values with their corresponding uncertainty intervals is graphed. Finally, a table of averages (temperatures, Flux, U-values, and surface-fluid HTC's) and their uncertainties is established to be taken forward informing model re-calibration.

5.1 Raw data

The following section illustrates the data capture from every phase:

- Baseline is shown between Figure 151 to Figure *156*
- The steel only is shown in Figure 157 to Figure *163*
- TBL 5mm Figure 164 to Figure *170*
- TBF 5mm Figure 171 to Figure *177*
- TBK 5mm Figure 178 to Figure *184*
- TBL 25mm Figure 185 to Figure *191*
- TBF 25mm Figure 192 to Figure *198*
- TBK 25mm Figure 199 to Figure *205*

5.1.1 Baseline Wall

The data was acquired between 29/03/21 07:30 and 01/04/21 08:51 collecting 4402 data points over 22 sensors (8x heat flux, 14x thermocouple) enabling the calculation of measurands U-value and surface-fluid HTC: Heat Flux measurements can be determined by converting mV readings into [W/m^2] using the conversion coefficient, then, after the relevant temperature difference – sensed using pairs of T-type thermocouples – is applied, either the U-value or surface-fluid HTC can be calculated and their errors propagated.

- Sensor locations (diagram of sensor array) are shown earlier in Figure 120 to Figure 125.

Temperature / time

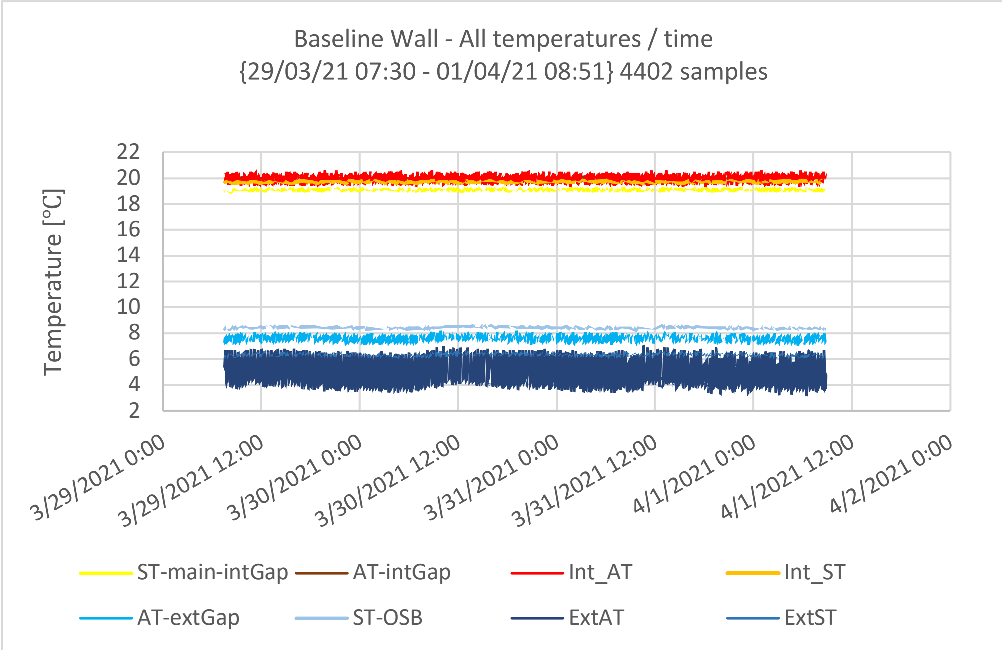

Figure 151 – Steady-state analysis window, temperature vs time graph of the baseline test.

U-value & dT / time

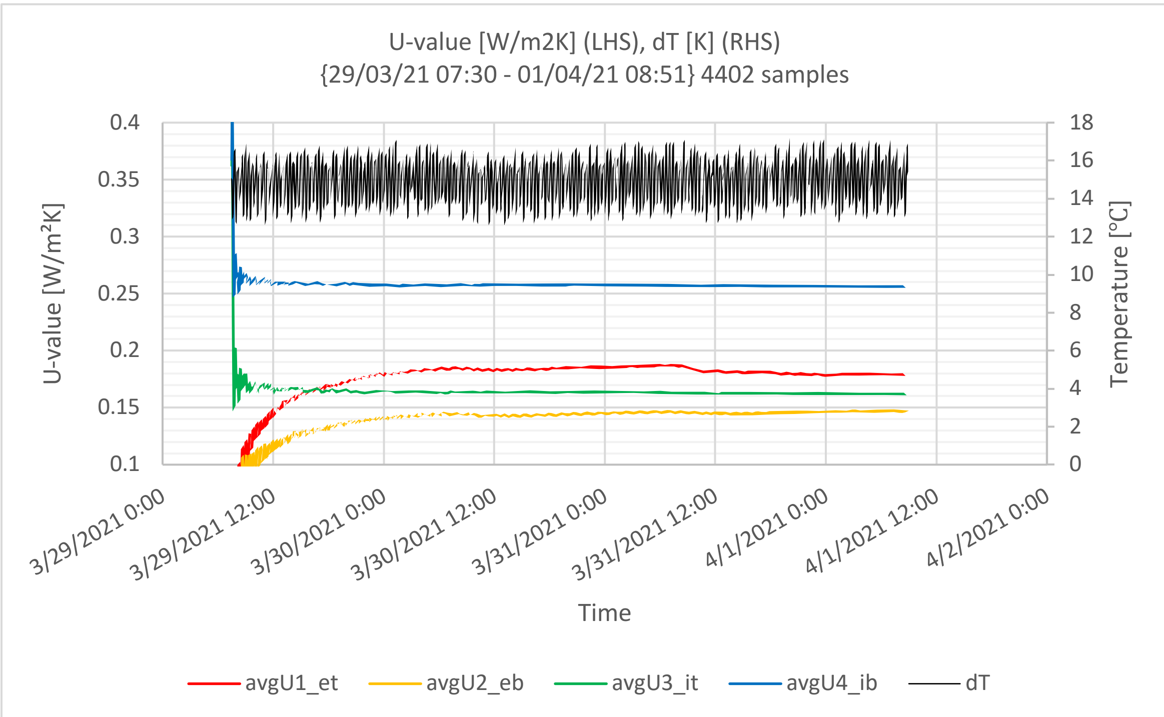

Figure 152 – U-values and temperature difference vs time graph.

U-values measurands, total average & uncertainty interval

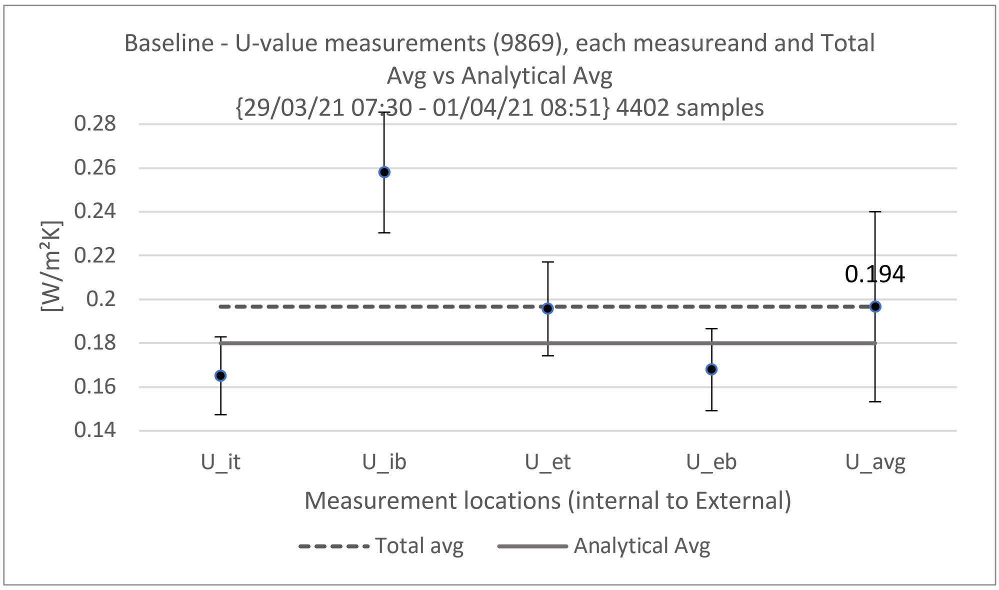

Figure 153 – U-value measurands with uncertainty.

Surface-fluid HTC measurand total, internal, and external

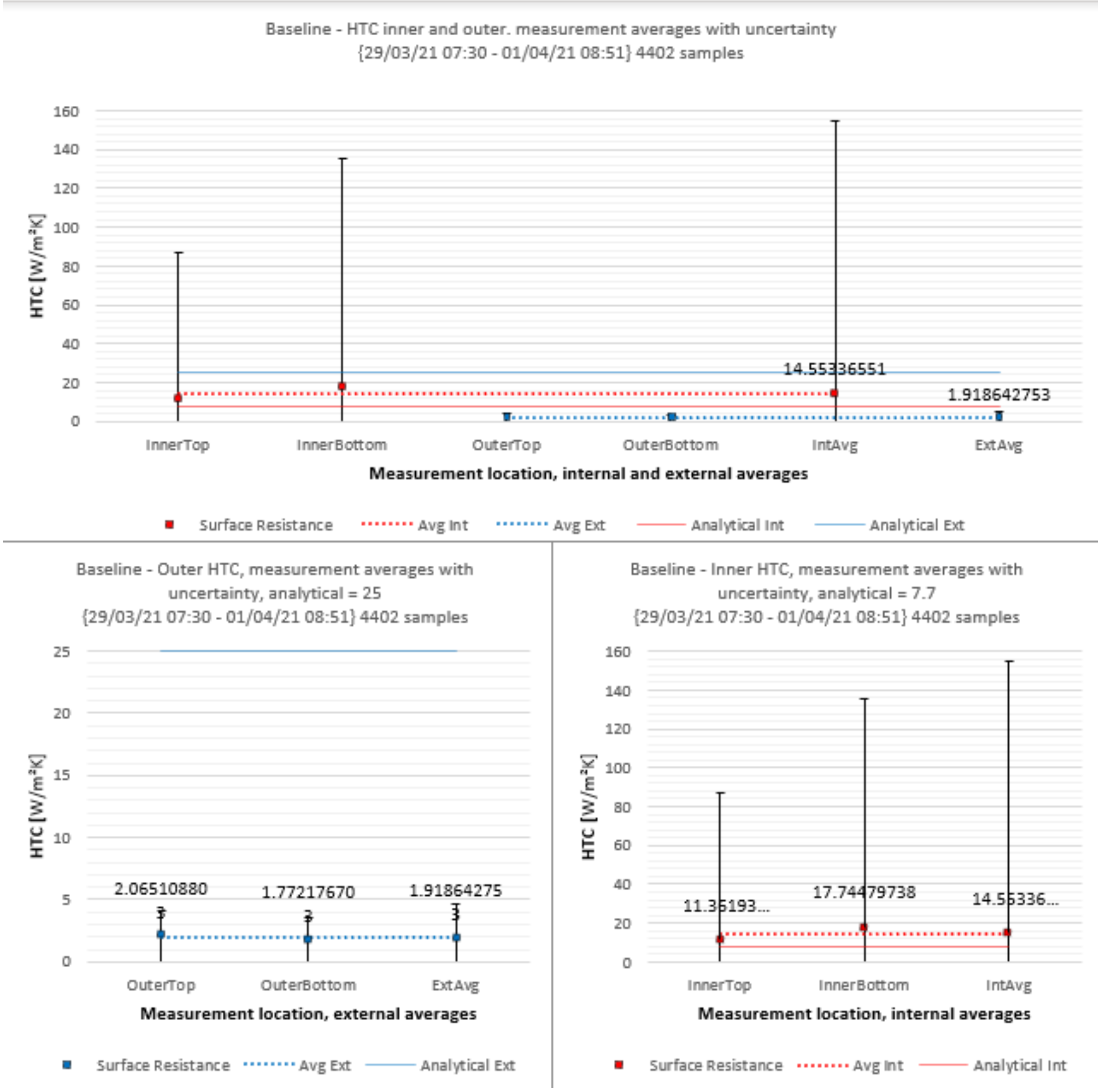

Figure 154 – Inner and outer surface-fluid HTC measurements and uncertainty.

Temperatures through wall thickness

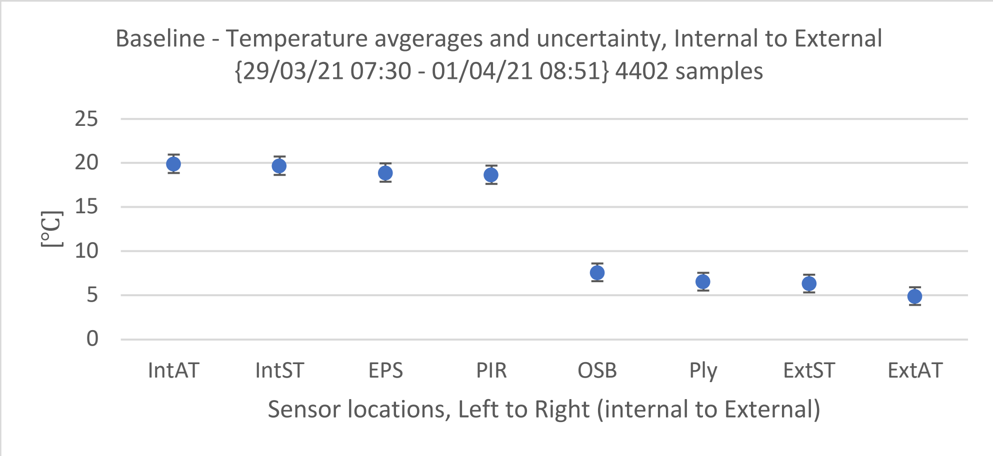

Figure 155 – Average temperatures and uncertainties recorded at various locations through the specimen wall.

Table of averages and their uncertainties:

	HF1	HF2	HF3	HF4	HF5	HF6	HF7	HF8	T1	T2	T3	T4	T5	T6	T7	T8	T11	T12	T13	T14
	CH1	CH2	CH3	CH4	CH5	CH6	CH7	CH8	CH9	CH10	CH11	CH12	CH13	CH14	CH15	CH16	CH19	CH20	CH21	CH22
	CH1	CH2	CH3	CH4	CH5	CH6	CH7	CH8	FT-inner	FT-Main	FT-OSB	FT-Ply	ST-main-i	AT-intGap	Int_AT	Int_ST	AT-extGa	ST-OSB	ExtAT	ExtST
avg	0.001202052	0.002484908	0.16832291	0.151901	0.004672826	0.00580029	0.151490281	0.2372514	18.92824	18.26486	6.807428	6.560359	19.09264	20.03478	19.9202	19.70223	7.588369	8.431327	4.925216	6.346206
sd	0.000322132	0.001319598	0.2277006	0.296839	0.000140792	0.000196693	0.146940987	0.1090132	0.063483	0.070876	0.081176	0.169273	0.075484	0.055307	0.338387	0.060209	0.283246	0.07474	0.966572	0.117313
N	4402	4402	4402	4402	4402	4402	4402	4402	4402	4402	4402	4402	4402	4402	4402	4402	4402	4402	4402	4402
uA	4.85522E-06	1.98892E-05	0.00343194	0.004474	2.12203E-06	2.96459E-06	0.002214715	0.0016431	0.000957	0.001068	0.001223	0.002551	0.001138	0.000834	0.0051	0.000907	0.004269	0.001126	0.014568	0.001768
uB	1.80308E-05	3.72736E-05	0.00252484	0.002279	7.00924E-05	8.70044E-05	0.002272354	0.0035588	1.039525	1.036852	1.0052	1.00483	1.040201	1.044181	1.043687	1.042756	1.006457	1.007966	1.002725	1.004521
uC	1.8673E-05	4.22481E-05	0.00426064	0.005021	7.01245E-05	8.70548E-05	0.003173099	0.0039198	1.039526	1.036852	1.005201	1.004833	1.040202	1.044181	1.0437	1.042756	1.006466	1.007966	1.002831	1.004522
	0.001009322	0.001485979	0.05736	0.06032	0.001440023	0.001430889	0.06117	0.06134	T1	T2	T3	T4	T5	T6	T7	T8	T11	T12	T13	T14
Flux[W/m2]	Flux1	Flux2	Flux3	Flux4	Flux5	Flux6	Flux7	Flux8	CH9	CH10	CH11	CH12	CH13	CH14	CH15	CH16	CH19	CH20	CH21	CH22
c_mV	990.764185	672.9569177	17.4337517	16.57825	694.4334059	698.8660867	16.34788295	16.302576	FT-inner	FT-Main	FT-OSB	FT-Ply	ST-main-i	AT-intGap	Int_AT	Int_ST	AT-extGa	ST-OSB	ExtAT	ExtST
c_Sc	-1179.95025	-1125.3427	-51.159343	-41.7481	-2253.41333	-2832.94188	-40.4862741	-63.05526												
UB_mV	6.26498E-05	8.63771E-05	0.00256874	0.002702	8.40372E-05	8.35703E-05	0.002598716	0.0026023			dT-T				dT-it	dT-PIR	dT-OSB	dT-eb		
uC	0.076203544	0.101276414	0.15095449	0.140193	0.195531526	0.244442172	0.117305115	0.1760937			14.99498				0.217969	0.94214	0.842958	1.42099		
[+/-]	6.40%	6.06%	5.14%	5.57%	6.03%	6.03%	4.74%	4.55%			1.447404				1.475347	1.473884	1.424419	1.419414		
AvgFlux	1.190949642	1.672235873	2.93449991	2.518246	3.244966782	4.0536262	2.476545389	3.8678096												
SR	SR1	SR2	SR3	SR4	SR5	SR6	SR7	SR8												
c_dT	0.839666066	0.598001763	0.34077357	0.397102	0.308169565	0.246692702	0.403788279	0.2585443												
c_Q		-0.30144684	-0.1650148	-0.22408	-0.08947358	-0.05733607	-0.03553869	-0.01457												
avgSR		0.504090218	0.48423599	0.564278	0.290338782	0.232418989	0.088013188	0.0563545												
uC		0.852352187	0.48433963	0.564526	0.539073181	0.363866467	0.584459791	0.3742269												
[+/-]		169.09%	100.02%	100.04%	185.67%	156.56%	664.06%	664.06%												
U			0.19569883	0.167939			0.165158304	0.2579403												
c_Q			0.06668899	0.066689			0.066688987	0.066689												
c_dt			-0.013051	-0.0112			-0.01101424	-0.017202												
uC			0.02140507	0.018713			0.017758039	0.0275285												
[+/-]			10.94%	11.14%			10.75%	10.67%												
			(5691 datapoints) < 4days																	
	dT-T				dT-it	dT-PIR	dT-OSB	dT-eb												
[°C]	14.99497956				0.217968654	0.942139702	0.842957746	1.4209905												
[+/-]	1.447404378				1.475347423	1.47388408	1.424419314	1.4194136												
	Ply	OSB	et	eb	PIR	EPS	it	ib												
AvgFlux	1.190949642	1.672235873	2.93449991	2.518246	3.244966782	4.0536262	2.476545389	3.8678096												
[+/-]	0.076203544	0.101276414	0.15095449	0.140193	0.195531526	0.244442172	0.117305115	0.1760937												
%	6.40%	6.06%	5.14%	5.57%	6.03%	6.03%	4.74%	4.55%												
										SR			HTC							
	OSB	et	eb	PIR	EPS	it	ib			Ext	Int		Ext	Int						
AvgSR	0.504090218	0.484235987	0.56427782	0.290339	0.232418989	0.088013188	0.056354546			0.524257	0.072184		1.907462	13.85351						
[+/-]	0.852352187	0.484339631	0.56452637	0.539073	0.363866467	0.584459791	0.374226899			0.524433	0.479343		1.908086	91.99544						
%	169.09%	100.02%	100.04%	185.67%	156.56%	664.06%	664.06%			100.03%	664.06%		100.03%	664.06%						
	et	eb		it	ib		Overall													
AvgU	0.195698827	0.181234385		0.151773	0.247142851		0.193962149													
[+/-]	0.021405071	0.023622983		0.016995	0.027027777		0.022262732													
%	10.94%	11.14%		10.75%	10.67%		10.88%													

	T1	T2	T3	T4	T5	T6	T7	T8	T9	T10	T11	T12	T13	T14
Barewall	IntST	IntAT	IntST	IntAT	ExtST	ExtAT	ExtST	ExtAT	ExtGap	ExtGap	ExtGap	IntGap	IntGap	IntGap
	top	top	Bott	Bott	top	top	bott	bott	Ply	AT	OSB	PIR	AT	EPS
Temps	18.92823707	18.2648568	6.807428442	6.560358928	19.09264	20.03477965	19.92019537	19.70222672	7.58836892	8.4313267	4.9252158	6.3462063	0	0
U-value	U1_int	U2_int	U3_ext	U4_ext	U1_int	U2_int	U3_ext	U4_ext		Uavg	[+/-]			
	0.151772533	0.247142851	0.195698827	0.181234385	10.75%	10.67%	10.94%	11.14%		0.193962	22.04%	0.042755		
S-HTC	SR1_int	SR2_int	SR3_ext	SR4_ext	SR1_int	SR2_int	SR3_ext	SR4_ext		SR_int_avg	[+/-]		SR_ext_avg	[+/-]
	0.088013188	0.056354546	0.484235987	0.564277816	664.06%	664.06%	100.02%	100.04%		14.55337	961.44%	139.9213	1.918643	141.88%
W/m2K	11.36193365	17.74479738	2.065108803	1.7721767									2.722109	
	75.44998114	117.8357555	2.065550808	1.7729573										

Figure 156 – All measurements recorded and uncertainty analysis.

5.1.2 Steel Only

The data was acquired between 16/09/21 14:24 and 17/09/21 09:01 collecting 1118 data points over 22 sensors (8x heat flux, 14x thermocouple) enabling the calculation of measurands U-value and surface-fluid HTC: Heat Flux measurements can be determined by converting mV readings into [W/m^2] using the conversion coefficient, then, after the relevant temperature difference – sensed using pairs of T-type thermocouples – is applied, either the U-value or surface-fluid HTC can be calculated, and their errors propagated.

- Sensor locations (diagram of sensor array) are shown earlier in Figure 120 to Figure 125.

Embedded flux & external temperatures / time

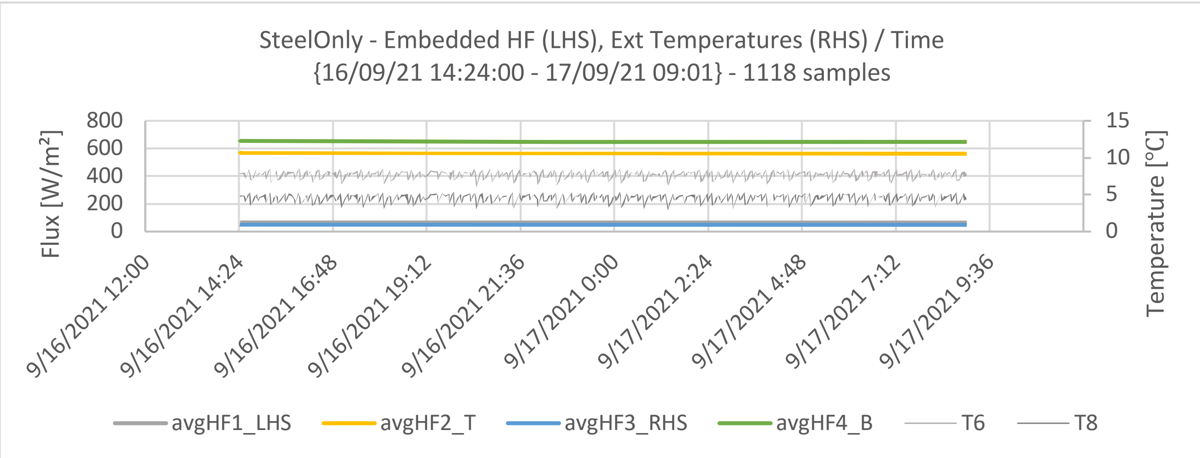

Figure 157 – Embedded flux and external temperatures vs time graph.

U-value & dT / time

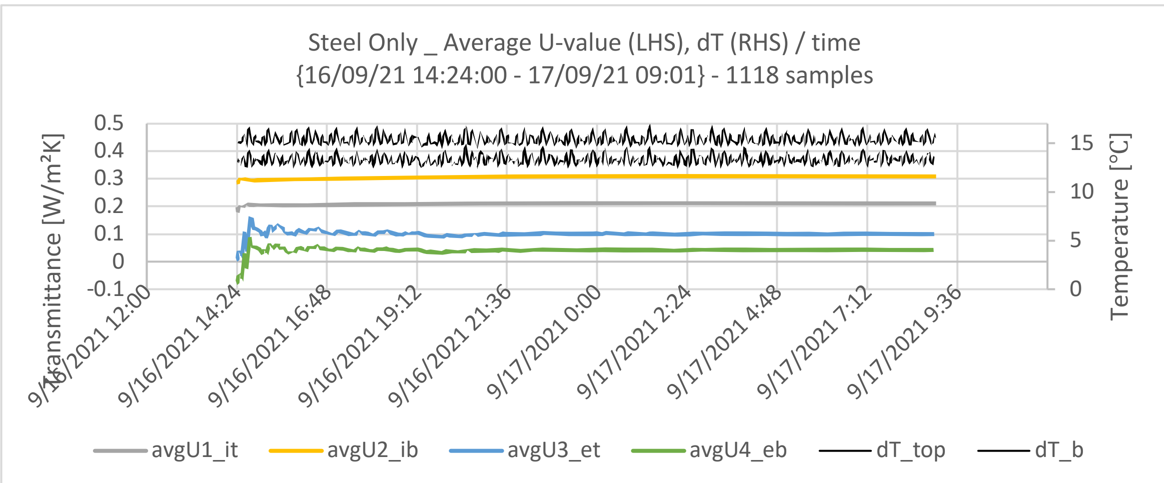

Figure 158 – U-values and temperature difference vs time graph.

U-values measurand and total average & uncertainty interval

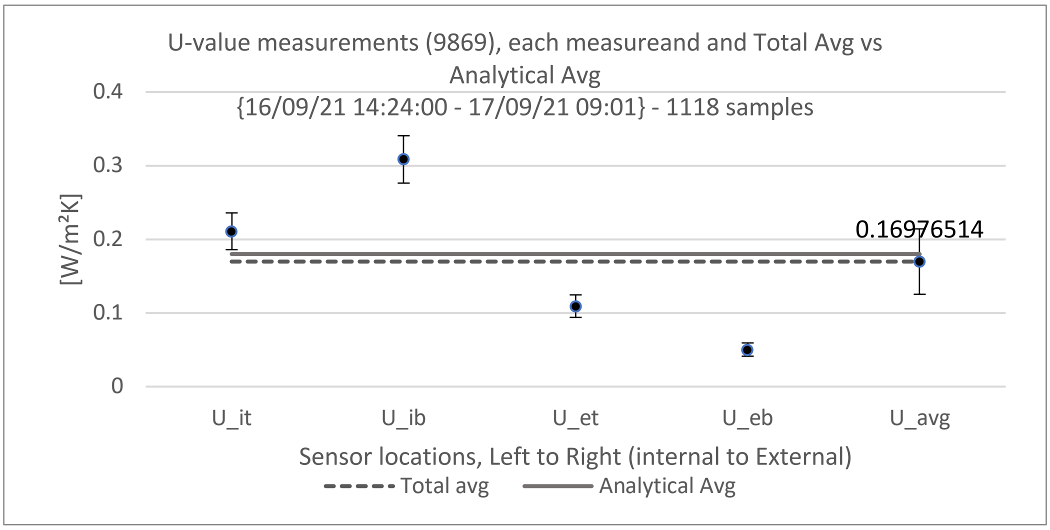

Figure 159 – U-value measurands with uncertainty.

Surface-fluid HTC measurand total, internal, and external

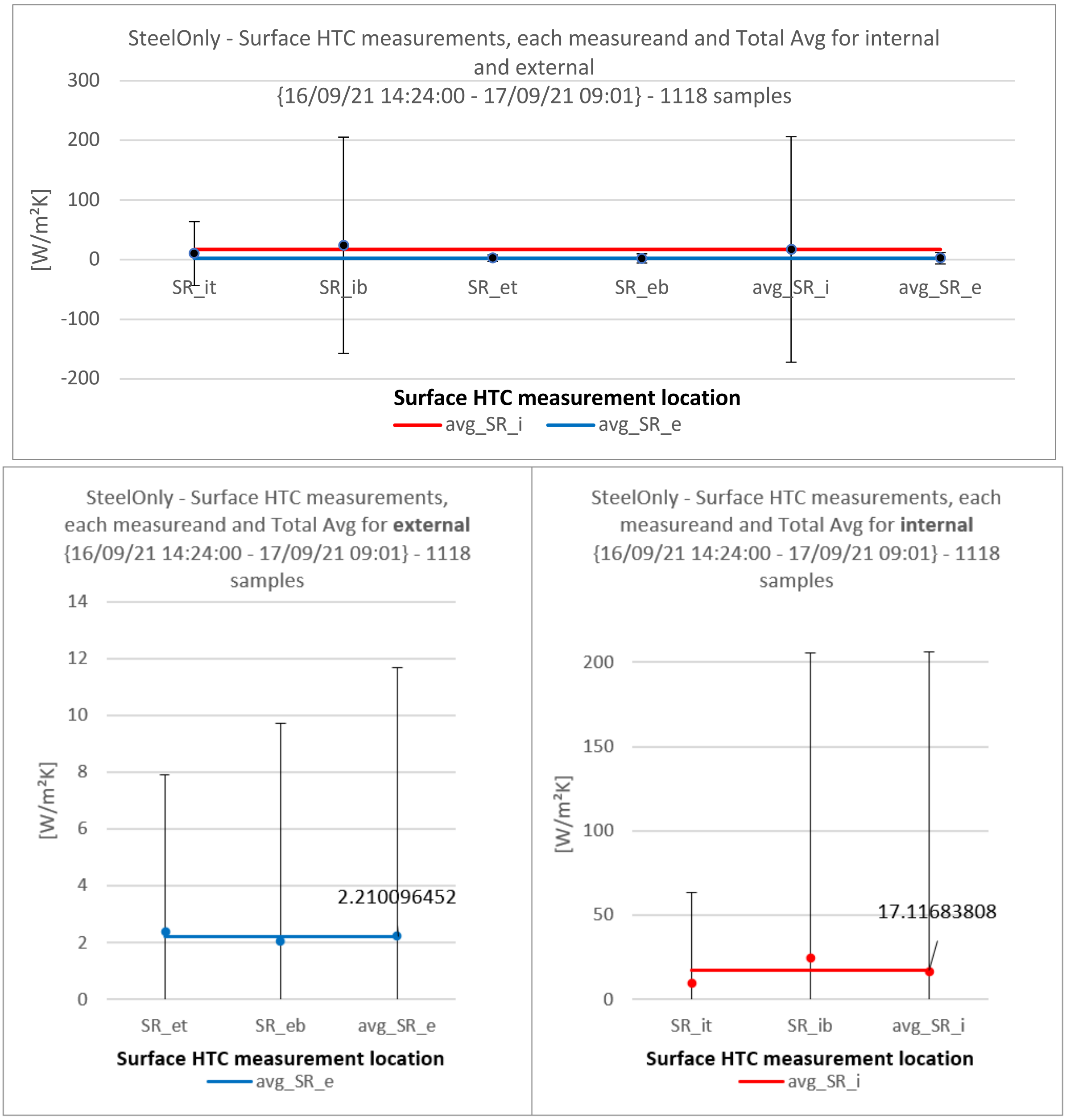

Figure 160 – Surface-fluid HTCs.

Embedded flux values top and side

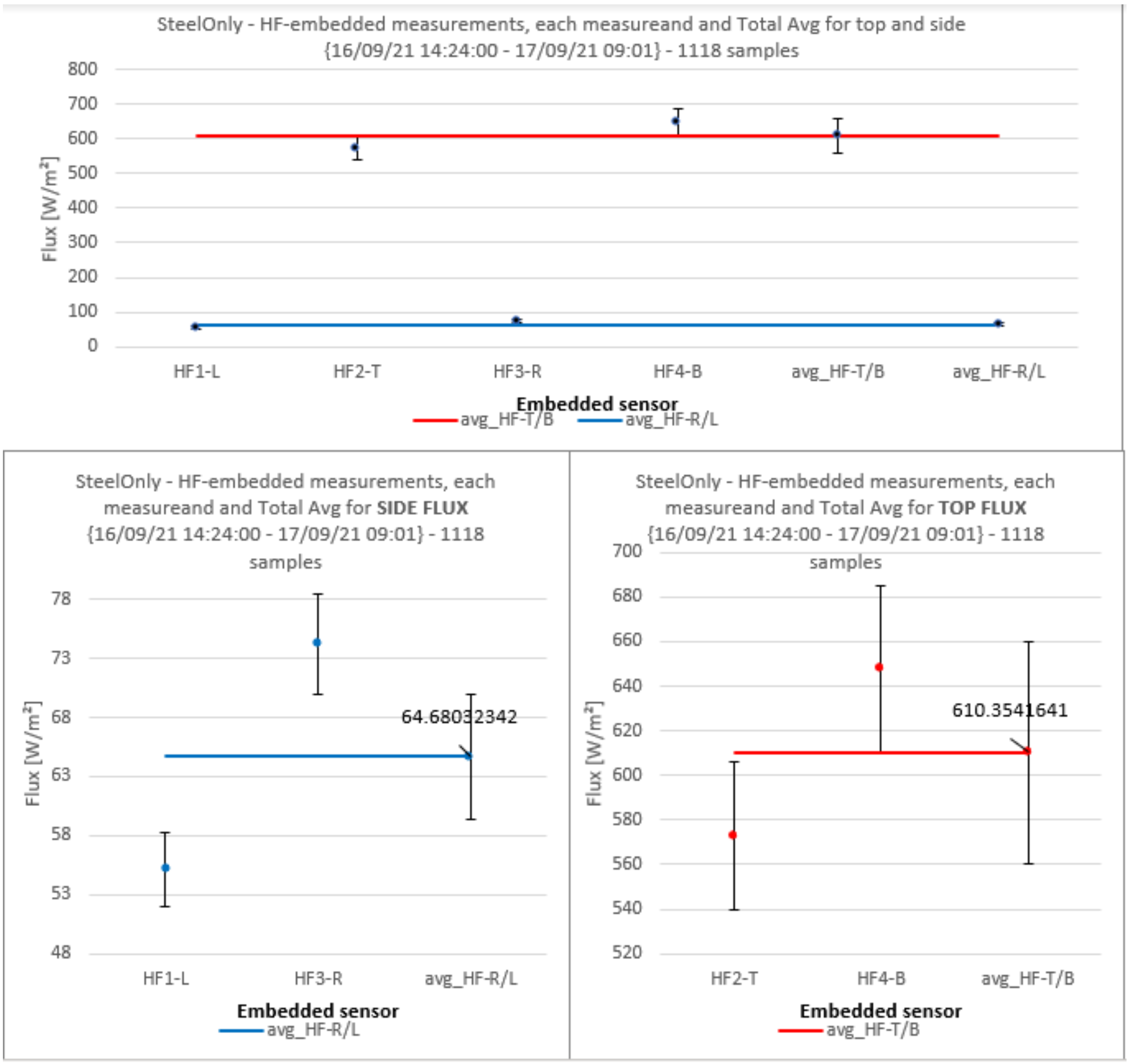

Figure 161 – Embedded flux measurements top, side, and average.

Table of averages and their uncertainties:

		2422	2419	2421	2423	'985 - int t	7984 - int bot	987 - Ext T	986 - Ext B	IntST_top	IntAT_top	IntST_Bot	IntAT_Bot	ExtST_top	ExtAT_top	ExtST_bot	ExtAT_bot	ExtGapPly	ExtGapAT	ExtGapOS	IntGapMa	IntGapAT	IntGapInn
		HF1	HF2	HF3	HF4	HF5	HF6	HF7	HF8	T1	T2	T3	T4	T5	T6	T7	T8	T9	T10	T11	T12	T13	T14
	avg	0.058996592	0.595901	0.07645	0.68659	0.171846	0.29103415	0.083472	0.046677	20.69785	20.97629691	19.69428	19.89079	8.271914132	7.659302	4.890161	4.511717	4.991055	5.094365	7.736852	16.44732	14.88032	15.86726
	sd	0.000510376	0.004656	0.002078	0.006078	0.025811	0.01428077	0.207728	0.225712	0.026336	0.103783215	0.024359	0.041604	0.262978168	0.495596	0.215856	0.523522	0.124145	0.123001	0.059528	0.081395	0.099763	0.076494
	N	1118	1118	1118	1118	1118	1118	1118	1118	1118	1118	1118	1118	1118	1118	1118	1118	1118	1118	1118	1118	1118	1118
	uA	1.5264E-05	0.000139	6.22E-05	0.000182	0.000772	0.0004271	0.006213	0.00675	0.000787	0.003103889	0.000729	0.001244	0.007865001	0.014822	0.006456	0.015657	0.003713	0.003679	0.00178	0.002434	0.002984	0.002288
logger	uB	0.000884949	0.008939	0.001147	0.010299	0.002578	0.00436551	0.001252	0.0007	1.047087	1.048332548	1.042722	1.043561	1.007668361	1.006578	1.002687	1.002287	1.002799	1.002915	1.006712	1.029983	1.024607	1.027934
	uC	0.000885081	0.00894	0.001148	0.0103	0.002691	0.00438636	0.006338	0.006787	1.047087	1.048337143	1.042722	1.043562	1.007699055	1.006687	1.002707	1.00241	1.002805	1.002922	1.006713	1.029986	1.024612	1.027937
				OpTemp	9.987343	1.433765																	
			5%		0.950358			3%					OpTemp										
		fluxteq	microV	±	milliV		UB	hukseflux	microV	±	milliV			±		UB							
		2422	1.07	0.03	0.00107	0.00003	5.9035E-05	17984	61.34	1.84	0.06134	0.00184	19.79253	1.475225869	1.27E-05	0.002602							
		2419	1.04	0.03	0.00104	0.00003	5.7812E-05	17985	61.17	1.84	0.06117	0.00184	20.83708	1.481688783	5.12E-05	0.002599							
		2421	1.03	0.03	0.00103	0.00003	5.7406E-05	17986	60.32	1.81	0.06032	0.00181	4.700939	1.41783194	0.000923	0.002721							
		2423	1.06	0.03	0.00106	0.00003	5.8626E-05	17987	57.36	1.72	0.05736	0.00172	7.965608	1.424386423	0.00069	0.002529							
		LHS(int-ext)	Top	RHS(int-e:	Bottom																		
		Flux1	Flux2	Flux3	Flux4	Flux5	Flux6	Flux7	Flux8		dT_t	dT_b		dT_it	dT_ib	dT_et	dT_eb						
W/m2		**55.13700199**	**572.982**	**74.22364**	**647.7263**	**2.809318**	**4.74460627**	**1.455231**	**0.773819**		13.31699458	15.37907		0.278442695	0.196511	0.612612	0.378444						
	c_mV	934.5794393	961.5385	970.8738	943.3962	16.34788	16.3025758	17.43375	16.57825		1.453420126	1.447013		1.481688783	1.475226	1.424386	1.417832						
	c_Ss	-51529.9084	-550944	-72061.8	-611063	-45.9264	-77.349303	-25.3701	-12.8286														
[+/-W/m2	uC	3.152521106	32.99055	4.284413	37.11882	0.127219	0.21361275	0.127766	0.1178														
		5.72%	5.76%	5.77%	5.73%	4.53%	4.50%	8.78%	15.22%														
						85-it	84-ib	87-et	86-eb														
						U1	U2	U3	U4														
					c_Q	0.075092	0.06502344	0.075092	0.065023														
					c_dT	-0.01584	-0.0200604	-0.00821	-0.00327														
					Avg_U	**0.210957**	**0.30851062**	**0.109276**	**0.050316**		0.259733993	0.079796		0.16976514									
					uC_U	0.024927	0.03217972	0.015306	0.009005		0.040705013	0.017759		0.022982084	0.04441								
					[+/-]	11.82%	10.43%	14.01%	17.90%		15.67%	22.26%		13.54%	26.16%								
						SR1	SR2	SR3	SR4	[HTC]													
					c_Q	3.591403	5.08878515	1.632355	2.642401														
					c_dT	-36.2351	-122.86506	-3.87758	-5.40302		int	ext		int	ext								
					Avg_SR	**10.08939**	**24.1442819**	**2.375454**	**2.044739**		17.11683808	2.210096		17.11683808	2.210096								
					uC_U	53.69106	181.256979	5.527114	7.666899		189.0418536	9.451472		109.7940501	6.714642								
					[+/-]	532.15%	750.72%	232.68%	374.96%		1104.42%	427.65%		641.44%	303.82%								

Figure 162 – All measurements recorded and uncertainty analysis.

	T1	T2	T3	T4	T5	T6	T7	T8	T9	T10	T11	T12	T13	T14
Steel	IntST	IntAT	IntST	IntAT	ExtST	ExtAT	ExtST	ExtAT	ExtGap	ExtGap	ExtGap	IntGap	IntGap	IntGap
Only	top	top	Bott	Bott	top	top	bott	bott	Ply	AT	OSB	PIR	AT	EPS
Temps	20.69785422	20.97629691	19.694276	19.890787	8.2719141	7.6593023	4.890161002	4.5117174	4.9910555	5.0943649	7.736851521	16.447317	14.880322	15.86726297
U-value	U1_int	U2_int	U3_ext	U4_ext	U1_int	U2_int	U3_ext	U4_ext		**Uavg**	**[+/-]**			
	0.210957368	0.308510617	0.1092762	0.0503163	11.82%	10.43%	14.01%	17.90%		**0.169765**	**26.16%**	0.04441		
S-HTC	SR1_int	SR2_int	SR3_ext	SR4_ext	SR1_int	SR2_int	SR3_ext	SR4_ext		**SR_int_avg**	**[+/-]**		**SR_ext_avg**	**[+/-]**
	0.1	0.04	0.42	0.49	532.15%	750.72%	232.68%	374.96%		**17.11684**	**1104.42%**	189.0419	**2.210096**	**427.65%**
W/m2K	10.08939427	24.1442819	2.375454	2.044739									**9.451472**	
	53.69106066	181.2569789	5.527114	7.666899										
Fluxes	Flux1 (side)	Flux2 (top)	Flux3 (side)	Flux4 (bot)	Flux1 (side)	Flux2 (top)	Flux3 (side)	Flux4 (bot)		**F(side)avg**	**[+/-]**		**F(top/bot) avg**	**[+/-]**
	55.13700199	572.9819982	74.223645	647.72633	5.72%	5.76%	5.77%	5.73%		**64.68032**	**8.22%**		**610.355**	**8.14%**

Figure 163 – All measurements taken forward as simulation input parameters (temperatures, transmittances, SRs) and output values.

5.1.3 TBL5

The data was acquired between 17/09/2021 11:00 and 20/09/2021 07:23 collecting 2580 data points over 22 sensors (8x heat flux, 14x thermocouple) enabling the calculation of measurands U-value and surface-fluid HTC: Heat Flux measurements can be determined by converting mV readings into [W/m^2] using the conversion coefficient, then, after the relevant temperature difference – sensed using pairs of T-type thermocouples – is applied, either the U-value or surface-fluid HTC can be calculated, and their errors propagated.

- Sensor locations (diagram of sensor array) are shown earlier in Figure 120 to Figure 125.

Embedded lux & external temperatures / time:

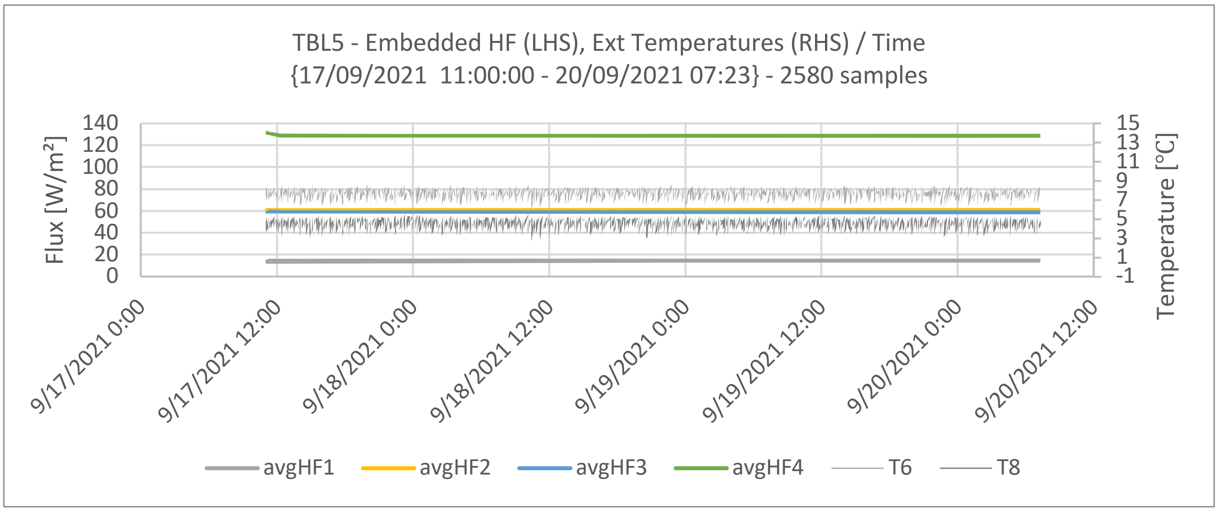

Figure 164 – Embedded flux and external temperatures vs time graph.

U-value & dT / time

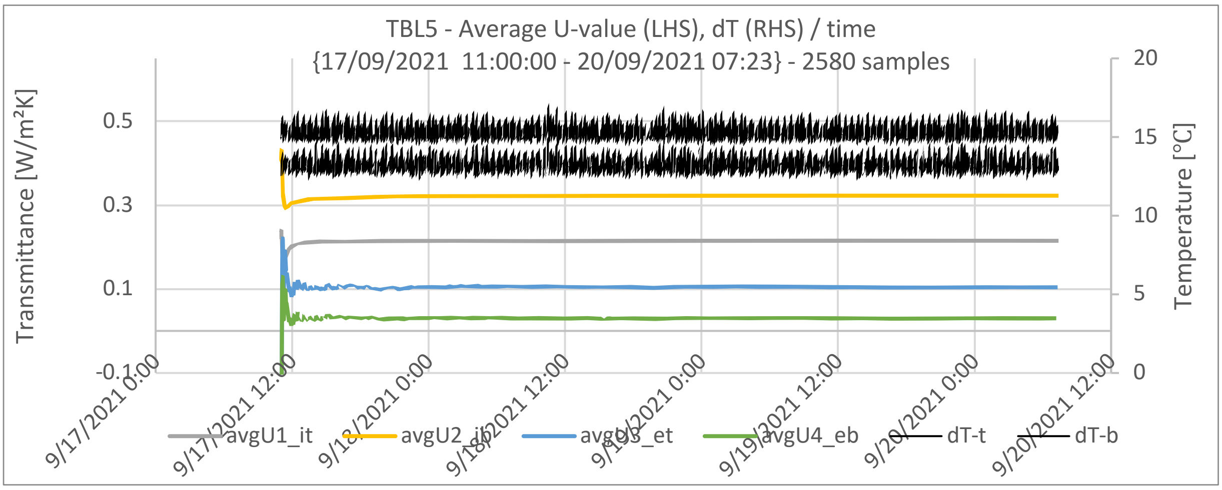

Figure 165 – U-values and temperature difference vs time graph.

U-values measurand and total average & uncertainty interval

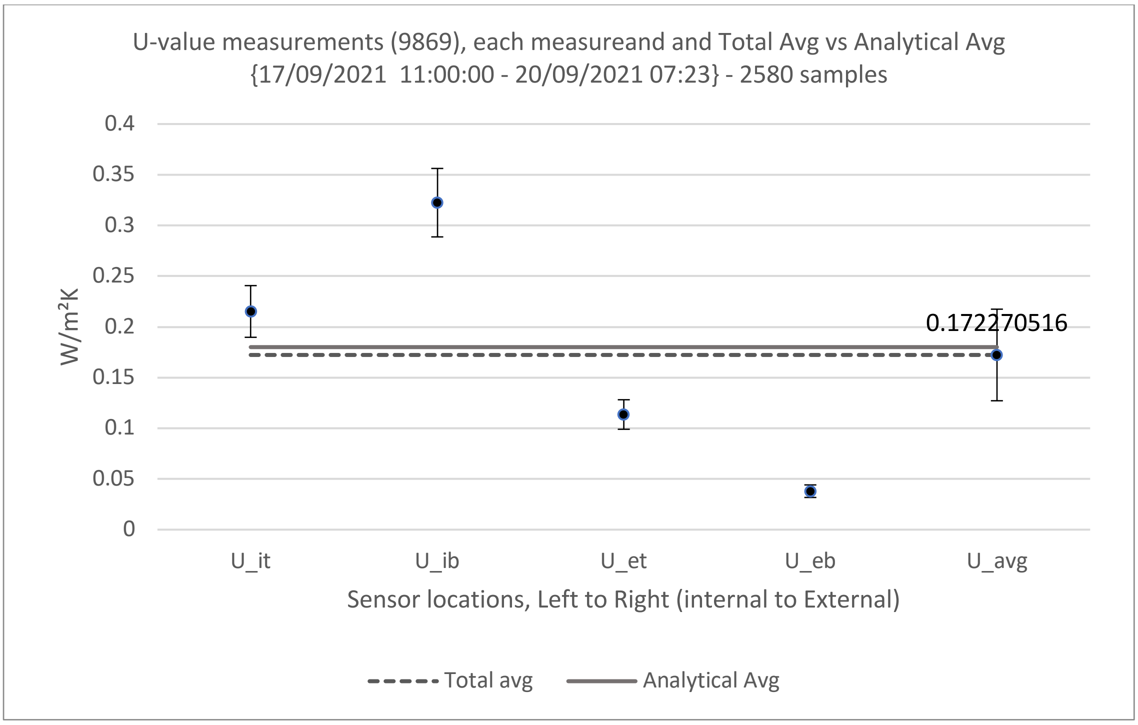

Figure 166 – U-value measurands with uncertainty.

Surface-fluid HTC measurand total, internal, and external

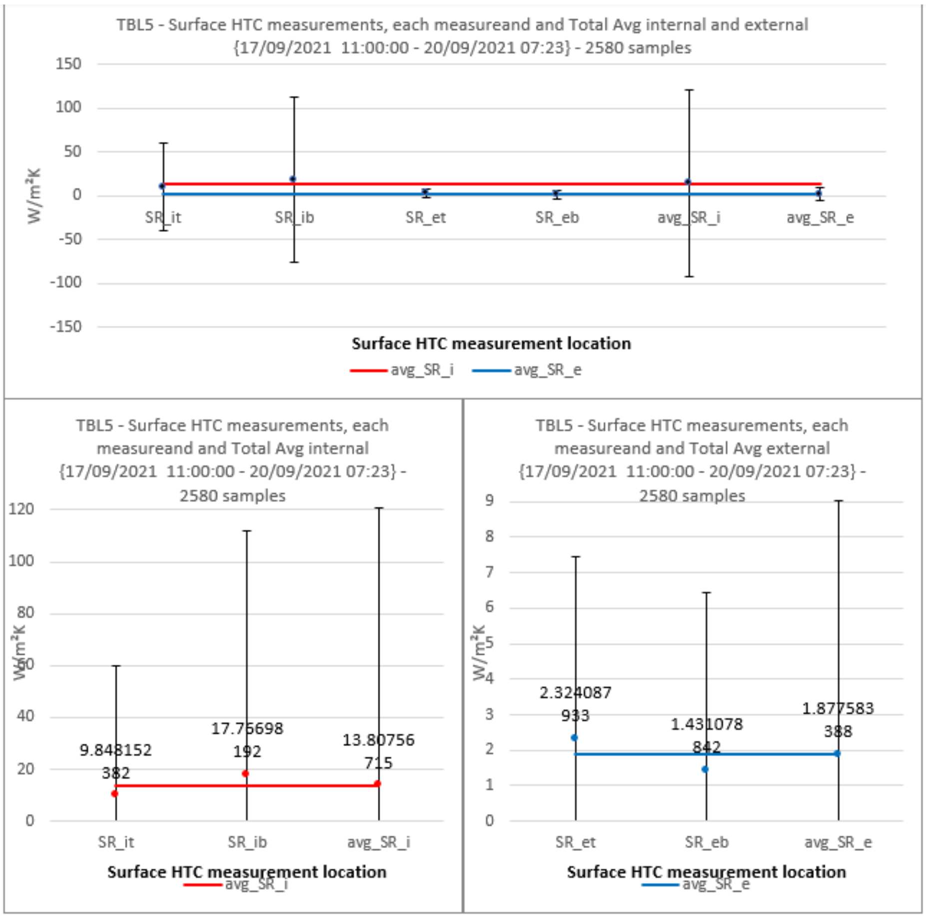

Figure 167 – Surface-fluid HTCs.

Embedded flux values all, top, side

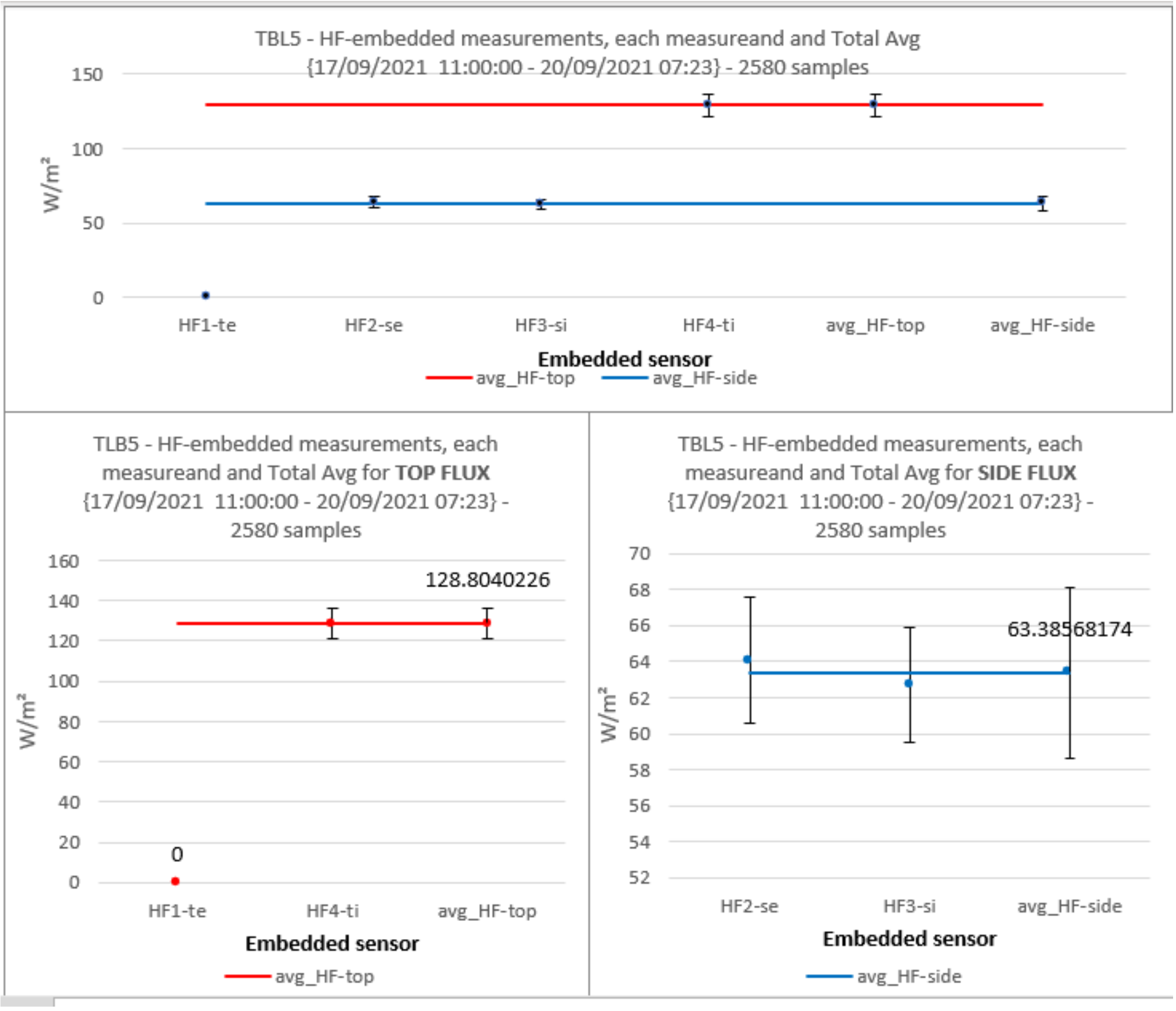

Figure 168 – Embedded flux measurements top, side, and average.

Table of averages and their uncertainties:

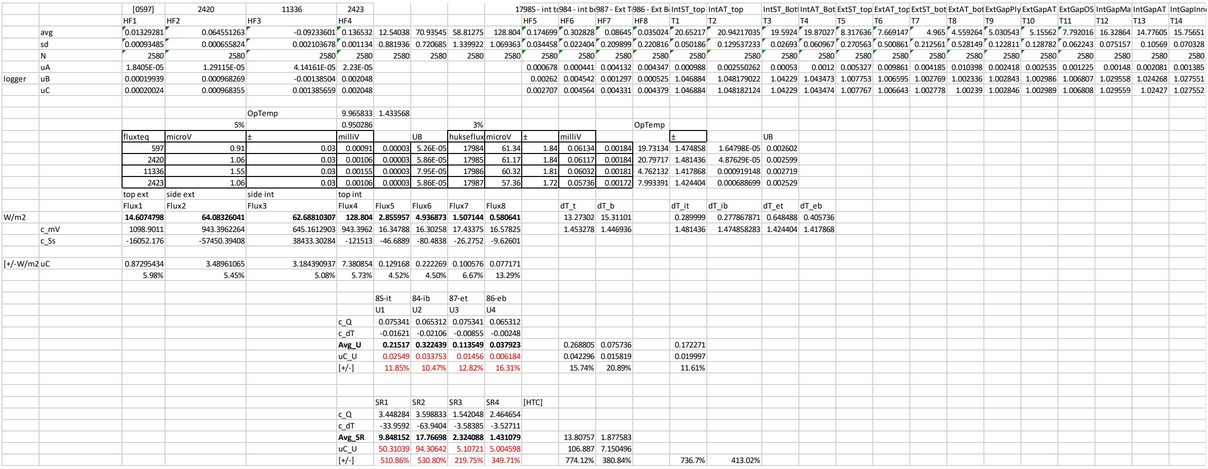

Figure 169 – All measurements recorded and uncertainty analysis.

	T1	T2	T3	T4	T5	T6	T7	T8	T9	T10	T11	T12	T13	T14
TBL 5mm	IntST	IntAT	IntST	IntAT	ExtST	ExtAT	ExtST	ExtAT	ExtGap	ExtGap	ExtGap	IntGap	IntGap	IntGap
	top	top	Bott	Bott	top	top	bott	bott	Ply	AT	OSB	PIR	AT	EPS
Temps	20.65217106	20.94217035	19.5924031	19.870271	8.3176357	7.6691473	4.965	4.5592636	5.0305426	5.1556202	7.7920155	16.328643	14.776047	15.75651163
U-value	U1_int	U2_int	U3_ext	U4_ext	U1_int	U2_int	U3_ext	U4_ext		Uavg	[+/-]			
	0.21517006	0.322439491	0.113549415	0.0379231	11.85%	10.47%	12.82%	16.31%		0.172271	26.21%	0.045158		
S-HTC	SR1_int	SR2_int	SR3_ext	SR4_ext	SR1_int	SR2_int	SR3_ext	SR4_ext		SR_int_avg	[+/-]		SR_ext_avg	[+/-]
	0.101541889	0.05628418	0.430276319	0.6987735	510.86%	530.80%	219.75%	349.71%		13.80757	774.12%	106.887	1.877583	380.84%
W/m2K	9.84815238	17.76698192	2.324087933	1.431079										
Fluxes	Flux1 (te)	Flux2 (se)	Flux3 (si)	Flux4 (ti)	Flux1 (te)	Flux2 (se)	Flux3 (si)	Flux4 (ti)		F(side)avg	[+/-]		F(top/bot) avg	[+/-]
		64.08326041	62.68810307	128.80402		5.45%	5.08%	5.73%		63.38568	7.45%		128.804	5.73%

Figure 170 – All measurements taken forward as simulation input parameters (temperatures, transmittances, SRs) and output values.

5.1.4 TBF5

The data was acquired between 20/09/2021 18:00 and 21/09/2021 12:29 collecting 1110 data points over 22 sensors (8x heat flux, 14x thermocouple) enabling the calculation of measurands U-value and surface-fluid HTC: Heat Flux measurements can be determined by converting mV readings into [W/m^2] using the conversion coefficient, then, after the relevant temperature difference – sensed using pairs of T-type thermocouples – is applied, either the U-value or surface-fluid HTC can be calculated, and their errors propagated.

- Sensor locations (diagram of sensor array) are shown earlier in Figure 120 to Figure 125.

Embedded flux & external temperature / time

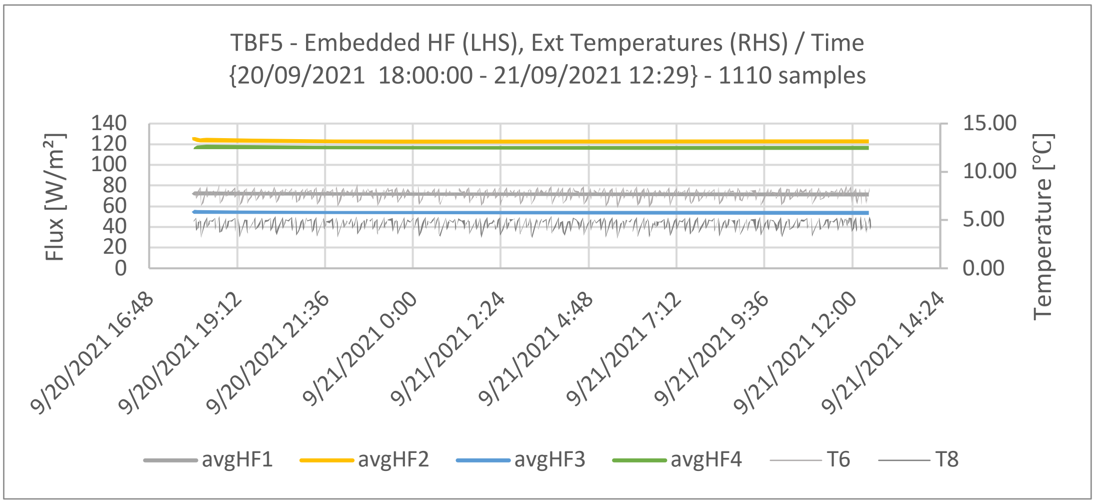

Figure 171 – Embedded flux and external temperatures vs time graph.

U-value & dT / time

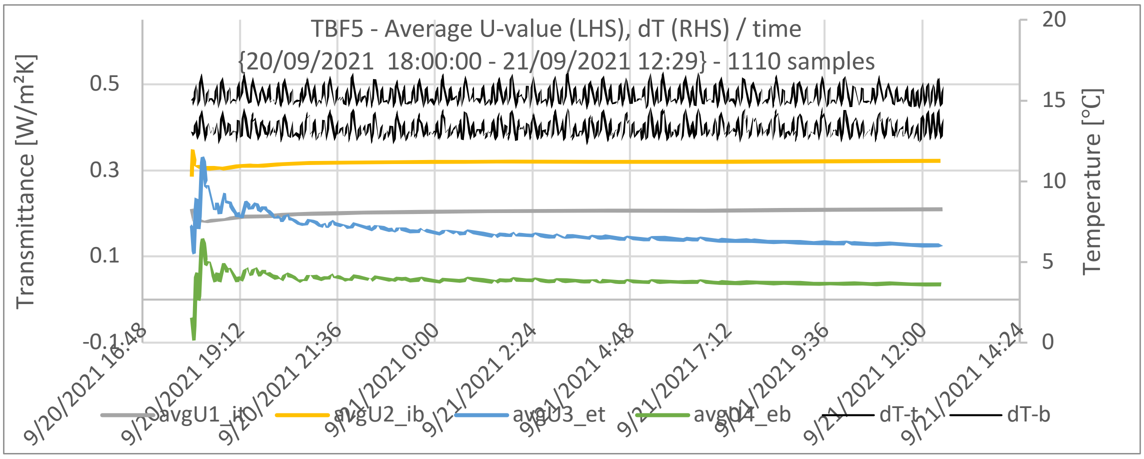

Figure 172 – U-values and temperature difference vs time graph.

U-values measurand and total average & uncertainty interval

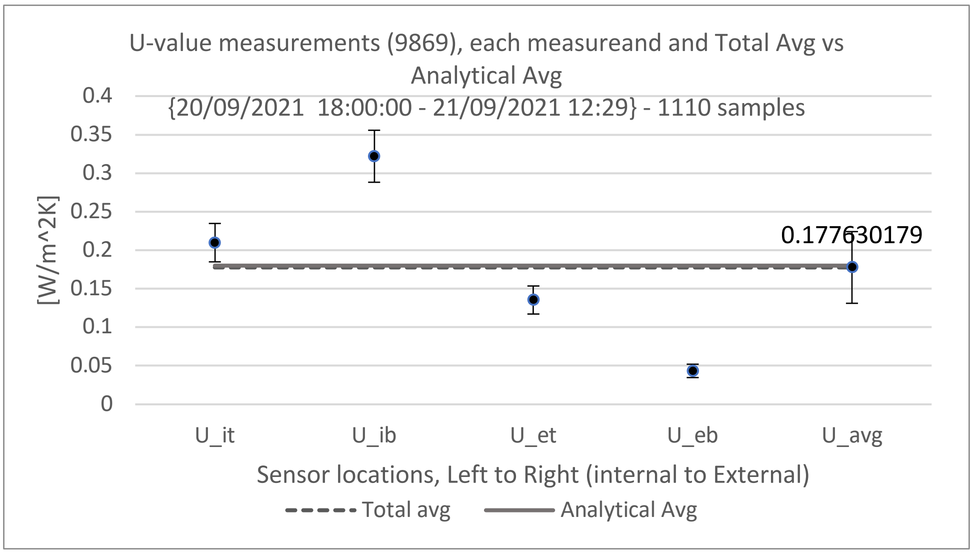

Figure 173 – U-value measurands with uncertainty.

Surface-fluid HTC measurand total, internal, and external

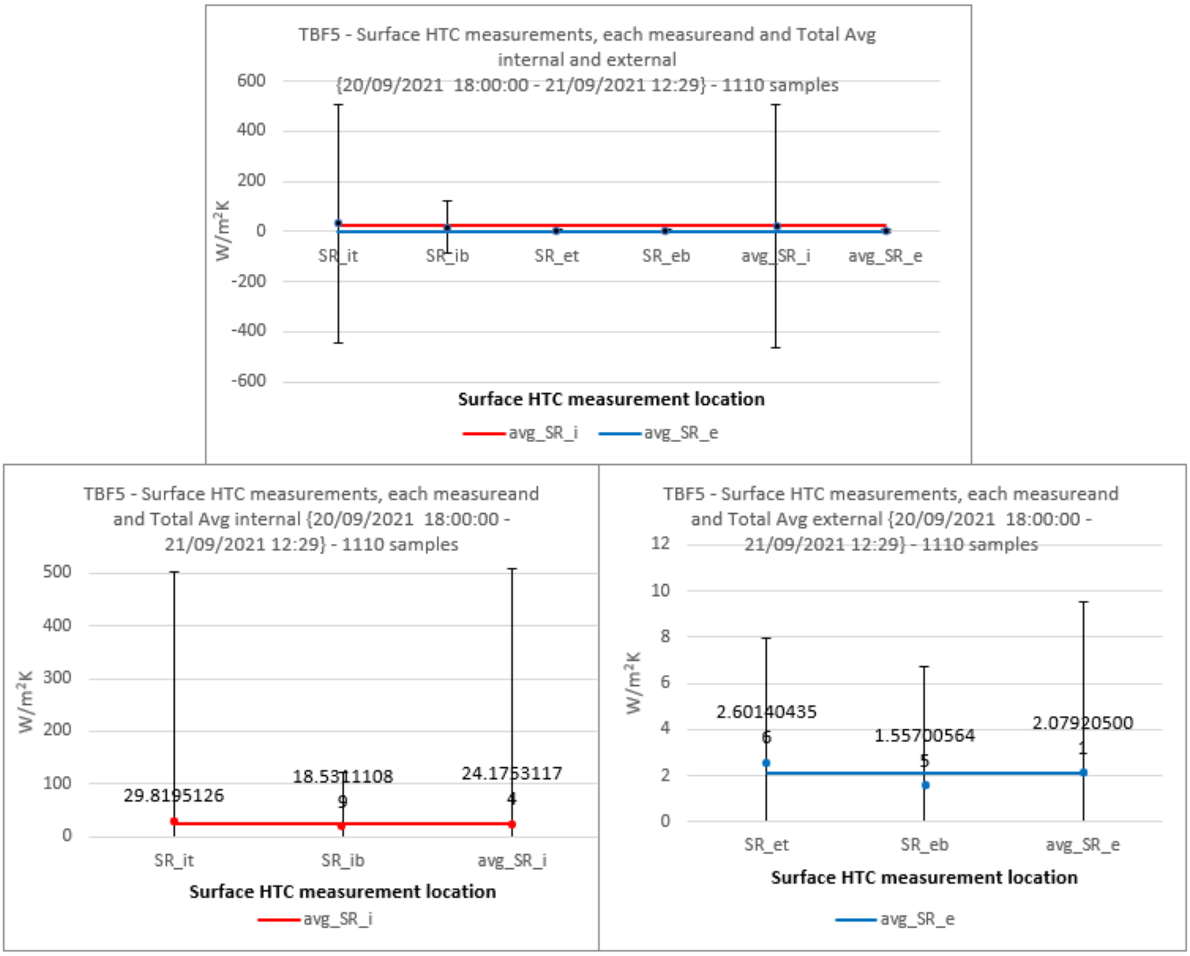

Figure 174 – Surface-fluid HTCs.

Embedded flux values all, top, side

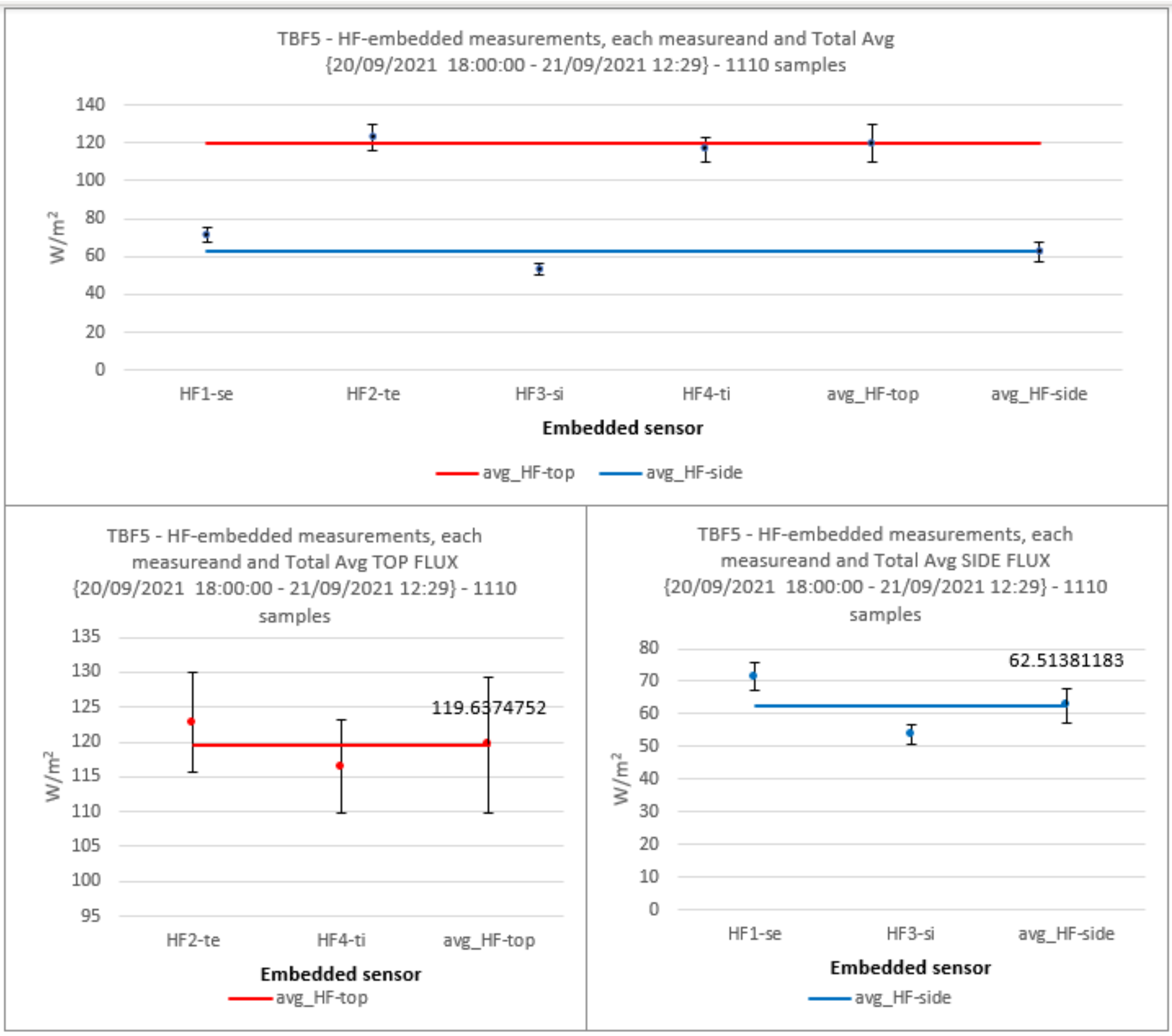

Figure 175 – Embedded flux measurements top, side, and average.

Table of averages and their uncertainties:

		2422	2419	2421	2423					17985 - int top	17984 - int bott	17987 - Ext Top	17986 - Ext Bott	IntST_top	IntAT_top	IntST_Bot	IntAT_Bot	ExtST_top	ExtAT_top	ExtST_bot	ExtAT_bot	ExtGapPly	ExtGapAT	ExtGapOS	IntGapMa	IntGapAT	IntGapInn
		HF1	HF2	HF3	HF4					HF5	HF6	HF7	HF8	T1	T2	T3	T4	T5	T6	T7	T8	T9	T10	T11	T12	T13	T14
	avg	0.076421686	0.127710059	0.055213651	0.123465425	71.4221369	122.7981341	53.60548675	116.4768163	0.170081989	0.302095057	0.10290565	0.040055005	20.82963898	20.92288264	19.60712	19.87288	8.36036	7.670721	5.000991	4.574505	5.098559	5.261892	7.919459	16.34721	14.80018	15.77604
	sd	0.000700348	0.001340611	0.000627409	0.001049593	0.654530453	1.289048731	0.609135366	0.990182367	0.030637442	0.022335103	0.213151715	0.226071627	0.050714675	0.11639815	0.029313	0.059984	0.268992	0.495455	0.212087	0.52485	0.132874	0.152747	0.104147	0.100567	0.126918	0.082651
	N	1110	1110	1110	1110	1110	1110	1110	1110	1110	1110	1110	1110	1110	1110	1110	1110	1110	1110	1110	1110	1110	1110	1110	1110	1110	1110
	uA	2.10209E-05	4.02384E-05	1.88317E-05	3.15036E-05					0.000919583	0.000670388	0.006397751	0.006785542	0.001522202	0.003493692	0.00088	0.0018	0.008074	0.014871	0.006366	0.015753	0.003988	0.004585	0.003126	0.003019	0.003809	0.002481
logger	uB	0.001146325	0.001915651	0.000828205	0.001851981					0.00255123	0.004531426	0.001543585	0.000600825	1.047674386	1.048092352	1.042353	1.043484	1.007833	1.006598	1.00281	1.002351	1.00292	1.00311	1.007031	1.029625	1.024346	1.027618
	uC	0.001146518	0.001916073	0.000828419	0.001852249					0.002711901	0.004580747	0.006581328	0.00681209	1.047675492	1.048098175	1.042353	1.043486	1.007865	1.006708	1.00283	1.002475	1.002928	1.00312	1.007036	1.029629	1.024353	1.027621
				OpTemp	10.03103604	1.433719087																					
			5%		0.95050366			3%					OpTemp														
		fluxteq	microV	±	milliV	UB		hukseflux	microV	±	milliV			±		UB											
		2422	1.07	0.03	0.00107	0.00003	5.90417E-05	17984	61.34	1.84	0.06134	0.00184	19.73999988	1.474910973	1.59484E-05	0.002602											
		2419	1.04	0.03	0.00104	0.00003	5.78182E-05	17985	61.17	1.84	0.06117	0.00184	20.87626081	1.481935802	5.36009E-05	0.002599											
		2421	1.03	0.03	0.00103	0.00003	5.74125E-05	17986	60.32	1.81	0.06032	0.00181	4.787747748	1.417964842	0.000917603	0.002719											
		2423	1.06	0.03	0.00106	0.00003	5.86329E-05	17987	57.36	1.72	0.05736	0.00172	8.015540541	1.424518109	0.000687429	0.002528											
		se	te	si	ti																						
		Flux1	Flux2	Flux3	Flux4	Flux5	Flux6	Flux7	Flux8		dT_t	dT_b		dT_it	dT_ib	dT_et	dT_eb										
W/m2		**71.4221369**	**122.7981341**	**53.60548675**	**116.4768163**	**2.780480451**	**4.924927564**	**1.794031563**	**0.664041867**		13.25216191	15.29837806		0.093243659	0.265765371	0.68964	0.426486										
	c_mV	934.5794393	961.5384615	970.8737864	943.3962264	16.34788295	16.30257581	17.43375174	16.57824934		1.453261822	1.44700358		1.481935802	1.474910973	1.424518	1.417965										
	c_Ss	-66749.66066	-118075.1289	-52044.16189	-109883.7889	-45.45496896	-80.28900495	-31.27670089	-11.00865164																		
[+/-W/m2	uC	4.084080875	7.071128669	3.094339597	6.675559513	0.126192557	0.221884058	0.139347048	0.116831877			side	top														
		5.72%	5.76%	5.77%	5.73%	4.54%	4.51%	7.77%	17.59%			62.51381183	119.6374752		chiller												
						85-it	84-ib	87-et	86-eb																		
side	62.51381183					U1	U2	U3	U4																		
top	119.6374752				c_Q	0.075459386	0.065366407	0.075459386	0.065366407																		
					c_dT	-0.015832386	-0.021043068	-0.010215429	-0.002837296					uavg													
					Avg_U	**0.209813347**	**0.321924817**	**0.13537652**	**0.043406031**		0.265869082	0.089391275		0.177630179													
					uC_U	0.024901248	0.033727212	0.018192326	0.008670508		0.041923704	0.020152876															
					[+/-]	11.87%	10.48%	13.44%	19.98%		15.77%	22.54%															
						SR1	SR2	SR3	SR4	[HTC]																	
					c_Q	10.72458991	3.762717451	1.450032658	2.344740177																		
					c_dT	-319.802044	-69.72733433	-3.772121275	-3.650773691																		
					Avg_SR	**29.8195126**	**18.53111089**	**2.601404356**	**1.557005645**		24.17531174	2.079205001															
					uC_U	473.9280308	102.8449994	5.377252706	5.183911899		484.9586295	7.469122388															
					[+/-]	1589.32%	554.99%	206.71%	332.94%		2006.01%	359.23%															

Figure 176 – All measurements recorded and uncertainty analysis.

	T1	T2	T3	T4	T5	T6	T7	T8	T9	T10	T11	T12	T13	T14
TBF 5mm	IntST	IntAT	IntST	IntAT	ExtST	ExtAT	ExtST	ExtAT	ExtGap	ExtGap	ExtGap	IntGap	IntGap	IntGap
	top	top	Bott	Bott	top	top	bott	bott	Ply	AT	OSB	PIR	AT	EPS
Temps	20.82963898	20.92288264	19.6071172	19.87288257	8.36036036	7.670720721	5.000990991	4.574504505	5.098558559	5.261891892	7.919459459	16.34720699	14.80018018	15.77603604
U-value	U1_int	U2_int	U3_ext	U4_ext	U1_int	U2_int	U3_ext	U4_ext		**Uavg**	**[+/-]**			
	0.209813347	0.321924817	0.13537652	0.043406031	11.87%	10.48%	13.44%	19.98%		**0.177630179**	**26.19%**	0.046515969		
S-HTC	SR1_int	SR2_int	SR3_ext	SR4_ext	SR1_int	SR2_int	SR3_ext	SR4_ext		**SR_int_avg**	**[+/-]**		**SR_ext_avg**	**[+/-]**
	0.033535089	0.05415494	0.251891453	0.361208647	1589.32%	554.99%	206.71%	332.94%		**24.17531174**	**2006.01%**	484.9586295	**2.079205001**	**359.23%**
W/m2K	29.8195126	18.53111089	2.601404356	1.557005645										
	2nd attempt chiller													
Fluxes	Flux1 (se)	Flux2 (te)	Flux3 (si)	Flux4 (ti)	Flux1 (se)	Flux2 (te)	Flux3 (si)	Flux4 (ti)		**F(side)avg**	**[+/-]**		**F(top/bot)avg**	**[+/-]**
	71.4221369	122.7981341	53.60548675	116.4768163	5.72%	5.76%	5.77%	5.73%		**62.51381183**	**8.20%**		**119.6374752**	**8.13%**

Figure 177 – All measurements taken forward as simulation input parameters (temperatures, transmittances, SRs) and output values.

5.1.5 TBK5

The data was acquired between 29/09/2021 16:59 and 30/09/2021 09:30 collecting 992 data points over 22 sensors (8x heat flux, 14x thermocouple) enabling the calculation of measurands U-value and surface-fluid HTC: Heat Flux measurements can be determined by converting mV readings into [W/m^2] using the conversion coefficient, then, after the relevant temperature difference – sensed using pairs of T-type thermocouples – is applied, either the U-value or surface-fluid HTC can be calculated, and their errors propagated.

- Sensor locations (diagram of sensor array) are shown earlier in Figure 120 to Figure 125.

Embedded Flux & Ext Temps / time

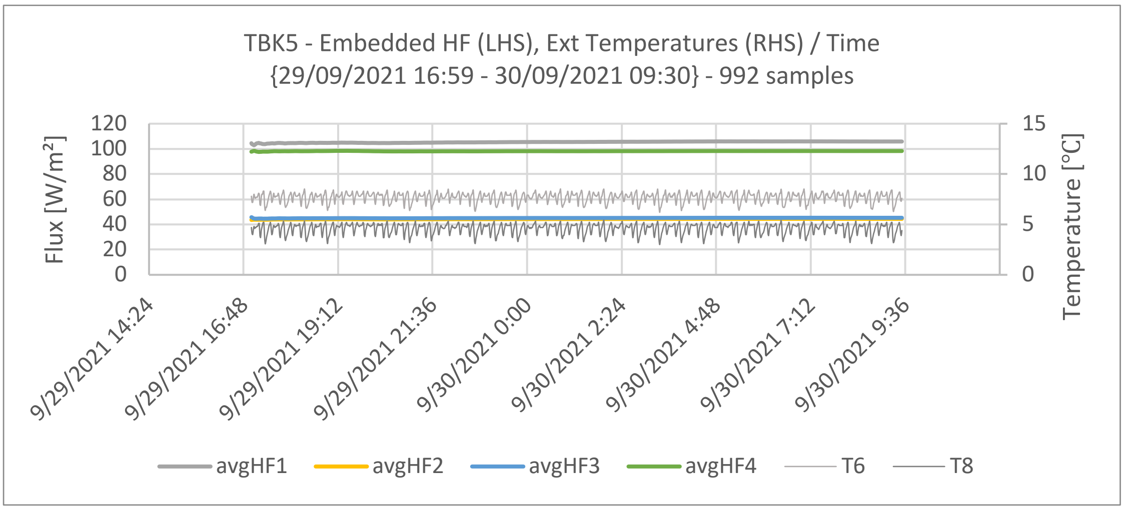

Figure 178 – Embedded flux and external temperatures vs time graph.

U-value & dT / time

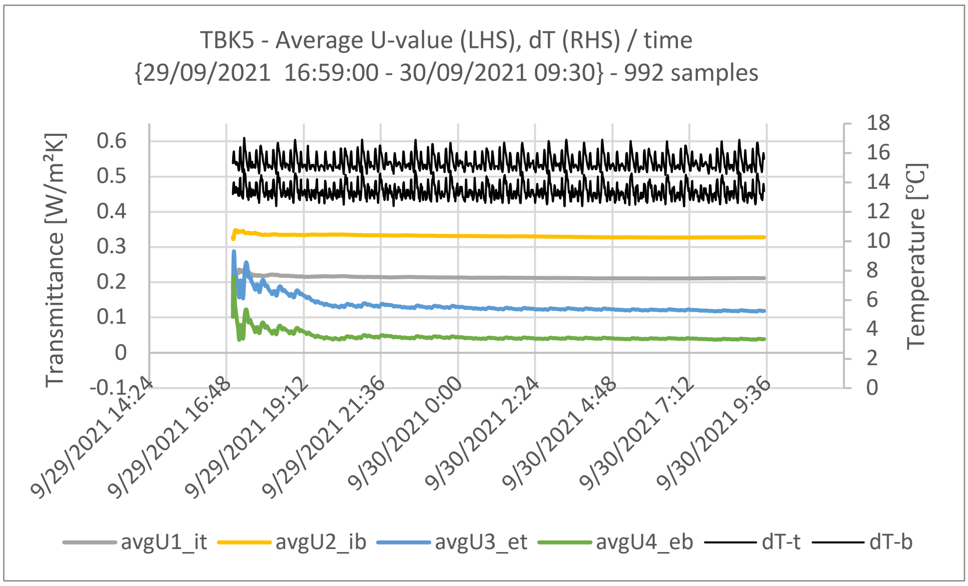

Figure 179 – U-values and temperature difference vs time graph.

U-values measurand and total average & uncertainty interval

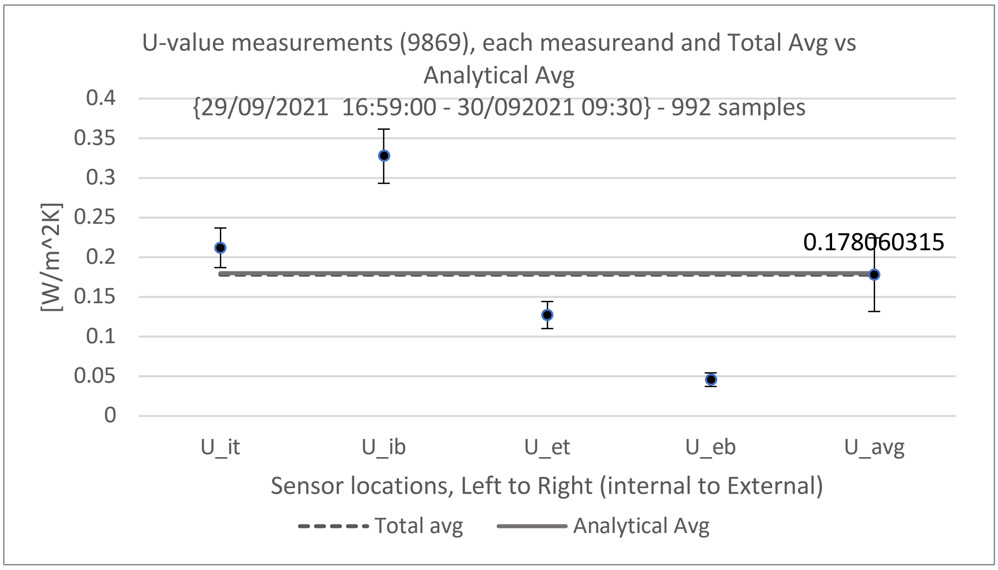

Figure 180 – U-value measurands with uncertainty.

Surface-fluid HTC measurand total, internal, and external

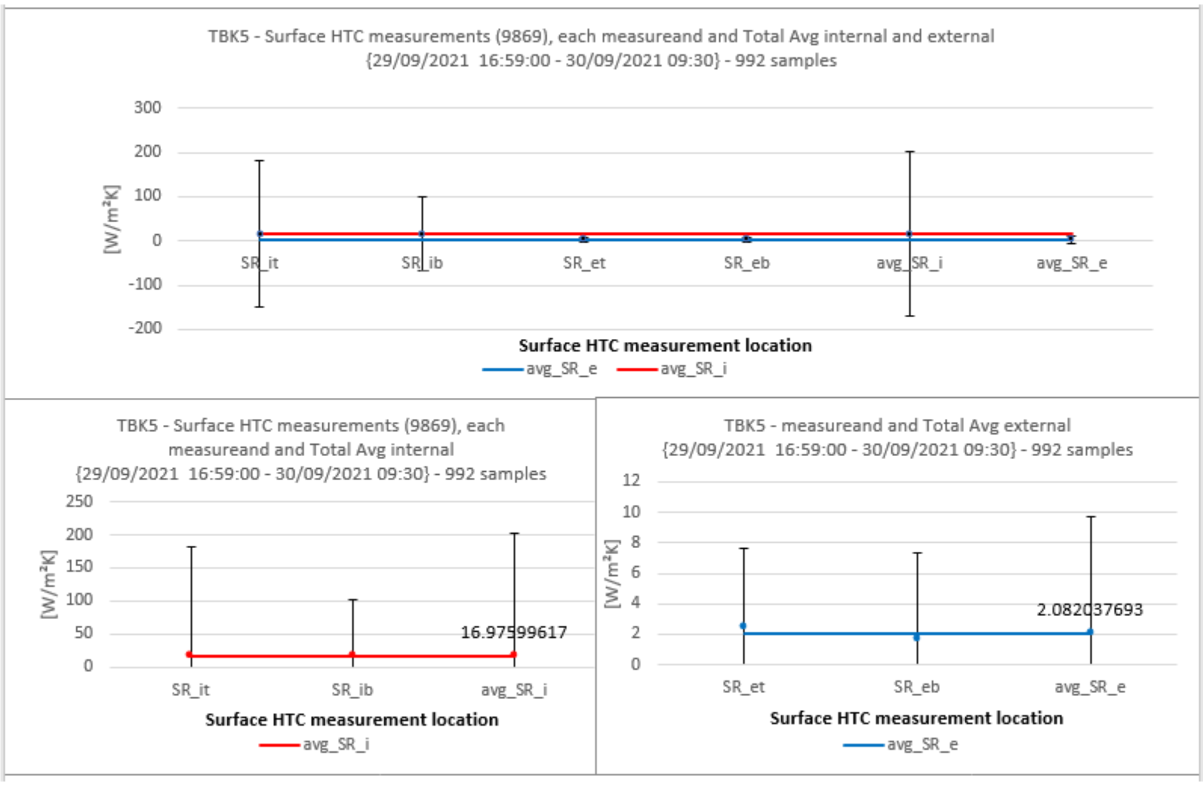

Figure 181 – Surface-fluid HTCs.

Embedded flux values all, top, side

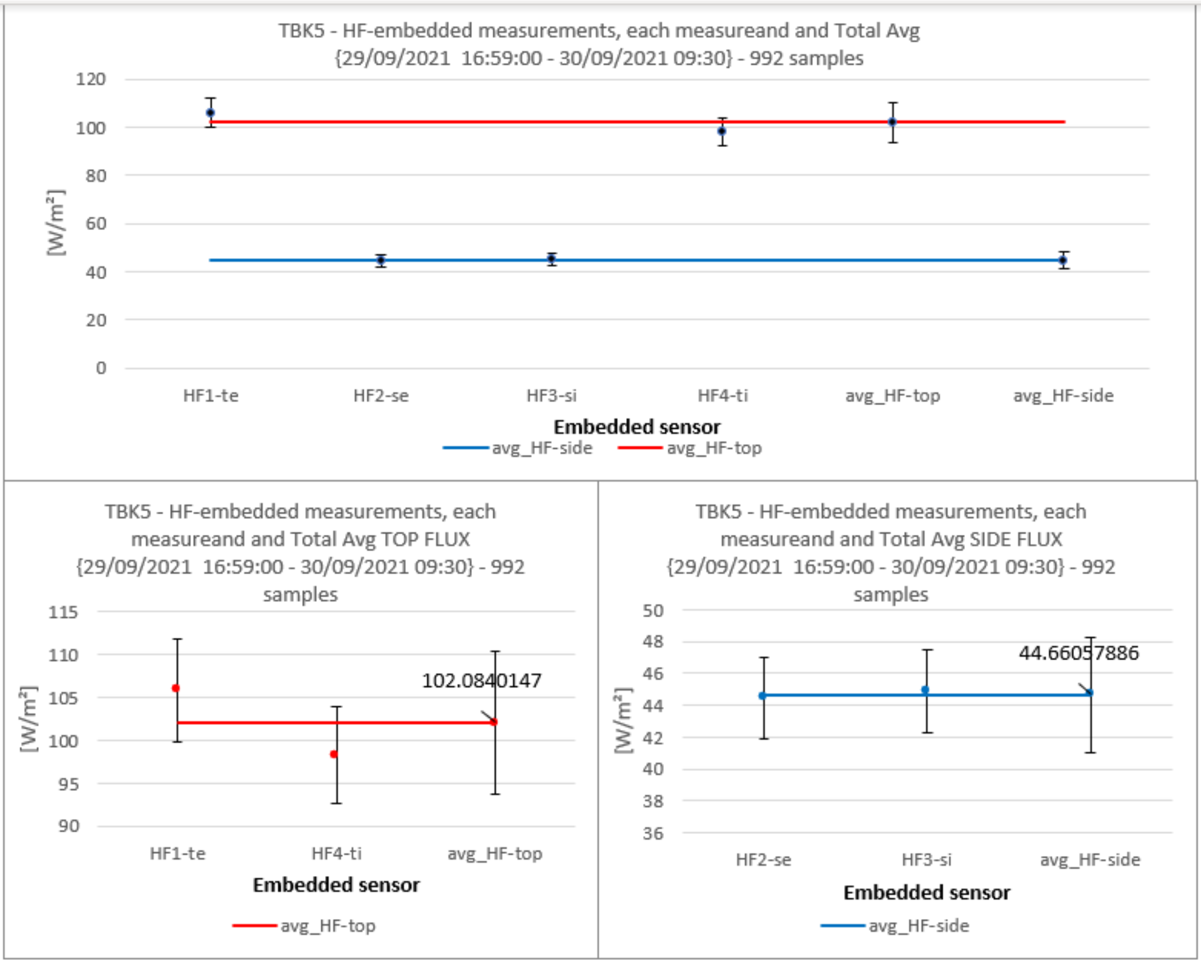

Figure 182 – Embedded flux measurements top, side, and average.

Table of averages and their uncertainties:

		2422	2419	2421	2423					17985 - int t	7984 - int bo	7987 - Ext Tc	986 - Ext B	IntST_top	IntAT_top	IntST_Bot	IntAT_Bot	ExtST_top	ExtAT_top	ExtST_bot	ExtAT_bot	ExtGapPly	ExtGapAT	ExtGapOS	IntGapMa	IntGapAT	IntGapInn
		HF1	HF2	HF3	HF4					HF5	HF6	HF7	HF8	T1	T2	T3	T4	T5	T6	T7	T8	T9	T10	T11	T12	T13	T14
	avg	0.113269	0.046235957	0.046658	0.104207	105.8591	44.45765	45.29908	98.30889	0.173623	0.308918	0.0976977	0.042448	20.90746	21.0746	19.67692	19.97369	8.366532	7.681956	5.010484	4.590625	5.098085	5.250806	7.900706	16.34879	14.78952	15.79476
	sd	0.002363	0.00039309	0.000683	0.000916	2.208852	0.377971	0.662922	0.864255	0.041155	0.0237171	0.1949619	0.206649	21	0.157922	0.042614	0.067377	0.243191	0.474137	0.19373	0.507348	0.111471	0.129435	0.061807	0.112784	0.138289	0.094574
	N	992	992	992	992	992	992	992	992	992	992	992	992	992	992	992	992	992	992	992	992	992	992	992	992	992	992
	uA	7.5E-05	1.24806E-05	2.17E-05	2.91E-05					0.001307	0.000753	0.00619	0.006561	0.6667507	0.005014	0.001353	0.002139	0.007721	0.015054	0.006151	0.016108	0.003539	0.00411	0.001962	0.003581	0.004391	0.003003
logger	uB	0.001699	0.000693539	0.0007	0.001563					0.002604	0.0046338	0.0014655	0.000637	1.0480231	1.048776	1.042648	1.043917	1.007844	1.006617	1.00282	1.002368	1.00292	1.003097	1.006998	1.02963	1.024312	1.027683
	uC	0.001701	0.000693652	0.0007	0.001563					0.002914	0.0046946	0.0063612	0.006592	1.2421388	1.048788	1.042649	1.04392	1.007874	1.00673	1.002839	1.002497	1.002926	1.003105	1.007	1.029637	1.024321	1.027687
				OpTemp	10.02016	1.433685																					
			5%		0.950467			3%					OpTemp														
		fluxteq	microV	±	milliV		UB	hukseflux	microV	±	milliV			±		UB											
		2422	1.07	0.03	0.00107	0.00003	5.9E-05	17984	61.34	1.84	0.06134	0.00184	19.8253	1.4754272	1.07E-05	0.002602											
		2419	1.04	0.03	0.00104	0.00003	5.78E-05	17985	61.17	1.84	0.06117	0.00184	20.99103	1.6256891	6.06E-05	0.002599											
		2421	1.04	0.03	0.00104	0.00003	5.78E-05	17986	60.32	1.81	0.06032	0.00181	4.800554	1.4179871	0.000917	0.002719											
		2423	1.06	0.03	0.00106	0.00003	5.86E-05	17987	57.36	1.72	0.05736	0.00172	8.024244	1.4245398	0.000687	0.002528											
		top ext	side ext	side int	top int																						
		Flux1	Flux2	Flux3	Flux4	Flux5	Flux6	Flux7	Flux8		dT_t	dT_b		dT_it	dT_ib	dT_et	dT_eb										
W/m2		**105.8591**	**44.45765063**	**44.86351**	**98.30889**	**2.83837**	**5.03616**	**1.703238**	**0.703708**		13.392641	15.383065		0.1671372	0.296773	0.684577	0.419859										
	c_mV	934.5794	961.5384615	961.5385	943.3962	16.34788	16.30258	17.43375	16.57825		1.4537747	1.4473317		1.6256891	1.475427	1.42454	1.417987										
	c_Ss	-98933.8	-42747.74099	-43138	-92744.2	-46.4013	-82.1024	-29.6938	-11.6662																		
[+/-W/m2	uC	6.053444	2.559943892	2.583369	5.634176	0.129681	0.22695	0.133918	0.113792		side	top															
		5.72%	5.76%	5.76%	5.73%	4.57%	4.51%	7.86%	16.17%		44.66	102.08															
						85-it	84-ib	87-et	86-eb																		
						U1	U2	U3	U4																		
					c_Q	0.074668	0.065007	0.074668	0.065007																		
					c_dT	-0.01582	-0.02128	-0.0095	-0.00297					uavg													
					Avg_U	**0.211935**	**0.327383**	**0.127177**	**0.045746**		0.2696592	0.0864614		0.1780603													
					uC_U	0.02496	0.034153	0.017046	0.008558		0.0423019	0.0190739															
					[+/-]	11.78%	10.43%	13.40%	18.71%		15.69%	22.06%															
						SR1	SR2	SR3	SR4	[HTC]																	
					c_Q	5.983109	3.369574	1.460757	2.381753																		
					c_dT	-101.607	-57.1807	-3.63439	-3.99196																		
					Avg_SR	**16.98228**	**16.96971**	**2.488017**	**1.676059**		16.975996	2.0820377															
					uC_U	165.1829	84.36943	5.181024	5.667028		185.48209	7.678426															
					[+/-]	972.68%	497.18%	208.24%	338.12%		1092.61%	368.79%															

Figure 183 – All measurements recorded and uncertainty analysis.

	T1	T2	T3	T4	T5	T6	T7	T8	T9	T10	T11	T12	T13	T14
TBK 5mm	IntST	IntAT	IntST	IntAT	ExtST	ExtAT	ExtST	ExtAT	ExtGap	ExtGap	ExtGap	IntGap	IntGap	IntGap
	top	top	Bott	Bott	top	top	bott	bott	Ply	AT	OSB	PIR	AT	EPS
Temps	20.9074596	21.074597	19.67691609	19.97369	8.3665323	7.6819556	5.0104839	4.590625	5.0980847	5.2508065	7.9007056	16.34879018	14.789516	15.794758
U-value	U1_int	U2_int	U3_ext	U4_ext	U1_int	U2_int	U3_ext	U4_ext		**Uavg**	**[+/-]**			
	0.211935069	0.3273834	0.127177162	0.0457456	11.78%	10.43%	13.40%	18.71%		**0.17806**	**26.06%**	0.0464033		
S-HTC	SR1_int	SR2_int	SR3_ext	SR4_ext	SR1_int	SR2_int	SR3_ext	SR4_ext		**SR_int_avg**	**[+/-]**		**SR_ext_avg**	**[+/-]**
	0.1	0.04	0.38	0.5	972.68%	497.18%	208.24%	338.12%		**16.976**	**1092.61%**	185.48209	**2.082038**	**368.79%**
W/m2K	16.98227958	16.96971	2.488016767	1.676059	Chill 3 [preliminary phase]									
Fluxes	Flux1 (te)	Flux2 (se)	Flux3 (si)	Flux4 (ti)	Flux1 (te)	Flux2 (se)	Flux3 (si)	Flux4 (ti)		**F(side)avg**	**[+/-]**		**F(top/bot) avg**	**[+/-]**
	105.8591414	44.457651	44.8635071	98.308888	5.72%	5.76%	5.76%	5.73%		**44.66058**	**8.14%**		**102.084**	**8.10%**

Figure 184 – All measurements taken forward as simulation input parameters (temperatures, transmittances, SRs) and output values.

5.1.6 TBL25

The data was acquired between 14/09/2021 13:00 and 16/09/2021 11:00 collecting 2760 data points over 22 sensors (8x heat flux, 14x thermocouple) enabling the calculation of measurands U-value and surface-fluid HTC: Heat Flux measurements can be determined by converting mV readings into [W/m^2] using the conversion coefficient, then, after the relevant temperature difference – sensed using pairs of T-type thermocouples – is applied, either the U-value or surface-fluid HTC can be calculated, and their errors propagated.

- Sensor locations (diagram of sensor array) are shown earlier in Figure 120 to Figure 125.

Embedded Flux & Ext Temps / time

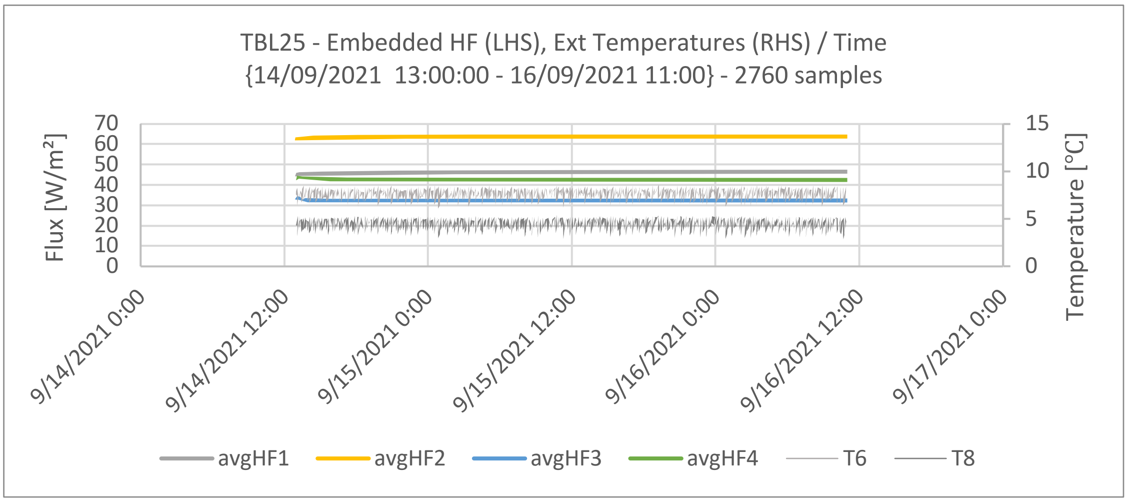

Figure 185 – Embedded flux and external temperatures vs time graph.

U-value & dT / time

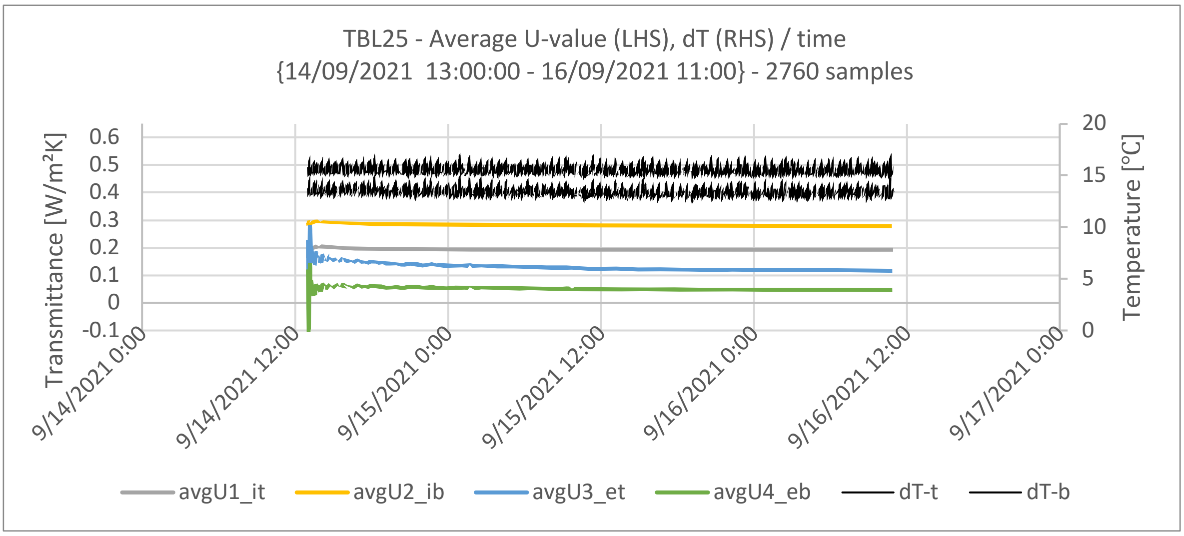

Figure 186 – U-values and temperature difference vs time graph.

U-values measurand and total average & uncertainty interval

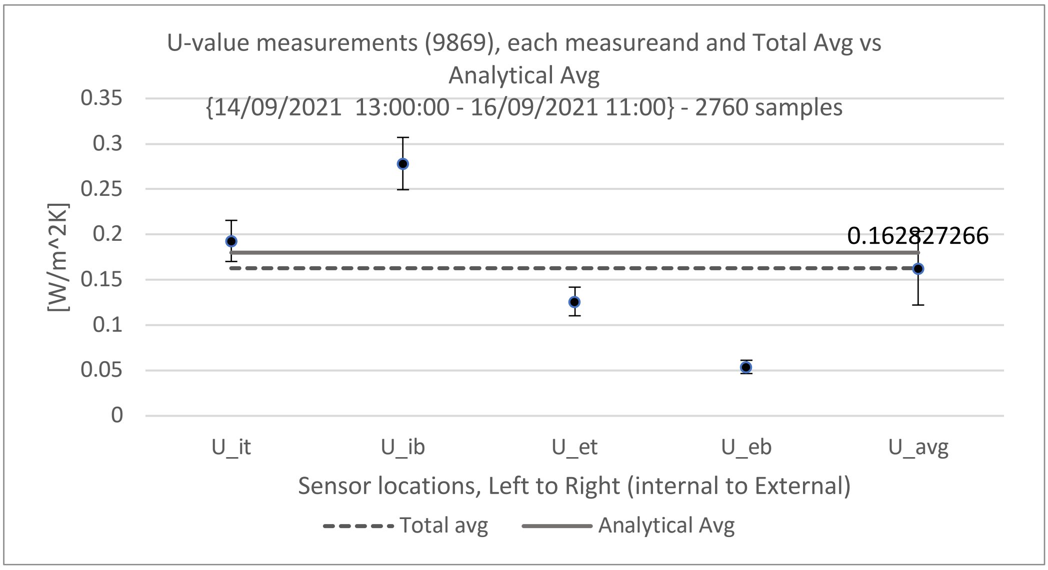

Figure 187 – U-value measurands with uncertainty.

Surface-fluid HTC measurand total, internal, and external

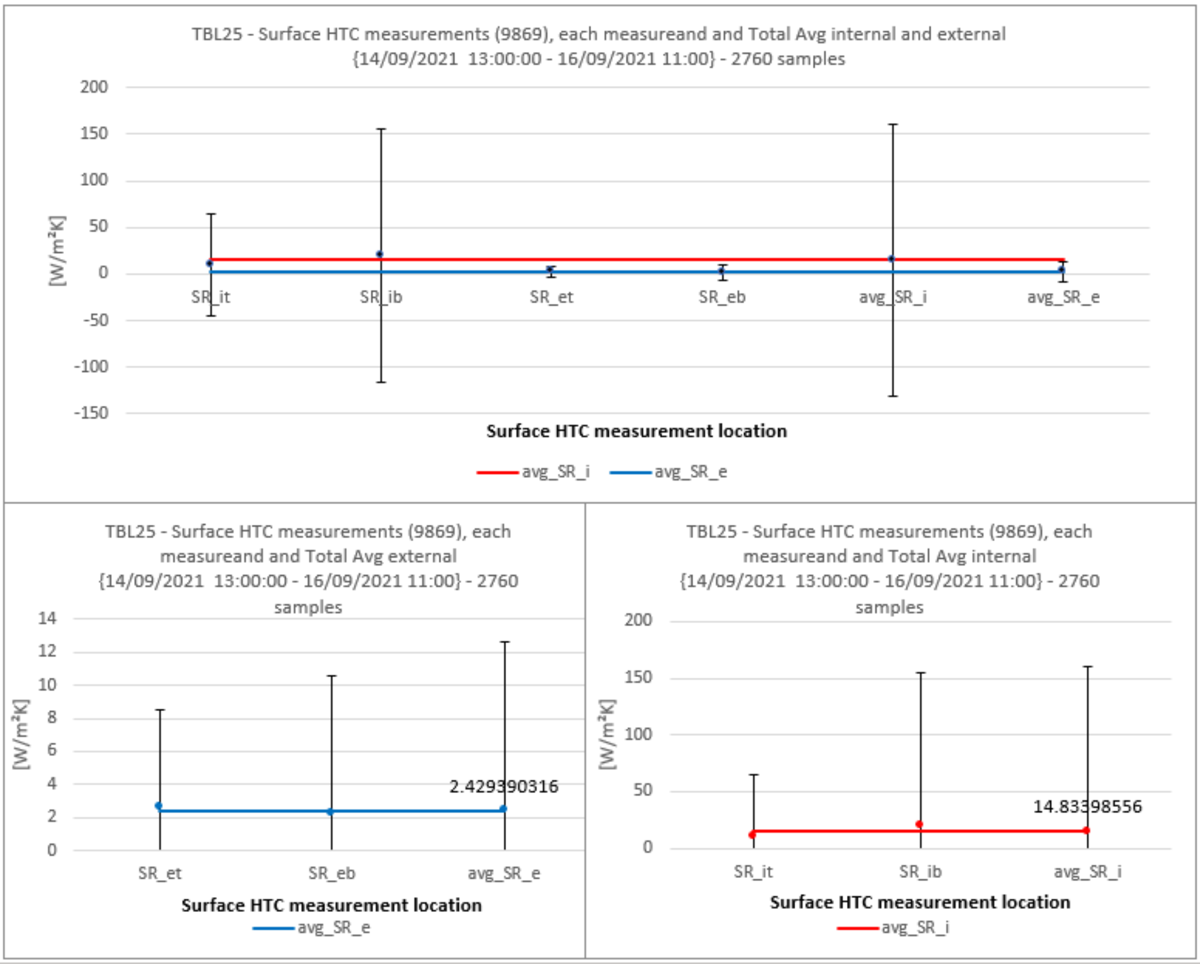

Figure 188 – Surface-fluid HTCs.

Embedded flux values all, top, side

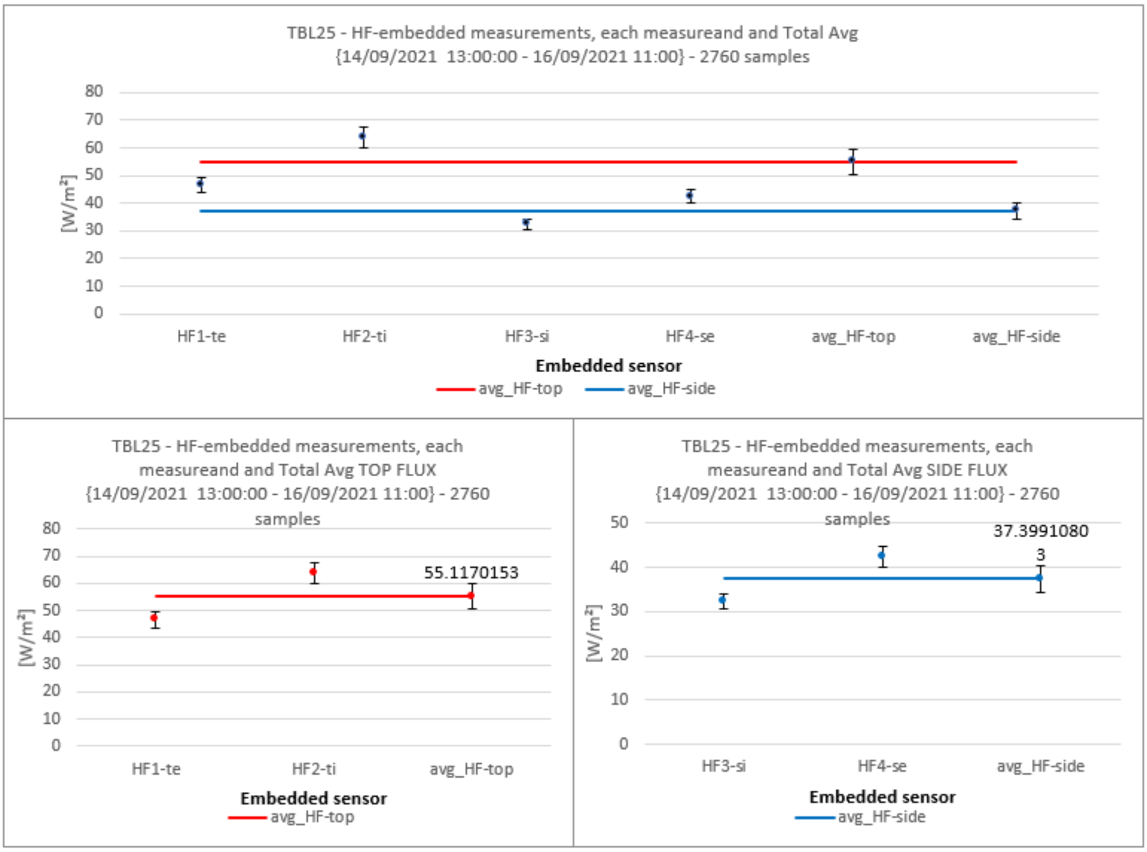

Figure 189 – Embedded flux measurements top, side, and average.

Table of averages and their uncertainties:

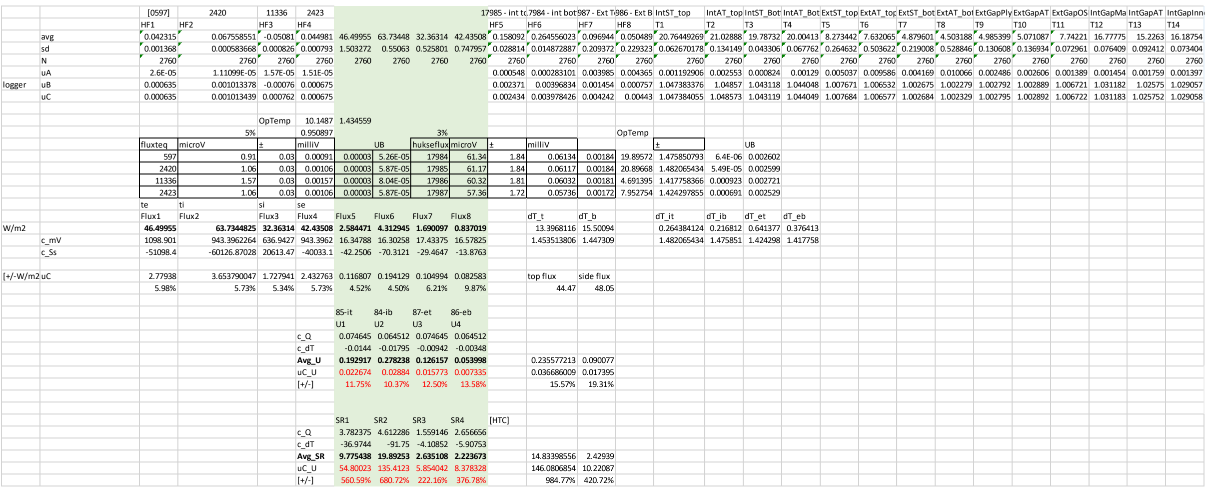

		[0597]	2420	11336	2423					17985 - int t	7984 - int bot	987 - Ext T	986 - Ext B	IntST_top	IntAT_top	IntST_Bot	IntAT_Bot	ExtST_top	ExtAT_top	ExtST_bot	ExtAT_bot	ExtGapPly	ExtGapAT	ExtGapOS	IntGapMa	IntGapAT	IntGapInn
		HF1	HF2	HF3	HF4					HF5	HF6	HF7	HF8	T1	T2	T3	T4	T5	T6	T7	T8	T9	T10	T11	T12	T13	T14
	avg	0.042315	0.067558551	-0.05081	0.044981	46.49955	63.73448	32.36314	42.43508	0.158092	0.264556023	0.096944	0.050489	20.76449269	21.02888	19.78732	20.00413	8.273442	7.632065	4.879601	4.503188	4.985399	5.071087	7.74221	16.77775	15.2263	16.18754
	sd	0.001368	0.000583668	0.000826	0.000793	1.503272	0.55063	0.525801	0.747957	0.028814	0.014872887	0.209372	0.229323	0.062670178	0.134149	0.043306	0.067762	0.264632	0.503622	0.219008	0.528846	0.130608	0.136934	0.072961	0.076409	0.092412	0.073404
	N	2760	2760	2760	2760	2760	2760	2760	2760	2760	2760	2760	2760	2760	2760	2760	2760	2760	2760	2760	2760	2760	2760	2760	2760	2760	2760
	uA	2.6E-05	1.11099E-05	1.57E-05	1.51E-05					0.000548	0.000283101	0.003985	0.004365	0.001192906	0.002553	0.000824	0.00129	0.005037	0.009586	0.004169	0.010066	0.002486	0.002606	0.001389	0.001454	0.001759	0.001397
logger	uB	0.000635	0.001013378	-0.00076	0.000675					0.002371	0.00396834	0.001454	0.000757	1.047383376	1.04857	1.043118	1.044048	1.007671	1.006532	1.002675	1.002279	1.002792	1.002889	1.006721	1.031182	1.02575	1.029057
	uC	0.000635	0.001013439	0.000762	0.000675					0.002434	0.003978426	0.004242	0.00443	1.047384055	1.048573	1.043119	1.044049	1.007684	1.006577	1.002684	1.002329	1.002795	1.002892	1.006722	1.031183	1.025752	1.029058
				OpTemp	10.1487	1.434559																					
			5%		0.950897			3%					OpTemp														
		fluxteq	microV	±	milliV	UB		hukseflux	microV	±	milliV			±		UB											
		597	0.91	0.03	0.00091	0.00003	5.26E-05	17984	61.34	1.84	0.06134	0.00184	19.89572	1.475850793	6.4E-06	0.002602											
		2420	1.06	0.03	0.00106	0.00003	5.87E-05	17985	61.17	1.84	0.06117	0.00184	20.89668	1.482065434	5.49E-05	0.002599											
		11336	1.57	0.03	0.00157	0.00003	8.04E-05	17986	60.32	1.81	0.06032	0.00181	4.691395	1.417758366	0.000923	0.002721											
		2423	1.06	0.03	0.00106	0.00003	5.87E-05	17987	57.36	1.72	0.05736	0.00172	7.952754	1.424297855	0.000691	0.002529											
		te	ti	si	se																						
		Flux1	Flux2	Flux3	Flux4	Flux5	Flux6	Flux7	Flux8		dT_t	dT_b		dT_it	dT_ib	dT_et	dT_eb										
W/m2		**46.49955**	**63.7344825**	**32.36314**	**42.43508**	**2.584471**	**4.312945**	**1.690097**	**0.837019**		13.3968116	15.50094		0.264384124	0.216812	0.641377	0.376413										
	c_mV	1098.901	943.3962264	636.9427	943.3962	16.34788	16.30258	17.43375	16.57825		1.453513806	1.447309		1.482065434	1.475851	1.424298	1.417758										
	c_Ss	-51098.4	-60126.87028	20613.47	-40033.1	-42.2506	-70.3121	-29.4647	-13.8763																		
[+/-W/m2	uC	2.77938	3.653790047	1.727941	2.432763	0.116807	0.194129	0.104994	0.082583		top flux	side flux															
		5.98%	5.73%	5.34%	5.73%	4.52%	4.50%	6.21%	9.87%		44.47	48.05															
						85-it	84-ib	87-et	86-eb																		
						U1	U2	U3	U4																		
					c_Q	0.074645	0.064512	0.074645	0.064512																		
					c_dT	-0.0144	-0.01795	-0.00942	-0.00348																		
					Avg_U	**0.192917**	**0.278238**	**0.126157**	**0.053998**		0.235577213	0.090077															
					uC_U	0.022674	0.02884	0.015773	0.007335		0.036686009	0.017395															
					[+/-]	11.75%	10.37%	12.50%	13.58%		15.57%	19.31%															
						SR1	SR2	SR3	SR4	[HTC]																	
					c_Q	3.782375	4.612286	1.559146	2.656656																		
					c_dT	-36.9744	-91.75	-4.10852	-5.90753																		
					Avg_SR	**9.775438**	**19.89253**	**2.635108**	**2.223673**		14.83398556	2.42939															
					uC_U	54.80023	135.4123	5.854042	8.378328		146.0806854	10.22087															
					[+/-]	560.59%	680.72%	222.16%	376.78%		984.77%	420.72%															

Figure 190 – All measurements recorded and uncertainty analysis.

	T1	T2	T3	T4	T5	T6	T7	T8	T9	T10	T11	T12	T13	T14
TBL	IntST	IntAT	IntST	IntAT	ExtST	ExtAT	ExtST	ExtAT	ExtGap	ExtGap	ExtGap	IntGap	IntGap	IntGap
25mm	top	top	Bott	Bott	top	top	bott	bott	Ply	AT	OSB	PIR	AT	EPS
Temps	20.76449269	21.028877	19.78731821	20.00413	8.273442	7.6320652	4.8796014	4.5031884	4.9853986	5.071087	7.74221014	16.777753	15.226304	16.187537
U-value	U1_int	U2_int	U3_ext	U4_ext	U1_int	U2_int	U3_ext	U4_ext		Uavg	[+/-]			
	0.192916844	0.2782376	0.126156669	0.053998	11.75%	10.37%	12.50%	13.58%		0.162827	24.93%	0.040601		
S-HTC	SR1_int	SR2_int	SR3_ext	SR4_ext	SR1_int	SR2_int	SR3_ext	SR4_ext		SR_int_avg	[+/-]		SR_ext_avg	[+/-]
	0.102297206	0.0502701	0.379491096	0.4497065	571.90%	694.20%	222.77%	378.44%		14.83399	1004.32%	148.9812	2.42939	422.35%
W/m2K	9.775438014	19.89253	2.635107942	2.223673										
Fluxes	Flux1 (te)	Flux2 (ti)	Flux3 (si)	Flux4 (se)	Flux1 (te)	Flux2 (ti)	Flux3 (si)	Flux4 (se)		F(side)avg	[+/-]		F(top/bot) avg	[+/-]
	46.4995481	63.734482	32.36314087	42.435075	5.98%	5.73%	5.34%	5.73%		37.39911	7.98%		55.11702	8.33%

Figure 191 – All measurements taken forward as simulation input parameters (temperatures, transmittances, SRs) and output values.

5.1.7 TBF25

The data was acquired between 26/07/2021 14:26 and 28/07/2021 07:56 collecting 2491 data points over 22 sensors (8x heat flux, 14x thermocouple) enabling the calculation of measurands U-value and surface-fluid HTC: Heat Flux measurements can be determined by converting mV readings into [W/m^2] using the conversion coefficient, then, after the relevant temperature difference – sensed using pairs of T-type thermocouples – is applied, either the U-value or surface-fluid HTC can be calculated, and their errors propagated.

- Sensor locations (diagram of sensor array) are shown earlier in Figure 120 to Figure 125.

Embedded Flux & Ext Temps / time

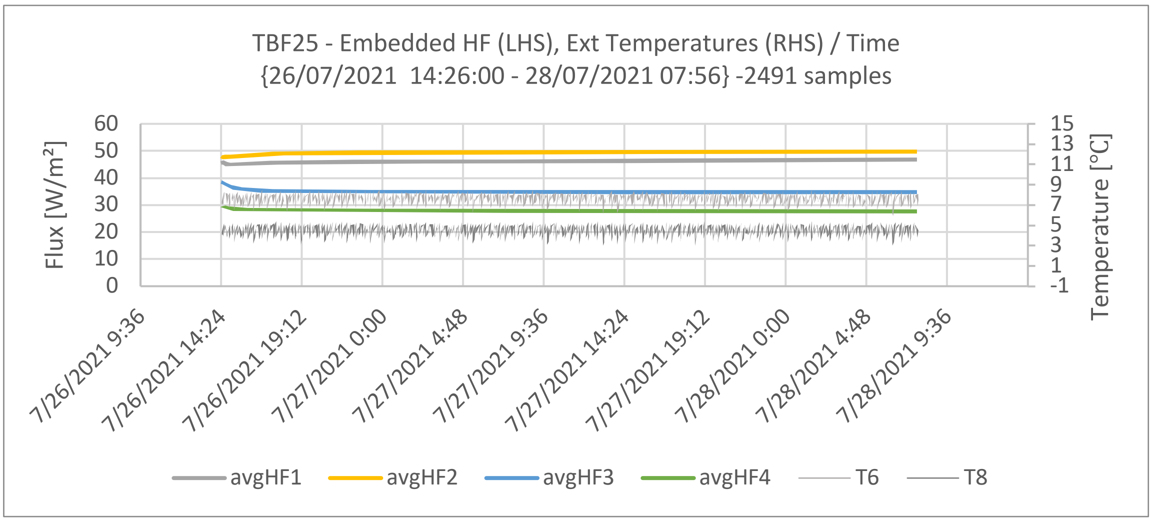

Figure 192 – Embedded flux and external temperatures vs time graph.

U-value & dT / time

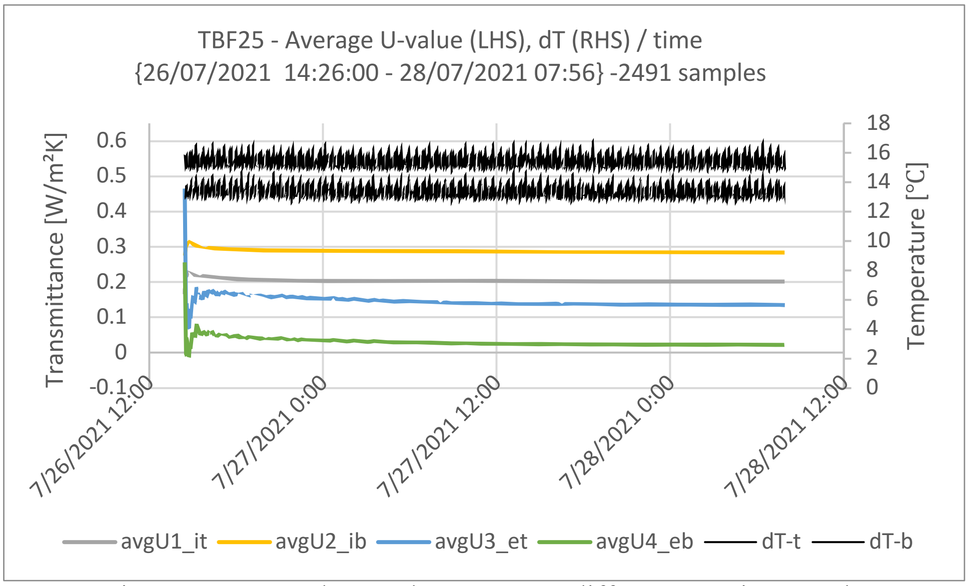

Figure 193 – U-values and temperature difference vs time graph.

U-values measurand and total average & uncertainty interval

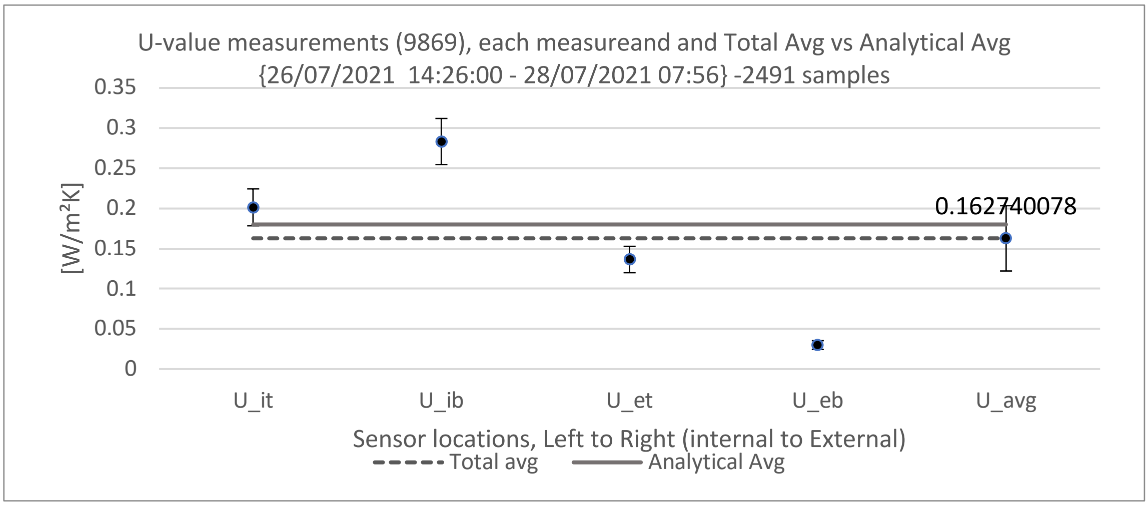

Figure 194 – U-value measurands with uncertainty.

Surface-fluid HTC measurand total, internal, and external

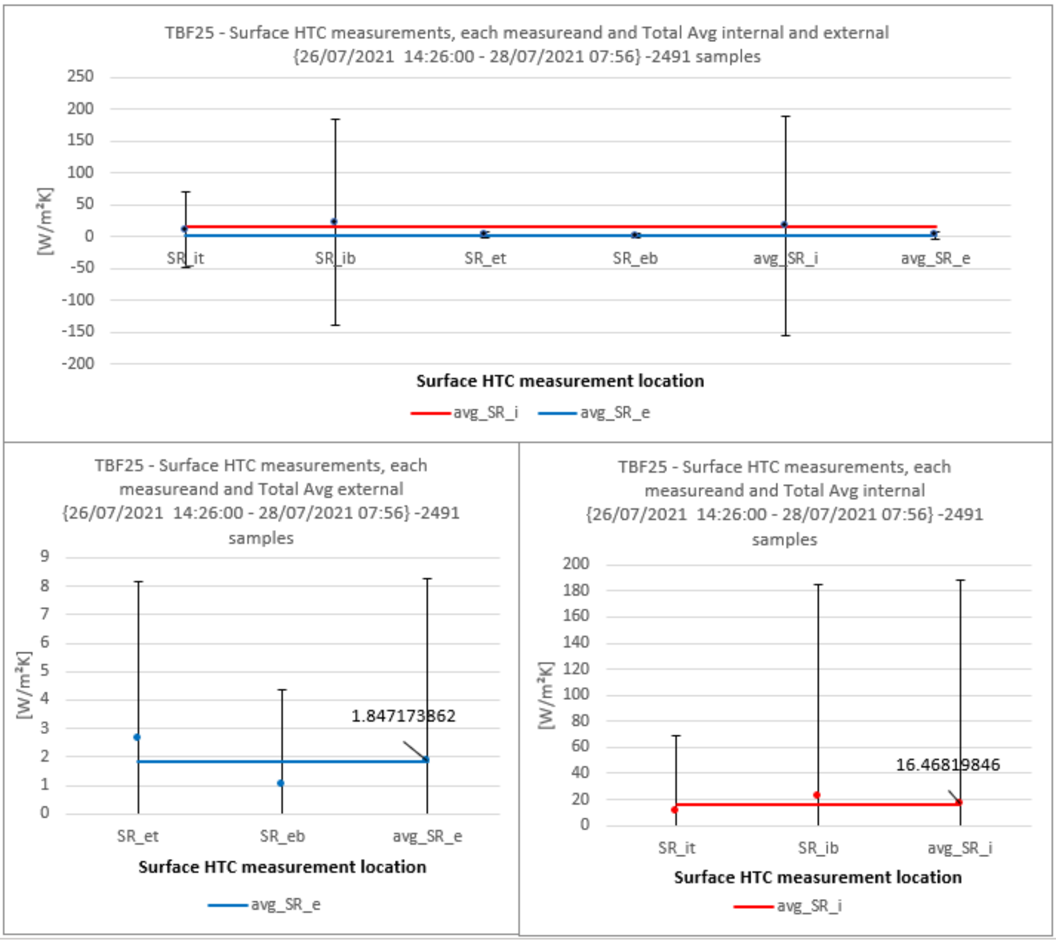

Figure 195 – Surface-fluid HTCs.

Embedded flux values all, top, side

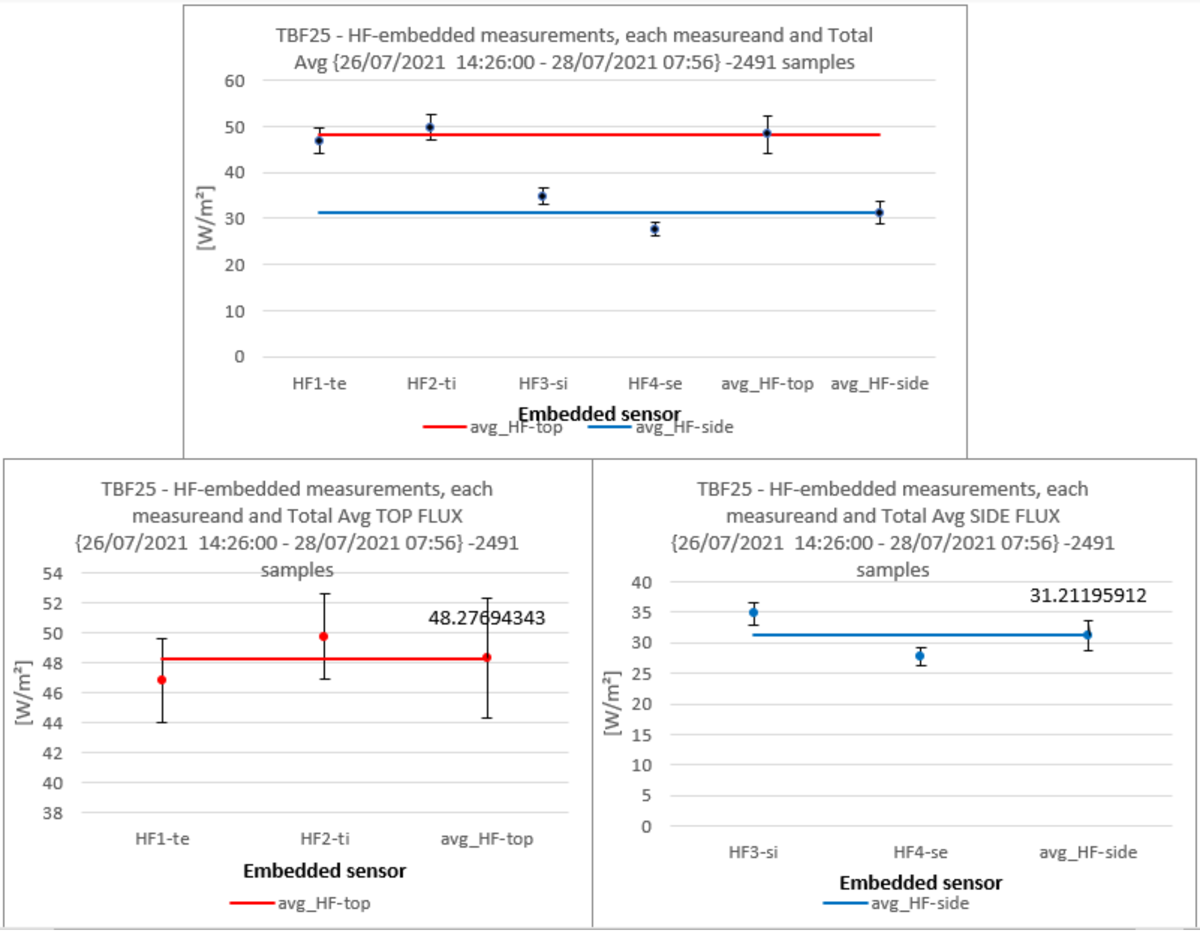

Figure 196 – Embedded flux measurements top, side, and average.

Table of averages and their uncertainties:

			0.91	1.06	1.57	1.06	61.17	61.34	57.36	60.32														
			[0597]	[2420]	[11336]	[2423]	[17985]	[17984]	[17987]	[17986]														
			HF1	HF2	HF3	HF4	HF5	HF6	HF7	HF8	T1	T2	T3	T4	T5	T6	T7	T8	T9	T10	T11	T12	T13	T14
		avg	0.042596675	0.052729015	0.0546	0.044788	0.164562	0.267457	0.109932	0.026397	20.75785	21.01204338	19.76544	19.9605	8.335889201	7.650221	5.014974	4.570935	5.04729	5.030108	7.772461	16.69755	15.18659	16.13898
		sd	0.001477424	0.000622771	0.000842	0.000532	0.028615	0.0168	0.201883	0.199872	0.051761	0.122955048	0.048227	0.058665	0.25270238	0.487313	0.200012	0.51672	0.123298	0.138324	0.067504	0.09993	0.120504	0.098208
		N	2491	2491	2491	2491	2491	2491	2491	2491	2491	2491	2491	2491	2491	2491	2491	2491	2491	2491	2491	2491	2491	2491
		uA	2.96018E-05	1.24779E-05	1.69E-05	1.07E-05	0.000573	0.000337	0.004045	0.004005	0.001037	0.002463539	0.000966	0.001175	0.00506317	0.009764	0.004007	0.010353	0.00247	0.002771	0.001353	0.002002	0.002414	0.001968
t-type	logger	uB	6.3895E-05	7.90935E-05	8.19E-05	6.72E-05	0.000247	0.000401	0.000165	3.96E-05	1.000485	1.000496571	1.000439	1.000448	1.00007817	1.000066	1.000028	1.000024	1.000029	1.000028	1.000068	1.000314	1.000259	1.000293
		uC	7.0419E-05	8.00717E-05	8.36E-05	6.8E-05	0.000624	0.000524	0.004048	0.004005	1.000485	1.000499604	1.00044	1.000449	1.000090987	1.000114	1.000036	1.000077	1.000032	1.000032	1.000069	1.000316	1.000262	1.000295
		OpT	0.954313405	0.954313405	0.954313	0.954313	5.41E-05	8.41E-06	0.000724	0.000872														
	Scali	micro-V	0.91	1.06	1.57	1.62	61.17	61.34	60.32	57.36		dT_t	dT_b	dT_it	dT_ib	dT_et	dT_eb			ST avg	AT avg	avg		
		[+/-]	0.03	0.03	0.03	0.03	1.84	1.84	1.81	1.72		13.36182258	15.38956	0.254195	0.195062522	0.685668	0.444039			12.23501	10.10835	11.17168		
		mV	0.00091	0.00106	0.00157	0.00162	0.06117	0.06134	0.06032	0.05736		1.41464712	1.414585	1.41491	1.414841962	1.414358	1.414294							
	[+/-]		0.00003	0.00003	0.00003	0.00003	0.00184	0.00184	0.00181	0.00172														
3%	5%		0.0000455	0.000053	7.85E-05	0.000081	0.001835	0.00184	0.00181	0.001721														
		uC	0.0000545	6.09016E-05	8.4E-05	8.64E-05	0.002599	0.002602	0.00266	0.002585														
			te	ti	si	se																		
			F1	**F2**	**F3**	**F4**	F5	F6	F7	F8		dT_t	dT_b	dT_it	dT_ib	dT_et	dT_eb							
			46.80953322	**49.74435364**	**34.77691**	**27.64701**	2.690244	4.360236	1.822488	0.46019	**W/m2**	14.32414876	16.5243	0.275852	0.324767364	0.77291	0.382508							
												1.414577472	1.414562	1.414529	1.414504964	1.414469	1.414435							
		c_mv	1098.901099	943.3962264	636.9427	617.284	16.34788	16.30258	16.57825	17.43375														
		c_S	-51439.0475	-46928.63551	-22150.9	-17066.1	-43.9798	-71.0831	-30.2137	-8.02284														
		uF	2.804495901	2.859025208	1.862261	1.474714	0.114769	0.185177	0.104705	0.072834														
			5.99%	5.75%	5.35%	5.33%	4.27%	4.25%	5.75%	15.83%														
							U1	**U2**	**U3**	**U4**														
							0.201338	**0.283324**	**0.136395**	**0.029903**	**W/m2K**		0.16274											
						c_F	0.07484	0.064979	0.07484	0.064979														
						c_dT	-0.01507	-0.01841	-0.01021	-0.00194														
						uU	0.022982	0.028688	0.01643	0.005473														
							11.41%	10.13%	12.05%	18.30%														
							SR1	**SR2**	**SR3**	**SR4**			**SR1**	**SR2**	**SR3**	**SR4**								
							0.094488	**0.044737**	**0.376227**	**0.964902**	**m2K/W**		**10.58338**	**22.35302**	**2.657972905**	**1.036375**								
						c_dT	0.371713	0.229345	0.5487	2.173014		c_F	3.933984	5.126561	1.458430913	2.252057								
						c_F	-0.03512	-0.01026	-0.20644	-2.09675		c_dT	-41.6348	-114.594	-3.87646985	-2.33397								
						uSR	0.525956	0.324493	0.77636	3.077072		uSR	58.91127	162.1354	5.484842908	3.304999								
							556.64%	725.34%	206.35%	318.90%			556.64%	725.34%	206.35%	318.90%								

Figure 197 – All measurements recorded and uncertainty analysis.

	T1	T2	T3	T4	T5	T6	T7	T8	T9	T10	T11	T12	T13	T14
TBF	IntST	IntAT	IntST	IntAT	ExtST	ExtAT	ExtST	ExtAT	ExtGap	ExtGap	ExtGap	IntGap	IntGap	IntGap
25mm	top	top	Bott	Bott	top	top	bott	bott	Ply	AT	OSB	PIR	AT	EPS
Temps	20.75784812	21.01204338	19.76543527	19.960498	8.3358892	7.6502208	5.0149739	4.5709354	5.0472902	5.0301084	7.7724609	16.697552	15.186592	16.138981
U-value	U1_int	U2_int	U3_ext	U4_ext	U1_int	U2_int	U3_ext	U4_ext		Uavg	[+/-]			
	0.201338126	0.283324258	0.136395169	0.0299028	11.41%	10.13%	12.05%	18.30%		0.16274	24.97%	0.040633		
S-HTC	SR1_int	SR2_int	SR3_ext	SR4_ext	SR1_int	SR2_int	SR3_ext	SR4_ext		SR_int_avg	[+/-]		SR_ext_avg	[+/-]
	0.094487795	0.044736686	0.376226559	0.9649019	556.64%	725.34%	206.35%	318.9%		16.4682	1047.51%	172.5063	1.847174	#VALUE!
W/m2K	10.5833775	22.35301942	2.657972905	1.036375	Chill 2 [preliminary phase]									
Fluxes	Flux1 (te)	Flux2 (ti)	Flux3 (si)	Flux4 (se)	Flux1 (te)	Flux2 (ti)	Flux3 (si)	Flux4 (se)		F(side)avg	[+/-]		F(top/bot) avg	[+/-]
	46.80953322	49.74435364	34.77690974	27.647008	6%	5.75%	5.35%	5.33%		31.21196	7.60%		48.27694	8.30%

Figure 198 – All measurements taken forward as simulation input parameters (temperatures, transmittances, SRs) and output values.

5.1.8 TBK25

The data was acquired between 11/07/2021 15:00 and 13/07/2021 08:00 collecting 2461 data points over 22 sensors (8x heat flux, 14x thermocouple) enabling the calculation of measurands U-value and surface-fluid HTC: Heat Flux measurements can be determined by converting mV readings into [W/m^2] using the conversion coefficient, then, after the relevant temperature difference – sensed using pairs of T-type thermocouples – is applied, either the U-value or surface-fluid HTC can be calculated, and their errors propagated.

- Sensor locations (diagram of sensor array) are shown earlier in Figure 120 to Figure 125.

Embedded Flux & Ext Temps / time

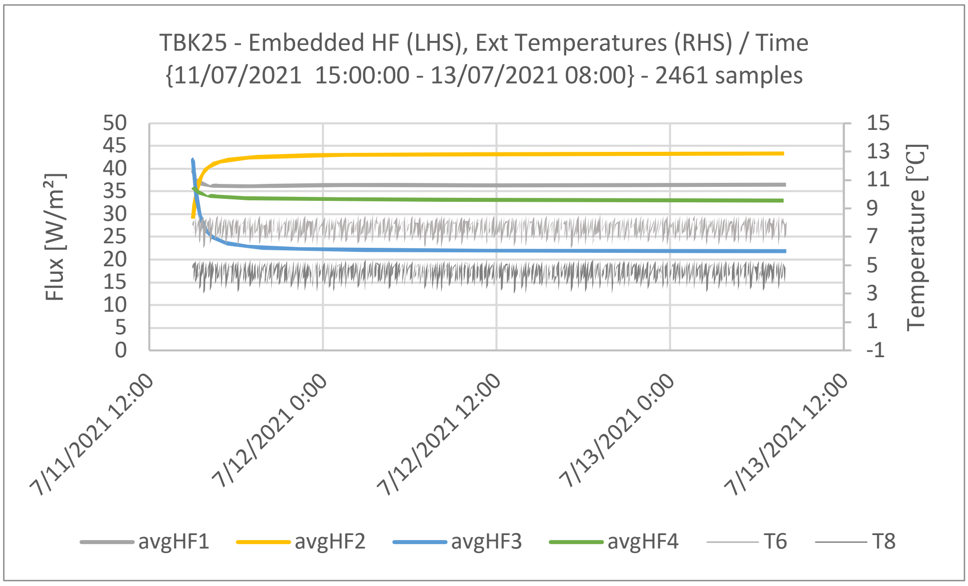

Figure 199 – Embedded flux and external temperatures vs time graph.

U-value & dT / time

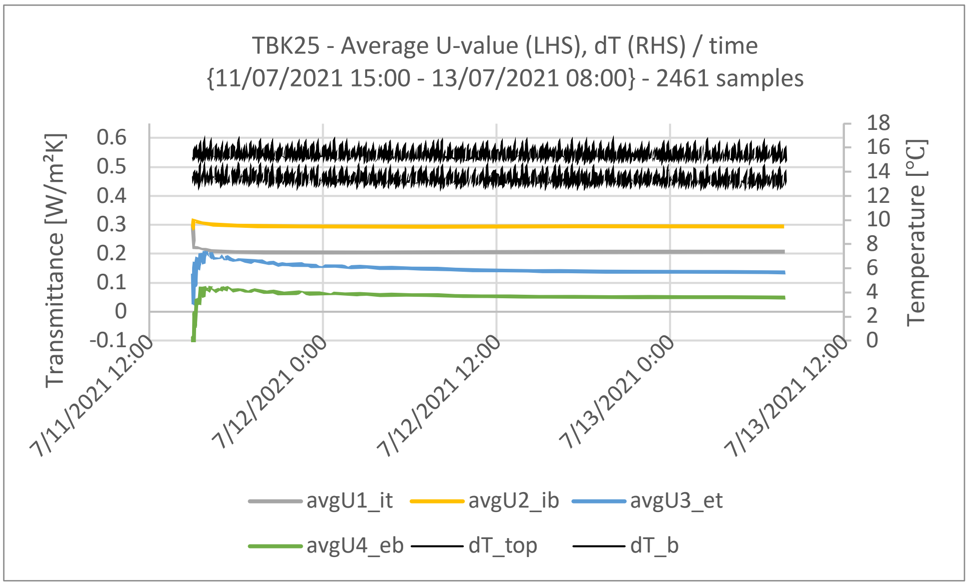

Figure 200 – U-values and temperature difference vs time graph.

U-values measurand and total average & uncertainty interval

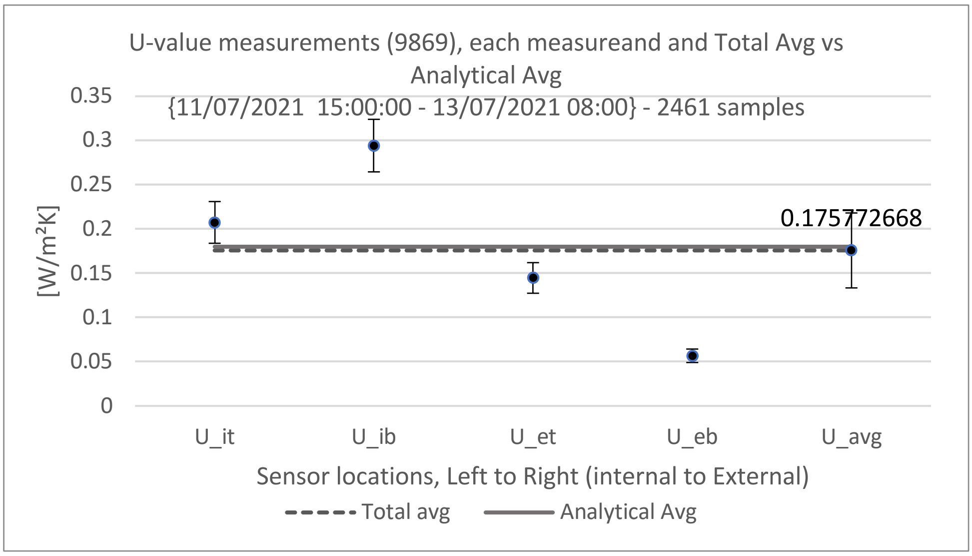

Figure 201 – U-value measurands with uncertainty.

Surface-fluid HTC measurand total, internal, and external

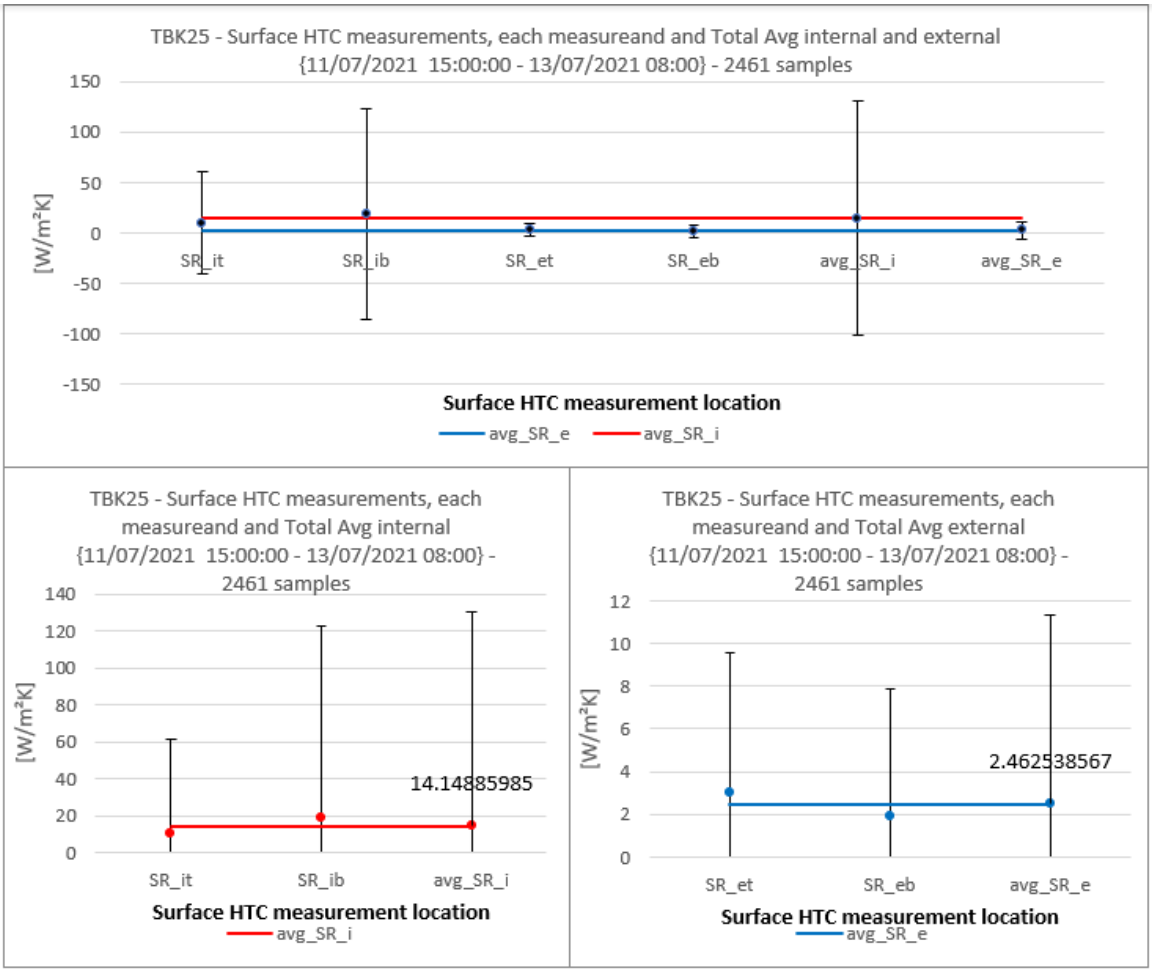

Figure 202 – Surface-fluid HTCs.

Embedded flux values all, top, side

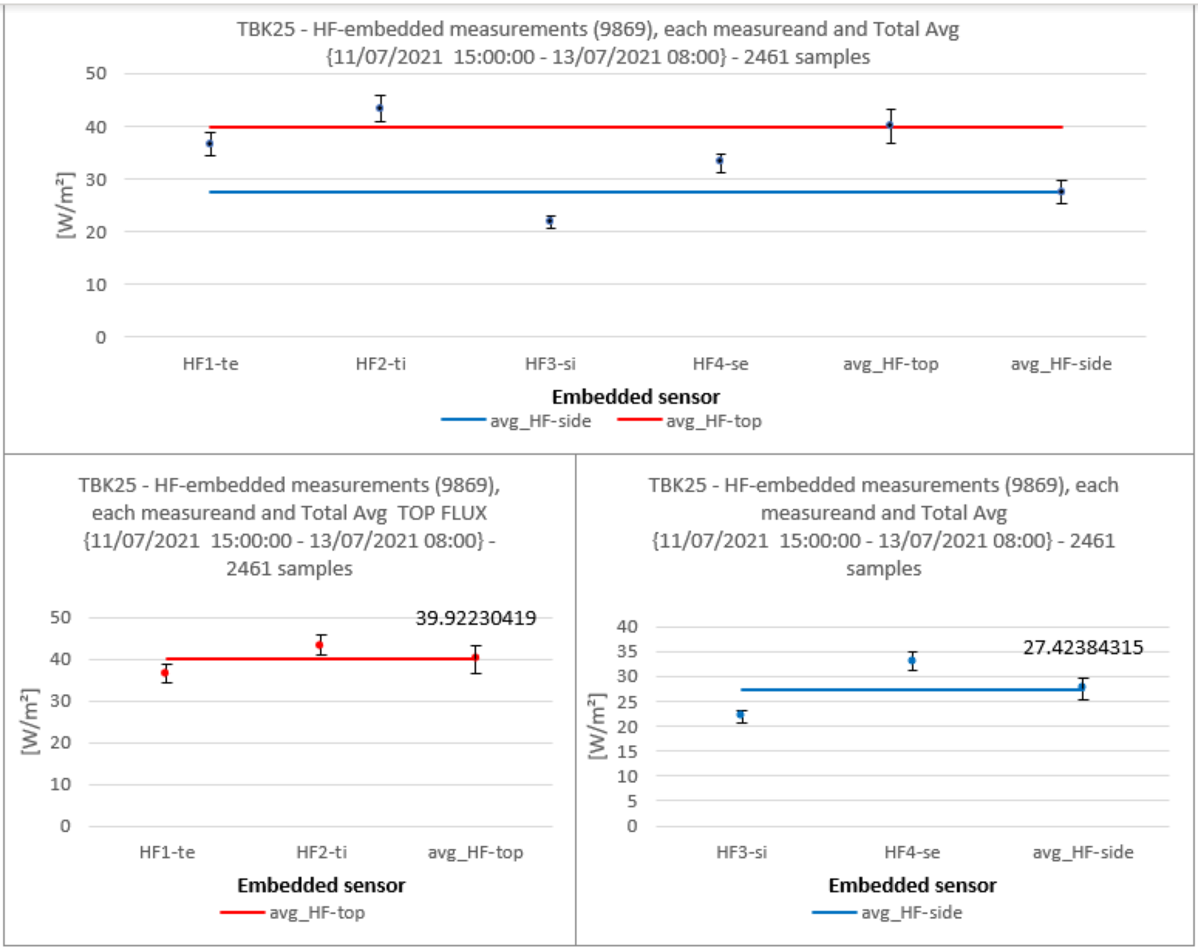

Figure 203 – Embedded flux measurements top, side, and average.

Table of averages and their uncertainties:

			top_ext	top_int	side_int	side_ext	Int_Top	Int_Bott	Ext_Top	Ext_Bott	ST_int_To	AT_int_To	ST_int_Bo	AT_int_Bc	ST_ext_Tc	AT_ext_Tc	ST_ext_Bc	AT_ext_Bc	ExtGap_pl	ExtGap_A	ExtGap_O	IntGap_M	IntGap_AT	IntGap_Inr
		CHILLER	HF1	HF2	HF3	HF4	HF5	HF6	HF7	HF8	T1	T2	T3	T4	T5	T6	T7	T8	T9	T10	T11	T12	T13	T14
		AVG	0.033209	0.045952	0.034317415	0.053443	0.170429	0.279009	0.117207	0.05027	20.7846	21.06294	19.72804	19.97676	8.277692	7.631735	4.977408	4.520236	5.035636	5.035473	7.779074	16.52243	15.01824	16.01495
		sd	0.001408	0.000871	0.001932513	0.000922	0.029858	0.016516	0.204571	0.216631	0.059341	0.133773	0.044917	0.064412	0.257709	0.507926	0.198965	0.527201	0.119943	0.154327	0.068157	0.068542	0.090218	0.066459
		N	2461	2461	2461	2461	2461	2461	2461	2461	2461	2461	2461	2461	2461	2461	2461	2461	2461	2461	2461	2461	2461	2461
		Ua	2.84E-05	1.76E-05	3.89553E-05	1.86E-05	0.000602	0.000333	0.004124	0.004367	0.001196	0.002697	0.000905	0.001298	0.005195	0.010239	0.004011	0.010627	0.002418	0.003111	0.001374	0.001382	0.001819	0.00134
		Ub	4.98E-05	6.89E-05	5.14761E-05	8.02E-05	0.000256	0.000419	0.000176	7.54E-05	1.000486	1.000499	1.000438	1.000449	1.000077	1.000066	1.000028	1.000023	1.000029	1.000029	1.000068	1.000307	1.000254	1.000288
		Uc	5.73E-05	7.11E-05	6.45547E-05	8.23E-05	0.000654	0.000535	0.004127	0.004367	1.000487	1.000503	1.000438	1.00045	1.000091	1.000118	1.000036	1.000079	1.000031	1.000033	1.000069	1.000308	1.000255	1.000289
		OpT	0.954037	0.954037	0.95403661	0.954037	5.65E-05	9.05E-06	0.000727	0.000875														
	Scali	micro-V	0.91	1.06	1.57	1.62	61.17	61.34	60.32	57.36		dT_t	dT_b	dT_it	dT_ib	dT_et	dT_eb			ST avg	AT avg	avg		
		[+/-]	0.03	0.03	0.03	0.03	1.84	1.84	1.81	1.72		13.43121	15.45652	0.278343	0.24872	0.645957	0.457172			12.15075	10.02686	11.08881		
		mV	0.00091	0.00106	0.00157	0.00162	0.06117	0.06134	0.06032	0.05736		1.414652	1.414588	1.414913	1.414841	1.414361	1.414295							
	[+/-]		0.00003	0.00003	0.00003	0.00003	0.00184	0.00184	0.00181	0.00172														
3%	5%		4.55E-05	0.000053	0.0000785	0.000081	0.001835	0.00184	0.00181	0.001721														
		uC	5.45E-05	6.09E-05	8.40372E-05	8.64E-05	0.002599	0.002602	0.002661	0.002586														
			te	ti	si	se																		
			F1	**F2**	**F3**	**F4**	F5	F6	F7	F8		dT_t	dT_b	dT_it	dT_ib	dT_et	dT_eb							
			36.49335	**43.35126**	**21.85822603**	**32.98946**	2.786151	4.548566	1.943093	0.876395	**W/m2**	14.32415	16.5243	0.275852	0.324767	0.77291	0.382508							
												1.414577	1.414562	1.414529	1.414505	1.414469	1.414435							
		c_mv	1098.901	943.3962	636.9426752	617.284	16.34788	16.30258	16.57825	17.43375														
		c_S	-40102.6	-40897.4	-13922.43696	-20363.9	-45.5477	-74.1533	-32.2131	-15.2789														
		uF	2.186499	2.49162	1.170724818	1.759704	0.118874	0.193167	0.10967	0.085779														
			5.99%	5.75%	5.36%	5.33%	4.27%	4.25%	5.64%	9.79%														
							U1	**U2**	**U3**	**U4**														
							0.207439	**0.294281**	**0.14467**	**0.056701**	**W/m2K**													
						c_F	0.074453	0.064698	0.074453	0.064698														
						c_dT	-0.01544	-0.01904	-0.01077	-0.00367														
						uU	0.023573	0.029691	0.017287	0.007598														
							11.36%	10.09%	11.95%	13.40%														
							SR1	**SR2**	**SR3**	**SR4**			**SR1**	**SR2**	**SR3**	**SR4**								
							0.099902	**0.054681**	**0.332438**	**0.52165**	**m2K/W**		**10.00979**	**18.28793**	**3.008084**	**1.916993**								
						c_dT	0.358918	0.21985	0.514643	1.141038		c_F	3.592695	4.020592	1.548091	2.187361								
						c_F	-0.03586	-0.01202	-0.17109	-0.59522		c_dT	-35.9621	-73.5283	-4.65679	-4.19316								
						uSR	0.507856	0.311061	0.728133	1.614571		uSR	50.88508	104.0338	6.588566	5.933328								
							508.35%	568.87%	219.03%	309.51%			508.35%	568.87%	219.03%	309.51%								

Figure 204 – All measurements recorded and uncertainty analysis.

	T1	T2	T3	T4	T5	T6	T7	T8	T9	T10	T11	T12	T13	T14
TBK	IntST	IntAT	IntST	IntAT	ExtST	ExtAT	ExtST	ExtAT	ExtGap	ExtGap	ExtGap	IntGap	IntGap	IntGap
25mm	top	top	Bott	Bott	top	top	bott	bott	Ply	AT	OSB	PIR	AT	EPS
Temps	20.78459939	21.062942	19.728038	19.97675742	8.277692	7.6317351	4.9774076	4.5202357	5.0356359	5.0354734	7.7790735	16.52243	15.018245	16.014953
U-value	U1_int	U2_int	U3_ext	U4_ext	U1_int	U2_int	U3_ext	U4_ext		Uavg	[+/-]			
	0.207438637	0.2942813	0.14467	0.056700681	11.36%	10.09%	11.95%	13.40%		**0.175773**	**24.10%**	0.042354		
S-HTC	SR1_int	SR2_int	SR3_ext	SR4_ext	SR1_int	SR2_int	SR3_ext	SR4_ext		**SR_int_avg**	[+/-]		**SR_ext_avg**	[+/-]
	0.09990218	0.0546809	0.3324375	0.52165031	508.35%	568.87%	219.03%	309.51%		**14.14886**	**818.52%**	115.8116	**2.462539**	**360.05%**
W/m2K	10.0097915	18.28793	3.008084	1.916993013	Chill 1 [preliminary phase]									
Fluxes	Flux1 (te)	Flux2 (ti)	Flux3 (si)	Flux4 (se)	Flux1 (te)	Flux2 (ti)	Flux3 (si)	Flux4 (se)		**F(side)avg**	[+/-]		**F(top/bot) avg**	[+/-]
	36.49334721	43.351261	21.858226	32.98946027	6%	6%	5%	5%		**27.42384**	**7.71%**		**39.9223**	**8.30%**

Figure 205 – All measurements taken forward as simulation input parameters (temperatures, transmittances, SRs) and output values.

The following collates all measurement phases into tables and graphs:

- Table 27 shows the measured U-values whilst Figure 206 represents them in graphical form including uncertainty.
- Table 28 shows the measured SR whilst Figure 207 graphs these values and uncertainties.
- Table 29 shows the embedded flux measurements per phase whilst Figure 208 graphs these with their uncertainty.
- Table 30 & Table *31* show the remaining average temperature measurement for each test phase.

5.2 Total summary of measurement results

Measured U-values and dT's are shown in the following Table 27 and Figure 206:

U-value	U1_it [W/m^{2}K]	U2_ib [W/m^{2}K]	U3_et [W/m^{2}K]	U4_eb [W/m^{2}K]		U_avg [W/m^{2}K]		dT_avg [°C]
Baseline	0.152	0.247	0.196	0.181		0.194		14.99
[+/-]	10.75%	10.67%	10.94%	11.14%		22.04%		1.41
SO	0.211	0.309	0.109	0.050		0.170		14.35
[+/-]	11.82%	10.43%	14.01%	17.90%		26.16%		1.41
TBL5	0.215	0.322	0.114	0.038		0.172		14.29
[+/-]	11.85%	10.47%	12.82%	16.31%		26.21%		1.41
TBF5	0.210	0.322	0.135	0.043		0.178		14.28
[+/-]	11.87%	10.48%	13.44%	19.98%		26.19%		1.41
TBK5	0.212	0.327	0.127	0.046		0.178		14.39
[+/-]	11.78%	10.43%	13.40%	18.71%		26.06%		1.41
TBL25	0.193	0.278	0.126	0.054		0.163		14.45
[+/-]	11.75%	10.37%	12.50%	13.58%		24.93%		1.41
TBF25	0.201	0.283	0.136	0.030		0.163		14.38
[+/-]	11.41%	10.13%	12.05%	18.30%		24.97%		1.41
TBK25	0.207	0.294	0.145	0.057		0.176		14.44
[+/-]	11.36%	10.09%	11.95%	13.40%		24.10%		1.41

Table 27 – Measured U-values (individual and average) and measured temperature °C difference with their respective uncertainties.

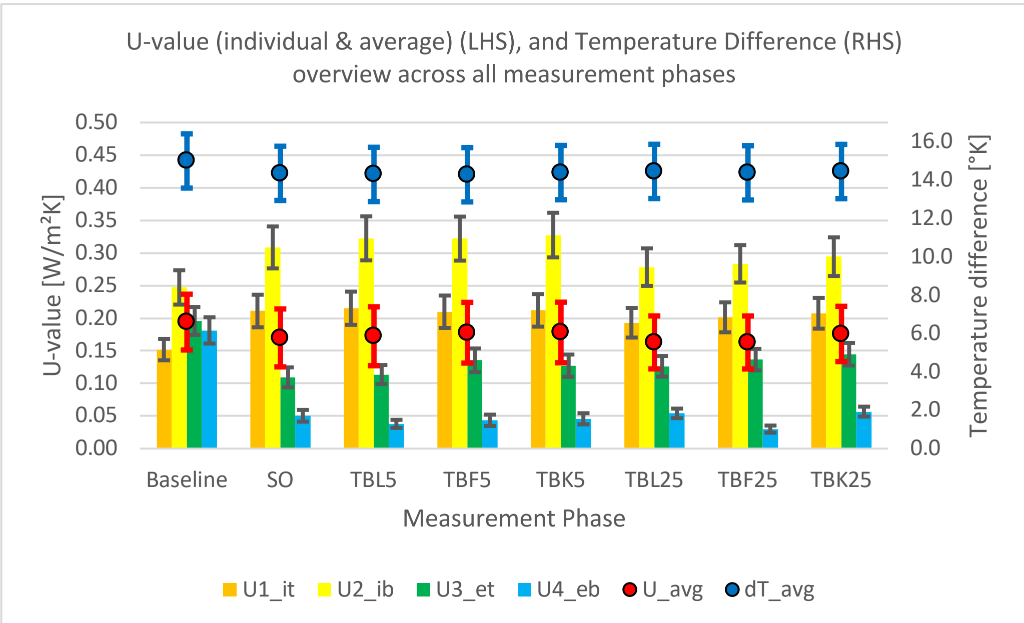

Figure 206 – U-values measured (individual and average) including uncertainty (LHS axis), temperature difference (RHS axis).

Surface-fluid HTC are seen in the following Table 28 and Figure 207:

Surface-fluid HTC	Int_T [W/m²K]	Int_B [W/m²K]	Ext_T [W/m²K]	Ext_B [W/m²K]		Int_avg [W/m²K]	Ext_avg [W/m²K]
Baseline	11.362	17.745	2.065	1.772		14.553	1.92
[+/-]	664.06%	664.06%	100.02%	100.04%		961.44%	141.88%
SO	10.089	24.144	2.375	2.045		17.117	2.21
[+/-]	532.15%	750.72%	232.68%	374.96%		1104.42%	427.65%
TBL5	9.848	17.767	2.324	1.431		13.808	1.88
[+/-]	510.86%	530.80%	219.75%	349.71%		774.12%	380.84%
TBF5	29.820	18.531	2.601	1.557		24.175	2.08
[+/-]	1589.32%	554.99%	206.71%	332.94%		2006.01%	359.23%
TBK5	16.982	16.970	2.488	1.676		16.976	2.08
[+/-]	972.68%	497.18%	208.24%	338.12%		1092.61%	368.79%
TBL25	9.775	19.893	2.635	2.224		14.834	2.43
[+/-]	571.90%	694.20%	222.77%	378.44%		1004.32%	422.35%
TBF25	10.583	22.353	2.658	1.036		16.468	1.85
[+/-]	556.64%	725.34%	206.35%	318.90%		1047.51%	346.67%
TBK25	10.01	18.29	3.01	1.92		14.15	2.46
[+/-]	508.35%	568.87%	219.03%	309.51%		818.52%	360.05%

Table 28 – Shows measured surface-fluid HTC's individually measured and averaged, with their uncertainties for each measurement phase.

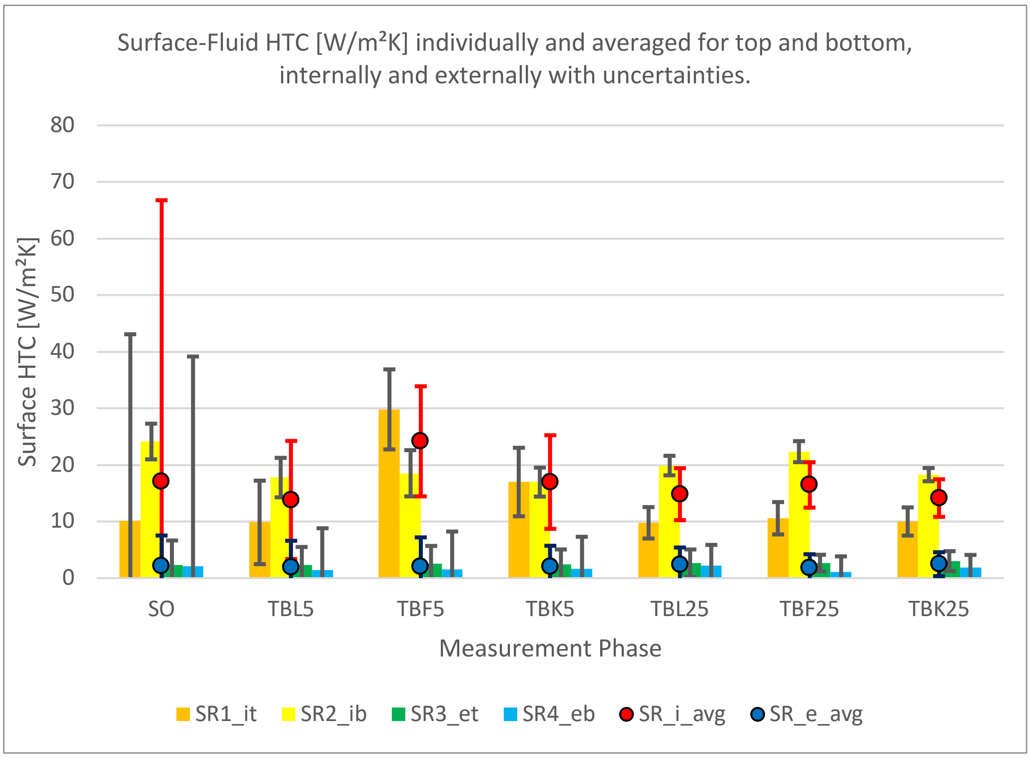

Figure 207 – Illustrates the measured surface-fluid HTC individually measured and averaged, with their uncertainties, for each measurement phase.

Embedded Flux are shown in Table 29 and Figure 208:

HF embedded	HF_te_1 [W/m²]	HF_se_2 [W/m²]	HF_si_3 [W/m²]	HF_ti_4 [W/m²]		HF_t_avg [W/m²]	HF_s_avg [W/m²]
SO	572.98	55.14	74.22	647.73		610.35	64.68
[+/-]	5.76%	5.72%	5.77%	5.73%		8.14%	8.22%
TBL5	128.80	64.08	62.69	128.80		128.80	63.39
[+/-]	5.73%	5.45%	5.08%	5.73%		8.10%	7.45%
TBF5	122.80	71.42	53.61	116.48		119.64	62.51
[+/-]	5.76%	5.72%	5.77%	5.73%		8.13%	8.20%
TBK5	105.86	44.46	44.86	98.31		102.08	44.66
[+/-]	5.72%	5.76%	5.76%	5.73%		8.10%	8.14%
TBL25	46.50	32.36	42.44	63.73		55.12	37.40
[+/-]	5.98%	5.34%	5.73%	5.73%		8.33%	7.98%
TBF25	49.74	34.78	27.65	46.81		48.28	31.21
[+/-]	5.75%	5.35%	5.33%	6.00%		8.30%	7.60%
TBK25	43.35	21.86	32.99	36.49		39.92	27.42
[+/-]	5.75%	5.36%	5.33%	5.99%		8.30%	7.71%

Table 29 – Shows the embedded flux measurements and the average for the top and bottom break section with their respective uncertainties.

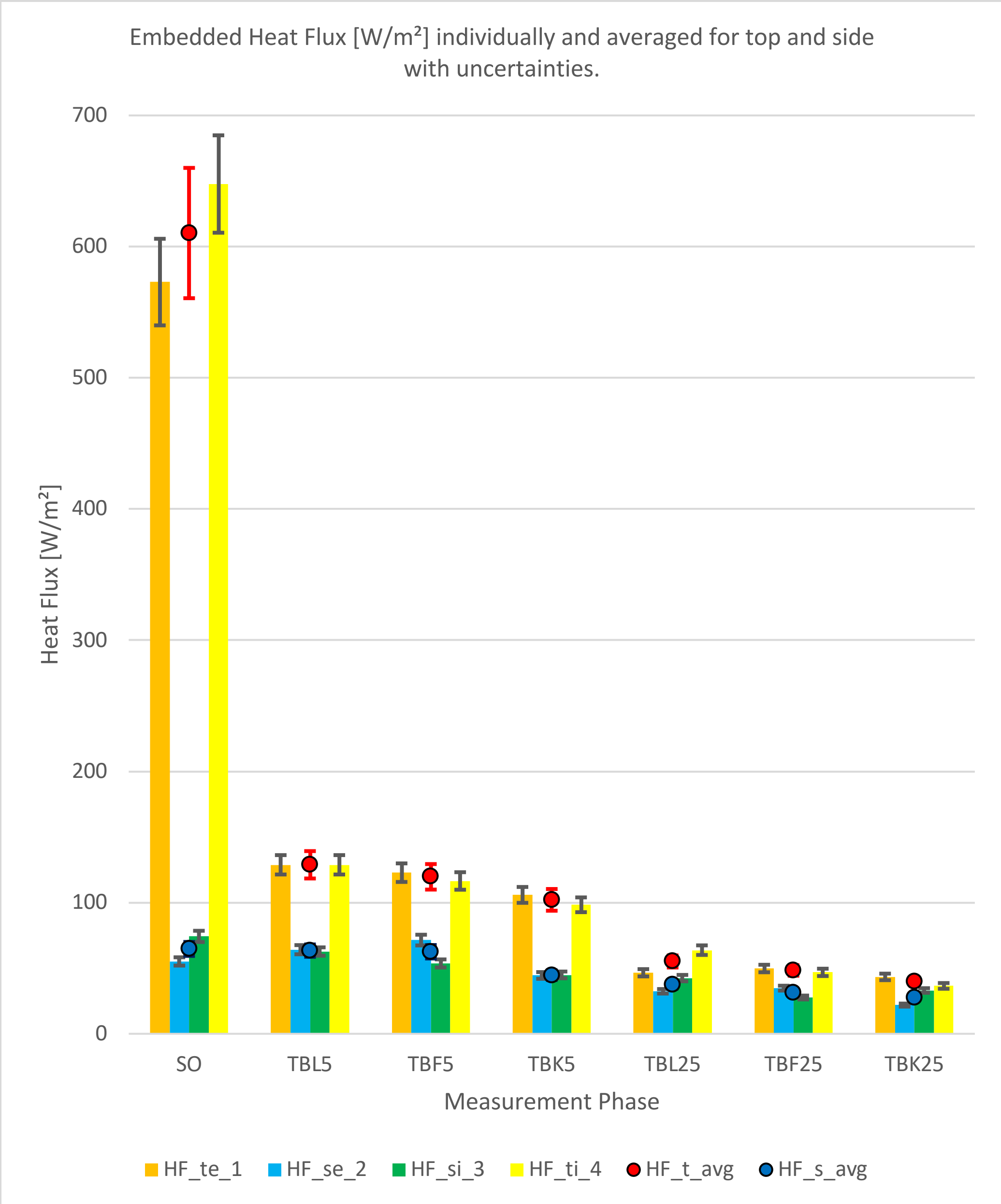

Figure 208 – Illustrates the embedded flux measurements and the average for the top and bottom break section with their respective uncertainties.

The average measured temperatures for each phase are shown in the following tables (Table 30 & Table 31) and referred to during model calibration. Table *30* shows the 'Bare-wall' phase:

	T1	T2	T3	T4	T5	T6	T7	T8	T11	T12	T13	T14
Bare wall	FT-inner	FT-Main	FT-OSB	FT-Ply	ST-main-intGap	AT-intGap	Int_AT	Int_ST	AT-extGap	ST-OSB	ExtAT	ExtST
Temps	18.93	18.26	6.81	6.56	19.09	20.03	19.92	19.70	7.59	8.43	4.93	6.35

Table 30 – Shows the Bare-wall baseline values.

The remaining single temperature measurements using the new sensor array can be seen in Table *31*Table *31* – Shows the remaining single temperature measurements using the new array.:

Temperatures	T1 IntST top	T2 IntAT top	T3 IntST Bott	T4 IntAT Bott	T5 ExtST top	T6 ExtAT top	T7 ExtST bott	T8 ExtAT bott	T9 ExtGap Ply	T10 ExtGap AT	T11 ExtGap OSB	T12 IntGap PIR	T13 IntGap AT	T14 IntGap EPS
Steel Only	20.70	20.98	19.69	19.89	8.27	7.66	4.89	4.51	4.99	5.09	7.74	16.45	14.88	15.87
TBL 5	20.65	20.94	19.59	19.87	8.32	7.67	4.97	4.56	5.03	5.16	7.79	16.33	14.78	15.76
TBF 5	20.83	20.92	19.61	19.87	8.36	7.67	5.00	4.57	5.10	5.26	7.92	16.35	14.80	15.78
TBK 5	20.91	21.07	19.68	19.97	8.37	7.68	5.01	4.59	5.10	5.25	7.90	16.35	14.79	15.79
TBL25	20.76	21.03	19.79	20.00	8.27	7.63	4.88	4.50	4.99	5.07	7.74	16.78	15.23	16.19
TBF 25	20.76	21.01	19.77	19.96	8.34	7.65	5.01	4.57	5.05	5.03	7.77	16.70	15.19	16.14
TBK 25	20.78	21.06	19.73	19.98	8.28	7.63	4.98	4.52	5.04	5.04	7.78	16.52	15.02	16.01

Table 31 – Shows the remaining single temperature measurements using the new array.

6.0 Modelling analysis

The modelling methodology alters thermophysical properties and boundary conditions within their respective sensible ranges – dictated by measurement and uncertainty analysis. Once the embedded flux locations, probed in the model, compared to the respective measurements with good agreement, the model is considered calibrated to within acceptable tolerance. Then, adopting OFAT, each STB model is simulated including a model without any STB solution – allowing the effect of utilising the various STB to be compared once the TB-transmittances are calculated following ISO 10211 and BRE guidance.

To highlight the PG, calibrated models of the experimental point-TB set-up can be compared to the current standardised numerical calculation methods since the methodology in this study – a measured and modelled evaluation of point transmittances through structural point TBs in-situ – reflects the real-world conditions more accurately as specific environmental conditions are monitored and used to parametrise the FE modelling rather than accepting standardised assumptions.

Insights can be gained into the assessment of this TB in-situ whilst observing the benefits when utilising STBs, to both improve future measurement/analysis and mitigate any detriments of TB in future building designs by proving the efficacy of STB solutions, respectively.

Calculation requires 3D heat transfer simulation software to generate a coupling coefficient, which describes the total energetic loss through the structure. This value is divided by the dT (temperature difference) before the analytical U-value (multiplied by its effective modelled area) is subtracted, leaving only the additional heat loss caused by the point TB (Passivhaus Institute, 2021; Ward & Sanders, 2016), see equation 76:

$$\chi = L_{3D} - \sum (U.A) \tag{76}$$

Where 'χ' is the chi-value, 'L_{3D}' is the coupling coefficients obtained from the simulation's total energetic loss through the structure divided by the imposed temperature difference, 'U' is the analytical U-value in the simulation, and 'A' is the area of the model.

The equations are taken from BS EN ISO 10211 (BSI, 2017c), which also stipulates the necessary requirements the chosen simulation software must meet, offering 4 cases in Annex C which the software must satisfy.

As mentioned, after an extensive trial of many bespoke TB software and multi-physics packages, the chosen software is ABAQUS. This software satisfies the 4 validation cases in BS EN ISO 10211 (BSI, 2017c) and is therefore adequate for the desired steady-state FE analysis. Fourier's law of conduction and the energy conservation laws are applied, populating a system of equations as a function of temperature at the nodes within the elements of the discretised geometry. A temperature distribution field is then determined and interpolation calculates the heat flows (BSI, 2017c).

6.1 Assumptions, and justifications

- Using the measured values initially showed that the model was not reflecting the measurements, therefore calibration is required before calculating the TB-transmittance. Variables used to calibrate the simulation: (meshing, BC temperatures and surface-fluid HTC's, conductivities, thicknesses, and geometry).

- Beam & break position: once installed the beam was fixed in position for both safety and repeatability. When altering the break variants between none, 5mm, and 25mm in the experimental measurement, only the balcony arm (external steel section) was removed and replaced. This means the breaks are slightly toward the external face of the conceived construction detail – not in the centre of the insulation. The model mirrors this by fixing the main body of the steelwork (edge-beam, backspan, stub-arm) and only adjusting the relative position of the balcony arm to accommodate the break thicknesses.

- Meshing: Because large flux and temperature gradients exist in the break connection, the mesh quality needs to be as fine as possible at the point of interest. The desired refinement would be 0.1mm to capture this 3D effect, however this is overreaching, and the simulation aborts due to burdensome computations. A mesh independency study was performed showing 1mm is likely to suffice, see meshing section.

- Partitioning was used to section off a through cut surrounding the break connection 50mm away from the beam penetration. A fine intermediate local refinement was applied to these new edges, whilst the finest remained focused on the break connection. In doing so a larger global mesh could be achieved using fewer calculation nodes away from the location of interested (3D flux) whilst providing less element distortion, again, reducing the computational cost whilst retaining adequate accuracy, see meshing section.

- On a similar endeavour to reduce computational cost (using information acquired from an earlier simulation looking at the flanking loss surrounding various sizes of specimen walls, both alone and in CV wall, before the experimental test was set-up to confirm no detrimental interference), 3 sizes were simulated and ran through the same calculation producing similar 3D chi-values, albeit not identical. The likeliest causation is unidentical meshing however the results are within acceptable agreement. Therefore, the smaller model (1x1m) was used, since no benefit would be gained by increasing the model size, see meshing section.

- Attempting to reach the optimum accuracy whilst reducing computational cost, the symmetry of the model was exploited by considering only a quarter in simulation. The results module in Abaqus allow the planes to be mirrored for visualisation. The outputs from this quarter model were compared with the full model, both targeting the same local refinement. This target was increased sequentially, and it was deduced that the smaller model produced satisfactory results, see meshing section.

- The 'Air Layer' conductivity could not be measured and was assumed using the standard BS EN ISO 6946 (BSI, 2017b) which shows that for unventilated air layers with high emissivity surfaces correspond to an equivalent thermal resistance, dependent upon the thickness of the air layer and the direction of heat flow (section 6.9.2, table 8, page 13 (BSI, 2017b)). The horizontal thermal resistance of a 50mm air layer is 0.18 [m^2K/W] which works out to have an equivalent thermal conductivity of 0.278 [W/mK].

- Preliminary FE studies suggest that the use of a STB causes a larger energetic loss conflicting with the hypothesis that: the greater the break resistance, the larger reductions in heat-loss. This is caused by performing 'Boolean geometry subtraction' replacing highly insulating elements in the modelled geometry with a highly conductive and bulky steel-to-steel connection (including bolts). In reality, and in my experimental investigation, this would not be the case. Hence why a block was considered to replace the low conductivity materials in the subtraction.

  I feel this is the right decision because the experimental set-up featured such a gap, although, this does add another variable built on assumption. Primarily the 'Air Block' is used to emulate the gap around the web and flange however, this could not be measured: in reality temperature and convective mechanisms within this 'Air Block' would drastically change over the various surfaces within the gap and large gradients through the model could exist, which is far too complex to measure accurately and parameterise using FE.

  The conductivity of the 'Air Block' was educationally guessed and altered to balance the side and top fluxes which were experimentally measured. Adjusting the BC values or conductance properties did not alter balancing (only the magnitude), only when the conductivity of the 'Air Block' or 'Steel' was altered did the balance between the top and side flux become sensible. As the conductivity of the 'Air Block' increases, the top flux decreases and the side flux increases, whereas increasing the steel conductivity does the opposite; it increases the top and decreases the side.

  If the model variables are constricted by the uncertainty budget of their measurand, the conductivity of the 'Air Block' or 'Steel' materials in the model could be adjusted to help achieve agreement with the measured embedded flux.

  A short analysis showed, although altering the 'Air Block' conductivity value to extremes does affect the overall Chi-value (TB transmittance), the altered ranges with which to balances the side and top embedded heat flux has negligible effect.

Initial investigations showed that the conductance could be fixed across all models including the 'Air Block' or the 'Steel' conductivity and only BCs were altered to converge probed model values to their corresponding measurement.

The above assumptions are justified in the following meshing section. Local refinement 1 (fine mesh) was applied to partitioned edges (20mm and 50mm away from the model centre, in the steel and in the wall, respectively) whilst local refinement 2 (most fine) was applied to the central penetrating elements. This allows a courser global mesh to be considered at the adiabatic edges creating less element distortion and reducing computational cost.
Similarly, all models were 1x1m and split into 1/4 taking advantage of the two symmetry planes, again reducing the computational load whilst retaining adequate accuracy.

6.2 Meshing

When refining the mesh on a model of a construction element, usually a basic quality is specified initially. The resulting minimum internal surface temperatures and heat flux will be significantly erroneous, however, as the model is refined by dividing the mesh element size, these metrics will converge to an asymptotic value. Care must be taken when dividing the mesh grid as the results are sensitive to the level of refinement. The easiest method is to divide each element in the grid by two until the results stabilise. This is simple for a 2D model but becomes increasingly complex for a 3D model since each division increases the number of nodes by a factor of 8 (if linear hexagon or tetrahedral elements are applied, even more if quadratic). In these cases, it is more important to concentrate the elements around features likely to cause significant heat flow, areas of interest, or high gradient locations (Ward & Sanders, 2016).

To calculate a sufficiently accurate thermal model the BRE recommend the following procedure in BR 497 (Ward & Sanders, 2016):

1. Define minimum grid necessary to specify materials.
2. Divide all the spaces between nodes by two.
3. Identify all areas where low thermal conductivity materials are penetrated by high conductivity materials. Also, identify areas close to the TB and consider adding more elements at these locations. (Including air spaces).
4. Calculate the heat flux and minimum internal surface temperatures.
5. Divide the elements and recalculate results. The model may become too large to compute, particularly in 3D models. If this is the case, dividing elements at step 5 may be restricted to step 3.

If the total heat flow from step 4 to 5 differs less than 1% and the minimum surface temperature differs less than 0.005[°K], the mesh refinement is sufficient. If the change in any is bigger than this, repeat step 3 to 5 until the criterion is met. If this procedure is not allowed by the software then a suitably refined mesh must be demonstrated separately (Ward & Sanders, 2016). One suggestion in BR 497 would be to create an equivalent division in steps 4 and 5 such that subsequent models with differing mesh densities can be manually compared, whilst considering the same stopping criteria of steps 4 and 5.

A model was initially made 2m x 2m creating an area of 4[m^2] which a U-value of approximately 0.18[W/ m^2K] affects. The following Table 32 shows the thickness and conductivity of wall layers, from internal to external:

	dx	lam
EPS	0.03	0.054
Air_int	0.05	0.3
PIR	0.1	0.023
OSB	0.011	0.13
Air_ext	0.05	0.3
Ply	0.009	0.13

Table 32 – Thermophysical properties used in the meshing simulation.

Internal and external boundary conditions were set to 7.7[W/ m^2K] at 25[°C] and 25[W/ m^2K] at 5[°C], respectively. As mentioned, this generates an approximate U-value = 0.18 [W/ m^2K] and a dT = 20[°C].

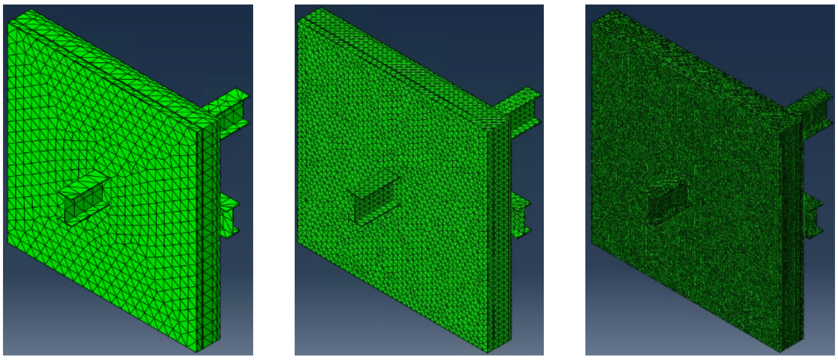

Figure 209 – Shows models M1, M2, M3, from left to right increasing in mesh quality.

quality	global m	local1 m	local2 m	elements #	sum RFLE W	Chi W/K	HF1-top W/m^2	HF2-bot W/m^2
M1	0.1	~	~	29909	30.2945	0.789099	962.688	211.783
					3.34%	6.41%	-32.56%	0.25%
M2	0.05	~	~	92680	29.2821	0.738479	1276.13	211.248
					2.70%	5.34%	11.67%	52.42%
M3	0.02	~	~	1023704	28.4929	0.699019	1127.19	100.509

Table 33 – Shows 'M1, 'M2', 'M3' mesh qualities.

Refining the global mesh to 20mm ('M3', see RHS of Figure 209) slowed the time to mesh, simulate, and retrieve data from results seen in Table 33. However, looking at the embedded flux 'HF1-top' and 'HF2-bot', further refinement is required to converge the mesh. To focus the analysis on this region, the global was left as default and the geometry edge at the connection was selected and prescribed a finer mesh granularity (local1), see the following Figure 210 and Table 34**.**

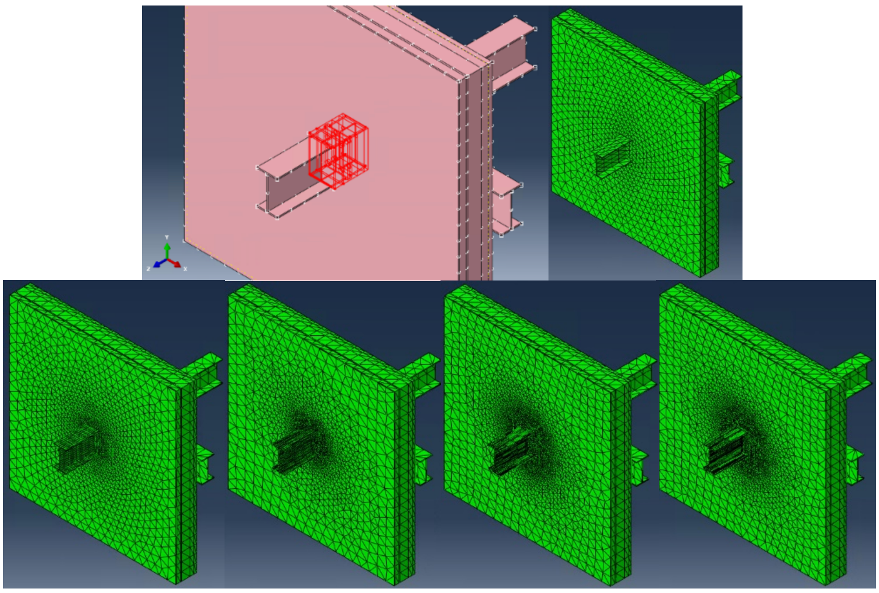

Figure 210 – Shows 'M4', 'M5', 'M6', 'M7', 'M8'. 'M9' did not simulate.

quality	global m	local1 m	local2 m	elements #	sum RFLE W	Chi W/K	HF1-top W/m^2	HF2-bot W/m^2
M4	0.1	0.05	~	41269	29.4545	0.747099	1298.68	213.312
					1.79%	3.53%	10.49%	52.12%
M5	0.1	0.02	~	96891	28.9274	0.720744	1162.41	102.142
					0.48%	0.96%	12.44%	-3.01%
M6	0.1	0.01	~	230764	28.7894	0.713844	1017.76	105.219

Table 34 – Shows ‘M4’, ‘M5’, ‘M6’.

The simulation output RFLE [W] and the processed Chi [W/K] for model ‘M6’ (seen in Table 34 above) converge to within 1% of the previous meshing – suggesting the courser of the two (‘M5’ using 20mm local seeding at the connection) is sufficiently accurate to describe theses metrics. However, as seen previously, the embedded flux ‘HF1-top’ and ‘HF2-bot’ require further refinement to converge the mesh.

To increase local refinement, the steel and wall were partitioned 20mm and 50mm away, respectively, offset from the central position of interest. These will have an intermediate ‘local1’ seeding applied to the edges whilst ‘local2’ seeding concentrates on the connection. This is seen in the following Table 35 where the finest refinement attempts to reduce the element size at the connection from 5mm down to 1mm.

quality	global m	local1 m	local2 m	elements #	sum RFLE W	Chi W/K	HF1-top W/m^2	HF2-bot W/ m^2
					0.51%	1.04%	0.69%	-0.72%
M7	0.1	0.01	0.005	722814	28.6416	0.706454	1010.69	105.981
					0.19%	0.39%	1.46%	0.50%
M8	0.1	0.01	0.002	3314717	28.587	0.703724	995.917	105.448
					~	~	~	~
M9	0.1	0.01	0.001	11488625	~	~	~	~

Table 35 – Shows ‘M7’, ‘M8’, ‘M9’.

Adequate accuracy is observed; the mesh has converged closer at these high flux gradient locations.

M8’ is the most accurate illustrating good convergence in most results – suggesting that in fact, ‘M7’ may be sufficiently accurate – although the ‘HF1-top’ deviated more than expected implying that a higher refinement is required.

M9 attempts to refine the elements at the connection interface (point of interest) to 1mm. A mesh is generated creating approximately 11.5 million elements, but it fails to compute.

The following models have been modified attempting to reduce the computational cost whilst retaining the required accuracy – aiming for a 1mm element size at the area of interest. The modifications reduce the model size from 2mx2m to 1mx1m and, by taking advantage of planes of symmetry, analysing only ¼ of the full model – which can be mirrored in results resolving the full model. These were considered in the following Figure 211 and Table 36.

Advice and guidance (Ward & Sanders, 2016) suggest flanking elements (adjacent to the TB) should be taken to 1m or three times the thickness (whichever is closer), away from the TB, or up to a plane of symmetry in the case of repeating features. Surface temperatures can be noted at the adiabatic edge, then, noted again in an extended model at the new adiabatic edge. If the difference in temperature factor is no more than 0.005 (or, for a 20 [°C] internal and 0 [°C] external temperature, a difference in temperature factor is equivalent to a difference in surface temperature of 0.1 [°C]), the smaller model is adequate, otherwise this process is repeated until the condition is met (Ward & Sanders, 2016).

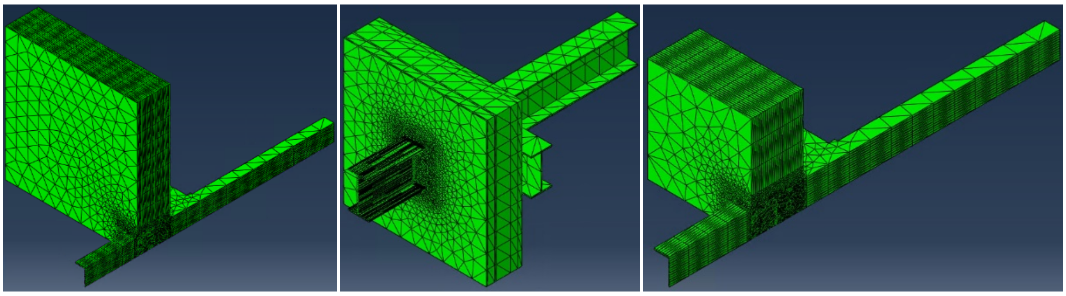

Figure 211 – Shows ‘M10’, ‘M11’, ’M12’

	quality	global m	local1 m	local2 m	elements #	sum RFLE W	Chi W/K	HF1-top W/m^2	HF2-bot W/m^2
						-0.73%	-1.48%	-1.87%	-1.78%
¼ 2mx2m	M10	0.1	0.01	0.001	3148626	7.19899	0.714172	1014.55	107.321
						~	0.23%	1.25%	1.24%
1mx1m	M11	0.1	0.01	0.001	12678498	17.8787	0.712529	1001.86	105.993
						~	-0.48%	-1.23%	-1.11%
¼ 1mx1m	M12	0.1	0.01	0.001	3109024	4.49513	0.71762	1014.2	107.172

Table 36 – Shows the ¼ 2mx2m, 1mx1m, and ¼ 1mx1m models.

Considering the surface temperature at the adiabatic edge the 1mx1m model was adequate as was the 2mx2m model, differing in surface temperature less than 0.1 [°C]. Also, the ¼ model versions were close to convergence (approximately rounded to 1%). Therefore, the ¼ 1mx1m model is deemed adequately accurate and was chosen to carry forward in the analysis. A slight modification, setting global = 0.06m and local1 = 0.03m helped reduce the mesh distortion whilst retaining accuracy, see Table 37.

	quality	global m	local1 m	local2 m	elements #	sum RFLE W	Chi W/K	HF1-top W/m^2	HF2-bot W/m^2
¼ 1mx1m	M13	0.06	0.03	0.001	3344261	4.46813	0.71222	1008.48	106.755

Table 37 – Shows the final meshing used in the analysis going forward.

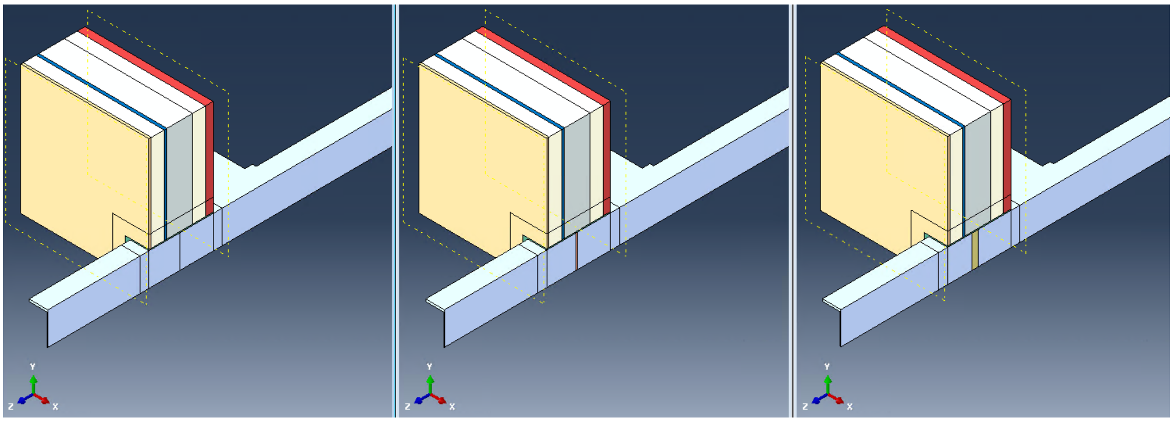

Figure 212 – Shows the isometric view of the ¼ 1m^2 models, from right to left, ‘Steel Only’, ‘TB5’, and ‘TB25’.

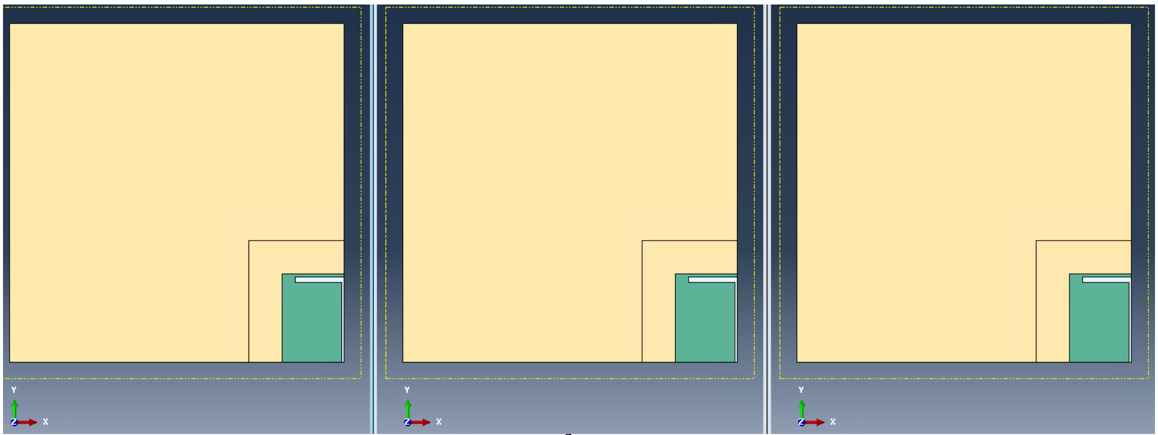

Figure 213 – Shows the front view of the ¼ 1m^2 models, from right to left, ‘Steel Only’, ‘TB5’, and ‘TB25’.

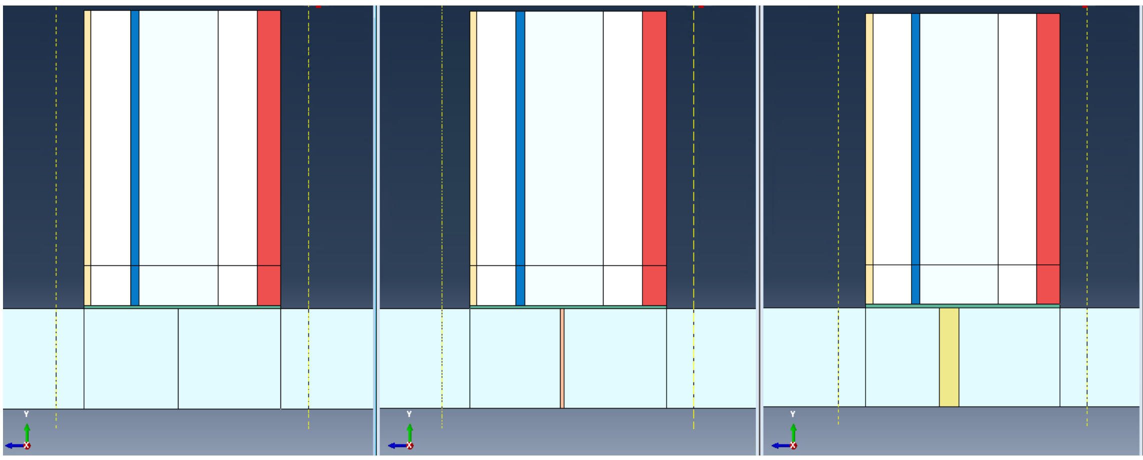

Figure 214 – Shows the side view of the ¼ 1m^2 models, from right to left, ‘Steel Only’, ‘TB5’, and ‘TB25’.

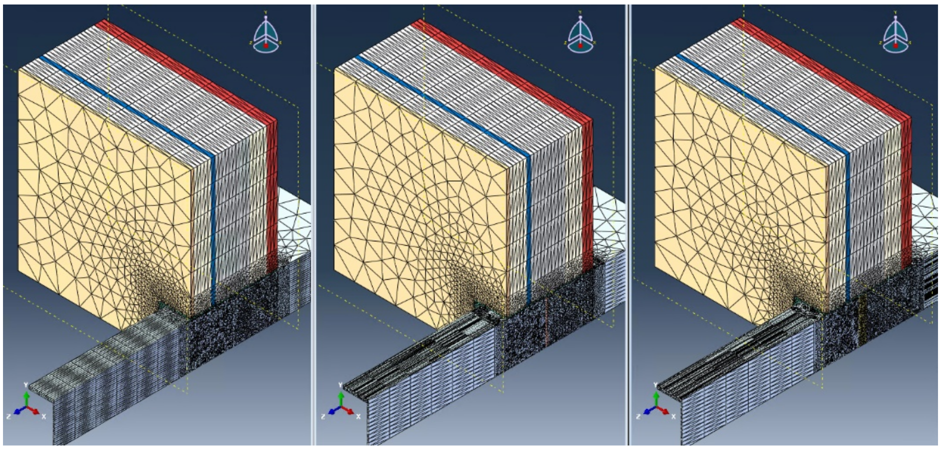

Figure 215 – Shows an isometric view of the simulation mesh, ¼ 1m^2 models, from right to left, 'Steel Only', 'TB5', and 'TB25'.

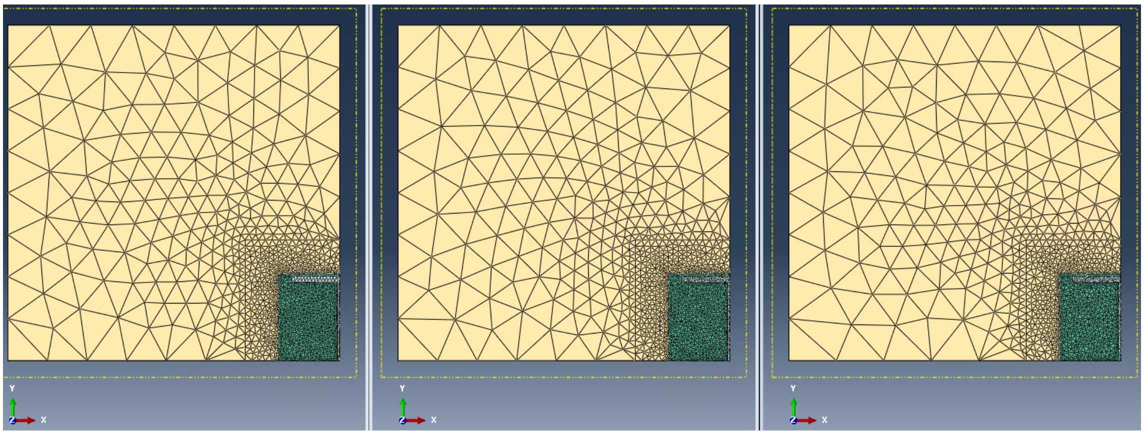

Figure 216 – Shows a front view of the simulation mesh, ¼ 1m^2 models, from right to left, 'Steel Only', 'TB5', and 'TB25'.

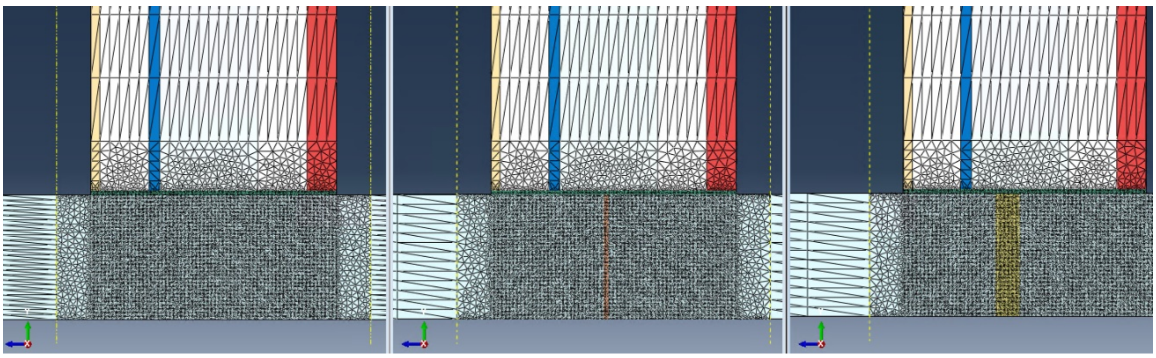

Figure 217 – Shows a side view of the simulation mesh, ¼ 1m^2 models, from right to left, 'Steel Only', 'TB5', and 'TB25'.

Individual part files were made for each component then assembled in an assembly file using SolidWorks: ply façade, OSB lay, PIR layer, EPS on Plasterboard layer, each Air Layer, 5mm break, 25mm break, steelwork (made as individual parts). SolidWorks is a useful CAD software which allows fast and accurate model generation, it is also a compatible interface with ABAQUS simulation software enabling rapid geometry alterations.

Once the model is generated in SolidWorks and saved in the correct unit system desired for ABAQUS simulation, the SolidWorks model can be imported so long as the SolidWorks CAD interface is enabled within the 'Assembly' module in ABAQUS (assigning a connection port linking the software). An individual part is generated, ready-assembled as per the SolidWorks model. Using the Boolean operators within ABAQUS 'Assembly' module, the geometry is selected and combined whilst retaining the edges between parts. This produces one merged single ABAQUS part, all the retained edges between component parts divide the part into cells with which the sections – defining the material properties – can be applied.

To set the simulation up the type of simulation needs to be defined (e.g., Heat Transfer), as does the transients (dynamic or steady-state), time-step, increment size, initial, and maximum increments. The geometry is then meshed – prescribing the element type and shape suitable for the simulation type and geometry. Models 'Steel Only' simulated just the beam without any breaks, 'TB5' simulated all the 5mm variants, and 'TB25' simulated all the 25mm variants. Each model was partitioned and meshed using the same method (global seeding, local refinement, element shape, and type), however, truly identical meshing cannot be expected. Cell or surface partitions are tools utilised for refining the geometry for more efficient meshing in terms of accuracy and computational cost. Surfaces partitions are particularly useful for isolating areas of interest, for example the embedded flux locations within the connection interface. History outputs can be requested from these surfaces at the end of the steady-state simulation step which coincide with the measurements made, allowing direct comparison. Also, the ¼ model can be mirrored over the 2 symmetry planes in the results to visualise isotherms and flux gradients through the 3D models.

Then, following the calibration flow chart **(**Figure 218) the material properties are fixed whilst altering BC's in each model, considering the specific measurements in that test phase, to calibrate the probed embedded flux values to as close as possible to the average measured value for that phase – within a tolerance dictated by their measurement uncertainty. The main decision points in the calibration are:

- Is the geometry representative?
- Are the material properties (conductivity and thickness) sensible?
- Are the boundary conditions sensible?
- Do these U-values and SRs converge to within measurement uncertainty?
- Is the mesh quality accurate?
- Is simplification or partitioning required?
- Have the embedded flux values converged to within their measurement uncertainty?

If no, the re-calibration would require revisiting and adjusting one or more of the operations, illustrated below in the next section, see Figure 218**:**

6.3 Calibration flow chart

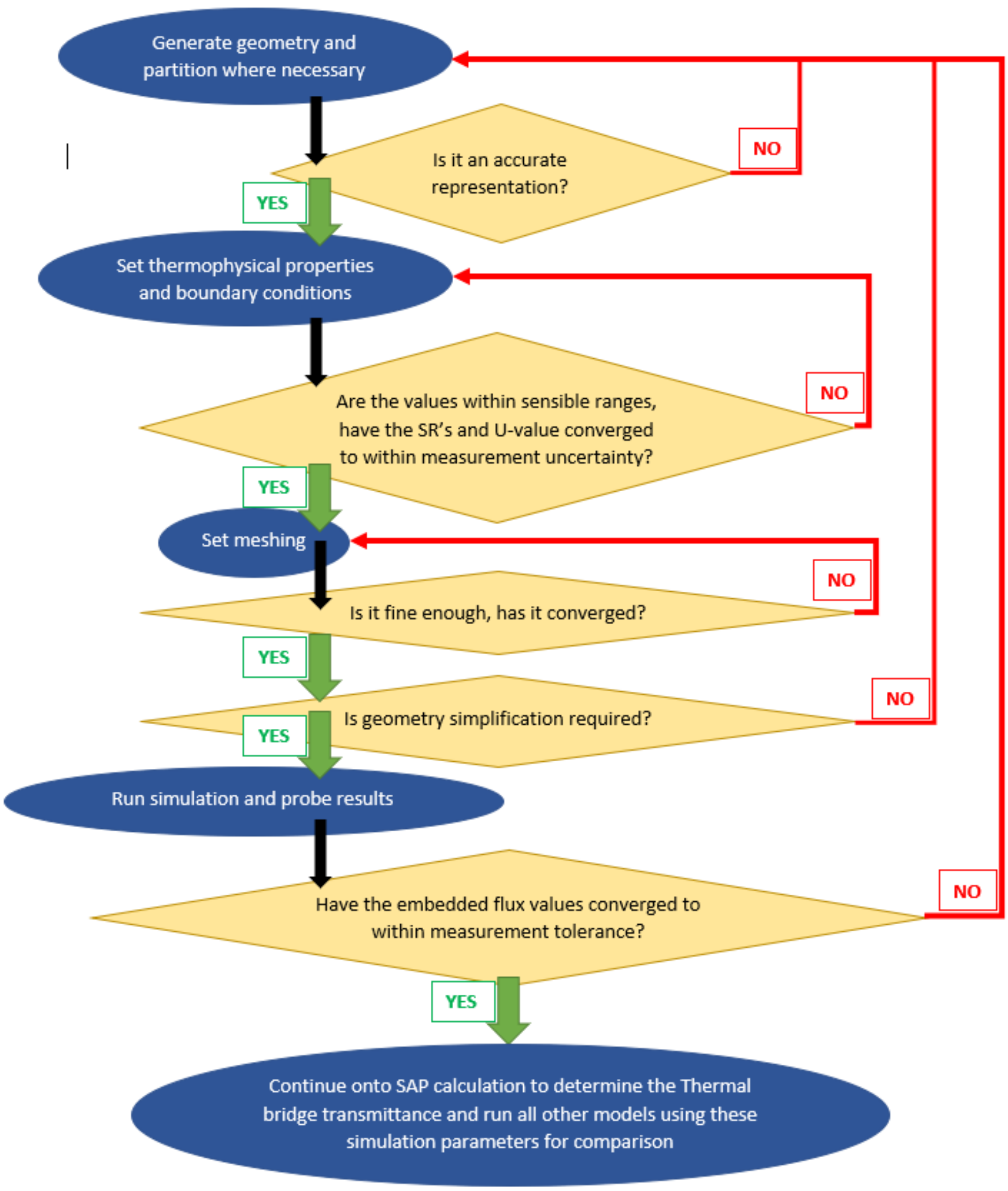

Figure 218 – Model calibration flow chart.

Once one phase was modelled and calibrated (by altering the dT and SR measurements considering the embedded heat fluxes relating to that phase), all the other models were simulated using the parameters at that calibration. Then, the coupling coefficients were recorded, then used to calculate the TB-transmittance following BS EN ISO 10211 and guidance from BRE 497, the only factor to change between models was the conductivity of the STB material. This gives comparable simulation results between the break variants, however, comparing break thickness (none, 5mm, 25mm) requires switching model geometry, hence re-meshing – which could cause discontinuity between compared models. This is performed for every calibrated state providing grounds for model comparison and showing STB impact. Standard numerical simulation settings were used on each model, allowing a PG comparison between each calibrated model and the standard assessment procedure.

6.4 Modelled parameters (material thickness, conductivities, and BC's)

Conductance settings were fixed across all models as seen in Table 38 below, with the assumed 'Air Block' and 'Steel' conductivities set to the most agreeable values across all models (1.7 [W/mK] for the 'AirBlock', and 50 [W/mK] for the steel).

Thermophysical Properties (thicknesses and conductivities)														
	SO		TBL5		TBF5		TBK5		TBL25		TBF25		TBK25	
	dx [m]	λ [W/mK]	dx [m]	λ [W/mK]	dx [m]	λ [W/mK]	dx [m]	λ [W/mK]	dx [m]	λ [W/mK]	dx [m]	λ [W/mK]	dx [m]	λ [W/mK]
EPS	0.03	0.054	0.03	0.054	0.03	0.054	0.03	0.054	0.03	0.054	0.03	0.054	0.03	0.054
Air layer_int	0.05	0.3	0.05	0.3	0.05	0.3	0.05	0.3	0.05	0.3	0.05	0.3	0.05	0.3
PIR	0.1	0.023	0.1	0.023	0.1	0.023	0.1	0.023	0.1	0.023	0.1	0.023	0.1	0.023
OSB	0.011	0.13	0.011	0.13	0.011	0.13	0.011	0.13	0.011	0.13	0.011	0.13	0.011	0.13
Air Layer_ext	0.05	0.3	0.05	0.3	0.05	0.3	0.05	0.3	0.05	0.3	0.05	0.3	0.05	0.3
Ply	0.009	0.13	0.009	0.13	0.009	0.13	0.009	0.13	0.009	0.13	0.009	0.13	0.009	0.13
Steel	~	50	~	50	~	50	~	50	~	50	~	50	~	50
Air Block	~	1.7	~	1.7	~	1.7	~	1.7	~	1.7	~	1.7	~	1.7
TB	~	~	0.005	0.292	0.005	0.2	0.005	0.187	0.025	0.292	0.025	0.2	0.025	0.187

Table 38 – Conductivities and thicknesses used to parameterise and calibrate each model.

The justification of the 'Air block' conductivity assumes a 300 mm through wall gap (approx.) divided by the 0.18 [m^2K/W] horizontal resistance as per BS EN ISO 6946. This approximates to an equivalent conductivity of 1.67 [W/mK] which is rounded up to 1.7 [W/mK].

As mentioned, prior to experimentation, wall samples were taken for accurate conductivity and thickness measurements, which did differ from manufacturer specification marginally, but the measurement provided an uncertainty which the reported manufacturer values were within. The analytical U-value determined from the abovementioned properties are used in the model calculations to determine TB-transmittances.

These parameters are fixed throughout each model and calibrated to a best fit within their measured uncertainty.

The U-value of the wall was measured in-situ following the BS EN ISO 9869 averaging method (BSI, 2014) verifying the analytical calculation. Heat flux plates were attached in two places on each surface, internal and external. The plates detect 1D heat flux, captured by the datalogger alongside environmental air temperatures from T-type thermocouple sensors, then used in calculation. The measured U-value has systemic and bias uncertainties, which, when propagated properly conclude in a 95% confident uncertainty statement. This is calculated using the sum of thermal resistances stemming from conductance (conductivity and thickness) and surface-to-fluid transfer (radiative and convective mechanisms).

Also measured throughout the experiment, the surface-fluid HTCs are calculated using the surface flux and the temperature difference between the surface and the fluid, measured twice on each environmental surface. The temperature difference is substantially smaller than the one used for the U-value calculation, hence why a much larger uncertainty is seen at the same confidence interval. These measured surface-fluid HTCs will be used to inform model parameter calibration and resolve the analytical U-value for the TB-transmittance calculation, instead of the standardised values (0.04 and 0.13 [m^2K/W], for external and internal horizontal surfaces, respectively).

The following Table 39 shows the model parameters used to calibrate the BCs and U-values, these were the only variables altered to inform the convergence of the probed embedded heat fluxes values to their measurement within associated uncertainty.

Modelled	Int HTC [W/m^2K]	Ext HTC [W/m^2K]	dT [°K]	U-value [W/m^2K]
SO	21	4	16	0.1758
TBL5	22	5	15.5	0.1774
TBF5	30	9	15.9	0.181
TBK5	23	6	16.3	0.1785
TBL25	21	3	16	0.1733
TBF25	25	4	16.3	0.1733
TBK25	20	3	15.3	0.1732

Table 39 – Shows the internal surface-fluid HTC, external surface-fluid HTC, temperature difference, and U-values.

Comparing these to the measurement, Table 40 shows the measured average, its uncertainty, and the modelled parameter of the internal and external surface-fluid HTC.

	Measured int_HTC	[+/-]	Modelled int_HTC	%Diff	Measured ext_HTC	[+/-]	Modelled ext_HTC	%Diff
SO	17.12	189.04	21.00	-23%	2.21	9.45	4.00	-81%
TBL5	13.81	106.89	22.00	-59%	1.88	7.15	5.00	-166%
TBF5	24.18	484.96	30.00	-24%	2.08	7.47	9.00	-381%
TBK5	16.98	185.48	23.00	-35%	2.08	7.68	6.00	-188%
TBL25	14.83	148.98	21.00	-42%	2.43	10.26	3.00	-23%
TBF25	16.47	172.51	25.00	-52%	1.85	11.83	4.00	-117%
TBK25	14.15	115.81	20.00	-41%	2.46	8.87	3.00	-22%

Table 40 – Shows the BC internal and external surface-fluid HTCs comparing the modelled with the measured.

Again, comparing the modelled BC with measurements, Table 41 shows the measured average, its uncertainty, and the modelled parameter of the temperature difference and U-value.

	Measured dT	[+/-]	Modelled dT	%Diff	Measured _U	[+/-]	Modelled_U	%Diff
SO	14.35	2.00	16.00	-12%	0.17	0.04	0.18	-4%
TBL5	14.29	2.00	15.50	-8%	0.17	0.05	0.18	-3%
TBF5	14.28	2.00	15.90	-11%	0.18	0.05	0.18	-2%
TBK5	14.39	2.00	16.30	-13%	0.18	0.05	0.18	0%
TBL25	14.45	2.00	16.00	-11%	0.16	0.04	0.17	-6%
TBF25	14.38	2.00	16.30	-14%	0.16	0.04	0.18	-8%
TBK25	14.44	2.00	15.30	-6%	0.18	0.04	0.17	1%

Table 41 – Shows the temperature difference and U-values comparing the modelled with the measured.

The following graphs illustrate each model input parameter with its corresponding measurand and uncertainty. The measured internal surface-fluid HTC is plotted with its uncertainty and modelled value to illustrate that the modelled value is within the measured uncertainty, see Figure 219.

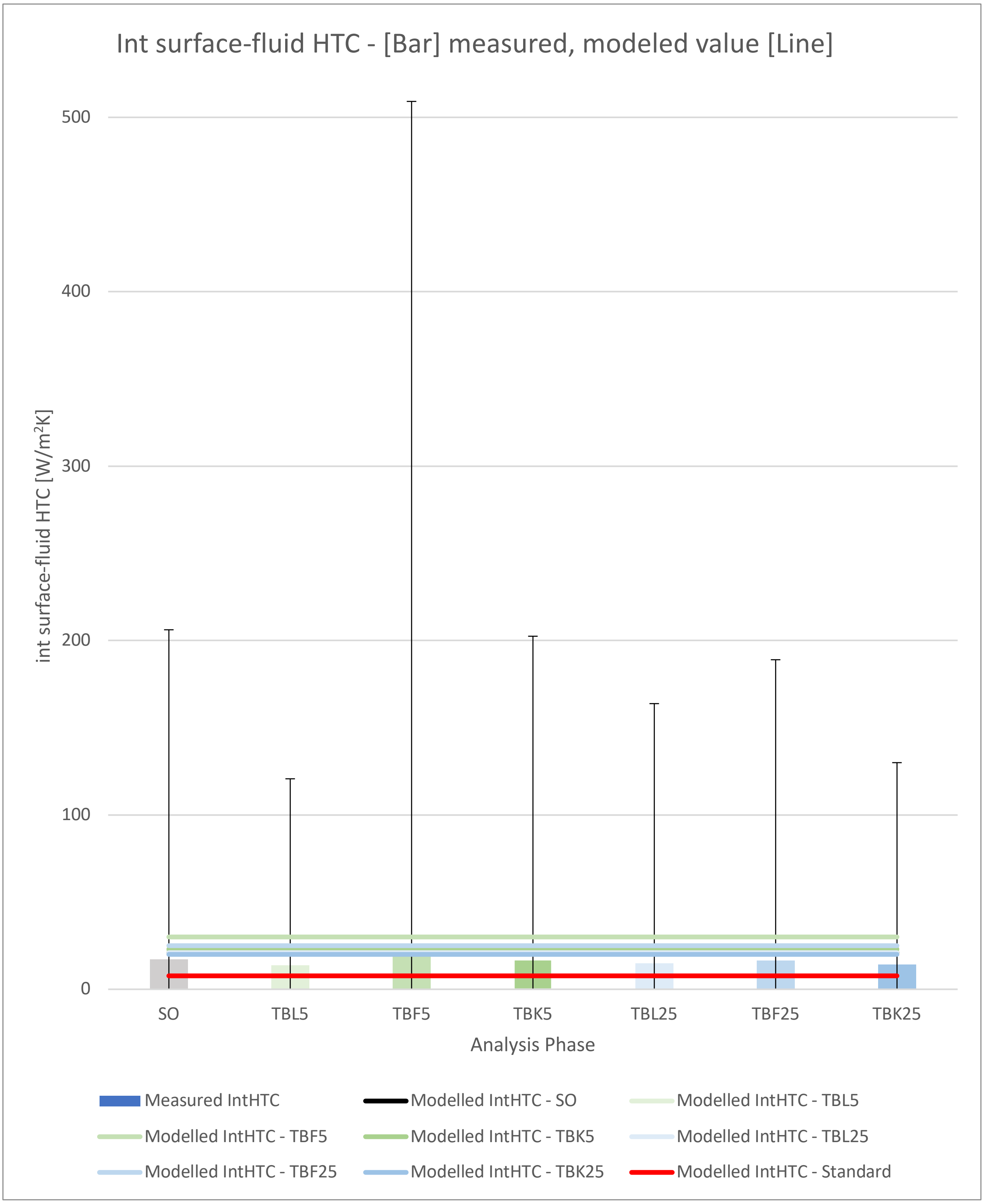

Figure 219 – Shows the internal surface-fluid HTC measurement [Bar] with its uncertainty and each modelled value [Line] colour coded as per plot ledged.

The measured external surface-fluid HTC is plotted with its uncertainty and modelled value to illustrate that the modelled value is within the measured uncertainty, see Figure 220:

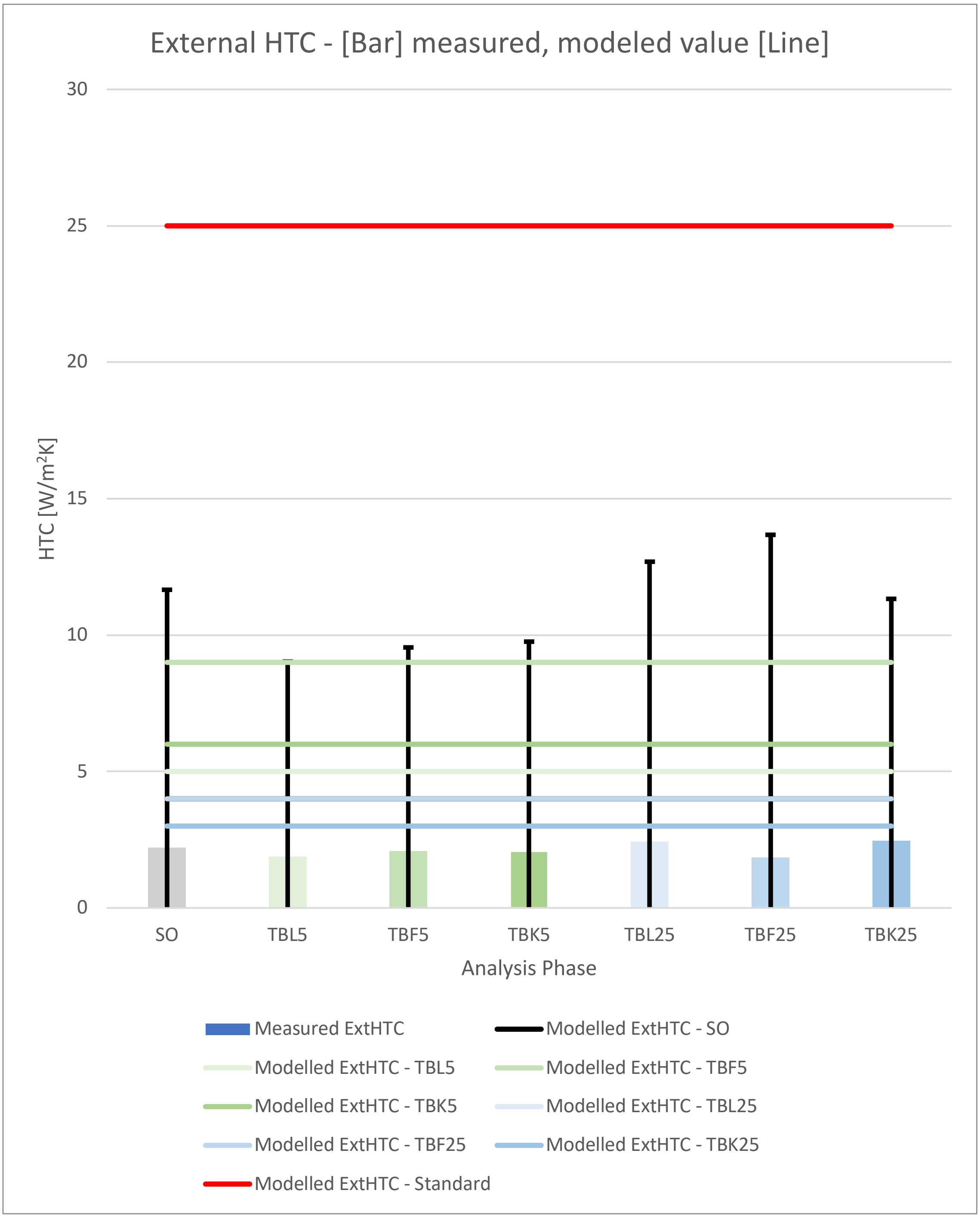

Figure 220 – Shows the internal surface-fluid HTC measurement [Bar] with its uncertainty and each modelled value [Line] colour coded as per plot ledged.

The measured temperature difference is plotted with its uncertainty and modelled value to illustrate that the modelled value is within the measured uncertainty, see Figure 221.

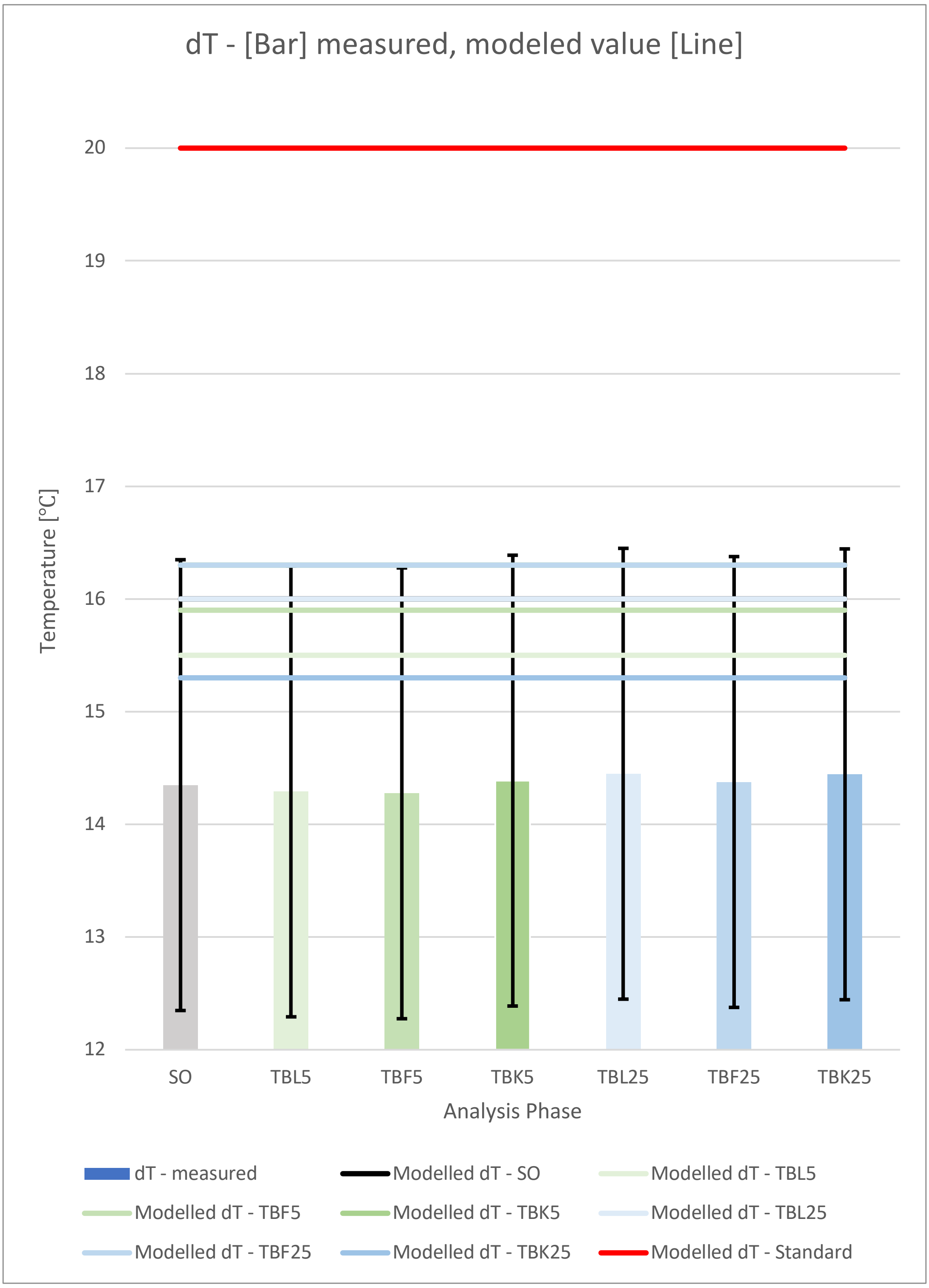

Figure 221 – Shows the temperature difference measurement [Bar] with its uncertainty and each modelled value [Line] colour coded as per plot ledged.

The measured U-value is plotted with its uncertainty and modelled value to illustrate that the modelled value is within the measured uncertainty, see Figure 222:

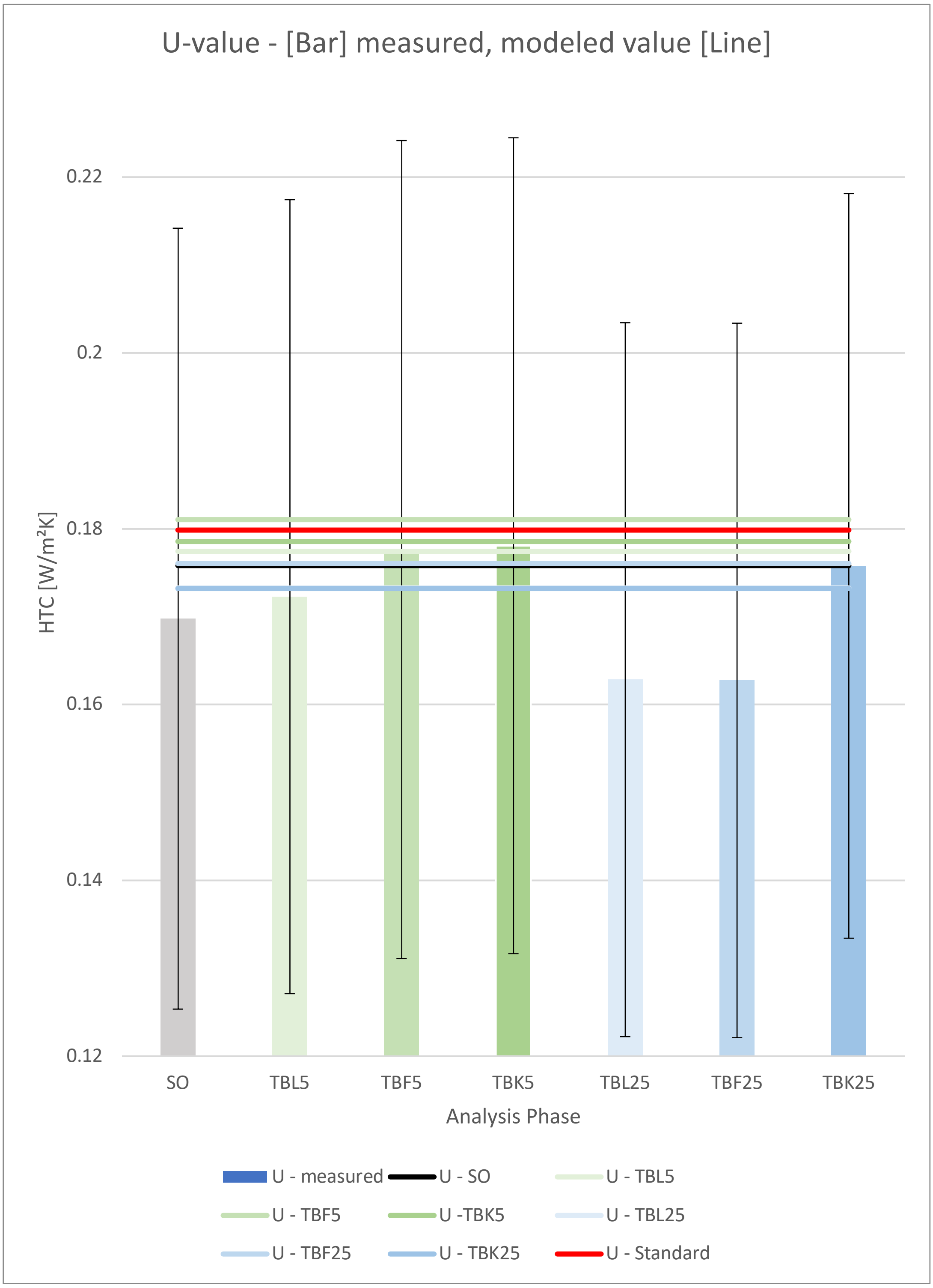

Figure 222 – Shows the internal U-value [Bar] with its uncertainty and each modelled value [Line] colour coded as per plot ledged.

The embedded flux (top and side) outputs from the simulations are shown in Table 42**.** The percentage change from the measurement is also reported showing every response is within 5-6% of the measurement.

Top	Measured	[+/-]	SO	TBL5	TBF5	TBK5	TBL25	TBF25	TBK25	% Diff
SO	610.35	8.2%	**622.30**	638.96	759.58	702.21	573.97	643.45	547.59	-1.96%
TBL5	128.80	7.5%	121.46	**124.21**	145.32	136.08	112.65	125.58	107.47	3.57%
TBF5	119.64	8.2%	97.15	99.31	**116.04**	108.76	90.16	100.44	86.01	3.01%
TBK5	102.08	8.1%	93.41	95.48	111.54	**104.56**	86.70	96.57	82.71	-2.42%
TBL25	55.12	8.0%	59.04	60.06	69.34	65.53	**55.15**	61.00	52.63	-0.06%
TBF25	48.28	7.6%	47.42	48.21	55.57	52.58	44.33	**48.99**	42.30	-1.48%
TBK25	39.92	7.7%	45.70	46.46	53.54	50.66	42.72	47.21	**40.77**	-2.12%

Side	Measured	[+/-]	SO	TBL5	TBF5	TBK5	TBL25	TBF25	TBK25	% Diff
SO	64.68	8.14%	**65.68**	67.74	82.11	74.77	60.39	68.26	57.53	-1.54%
TBL5	63.39	5.73%	63.81	**65.38**	77.07	71.76	59.08	66.09	56.34	-3.15%
TBF5	62.51	8.13%	53.77	55.06	**64.81**	60.41	49.82	55.68	47.51	-3.67%
TBK5	44.66	8.10%	52.03	53.28	62.69	**58.45**	48.22	53.88	45.98	-30.87%
TBL25	37.40	8.33%	40.52	41.28	47.91	45.10	**37.80**	41.91	36.06	-1.08%
TBF25	31.21	8.30%	31.93	32.51	37.68	35.50	29.81	**33.02**	28.44	-5.79%
TBK25	27.42	8.30%	30.62	31.17	36.12	34.04	28.59	31.66	**27.27**	0.55%

Table 42 – Shows the top flux and side flux, comparing the measurement and uncertainty with the simulation response.

The following graphs (Figure 223 to Figure 226) visualises these embedded flux values, showing the measurement, uncertainty, and the simulation response, proving the models are calibrated to the embedded flux readings.

Top flux measured in each phase with uncertainty and every probed response from each simulation model, see Figure 223.

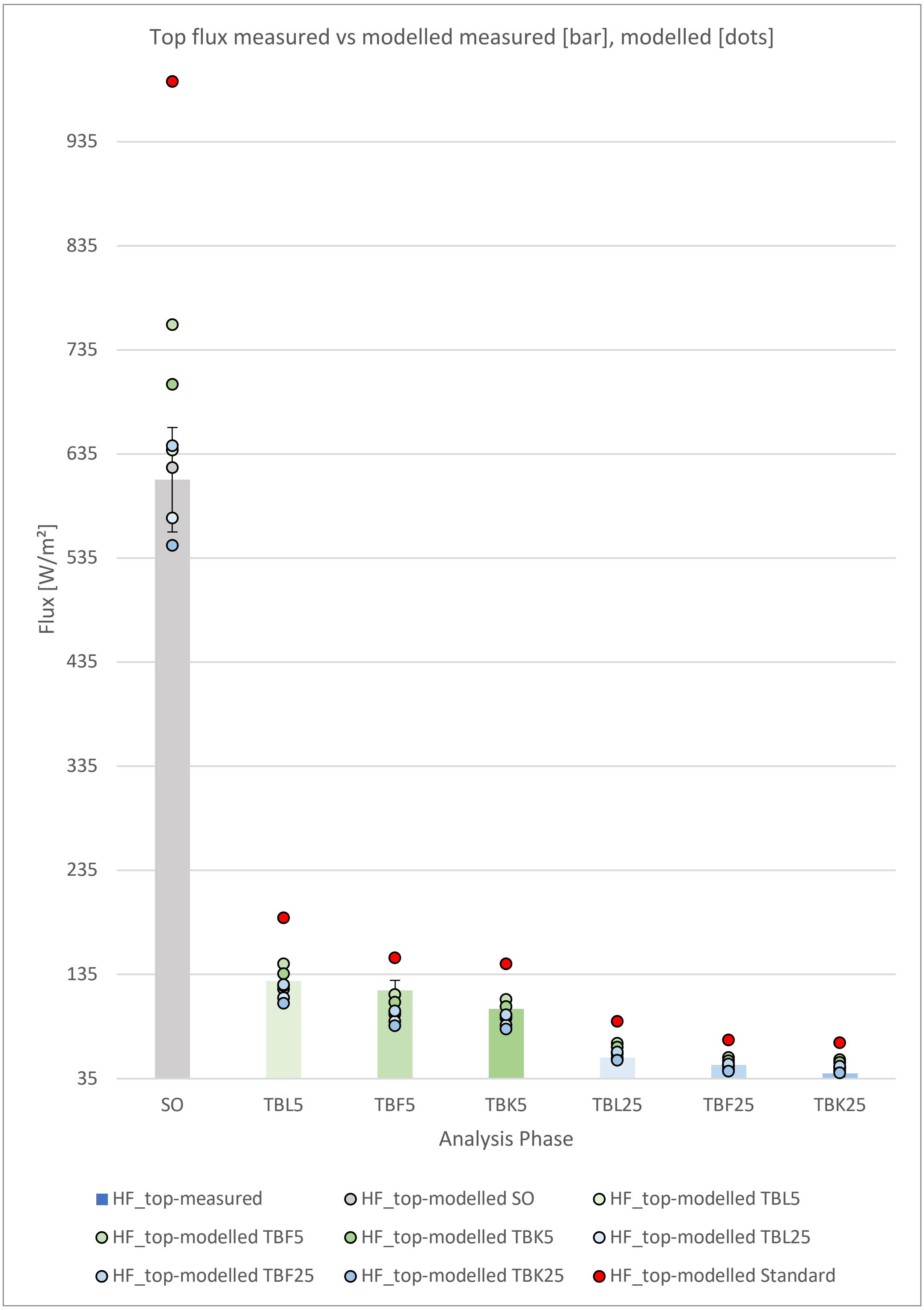

Figure 223 – Shows the embedded top flux measurement [Bar] and uncertainty with every probed response from each simulation model [Dots]

Side flux measured in each phase with uncertainty and every probed response from each simulation model, see Figure 224.

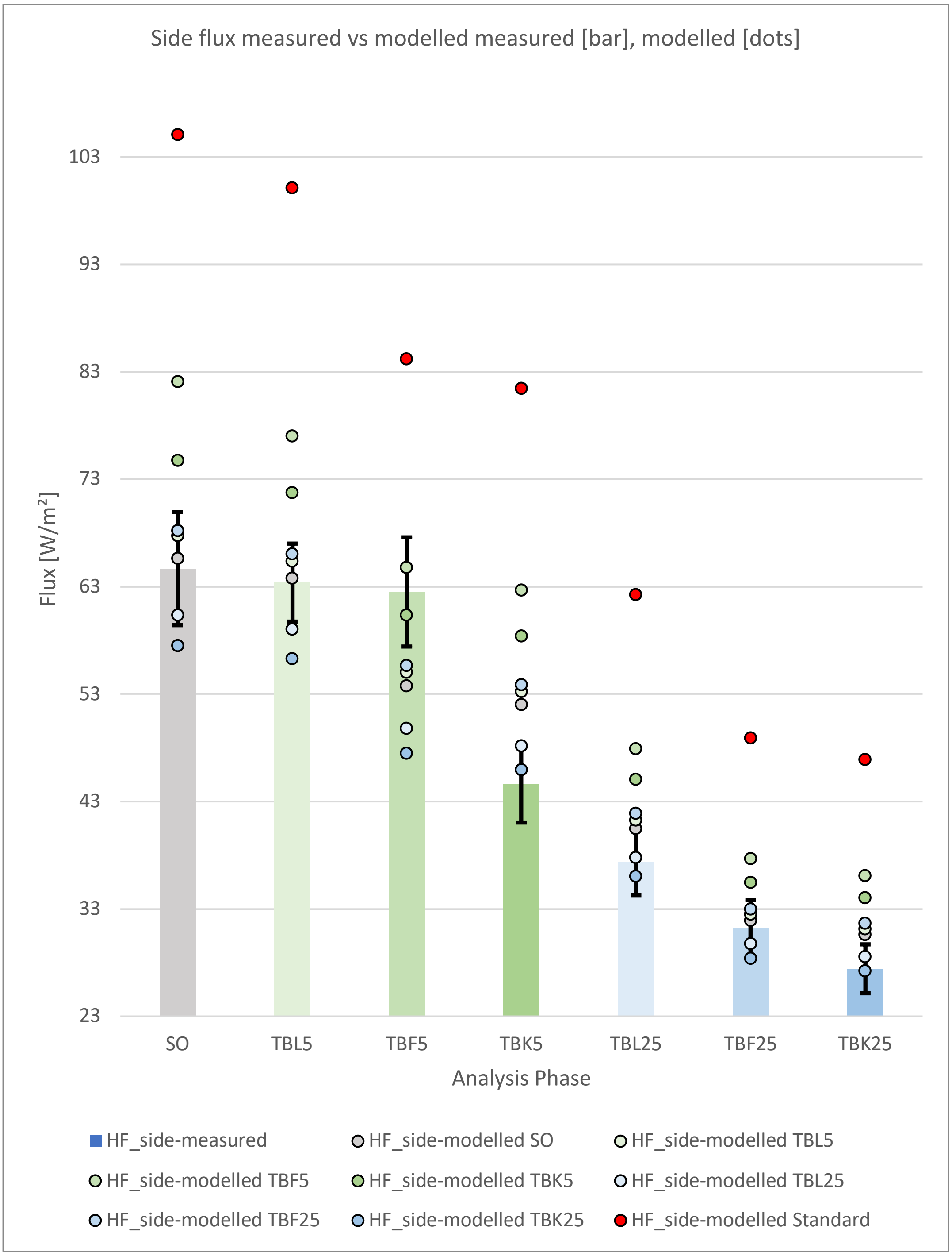

Figure 224 – Shows the embedded side flux measurement [Bar] and uncertainty with every probed response from each simulation model [Dots].

The scale is unfavourable for the STB phases, therefore the 'Steel Only' phase will be removed and the scale reset improving visualisation of the calibrated break phases.

The measured top flux in each phase with uncertainty and every probed response from each simulation model – excluding the 'Steel Only' phase and the response from assuming standardised BC's settings, see Figure 225.

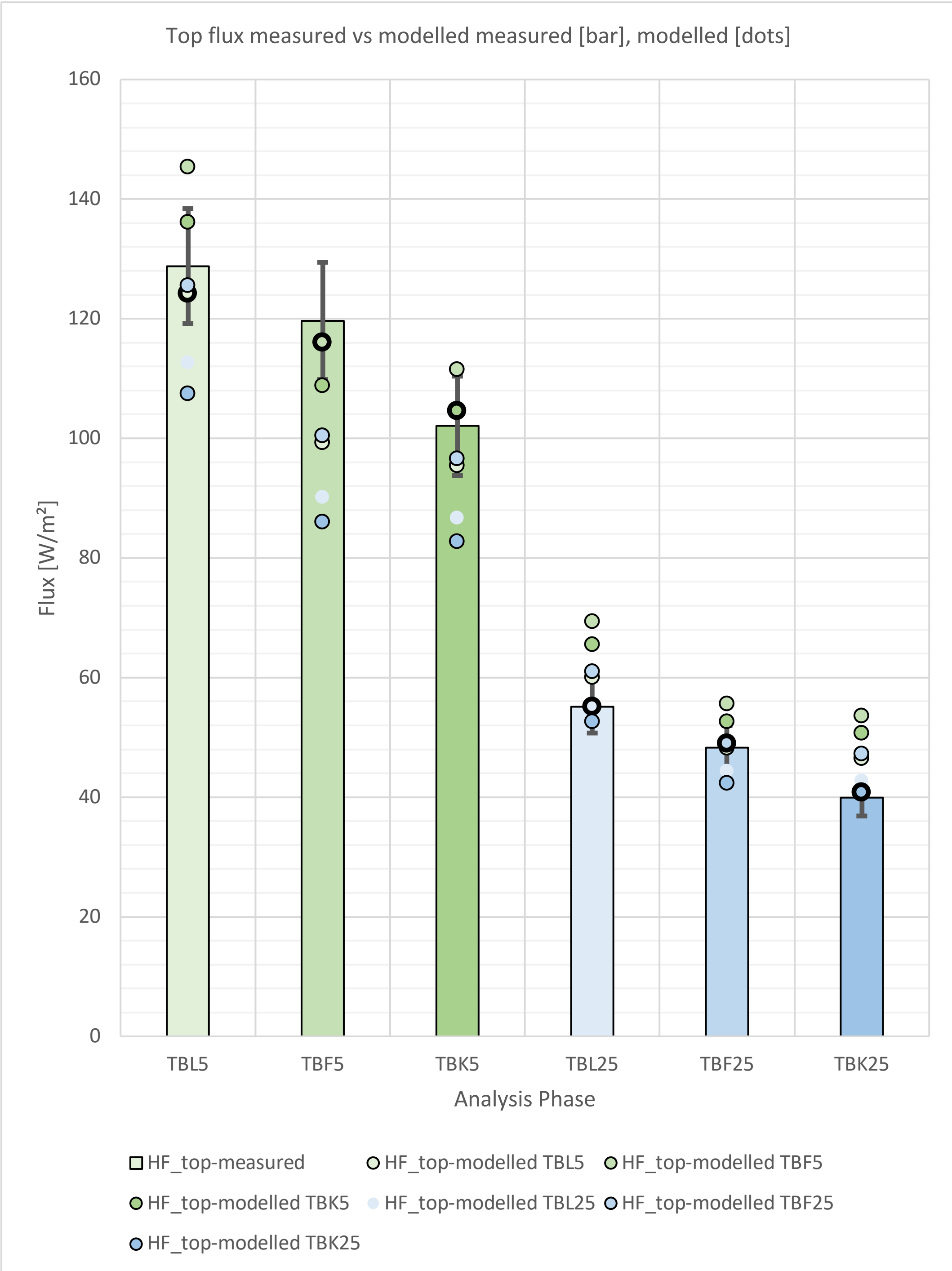

Figure 225 – Shows the embedded top flux measurement [Bar] and uncertainty with every probed response from each simulation model [Dots] – excluding the 'Steel Only' phase and the response from assuming standardised BC's.

The measured side flux in each phase with uncertainty and every probed response from each simulation model – excluding the 'Steel Only' phase and the response from assuming standardised BC's settings, see Figure 226.

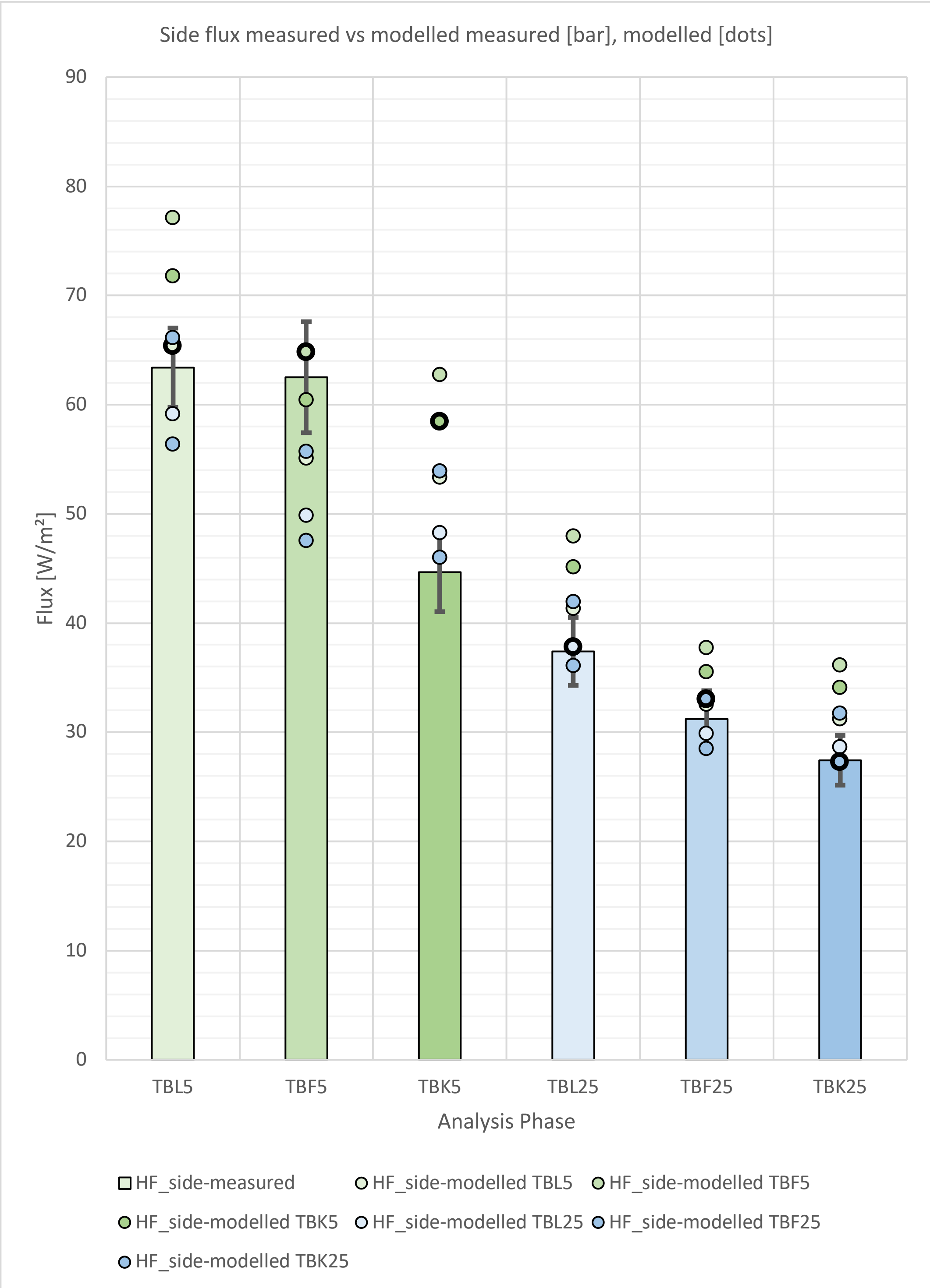

Figure 226 – Shows the embedded side flux measurement [Bar] and uncertainty with every probed response from each simulation model [Dots] – excluding the 'Steel Only' phase and the response from assuming standardised BC's.

6.5 Simulated transmittance results (Chi-values)

As mentioned, once one modelled phase was calibrated, all the other models were simulated using the parameters at that calibration. The TB-transmittance (chi value) can then be calculated, see Table 43 below.

	chi [W/K]	SO	TBL5	TBF5	TBK5	TBL25	TBF25	TBK25
Sim Settings	SO	**0.5447**	0.5043	0.4997	0.4989	0.4606	0.4552	0.4544
	TBL5	0.5797	**0.5343**	0.5291	0.5282	0.4853	0.4793	0.4784
	TBF5	0.6800	0.6144	**0.6076**	0.6065	0.5502	0.5426	0.5414
	TBK5	0.6077	0.5581	0.5524	**0.5515**	0.5048	0.4983	0.4973
	TBL25	0.4997	0.4654	0.4614	0.4608	**0.4283**	0.4235	0.4228
	TBF25	0.5577	0.5163	0.5115	0.5108	0.4715	**0.4659**	0.4651
	TBK25	0.4983	0.4642	0.4602	0.4595	0.4272	0.4225	**0.4218**
	Standard	0.7020	0.6366	0.6293	0.6281	0.5687	0.5605	0.5593

Table 43 – Shows all the calculated point-transmittance for each model under every simulation setting.

By comparing the difference between the actual (calibrated thermal model, informed via measurement) chi-value and that obtained using standardised modelling methodologies, the PG can be determined, as shown in the following Table 44:

PG %	SO	TBL5	TBF5	TBK5	TBL25	TBF25	TBK25
SO	**-22%**	-21%	-21%	-21%	-19%	-19%	-19%
TBL5	-17%	**-16%**	-16%	-16%	-15%	-14%	-14%
TBF5	-3%	-3%	**-3%**	-3%	-3%	-3%	-3%
TBK5	-13%	-12%	-12%	**-12%**	-11%	-11%	-11%
TBL25	-29%	-27%	-27%	-27%	**-25%**	-24%	-24%
TBF25	-21%	-19%	-19%	-19%	-17%	**-17%**	-17%
TBK25	-29%	-27%	-27%	-27%	-25%	-25%	**-25%**

Table 44 – Shows the % differences between the chi-values evaluated using the model calibration techniques developed in these works and the standardised method of calculation.

This shows an underestimation of the chi-value in every case with an average PG of -17% (ranging from -3% to -29%). Speculations can therefore be made that the effect of TB is overestimated in current BPE and heat loss calculations; when bespoke conditions are measured and used to inform the model, less transmittance is seen. This could be due to worst-case values are assumed in standard assessment and the experimental set-up (laboratory based, steady-state conditions) in these works idealises the situation and fails to reflect actual in-situ conditions (solar/wind etc.) accurately.

The % difference between the unbroken ‘Steel Only’ model and each STB models (TBL/F/K 5mm to TBL/F/K 25mm) was calculated for each chi-value. This shows the % saving in transmittance when each STB is employed in the connection interface for each calibrated model settings, see the following Table 45.

	% saving	TBL5	TBF5	TBK5	TBL25	TBF25	TBK25
Simulation setting	SO	7.42%	8.27%	8.41%	15.44%	16.44%	16.59%
	TBL5	7.83%	8.73%	8.87%	16.29%	17.32%	17.48%
	TBF5	9.64%	10.64%	10.80%	19.08%	20.21%	20.37%
	TBK5	8.16%	9.09%	9.24%	16.94%	18.00%	18.16%
	TBL25	6.87%	7.67%	7.80%	14.30%	15.25%	15.39%
	TBF25	7.42%	8.28%	8.42%	15.47%	16.47%	16.62%
	TBK25	6.85%	7.66%	7.78%	14.27%	15.22%	15.36%
	Standard	9.31%	10.35%	10.52%	18.99%	20.15%	20.32%

Table 45 – Shows the % saving when utilising STBs.

To illustrate this further, Figure 227 plots the chi-value response from each model for every calibrated simulation setting on the left-hand-side axis. Whilst the right-hand-side axis shows the % saving when utilising each STB under the calibrated setting. Maximum and minimum % savings are highlighted, see Figure 227.

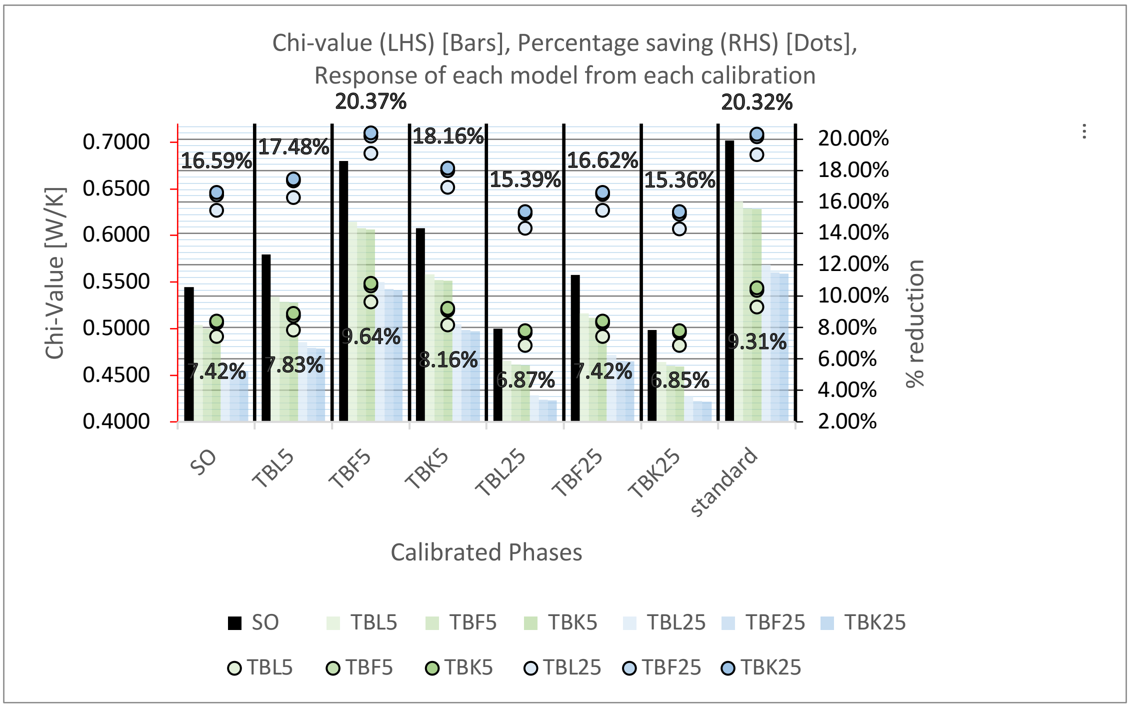

Figure 227 – Shows the point thermal transmittance [Bar] calculated for each model, simulated using the parameters at that calibration (LHS). Also, the % saving [Dots] when using breaks is shown for each calibrated state (RHS).

6.6 f_{Rsi} – Internal surface temperature factor

The results from the studied experiment – comparing the unbroken TB with STB solutions – are shown in the following Table 46:

f_{Rsi}	SO	TBL5	TBF5	TBK5	TBL25	TBF25	TBK25
Minimum Surface temperature [°C]	10.65	11.26	11.35	11.37	12.12	12.26	12.28
External Air Temperature [°C]	-5	-5	-5	-5	-5	-5	-5
Internal Air Temperature [°C]	20	20	20	20	20	20	20
f_{Rsi}	0.626	0.6504	0.654	0.6548	0.6848	0.6904	0.6912

Table 46 – Results from the temperature factor simulation.

That said, the minimum temperature in the model was found to be in the middle of the 'AirBlock', see Figure 228**.**

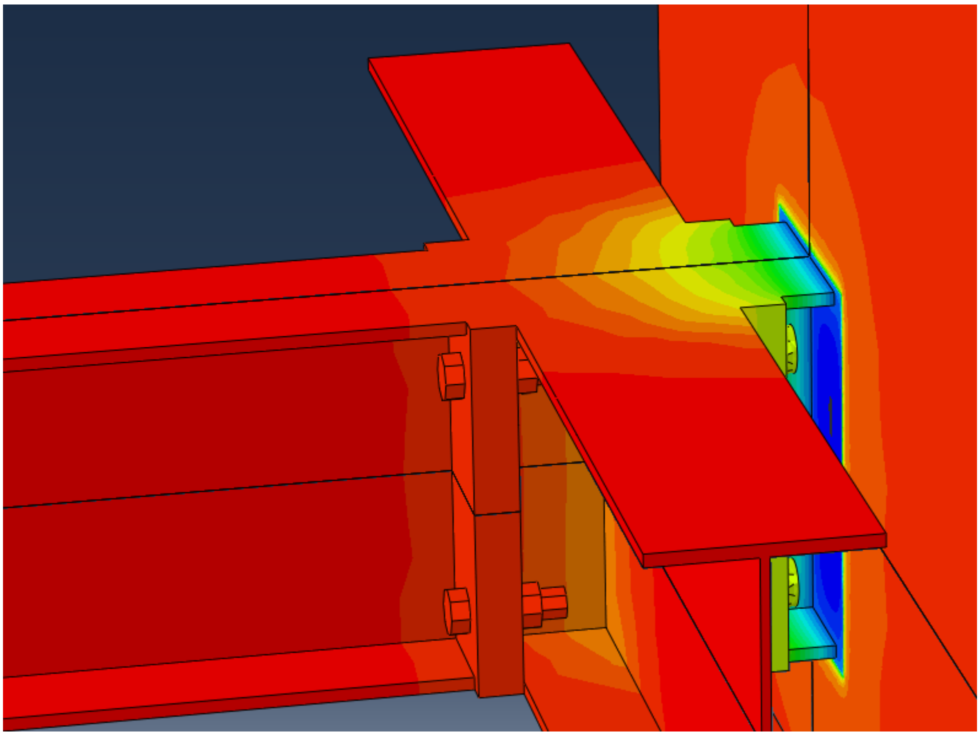

Figure 228 – internal view of the modelled experiment showing minimum inter surface temperature location.

This is an unrealistic location to extract a minimum internal surface temperature from in a real-world construction; no ceiling/floor layers exist in the experimental set-up as it was deemed unsafe to include and too difficult to actualise realistic conditions for the underfloor air cavity where any meaningful measurements to be taken. Therefore, it can be presumed that under proper circumstances the minimum internal surface temperature within the dwelling will be much higher, increasing the f_{Rsi} value to within a safe f_{CRsi}, where the hygiene criterion for domestic residential dwellings, from both BRE and passive house documentations, will be satisfied.

7.0 Discussion

The results presented in these works have fixed all wall layer thicknesses and material properties throughout each simulation, as well as the 'Steel' and 'Air Block' conductivities. Only the BCs were altered attempting to inform the probed embedded flux values in the models (at the break location) to within their associated measurement.

The parameters prescribed at each BC are the surface-fluid HTC and temperature, the former having considerably large uncertainty intervals which broadens the possible sensible range the true values might fall within. Altering the SRs in individual models, however, marginally affects the U-value, which is subsequently used to calculate chi-value.

The chi-value was calculated for each calibrated model once the embedded flux matched the measurement within its uncertainty interval at a 95% confidence level.

The modelled embedded flux (used to calibrate the models) is affected by the simulation BC's and is most sensitive to the SR and the temperature difference (dT). However, prescribing standard BC settings produced higher values in every modelled case, primarily due to the elevated prescribed temperature difference in the simulation, since the greater the dT, the greater the flux experienced at through the break location. The dT however, does not affect the calculated chi-value since this metric is independent of temperature – as is the U-value.

Applying the fixed material property assumption provides decent agreement between the modelled and measured embedded flux in almost every case. The only exception being the TBK5 modelled phase which exhibits large deviation in the side flux, around 31% different than the measured value (see Figure 229 below illustrating this deviation).

The results presented in the previous section show top and side embedded flux values deviating outside their measured uncertainty, Figure 226 is illustrated again below in Figure *229* marking the observed deviation between modelled and measured side flux in the TBK5 model.

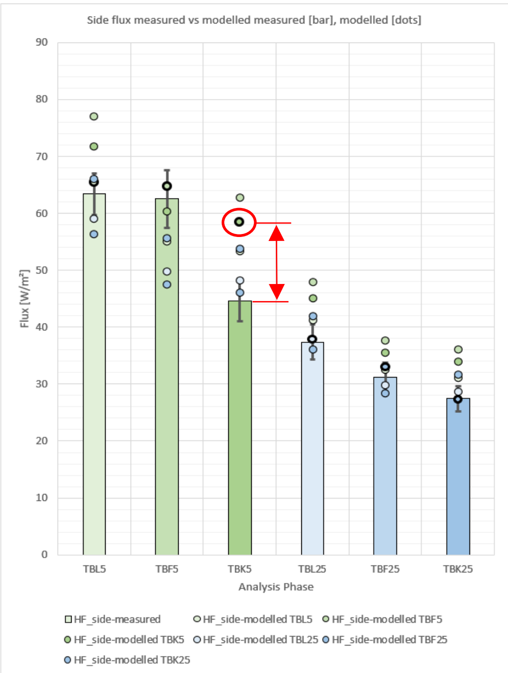

Figure 229 – A copy of Figure 226, illustrating the deviation in TBK5 analysis phase.

The most likely cause of this deviation stems from bias sensor errors in data capture. Also, perfect thermal contact is assumed in the model whereas in reality we know that small air gaps can cause an increased resistance, reducing the flux at the point of measure. The experimental procedure in data capture made every effort to reduce or eliminate these sources of contact error by; ensuring no dust or foreign bodies were presented around the sensors in the connection; applying silicone heat-sink gel to the sensors and the break; the same torque was applied in mechanical tightening which was sequenced over each bolt head ensuring a flush connection and that no twist was present; and cutting recess into the breaks (which not only reduced potential damage to the sensors, but ensured both precise location of the sensors, as well as mitigating air gaps caused by the sensors in the connection). Although, some human error must be allowed for in the test-rig assembly and experimental reproducibility – when altering measurement set-up phases.

Additionally, the 0.5mm recesses cut into the opposite faces of the breaks (to locate and sit the sensors in flush with the break surface) reduce the STB thickness locally at the point of measure by 1mm. For example, the thicker breaks (25mm) are reduced to 24mm whereas the thinner breaks (5mm) are reduced to 4mm, causing a 4% and 20% reduction, respectively. Hence, a greater impact is seen in the 5mm variants oppose to the 25mm, which could explain the error seen in the side flux of the TBK5 simulated model.

The FluxTeq sensors were reused throughout each data capture phase; the flimsy nature quickly became apparent. In retrospect, these thin-film flux sensors are best suited for one use, not to be re-deployed as seen in this experiment. A number of these sensors broke when disassembling the construction and replacements were applied in subsequent measurement phases, leading to potential precision errors.

The chi-values were presented for every model under each calibrated simulation setting allowing a comparison of the breaks at each calibrated simulated state, including standardised simulation setting to illustrate the PG. Compared with using standardised assumptions, all recalibrated model parameters (material properties, BC's) were within their measured uncertainty and therefore reflected a more accurate estimation of the in-situ thermal performance of the unique construction detail investigated.

When comparing the calibrated models (informed with measurement) with simulations assuming standard HTC's and temperatures, the PG becomes obvious. Calculated as the percentage difference between the calibrated model result and standard simulation, the PG ranged from -3% to -29% with an average of -17%. This shows that setting-up the simulation using standardised assumptions over-estimated the transmittance in every case. This is probably because idealistic conditions were observed in the laboratory-based experiments where the measurements informing model re-calibration were taken, compared with inherent uncertainties in conditions experienced in-situ (solar, wind, dynamics, etc), which the standard presumably convertibly considers.

The TBF5 calibrated simulation settings produce very similar chi-values to the standard settings in all models and therefore similar % savings when using the STB solutions were observed – compared to the unbroken model (steel only). The most probably reasoning for this similarity is that the surface-fluid HTC's, used as the BC, were very similar.

The chi-values calculated for the unbroken models ranged from 0.4983–0.7020 [W/K] (see Table 43), depending on the simulated settings prescribed. The minimum value resulted from applying the TBK25 calibrated setting to the SO model (lowest TB resistance) and the maximum – as in every case – resulted from applying the standard settings to the TBK25 model (highest TB resistance). This trend was true for each modelled case: each calibration setting found the maximum chi-value occurred, as expected, to the unbroken model whilst the minimum occurred to the most thermally resistive STBs model (TBK25).

The percentage saving in TB transmittance when utilising breaks, oppose to using none, ranged from:

- 6.85%-9.64% in the TBL5 model
- 7.66%-10.64% in the TBF5 model
- 7.78%-10.8% in the TBK5 model
- 14.27%-19.08% in the TBL25 model
- 15.22%-20.21% in the TBF25 model
- 15.36%-20.37% in the TBK25 model

These findings show that when using a 25mm break oppose to 5mm, the heat loss saving is roughly doubled and, in each case, as the STB resistance increases, so does the percentage saving. The differing material conductivity of the STBs is less significant than the increase in thickness since the conductivities do not vary greatly (L=0.292, F=0.2, and K=0.187 [W/m^{2}K]).

The critical temperature factor was calculated for each model using standardised BCs: internally 20 [°C] at 4 [W/m^{2}K] and externally -5 [°C] at 25 [W/m^{2}K].

A minimum internal surface temperature was found in the least resistive TB phase as 10.65 [°C] producing an f_{Rsi} of 0.626, whilst in the most resistive TB phase a minimum surface temperature of 12.28 [°C] produced an f_{Rsi} of 0.6912, see Table 46.

The BRE state a f_{CRsi} value of 0.75 limits the risk of mould growth in residential buildings. The findings here show, even utilising the most resistive structural thermal break, the critical value is underachieved with a maximum f_{Rsi} value of 0.6912. However, the risk of condensation is mitigated for storage buildings (f_{CRsi} = 0.3) and offices/retail premises (f_{CRsi} = 0.5), but not for high humidity operations such as swimming pools (f_{CRsi} = 0.8-0.9).

Passive house hygiene criteria for a cool, temperate climate (as found in northern Europe, for example) states a critical temperature factor (f_{CRsi} = 0.7), which is very nearly achieved with the most resistive breaks.

Comparing the f_{Rsi} result with the criterion from BRE and passive house, the minimum internal surface temperature failed to meet the threshold of condensation risk aversion for residential buildings in every case. Without thermally breaking the structural connection the minimum internal surface temperature was calculated as 10.65 [°C] producing an f_{Rsi} of 0.626, and by including thermal breaks, the minimum internal surface temperature increases – subsequently reducing condensation risk with an increasing f_{Rsi} – as the resistance of the break increases. Utilising STBs was found to increase the minimum internal temperature between 0.6°C and 1.63°C, corresponding to an increase in f_{Rsi} between 0.0244 and 0.0652 illustrating low impact. The material choice of the surrounding wall composition may be of more influence on the f_{Rsi} compared with the STBs.

HOW DOES THIS FIT INTO THE WIDER CONTEXT AND AGREE WITH THE LITERATURE ALREADY DONE.

8.0 Conclusion

8.1 Overall findings

The experimental design proposed in these works attempts to combine measurement and modelling to evaluate in-situ TB-transmittance. Since numerical solutions are the only way to quantify 3D point transmittances, like them caused by cantilever balcony supports, temperature and heat flux measurements informed bespoke thermal simulation parameterisation. Currently, standardised numerical solutions assume BC (SR and dT). Comparing the experimental designs calibrated models to these standardised approaches allows the PG to be calculated.

The experimental design was initially validated by comparing two novel measurement methods found in literature, measuring the linear transmittance from a common 2D TB using HFM and IR, with the proposed recalibration method using measurements taken from the investigated construction detail.

A simple corner wall junction was chosen for analysis in the EH facility at UoS. The experiment showed good agreement between the two measurements and the calibrated model results.

Developing the experimental design further, it was subsequently applied to analyse a point transmittance, where no comparable novel measurement methodologies are available, caused by a single beam anchored to the external wall of the EH.

No standardised or novel measurement methodologies exist to evaluate the heat loss through this complex 3D geometry unlike simpler bridges (T. Theodosiou et al., 2021), as investigated in the preliminary 2D experiment. Hence 3D FE modelling is required for bespoke thermal performance estimations of point-TB with good knowledge of the surrounding details as simplifications can cause erroneous gaps between expectations and reality.

In-situ conditions were sort after although, since it is a laboratory-based experiment, idealisations were realised. Issues regarding imperfect thermal contact, internal stratification / proximity to surrounding TBs, and minimal bridging due steel beam penetration were observed. These were respectively mitigated by smoothing the steel–brick interface with a soft mortar mix; exciting the internal air with a fan to mitigate stratification and internal obstructions; and applying EWI to exacerbate the TB affect.

In this experiment, thin-film flux sensors were applied within the connection STB interface. These were used to inform model calibration; the material properties and BCs were altered in subsequent simulation iterations until the probed flux (modelled) in the connection interface matched the embedded thin-film sensor measurements within a sensible tolerance dictated by the uncertainty analysis.

Comparisons were made between a thermally broken and unbroken connection in a bare wall configuration and an externally insulated wall configuration. The results were purely numerical and a reduction in TB-transmittance was observed in both cases: a 6.7% transmittance reduction was seen when using a STB solution in the bare wall configuration and a larger transmittance reduction of 15.4% was seen in the EWI configuration. The minimum internal surface temperature was raised from 20.56℃ to 20.61℃ in the bare wall configuration when the STB was in the connection, whereas it was increased from 21.62℃ to 26.5℃ in the EWI configuration. Even the lowest temperature reported here passes the criterion for condensation or mould formation on the internal surface, most likely because the bridging effect was not detrimental to the structure, unrepresentative of the worst-case scenarios which this nuanced type of structural TB is manifested.

Findings suggested that to develop the experimental design further, SR measurements and thorough uncertainty analysis is required to accurately capture the heat transfer mechanisms experienced by any individual investigated construction detail. Further experiments should consider a real-world connection, representative of a worst-case scenario, in a wall configuration reflecting modern new-builds – where this TB phenomena is pertinent – and with dynamic in-situ conditions.

Therefore, the final experiment initially attempted to monitor a real balcony construction, but because of onsite collaboration failure and the global pandemic, the final experiment used the EH facility at UoS once more.

The upstairs window was removed from the neighbouring building to the EH (built within the same climatic chamber) and used to facilitate the test rig. The test rig was comprised of a representative lightweight cladding wall system aiming to achieve a U-value <0.18 [W/m^{2}K] – as per recent building regulation for new-builds, with which could then be bridged with a fabricated mock-up of a cantilever beam balcony system (steel-to-steel connection), then subsequently broken by various STB solutions. The modular steel design allowed various breaks to be tested – 2 thicknesses (5mm and 25mm) of 3 materials (TBL, TBF, and TBK).

Surface heat flux and temperature measurement (both air and surface) were used to process U-values (supporting the material thickness and conductivity assumptions in the calibrated model) and SR-values (informing the simulated BC settings). Prior to experimentation, samples of each wall layer and thermal break materials were tested for their conductivity in a separate laboratory apparatus which also informed the material properties within the models.

Again, thermal models were calibrated using measured BCs (SR and dT) whilst considering the embedded flux measurements within the connection. Once the probed simulation values correlated to their measured counterpart – to within their respective measurement uncertainty – the model was considered calibrated. Then, each model was simulated using these calibrated settings, allowing comparison of STB impact. Each model was also simulated considering standardised simulation settings allowing the PG to be calculated between calibrated and standard assessed models.

Results showed that the TB-transmittance reduced and the f_{Rsi} increased as the STB resistance increased, saving between 6.85% and 20.37% depending on the break and calibration settings applied. The calibrated models outperformed (showed less transmittance) the standardised models in every case with PG ranging from -3% to -29% with an average of -17%.

The reason standard assessments overestimate the transmittance is due to the worst-case assumed BCs geared to encapsulate dynamic environmental conditions (solar, wind speed variations) within a steady calculation, whereas the calibrated models have measured these convective and radiative interactions effecting a bespoke construction.

The largest limitations to this measurement and modelling study are due to the geometry investigated (single balcony support with no internal ceiling void or external balcony) and real-world dynamic conditions. As mentioned, due to unsuccessful industry collaboration and the global pandemic, the well-instrumented EH test facility at the UoS was used again in this final experiment. Steady-state temperatures were realised allowing rapid testing of many STB variation. However, this is laboratory controlled and lacks the dynamic natural mechanisms which real buildings are exposed to.

Findings suggest future works could address questions such as:

- Do we need thicker breaks at the top of the building?
- Or do south facing facades need less thermal breakage?

Considering an increased convection and solar radiation, respectively, since the TB-transmittance calculation is sensitive to these parameters.

The measurement informed (calibrated) models have been proven within the laboratory environment, now onsite field testing, where a real balcony detail experiences dynamic external weather conditions, should be tested.

8.2 Review of objectives

Bring in objectives – Did I meet them – go through each one

- Identify the causes of the PG in both measurement and thermal FE modelling.
- Understand and criticise existing methodologies assessing building performance.
- Explore assumptions in modelling building performance.
- Design and conduct experiments to correlate the performance of the product by comparing results using standardised numerical modelling to simulations informed with physical measurement.
- Formulate findings and provide insights/recommendations related to the evaluation of this nuanced TB and break product.

8.3 Original contribution to knowledge

Have I achieved what I set out to – they key 2 SHOW

The proposed body of research makes an original contribution to knowledge in the following areas:

- Calibrating models using measured data (taken in and around bespoke structural TB details and STB solutions) to reflect real world performance. The numerical estimation maps the multi-dimensional heat flows and complex temperature distributions through a FE model of the investigated detail. Informing the model using measurements reduces some uncertainties stemming from assumptions in the model data and enables quantification of the accepted TB transmittance metric with greater accuracy compared with standard numerical assessments.

- The experimental design is developed by testing a range of STB products in a well-instrumented laboratory under climatic-controlled conditions; emulating steady-state conditions allows validation of novel measurement methodologies and theory which the adopted grey-box parametric model re-calibration method can then be verified against. Ensuring a thorough understanding of the measurement uncertainties hopes to produce a robust interpretation of heat loss and cold spots cause by structural point-connections.

- Energy performance practitioners are provided with a greater understanding of possible evaluation methods assessing the associated heat loss and corresponding cold spots attributed to structural TBs in-situ, post construction.

- Broadening the knowledge around the impacts of STB solutions increases their application and accurate inclusion in whole building energy performance calculations.

8.4 Further work

In-situ evaluation

External live monitoring of SR could be achieved

Because if we just simply monitor the effect of convection or radiation without embedding sensors, we may not understand if a thermal model is calibrated and deduce the effectiveness of the STB solution, *since, as we have seen in this study, the flux through the connection depends heavily on exposure to convection – when the HVAC was used. Interestingly enough, the measured SRext didn't alter all that much between chiller and HVAC conditioning periods.*

Therefore, case studies should consider monitoring breaks at different Height in building on the north and south facing façades.

Different connection types should be investigated also:

- concrete-to-concrete
- steel-to-concrete connection

Either in horizontal or vertical situations

- column sections to the ground
- roof penetrations

extreme applications

- ice cream factory in the desert
- sauna on the moon

8.5 Summary and conclusion

4-5 big take aways – and their implication

Solid state thermal breaks have shown to be effective at isolating heat-flow. In this study, a 20% saving in transmittance was found when the most resistive STB tested was breaking the connection

The verifies the efficacy of this solution

When understanding measurement uncertainty needs to be thorough, accurate, and precise – or you won't get good data to inform the model. All measurements in this study were lab based which reduced variability of conditions. The test was steady-state, not dynamic, so this may have implications on the data when measuring in-situ.

Surface resistances were measured using a basic technique; essentially the heat flux was captured on the surface of the wall whilst measuring its surface and local air temperature. Knowing the temperature difference either side of the flux plate, and the flux going through the plate, the fluid/solid heat transfer can be deduced. This was a fairly simple and effective method in this laboratory-based situation, but large uncertainties remained in its calculated SR measurand due to the miniscule temperature difference used in the propagation of errors.

Not only are the uncertainties high with this method, but it may also be hard to apply the sensors in-situ due to access, and an alternative method, one that measures radiation and convection individually – combining metrics in a more in-depth calculation to estimate the SR – could be more effective and accurate. However, this generally requires expensive measurement instruments and significantly more analysis time. Good data was realised and averaged over 12hr measurement periods in this steady-state study, but in-situ, long data captures over a few months may be required to represent the SR.

Model assumptions need to be thorough, accurate, and precise – or you won't get a good outcome; its all right having good measured data to parameterise a simulation, but if you are not vigilant in following standardised guidance when preparing the meshed geometry, prescribing properties, and applying conditions, the outcome will be different to others if repeated and could be wildly wrong.

The performance gap, when measured, showed that using standardised assumptions overestimated the thermal transmittance. This occurred due to the boundary conditions used; the measured SR was much lower than the standard assumption, both internally and externally. Although this study was performed in controlled laboratory environment where quasi steady-state conditions were realised, the implications of overestimating thermal transmittances means building evaluators underestimates how well the building performs, causing designers/specifiers/architects to over-engineer the construction, inflating costs unnecessarily. Since the model response is somewhat sensitive to the BCs, it is probable that the convective and radiative mechanisms, experienced in-reality, affect TB transmittance in the same way. Therefore, individual connections, positioned at different locations in the façade, would experience a variety of effects based on orientation to the sun and external convection fluctuations – which could conceivably be caused by abnormal façades or other wind augmenting objects. In this sense, every detail is unique and may not abide by government approved assumptions, standardised as guidance. Therein, another performance gap contributor when performing external surveys – which is the essence off the advised future work.

9.0 References

ABAQUS. (2021). *Uncoupled heat transfer analysis*.

Abdul, Y., & Hadi, M. (2016). *Performance of exemplar buildings in use Bridging the performance gap*.

Akarcay, A., Lister, C., & Pemberton, J. (2020). *Want less bounce in your balcony ? 44*(0).

Albatici, R., Passerini, F., Tonelli, A. M., & Gialanella, S. (2013). Assessment of the thermal emissivity value of building materials using an infrared thermovision technique emissometer. *Energy and Buildings*, *66*, 33–40. https://doi.org/10.1016/J.ENBUILD.2013.07.004

Albatici, R., & Tonelli, A. M. (2010). Infrared thermovision technique for the assessment of thermal transmittance value of opaque building elements on site. *Energy and Buildings*, *42*(11), 2177–2183. https://doi.org/10.1016/J.ENBUILD.2010.07.010

Albatici, R., Tonelli, A. M., & Chiogna, M. (2015). A comprehensive experimental approach for the validation of quantitative infrared thermography in the evaluation of building thermal transmittance. *Applied Energy*, *141*, 218–228. https://doi.org/10.1016/J.APENERGY.2014.12.035

Al-Sanea, S. A., & Zedan, M. F. (2012). Effect of thermal bridges on transmission loads and thermal resistance of building walls under dynamic conditions. *Applied Energy*, *98*, 584–593. https://doi.org/10.1016/j.apenergy.2012.04.038

Alzetto, F., Farmer, D., Fitton, R., Hughes, T., & Swan, W. (2018). Comparison of whole house heat loss test methods under controlled conditions in six distinct retrofit scenarios. *Energy and Buildings*, *168*, 35–41. https://doi.org/10.1016/j.enbuild.2018.03.024

Ambrosini, D., Paoletti, D., Sfarra, S., Nardi, I., & Sfarra, S. (2015). *Combining Infrared Thermography and Numerical Analysis for Evaluating Thermal Bridges In Buildings: A Case Study* (Vol. 5, Issue 1).

Anderson, B. (2006). *Conventions for U-value calculations BR 443*.

ANSYS. (2021). *Ansys Mechanical Heat Transfer*. https://www.ansys.com/en-gb/training-center/course-catalog/structures/ansys-mechanical-heat-transfer

Antherm. (2020). *AnTherm*. http://www.antherm.at/antherm/EN/Downloads.htm

Ascione, F., Bianco, N., De Masi, R. F., de' Rossi, F., & Vanoli, G. P. (2013). Simplified state space representation for evaluating thermal bridges in building: Modelling, application and validation of a methodology. *Applied Thermal Engineering*, *61*(2), 344–354. https://doi.org/10.1016/J.APPLTHERMALENG.2013.07.052

Ascione, F., Bianco, N., De Masi, R. F., Mauro, G. M., Musto, M., & Vanoli, G. P. (2014). Experimental validation of a numerical code by thin film heat flux sensors for the resolution of thermal bridges in dynamic conditions. *Applied Energy*, *124*, 213–222. https://doi.org/10.1016/J.APENERGY.2014.03.014

Ascione, F., Bianco, N., Rossi, F. de', Turni, G., & Vanoli, G. P. (2012). Different methods for the modelling of thermal bridges into energy simulation programs: Comparisons of accuracy for flat heterogeneous roofs in Italian climates. *Applied Energy*, *97*, 405–418. https://doi.org/10.1016/J.APENERGY.2012.01.022

Asdrubali, F., & Baldinelli, G. (2011). Thermal transmittance measurements with the hot box method: Calibration, experimental procedures, and uncertainty analyses of three different approaches. *Energy and Buildings*, *43*(7), 1618–1626. https://doi.org/10.1016/J.ENBUILD.2011.03.005

Asdrubali, F., Baldinelli, G., & Bianchi, F. (2012). A quantitative methodology to evaluate thermal bridges in buildings. *Applied Energy*, *97*, 365–373. https://doi.org/10.1016/J.APENERGY.2011.12.054

Asdrubali, F., Baldinelli, G., Bianchi, F., Costarelli, D., Rotili, A., Seracini, M., & Vinti, G. (2018). Detection of thermal bridges from thermographic images by means of image processing approximation algorithms. *Applied Mathematics and Computation*, *317*, 160–171. https://doi.org/10.1016/J.AMC.2017.08.058

Asdrubali, F., D'Alessandro, F., Baldinelli, G., & Bianchi, F. (2014). Evaluating in situ thermal transmittance of green buildings masonries—A case study. *Case Studies in Construction Materials*, *1*, 53–59. https://doi.org/10.1016/J.CSCM.2014.04.004

ASTM. (2013a). *C1046 - Standard Practice for In-Situ Measurement of Heat Flux and Temperature on Building Envelope Components*. https://doi.org/10.1520/C1046-95R13

ASTM. (2013b). *C1155 - Standard Practice for Determining Thermal Resistance of Building Envelope Components from the In-Situ Data 1*. https://doi.org/10.1520/C1155-95R13

ASTM. (2015). C518-17: Standard Test Method for Steady-State Thermal Transmission Properties by Means of the Heat Flow Meter Apparatus. *ASTM*, 1–15. https://doi.org/10.1520/C0518-17.2

ASTM. (2017). *C1130 - Standard Practice for Calibration of Thin Heat Flux Transducers 1*. https://doi.org/10.1520/C1130-17

ASTM. (2022). *Standard Practices for Air Leakage Site Detection in Building Envelopes and Air Barrier Systems*. https://doi.org/10.1520/E1186-22.2.

Atsonios, I. A., Mandilaras, I. D., Kontogeorgos, D. A., & Founti, M. A. (2018). Two new methods for the in-situ measurement of the overall thermal transmittance of cold frame lightweight steel-framed walls. *Energy and Buildings*, *170*, 183–194. https://doi.org/10.1016/J.ENBUILD.2018.03.069

Baba, F., & Ge, H. (2016a). Dynamic effect of balcony thermal bridges on the energy performance of a high-rise residential building in Canada. *Energy and Buildings*, *116*, 78–88. https://doi.org/10.1016/J.ENBUILD.2015.12.044

Baba, F., & Ge, H. (2016b). Dynamic effect of balcony thermal bridges on the energy performance of a high-rise residential building in Canada. *Energy and Buildings*, *116*, 78–88. https://doi.org/10.1016/j.enbuild.2015.12.044

Baker, P. (2009). *Research into the thermal performance of traditional windows: timber sash windows*.

Baker, P. (2011). Technical Paper 10 - U-values and traditional buildings. *Kardiologiya*, *19*(1), 17–23.

Balaras, C. A. (1996). The role of thermal mass on the cooling load of buildings. An overview of computational methods. *Energy and Buildings*, *24*(1), 1–10. https://doi.org/10.1016/0378-7788(95)00956-6

Balaras, C. A., & Argiriou, A. A. (2002). Infrared thermography for building diagnostics. *Energy and Buildings*, *34*(2), 171–183. https://doi.org/10.1016/S0378-7788(01)00105-0

Baldinelli, G., Bianchi, F., Rotili, A., Costarelli, D., Seracini, M., Vinti, G., Asdrubali, F., & Evangelisti, L. (2018). A model for the improvement of thermal bridges quantitative assessment by infrared thermography. *Applied Energy*, *211*, 854–864. https://doi.org/10.1016/J.APENERGY.2017.11.091

Ballarini, I., & Corrado, V. (2009). Application of energy rating methods to the existing building stock: Analysis of some residential buildings in Turin. *Energy and Buildings*, *41*(7), 790–800. https://doi.org/10.1016/J.ENBUILD.2009.02.009

Barreira, E., De Freitas, V. P., Delgado, J. M. P. Q., & Ramos, N. M. M. (2012). *Thermography Applications in the Study of Buildings Hygrothermal Behaviour*.

Bauwens, G., & Roels, S. (2014). Co-heating test: A state-of-the-art. *Energy and Buildings*, *82*, 163–172. https://doi.org/10.1016/j.enbuild.2014.04.039

BC Hydro. (2016). *Building Envelope Thermal Bridging Guide*.

BEIS. (2020). *Department for Business, Energy & Industrial Strategy*. https://www.gov.uk/government/organisations/department-for-business-energy-and-industrial-strategy?utm_source=BEIS&utm_medium=shorturl&utm_campaign=BEIS-shorturl

BEIS. (2021a). *Energy Consumption in the UK (ECUK) 1970 to 2020*.

BEIS. (2021b). *HM Government – Heat and Buildings Strategy*.

BEIS. (2021c). *National Energy Efficiency Data-Framework (NEED) report: June 2021*.

BEIS ECUK. (2018). *Energy consumption in the UK*.

Ben Larbi, A., Couchaux, M., & Bouchair, A. (2017). Thermal and mechanical analysis of thermal break with end-plate for attached steel structures. *Engineering Structures*, *131*, 362–379. https://doi.org/10.1016/J.ENGSTRUCT.2016.10.049

Benko, I. (2002). *Quantitative analysis of thermal bridges of structures through infrared thermograms*. https://doi.org/10.21611/qirt.2002.027

Berggren, B., & Wall, M. (2013). Calculation of thermal bridges in (Nordic) building envelopes – Risk of performance failure due to inconsistent use of methodology. *Energy and Buildings*, *65*, 331–339. https://doi.org/10.1016/J.ENBUILD.2013.06.021

Berggren, B., & Wall, M. (2018). State of Knowledge of Thermal Bridges—A Follow up in Sweden and a Review of Recent Research. *Buildings*, *8*(11), 154. https://doi.org/10.3390/buildings8110154

Bianchi, F., Pisello, A. L., Baldinelli, G., & Asdrubali, F. (2014). Infrared thermography assessment of thermal bridges in building envelope: Experimental validation in a test room setup. *Sustainability (Switzerland)*. https://doi.org/10.3390/su6107107

Biddulph, P., Gori, V., Elwell, C. A., Scott, C., Rye, C., Lowe, R., & Oreszczyn, T. (2014). Inferring the thermal resistance and effective thermal mass of a wall using frequent temperature and heat flux measurements. *Energy and Buildings*, *78*, 10–16. https://doi.org/10.1016/j.enbuild.2014.04.004

Black, R. (2021). *Energy & Climate Intelligence Unit | How is the UK tackling climate….* https://eciu.net/analysis/briefings/uk-energy-policies-and-prices/how-is-the-uk-tackling-climate-change

Blomberg, T. (1996). *HEAT CONDUCTION IN TWO AND THREE DIMENSIONS Computer Modelling of Building Physics Applications*.

Bordass, B., Bordass, B., & Associates, W. B. (2004). Energy Performance of Non-Domestic Buildings: Closing the Credibility Gap. *IMPROVING ENERGY EFFICIENCY OF COMMERCIAL BUILDINGS CONFERENCE*, 21--22.

BRE. (2017). *RdSAP Conventions*.

BRE. (2019a). *Certified Thermal Details and Products scheme : BRE Group*. https://www.bregroup.com/certifiedthermalproducts/podpage.jsp?id=3590

BRE. (2019b). *The Passivhaus Standard*. https://www.bregroup.com/a-z/the-passivhaus-standard/

BRE. (2022). *New BRE Global certification scheme for the thermal performance of details and products is launched - BRE Group*. https://bregroup.com/press-releases/new-bre-global-certification-scheme-for-the-thermal-performance-of-details-and-products-is-launched/

Broome, J., Clarke, A., Smyth, P., Taylor, M., Allen, M., Bere, J., Bootland, J., Butcher, B., Goodman, A., Herring, C., Hines, J., Pelsmakers, S., Tuohy, P., Warm, P., Mead, K., & Everhart, T. (2015). *Claiming the Passivhaus Standard: Technical briefing document*.

Bros-Williamson, J., Stinson, J., Garnier, C., & Currie, J. (2014). In-situ monitoring of thermal refurbishment on pre-1919 properties in Scotland Introduction-context & background. *International Journal of Sustainable Construction*, *2*(1), 26–33. https://doi.org/10.14575/gl/ijsc/02-01/003

BSI. (1991a). *ISO 8301-1991*.

BSI. (1991b). *ISO 8302-1991*.

BSI. (2008a). *Industrial platinum resistance thermometers and platinum temperature sensors*. *EN 60751:2008*, 28.

BSI. (2012a). *BSI Standards Publication (ISO 13788:2012) Hygrothermal performance of building components and building elements-Internal surface temperature to avoid critical surface humidity and interstitial condensation-Calculation methods*.

BSI. (2015a). *BS EN ISO 9972-2015Thermal performance of buildings - Determinatino of sir permeability of buildings - Fan pressurization*.

BSI. (2017a). *PD CEN ISO/TR 52019-2:2017 Energy performance of buildings - Hygrothermal performance of building components and building elements — Part 2: Explanation and justification 1*.

BSI. (2022). *BS 40101-2022 - Building Performance evaluation and operational buildings (using data gathered from tests, measurements, observation and user experience) - Specifications*.

BSI, B. S. I. (1996a). ISO 8990 Thermal insulation — Determination of steady-state thermal transmission properties — Calibrated and guarded hot box. *Bsi*, 26.

BSI, B. S. I. (1996b). *Thermal insulation-Determination of steady-state thermal transmission properties-Calibrated and guarded hot box. BS EN ISO 8990:1996*.

BSI, B. S. I. (1998). *Thermal performance of buildings -Determination of thermal resistance by hot box method using heat flow meter - Masonry. BS EN 1934-1998*.

BSI, B. S. I. (2000). *Thermal performance of building products and components – Specific criteria for the assessment of laboratories measuring heat transfer properties – Part 4: Measurements by hot box methods. BS EN 1946-4:2000*.

BSI, B. S. I. (2003). *Thermal performance of windows, doors and shutters-Determination of thermal transmittance by hot box method-Part 2: Frames 12412-2:2003*.

BSI, B. S. I. (2007). *10456:2007 Building materials and products - hygrothermal properties - tabulated design values got determining declared and design thermal values*.

BSI, B. S. I. (2008b). *Condition monitoring and diagnostics of machines — Thermography — ISO 18434*. *3*.

BSI, B. S. I. (2010). *BSI Standards Publication Thermal performance of windows and doors-Determination of thermal transmittance by the hot-box method. BS EN ISO 12567-1: 2010*.

BSI, B. S. I. (2012b). *BSI Standards Publication Masonry and masonry products-Methods for determining thermal properties. BS EN 1745:2012*.

BSI, B. S. I. (2014). *BS ISO 9869-1 Thermal insulation — Building elements — In- situ measurement of thermal resistance and thermal transmittance Part 1 : Heat flow meter method*.

BSI, B. S. I. (2015b). *BS EN ISO 6781-3:2015 Performance of buildings — Detection of heat , air and moisture irregularities in buildings by infrared methods Part 3 : Qualifications of equipment operators , data analysts and report writers*.

BSI, B. S. I. (2017b). *BS EN ISO 6946:2017 - Building components and building elements-Thermal resistance and thermal transmittance-Calculation methods*.

BSI, B. S. I. (2017c). *BS EN ISO 10211:2017 - Thermal bridges in building construction-Heat flows and surface temperatures-Detailed calculations*.

BSI, B. S. I. (2017d). *BS EN ISO 12631:2017 BSI Standards Publication Thermal performance of curtain walling - Calculation of thermal transmittance*.

BSI, B. S. I. (2017e). *BS EN ISO 13370 : 2017 Thermal performance of buildings - Heat transfer via the ground - Calculation methods*. 1–49.

BSI, B. S. I. (2017f). *BS EN ISO 13786:2017 Thermal performance of building components - Dynamic thermal characteristics - Calculation methods*.

BSI, B. S. I. (2017g). *BS EN ISO 13789 -Thermal performance of buildings-Transmission and ventilation heat transfer*.

BSI, B. S. I. (2017h). *BS EN ISO 14683:2017 - Thermal bridges in building construction-Linear thermal transmittance-Simplified methods and default values*.

BSI, B. S. I. (2018a). *BS EN ISO 7345 : 2018 BSI Standards Publication Thermal performance of buildings and building components - Physical quantities and definitions (ISO 7345 : 2018)*.

BSI, B. S. I. (2018b). *Thermal insulation — Building elements — In-situ measurement of thermal resistance and thermal transmittance. BS ISO 9869-2:2018*.

Budaiwi, I., & Abdou, A. (2013). The impact of thermal conductivity change of moist fibrous insulation on energy performance of buildings under hot-humid conditions. *Energy and Buildings*, *60*, 388–399. https://doi.org/10.1016/j.enbuild.2013.01.035

Butler, D., Diagnostics, B., & Dengel, A. (2013). *Review of co-heating test methodologies*.

Cambridge Consultants. (2021). *Veritherm: System Overview and Verification Results*.

Campbell Scientific Inc. (2021). *Rugged Monitoring: Measurement and control instrumentation for any application*. https://www.campbellsci.com/

Capgo. (2014a). *RTDs*. https://www.capgo.com/Resources/Temperature/RTDs/RTD.html

Capgo. (2014b). *Thermistor Temperature Sensors*. https://www.capgo.com/Resources/Temperature/Thermistor/Thermistor.html

Capozzoli, A., Gorrino, A., & Corrado, V. (2013). A building thermal bridges sensitivity analysis. *Applied Energy*, *107*, 229–243. https://doi.org/10.1016/J.APENERGY.2013.02.045

Carpi, A., & Egger, Anne. E. (2008). *Uncertainty, Error, and Confidence | Process of Science | Visionlearning*. https://www.visionlearning.com/en/library/Process-of-Science/49/Uncertainty-Error-and-Confidence/157

Carrié, F. R., & Leprince, V. (2016). Uncertainties in building pressurisation tests due to steady wind. *Energy and Buildings*, *116*, 656–665. https://doi.org/10.1016/J.ENBUILD.2016.01.029

CEN/TC 89. (2020). *CEN/TC 89 - Thermal performance of buildings and building components*. https://standards.iteh.ai/catalog/tc/cen/eef2e6c2-d573-4840-8430-93a371a172cc/cen-tc-89

Cesaratto, P. G., & De Carli, M. (2013). A measuring campaign of thermal conductance in situ and possible impacts on net energy demand in buildings. *Energy and Buildings*, *59*, 29–36. https://doi.org/10.1016/j.enbuild.2012.08.036

CIBSE. (2021). *Environmental design - Guide A*.

Cluni, F., Costarelli, D., Minotti, A. M., & Vinti, G. (2014). *Applications of sampling Kantorovich operators to thermographic images for seismic engineering* (Vol. 47, Issue 38).

Cluni, F., Costarelli, D., Minotti, A. M., & Vinti, G. (2015). Enhancement of thermographic images as tool for structural analysis in earthquake engineering. *NDT and E International*, *70*, 60–72. https://doi.org/10.1016/j.ndteint.2014.10.001

COMSOL. (2021). *Heat Transfer Module Application Gallery Examples*. https://www.comsol.ch/models/heat-transfer-module

COP26. (2022). *UK Climate Leadership - UN Climate Change Conference at the SEC – Glasgow 2021*. https://ukcop26.org/uk-presidency/uk-climate-leadership/

Costarelli, D., Minotti, A. M., & Vinti, G. (2017). Approximation of discontinuous signals by sampling Kantorovich series. *Journal of Mathematical Analysis and Applications*, *450*(2), 1083–1103. https://doi.org/10.1016/j.jmaa.2017.01.066

Costarelli, D., & Vinti, G. (2013). Approximation by Nonlinear Multivariate Sampling Kantorovich Type Operators and Applications to Image Processing. *Numerical Functional Analysis and Optimization*, *34*(8), 819–844. https://doi.org/10.1080/01630563.2013.767833

Cozza, S., Chambers, J., & Patel, M. K. (2020). Measuring the thermal energy performance gap of labelled residential buildings in Switzerland. *Energy Policy*, *137*, 111085. https://doi.org/10.1016/J.ENPOL.2019.111085

Crawley, J., Biddulph, P., Northrop, P. J., Wingfield, J., Oreszczyn, T., & Elwell, C. (2019). Quantifying the Measurement Error on England and Wales EPC Ratings. *Energies 2019, Vol. 12, Page 3523*, *12*(18), 3523. https://doi.org/10.3390/EN12183523

Creswell, J. W. (2009). *Research design: Qualitative, quantitative, and mixed methods approaches* (3rd ed.).

Dall'O', G., Sarto, L., Panza, A., Dall'O', G., Sarto, L., & Panza, A. (2013). Infrared Screening of Residential Buildings for Energy Audit Purposes: Results of a Field Test. *Energies*, *6*(8), 3859–3878. https://doi.org/10.3390/en6083859

Dascalaki, E., Santamouris, M., Balaras, C. A., & Asimakopoulos, D. N. (1993). *Natural convection heat transfer coefficients from vertical and horizontal surfaces for building applications*. https://reader.elsevier.com/reader/sd/pii/0378778894900272?token=98E71F87C08DF14A18B977C8663A018BAB2170B812B2DDD1C2C4B0B56CA369ACF8579E95CC6416F94AED969D40173A67

Datcu, S., Ibos, L., Candau, Y., & Matteï, S. (2005). Improvement of building wall surface temperature measurements by infrared thermography. *Infrared Physics & Technology*, *46*(6), 451–467. https://doi.org/10.1016/J.INFRARED.2005.01.001

de Sousa Dias Prata, J., & de Sousa Dias Prata Joana, J. (2017). *DYNAMIC BEHAVIOUR OF LINEAR AND POINT THERMAL BRIDGES OF BUILDINGS-NUMERICAL AND EXPERIMENTAL SIMULATIONS*.

Deb, C., Gelder, L. V., Spiekman, M., Pandraud, G., Jack, R., & Fitton, R. (2021). Measuring the heat transfer coefficient (HTC) in buildings: A stakeholder's survey. *Renewable and Sustainable Energy Reviews*, *144*, 111008. https://doi.org/10.1016/J.RSER.2021.111008

Déqué, F., Ollivier, F., & Roux, J. J. (2001). Effect of 2D modelling of thermal bridges on the energy performance of buildings - Numerical application on the Matisse apartment. *Energy and Buildings*, *33*(6), 583–587. https://doi.org/10.1016/S0378-7788(00)00128-6

DesignBuilder Software Ltd. (2021). *DesignBuilder*. https://designbuilder.co.uk//

Designing Buildings Wiki. (2021a). *Zero carbon homes*. https://www.designingbuildings.co.uk/wiki/Zero_carbon_homes

Designing Buildings Wiki. (2021b). *Zero carbon non-domestic buildings* . https://www.designingbuildings.co.uk/wiki/Zero_carbon_non-domestic_buildings

Desogus, G., Mura, S., & Ricciu, R. (2011). Comparing different approaches to in situ measurement of building components thermal resistance. *Energy and Buildings*, *43*(10), 2613–2620. https://doi.org/10.1016/j.enbuild.2011.05.025

Dikarev, K., Berezyuk, A., Kuzmenko, O., & Skokova, A. (2016). Experimental and Numerical Thermal Analysis of Joint Connection «Floor Slab – Balcony Slabe» with Integrated Thermal Break. *Energy Procedia*, *85*, 184–192. https://doi.org/10.1016/J.EGYPRO.2015.12.325

Dilmac, S., Guner, A., Senkal, F., & Kartal, S. (2007). Simple method for calculation of heat loss through floor/beam-wall intersections according to ISO 9164. *Energy Conversion and Management*, *48*(3), 826–835. https://doi.org/10.1016/j.enconman.2006.08.015

DOE. (2018). *EnergyPlus*. https://energyplus.net/

Doran, S. (2001). Field investigations of the thermal performance of construction elements as built. *BRE East Kilbride*, *June*. https://doi.org/10.13140/RG.2.1.3397.9042

ee power. (2020). *Thermistor Guide*. https://eepower.com/resistor-guide/resistor-types/thermistor/

Elshafie, M. (2013). Arab World English Journal العريب العامل يف ية الانلكزي للغة ا جمةل. *AWEJ*, *2*, 4–13.

Energy Saving Trust. (2008). *Enhanced Construction Details : introduction and use Contents*.

EnergyTest. (2017). *SBEM Calculations*. http://energy-test.co.uk/sbem-calculations-3/

European Union. (2020). *Renovation wave*. https://energy.ec.europa.eu/topics/energy-efficiency/energy-efficient-buildings/renovation-wave_en

European Union. (2021a). *DIRECTIVE OF THE EUROPEAN PARLIAMENT AND OF THE COUNCIL on the energy performance of buildings (recast) COM(2021) 802 final (Text with EEA relevance)*.

European Union. (2021b). *European Green Deal - Delivering on our targets*. https://ec.europa.eu/commission/presscorner/detail/en/fs_21_3688

European Union. (2021c). *Factsheet - Energy Performance of Buildings*. https://ec.europa.eu/commission/presscorner/detail/en/fs_21_6691

Evangelisti, L., Guattari, C., Gori, P., & Bianchi, F. (2017). Heat transfer study of external convective and radiative coefficients for building applications. *Energy and Buildings*, *151*, 429–438. https://doi.org/10.1016/j.enbuild.2017.07.004

Evangelisti, L., Guattari, C., Gori, P., & De Lieto Vollaro, R. (2015). In situ thermal transmittance measurements for investigating differences between wall models and actual building performance. *Sustainability (Switzerland)*, *7*(8), 10388–10398. https://doi.org/10.3390/su70810388

Evangelisti, L., Guattari, C., Gori, P., de Lieto Vollaro, R., & Asdrubali, F. (2016). Experimental investigation of the influence of convective and radiative heat transfers on thermal transmittance measurements. *International Communications in Heat and Mass Transfer*, *78*, 214–223. https://doi.org/10.1016/j.icheatmasstransfer.2016.09.008

Farmer, D., Johnston, D., & Miles-Shenton, D. (2016). Obtaining the heat loss coefficient of a dwelling using its heating system (integrated coheating). *Energy and Buildings*, *117*, 1–10. https://doi.org/10.1016/j.enbuild.2016.02.013

Farrat. (2020). *Structural Thermal Break Connections FTB*.

Farrat. (2021). *TBK Data Sheet - Farrat*. https://www.farrat.com/wp-content/uploads/2021/09/DS-FTB-Farrat-TBK-21a.pdf

Fels, M. F. (1986). PRISM: An introduction. *Energy and Buildings*, *9*(1–2), 5–18. https://doi.org/10.1016/0378-7788(86)90003-4

Fitton. (2021a). *Building energy performance assessment based on in-situ measurements : challenges and general framework Title Building energy performance assessment based on in-situ measurements : challenges and general framework*.

Fitton, R. (2016). *The Thermal Energy Performance of Domestic Dwellings in the UK*.

Fitton, R. (2021b). *IEA ANNEX 71- Building Energy Performance Assessment Based on In-situ Measurements* (Issue August).

Fitton, R., Swan, W., Hughes, T., & Benjaber, M. (2017). *The thermal performance of window coverings in a whole house test facility with single-glazed sash windows*. https://doi.org/10.1007/s12053-017-9529-0

Flir Systems. (2019). *User's manual FLIR T8xx series*.

FluxTeq. (2018). *FAQ | fluxteq*. https://www.fluxteq.com/faq-s

FluxTeq LLC. (2022). *PHFS -01e Heat Flux Sensor Datasheet*. 3735.

Fokaides, P. A., & Kalogirou, S. A. (2011). Application of infrared thermography for the determination of the overall heat transfer coefficient (U-Value) in building envelopes. *Applied Energy*, *88*(12), 4358–4365. https://doi.org/10.1016/J.APENERGY.2011.05.014

François, A., Ibos, L., Feuillet, V., & Meulemans, J. (2020a). Estimation of the thermal resistance of a building wall with inverse techniques based on rapid active in situ measurements and white-box or ARX black-box models. *Energy and Buildings*, *226*, 110346. https://doi.org/10.1016/j.enbuild.2020.110346

François, A., Ibos, L., Feuillet, V., & Meulemans, J. (2020b). Novel in situ measurement methods of the total heat transfer coefficient on building walls. *Energy and Buildings*, *219*, 110004. https://doi.org/10.1016/j.enbuild.2020.110004

Fraunhofer. (2018a). *Detailed product overview*. https://wufi.de/en/software/product-overview/detailed-product-overview/

Fraunhofer. (2018b). *The past method: Glaser*. https://wufi.de/en/software/what-is-wufi/

Fraunhofer. (2018c). *WUFI*. https://wufi.de/en/

Fraunhofer IBP. (2017). *WUFI Plus Product overview*. https://wufi.de/en/software/product-overview/

Galvin, R. (2014). Making the 'rebound effect' more useful for performance evaluation of thermal retrofits of existing homes: Defining the 'energy savings deficit' and the 'energy performance gap.' *Energy and Buildings*, *69*, 515–524. https://doi.org/10.1016/J.ENBUILD.2013.11.004

Gao, Y., Roux, J. J., Zhao, L. H., & Jiang, Y. (2008). Dynamical building simulation: A low order model for thermal bridges losses. *Energy and Buildings*, *40*(12), 2236–2243. https://doi.org/10.1016/J.ENBUILD.2008.07.003

Garay Martinez, R. (2017). Caracterización térmica dinámica de la transferencia de calor multidimensional en edificios. Dynamic performance assessment of multidimensional heat transfer in buildings. *TDX (Tesis Doctorals En Xarxa)*, *c*.

Garay Martinez, R. (2018). Hybrid numerical and experimental performance assessment of structural thermal bridge retrofits. *Journal of Facade Design and Engineering*, *6*(2), 95–106. https://doi.org/10.7480/jfde.2018.2.2206

Garay, R., Uriarte, A., & Apraiz, I. (2014). Performance assessment of thermal bridge elements into a full scale experimental study of a building façade. *Energy and Buildings*, *85*, 579–591. https://doi.org/10.1016/j.enbuild.2014.09.024

Garrido, I., Lagüela, S., Arias, P., & Balado, J. (2018). Thermal-based analysis for the automatic detection and characterization of thermal bridges in buildings. *Energy and Buildings*, *158*, 1358–1367. https://doi.org/10.1016/J.ENBUILD.2017.11.031

Gaspar, K., Casals, M., & Gangolells, M. (2016). A comparison of standardized calculation methods for in situ measurements of façades U-value. *Energy and Buildings*, *130*, 592–599. https://doi.org/10.1016/j.enbuild.2016.08.072

Ge, H., & Baba, F. (2017). Effect of dynamic modeling of thermal bridges on the energy performance of residential buildings with high thermal mass for cold climates. *Sustainable Cities and Society*, *34*, 250–263. https://doi.org/10.1016/J.SCS.2017.06.016

Ge, H., McClung, V. R., & Zhang, S. (2013). Impact of balcony thermal bridges on the overall thermal performance of multi-unit residential buildings: A case study. *Energy and Buildings*, *60*, 163–173. https://doi.org/10.1016/J.ENBUILD.2013.01.004

Ghazi Wakili, K., Simmler, H., & Frank, T. (2007). Experimental and numerical thermal analysis of a balcony board with integrated glass fibre reinforced polymer GFRP elements. *Energy and Buildings*, *39*(1), 76–81. https://doi.org/10.1016/J.ENBUILD.2006.05.002

Ghazi Wakili, K., & Tanner, Ch. (2003). U-value of a dried wall made of perforated porous clay bricks: Hot box measurement versus numerical analysis. *Energy and Buildings*, *35*(7), 675–680. https://doi.org/10.1016/S0378-7788(02)00209-8

Gomes, A. P., De Souza, H. A., & Tribess, A. (2013). Impact of thermal bridging on the performance of buildings using Light Steel Framing in Brazil. *Applied Thermal Engineering*, *52*(1), 84–89. https://doi.org/10.1016/j.applthermaleng.2012.11.015

Gorse, C. A., Miles-Shenton, D., Farmer, D., & Fletcher, M. (2013). *BUILDING PERFORMANCE: FABRIC, IMPACT AND IMPLICATIONS*.

Gorse, C., Brooke-Peat, M., Parker, J., & Thomas, F. (2016). Building Simulation and Models: Closing the Performance Gap. In M. Dastbaz, I. Strange, & S. Selkowitz (Eds.), *Building Sustainable Futures : Design and the Built Environment* (pp. 209–226). Springer International Publishing AG.

Gorse, C., Stafford, A., Miles Shenton, D., Johnston, D., Sutton, R., & Farmer, D. (2012). *Association of Researchers in Construction Management*.

GOV. (2018). *Energy Company Obligation: ECO3, 2018 to 2022*. https://www.gov.uk/government/consultations/energy-company-obligation-eco3-2018-to-2022

GOV. (2021). *Volume 1: Dwellings Requirement L1: Conservation of fuel and power Requirement L2: On-site generation of electricity - for use in England*.

GOV.UK. (2015). *Cambridge Housing Model and user guide*. https://www.gov.uk/government/publications/cambridge-housing-model-and-user-guide

GOV.UK. (2019a). *English Housing Survey*.

GOV.UK. (2019b). *The Climate Change Act 2008 (2050 Target Amendment) Order 2019*.

GOV.UK. (2020). *UK sets ambitious new climate target ahead of UN Summit - GOV.UK*. https://www.gov.uk/government/news/uk-sets-ambitious-new-climate-target-ahead-of-un-summit

GOV.UK. (2021). *Standard Assessment Procedure*. https://www.gov.uk/guidance/standard-assessment-procedure

GOV.UK. (2022). *COP 26 declaration: International Aviation Climate Ambition Coalition*. https://www.gov.uk/government/publications/cop-26-declaration-international-aviation-climate-ambition-coalition/cop-26-declaration-international-aviation-climate-ambition-coalition

Graphtec Corporation. (2005). *Instrument products*. http://www.graphteccorp.com/product/instrument.html

greenTEG. (2021). *Heat Flux Sensor Explanation* . https://www.greenteg.com/heat-flux-sensor/about-heat-flux/heat-flux-sensor-explanation/

Guba, E. G., & Lincoln, Y. S. (1994). *Competing paradigms in qualitative research* (p. 13).

Hens, H., Janssens, A., Depraetere, W., Carmeliet, J., & Lecompte, J. (2007). Brick Cavity Walls: A Performance Analysis Based on Measurements and Simulations. *Journal of BUILDING PHYSICS*, *31*(2). https://doi.org/10.1177/1744259107082685

Hensen, J. L. M. (1992). Energy simulation in building design. *Research on Building Structures and Building Physics.* , 101–112.

HM Government. (2007). *Accredited Construction Details*.

HM Government. (2017). *Building Regulations 2017 Technical Guidance Document L-Buildings other than Dwellings Conservation of Fuel and Energy*.

HM Government. (2021a). *Building Regulations Conservation of fuel and power Approved Document Part L Volume 1: Dwellings*.

HM Government. (2021b). *Building Regulations Conservation of fuel and power Volume 2: Buildings other than dwellings*.

Holman, J. (1988). *Thermodynamics* (4th ed.). McGraw-Hill.

Holman, J. P. (1972). *Heat Transfer* (p. 512). McGraw-Hill.

Hosch, W. L. (2009). *Thermoelectricity | physics | Britannica*. https://www.britannica.com/science/thermoelectricity

Hoyano, A., Asano, K., & Kanamaru, T. (1999). Analysis of the sensible heat flux from the exterior surface of buildings using time sequential thermography. *Atmospheric Environment*, *33*(24–25), 3941–3951. https://doi.org/10.1016/S1352-2310(99)00136-3

HTflux. (2018). *HTflux - Hygric and Thermal Simulation*. https://www.htflux.com/en/

Hukseflux. (2021a). *Hukseflux Thermal Sensors*.

Hukseflux. (2021b). *Hukseflux Thermal Sensors*.

Hulme, J., Doran, S., & John Riley, N. (2014). *In-situ measurements of wall U-values in English housing*.

International Energy Agency. (2018). *Market Report Series: Energy Efficiency 2018*.

International Energy Agency. (2021). *Tracking Buildings 2021*. https://www.iea.org/fuels-and-technologies/building-envelopes

Iodice, P., Massarotti, N., Mauro, A., Iodice, P., Massarotti, N., & Mauro, A. (2016). Effects of Inhomogeneities on Heat and Mass Transport Phenomena in Thermal Bridges. *Energies*, *9*(3), 126. https://doi.org/10.3390/en9030126

Jack, R., Loveday, D., Allinson, D., & Lomas, K. (2017). *Building Research & Information First evidence for the reliability of building co-heating tests*. https://doi.org/10.1080/09613218.2017.1299523

Janssens, a, Londersele, E. Van, Vandermarcke, B., Roels, S., Standaert, P., & Wouters, P. (2007). Development of Limits for the Linear Thermal Transmittance of Thermal Bridges in Buildings. *Thermal Performance of Exterior Envelopes of Whole Buildings X International Conference*.

JCGM. (2008). Evaluation of measurement data — Guide to the expression of uncertainty in measurement. *International Organization for Standardization Geneva ISBN*, *50*(September), 134.

Ji, Y., Fitton, R., Swan, W., & Webster, P. (2014). Assessing overheating of the UK existing dwellings - A case study of replica Victorian end terrace house. *Building and Environment*, *77*, 1–11. https://doi.org/10.1016/j.buildenv.2014.03.012

Jiménez, M. J., Porcar, B., & Heras, M. R. (2009). Application of different dynamic analysis approaches to the estimation of the building component U value. *Building and Environment*, *44*(2), 361–367. https://doi.org/10.1016/j.buildenv.2008.03.010

Johnston, D., Miles-Shenton, D., & Farmer, D. (2015a). Quantifying the domestic building fabric "performance gap." *Building Services Engineering Research and Technology*, *36*(5), 614–627. https://doi.org/10.1177/0143624415570344

Johnston, D., Miles-Shenton, D., & Farmer, D. (2015b). *Quantifying the domestic building fabric "performance gap" Title Quantifying the domestic building fabric "performance gap" Quantifying the domestic building fabric "performance gap."* https://doi.org/10.1177/0143624415570344

Johnston, D., Miles-Shenton, D., Wingfield, J., Farmer, D., & Bell, M. (2012). *Whole House Heat Loss Test Method (Coheating)*.

Johnston, D., Siddall, M., Ottinger, O., Peper, S., & Feist, W. (2020). Are the energy savings of the passive house standard reliable? A review of the as-built thermal and space heating performance of passive house dwellings from 1990 to 2018. *Energy Efficiency*, *13*(8), 1605–1631. https://doi.org/10.1007/S12053-020-09855-7/FIGURES/14

Jones, R. V., Fuertes, A., Boomsma, C., & Pahl, S. (2016). Space heating preferences in UK social housing: A socio-technical household survey combined with building audits. *Energy and Buildings*, *127*, 382–398. https://doi.org/10.1016/J.ENBUILD.2016.06.006

Kato, S., Kuroki, K., & Hagihara, S. (2007). *METHOD OF IN-SITU MEASUREMENT OF THERMAL INSULATION PERFORMANCE OF BUILDING ELEMENTS USING INFRARED CAMERA*.

Kirimtat, A., Koyunbaba, B. K., Chatzikonstantinou, I., & Sariyildiz, S. (2016). Review of simulation modeling for shading devices in buildings. *Renewable and Sustainable Energy Reviews*, *53*, 23–49. https://doi.org/10.1016/J.RSER.2015.08.020

Kittel, C. (2004). Introduction to Solid State Physics, 8th edition. In *Wiley & Sons, New York, NY*.

Kline, S. J., & McClintock, F. A. (1953). *Describing uncertainty in single sample experiments*.

Kordatos, E. Z., Exarchos, D. A., Stavrakos, C., Moropoulou, A., & Matikas, T. E. (2013). Infrared thermographic inspection of murals and characterization of degradation in historic monuments. *Construction and Building Materials*, *48*, 1261–1265. https://doi.org/10.1016/j.conbuildmat.2012.06.062

Kośny, J., Curcija, C., Fontanini, A.D., Liu, H. and Kossecka, E., A. N. A. for A. of C. B. E. in W. B. E. Simulations. (2016). *A New Approach for Analysis of Complex Building Envelopes in Whole Building Energy Simulations*.

Kosny, J., & Desjarlais, A. O. (1994). Influence of Architectural Details on the Overall Thermal Performance of Residential Wall Systems. In *J. THERMAL INSUL. AND BLDG. ENVS* (Vol. 18).

Kośny, J., & Kossecka, E. (2002). Multi-dimensional heat transfer through complex building envelope assemblies in hourly energy simulation programs. *Energy and Buildings*, *34*(5), 445–454. https://doi.org/10.1016/S0378-7788(01)00122-0

Kossecka, E., & Kosny, J. (1997). Equivalent Wall as a Dynamic Model of a Complex Thermal Structure. *Journal of Thermal Envelope and Building Science*. https://doi.org/10.1177/109719639702000306

Kossecka, E., & Kosny, J. (2005). Three-dimensional conduction z-transfer function coefficients determined from the response factors. *Energy and Buildings*. https://doi.org/10.1016/j.enbuild.2004.06.026

Kothari, C. R. (2004). *Research Methodolgy: Methods and Techniques*. New Age. http://dspace.sfit.co.in:8004/xmlui/bitstream/handle/123456789/1120/Research Methodology C R Kothari %28Eng%29 1.81 MB.pdf?sequence=1&isAllowed=y

Kubba, S. (2017). Components of Sustainable Design and Construction. *Handbook of Green Building Design and Construction*, 55–110. https://doi.org/10.1016/B978-0-12-810433-0.00002-2

Kuusk, K., Kurnitski, J., & Kalamees, T. (2017). Calculation and compliance procedures of thermal bridges in energy calculations in various European countries. *Energy Procedia*, *132*, 27–32. https://doi.org/10.1016/j.egypro.2017.09.626

Kylili, A., Fokaides, P. A., Christou, P., & Kalogirou, S. A. (2014). Infrared thermography (IRT) applications for building diagnostics: A review. *Applied Energy*, *134*, 531–549. https://doi.org/10.1016/J.APENERGY.2014.08.005

Larbi, A. Ben. (2005). Statistical modelling of heat transfer for thermal bridges of buildings. *Energy and Buildings*, *37*(9), 945–951. https://doi.org/10.1016/J.ENBUILD.2004.12.013

Larbi, A. Ben, Couchaux, M., & Alhasawi, A. (2019). Experimental tests on bolted end-plate connections using thermal insulation layer attached to steel structures. *Stability and Ductility of Steel Structures 2019 Wald & Jandera (Eds)*, 269–276.

Larbi, A. Ben, Couchaux, M., & Bouchaïr, A. (2017). 03.14: Steel connections with thermal barrier for nearly zero-energy buildings (NZEB). *Ce/Papers*, *1*(2–3), 609–618. https://doi.org/10.1002/cepa.99

Lawrence Berkeley National Laboratory. (2012). *THERM | Windows and Daylighting*. https://windows.lbl.gov/software/therm

Lecompte, J. (1990). Energy-insulation The influence of natural convection on the thermal quality of insulated cavity construction. *Building Research and Practice: CIB*, *6*.

Lewis, V., Woods, M., Burgess, P., Green, S., Birmingham, R., Simpson, J., & Wardle, J. (2005). *The Assessment of Uncertainty in Radiological Calibration and Testing*.

Li, F. G. N., Smith, A. Z. P., Biddulph, P., Hamilton, I. G., Lowe, R., Mavrogianni, A., Oikonomou, E., Raslan, R., Stamp, S., Stone, A., Summerfield, A. J., Veitch, D., Gori, V., & Oreszczyn, T. (2015). Solid-wall U-values: Heat flux measurements compared with standard assumptions. *Building Research and Information*, *43*(2), 238–252. https://doi.org/10.1080/09613218.2014.967977

Little, J., & Beñat, A. (2011). *Thermal Bridging Understanding its critical role in energy efficiency*.

Lomas, K. J., Eppel, H., Martin, C. J., & Bloomfield, D. P. (1997). Empirical validation of building energy simulation programs. *Energy and Buildings*, *26*(3), 253–275. https://doi.org/10.1016/S0378-7788(97)00007-8

Lucchi, E. (2017a). Thermal transmittance of historical brick masonries: A comparison among standard data, analytical calculation procedures, and in situ heat flow meter measurements. *Energy and Buildings*, *134*, 171–184. https://doi.org/10.1016/J.ENBUILD.2016.10.045

Lucchi, E. (2017b). Thermal transmittance of historical stone masonries: A comparison among standard, calculated and measured data. *Energy and Buildings*, *151*, 393–405. https://doi.org/10.1016/J.ENBUILD.2017.07.002

Lucchi, E. (2018). Applications of the infrared thermography in the energy audit of buildings: A review. In *Renewable and Sustainable Energy Reviews* (Vol. 82, pp. 3077–3090). Pergamon. https://doi.org/10.1016/j.rser.2017.10.031

Luscietti, D., Gervasio, P., & Lezzi, A. M. (2014). Computation of linear transmittance of thermal bridges in precast concrete sandwich panels. *Journal of Physics: Conference Series*. https://doi.org/10.1088/1742-6596/547/1/012014

Ma, Z., Bao, H., & Roskilly, A. P. (2019). Seasonal solar thermal energy storage using thermochemical sorption in domestic dwellings in the UK. *Energy*, *166*, 213–222. https://doi.org/10.1016/j.energy.2018.10.066

Madding, R. (2008). Finding R-values of Stud-Frame Constructed Houses with IR Thermography Finding R-Values of Stud Frame Constructed Houses with IR Thermography. In *Proceedings ITC* (Vol. 126).

Mangematin, E., Pandraud, G., & Roux, D. (2012). Quick measurements of energy efficiency of buildings. *Comptes Rendus Physique*, *13*(4), 383–390. https://doi.org/10.1016/J.CRHY.2012.04.001

Marino, B. M., Muñoz, N., & Thomas, L. P. (2017). Estimation of the surface thermal resistances and heat loss by conduction using thermography. *Applied Thermal Engineering*, *114*, 1213–1221. https://doi.org/10.1016/J.APPLTHERMALENG.2016.12.033

Marshall, A., Fitton, R., Swan, W., Farmer, D., Johnston, D., Benjaber, M., & Ji, Y. (2017). Domestic building fabric performance: Closing the gap between the in situ measured and modelled performance. *Energy and Buildings*, *150*, 307–317. https://doi.org/10.1016/J.ENBUILD.2017.06.028

Marshall, A., Francou, J., Fitton, R., Swan, W., Owen, J., & Benjaber, M. (2018). Variations in the U-Value Measurement of a Whole Dwelling Using Infrared Thermography under Controlled Conditions. *Buildings*. https://doi.org/10.3390/buildings8030046

Martin, K., Campos-Celador, A., Escudero, C., Gómez, I., & Sala, J. M. (2012). Analysis of a thermal bridge in a guarded hot box testing facility. *Energy and Buildings*, *50*, 139–149. https://doi.org/10.1016/J.ENBUILD.2012.03.028

Martin, K., Escudero, C., Erkoreka, A., Flores, I., & Sala, J. M. (2012). Equivalent wall method for dynamic characterisation of thermal bridges. *Energy and Buildings*, *55*, 704–714. https://doi.org/10.1016/J.ENBUILD.2012.08.024

Martinez, R. G., Riverola, A., & Chemisana, D. (2017). Disaggregation process for dynamic multidimensional heat flux in building simulation. *Energy and Buildings*, *148*, 298–310. https://doi.org/10.1016/J.ENBUILD.2017.05.029

Martín Ocaña, S., Cañas Guerrero, I., & González Requena, I. (2004). Thermographic survey of two rural buildings in Spain. *Energy and Buildings*, *36*(6), 515–523. https://doi.org/10.1016/J.ENBUILD.2003.12.012

Mauriello, M. L., Mcnally, B., & Froehlich, J. E. (2019). *Thermporal: An Easy-to-Deploy Temporal Thermographic Sensor System to Support Residential Energy Audits*. 14. https://doi.org/10.1145/3290605.3300343

Mclean, S., & Fitton, R. (2017). Smart surveys: A review of available technologies. *Number 1 Journal of Building Survey*, *6*(1), 67–77.

Meng, X., Yan, B., Gao, Y., Wang, J., Zhang, W., & Long, E. (2015). Factors affecting the in situ measurement accuracy of the wall heat transfer coefficient using the heat flow meter method. *Energy and Buildings*, *86*, 754–765. https://doi.org/10.1016/j.enbuild.2014.11.005

Mitchell, R., & Natarajan, S. (2020). UK Passivhaus and the energy performance gap. *Energy and Buildings*, *224*, 110240. https://doi.org/10.1016/J.ENBUILD.2020.110240

Moffat, R. J. (1988). Describing the uncertainties in experimental results. *Experimental Thermal and Fluid Science*, *1*(1), 3–17. https://doi.org/10.1016/0894-1777(88)90043-X

Munson, B. R., Okiishi, T. H. (Theodore H., Huebsch, W. W., & Rothmayer, A. P. (2013). *Fluid mechanics*.

Nardi, I., de Rubeis, T., Taddei, M., Ambrosini, D., & Sfarra, S. (2017). The energy efficiency challenge for a historical building undergone to seismic and energy refurbishment. *Energy Procedia*, *133*, 231–242. https://doi.org/10.1016/J.EGYPRO.2017.09.357

Nardi, I., Lucchi, E., de Rubeis, T., & Ambrosini, D. (2018). Quantification of heat energy losses through the building envelope: A state-of-the-art analysis with critical and comprehensive review on infrared thermography. *Building and Environment*, *146*, 190–205. https://doi.org/10.1016/J.BUILDENV.2018.09.050

Nardi, I., Paoletti, D., Ambrosini, D., de Rubeis, T., & Sfarra, S. (2016). U-value assessment by infrared thermography: A comparison of different calculation methods in a Guarded Hot Box. *Energy and Buildings*, *122*, 211–221. https://doi.org/10.1016/J.ENBUILD.2016.04.017

Nardi, I., Sfarra, S., & Ambrosini, D. (2014). Quantitative thermography for the estimation of the U-value: state of the art and a case study. *Journal of Physics: Conference Series*, *547*(1), 012016. https://doi.org/10.1088/1742-6596/547/1/012016

NBS. (2016). *Building Regulations Part L1A*.

NBS. (2018a). *Building regulation Part L-1B*.

NBS. (2018b). *Part L of the Building Regulations*. https://www.isurv.com/info/35/part_l_of_the_building_regulations

NI. (2021). *Overview of Temperature Sensors*. https://www.ni.com/en-gb/innovations/white-papers/06/overview-of-temperature-sensors.html

Nimiya, H., Akasaka, H., Obara, S., & Itami, K. (1999). Thermal Analysis of 3-Dimensional Heat Bridges Included in Steel Frames Houses - Method of Making Models and Analysis Examples. *Proceedings of the IBSPA 6th International Conference on Building Simulation 99*, 747–753.

Novus Automation Inc. (2021). *FieldLogger -*. https://www.novusautomation.com/site/default.asp?Idioma=1&TroncoID=608027&SecaoID=549361&SubsecaoID=705280&Template=../catalogos/layout_produto.asp&ProdutoID=506190

NSAI. (2017). *Energy performance of buildings - Overarchin EPB assessment - Part 1: General framework and procedures (ISO 52000-1:2017)*.

Office for National Statistics. (2019). National population projections: 2018. *Popuation Projections*, *June*, 1–16.

Office for National Statistics. (2020). *Household projections for England: 2018*. *March*, 1–13.

ofgem. (2018). *About the ECO scheme | Ofgem*. https://www.ofgem.gov.uk/environmental-programmes/eco/about-eco-scheme

OFGEM. (2021). *Overview of previous schemes*. https://www.ofgem.gov.uk/environmental-programmes/eco/overview-previous-schemes

O'grady, M. (2018). *Building envelope thermal bridging heat loss assessment using infrared thermography*.

O'Grady, M., Lechowska, A. A., & Harte, A. M. (2017a). Infrared thermography technique as an in-situ method of assessing heat loss through thermal bridging. *Energy and Buildings*, *135*, 20–32. https://doi.org/10.1016/J.ENBUILD.2016.11.039

O'Grady, M., Lechowska, A. A., & Harte, A. M. (2017b). Quantification of heat losses through building envelope thermal bridges influenced by wind velocity using the outdoor infrared thermography technique. *Applied Energy*, *208*, 1038–1052. https://doi.org/10.1016/J.APENERGY.2017.09.047

O'Grady, M., Lechowska, A. A., & Harte, A. M. (2018). Application of infrared thermography technique to the thermal assessment of multiple thermal bridges and windows. *Energy and Buildings*, *168*, 347–362. https://doi.org/10.1016/j.enbuild.2018.03.034

Oh, J., Yoo, H., & Kim, S. (2016). Evaluation of Strategies to Improve the Thermal Performance of Steel Frames in Curtain Wall Systems. *Energies*, *9*(12), 1055. https://doi.org/10.3390/en9121055

Optris. (2021). *Optris PI Precision Line: infrared cameras for fast processes*.

Palmer, J., & Cooper, I. (2013). *UK Housing Energy Fact File 2013*.

Papadakos, G., Marinakis, V., Konstas, C., Doukas, H., & Papadopoulos, A. (2021). Managing the uncertainty of the U-value measurement using an auxiliary set along with a thermal camera. *Energy and Buildings*, *242*, 110984. https://doi.org/10.1016/j.enbuild.2021.110984

Passipedia. (2019). *PHPP – Passive House Planning Package*. https://passipedia.org/planning/calculating_energy_efficiency/phpp_-_the_passive_house_planning_package

Passive House. (2015). *How to build a Passivhaus: Rules of thumb*.

Passive House. (2021). Thermal Bridges Catalogue. *Energy Conservation in Buildings*, 188–198. https://doi.org/10.1002/9780470773802.ch15

Passivehaus. (2015). *Passivhaus Institute*. https://passivehouse.com/

Passivhaus Institut. (2022). *Criteria and Algorithms for Certified Passive House Components: Opaque Construction Systems*.

Passivhaus Institute. (2021). *Passipedia - The Passive House Resource*. Passipedia. https://www.passipedia.org/start

Passivhaus-Trust. (2019). *What is Passivhaus?* http://passivhaustrust.org.uk/what_is_passivhaus.php

Pearson, C. (2011). Thermal Imaging of Building Fabric A BSRIA Guide THERMAL IMAGING OF BUILDING FABRIC 1. *BSRIA*, *39*(11).

Peng, C., & Wu, Z. (2008). In situ measuring and evaluating the thermal resistance of building construction. *Energy and Buildings*, *40*(11), 2076–2082. https://doi.org/10.1016/j.enbuild.2008.05.012

Physibel. (2017a). *TRISCO*. http://www.physibel.be/v0n2tr.htm

Physibel. (2017b). *VOLTRA*. https://doi.org/VOLTRA

Pineda, D. D., & Rezaniakolaei, A. (2017). *Thermoelectric Energy Conversion: Basic Concepts and Device Applications*.

Pipes, L. A. (1957). Matrix analysis of heat transfer problems. *Journal of the Franklin Institute*, *263*(3), 195–206. https://doi.org/10.1016/0016-0032(57)90927-4

Pollock, D. D. (1991). *Thermocouples: Theory and Properties -*. https://books.google.co.uk/books?id=_CK8U_bzgKQC&pg=PA249&redir_esc=y#v=onepage&q=fermi&f=false

Prasad, A. (2016). *A Detailed Uncertainty Analysis of Heat Transfer Experiments Using Temperature Sensitive Paint*.

Prata, J., Simões, N., & Tadeu, A. (2018). Heat transfer measurements of a linear thermal bridge in a wooden building corner. *Energy and Buildings*, *158*, 194–208. https://doi.org/10.1016/J.ENBUILD.2017.09.073

Preiser, W. F. E., Hardy, A. E., & Schramm, U. (2018). *Building Performance Evaluation From Delivery Process to Life Cycle Phases Second Edition*.

PSI THERM. (2018). *PSI-Therm 3D Features*. https://www.psitherm.uk/psi-features/psi-therm-3d-features

Purdy, J., & Beausoleil-Morrison, I. (2001). *THE SIGNIFICANT FACTORS IN MODELLING RESIDENTIAL BUILDINGS*.

Quinten, J., & Feldheim, V. (2016). Dynamic modelling of multidimensional thermal bridges in building envelopes: Review of existing methods, application and new mixed method. *Energy and Buildings*, *110*, 284–293. https://doi.org/10.1016/j.enbuild.2015.11.003

Ramsden, E. (2000). *Temperature Measurement - FierceElectronics*. https://www.fierceelectronics.com/components/temperature-measurement

Rashid Shah, S., & Al-Bargi, A. (2013). Arab World English Journal العريب العامل يف ية الانلكزي للغة ا جمةل. *AWEJ*, *4*(4), 252–264.

Roberts, B. M., Allinson, D., Diamond, S., Abel, B., Das Bhaumik, C., Khatami, N., & Lomas, K. J. (2019). Predictions of summertime overheating: Comparison of dynamic thermal models and measurements in synthetically occupied test houses. *Building Serv. Eng. Res. Technol*, *40*(4), 512–552. https://doi.org/10.1177/0143624419847349

Rosina, E., & Spodek, J. (2003). Using Infrared Thermography to Detect Moisture in Historic Masonry: A Case Study in. In *Source: APT Bulletin: The Journal of Preservation Technology* (Vol. 34, Issue 1).

Rouleau, J., Gosselin, L., & Blanchet, P. (2018). Understanding energy consumption in high-performance social housing buildings: A case study from Canada. *Energy*, *145*, 677–690. https://doi.org/10.1016/J.ENERGY.2017.12.107

Rowe, M. (2016). *Thermocouple physics – How it works – Passive Components Blog*. https://passive-components.eu/thermocouple-physics-how-it-works/

Rye, C., & Scott, C. (2012). *U-value report*.

Šadauskiene, J., Ramanauskas, J., Šeduikyte, L., Daukšys, M., & Vasylius, A. (2015). A simplified methodology for evaluating the impact of point thermal bridges on the high-energy performance of a Passive House. *Sustainability (Switzerland)*. https://doi.org/10.3390/su71215840

Šadauskienė, J., Ramanauskas, J., Šeduikytė, L., Daukšys, M., Vasylius, A., Šadauskienė, J., Ramanauskas, J., Šeduikytė, L., Daukšys, M., & Vasylius, A. (2015). A Simplified Methodology for Evaluating the Impact of Point Thermal Bridges on the High-Energy Performance of a Passive House. *Sustainability*, *7*(12), 16687–16702. https://doi.org/10.3390/su71215840

Sadineni, S. B., Madala, S., & Boehm, R. F. (2011). Passive building energy savings: A review of building envelope components. *Renewable and Sustainable Energy Reviews*, *15*(8), 3617–3631. https://doi.org/10.1016/J.RSER.2011.07.014

Sallée, H., Quenard, D., Valenti, E., & Galan, M. (2014). VIP as thermal breaker for internal insulation system. *Energy and Buildings*, *85*, 631–637. https://doi.org/10.1016/j.enbuild.2014.08.039

Salman, A. (2003). Seebeck and Peltier Effects Introduction. *Seebeck and Peltier Effects Introduction*, 1–8.

Sapphire balconies Ltd. (2022). *Trends in balconies in the UK past, present and future*. https://balconies.global/industry-news/trends-in-balconies-and-balustrades/

Saunders, M. N. K., Lewis, P., & Thornhill, A. (1997). *Research Methods for Business Students: Vol. ProQuest E*. Pearson Education UK.

Schneider, M., & Fischer, H.-M. (2008). *Vibration reduction of thermal break balcony connections*.

Schöck Ltd. (2022). *Thermal insulation - Schöck Ltd*. https://www.schoeck.com/en-gb/thermal-insulation

Scotland, J. (2012). *Exploring the Philosophical Underpinnings of Research: Relating Ontology and Epistemology to the Methodology and Methods of the Scientific, Interpretive, and Critical Research Paradigms* . *5*(9). https://doi.org/10.5539/elt.v5n9p9

Simões, I., Simões, N., Tadeu, A., & Riachos, J. (2014). *Laboratory assessment of thermal transmittance of homogeneous building elements using infrared thermography*.

Stamp, S. F. (2015). *Assessing uncertainty in co-heating tests: Calibrating a whole building steady state heat loss measurement method*. https://www.researchgate.net/publication/306258202_Assessing_uncertainty_in_co-heating_tests_Calibrating_a_whole_building_steady_state_heat_loss_measurement_method

StirlingSensors. (2019). *Thermocouple technical reference information*. https://www.sterlingsensors.co.uk/thermocouples#Different Thermocouple types

Strachan, P., Svehla, K., Heusler, I., & Kersken, M. (2016). Whole model empirical validation on a full-scale building. *Journal of Building Performance Simulation*, *9*(4), 331–350. https://doi.org/10.1080/19401493.2015.1064480/SUPPL_FILE/TBPS_A_1064480_SM0875.ZIP

Subbarao, K., Burch, J. D., Hancock, C. E., Lekov, A., & Balcomb, J. D. (1988). *Short-Term Energy Monitoring (STEM): Application of the PSTAR Method to a Residence in Fredericksburg, Virginia*.

Sun, J., & Reddy, T. A. (2006). Calibration of building energy simulation programs using the analytic optimization approach (RP-1051). *HVAC and R Research*. https://doi.org/10.1080/10789669.2006.10391173

Swan, W., Fitton, R., & Brown, P. (2015). *A UK practitioner view of domestic energy performance measurement Title A UK practitioner view of domestic energy performance measurement*. https://doi.org/10.1680/ensu.14.00056

Tadeu, A., Simões, I., Simões, N., & Prata, J. (2011). Simulation of dynamic linear thermal bridges using a boundary element method model in the frequency domain. *Energy and Buildings*, *43*(12), 3685–3695. https://doi.org/10.1016/j.enbuild.2011.10.001

Tadeu, A., Simoes, N., Simões, I., Pedro, F., & Škerget, L. (2015). In-Situ Thermal Resistance Evaluation of Walls Using an Iterative Dynamic Model. *An International Journal of Computation and Methodology ISSN: Numerical Heat Transfer, Part A: Applications*, *67*(1), 33–51. https://doi.org/10.1080/10407782.2014.901032

Taylor, J. R. (1982). *An Introduction To Error Analysis: The Study Of Uncertainties In Physical Measurement*.

Taylor, T., Counsell, J., & Gill, S. (2014). Combining thermography and computer simulation to identify and assess insulation defects in the construction of building façades. *Energy and Buildings*, *76*, 130–142. https://doi.org/https://doi.org/10.1016/j.enbuild.2014.02.080

Tejedor, B., Casals, M., & Gangolells, M. (2018). Assessing the influence of operating conditions and thermophysical properties on the accuracy of in-situ measured U-values using quantitative internal infrared thermography. *Energy and Buildings*, *171*, 64–75. https://doi.org/10.1016/j.enbuild.2018.04.011

Tejedor, B., Casals, M., Gangolells, M., & Roca, X. (2017). Quantitative internal infrared thermography for determining in-situ thermal behaviour of façades. *Energy and Buildings*, *151*, 187–197. https://doi.org/10.1016/J.ENBUILD.2017.06.040

Theodosiou, T. G., & Papadopoulos, A. M. (2008). The impact of thermal bridges on the energy demand of buildings with double brick wall constructions. *Energy and Buildings*, *40*(11), 2083–2089. https://doi.org/10.1016/J.ENBUILD.2008.06.006

Theodosiou, T. G., Tsikaloudaki, A. G., Kontoleon, K. J., & Bikas, D. K. (2015). Thermal bridging analysis on cladding systems for building facades. *Energy and Buildings*, *109*, 377–384. https://doi.org/10.1016/J.ENBUILD.2015.10.037

Theodosiou, T., Tsikaloudaki, K., & Bikas, D. (2017). Analysis of the Thermal Bridging Effect on Ventilated Facades. *Procedia Environmental Sciences*, *38*, 397–404. https://doi.org/10.1016/J.PROENV.2017.03.121

Theodosiou, T., Tsikaloudaki, K., Kontoleon, K., & Giarma, C. (2021). Assessing the accuracy of predictive thermal bridge heat flow methodologies. *Renewable and Sustainable Energy Reviews*, *136*, 110437. https://doi.org/10.1016/J.RSER.2020.110437

Theodosiou, T., Tsikaloudaki, K., Tsoka, S., & Chastas, P. (2019). Thermal bridging problems on advanced cladding systems and smart building facades. *Journal of Cleaner Production*, *214*, 62–69. https://doi.org/10.1016/J.JCLEPRO.2018.12.286

Thermometrics Corporation. (2012). *Thermocouple type*. https://www.thermometricscorp.com/thertypk.html

Thermo-Sensor. (2021). *Physical Principles of Temperature Measurement*. https://www.thermo-sensor.de/physical-principles.html

Tilmans, A., & Van Orshoven, D. (2010). *Software and atlases for evaluating thermal bridges*.

Touloupaki, E., & Theodosiou, T. (2017a). Energy Performance Optimization as a Generative Design Tool for Nearly Zero Energy Buildings. *Procedia Engineering*, *180*, 1178–1185. https://doi.org/10.1016/J.PROENG.2017.04.278

Touloupaki, E., & Theodosiou, T. (2017b). Optimization of External Envelope Insulation Thickness: A Parametric Study. *Energies*, *10*(3), 270. https://doi.org/10.3390/en10030270

Tudiwer, D., Teichmann, F., & Korjenic, A. (2019). Thermal bridges of living wall systems. *Energy and Buildings*, *205*. https://doi.org/10.1016/j.enbuild.2019.109522

Tye, R. P. (1977). Forced convection: Practical thermal conductivity in an insulated structure under the influence of workmanship and wind. *ASTM: Thermal Transmission Measurements of Insulation*, *660*, pp 409-425.

UK Gov. (2019). *Climate Change Act 2008 - Legislation*. *2050*(August), 108.

UK Government. (2008). *Climate Change Act 2008*.

UK Parliament. (2021). *Climate change targets: the road to net zero? - House of Lords Library*. https://lordslibrary.parliament.uk/climate-change-targets-the-road-to-net-zero/

USGBC. (2019). *LEED green building certification*. https://new.usgbc.org/leed

Viot, H., Sempey, A., Pauly, M., & Mora, L. (2015). Comparison of different methods for calculating thermal bridges: Application to wood-frame buildings. *Building and Environment*, *93*, 339–348. https://doi.org/10.1016/J.BUILDENV.2015.07.017

Walker, N. J. (2004). *Infrared Thermography Volume 1: Principles and Practice*. The British Institute of Non-Destructive Testing.

Ward, T. (2006). *IP 1/06*.

Ward, T., & Sanders, C. (2016). *BR 497 Conventions for calculating linear thermal transmittance and temperature factors*.

Whale, Dr. L. (2012). *Thermal Bridging Guide, An introductory guide to thermal bridging in homes* (Issue May).

Wilkerson, J. E. (2012). *Thermocouple Two Wire Transmitters*. https://www.wici.com/blogs/2012/06/thermocouple-two-wire-transmitters/

Wrobel, L. C., & Brebbia, C. A. (1981). A formulation of the boundary element method for axisymmetric transient heat conduction. *International Journal of Heat and Mass Transfer*, *24*(5), 843–850. https://doi.org/10.1016/S0017-9310(81)80007-5

Xu, J., Kim, J. H., Hong, H., & Koo, J. (2015). A systematic approach for energy efficient building design factors optimization. *Energy and Buildings*, *89*, 87–96. https://doi.org/10.1016/j.enbuild.2014.12.022

Zalewski, L., Lassue, S., Rousse, D., & Boukhalfa, K. (2010). Experimental and numerical characterization of thermal bridges in prefabricated building walls. *Energy Conversion and Management*, *51*(12), 2869–2877. https://doi.org/10.1016/j.enconman.2010.06.026

Zero Carbon Hub. (2013). Closing the gap between design and as-built performance. In *(BRE) British Research Establishment* (Issue July). https://doi.org/10.1136/bmj.a1770

Zou, P. X. W., Wagle, D., & Alam, M. (2019). Strategies for minimizing building energy performance gaps between the design intend and the reality. *Energy and Buildings*, *191*, 31–41. https://doi.org/10.1016/j.enbuild.2019.03.013